

EDITORS' SHOWCASE: CHEMICAL BIOLOGY

EDITED BY: John D. Wade
PUBLISHED IN: Frontiers in Chemistry





frontiers

Frontiers eBook Copyright Statement

The copyright in the text of individual articles in this eBook is the property of their respective authors or their respective institutions or funders. The copyright in graphics and images within each article may be subject to copyright of other parties. In both cases this is subject to a license granted to Frontiers.

The compilation of articles constituting this eBook is the property of Frontiers.

Each article within this eBook, and the eBook itself, are published under the most recent version of the Creative Commons CC-BY licence.

The version current at the date of publication of this eBook is CC-BY 4.0. If the CC-BY licence is updated, the licence granted by Frontiers is automatically updated to the new version.

When exercising any right under the CC-BY licence, Frontiers must be attributed as the original publisher of the article or eBook, as applicable.

Authors have the responsibility of ensuring that any graphics or other materials which are the property of others may be included in the CC-BY licence, but this should be checked before relying on the CC-BY licence to reproduce those materials. Any copyright notices relating to those materials must be complied with.

Copyright and source acknowledgement notices may not be removed and must be displayed in any copy, derivative work or partial copy which includes the elements in question.

All copyright, and all rights therein, are protected by national and international copyright laws. The above represents a summary only. For further information please read Frontiers' Conditions for Website Use and Copyright Statement, and the applicable CC-BY licence.

ISSN 1664-8714

ISBN 978-2-83250-064-4

DOI 10.3389/978-2-83250-064-4

About Frontiers

Frontiers is more than just an open-access publisher of scholarly articles: it is a pioneering approach to the world of academia, radically improving the way scholarly research is managed. The grand vision of Frontiers is a world where all people have an equal opportunity to seek, share and generate knowledge. Frontiers provides immediate and permanent online open access to all its publications, but this alone is not enough to realize our grand goals.

Frontiers Journal Series

The Frontiers Journal Series is a multi-tier and interdisciplinary set of open-access, online journals, promising a paradigm shift from the current review, selection and dissemination processes in academic publishing. All Frontiers journals are driven by researchers for researchers; therefore, they constitute a service to the scholarly community. At the same time, the Frontiers Journal Series operates on a revolutionary invention, the tiered publishing system, initially addressing specific communities of scholars, and gradually climbing up to broader public understanding, thus serving the interests of the lay society, too.

Dedication to Quality

Each Frontiers article is a landmark of the highest quality, thanks to genuinely collaborative interactions between authors and review editors, who include some of the world's best academicians. Research must be certified by peers before entering a stream of knowledge that may eventually reach the public - and shape society; therefore, Frontiers only applies the most rigorous and unbiased reviews.

Frontiers revolutionizes research publishing by freely delivering the most outstanding research, evaluated with no bias from both the academic and social point of view. By applying the most advanced information technologies, Frontiers is catapulting scholarly publishing into a new generation.

What are Frontiers Research Topics?

Frontiers Research Topics are very popular trademarks of the Frontiers Journals Series: they are collections of at least ten articles, all centered on a particular subject. With their unique mix of varied contributions from Original Research to Review Articles, Frontiers Research Topics unify the most influential researchers, the latest key findings and historical advances in a hot research area! Find out more on how to host your own Frontiers Research Topic or contribute to one as an author by contacting the Frontiers Editorial Office: frontiersin.org/about/contact

EDITORS' SHOWCASE: CHEMICAL BIOLOGY

Topic Editor:

John D. Wade, University of Melbourne, Australia

Citation: Wade, J. D., ed. (2022). Editors' Showcase: Chemical Biology.

Lausanne: Frontiers Media SA. doi: 10.3389/978-2-83250-064-4

Table of Contents

- 05 Editorial: Editors' Showcase: Chemical Biology**
John D. Wade
- 08 The Potential of Modified and Multimeric Antimicrobial Peptide Materials as Superbug Killers**
Tamara Matthyssen, Wenyi Li, James A. Holden, Jason C. Lenzo, Sara Hadjigol and Neil M. O'Brien-Simpson
- 31 Functional Effects of ARV-1502 Analogs Against Bacterial Hsp70 and Implications for Antimicrobial Activity**
Alexandra Brakel, Lisa Kolano, Carl N. Kraus, Laszlo Otvos Jr and Ralf Hoffmann
- 44 Recent Progress of Exosome Isolation and Peptide Recognition-Guided Strategies for Exosome Research**
Kun Xu, Yulong Jin, Yongming Li, Yanyan Huang and Rui Zhao
- 56 Post-Translational Modifications of G Protein–Coupled Receptors Revealed by Proteomics and Structural Biology**
Bingjie Zhang, Shanshan Li and Wenqing Shui
- 65 Label-Free Target Identification Reveals the Anticancer Mechanism of a Rhenium Isonitrile Complex**
Junhyeong Yim and Seung Bum Park
- 76 An Efficient Approach for the Design and Synthesis of Antimicrobial Peptide–Peptide Nucleic Acid Conjugates**
Nitin A. Patil, Varsha J. Thombare, Rong Li, Xiaoji He, Jing Lu, Heidi H. Yu, Hasini Wickremasinghe, Kavya Pamulapati, Mohammad A. K. Azad, Tony Velkov, Kade D. Roberts and Jian Li
- 86 Mucin-Type O-Glycosylation Proximal to β -Secretase Cleavage Site Affects APP Processing and Aggregation Fate**
YashoNandini Singh, Deepika Regmi, David Ormaza, Ramya Ayyalasomayajula, Nancy Vela, Gustavo Mundim, Deguo Du, Dmitriy Minond and Maré Cudic
- 99 The Cytochrome P450 OxyA from the Kistamicin Biosynthesis Cyclization Cascade is Highly Sensitive to Oxidative Damage**
Anja Greule, Thierry Izoré, Daniel Machell, Mathias H. Hansen, Melanie Schoppet, James J. De Voss, Louise K. Charkoudian, Ralf B. Schittenhelm, Jeffrey R. Harmer and Max J. Cryle
- 117 Signaling Pathway and Small-Molecule Drug Discovery of FGFR: A Comprehensive Review**
Jia Zheng, Wei Zhang, Linfeng Li, Yi He, Yue Wei, Yongjun Dang, Shenyong Nie and Zufeng Guo
- 141 3D Single Molecule Super-Resolution Microscopy of Whole Nuclear Lamina**
Ashley M. Rozario, Alison Morey, Cade Elliott, Brendan Russ, Donna R. Whelan, Stephen J. Turner and Toby D. M. Bell

152 Approaches to Improve the Quantitation of Oxytocin in Human Serum by Mass Spectrometry

Anke Hering, Beverly Jieu, Alun Jones and Markus Muttenthaler

163 Role of Helical Structure in MBP Immunodominant Peptides for Efficient IgM Antibody Recognition in Multiple Sclerosis

Agnieszka Staśkiewicz, Michael Quagliata, Feliciano Real-Fernandez, Francesca Nuti, Roberta Lanzillo, Vincenzo Brescia-Morra, Hendrik Rusche, Michal Jewginski, Alfonso Carotenuto, Diego Brancaccio, Rina Aharoni, Ruth Arnon, Paolo Rovero, Rafal Latajka and Anna Maria Papini



OPEN ACCESS

EDITED AND REVIEWED BY

Qingfei Zheng,
The Ohio State University, United States

*CORRESPONDENCE

John D. Wade,
john.wade@florey.edu.au

SPECIALTY SECTION

This article was submitted to Chemical Biology, a section of the journal Frontiers in Chemistry

RECEIVED 27 July 2022

ACCEPTED 28 July 2022

PUBLISHED 15 August 2022

CITATION

Wade JD (2022), Editorial: Editors' showcase: Chemical biology.
Front. Chem. 10:1004363.
doi: 10.3389/fchem.2022.1004363

COPYRIGHT

© 2022 Wade. This is an open-access article distributed under the terms of the [Creative Commons Attribution License \(CC BY\)](#). The use, distribution or reproduction in other forums is permitted, provided the original author(s) and the copyright owner(s) are credited and that the original publication in this journal is cited, in accordance with accepted academic practice. No use, distribution or reproduction is permitted which does not comply with these terms.

Editorial: Editors' showcase: Chemical biology

John D. Wade^{1,2*}

¹Florey Institute of Neuroscience and Mental Health, University of Melbourne, Melbourne, VIC, Australia, ²School of Chemistry, University of Melbourne, Melbourne, VIC, Australia

KEYWORDS

antimicrobial peptides, chemical biology, DnaK, exosomes, GPCRs, LC-MS, peptides, small molecule inhibitors

Editorial on the Research Topic

Editor's showcase: Chemical biology

Today, chemical biology is a mature and widely recognized scientific discipline that seeks to translate knowledge of the structural and chemical basis of biology to better regulate or modulate biological processes. This can be achieved by a myriad of ways ranging from chemical synthesis, recombinant DNA production, biomolecular conjugation, selective detection, organic chemistry, structural and conformational analyses to affinity chromatography and proteomics. This array of resources and tools available to the chemical biologist today can enable even the most complex of biomolecular interactions and pathways be studied and manipulated with incredible sensitivity and control.

In this special Research Topic, twelve leading international exponents of chemical biology together with their teams present their latest results across a wide spectrum of research. These highlight the importance of novel methods and technology together with the development of novel chemical compounds, be they small organic molecules, peptides, proteins, nucleic acids, lipids, glycans or hybrid molecules to better understand the chemical basis of biology and to use this knowledge for the preparation of more selective and potent mediators of biological function. The first of these by [Matthyssen et al.](#) examine the influence of multimerization (dimers, oligomer conjugates, dendrimers, polymers and self-assembly) of antimicrobial peptides (AMPs) on their potency and bacterial selectivity. Of particular importance is the role of such modifications against bacteria that are responsible for the production of antibiotic-resistant biofilms which remain the most difficult to prevent or treat.

AMP drug design and development is also the focus of the second contribution to this Research Topic. Here, [Brakel et al.](#) focus on the systematic structure-activity relationship study of the short proline-rich analogue ARV-1502 to determine the features that dictate binding to and inhibition of the bacterial chaperone DnaK. More than 180 synthetic analogues were prepared by chemical synthesis and assayed for activity against *E. coli* and *S. aureus*. Interestingly, those analogues that possessed increased inhibition of the DnaK chaperone system did not necessarily have increased antimicrobial activity which highlights the challenges associated with designing novel peptide-based antibiotics.

An alternative approach to the development of antibacterial agents is provided by Patil et al.. They describe the design and synthesis of AMP-peptide nucleic acid (PNA) conjugates as a means of targeting essential bacterial genes. Such antisense antimicrobials possess multimodal activity which is likely to confound the onset of antimicrobial resistance. Elegant organic chemical approaches to the conjugation for the chemically disparate AMP and PNA are investigated and used to develop conjugates that specifically target the acyl carrier protein gene of the Gram-negative bacteria *A. baumannii*. A cysteine-based click chemical method was shown to be most effective leading the way to the ready production of such compounds for antimicrobial drug development.

G protein coupled receptors (GPCRs), seven-transmembrane proteins, make up the largest family of cell surface receptors in mammalian cells and thus represent important drug targets with over 30% of FDA approved therapeutics. While there is good knowledge of the structural features that regulate GPCR action, comparatively much less is known about the role of post-translational modifications (PTMs) on receptor function. The manuscript by Zhang et al. describes the use of powerful mass spectrometry-based proteomics for profiling PTMs. The results shed important light on the role that PTMs play in increasing the functional diversity of GPCR regulation leading to new opportunities for selective GPCR-targeted drug development.

Xu et al. report in their manuscript the utility of modern and highly specific affinity capture strategies based upon molecular recognition for the isolation of exosomes, membrane extracellular vesicles that are secreted by all eukaryotic cells and which play critical roles in biological processes including cell-to-cell communication, immune response, and cell growth. The most common methods each have limitations which are described in detail, and which dictate careful consideration for use in specific applications. The ability to automate these methods currently remains beyond reach but is an attractive goal for the future.

The development of novel anticancer agents remains a subject of considerable research effort. Platinum-based drugs are of notable interest given their selectivity and site of action on DNA rather than proteins. Despite their effectiveness, non-selective cytotoxic effects and resistance development has motivated the development of new drugs. Rhenium based compounds were subsequently shown to possess potent anticancer activity with tricarbonyl rhenium isonitrile polypyridyl (TRIP) complex being notably effective. Yim and Park report the use of a label-free process, inductively coupled plasma mass spectrometry (ICP-MS), to conclusively demonstrate that TRIP acts on a protein, HSP60, and not DNA, to inhibit its chaperone function leading to cancer-specific cell death. The study highlights the importance of such tools for determining the molecular basis of metal-based drugs.

Post-translational modifications (PTMs) of peptides and proteins is a critical cellular process that adds significant structural and functional diversity. Glycosylation is arguably the most common PTM but is highly complex and generally leads to heterogeneous glycan structures that are challenging to discriminate and characterize. The manuscript by Singh et al. reports the use of chemical synthesis of O-GalNac peptides to examine the influence of O-glycosylation on amyloid- β precursor protein (APP) proteolysis by β - and γ -secretases to produce amyloid- β peptides and possible subsequent Alzheimer's disease pathology. The use of defined glycans obviates issues associated with typical glycosylation PTMs and enabled the authors to show that O-glycosylation can render APP model glycopeptides more susceptible to cleavage by β -secretase thus contributing to knowledge regarding the role of this PTM on amyloid- β aggregation.

The mammalian fibroblast growth factors (FGFs) are a family of 23 proteins that regulate a variety of cellular processes following interaction with one or more of 5 transmembrane receptor kinases (RTKs) known as fibroblast growth factor receptors (FGFRs). Abnormal FGF/FGFR interaction and signaling is frequently associated with tumor development including breast cancer and lung cancer. Consequently, the development of small molecule FGFR inhibitors has been an area of substantial research in the past 2 decades. The review by Zheng et al. provides an excellent survey of the early efforts to construct FGFR-targeting small molecules leading to subsequent *de novo* design of next-generation compounds with improved selectivity and potency. The roles of computer-aided design and, increasingly, artificial intelligence to expand the chemical space of potential inhibitors is discussed. Finally, the development and use of alternatives to small molecule inhibitors are described, notably PROTAC and molecular glues, and highlight the continuing importance of medicinal chemistry in oncology research.

One of the most important tools in chemical biology research is fluorescence microscopy in which a range of fluorophore labels are used to permit specific visualization of cellular structures and dynamics. Rozario et al. together with their colleagues report the development of improved single molecule (SM) super-resolution microscopy to undertake a remarkably detailed examination of the nuclear lamina of cultured COS-7 and T cells in 3D. The authors described the use of SM imaging using optical astigmatism together with multiplane acquisition and the photoswitchable fluorophore AlexFluor 647 to enable super-resolution discrimination of the entire nuclear lamina morphology leading to quantification of overall nuclear dimensions and local membrane features.

Greule et al. describe the use of combination of approaches including chemical synthesis, structural biology, biochemistry, enzymatic catalysis and protein engineering to examine the structure and function of the monooxygenase, cytochrome P450 OxyA from kistamycin. The enzyme plays a significant

role in the cellular glycopeptide antibiotic biosynthesis. It was revealed that the precise heme orientation is crucial to enzyme function which, in turn, highlights the great potential of P450s for use as biocatalysts to perform synthetically challenging transformations both *in vitro* and *in vivo* and to produce new medically important bioactive compounds.

Demyelination is a hallmark of multiple sclerosis (MS) although numerous debates continue as to its cause. It is generally agreed that a T-cell mediated inflammatory process directed against myelin is a critical contributory event. Myelin basic protein (MBP) is a major component of the myelin sheath and is thought to be a target by antibodies which may lead to the pathogenicity observed in MS. To contribute to a better understanding of the possible role of MBP in the immune response, [Staśkiewicz et al.](#) undertook to chemically assemble several peptide fragments of MBP and to measure their association with IgM antibodies derived from MS patient sera and to correlate the findings with the helical conformation of the peptides. They showed that such synthetic antigenic probes can be valuable tools for discriminating between different ELISAs and subsequent further understanding of the role of MBP in MS.

The role of peptide hormones in health and disease requires sophisticated and sensitive detection and quantification methods which has typically been afforded by immunoassay. The necessity for increased sensitivity has led to the development of mass spectrometry methods although the reproducibility and reliability of these have yet to enable their ready utility. The manuscript by [Hering et al.](#) report a systematic evaluation of sample preparation as a critical component of peptide quantification using tandem triple quadrupole mass spectrometer together with peptide modification with a quaternary pyridinium ion. Such approaches enabled a substantial improvement in quantifying serum oxytocin levels which in turn will aid research into the role of this hormone in psychiatric disease.

Together this collection of contributions highlights the continuing and powerful role chemical biology makes in our understanding of complex cellular processes and in the development of novel tools, diagnostics and therapeutics. It is

hoped that the reader will enjoy and appreciate this Research Topic.

Author contributions

The author confirms being the sole contributor of this work and has approved it for publication.

Funding

JW thanks the National Health and Medical Research Council (NHMRC) of Australia for an Idea research grant (APP2010781).

Acknowledgments

The editor thanks all the contributing authors for their considerable efforts in producing the enclosed articles.

Conflict of interest

The author declares that the research was conducted in the absence of any commercial or financial relationships that could be construed as a potential conflict of interest.

Publisher's note

All claims expressed in this article are solely those of the authors and do not necessarily represent those of their affiliated organizations, or those of the publisher, the editors and the reviewers. Any product that may be evaluated in this article, or claim that may be made by its manufacturer, is not guaranteed or endorsed by the publisher.



The Potential of Modified and Multimeric Antimicrobial Peptide Materials as Superbug Killers

Tamara Matthyssen¹, Wenyi Li¹, James A. Holden², Jason C. Lenzo², Sara Hadjigol¹ and Neil M. O'Brien-Simpson^{1*}

¹ACTV Research Group, The University of Melbourne, Melbourne Dental School, Centre for Oral Health Research, Royal Dental Hospital, Melbourne, VIC, Australia, ²Centre for Oral Health Research, The University of Melbourne, Melbourne Dental School, Royal Dental Hospital, Melbourne, VIC, Australia

OPEN ACCESS

Edited by:

Laszlo Otvos,
Olpe LLC, United States

Reviewed by:

Suzana Katarina Straus,
University of British Columbia, Canada
Annelise Emily Barron,
Stanford University, United States

*Correspondence:

Neil M. O'Brien-Simpson
neil.obs@unimelb.edu.au

Specialty section:

This article was submitted to
Chemical Biology,
a section of the journal
Frontiers in Chemistry

Received: 15 October 2021

Accepted: 24 November 2021

Published: 10 January 2022

Citation:

Matthyssen T, Li W, Holden JA,
Lenzo JC, Hadjigol S and
O'Brien-Simpson NM (2022) The
Potential of Modified and Multimeric
Antimicrobial Peptide Materials as
Superbug Killers.
Front. Chem. 9:795433.
doi: 10.3389/fchem.2021.795433

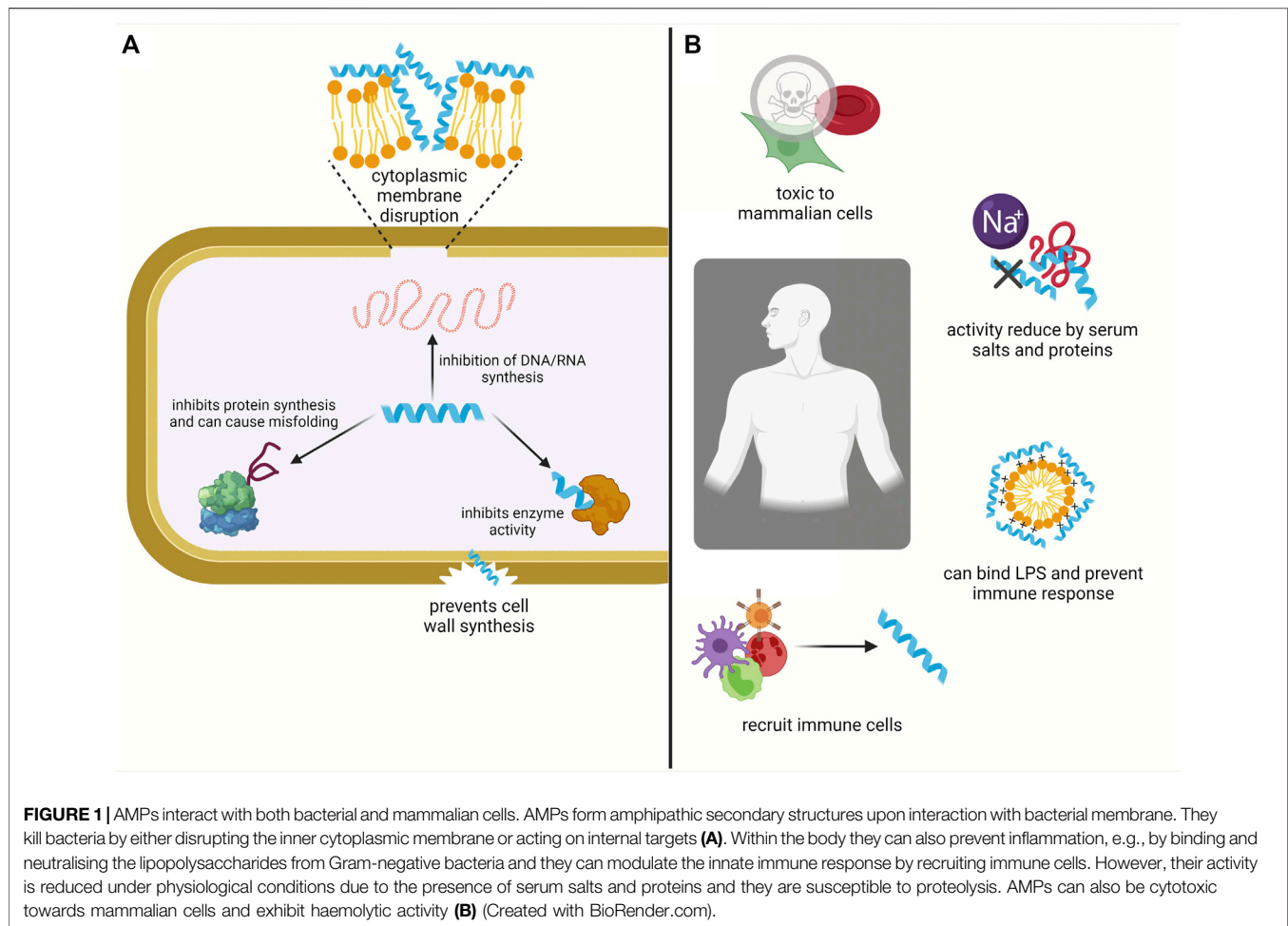
Antimicrobial peptides (AMPs) are found in nearly all living organisms, show broad spectrum antibacterial activity, and can modulate the immune system. Furthermore, they have a very low level of resistance induction in bacteria, which makes them an ideal target for drug development and for targeting multi-drug resistant bacteria 'Superbugs'. Despite this promise, AMP therapeutic use is hampered as typically they are toxic to mammalian cells, less active under physiological conditions and are susceptible to proteolytic degradation. Research has focused on addressing these limitations by modifying natural AMP sequences by including e.g., D-amino acids and N-terminal and amino acid side chain modifications to alter structure, hydrophobicity, amphipathicity, and charge of the AMP to improve antimicrobial activity and specificity and at the same time reduce mammalian cell toxicity. Recently, multimerisation (dimers, oligomer conjugates, dendrimers, polymers and self-assembly) of natural and modified AMPs has further been used to address these limitations and has created compounds that have improved activity and biocompatibility compared to their linear counterparts. This review investigates how modifying and multimerising AMPs impacts their activity against bacteria in planktonic and biofilm states of growth.

Keywords: antimicrobials1, peptides2, multimerisation3, superbugs4, AMPs5

INTRODUCTION

As drug resistant bacterial infections increase globally, the age of antibiotics is reported to be coming to an end (O'Neill, 2016). Antibiotics are crucial to modern healthcare as they are used not only for treating bacterial infections, but for making important medical procedures and treatments requiring immune suppression possible (Interagency Coordination Group on Antimicrobial Resistance, 2019). The World Health Organisation (WHO) estimates that, globally, over 700,000 deaths per year are due to drug resistant diseases, with this number predicted to rise to 10 million deaths by 2050 if nothing is done to change the current situation (O'Neill, 2016). The need for alternative antibacterial therapeutics that are less likely to induce antimicrobial resistance are therefore needed more than ever.

A promising avenue of research stems from naturally occurring antimicrobial peptides (AMPs) that have a broad spectrum of activity (Zasloff, 2002). AMPs are found in all living organisms and are also referred to as host defense peptides, or defensins (Campopiano et al., 2004; Qian et al., 2018; Zasloff, 2002). AMPs have been shown to directly kill bacteria by disrupting the cellular membrane



or acting on intracellular targets. They can also modulate the body's inflammatory and innate immune response, recruiting immune cells to promote wound healing or angiogenesis (**Figure 1**) (Dong et al., 2018; Hancock and Sahl, 2006; Afacan et al., 2012; Zasloff, 2002).

AMPs have demonstrated strong antimicrobial activity both *in vitro* and *in vivo* and are of special interest as they do not readily induce antimicrobial resistance (Zasloff, 2002). According to the Antimicrobial Peptide database (APD3), at least 3,000 active natural AMPs have been discovered in various organisms (Wang G. et al., 2016). Despite the large number of known natural AMPs, their clinical application has been constrained by their various limitations. These limitations include cytotoxicity, susceptibility to protease degradation and a short *in vivo* half-life (Hancock and Sahl, 2006). Various studies have revealed that certain amino acids are more prevalent than others among AMPs and that charge, hydrophobicity, and overall structure affect the level of antimicrobial activity (Kumar et al., 2018). Manipulating these inherent properties of AMPs has helped overcome some of their limitations. It has also been demonstrated that multimerisation of AMPs is another technique that can improve their activity and biocompatibility to help overcome issues of cytotoxicity and stability (Giuliani and Rinaldi, 2011;

Sobczak et al., 2013; Ortega et al., 2020). This review provides a summary of some of the modifications made to AMPs that increase their activity and aims to highlight their effects on AMP structure. The review also explores different multimerisation strategies and the features of multimerised compounds that affect activity and biocompatibility.

PROPERTIES AND LIMITATIONS OF ANTIMICROBIAL PEPTIDES

General Properties

AMPs show antimicrobial activity towards both Gram-negative and Gram-positive bacteria, parasites, fungi and some viruses (Gordon et al., 2005). Natural AMPs can vary greatly in length, from 2 to >200 amino acids in length. However, the majority are 10–50 amino acid residues in length, at least 30% of their residues are hydrophobic, have an overall positive charge and form amphipathic secondary structures of α -helices, β -sheets, looped peptides or extended structures upon interaction with a lipid membrane (Hancock and Sahl, 2006; Nguyen et al., 2011; Takahashi et al., 2013; Wang J. et al., 2016). Modifying AMP size, sequence, net charge, conformation, structure,

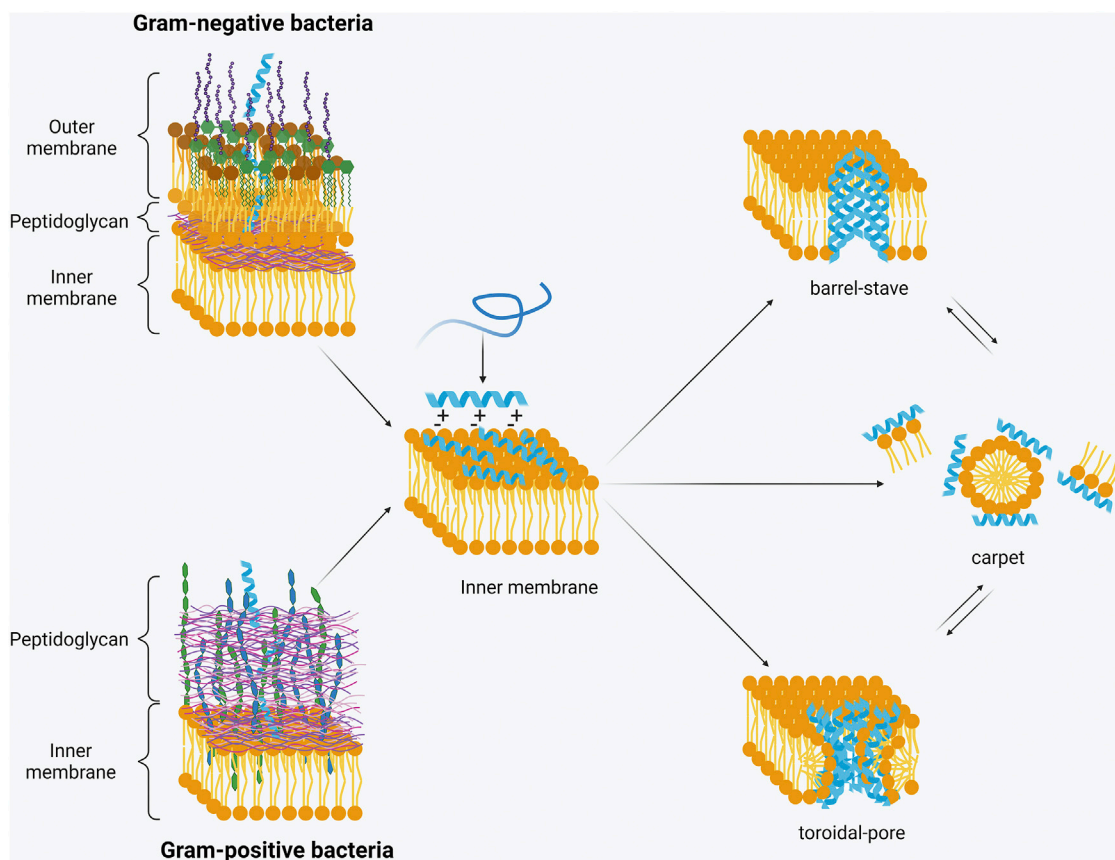


FIGURE 2 | Permeabilisation of the inner membrane. Upon interaction with the negatively charged bacterial membrane AMPs form a secondary structure. Once a threshold concentration has been reached, they insert into the membrane with three models being the most widely accepted – barrel-stave, toroidal pore or carpet model (Created with BioRender.com).

hydrophobicity and amphipathicity can all affect AMP antimicrobial activity and specificity for certain cell types (Hong, 2001; Dennison et al., 2005; Gagnon et al., 2017; Chen W. et al., 2019).

Mode of Action

The overall positive net charge of AMPs attracts them to the negatively charged surface of bacteria where they interact and transit through either the outer-membrane or peptidoglycan layers of Gram-negative or Gram-positive bacteria, respectively, and then embed in to the inner/cytoplasmic membrane. Once a certain threshold concentration of AMPs is reached at the inner membrane, AMPs insert themselves into the membrane through hydrophobic and electrostatic interactions (Hale and Hancock, 2007). These membrane-active AMPs are believed to form pores in the inner membrane, with two popular modes of action having been proposed – toroidal-pore and barrel-stave (Figure 2) (Avci et al., 2018). In the barrel-stave model, peptides interact to form a structure within the membrane to create a channel similar to that of a membrane protein ion channel. In the toroidal pore model, however, there is little to no peptide-peptide interaction. Rather, the peptides affect the curve of the lipid bilayer by interacting with the lipid hydrocarbons and

headgroups to disrupt the separation of the polar and non-polar parts (Wimley, 2010).

It is also proposed that some AMPs permeabilise the membrane through non-pore forming models, such as the carpet model (Figure 2). This model suggests that the peptides cover the bacterial membrane surface and then reorient themselves, so that the hydrophobic face is towards the lipids, and the hydrophilic part faces the phospholipid head group. The peptides then cause the membrane to disintegrate by disrupting the bilayer curvature (Shai, 2002). Membrane disruption is the predominant mode of action for many AMPs. However, it is not always essential for activity. Some AMPs translocate across the membrane and act on internal targets. For example, human β -defensin 3 (hBD3) binds lipid II and inhibits cell wall synthesis, resulting in bacterial death (Sass et al., 2010). On the other hand, proline-rich AMPs, such as pyrrolicorin, can inhibit DnaK or bind to the 70S ribosome. This respectively leads to protein misfolding or inhibition of protein translation and, in both cases, to cell death (Kragol et al., 2001; Krizsan et al., 2014). The definition and mode of action of proline-rich AMPs has been recently reviewed by Welch et al. (2020). AMPs have also been shown to cause aggregation of anionic intracellular molecules such as DNA and ribosomes (Chongsiriwatana et al., 2017; Zhu

Y. et al., 2019). It is proposed that flocculation of these molecules can lead to inhibition of growth or cell death and is an important mechanism representative of the breadth of AMP activity. Other internal/cytosolic mechanisms of action are inhibition of DNA/RNA synthesis (butorin II), protein synthesis (pleurocidin), cell division (indolicidin), and enzymes (histatin 5) (Park et al., 1998; Subbalakshmi, 1998; Gusman et al., 2001; Patrzykat et al., 2002).

Effect of Structure, Hydrophobicity, Amphipathicity and Charge on Antimicrobial Peptide Activity and Selectivity

Antimicrobial Peptide Structure

Modification of certain predominant features of AMPs (amino acid length, hydrophobicity, charge and amphipathicity) can lead to changes in their activity. An *in-silico* study of 100,000 9-mer peptides also indicated that AMP structure impacts its antimicrobial activity (Cherkasov et al., 2009). From this virtual library, 200 peptides were tested *in vitro* against *Pseudomonas aeruginosa*. Interestingly, this showed that peptides with very similar hydrophobicity, amphipathicity and charge, had varying antibacterial activity towards *P. aeruginosa*. The two lead compounds KRWWKWIRW and KRWWKWRRR had high antibacterial activity whereas AIRRWIRK and WVRVYRYW were virtually inactive while being considered to have similar amino acid composition to the lead compounds by the authors. It was suggested that the order of amino acids within the sequence affects antimicrobial activity and that this change in activity is likely due to the different final structures formed by these peptides. Unfortunately, the study did not determine the structure of these compounds, so it is unclear whether the increased activity was due to the final structures formed or due to other aspects such as overall charge and hydrophobicity. As many naturally occurring AMPs form α -helices or β -sheets and these structures have different impacts on AMP activity, the conclusion that the order of the amino acid sequence would affect this is not surprising. Non-covalent interactions between residues within a sequence determine what secondary structures can be formed. As such, disrupting or changing a specific sequence can alter their possible interactions, and hence formation of an α -helix or β -sheet.

The largest and most well studied group of AMPs are those that form α -helices and many β -sheet AMPs have been discovered in animals and plants (Hancock and Lehrer, 1998; Koebach and Craik, 2019). Both α -helical and β -sheet AMPs are believed to exert their activity via membrane disruption but have been shown to have differing specificities. In general, the propensity to form an α -helix results in more potent activity whilst many β -sheet peptides are stabilised by disulfide bonds and their activity correlated to their amphipathicity. For example, two peptides derived from PGLa (all peptide sequences found in **Supplementary Appendix A**) shared similar hydrophobicity and the same charge but differed in their secondary structure (Blazyk et al., 2001; Jin et al., 2005). One adopted an α -helix ((KIAGKIA)₃-NH₂) whilst the other formed a β -sheet ((KIGAKI)₃-NH₂). Both these peptides had similar

antibacterial activity, however the β -sheet was not haemolytic and the α -helical structure better at inducing leakage in *E. coli* cells. This similarity in antibacterial activity but difference in haemolytic activity and membrane leakage indicate differences in the mode of action of these two structures.

The comparison of a number of β -sheet peptides, revealed a correlation between their amphipathicity and activity as well as a conserved C-terminal cysteine (Edwards et al., 2016). The most amphipathic compounds were tachyplesin-1 and protegrin-1, closely followed by arenicin-3 and polyphemusin-1 with gomesin and thanatin the least amphipathic. Overall, the more amphipathic compounds exhibited better activity towards both Gram-negative and Gram-positive bacteria (e.g., MIC range of 0.016–0.25 μ g/ml for tachyplesin-1 compared to 2–256 μ g/ml for thanatin). The role of the conserved C-terminal cysteine found in these AMPs was not explored in this study but another study that deleted the cysteines that formed the first disulfide bond of an arenicin-3 analogue and named N6 found that it did not significantly impact its antimicrobial activity (Yang et al., 2017). β -sheets are often stabilised by disulfide bonds which offers such AMPs better proteolytic stability (Koebach and Craik, 2019). The role of the conserved cysteine found in the aforementioned AMPs may hence be limited to overall peptide stability. To further understanding of AMP activity, a comparative study of the proteolytic stability of α - and β -structures that have similar hydrophobicity, charge, and amino acid sequence to determine whether β -sheet-containing peptides have more to offer than reduced haemolytic activity, is needed. Additionally, comparison of whether the number of β -turns within a compound affect its activity could be of interest to rational AMP design and optimisation.

The role of helicity and its correlation with AMP antibacterial activity has been explored by replacing one or more of the residues of an helical peptide derived from CP2600 (peptide *p*) with their D-amino acid counterparts (Huang et al., 2014). This resulted in analogues with decreased helicity but varying antimicrobial activity. Substituting 1, 2 or 3 residues with their D-amino equivalents not only increased antimicrobial activity towards the Gram-negative *E. coli* and *P. aeruginosa* bacteria compared to the parent peptide, but also reduced their haemolytic activity. However, substituting 4 or more residues resulted in a decrease in antimicrobial activity. When tested against the Gram-positive bacteria *S. aureus*, it was only substitution of K14 that showed improved antimicrobial activity, all other analogues showed similar or decreased activity. However, against Gram-positive *Bacillus subtilis*, substituting 1, 2, 3 or 4 residues with D-amino acids resulted in analogues with improved antimicrobial activity. Scanning electron microscopy (SEM) images of *P. aeruginosa* and *S. aureus* treated with the lead analogue (L12_D/L20_D) indicated that the peptide interacted with and damaged the bacterial cell membrane. As L12_D/L20_D appears to exert its activity on the cell membrane, the difference in activity between the two Gram-positive strains may be due to differences in their membrane composition. According to a review on cell membrane composition by Sohlenkamp and Geiger, the major membrane lipids in *S. aureus* are phosphatidylglycerol (PG), cardiolipin (CL), lysyl-phosphatidylglycerol (LPG) and

glycophospholipid (GPL) (Sohlenkamp and Geiger, 2015). In addition to these membrane lipids, *B. subtilis* also contains phosphatidylethanolamine (PE) and glycolipid (GL). According to this review *E. coli* and *P. aeruginosa* membranes also contain pE. AMPs may interact with specific membrane lipids in specific ways which may account for their varying specificity for different bacteria. An exploration of bacterial membrane composition and susceptibility to AMPs could help in AMP design and specific targeting but is outside the scope of this review. In general, amongst the analogues, decreasing helicity resulted in weaker antimicrobial activity. However, analogues with 1, 2 or 3 D-amino substitutions and reduced helicity exhibited improved activity compared to the parent peptide which was the most helical. In addition to improved activity, the aforementioned D-amino substituted analogues also exhibited lower haemolytic activity than the parent peptide which resulted in all of the analogues having higher therapeutic indices. Substitution with D-amino acid residues also affected the overall hydrophobicity of these peptides. A decrease in hydrophobicity was seen to be correlated with an increase in the number of D-amino substitution in this series of analogues which may account for the observed decrease in haemolytic activity. Peptides with multiple D-amino substitutions and hence lower helicity were the least haemolytic, indicating that the degree of helicity also contributed to toxicity.

More recently, the role of helicity was further explored using peptoid 1, a peptoid (residues with the side-chain moiety connected to the backbone nitrogen rather than the α -carbon of the amino acid) mimic of magainin 2 (Patch and Barron, 2003). This peptoid was made using N-(4-aminobutyl)-glycine (NLys), a peptoid analogue of lysine (Lys (K)), and (S)-N-(1-phenylethyl) amine (Nspe), an analogue of phenylalanine (Phe (F)) that acts as a helix inducer (Nam et al., 2020). Peptoid 1 was reported to be fully helical and a non-helical peptoid 2 was also created by substituting all Nspe with N-(phenylmethyl)glycine (Npm). A series of 17 peptoids were also made by substituting 1 or more Nspe at different positions with Npm and these peptoids exhibited varying degrees of helicity but similar hydrophobicity to peptoids 1 and 2. The fully helical peptoid 1 was the most potent but also displayed strong haemolytic activity whilst peptoid 2 was the least active and the least haemolytic. The antimicrobial activity and toxicity of all other moderately helical peptoids fell within a range between peptoid 1 and 2 but there was no explicit correlation between helicity and activity determined by the authors. However, of interest was the degree to which helices were formed in different environments. The degree of helical fold of peptoids 1, 16 and 17 were compared using circular dichroism (CD) spectroscopy in three different environments: aqueous buffer, lipid vesicles mimicking *E. coli* membranes and vesicles mimicking erythrocyte membranes. Both peptoid 16 and 17 had 4 Nspe substituted with Npm but at different positions. Peptoid 16 had substitutions at the C- and N-terminus whereas peptoid 17 had substitution in the middle which was shown to affect the flexibility of these peptoids. Peptoids 1 and 16 displayed strong and weak CD intensity, respectively, which did not vary between different environments. Peptoid 17, however, which showed a weaker degree of helicity than peptoid 16 in aqueous

buffer exhibited a much greater degree of helicity in the bacterial membrane mimic environment. A comparison of their MICs showed that against *E. coli*, peptoid 1 was the most potent (3.1 μ M) followed by peptoid 17 (6.3 μ M) with peptoid 16 the weakest (12.5 μ M). Peptoids 16 and 17 were also much less haemolytic than peptoid 1 with peptoid 17 having the greatest selectivity index (calculated as HC_{10}/MIC in *E. coli*). The flexibility of peptoid 17 was considered to be the reason for its selectivity towards the bacterial membrane. Such conformational flexibility can also be found in nature and the ability of this feature to improve AMP activity and selectivity has been more thoroughly explored in several papers (Juretić and Simunić, 2019; Liu et al., 2013; Rončević et al., 2018). Whilst the degree of helicity is important for AMP activity, the environment in which the AMP forms this structure, and its flexibility should be considered as equally important for AMP design.

Hydrophobicity

An earlier study on a variant of CP2600 explored how single amino acid substitution of this peptide could alter hydrophobicity and subsequently, activity. The variant was created via DNA mutagenesis and named V₆₈₁ (Zhang et al., 1998). Valine (Val) 13 of this peptide was then substituted with lysine (V13KL) and was shown to have good antimicrobial activity and a higher therapeutic index (TI) (Chen et al., 2005). Val 16 of V13KL was then substituted with various amino acids and it was found that a single amino acid substitution could greatly alter the peptide's overall hydrophobicity. The analogue V16L (Val 16 of V13KL substituted with Leucine (Leu)), was the most hydrophobic as shown by its increased retention time when analysed using RP-HPLC. This resulted in V16L being slightly more active than V13KL but it was also considerably more haemolytic, causing 53.9% haemolysis compared to 28.3%, respectively (Tan et al., 2014). Substitution with less hydrophobic amino acids and at hydrophobic positions other than Val 16 may result in analogues with reduced haemolysis. In this same study, V16A (substitution with Alanine (Ala)) was less hydrophobic than V13KL, had the same MIC towards a clinical isolate of *E. coli* and *P. aeruginosa* ATC2853 but was less haemolytic. It caused only 14.3% haemolysis. This shows that the issues of cytotoxicity may be addressed by using different hydrophobic amino acids to maintain amphipathicity of an AMP but reduce the overall hydrophobicity.

This concept of substituting hydrophobic residues with other hydrophobic residues to observe their effects on activity and toxicity has been explored using the platelet factor IV derived AMP C18G (Saint Jean et al., 2018). A series of peptides were made by replacing Leu of C18G with Phe, isoleucine (Ile), Val or α -aminoisobutyric acid (Aib). The change of Leu to Phe or Ile did not change the MIC of the peptide when tested against *E. coli*, *S. aureus*, *Salmonella enterica*, *P. aeruginosa* or *Staphylococcus epidermidis*. However, the change to Val increased the MIC values against all bacteria tested and the change to Aib increased the MIC even more. This agrees with the previously discussed study in which substitution of Val with Leu resulted in a decreased MIC. A similar trend was observed in lipid vesicle and bacterial membrane permeabilisation studies in which C18G

displayed the highest activity (~95% lipid vesicle content leakage at 1.5 μM), followed by the Leu \rightarrow Phe (~35% at 1.5 μM) and Leu \rightarrow Ile (~40% at 1.5 μM) variants that also showed considerable permeabilisation. The Leu \rightarrow Val and Leu \rightarrow Aib showed some, albeit considerably less, permeabilisation (lipid vesicle content leakage ~30% for Val and Aib at 1.5 μM and ~35% at 15 μM compared to 100% for Leu, Phe and Ile also at 15 μM). C18G and Leu \rightarrow Phe did the most damage to the *E. coli* outer membrane followed by the Leu \rightarrow Ile variant. The Val and Aib were also capable of causing some damage but to a much lesser extent. However, C18G was the only peptide that showed any considerable damage to the inner membrane of *E. coli*. C18G was also the most toxic to HEK-293 cells (10% cell viability at 15 μM) compared to ~50% viability for Phe substitution, ~65% for Aib, ~80% for Ile and ~88% for Val all at 15 μM . Although, at 1.5 μM (close to the MIC for C18G), cell viability ranged from ~80–100% for all peptides. It was postulated that the variation in antimicrobial activity and cell toxicity observed was not solely due to overall hydrophobicity but was affected by the side chain length and bulkiness of the hydrophobic residues. Order of side chain length was considered to be Phe > Ile > Leu > Val > Aib and for bulkiness Phe > Leu > Ile > Val/Aib. Substitution of Leu with Phe or Ile did not significantly impact activity, indicating that the increased side chain bulk of Phe had little effect on activity. However, substitution with Val showed that a significant decrease in side-chain length and bulk decreased activity considerably which was even more pronounced for analogues with the shorter chain Aib substitutions. Amino acids with bulky side-chains, such as tryptophan (Trp), can disrupt the equilibrium of bacterial membranes and have been shown to cause disorganisation of the lipopolysaccharide (LPS) leaflet found in Gram-negative bacteria. Isothermal calorimetric titration of LPS with Trp containing peptides demonstrated that an exothermic process occurred first, followed by an endothermic reaction (Shang et al., 2016). This resulted in disruption of the outer membrane of Gram-negative bacteria as the peptide buried into the LPS leaflet. Shifts in the emission spectra of Trp fluorescence in the presence of a negatively charged membrane has also been observed and shows that Trp residues bury deeply into the membrane (Bi et al., 2013). Once peptides bury into the lipid bilayer, the bulky side chain of Trp can then disrupt the hydrophobic interactions of the acyl chains and hence the membrane structure (Chan et al., 2006). This ability to traverse the outer membrane, bury into the lipid bilayer and disrupt the entropy of the membrane, can increase the overall antimicrobial activity of peptides containing residues with bulky side-chains.

Increasing overall hydrophobicity has also been shown to increase activity and haemolysis, although the evidence is less distinct (Tan et al., 2014). As reviewed by Moret and Zebende, different methods have been developed for determining the level of hydrophobicity of amino acid residues with each method ordering them differently (Moret and Zebende, 2007). However generally, alanine is the least hydrophobic with valine almost always more hydrophobic than methionine. The order of hydrophobicity of leucine, isoleucine, phenylalanine, tryptophan, tyrosine, and cysteine then vary depending on the method used. It is important to note that pH also affects

hydrophobicity. The amino acid residues that are chosen to increase the hydrophobicity of an AMP, and their position within the final construct, can determine the extent to which activity and toxicity is affected. If a certain residue increases hydrophobicity but also disrupts other key features such as amphipathicity, helicity or net charge, then increased activity may not be observed. Additionally, replacing a less hydrophobic residue with a more hydrophobic one will not necessarily result in increased activity. Some studies suggest this may be due to how residue side chains insert and interact with the lipid bilayer of bacterial membranes (Saint Jean et al., 2018). In addition to changing hydrophobicity and helicity, changing the amphipathic profile of an AMP also affects its activity.

Amphipathicity

To explore how amphipathicity affects activity and toxicity, alanine 8 on the polar face of AR-23 (an AMP from *Rana tagoi*, Brown frog) was substituted with positively charged Arg (R) (named A (A8R)), which increased its amphipathicity (Zhang et al., 2016). Conversely, Ala1 and Ile 17 on the non-polar face was substituted with Arg (A (A1R)) and Lys (K) (A (I17K)) respectively. A (A1R) had the same degree of amphipathicity as the parent peptide, but A (I17K) was slightly less amphipathic than the parent AR-23 peptide. The more amphipathic A (A8R) analogue showed increased antimicrobial activity towards *S. aureus* and *E. coli* as well as decreased haemolytic activity. Conversely, A (I17K) showed no change or a decrease in activity towards *E. coli* and *S. aureus* respectively but was much less haemolytic than both AR-23 and A (A8R). As for A (A1R), which displayed the same degree of amphipathicity as AR-23, it had the same MIC as A (A8R) towards *E. coli* but towards *S. aureus* its MIC was the same as AR-23. It was also less haemolytic than AR-23 but slightly more so than A (A8R). Considering the changed amphipathicity of these analogues and the effect on the MIC values, an increase in amphipathicity appeared to increase the antimicrobial activity of the peptide.

Other analogues that consisted of a mix of more than 1 of the above substitutions were also made. These analogues varied in their degree of amphipathicity and activity towards *S. aureus* and *E. coli*, but all of them were less haemolytic than AR-23. Along with the single substitution analogues, they also caused more membrane damage to *E. coli* cells than AR-23 (except for A (A8R, I17K)). However, they all caused less membrane damage to *S. aureus* compared to AR-23. These substitutions also affected the overall hydrophobicity, helicity, and charge on these AMPs, making it difficult to determine the exact effect changes to amphipathicity have on antibacterial activity and toxicity. Although A (A8R) and A (A1R, A8R) both had an increased amphipathic profile and lower haemolytic activity, they differed in their antimicrobial activity and α -helical content. The A (A8R) analogue had a higher α -helical content than both the parent peptide and A (A1R, A8R) in 50% v/v TFE. It also had lower MIC values than AR-23 towards *E. coli* and *S. aureus*, was less active than A (A1R, A8R) towards *E. coli* but more active towards *S. aureus*. The degree of helicity may be responsible for the general increase in bacterial activity however, a balance between helicity and amphipathicity could be contributing to the bacterial

selectivity of A (A1R, A8R) towards *E. coli* and of A (A8R) towards *S. aureus*. All analogues had lower α -helical content compared to the parent peptide which may account for the observed decrease in toxicity. Interestingly, unlike A (I17K) that showed no improvement in antimicrobial activity, substitution of I17 with R (A (I17R) did improve its activity towards *E. coli* to the same extent as A (A8R). This indicated that individual residues and not just disruption of amphipathicity affects activity against different bacteria in different ways. This again suggests that the different side groups of amino acids may play specific and important roles in AMP activity and interaction with bacterial membranes. These specific interactions may also mitigate any change in activity due to changes in other parameters that contribute to AMP activity.

Another study which modified an AMP sequence with the aim of creating a more regular amphipathic profile showed that the increased amphipathicity resulted in increased activity but also increased toxicity. Interchanging the first two residues of SB056-lin resulted in β -SB056-lin, also known as lin-SB056-1 (Manzo et al., 2015). This modified peptide was reported to have a perfect β -stranded amphiphilic structure. This structural change significantly decreased its MIC when tested against *E. coli*, *P. aeruginosa*, *S. aureus* and *E. faecalis*. This also led to increased haemolytic activity, although overall minimal haemolysis was observed at concentrations close to its MIC. Conversely, comparison of synthetic poly (vinyl ether) block and random copolymers, made of hydrophobic isobutyl vinyl ether and cationic amine vinyl ether, indicated that the more regulated amphiphilic profile of the block copolymer resulted in similar bactericidal activity to the random copolymer. However, it did exhibit lower haemolytic activity due to selectivity for bacterial membranes over erythrocyte membranes (Oda et al., 2011).

More recently, ring-opening polymerisation (ROP) of Phe and Lys N-carboxyanhydrides (NCA) was used to create amphiphilic diblock copolymers which also showed lower MICs and haemolytic activity compared to their random copolypeptide equivalents (Zhou et al., 2010; Su et al., 2017). This study suggested that the improved activity was due to the long section of hydrophobic residues present in the diblock copolymers which were able to insert into the membrane more effectively. It must be noted though that the most active random copolymer contained 10 Lys-NCA and 15 Phe-NCA building blocks whilst the diblock copolymers contained 30 Lys-NCA and 15, 30 or 45 Phe-NCA building blocks. Therefore, increased hydrophobicity and charge rather than regulated amphipathicity may have influenced the activity of these AMP polymers.

Unlike the previous examples, a non-amphipathic, charge-clustered AMP showed quite different results when compared to increasingly amphipathic versions of itself (Stone et al., 2019). The charge clustered AMP 6K-F17 exhibited significantly better antimicrobial activity, MIC 1.6 μ M towards *E. coli*, than its most amphipathic counterpart, 1KAMP which had an MIC of 12.5 μ M. Additionally, at 40 μ M they both showed 0% haemolysis. However, in another set of synthesised peptides where 4 alanines were substituted with 4 leucines to increase overall hydrophobicity, 6K-F17-4L and 1KAMP-4L were created and the charge clustered 6K-F17-4L exhibited lower antimicrobial activity but was also less haemolytic (33% haemolysis at 40 μ M) than the more amphipathic analogues. The general trend indicated that in this peptide series

with overall higher average hydrophobicity, the more amphipathic the peptide the better its antimicrobial activity. However, even though 1KAMP-4L exhibited strong antimicrobial activity towards *E. coli* (MIC 1.6 μ M), it caused 81% haemolysis at 40 μ M, making it a weaker therapeutic than the less hydrophobic 6K-F17. Of note was the ability of these AMPs to disrupt bacterial and mammalian lipid vesicles. Both charge clustered AMPs, 6K-F17 and 6K-F17-4L, caused more damage to bacterial lipid vesicles than their respective amphipathic counterparts, 1KAMP and 1KAMP-4L. Conversely, for the Leu substituted AMPs, 6K-F17-4L caused the least disruption to liposomes mimicking mammalian membranes. Similar to the amphiphilic diblock copolymers, it may be that the long section of hydrophobic residues present in these charge clustered AMPs allows for better bacterial membrane insertion and therefore disruption. It was also suggested that due to the charge cluster, it is only after an electrostatic interaction occurs with an anionic membrane that the hydrophobic domain causes membrane disruption. This may also explain the reduced haemolysis observed in 6K-F17-4L compared to 1KAMP-4L. The charge clustered variants were also more resistant to proteolytic degradation. After 60 min incubation with proteinase K, ~ 60% of 6K-F17 still remained compared to <10% for other peptide variants with a lower charge cluster.

Amphipathicity is a key feature of natural AMPs, but it is unclear whether a more regulated amphipathic profile is always desired in AMP design. In some cases, it can improve antibacterial activity whilst in others, it decreases activity, and the same inconsistency is seen in haemolytic activity. The length of the polar and non-polar sections within an amphipathic AMP may possibly account for this variation. For high antimicrobial activity the hydrophobic sections may need to be a certain length to cause significant membrane damage whilst longer sections of charged residues may improve selectivity for bacterial membranes over mammalian membranes. It is difficult to determine the exact influence of amphipathicity on antibacterial activity as changing amphipathicity also result in changes to helicity, hydrophobicity, and overall positive charge. Each of these parameters are important to AMP activity and are not independent of each other, thus making it difficult to pinpoint precisely how natural AMP features can be optimised through a rational evidence-based strategy, rather than a semi-rational trial and error approach.

Overall Charge

In addition to observing the effects of changing amphipathicity, the AR-23 analogues also allowed for analysis of the correlation between overall positive charge and AMP activity and selectivity (Zhang et al., 2016). As alanine was being replaced by the positively charged residues Arg and Lys, the overall net charge of the analogues therefore increased, ranging from +4 for AR-23 to +7 for analogues with 3 substitutions. An increase in charge was well correlated with reduced haemolytic activity. In analogues where I17 was replaced with Arg or Lys, the Arg substitution was more haemolytic than the Lys substitution but nonetheless remained much less toxic than analogues with a lower overall net positive charge. Arg interacts with lipid membranes more strongly than Lys and is further discussed in **Section 4.1**. As for antibacterial activity, there was no clear

correlation with charge and activity. As previously discussed, this may be more a result of the substitutions affecting amphipathicity, helicity and hydrophobicity than a reflection on the effects of increased charge.

An example of the effects of increased charge whilst maintaining amphipathicity, hydrophobicity and length was shown through an analogue of aurein 1.2 (Ramezanzadeh et al., 2021). Substituting Asp 4 and Glu 11 of aurein 1.2 with Lys resulted in the peptide named aurein M2. These substitutions increased the net positive charge from +1 to +5. When tested against *S. aureus*, aurein M2 had an MIC of 12.5 µg/ml which was two-fold better than aurein 1.2 (25 µg/ml), but against *E. faecalis*, the MIC values were the same (50 µg/ml). However, M2 exhibited improved antibacterial activity towards two Gram-negative strains, *E. coli* (MIC of 25 µg/ml) and *P. aeruginosa* (MIC of 6.25 µg/ml), whilst the MIC of aurein 1.2 was >200 µg/ml for both strains. Although M2 was the most helical (78.44% α -helix compared to 53.04% for aurein 1.2), another analogue which in addition to the substituted Lys also substituted Ala 10 for tryptophan (aurein M3), had a lower α -helical content (36.36%) but even better antimicrobial activity. The MIC values for aurein M3 were 3.12 µg/ml (*S. aureus*), 25 µg/ml (*E. faecalis*), 6.25 µg/ml (*E. coli*) and 3.12 µg/ml (*P. aeruginosa*). This suggests that the increased charge rather than increased α -helicity of M2 may be responsible for the increase in activity and the addition of tryptophan (Trp) further improves activity despite an even lower α -helical content. Overall, M2 was also the least haemolytic with 5% haemolysis of human red blood cells being caused by 100 µg/ml of M2 compared to 50 µg/ml and 25 µg/ml for aurein 1.2 and aurein M3 respectively.

Similarly, the overall net charge of the 26-residue V13KL peptide was altered by varying the number of positively charged residues but only on the polar face to determine how charge affects activity, while maintaining the non-polar face unchanged (Jiang et al., 2008). Decreasing the charge from +7 to +4 significantly reduced both its antimicrobial and haemolytic activity. However, increasing the charge to +8 increased its activity towards some bacteria whilst maintaining the same haemolytic activity as V13KL. Further increasing the charge continued to improve activity, although it also made the peptide significantly more haemolytic.

Generally, an increase in net charge results in increased activity, but only to a certain extent. Studies in which the net charge of various AMPs have been altered show that once the net positive charge reaches a certain point, no further increase in antibacterial activity is observed although haemolytic activity does increase (Dathe et al., 2001; Jiang et al., 2008). The turning point at which activity decreases with increasing charge varies for different AMPs with an overall positive charge of +8 or +9 often considered the maximum charge that offers increased activity without significantly increasing the toxicity of the peptide (Zelezetsky and Tossi, 2006).

Altering the structure, hydrophobicity, amphipathicity and net charge of AMPs can have either positive or negative results, indicating that a balance between these different factors is crucial to AMP design and function. It may be reasonable to rationalise that perfect helicity, amphipathicity and increased net charge will

dramatically improve the antimicrobial activity of *de novo* AMPs as they are defining features of natural AMPs. However, such perfectly structured and highly charged AMPs are not found in nature and synthetic AMPs where these parameters have been improved often display high levels of toxicity. Over the years there has been a lot of effort put into better understanding these common characteristics of AMPs and although considerable progress has been made, it has indicated that a fine balance between them is needed for improving and targeting activity. Additionally, despite their main mode of action being membrane disruption, there are certainly differences observed in their activity towards different species of bacteria. Although outside the scope of this review, a comprehensive analysis of differences between bacterial membranes and correlations between AMP activity and bacterial membrane composition would greatly further our understanding of AMPs and the process of rational design. Effects of changing membrane composition on antimicrobial activity has been explored to some extent. For example, the degree of membrane insertion of aurein 2.2 and aurein 2.3 varied between model membranes composed of different lipid combinations (Cheng et al., 2011). Furthermore, a change in membrane fatty acid composition in *S. aureus* was shown to impact the activity of daptomycin and its ability to form pores (Boudjemaa et al., 2018). Bacterial membranes are constantly changing and are affected by their external environment (Sohlenkamp and Geiger, 2015; Siliakus et al., 2017). A better understanding of the specific interactions between AMPs and bacterial membranes may therefore not only assist in designing AMPs with increased antimicrobial activity but may also allow for better cell specificity.

Limitations *In Vivo*

Whilst there has been some success in using AMPs topically, systemic therapy has been limited for several reasons (Costa et al., 2019). AMPs are disadvantageous from a therapeutic standpoint as they are susceptible to proteolytic degradation, less active under physiological conditions due to the presence of serum salts and proteins, have high MICs, low selectivity for pathogens over mammalian cells, are toxic to mammalian cells and have a short half-life *in vivo* (Drayton et al., 2020; Hancock and Sahl, 2006; Liu et al., 2010). These limitations are progressively being addressed as AMPs are modified to improve their stability, activity, and biocompatibility (Table 1).

OPTIMISING LINEAR ANTIMICROBIAL PEPTIDES

Type and Sequence Position of Amino Acids Enhance Antimicrobial Activity of Antimicrobial Peptides

Engineered AMPs that are high in hydrophobic and basic amino acids have been shown to have improved antimicrobial activity (Wimley, 2010). Identification of specific amino acid residues that contribute to improvement has been aided by using the technique of alanine scanning (sequential substitution of each peptide

residue with Ala) of naturally occurring AMPs. When analogues of aurein 1.2 were synthesised by substituting each amino acid for Ala one at a time, it was only the replacement of aspartic acid (Asp), glutamic acid (Glu) and serine (Ser) at positions 4, 11 and 12, respectively, that resulted in improved activity (Migoñ et al., 2019). All other substitutions reduced activity when compared to native aurein 1.2. These substitutions highlighted how hydrophobicity, resistance to proteolytic degradation and helical structure are affected by different residues. Replacement of Asp and Glu improved antimicrobial activity, but their removal also resulted in lower proteolytic stability and reduced α -helicity. The increase in activity was therefore best explained by their removal resulting in an increase in the overall positive charge of the analogue. The increase in activity observed by substituting Ser12 with Ala was contributed to the resulting increase in hydrophobicity and stability. However, the Ser12 analogue was less active towards *P. aeruginosa*, indicating that Ser may be important for interacting with the bacterial membrane. Phenylalanine 3 and 13 had previously been noted as being important for membrane anchoring, and their contribution to aurein 1.2 activity was further demonstrated in this study as substitution with Ala resulted in decreased activity (Shahmiri et al., 2017). Varying the position of Lys within the sequence also produced very different results, despite both the Lys being located next to each other at positions 7 and 8. Both K7A and K8A exhibited reduced activity compared to aurein 1.2, yet K8A had a lower MIC than K7A when tested against *E. faecalis*, *E. coli* and *Candida albicans*. K8A was also more haemolytic and had a higher α -helical content in dodecylphosphocholine (mammalian membrane mimic) but it had lower α -helical content in sodium dodecyl sulfate (bacterial membrane mimic) and was less stable than K7A.

Other *in vitro* studies have illustrated that Trp can improve the antimicrobial activity of AMPs and increase their resistance to proteolytic degradation (Deslouches et al., 2005; Hilpert et al., 2005; Shang et al., 2016; Han et al., 2020). It was also noted that Trp is particularly suited for targeting Gram-negative bacteria, as it can strongly bind to the LPS that make up the outer membrane. The Trp residues are thought to help dissociate the LPS of Gram-negative bacteria, allowing the peptide to pass the outer membrane and then disrupt the cytoplasmic membrane. Within the overall context of a peptide, these studies showed that the addition of Trp was more effective when it was located at the amino terminus compared to the carboxyl terminus (Bi et al., 2013; Shang et al., 2016).

Arg and Lys are also regularly used in AMP design. However, despite both residues having the same charge, substitution of Lys with Arg can further improve activity (Torcato et al., 2013). This was shown by replacing all Lys of the synthetic AMP BP100 with Arg to create R-BP100. This substitution resulted in a twofold decrease of its MIC when tested against *E. coli* and a fivefold decrease against *S. aureus*. This increase in activity is possibly due to the side chain of Arg containing a guanidino group which can interact with two lipid headgroups, whereas the side chain of Lys can only bind one (Rothbard et al., 2005). The amine side chain of Lys is also known to become deprotonated in a lipid membrane. This leads to weaker interactions with water and lipid headgroups

and does not cause extensive damage to the membrane. Arg, however, maintains its positive charge in the membrane environment and its ability to form more H-bonds with lipid head groups leads to membrane thinning and pore formation (Li et al., 2013). With certain residues exhibiting the ability to improve AMP activity, peptides enriched in these residues have been developed as another means to create optimised compounds.

The occurrence of natural AMPs enriched in certain residues has led to the development of synthetic AMPs also enriched with certain residues, to further increase their charge and hydrophobicity and improve activity (Chan et al., 2006; Stensvåg et al., 2008). For example, substituting different residues of the neuropeptide α -melanocyte stimulating hormone (α -MSH (6–13)) with Arg and Trp created different combinations of Arg/Trp rich peptides with enhanced charge and hydrophobicity (Singh et al., 2020). The most charged and hydrophobic peptide from this group (Ana-5) exhibited improved antibacterial activity and serum stability compared to its parent peptide. Similarly, analogues of a truncated aurein 2.2- Δ 3 enriched with Arg and Trp exhibited improved activity but were also more cytotoxic (Kumar et al., 2017, 2019; Raheem et al., 2020). Replacing neutral and non-polar residues on the polar face of the α -helical AMP Temporin-1CEb with Lys is another example of an AMP that was modified to decrease haemolytic activity and increase antimicrobial activity (Shang et al., 2012). This resulted in a series of Lys-rich AMPs whereby replacement with six lysine (analogue named L-K6) resulted in high antimicrobial activity and low haemolysis. This Lys-rich analogue was also shown to be able to neutralise LPS and prevent it from inducing a proinflammatory response (Dong et al., 2018).

Proline (Pro) rich AMPs (PrAMPs) are another group of antimicrobials, predominantly found in insects, that translocate across the bacterial membrane to act on internal targets and can modulate the immune system (Otvos and Otvos, 2002; Li et al., 2014). Based on naturally occurring pyrrolicorin, drosocin and apidaecin, a series of PrAMPs was created and then further optimised by creating C-terminally linked dimeric structures and adding an amino-cyclohexyl carboxylic acid moiety (Chex) to the N-terminal (Otvos et al., 2005; Otvos et al., 2014). From this series, A3-APO was identified as the best peptide and showed considerably better activity towards a range of fluoroquinolone-resistant *E. coli* and *K. pneumoniae*, compared to the clinically used antibiotic ciprofloxacin. Reviews by Welch et al. and Li et al. provide a more in depth look at this class of AMPs (Li et al., 2014; Welch et al., 2020).

Side-Chain Length, D-amino Acids and N-Terminal Modification

Altering the side-chain length of AMP residues is another way in which activity can be manipulated. With regards to activity against *P. aeruginosa*, peptide/ α -peptoid oligomers with shorter cationic side-chain lengths resulted in a more hydrophobic surface and improved membrane disruption. This

increased hydrophobicity is believed to be due to the aromatics in the oligomers shielding the cationic side chains, since longer cationic side chains resulted in reduced hydrophobicity. As previously noted in other AMPs, an increase in hydrophobicity also correlated with an increase in haemolysis and cytotoxicity (Frederiksen et al., 2019). Using D-amino acids instead of L-amino acids can also sometimes improve activity. The D-enantiomer of a sapecin B analogue, named D-L5, was compared to its L-isomer and was found to have a much lower MIC value when tested against *S. aureus* and *E. coli*. Of note, its activity towards *S. aureus* was improved by 16-fold compared to only a two-fold increase in activity towards *E. coli*. This is potentially due to its higher affinity for *S. aureus* peptidoglycan than the L-form (Manabe and Kawasaki, 2017). However, using D-amino acids does not always improve activity. The D-form and L-forms of Kn2-7, Mastoparan M and Temporin A were also tested but their D-forms did not show improved activity.

Another study compared the L-enantiomers of V681, V13KL, and V13AD with their corresponding D-isomers (D-V681, D-V13KD, and D-V13AL) (Chen et al., 2006). Again, it was observed that, generally, D-isomers did not display significantly different antimicrobial or haemolytic activity compared to their L-isomer counterparts. Nevertheless, they did show significantly improved resistance to proteolytic degradation. The peptides were incubated with trypsin at a 20,000:1 (peptide: trypsin) ratio for 8 h at 37°C. After 60 min, all L-peptides were fully degraded as determined by RP-HPLC. On the other hand, all D-peptides were fully intact even after 8 h incubation. The peptide D-V13KD stood out with the highest therapeutic index (TI). Its antibacterial activity in physiological conditions was further investigated along with its L-isomer (Huang et al., 2011). Again, both isomers had similar haemolytic activity and MIC values when tested against human red blood cells and Gram-negative bacteria. However, D-V13KD had lower MIC values towards Gram-positive bacteria compared to V13KL. The MIC of these peptides towards *E. coli*, *P. aeruginosa*, *S. epidermidis* and *B. subtilis* was also evaluated when in the presence of either NaCl (150 mM), CaCl₂ (2.5 mM) or human serum albumin (HSA, 0.6 mM). For both peptides, their antibacterial activity was decreased when tested in these mediums, but the decrease in activity of D-V13KD was significantly less than for V13KL.

N-terminal modification is another method for improving AMP activity. Analogues of Hy-a1, an AMP isolated from the South American frog *Hypsiboas albopunctatus*, were made via solid phase peptide synthesis (SPPS) that had either an acetyl group, Lys or Asp added to the N-terminus (Crusca et al., 2011). These additions resulted in analogues with N-terminal no charge (Ac⁰-W⁶-Hy-a1), positive charge (K⁰-W⁶-Hy-a1) or negative charge (D⁰-W⁶-Hy-a1) respectively. At position 6, Leu was also substituted with Trp, and an unmodified-N-terminus analogue made (W⁶-Hy-a1). The addition of Trp did not change the MIC compared to unmodified Hy-a1 but did significantly increase its haemolytic activity. This increase in haemolytic activity was observed for all N-terminally modified analogues, although K⁰-W⁶-Hy-a1 also exhibited increased antimicrobial activity against *E. coli*, *S. aureus*, *P.*

aeruginosa and *B. subtilis*, thus increasing the TI of this analogue.

Some other N-terminal modifications that lead to improved activity include the addition of acyl groups or fatty acid chains. Amino acid residues 21–31 of lactoferrin were synthesised to create LF11, which exhibited weak antibacterial activity (Zweyck et al., 2011). In one example, the authors sought to improve the activity of LF11 by exchanging Lys 9 and Val 10 for Ile and Arg respectively and deleting Gln 2 and 4 and asparagine (Asn) 6 which resulted in LF11-215. They then added either octanoyl (O-LF11-215) or 6-methyl-octanoyl (6-MO-LF11-215) to the N-terminus of this optimised analogue. This additionally reduced the MIC of LF11-215 from 16 to 32 µg/ml to 10 µg/ml for both analogues when tested against *E. coli*. Other studies have added different length fatty acid chains to AMPs and have found that this addition increases overall hydrophobicity, resulting in improved activity. One study added different length alkyl chains to the LL-37 derived peptide KR12. They found that increasing alkyl chain length up to 8 carbons (C₈) improved activity but beyond that a decrease in activity was observed despite compounds with longer chains being more hydrophobic (Kamysz et al., 2020). This was possibly due to compounds with longer chains being more prone to self-assembly. Addition of fatty acid chains also increased haemolytic activity but C₈-KR12-NH₂ showed <10% haemolysis at concentrations well above its MIC. However, addition of a longer chain, C₁₀, significantly increased the haemolytic activity. In another study, adding fatty acid chains of increasing length to an anoplin analogue (anoplin-D4, 7) also resulted in improved activity and increased haemolysis that correlated to chain length (though haemolysis was again only 10% at concentrations above the MIC values of C₁₀-D4, 7 and C₁₂-D4, 7, and C₈-D4, 7 was not haemolytic) (Zhong et al., 2019). The effect of lipidation on AMP activity is further reviewed by Rounds and Straus (2020) and Li et al. (2021).

Optimal Peptide Length

Overall charge affects AMP activity, making it difficult to determine the effect of peptide length. One study overcame this by building on repeats of KIAGKIA (the repeating unit of the peptide MSI-103, to create α-helical analogues of different lengths but with a constant charge of 7⁺ by substituting certain Lys for Ala (KIA peptides) or Lys for Ser (KISA peptides) in subsequently longer analogues (Gagnon et al., 2017). This study showed that independent of charge, longer peptides were generally more active than their shorter counterparts and that a minimal length of ~17–19 residues was required for membrane disruption of *E. coli*, *P. aeruginosa* and *S. aureus*. Activity increased with increasing length, but this came at a cost. Peptides ≤17–19 residues long showed no haemolysis (or activity), but peptides ≥21 residues long showed high haemolysis at varying concentrations. Interestingly, this study also observed that in some cases the longer peptide was slightly less active than the previous shorter peptide in their series. It was noted that these longer, less active peptides contained Lys at the C-terminus, whereas the next shorter, more active peptides contained the hydrophobic residues Ile and Ala. This suggests

TABLE 1 | Summary of how different modifications can increase or decrease the antimicrobial activity and toxicity of AMPs.

Modification	Unmodified				Name	Modified ^a			Ref	
	Name	MIC		Haemolytic activity ^b		Name	MIC			Haemolytic activity ^b
		<i>S. aureus</i>	<i>E. coli</i>				<i>S. aureus</i>	<i>E. coli</i>		
Increase in amphipathicity due to substitution on polar face	AR-23, 4 + charge	6.25 μM	25 μM	3.13 μM = 37.9%	A (A8R), 5 + charge	3.13 μM	12.5 μM	3.13 μM = 12.9%	Zhang et al. (2016)	
Decrease in amphipathicity due to substitution on non-polar face					A (I17K), 5 + charge	50 μM	25 μM	100 μM = 33%	Zhang et al. (2016)	
replacement of all Lys with Arg	BP100	32 μM	2 μM	>100 μM = 50%	R-BP100	6 μM	0.9 μM	50.9 μM = 50%	Torcatto et al. (2013)	
using D-amino acids instead of L-amino acids	L form	16 μg/ml	16 μg/ml	N/A	D form	1 μg/ml	8 μg/ml	N/A	Manabe and Kawasaki, (2017)	
	KLKLLLLLKLK-NH2 (L5)				D form					
	L form	8 μg/ml	N/A	N/A	D form	8 μg/ml	N/A	N/A	Manabe and Kawasaki, (2017)	
	Temporin A				Temporin A					
Peptoid mimic of a peptide	GN-4 peptide	6.25 μg/ml	6.25 μg/ml	100 μg/ml = 10%	GN-4 peptoid	32 μg/ml	64 μg/ml	>128 μg/ml = 10%	Mojsoska et al. (2015)	
addition of a positive charge at the N-terminus	W6-Hy-a1	8 μM	32 μM	4 μM = 50%	K0-W6-Hy-a1	4 μM	4 μM	4 μM = 50%	Crusca et al. (2011)	
increased peptide length from 19 residues to 26, but same overall charge	KIA19, +7 charge	>256 μg/ml	64 μg/ml	512 μg/ml = 10%	KIA (7)26	8 μg/ml	4 μg/ml	8 μg/ml = 39% 32 μg/ml = 72%	Gagnon et al. (2017)	
dimerisation of magainin 2 at C-terminal	MG2	128 μM	16 μM	32 μM = 0%	(MG2)2K	16 μM	1 μM	32 μM = 60%	(Lorenzón et al., 2016)	
dimerisation of magainin 2 at N-terminal	MG2	128 μM	16 μM	32 μM = 0%	E (MG2)2	128 μM	16 μM	32 μM = 5%	Lorenzón et al. (2016)	
multimerising the AMP R4 (RLYR) via attachment onto a dendrimeric core	(R4)4	1.8 μM	1 μM	338 μM = 50%	D4 (R4)	0.8 μM	0.6 μM	1,510 μM = 50%	Tam et al. (2002)	
change in architecture from linear to star-shaped	L-Lys	16 μg/ml	64 μg/ml	N/A	S-Lys	16–32 μg/ml	32 μg/ml	>10,000 μg/ml = 50%	Wong et al. (2016)	
change in architecture from linear to star-shaped	Lys-Val linear polymer	213.37 μM (MBC)	29.5 μM (MBC)	674.5 μM = 50%	S16	4.58 μM (MBC)	0.72 μM (MBC)	58.3 μM = 50%	Lam et al. (2016a)	
increasing arm length from medium to very long	SNAPP S4 _M	N/A	2.636 μM	14.727 μM = IC ₅₀	S4 _{VL}	N/A	0.403 μM	2.531 μM = IC ₅₀	Shirbin et al. (2018)	
increasing arm number from 4 to 16	SNAPP S4 _M	N/A	2.636 μM	14.727 μM = IC ₅₀	S16 _M	N/A	0.127 μM	1.090 μM = IC ₅₀	Shirbin et al. (2018)	

^aFor modified compounds as compared to unmodified, green highlighted sections indicate improved activity, red highlighted sections reduced activity and yellow highlighted sections indicating no change.

^bHaemolytic activity = concentration of compound that causes x % haemolysis expressed as μ M unless otherwise indicated.

that a more hydrophobic C-terminus may aid in membrane insertion and can result in a shorter peptide being more active than a longer peptide. The peptides were also tested in vesicle leakage experiments using lipid vesicles of different membrane thickness. Short peptides (<17 residues), that were inactive towards bacteria, could cause leakage in vesicles with thinner membranes but were unable to in vesicles with thicker membranes. A clear correlation between peptide length and membrane thickness was observed. This indicated that for this

series of peptides, they needed to be able to span the bacterial membrane in order to exert activity. As such, optimal peptide length would depend on the bacteria it is being tested against and the thickness of its membrane.

Short, 6 residues peptides have nonetheless shown to be active against bacteria, suggesting that not all AMPs need to be able to span the membrane to exert activity. The Arg/Trp-rich nature of these short peptides also contribute to their activity, making their activity as a function of length incomparable to the activity of the

KIA peptide series (Strøm et al., 2002). Ultrashort 3 residues long Arg/Trp-rich peptides are another inactive peptide, although when they are multimerised onto divalent and trivalent benzene scaffolds, the resulting compounds have higher activity that show negligible haemolysis, revealing multimerisation as another tool for improving AMPs (Hoffknecht et al., 2015).

MULTI-UNIT MATERIALS WITH ANTIMICROBIAL ACTIVITY

Multimeric Antimicrobial Peptides

Synthetic AMPs made of repeat units and constructed into branching forms can help resolve some of the limitations currently faced by linear AMPs (Figure 3). Multimerisation has been shown to increase AMP ability to disrupt bacterial membranes as well as their stability in physiological conditions to such an extent that any increase in cytotoxicity and haemolytic activity is negligible (Wiradharma et al., 2012; Li et al., 2015). These multimeric constructs can be made in various ways such as polymerisation, intermolecular covalent linking, multigeneration dendrimers or attachment to unnatural scaffolds or core molecules.

Peptide Based Antimicrobial Polymers

AMP-based polymerisation has also been employed to help overcome some AMP limitations. Anionic ring-opening polymerisation (ROP) was used to create poly- β -peptides, around 20 residues in length, with un-natural β -amino acids. The final structure of these compounds contained hydrophobic and cationic subunits (Zhang et al., 2019). Unlike standard AMPs, this polymer did not have a defined secondary structure but showed considerable activity towards a variety of Gram-positive and Gram-negative bacteria, low haemolytic activity and negligible cytotoxicity. Its MIC values were 12.5 $\mu\text{g/ml}$, 25–50 $\mu\text{g/ml}$, and 3.13–12.5 $\mu\text{g/ml}$ for various strains of *S. aureus*, *E. coli* and *P. aeruginosa*, respectively. A 20:80 ratio of hydrophobic to cationic subunits showed the best activity, with more than 20% hydrophobicity leading to increased toxicity whilst less than 20% reduced its activity (Chen A. et al., 2020). N^ϵ -tert-butyloxycarbonyl-D,L-lysine (Boc-DLL) and γ -benzyl-L-glutamate (BLG) polymerised in a 90:10 ratio also exhibited high activity against various clinical strains of multi-drug resistant (MDR) *P. aeruginosa* with an MIC of 50 $\mu\text{g/ml}$ (Jiang et al., 2020). Extremely low haemolytic activity and no cytotoxicity at its MIC was observed. Other interesting polymeric compounds are poly (ester amide) (PEA) random copolymers made from Lys, Arg and Phe (Zhu J. et al., 2019). The amphiphilic profile of this polymer allowed it to form micelles in water with the hydrophobic Phe protected by Lys and Arg. MIC values were not calculated but the OD growth curves of *E. coli* and *S. aureus* increased more slowly in the presence of PEA micelles. SEM images of treated and untreated bacteria also suggested a membrane lytic mode of action. Haemolysis and cytotoxicity were observed at concentrations of 500 $\mu\text{g/ml}$ and 2 mg/ml, respectively, and displayed no significant toxicity. A wound

infection mouse model also showed that treatment with PEA micelles reduced both bacteria load and the amount of various inflammatory cytokines in the wound tissue and serum. AMP activity was further increased by conjugation of the antibiotic levofloxacin (LV) or by preloading the micelles with LV, showing that they could also be used as nanocarriers for drug delivery.

Dimeric and Branched Antimicrobial Peptides

Dimeric AMPs (Figure 3A) exist in nature and exhibit certain antimicrobial advantages over linear forms. The naturally occurring AMP distinctin has a unique structure of two independent peptide chains (chain A and chain B) that form a heterodimer via a disulfide bond (formed between the C-terminal cysteines) (Batista et al., 2001). Analogues of this natural dimer, either linear forms of just chain A or B as well as A-A and B-B homodimers, were compared to distinctin and demonstrated how different structures affect activity and biocompatibility (Dalla Serra et al., 2008). The analogues were highly susceptible to protease degradation by elastase, whereas distinctin exhibited good stability. When tested against a variety of Gram-positive and Gram-negative bacteria, the homodimers had similar MIC values compared to distinctin and were lower than their linear counterparts, but both the heterodimers and homodimers were marginally more cytotoxic than the linear A and B chains.

The presence of such dimers in nature has led to synthetic AMP dimers being created, although with varying results (Liu et al., 2010). Dimerisation of magainin 2 was achieved either by replacing the C-terminal asparagine with a cysteine and forming a disulfide bond or by using Lys at the C-terminus or Glu at the N-terminus as ligands for the two chains (Dempsey et al., 2003; Lorenzón et al., 2016). N-terminal dimerisation did not improve the activity of magainin 2, however, C-terminal dimerisation using Lys or a disulfide linkage significantly improved its activity, albeit at the cost of increased haemolysis. Conversely, dimerisation of aurein 1.2 at both the C-terminal and N-terminal showed decreased activity compared to its linear form but had minimal haemolytic activity (Lorenzón et al., 2013). N-terminal dimerisation of PST13-RK also exhibited decreased activity and increased cytotoxicity compared to its linear form (Yang et al., 2009).

While acknowledging that dimerisation does not always lead to AMP improvement, by expanding on the concept that multiples of a peptide can improve overall activity, leads us to branched AMPs (Figures 3B,C). Branched AMPs can be formed through several methods and show improved activity. Comparison of dimeric (K-2A), trimeric (2K-3A), and tetrameric (3K-4A) anoplin, which were additionally lipidated at the N-terminal, revealed the trimer with *n*-butyric acid (2K-3A-C4) to have the best antibacterial activity (Gou et al., 2021). All of the multimers were built from a branched lysine core and tested against *S. aureus*, *B. subtilis*, *E. coli*, *P. aeruginosa* and *K. pneumoniae*. Overall, the trimer was found to be the most active followed by the dimer, and then the tetramer with all multimers more potent than linear anoplin-C4. This showed that like many other modification strategies, there is an optimal state for each compound whereby optimisation past a certain point does not further improve activity. Unfortunately, these multimers also

showed increasing haemolytic activity and cytotoxicity with increasing multimerisation. Another example of a branched AMP is the optimised proline-rich AMP (Chex1-Arg20) that used 2,4-diaminobutyric acid (Dab) to form a C-terminally linked homodimer (A3-APO) (Otvos et al., 2005). APO tetramers were then formed from this homodimer by either further building upon small molecule scaffolds or by adding a cysteine to its C-terminus and forming a disulfide bridge between two A3-APO molecules (Otvos et al., 2014; Li et al., 2015). It was shown that in the case of Chex-Arg20, the MIC and minimum bactericidal concentration (MBC) values of the dimer and tetramer were not significantly lower than the monomer. However, their ability to permeabilise *E. coli* membrane was increased through dimerisation with the tetramer further showing much stronger activity at lower concentrations. It can therefore be seen how, in some cases, further multimerisation provides an alternative strategy to increase activity and can change the mode of action of an AMP.

Dendrimeric Antimicrobial Peptides

Multimerising AMPs by tethering them onto dendrimers is another method for creating improved antimicrobial molecules (Figure 3D). Lysine is often used to create dendrimeric cores as it is a facile method for creating multivalent structures (known as multiple antigen peptides (MAPs)). Early work by Tam et al. showed that AMPs with low activity in their monomeric forms display potent activity when incorporated into tetra- and octavalent dendrimers (Tam et al., 2002).

Linear compounds of RLYR (R4) and two, four and eight repeats thereof were synthesised ((R4)₂ (R4)₄, and (R4)₈ respectively), and their antimicrobial activity was compared to divalent, tetravalent and octavalent lysine-core dendrimers (D₂, D₄ and D₈, respectively) which were decorated with R4 peptide to form the Lys-dendrimer-R4 constructs D₂R4, D₄R4 and D₈R4 respectively (Tam et al., 2002). A longer R8 peptide attached to a single Lys (RLYRKVYG(K)) was also synthesised as well as its divalent, tetravalent and octavalent analogues (D₂R8, D₄R8, D₈R8 respectively). Antimicrobial activity assays were conducted in both low and high salt conditions (as a simulation of physiological conditions) for a variety of Gram-negative and Gram-positive bacteria as well as some fungi. The monomeric R4 and R8 peptides showed no and low activity respectively in low salt conditions and R8 activity was completely abolished in high salt concentrations. The divalent dendrimers of each group showed better activity than their linear counterparts under low salt concentrations, but this was also diminished when tested in high salt. Notably, D₄R4 and D₄R8 not only showed improved activity compared to the monomers and divalent dendrimers (e.g., low salt MIC values of >500 µM for R4 and 6.1 µM for D₂R4 compared to 0.6 µM for D₄R4 against *E. coli*), but also retained their activity at high salt concentrations (with only a very slight increase in MIC observed). D₄R4 was generally slightly more active than D₄R8 and the octavalent dendrimers of R4 and R8 showed only small improvements in activity. The dendrimers did show increased haemolysis compared to R4 but based on molecular size, the dendrimers consistently showed reduced haemolytic activity (EC₅₀ of (R4)₄ was 338 µM compared to

1,510 µM for D₄R4). The EC₅₀ values for all linear and dendrimeric compounds were, however, well above their respective MIC values and thus considered nontoxic. Their activity after exposure to the proteolytic enzymes trypsin and chymotrypsin was also measured. After 24 h incubation with trypsin, D₄R4 retained 80% of its activity against *E. coli* whereas (R4)₄ only retained ~20% activity, indicating that the branched dendrimeric structure provided improved proteolytic stability.

The tetravalent dendrimer decorated with RW ((RW)_{4D}) is another example of a multivalent dendrimer that showed increased activity and a reduced haemolytic index (HI) in physiological salt conditions compared to the naturally occurring Arg/Trp rich AMP indolicidin (Liu et al., 2007b). Its increased activity towards *E. coli* and *S. aureus* correlated with increased haemolysis but its HI was much higher than that of indolicidin. Interestingly (RW)_{4D} was more active towards *E. coli* than *S. aureus*, whereas the reverse was observed for a series of linear peptides made from repeating units of RW, suggesting that AMPs multimerised onto a dendrimeric core may preferentially target Gram-negative bacteria (Liu et al., 2007a). Conversely, dendrimerisation of the linear peptide lin-SB056-1 onto a divalent lysine scaffold with an 8-aminooctanamide (Aoc) hydrophobic tail (den-SB056-1) did not improve its antibacterial activity when tested against *E. coli* and *S. aureus* in Mueller Hinton broth (MHB) (Batoni et al., 2016). However, when tested in MHB media in the presence of salts, den-SB056-1 had a much lower MIC than lin-SB056-1 (MIC value of 3.125 and 12.5 µM respectively against *E. coli* and 6.25 µM and >100 µM against *S. aureus*). This indicated that a multimerised peptide form may help AMPs maintain their activity in salt environments. Again, although the dendrimer did display increased haemolysis, at concentrations close to its MIC <20% haemolysis was observed.

Another dendrimer that has shown potent antimicrobial activity is the amphiphilic branched analogue of lysine termed BALY (Lind et al., 2014). The MIC of BALY towards *S. aureus*, MRSA, *E. coli*, and *P. aeruginosa* was 0.93, 10, 12, and 51 µM, respectively. The interaction of BALY with bilayer membranes that were in either a gel-phase or a fluid-phase, was closely studied and membrane thinning was observed in a gel-phase membrane whereas spherical aggregates were observed in fluid phase membranes. Further studies also revealed that BALY only interacted with the outer leaflet of homologous fluid- or gel-phase membranes, but that it caused increased disruption to mixed membranes and could penetrate across the lipid bilayer (Lind et al., 2015). These studies indicate that forming AMP dendrimers can impact their mode of action.

Recent research has also reported the creation of a series of dendrimer-based AMP-like compounds that take on an umbrella architecture and exhibit strong antimicrobial activity and low haemolysis and cytotoxicity (Chen S. et al., 2020). This series is comprised of 2,2-bis(hydroxymethyl) propionic acid (bis-MPA) dendrons of first (G₁), second (G₂) and third (G₃) generation displaying two, four and eight β-alanine groups respectively that form a cationic canopy. This canopy acts as a shield and is bound to hydrophobic alkyl chains varying from two to fourteen carbons long (C₂-C₁₄), creating the umbrella-like structure. The division

of the cationic canopy on one side and the hydrophobic tail on the other is reminiscent of the amphiphilic profile of AMPs. When tested against *E. coli* and *S. aureus*, increasing alkyl chain length correlated with an increase in antimicrobial activity. The most active compound was a second generation dendron with an alkyl chain of C₁₄ (C₁₄G₂) with MIC values of 3.9 and 1.95 µg/ml for *E. coli* and *S. aureus*, respectively. As previously noted, haemolysis is often associated with the overall hydrophobicity of a compound. When comparing dendrons of the same generation, increasing alkyl chain length, hence overall hydrophobicity, resulted in increasing haemolysis (HC₅₀ 1,514, 79.6, and 10.1 µg/ml for C₈G₁, C₁₀G₁ and C₁₄G₁ respectively). However, higher generation dendrons altered overall hydrophobicity, as seen by comparison of C₁₄G₁, C₁₄G₂ and C₁₄G₃ which have HC₅₀ values of 10.1, 63 and ~5,000 µg/ml, respectively. C₁₄G₃ was highlighted as the most promising compound and its cytotoxicity towards HeLa cells was considered mild with an LC₅₀ of 85 µg/ml. The cytotoxicity of C₂G₃ and C₁₄G₂ was also tested and comparison of their LC₅₀ values (>250 and 32 µg/ml respectively) with that of C₁₄G₃ showed that again increased tail length correlated with increased toxicity and that higher generation dendrons can mitigate this toxicity to an extent.

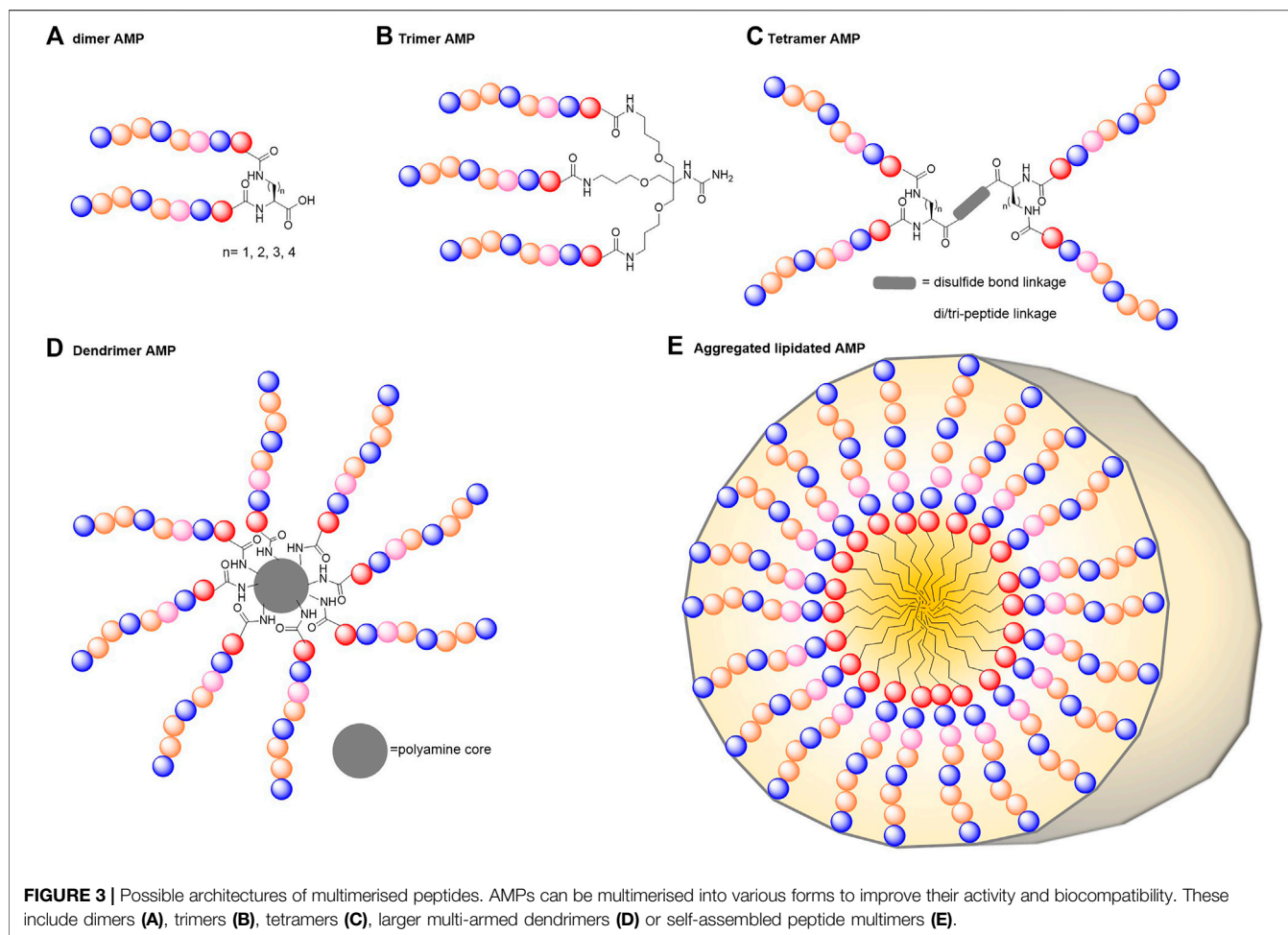
Star-Shaped Antimicrobials

An extension of branched and dimeric architecture is the collection of molecules known as star-shaped polymers. Their star architecture further confers enhanced activity, biocompatibility and stability compared to their linear counterparts. Arms made of polylysine and polyglucosamine radiating from a cross-linked core form a type of star-shaped polymer in which antimicrobial activity and biocompatibility can be regulated by varying the ratio of polylysine to polyglucosamine (Wong et al., 2016). Various star polymers with an estimated number of arms ranging from 12 to 19 were made via a combination of reversible addition–fragmentation chain-transfer (RAFT) polymerisation, N-carboxyanhydride ring-opening polymerisation (NCA-ROP) and click chemistry. The mol percentage of the glycopolymer polyglucosamine (GSA) arms to polylysine was also adjusted so that star polymers were generated with either 25, 50, 65 or 100 per cent of GSA arms for star molecules with a total of about 13 (S-GSA 25), 19 (S-GSA 50), 13 (S-GSA65) or 12 (S-GSA 100) arms respectively. Linear (L-Lys) and star (S-Lys) molecules containing only polylysine were also constructed. Their activity in MHB showed that the star architecture provided increased activity against *E. coli*, *P. aeruginosa* and *S. aureus* as indicated by their respective MIC values (Table 2). At 100 µg/ml, both compounds were extremely cytotoxic towards human aortic smooth muscle cells (AoSMC) however, all other S-GSA compounds resulted in >80% cell viability (improving with higher GSA content), indicating that the GSA arms were needed for reduced cytotoxicity. A mixture of L-Lys and linear GSA (L-GSA) at a 75:25 M ratio was also tested and shown to be more cytotoxic than S-GSA 25, highlighting that the star architecture also plays a role in improving biocompatibility.

This is possibly due to this star-structure allowing the GSA arms to shield the polylysine arms from non-specific interactions with other cells. Additionally, none of the star molecules were haemolytic at concentrations of 10,000 µg/ml, which was attributed to the lack of hydrophobic groups. S-GSAs also exhibited preferential activity towards Gram-positive bacteria compared to Gram-negative. It was suggested that the glucosamine shielded the Lys arms from interacting with the outer membrane of Gram-negative bacteria. Conversely, glucosamine, which resembles peptidoglycan structure, was thought to be responsible for penetrating the Gram-positive peptidoglycan layer so that the polylysine could then induce cell death. Unfortunately, the mechanism of action of these molecules was not described. Of all the compounds tested, S-GSA 25 was highlighted as the most promising antimicrobial as it had the highest TI of 7.0 as determined by its MIC against *S. aureus*.

Star-shaped structurally nanoengineered antimicrobial peptide polymers (SNAPPs), created through ROP of Lys and Val NCA building blocks at a theoretical ratio of 2:1 onto an amine core have also been shown to be effective in killing pathogenic bacteria (Lam et al., 2016a; Lam et al., 2016b). Compared to a linear analogue that represented one arm of these star molecules, the star architecture showed improved activity. Both the 16-arm (S16) and 32-arm (S32) SNAPPs had much lower MBCs in MHB compared to the linear analogue against *E. coli* and *S. aureus* (Table 2). These SNAPPs were also highly active against *K. pneumoniae* and *A. baumannii* with MBCs of 1.54 and 0.83 µM (S16 and S32) and 0.85 and 0.79 µM (S16 and S32) for *K. pneumoniae* and *A. baumannii*, respectively. The S16 and S32 SNAPPs exhibited considerably better activity towards these Gram-negative bacteria than towards the Gram-positive bacteria *S. aureus* (MBC of 4.58 and 2.23 µM for S16 and S32 respectively) and *S. mutans* (MBC of 3.55 and 1.80 µM for S16 and S32 respectively). They also showed very low haemolytic activity, with concentrations >100 × MBC resulting in <30% haemolysis and they were compatible with human embryonic kidney cells and rat hepatoma cells (IC₅₀ values well above MBC values). When tested *in vivo* in a mouse peritonitis model infected with colistin and multi-drug resistant (CMDR) *Acinetobacter baumannii* (*A. baumannii*), S16 was effective in reducing bacteria in the peritoneal cavity, blood, and spleen. It also increased the neutrophil count in the peritoneal cavity, demonstrating that SNAPPs can also enhance host cell innate immunity (though the role of the recruited neutrophils was unclear).

Further experimentation revealed that the degree of polymerisation (DP, arm length) and the number of arms on the SNAPPs can modulate their minimum membrane disruptive concentration (MDC), MIC, and MBC values (Shirbin et al., 2018). When tested against *E. coli*, SNAPPs with 4 arms but varying DP showed that increasing DP resulted in lower MIC values. Similarly, SNAPPs with medium arm length (DP of ~14 repeat units) but a different number of arms showed that an increase in arm number also decreased the MIC value (Table 2). Increasing activity (due to increases in DP and arm number) did correlate with an increase in cytotoxicity, but when tested *in vivo* in a murine model, no systemic organ damage was observed. The IC₅₀ values *in vitro* were consistently higher than the MICs with



S16_M showing the highest TI of 8.6 and S4_L a close second with a TI of 8.0 (based on its MIC for *E. coli*), indicating that a balance between activity and biocompatibility is important when determining the therapeutic use of new compounds.

Another star-shaped molecule using hyperbranched polyethylenimine (PEI) as the core and poly (L-lysine) (PLL) as the attached antimicrobial component (PEI-g-PLL) also exhibited better activity than its linear counterpart and did not include any hydrophobic components (Lu et al., 2019). This study tested 8 and 15-arm star shaped molecules in combination with arms that had DP of 5, 10, 15 or 20. A linear molecule (linear PLL) with a molecular weight close to that of an 8 arm and 10 DP star-shaped PLL (P2) was also tested. The P2 molecule showed consistently better activity against methicillin-resistant *S. aureus* (MRSA), methicillin-resistant *S. epidermidis* (MRSE), *P. aeruginosa* and *A. baumannii* compared to its linear PLL counterpart. All star-shaped PLLs showed better activity towards Gram-positive than Gram-negative bacteria, as previously noted with the S-GSA molecules that also lacked any hydrophobic groups (Table 2). Arm number and length also impacted the antimicrobial activity of these star PLLs. Converse to SNAPPs, the 8 arm molecules generally had lower MIC values than 15 arm molecules with the same DP. However,

like SNAPPs, an increase in DP also resulted in a lower MIC. As expected, all of these star molecules and the linear PLL showed negligible haemolysis due to the lack of hydrophobic groups. P2 was also more resistant to proteolytic degradation by trypsin compared to linear PLL. After a 3-h incubation only 13.5% degradation was noted for P2 compared to 67.3% for linear PLL, demonstrating again how this star-architecture improves stability. The lack of hydrophobic components contributes to improved biocompatibility of these compounds but star-molecules lacking these groups also tend to show preference for Gram-positive over Gram-negative bacteria.

According to the Centers for disease Control and Prevention, Gram-negative bacteria make up three out of the five pathogens that are considered urgent threats and seven out of the eleven that are considered serious threats (Frieden, 2019). As such, targeting Gram-negative bacteria, by including hydrophobic groups and finding a balance between activity and biocompatibility, is an important step in developing broad spectrum antimicrobials into therapeutic compounds.

Self-Assembling Peptides as Multimers

Self-assembling of antimicrobials is another approach shown to create multimerised compounds (Figure 3E). This topic has been

extensively and recently reviewed by Tian et al. (2015), Malekhaat Hä ffer and Malmsten, 2018, Lombardi et al. (2019), Zou et al. (2020) and Yang et al. (2021). Briefly, self-assembly occurs through noncovalent interactions and is often influenced by e.g., peptide length, distribution of hydrophobic and charged residues, and the presence of metal ions. This approach modifies the native AMP to alter its chemical characteristics (see **Sections 2 and 3**, this review) so that under specific environmental conditions the peptides self-assemble/aggregate. These self-assembled multimers can form micelles (DP7-C), nanofibers ((QL)₆-Melittin + (QL)₆-K), lamellae (V₄D) or fibrils (K₃(FA)₄K₃) (Chen Y.-F. et al., 2019; Kornmueller et al., 2018; Sha et al., 2020; Zhang et al., 2018). To aid peptide self-assembly, AMP sequences can be modified or conjugated to self-assembling sequences or hydrophobic moieties (e.g., lipids or alkyl chains). Self-assembly is also affected by the environment such that changes in the pH, temperature or ionic strength can control self-assembly (Wang J. et al., 2016). These self-assembled antimicrobials often display not only increased antibacterial activity, but reduced toxicity and improved stability. For example, the self-assembling peptide (QL)₆-Melittin + (QL)₆-K exhibited similar antibacterial activity towards *E. coli* but had significantly reduced toxicity to NIH 3T3 cells, compared to melittin (Chen Y.-F. et al., 2019). Another self-assembling peptide A₉K also exhibited antimicrobial activity towards *E. coli* and *B. subtilis* and could kill cancerous HeLa cells, but displayed minimal toxicity towards NIH 3T3 and human red blood cells (Chen et al., 2012). Some advantages of these self-assembling peptides include improved cell selectivity, sustained AMP release and improved stability.

Penetrating Biofilms

In addition to targeting a broad spectrum of bacteria with AMPs, it is also essential to evaluate their potency against biofilms. When bacteria grow in biofilms, they become harder to kill and can result in chronic infections (Bjarnsholt et al., 2013). Many AMPs and AMP-like compounds are only tested against planktonic bacteria *in vitro* under conditions that do not mimic the *in vivo* host environment. Already it has been shown that physiological salts and proteins can negatively affect AMP activity and not all studies explore whether AMPs are effective against biofilms or under physiologically relevant conditions, resulting in poor translation from *in vitro* models to *in vivo* ones. Those that have explored biofilm inhibition indicate that some AMPs do possess antibiofilm activity and that multimerisation can improve this inhibitory action.

Single-Chain Polymeric Nanoparticles (SCPN) that fold into a circular structure with extending oligoethylene glycol (OEG) arms are a type of branched multivalent molecule that are effective in killing *P. aeruginosa* planktonic cells and biofilm (Nguyen et al., 2017). These SCPN compounds are made of amine and hydrophobic groups polymerised at a molar ratio of 2.5:1 along with OEG to create a linear random copolymer that collapses into a micelle when in water. Two of these SCPNs, P_{Dab-EH} and P_{Dab-F}, were identified as lead compounds with MIC values of 1.4–2.8 μ M and 2.8–5.6 μ M against *P. aeruginosa*, respectively, and showed good biocompatibility with H4IIE

cells and sheep red blood cells. These compounds were also tested against *P. aeruginosa* PAO1 biofilms at 4 x MIC and CFUs within the biofilm were determined by a drop-plate method. This revealed a 2.6 and 3.3 log₁₀ reduction in biofilm CFUs, respectively, compared to an untreated control after 60 min incubation. Colistin was also tested at 4 x MIC for 60 min but only resulted in <1 log₁₀ reduction. These compounds were also shown to disperse approximately 72% of pre-formed biofilm mass after a 60 min incubation period as determined by a reduction in biofilm biomass via crystal violet staining.

Another AMP dendrimer consisting of Arg-Trp-Arg and Arg-Tbt-Arg (2) (Tbt: β -(2,5,7-tri-*tert*-butylindol-3-yl)alanine) tripeptide branches (called 2D-24), also exhibited antibiofilm activity against *P. aeruginosa* strains PAO1 and PDO300 (Bahar et al., 2015). At a concentration of 20 μ M, 2D-24 killed ~87.8 and ~81.7% of PAO1 and PDO300 biofilm cells respectively as determined via a drop-plate method and live/dead staining using membrane permeable dye SYTO9 and membrane impermeable dye propidium iodide. However, no linear compounds were used as a control. The previously mentioned (RW)_{4D} dendrimer also showed antibiofilm activity towards *E. coli* RP473 (Hou et al., 2009). Biofilm formation on a polystyrene surface was determined by crystal violet staining and was reduced by ~21.8, 47.1, 84.4 and 93.5% by 5, 10, 20 and 40 μ M of (RW)_{4D} respectively after 24 h incubation compared to a 0 μ M control. The aforementioned multivalent AMPs do not have linear analogues to be compared to and with many linear AMPs also showing antibiofilm activity, it is difficult to determine to what extent multimerisation affects antibiofilm activity.

The previously mentioned lin-SB056-1 AMP, however, is an example where the effect of multimerisation on biofilm formation has been demonstrated. The dendrimeric form of this peptide was again synthesised, but this time without the hydrophobic tail, to create (lin-SB056-1)₂-K and was tested against *P. aeruginosa* PAO1 biofilm in *in vivo*-like lung epithelial cell and artificial wound models (Grassi et al., 2019). A combination of lin-SB056-1 and EDTA was also tested as a comparison and combinatorial treatment. EDTA has been shown to break up the biofilm extracellular matrix and disrupt the outer membrane of Gram-negative bacteria, making them more susceptible to AMPs (Banin et al., 2006). At concentrations that caused less than 20% haemolysis and epithelial cell death (lin-SB056-1)₂-K (at 19.25 μ M) proved more effective at reducing the number of biofilm-forming *P. aeruginosa* (determined via drop-plate method and subsequent CFU count) than 38.5 μ M of its linear counterpart combined with 0.3 mM EDTA. After 4 h incubation, lin-SB056-1/EDTA resulted in a 1-Log unit reduction of biofilm-forming bacteria whereas (lin-SB056-1)₂-K resulted in a 2-Log unit reduction.

Another example is the modification of naturally occurring anoplin via substitution of residues 4 and 7 with their D-enantiomers that resulted in a more potent and selective compound named anoplin-D4, 7 (Zhong et al., 2019). This compound was further modified with the addition of different length fatty acids at the N-terminus (C₄, 6, 8, 10 or 12-D4,7).

Additionally, anoplin-D4,7 was also dimerised using copper click chemistry, the N-terminal residues acetylated, and fatty acid chains added to create J-AA-(C₄, 6, 8, 10 or 12-D4,7 + D4,7). Increasing fatty acid chain length led to increasing antimicrobial activity with the dimers being even more potent against a variety of Gram-positive and Gram-negative bacteria. These analogues (both linear and dimeric compounds) were tested for antibiofilm formation against *S. aureus* ATCC 25923, *E. coli* ATCC 25922 and *P. aeruginosa* ATCC 27853. All compounds could inhibit biofilm formation in a dose dependent manner as indicated by crystal violet staining and absorbance compared to a control sample (no peptide added). However, they were tested and compared to each other at 0.25, 0.5, 1 and 2 times their MIC values rather than at equal concentrations which makes it difficult to determine to what extent D-amino acids and dimerisation affect biofilm inhibition. Estimates for C₈-D4,7 and J-AA-(C₈-D4,7 + D4,7) indicate that at equal concentrations the dimerised compounds are more potent at inhibiting biofilm formation in *S. aureus* and *E. coli* but are less potent towards *P. aeruginosa* biofilm compared to their monomer counterpart.

Synergistic Effects of Antimicrobial Peptides

Synergy Between Antimicrobial Peptides and Antibiotics

Clinical use of AMPs alone as a therapeutic still faces some hurdles. However, AMPs as adjuvants for currently used antibiotics may be the first steppingstone to clinical approval. An antimicrobial polymer made up of oligoethylene glycol, hydrophobic and amine groups was tested alongside ten antibiotics (doxycycline, clarithromycin, azithromycin, gentamicin, tobramycin, ampicillin, amoxicillin, ceftriaxone, colistin and ciprofloxacin) that exhibit different modes of action. Out of this group of ten, the polymer only showed synergy with doxycycline and colistin methanesulfonate when tested against *P. aeruginosa* and *E. coli* (Namivandi-Zangeneh et al., 2019). Individually administered, the polymer and doxycycline had MIC values of 32 µg/ml and 8 µg/ml respectively but when used in combination these values were lowered to 8 µg/ml and 1 µg/ml when tested against *P. aeruginosa* PAO1. Against *E. coli* K12, the MIC lowered from 32 µg/ml to 8 µg/ml for the polymer and from 2 µg/ml to 0.5 µg/ml for doxycycline. The mechanisms involved in this synergy are unclear, but it is believed that the polymer increased the uptake of doxycycline via membrane disruption and acted additively with colistin as both compounds act via membrane disruption. However, there was no explanation as to why synergy was not observed with other antibiotics that also act on internal targets, and this may be a result of the size of the pore formed versus the size of the antibiotic.

Delivery of Synergistic Molecules

Given that AMPs can act in synergy with each other and antibiotics, it follows that they must somehow be co-delivered. Nanoparticles and self-assembling compounds are currently being explored as not only delivery vehicles, but as

compounds that also have inherent antibacterial properties. One such example are the previously mentioned star-shaped PLL molecules (also known as multi-armed poly (L-lysine) (MPLL) molecules) which can be crosslinked with poly (ethylene glycol) (PEG) (MPLL-*alt*-PEG) (Lu et al., 2020). The MPLL polymer is positively charged, allowing it to disrupt bacterial membranes, and when crosslinked with PEG can encapsulate negatively charged drugs and self-assemble into micelles. The authors suggested that the cross-linking improves stability of the micelles, allows for more efficient drug loading, and protects the encapsulated drug from degradation and premature release. They also proposed that the cross-linking improves the antibacterial activity of MPLL as it increases the molecular weight, makes it more stable against proteolysis and increases its *in vivo* half-life. Drug release is then based on the pH of the environment. At physiological pH, the MPLL micelles are positively charged and through electrostatic interactions encapsulated the protein tested (interferon α-2b), which is negatively charged. At infectious sites which have an acidic environment, the charge of the encapsulated protein changes from net negative to net positive whilst the side chains of the MPLL molecules remain positively charged. This change in charging state of the protein weakens its electrostatic interaction with the MPLL-*alt*-PEG molecule and results in accelerated drug release. The release rate of interferon α-2b was measured at varying pH and was shown to be fastest at a lower pH. The antimicrobial activity of MPLL was also tested against MRSA and *P. aeruginosa* and compared to the activity of MPLL-*alt*-PEG. The crosslinked MPLL polymers exhibited better antimicrobial activity compared to MPLL alone, with MIC values of 3.8 and 7.5 µM against MRSA and *P. aeruginosa* respectively compared to 7.5 and 15 µM for MPLL alone. Both compounds also exhibited minimal haemolysis with their HC₅₀ values being more than 1,000 µg/ml. Field-emission scanning electron microscopy (FE-SEM) and transmission electron microscopy (TEM) of treated and untreated MRSA and *P. aeruginosa* also revealed that the MPLL-*alt*-PEG molecules inhibited bacteria via a membrane-disruption mechanism.

The previous example demonstrates a possible avenue for co-delivery of an AMP-like compound and an anionic drug based on their electrostatic interaction. However, for synergistic AMPs that are both cationic, an alternative method is required. Nanoparticles can be made from various materials and in addition to inherent antibacterial activity, can also act as a delivery system. Porous silicon nanoparticles (pSiNPs) loaded with the cationic bacterial toxin [KLAKLAK]₂ made of D-amino acids (dKK), and the AMP lactoferrin (KCFQWQRNMRKVRGPPVSCI₁R), is one example (Kwon et al., 2017). In this study, lactoferrin was grafted to dKK which resulted in LACT-dKK that exhibited stronger antibacterial activity than dKK or LACT alone. This tandem peptide was then loaded in pSiNPs and was shown capable of killing *P. aeruginosa*, exhibited low toxicity towards NIH-3T3 cells and low haemolysis. Mice were also treated with unloaded pSiNPs, peptide-pSiNPs, free peptide or PBS (delivered to their lungs via a catheter) and adverse effects to their respiration observed. Compared to the PBS control,

TABLE 2 | Summary of activity of star-shaped antimicrobials^a.

Antimicrobial Activity	Compound name ^b	<i>E. coli</i>	<i>P. aeruginosa</i>	<i>A. baumannii</i>	<i>S. aureus</i>	HC ₅₀
MIC (μg/ml)	L-Lys	64	256		16	
	S-Lys	32	256		16–32	>10,000
	S-GSA 25	>512	>512		32–64	>10,000
MBC (μM)	Lys/Val linear analogue	29.50			213.37	674.5
	S16	0.72	1.42	0.85	4.58	58.3
	S32	0.72	0.97	0.79	2.23	45.3
MIC (μM)	S16_M (14 DP)	0.127				
	S4_M (12 DP)	2.64				
	S4_L (19 DP)	0.56				
MIC (μM)	Linear PLL		5.3	10.5	2.6 (MRSA)	>4,000
	P2 (8 arm, 10 DP)		2.3	4.5	1.1 (MRSA)	>4,000
	P4 (8 arm, 20DP)		2.3	2.3	0.6 (MRSA)	>2000
	P6 (15 arm, 10 DP)		2.4	2.4	1.2 (MRSA)	>2000

The bold values/text is to highlight the compounds, the meaning of each of these is in the text

^aReferences: (Lam et al., 2016a; Shirbin et al., 2018; Lu et al., 2019).

^bHighlighted in orange are the lead compounds for each class of star-shaped antimicrobial.

mice injected with the free peptide displayed laboured breathing whereas those injected with the peptide-pSiNPs showed no adverse respiration. However, hemotoxylin and eosin staining of lung sections revealed mild bronchial epithelial damage in mice treated with peptide-pSiNPs. The free peptide further caused substantial damage to the lungs, including sloughing of the bronchial epithelium, bronchitis, and interstitial pneumonitis. The more severe adverse response caused by the free peptide highlights the multifaceted need for drug carriers to act not only as delivery vehicles, but to also improve the safety profile of potential antibacterial. Whilst delivery systems for synergistic compounds are needed for efficient co-delivery, they can also be beneficial for delivery of single compounds. With many AMPs having short *in vivo* half-lives, being susceptible to proteolysis and toxic to mammalian cells, efficient delivery systems can help mitigate these limitations. They can also help antimicrobials penetrate biofilms and reach therapeutic concentrations at the target site. Reviews by Liu et al., Teixeira et al. and Drayton et al. give a more comprehensive overview of current nanotechnologies being explored as drug delivery vehicles (Drayton et al., 2020; Liu et al., 2019; Teixeira et al., 2020).

CONCLUSION

Much is known about the general properties of AMPs and how they can be manipulated to render them more potent, but this often comes at a cost of increased toxicity. Additionally, there remain the issues of proteolytic instability and reduced activity under physiological conditions and towards biofilms that need to be overcome. Although similar in many respects, the many differences between AMPs means that the modifications that improve activity in some cannot be applied universally and may have limited or detrimental effects on activity of other AMPs. The examples above highlight how dimerisation is not a solution for

all AMPs, and that maximising on each individual feature of natural AMPs – helicity, hydrophobicity, amphipathicity and charge – will not necessarily result in a superior compound. Furthermore, as well as the AMP sequence, the order of the amino acid sequence impacts activity. Sequence modifications that do improve linear peptides, do not always lead to increased improvement when these peptides are multimerised. Multimerisation of weaker, non-modified linear AMPs sometimes results in molecules that are more potent than the multimerised forms of their improved linear analogues. As such, a balance between the different adjustments that can be made to improve AMP activity needs to be achieved.

Research is focusing on structure-activity relationships by altering the overall sequence and structure of AMPs and has shown that multimerisation can result in AMP-like compounds that address the limitations faced by many AMPs. However, many multi-unit AMPs are derived through polymer chemistry, as polymerisation is generally faster and cheaper than peptide synthesis. However, an issue with polymers is that their sequence cannot be controlled, the final structure is not precise and there is only partial control over polymerisation (Kuroda and Caputo, 2013). This leads to a range in their molecular weight; a major issue in drug development and regulation since defined molecular weight materials are required for clinical use. Thus, there is a need for future research to address the ideas behind these architecturally unique compounds and create chemically defined molecules that have the potential to overcome the shortcomings of natural AMPs.

AUTHOR CONTRIBUTIONS

Conceptualization, TM and NO'B-S, writing and original draft preparation TM; writing—review and editing TM, NO'B-S, WL, JH, JL and SH, supervision of TM by NO'B-S, WL, JH, JL and SH. All authors have read and agreed to the published version of the manuscript.

FUNDING

The National Health and Medical Research Council (NHMRC) of Australia and Australian Research Council (ARC) are thanked for financial support over many years for the peptide chemistry and chemical biology studies reported in the authors' laboratories. NO'B-S is the recipient of NHMRC funding (APP1142472, APP1158841, APP1185426), ARC funding (DP210102781, DP160101312, LE200100163), Cancer Council Victoria funding (APP1163284) and Australian Dental Research. Funding in

antimicrobial materials and research is supported by the Centre for Oral Health Research in the Basic and Clinical Oral Sciences Division at The Melbourne Dental School.

SUPPLEMENTARY MATERIAL

The Supplementary Material for this article can be found online at: <https://www.frontiersin.org/articles/10.3389/fchem.2021.795433/full#supplementary-material>

REFERENCES

- Afacan, N. J., Yeung, A. T. Y., Pena, O. M., and Hancock, R. E. W. (2012). Therapeutic Potential of Host Defense Peptides in Antibiotic-Resistant Infections. *Cpd* 18 (6), 807–819. doi:10.2174/138161212799277617
- Avci, F. G., Akbulut, B. S., and Ozkirimli, E. (2018). Membrane Active Peptides and Their Biophysical Characterization. *Biomolecules* 8 (3), 77–44. doi:10.3390/biom8030077
- Bahar, A. A., Liu, Z., Totsingan, F., Buitrago, C., Kallenbach, N., and Ren, D. (2015). Synthetic Dendrimeric Peptide Active against Biofilm and Persister Cells of *Pseudomonas aeruginosa*. *Appl. Microbiol. Biotechnol.* 99 (19), 8125–8135. doi:10.1007/s00253-015-6645-7
- Banin, E., Brady, K. M., and Greenberg, E. P. (2006). Chelator-induced Dispersal and Killing of *Pseudomonas aeruginosa* Cells in a Biofilm. *Appl. Environ. Microbiol.* 72 (3), 2064–2069. doi:10.1128/AEM.72.3.2064-2069.2006
- Batista, C. V., Scaloni, A., Rigden, D. J., Silva, L. R., Rodrigues Romero, A., Dukor, R., et al. (2001). A Novel Heterodimeric Antimicrobial Peptide from the Tree-Frog *Phyllomedusa distincta*. *FEBS Lett.* 494 (1–2), 85–89. doi:10.1016/S0014-5793(01)02324-9
- Batoni, G., Casu, M., Giuliani, A., Luca, V., Maisetta, G., Mangoni, M. L., et al. (2016). Rational Modification of a Dendrimeric Peptide with Antimicrobial Activity: Consequences on Membrane-Binding and Biological Properties. *Amino Acids* 48 (3), 887–900. doi:10.1007/s00726-015-2136-5
- Bi, X., Wang, C., Ma, L., Sun, Y., and Shang, D. (2013). Investigation of the Role of Tryptophan Residues in Cationic Antimicrobial Peptides to Determine the Mechanism of Antimicrobial Action. *J. Appl. Microbiol.* 115 (3), 663–672. doi:10.1111/jam.12262
- Bjarnsholt, T., Alhede, M., Alhede, M., Eickhardt-Sørensen, S. R., Moser, C., Kühl, M., et al. (2013). The *In Vivo* Biofilm. *Trends Microbiol.* 21 (9), 466–474. doi:10.1016/j.tim.2013.06.002
- Blazzyk, J., Wiegand, R., Klein, J., Hammer, J., Epand, R. M., Epand, R. F., et al. (2001). A Novel Linear Amphipathic β -Sheet Cationic Antimicrobial Peptide with Enhanced Selectivity for Bacterial Lipids. *J. Biol. Chem.* 276 (30), 27899–27906. doi:10.1074/jbc.M102865200
- Boudjemaa, R., Cabriel, C., Dubois-Brissonnet, F., Bourg, N., Dupuis, G., Gruss, A., et al. (2018). Impact of Bacterial Membrane Fatty Acid Composition on the Failure of Daptomycin to Kill *Staphylococcus aureus*. *Antimicrob. Agents Chemother.* 62 (7), 1–12. doi:10.1128/AAC.00023-18
- Campopiano, D. J., Clarke, D. J., Polfer, N. C., Barran, P. E., Langley, R. J., Govan, J. R. W., et al. (2004). Structure-Activity Relationships in Defensin Dimers. *J. Biol. Chem.* 279 (47), 48671–48679. doi:10.1074/jbc.M404690200
- Chan, D. I., Prenner, E. J., and Vogel, H. J. (2006). Tryptophan- and Arginine-Rich Antimicrobial Peptides: Structures and Mechanisms of Action. *Biochim. Biophys. Acta (Bba) - Biomembranes* 1758 (9), 1184–1202. doi:10.1016/j.bbame.2006.04.006
- Chen, A., Karanastasis, A., Casey, K. R., Necelis, M., Carone, B. R., Caputo, G. A., et al. (2020). Cationic Molecular Umbrellas as Antibacterial Agents with Remarkable Cell-type Selectivity. *ACS Appl. Mater. Inter.* 12 (19), 21270–21282. doi:10.1021/acsami.9b19076
- Chen, C., Hu, J., Zhang, S., Zhou, P., Zhao, X., Xu, H., et al. (2012). Molecular Mechanisms of Antibacterial and Antitumor Actions of Designed Surfactant-like Peptides. *Biomaterials* 33 (2), 592–603. doi:10.1016/j.biomaterials.2011.09.059
- Chen, S., Shao, X., Xiao, X., Dai, Y., Wang, Y., Xie, J., et al. (2020). Host Defense Peptide Mimicking Peptide Polymer Exerting Fast, Broad Spectrum, and Potent Activities toward Clinically Isolated Multidrug-Resistant Bacteria. *ACS Infect. Dis.* 6 (3), 479–488. doi:10.1021/acscinfecdis.9b00410
- Chen, W., Yang, S., Li, S., Lang, J. C., Mao, C., Kroll, P., et al. (2019). Self-Assembled Peptide Nanofibers Display Natural Antimicrobial Peptides to Selectively Kill Bacteria without Compromising Cytocompatibility. *ACS Appl. Mater. Inter.* 11 (32), 28681–28689. doi:10.1021/acsami.9b09583
- Chen, Y.-F., Lai, Y.-D., Chang, C.-H., Tsai, Y.-C., Tang, C.-C., and Jan, J.-S. (2019). Star-shaped Polypeptides Exhibit Potent Antibacterial Activities. *Nanoscale* 11 (24), 11696–11708. doi:10.1039/C9NR02012H
- Chen, Y., Mant, C. T., Farmer, S. W., Hancock, R. E. W., Vasil, M. L., and Hodges, R. S. (2005). Rational Design of α -Helical Antimicrobial Peptides with Enhanced Activities and Specificity/Therapeutic Index. *J. Biol. Chem.* 280 (13), 12316–12329. doi:10.1074/jbc.M413406200
- Chen, Y., Vasil, A. I., Rehaume, L., Mant, C. T., Burns, J. L., Vasil, M. L., et al. (2006). Comparison of Biophysical and Biologic Properties of Alpha-Helical Enantiomeric Antimicrobial Peptides. *Chem. Biol. Drug Des.* 67 (2), 162–173. doi:10.1111/j.1747-0285.2006.00349.x
- Cheng, J. T. J., Hale, J. D., Elliott, M., Hancock, R. E. W., and Straus, S. K. (2011). The Importance of Bacterial Membrane Composition in the Structure and Function of Aurein 2.2 and Selected Variants. *Biochim. Biophys. Acta (Bba) - Biomembranes* 1808 (3), 622–633. doi:10.1016/j.bbame.2010.11.025
- Cherkasov, A., Hilpert, K., Jenssen, H., Fjell, C. D., Waldbrook, M., Mullaly, S. C., et al. (2009). Use of Artificial Intelligence in the Design of Small Peptide Antibiotics Effective against a Broad Spectrum of Highly Antibiotic-Resistant Superbugs. *ACS Chem. Biol.* 4 (1), 65–74. doi:10.1021/cb800240j
- Chongsiriwatana, N. P., Lin, J. S., Kapoor, R., Wetzler, M., Rea, J. A. C., Didwania, M. K., et al. (2017). Intracellular Biomass Flocculation as a Key Mechanism of Rapid Bacterial Killing by Cationic, Amphipathic Antimicrobial Peptides and Peptoids. *Sci. Rep.* 7 (1), 16718. doi:10.1038/s41598-017-16180-0
- Costa, F., Teixeira, C., Gomes, P., and Martins, M. C. L. (2019). Clinical Application of AMPs. *Curr. Biol.* 26 (Issue 1), 281–298. doi:10.1007/978-981-13-3588-4_15
- Crusca, E., Rezende, A. A., Marchetto, R., Mendes-Giannini, M. J. S., Fontes, W., Castro, M. S., et al. (2011). Influence of N-Terminus Modifications on the Biological Activity, Membrane Interaction, and Secondary Structure of the Antimicrobial Peptide Hylin-A1. *Biopolymers* 96 (1), 41–48. doi:10.1002/bip.21454
- Dalla Serra, M., Cironi, O., Vitale, R. M., Renzone, G., Coraiola, M., Giacometti, A., et al. (2008). Structural Features of Distinctin Affecting Peptide Biological and Biochemical Properties. *Biochemistry* 47 (30), 7888–7899. doi:10.1021/bi800616k
- Dathe, M., Nikolenko, H., Meyer, J., Beyermann, M., and Bienert, M. (2001). Optimization of the Antimicrobial Activity of Magainin Peptides by Modification of Charge. *FEBS Lett.* 501 (2–3), 146–150. doi:10.1016/S0014-5793(01)02648-5
- Dempsey, C. E., Ueno, S., and Avison, M. B. (2003). Enhanced Membrane Permeabilization and Antibacterial Activity of a Disulfide-Dimerized Magainin Analogue. *Biochemistry* 42 (2), 402–409. doi:10.1021/bi026328h
- Dennison, S., Wallace, J., Harris, F., and Phoenix, D. (2005). Amphiphilic α -Helical Antimicrobial Peptides and Their Structure/Function Relationships. *Ppl* 12 (1), 31–39. doi:10.2174/0929866053406084

- Deslouches, B., Phadke, S. M., Lazarevic, V., Cascio, M., Islam, K., Montelaro, R. C., et al. (2005). De Novo generation of Cationic Antimicrobial Peptides: Influence of Length and Tryptophan Substitution on Antimicrobial Activity. *Antimicrob. Agents Chemother.* 49 (1), 316–322. doi:10.1128/AAC.49.1.316-322.2005
- Dong, W., Zhu, X., Zhou, X., Yang, Y., Yan, X., Sun, L., et al. (2018). Potential Role of a Series of Lysine-leucine-Rich Antimicrobial Peptide in Inhibiting Lipopolysaccharide-Induced Inflammation. *Biochem. J.* 475 (22), 3687–3706. doi:10.1042/BCJ20180483
- Drayton, M., Kizhakkedathu, J. N., and Straus, S. K. (2020). Towards Robust Delivery of Antimicrobial Peptides to Combat Bacterial Resistance. *Molecules* 25 (13), 3048. doi:10.3390/molecules25133048
- Edwards, I. A., Elliott, A. G., Kavanagh, A. M., Zuegg, J., Blaskovich, M. A. T., and Cooper, M. A. (2016). Contribution of Amphipathicity and Hydrophobicity to the Antimicrobial Activity and Cytotoxicity of β -Hairpin Peptides. *ACS Infect. Dis.* 2 (6), 442–450. doi:10.1021/acsinfectdis.6b00045
- Frederiksen, N., Hansen, P. R., Björklund, F., and Franzky, H. (2019). Peptide/peptid Hybrid Oligomers: the Influence of Hydrophobicity and Relative Side-Chain Length on Antibacterial Activity and Cell Selectivity. *Molecules* 24 (24), 4429. doi:10.3390/molecules24244429
- Frieden, C. D. C. (2019). “Antibiotic Resistance Threats in the United States,” in *Centers for Disease Control and Prevention* (Atlanta, GA: U.S. Department of Health and Human Services). Available at: <https://www.cdc.gov/drugresistance/biggest-threats.html>.
- Gagnon, M.-C., Strandberg, E., Grau-Campistany, A., Wadhvani, P., Reichert, J., Bürck, J., et al. (2017). Influence of the Length and Charge on the Activity of α -Helical Amphipathic Antimicrobial Peptides. *Biochemistry* 56 (11), 1680–1695. doi:10.1021/acs.biochem.6b01071
- Giuliani, A., and Rinaldi, A. C. (2011). Beyond Natural Antimicrobial Peptides: Multimeric Peptides and Other Peptidomimetic Approaches. *Cell. Mol. Life Sci.* 68 (13), 2255–2266. doi:10.1007/s00018-011-0717-3
- Gordon, Y. J., Romanowski, E. G., and McDermott, A. M. (2005). A Review of Antimicrobial Peptides and Their Therapeutic Potential as Anti-infective Drugs. *Curr. Eye Res.* 30 (7), 505–515. doi:10.1080/02713680590968637
- Gou, S., Li, B., Ouyang, X., Ba, Z., Zhong, C., and Ni, J. (2021). Tuning the Activity of Anoplin by Dendrimerization of Lysine and Lipidation of the N-Terminal. *ACS Omega* 6 (33), 21359–21367. doi:10.1021/acsomega.1c01854
- Grassi, L., Batoni, G., Ostyn, L., Rigole, P., Van Den Bossche, S., Rinaldi, A. C., et al. (2019). The Antimicrobial Peptide Lin-Sb056-1 and its Dendrimeric Derivative Prevent *Pseudomonas aeruginosa* Biofilm Formation in Physiologically Relevant Models of Chronic Infections. *Front. Microbiol.* 10 (FEB), 1–14. doi:10.3389/fmicb.2019.00198
- Gusman, H., Grogan, J., Kagan, H. M., Troxler, R. F., and Oppenheim, F. G. (2001). Salivary Histatin 5 Is a Potent Competitive Inhibitor of the Cysteine Proteinase Clostripain. *FEBS Lett.* 489 (1), 97–100. doi:10.1016/S0014-5793(01)02077-4
- Hale, J. D., and Hancock, R. E. (2007). Alternative Mechanisms of Action of Cationic Antimicrobial Peptides on Bacteria. *Expert Rev. Anti-Infective Ther.* 5 (6), 951–959. doi:10.1586/14787210.5.6.951
- Han, X., Kou, Z., Jiang, F., Sun, X., and Shang, D. (2020). Interactions of Designed Trp-Containing Antimicrobial Peptides with DNA of Multidrug-Resistant *pseudomonas aeruginosa*. *DNA Cel Biol.* 40 (00), 414–424. doi:10.1089/dna.2019.4874
- Hancock, R. E. W., and Lehrer, R. (1998). Cationic Peptides: A New Source of Antibiotics. *Trends Biotechnol.* 16 (2), 82–88. doi:10.1016/S0167-7799(97)01156-6
- Hancock, R. E. W., and Sahl, H.-G. (2006). Antimicrobial and Host-Defense Peptides as New Anti-infective Therapeutic Strategies. *Nat. Biotechnol.* 24 (12), 1551–1557. doi:10.1038/nbt1267
- Hilpert, K., Volkmer-Engert, R., Walter, T., and Hancock, R. E. W. (2005). High-throughput Generation of Small Antibacterial Peptides with Improved Activity. *Nat. Biotechnol.* 23 (8), 1008–1012. doi:10.1038/nbt1113
- Hoffknecht, B. C., Worm, D. J., Bobersky, S., Prochnow, P., Bandow, J. E., and Metzler-Nolte, N. (2015). Influence of the Multivalency of Ultrashort Arg-Trp-Based Antimicrobial Peptides (AMP) on Their Antibacterial Activity. *ChemMedChem* 10 (9), 1564–1569. doi:10.1002/cmdc.201500220
- Hong, S. (2001). The Effect of Charge Increase on the Specificity and Activity of a Short Antimicrobial Peptide. *Peptides* 22 (10), 1669–1674. doi:10.1016/S0196-9781(01)00502-2
- Hou, S., Zhou, C., Liu, Z., Young, A. W., Shi, Z., Ren, D., et al. (2009). Antimicrobial Dendrimer Active against *Escherichia coli* Biofilms. *Bioorg. Med. Chem. Lett.* 19 (18), 5478–5481. doi:10.1016/j.bmcl.2009.07.077
- Huang, J., Hao, D., Chen, Y., Xu, Y., Tan, J., Huang, Y., et al. (2011). Inhibitory Effects and Mechanisms of Physiological Conditions on the Activity of Enantiomeric Forms of an α -helical Antibacterial Peptide against Bacteria. *Peptides* 32 (7), 1488–1495. doi:10.1016/j.peptides.2011.05.023
- Huang, Y., He, L., Li, G., Zhai, N., Jiang, H., and Chen, Y. (2014). Role of Helicity of α -helical Antimicrobial Peptides to Improve Specificity. *Protein Cell* 5 (8), 631–642. doi:10.1007/s13238-014-0061-0
- Interagency Coordination Group on Antimicrobial Resistance (2019). “No Time to Wait: Securing the Future from Drug-Resistant Infections,” in *World Health Organisation* (Atlanta, GA: United Nations Interagency Coordination Group on Antimicrobial Resistance). Available at: <https://www.who.int/antimicrobial-resistance/interagency-coordination-group/final-report/en/>.
- Jiang, W., Xiao, X., Wu, Y., Zhang, W., Cong, Z., Liu, J., et al. (2020). Peptide Polymer Displaying Potent Activity against Clinically Isolated Multidrug Resistant *Pseudomonas aeruginosa* In Vitro and In Vivo. *Biomater. Sci.* 8 (2), 739–745. doi:10.1039/C9BM01726G
- Jiang, Z., Vasil, A. I., Hale, J. D., Hancock, R. E. W., Vasil, M. L., and Hodges, R. S. (2008). Effects of Net Charge and the Number of Positively Charged Residues on the Biological Activity of Amphipathic α -helical Cationic Antimicrobial Peptides. *Biopolymers* 90 (3), 369–383. doi:10.1002/bip.20911
- Jin, Y., Hammer, J., Pate, M., Zhang, Y., Zhu, F., Zmuda, E., et al. (2005). Antimicrobial Activities and Structures of Two Linear Cationic Peptide Families with Various Amphipathic β -Sheet and α -Helical Potentials. *Antimicrob. Agents Chemother.* 49 (12), 4957–4964. doi:10.1128/AAC.49.12.4957-4964.2005
- Juretić, D., and Simunić, J. (2019). Design of α -helical Antimicrobial Peptides with a High Selectivity index. *Expert Opin. Drug Discov.* 14 (10), 1053–1063. doi:10.1080/17460441.2019.1642322
- Kamysz, E., Sikorska, E., Jaśkiewicz, M., Bauer, M., Neubauer, D., Bartoszewska, S., et al. (2020). Lipidated Analogs of the LL-37-Derived Peptide Fragment KR12-Structural Analysis, Surface-Active Properties and Antimicrobial Activity. *Ijms* 21 (3), 887. doi:10.3390/ijms21030887
- Koebach, J., and Craik, D. J. (2019). The Vast Structural Diversity of Antimicrobial Peptides. *Trends Pharmacol. Sci.* 40 (7), 517–528. doi:10.1016/j.tips.2019.04.012
- Kornmueller, K., Lehofer, B., Leitinger, G., Amenitsch, H., and Prassl, R. (2018). Peptide Self-Assembly into Lamellar Phases and the Formation of Lipid-Peptide Nanostructures. *Nano Res.* 11 (2), 913–928. doi:10.1007/s12274-017-1702-4
- Kragol, G., Lovas, S., Varadi, G., Condie, B. A., Hoffmann, R., and Otvos, L. (2001). The Antibacterial Peptide Pyrrocoricin Inhibits the ATPase Actions of DnaK and Prevents Chaperone-Assisted Protein Folding. *Biochemistry* 40 (10), 3016–3026. doi:10.1021/bi002656a
- Krizsan, A., Volke, D., Weinert, S., Sträter, N., Knappe, D., and Hoffmann, R. (2014). Insect-derived Proline-Rich Antimicrobial Peptides Kill Bacteria by Inhibiting Bacterial Protein Translation at the 70 S Ribosome. *Angew. Chem. Int. Ed.* 53 (45), 12236–12239. doi:10.1002/anie.201407145
- Kumar, P., Kizhakkedathu, J., and Straus, S. (2018). Antimicrobial Peptides: Diversity, Mechanism of Action and Strategies to Improve the Activity and Biocompatibility In Vivo. *Biomolecules* 8 (1), 4. doi:10.3390/biom8010004
- Kumar, P., Pletzer, D., Haney, E. F., Rahanjam, N., Cheng, J. T. J., Yue, M., et al. (2019). Aurein-derived Antimicrobial Peptides Formulated with Pegylated Phospholipid Micelles to Target Methicillin-Resistant *Staphylococcus aureus* Skin Infections. *ACS Infect. Dis.* 5 (3), 443–453. doi:10.1021/acsinfectdis.8b00319
- Kumar, P., Takayasu, A., Abbasi, U., Kalathottukaren, M. T., Abbina, S., Kizhakkedathu, J. N., et al. (2017). Antimicrobial Peptide-Polymer Conjugates with High Activity: Influence of Polymer Molecular Weight and Peptide Sequence on Antimicrobial Activity, Proteolysis, and Biocompatibility. *ACS Appl. Mater. Inter.* 9 (43), 37575–37586. doi:10.1021/acsami.7b09471
- Kuroda, K., and Caputo, G. A. (2013). Antimicrobial Polymers as Synthetic Mimics of Host-Defense Peptides. *WIREs Nanomed Nanobiotechnol* 5 (1), 49–66. doi:10.1002/wnan.1199
- Kwon, E. J., Skalak, M., Bertucci, A., Braun, G., Ricci, F., Ruoslahti, E., et al. (2017). Porous Silicon Nanoparticle Delivery of Tandem Peptide Anti-Infectives for the

- Treatment of *Pseudomonas aeruginosa* Lung Infections. *Adv. Mater.* 29 (35), 1701527. doi:10.1002/adma.201701527
- Lam, S. J., O'Brien-Simpson, N. M., Pantarat, N., Sulistio, A., Wong, E. H. H., Chen, Y.-Y., et al. (2016a). Combating Multidrug-Resistant Gram-Negative Bacteria with Structurally Nanoengineered Antimicrobial Peptide Polymers. *Nat. Microbiol.* 1 (11), 16162. doi:10.1038/nmicrobiol.2016.162
- Lam, S. J., Wong, E. H. H., O'Brien-Simpson, N. M., Pantarat, N., Blencowe, A., Reynolds, E. C., et al. (2016b). Bionano Interaction Study on Antimicrobial Star-Shaped Peptide Polymer Nanoparticles. *ACS Appl. Mater. Inter.* 8 (49), 33446–33456. doi:10.1021/acsami.6b11402
- Li, L., Vorobyov, I., and Allen, T. W. (2013). The Different Interactions of Lysine and Arginine Side Chains with Lipid Membranes. *J. Phys. Chem. B* 117 (40), 11906–11920. doi:10.1021/jp405418y
- Li, W., O'Brien-Simpson, N. M., Tailhades, J., Pantarat, N., Dawson, R. M., Otvos, L., et al. (2015). Multimerization of a Proline-Rich Antimicrobial Peptide, Chex-Arg20, Alters its Mechanism of Interaction with the *Escherichia coli* Membrane. *Chem. Biol.* 22 (9), 1250–1258. doi:10.1016/j.chembiol.2015.08.011
- Li, W., Sani, M.-A., Jamasbi, E., Otvos, L., Hossain, M. A., Wade, J. D., et al. (2016). Membrane Interactions of Proline-Rich Antimicrobial Peptide, Chex1-Arg20, Multimers. *Biochim. Biophys. Acta (Bba) - Biomembranes* 1858 (6), 1236–1243. doi:10.1016/j.bbamem.2016.02.035
- Li, W., Separovic, F., O'Brien-Simpson, N. M., and Wade, J. D. (2021). Chemically Modified and Conjugated Antimicrobial Peptides against Superbugs. *Chem. Soc. Rev.* 50 (8), 4932–4973. doi:10.1039/d0cs01026j
- Li, W., Tailhades, J., O'Brien-Simpson, N. M., Separovic, F., Otvos, L., Hossain, M. A., et al. (2014). Proline-rich Antimicrobial Peptides: Potential Therapeutics against Antibiotic-Resistant Bacteria. *Amino Acids* 46 (10), 2287–2294. doi:10.1007/s00726-014-1820-1
- Lind, T. K., Darré, L., Domene, C., Urbanczyk-Lipkowska, Z., Cárdenas, M., and Wacklin, H. P. (2015). Antimicrobial Peptide Dendrimer Interacts with Phosphocholine Membranes in a Fluidity Dependent Manner: A Neutron Reflection Study Combined with Molecular Dynamics Simulations. *Biochim. Biophys. Acta (Bba) - Biomembranes* 1848 (10), 2075–2084. doi:10.1016/j.bbamem.2015.05.015
- Lind, T. K., Zielińska, P., Wacklin, H. P., Urbanczyk-Lipkowska, Z., and Cárdenas, M. (2014). Continuous Flow Atomic Force Microscopy Imaging Reveals Fluidity and Time-dependent Interactions of Antimicrobial Dendrimer with Model Lipid Membranes. *ACS Nano* 8 (1), 396–408. doi:10.1021/nn404530z
- Liu, L., Fang, Y., and Wu, J. (2013). Flexibility Is a Mechanical Determinant of Antimicrobial Activity for Amphipathic Cationic α -helical Antimicrobial Peptides. *Biochim. Biophys. Acta (Bba) - Biomembranes* 1828 (11), 2479–2486. doi:10.1016/j.bbamem.2013.06.017
- Liu, S. P., Zhou, L., Lakshminarayanan, R., and Beuerman, R. W. (2010). Multivalent Antimicrobial Peptides as Therapeutics: Design Principles and Structural Diversities. *Int. J. Pept. Res. Ther.* 16 (3), 199–213. doi:10.1007/s10989-010-9230-z
- Liu, Y., Shi, L., Su, L., Van der Mei, H. C., Jutte, P. C., Ren, Y., et al. (2019). Nanotechnology-based Antimicrobials and Delivery Systems for Biofilm-Infection Control. *Chem. Soc. Rev.* 48 (2), 428–446. doi:10.1039/c7cs00807d
- Liu, Z., Brady, A., Young, A., Rasimick, B., Chen, K., Zhou, C., et al. (2007a). Length Effects in Antimicrobial Peptides of the (RW) N Series. *Antimicrob. Agents Chemother.* 51 (2), 597–603. doi:10.1128/AAC.00828-06
- Liu, Z., Young, A. W., Hu, P., Rice, A. J., Zhou, C., Zhang, Y., et al. (2007b). Tuning the Membrane Selectivity of Antimicrobial Peptides by Using Multivalent Design. *ChemBioChem* 8 (17), 2063–2065. doi:10.1002/cbic.200700502
- Lombardi, L., Falanga, A., Del Genio, V., and Galdiero, S. (2019). A New Hope: Self-Assembling Peptides with Antimicrobial Activity. *Pharmaceutics* 11 (4), 166. doi:10.3390/pharmaceutics11040166
- Lorenzón, E. N., Ramos, M. A. S., Bauab, T. M., Camargo, I. L. B. C., and Cilli, E. M. (2016). C-terminal Lysine-Linked Magainin 2 with Increased Activity against Multidrug-Resistant Bacteria. *Ppl* 23 (8), 738–747. doi:10.2174/0929866523666160511150907
- Lorenzón, E. N., Sanches, P. R. S., Nogueira, L. G., Bauab, T. M., and Cilli, E. M. (2013). Dimerization of Aurein 1.2: Effects in Structure, Antimicrobial Activity and Aggregation of Cándida Albicans Cells. *Amino Acids* 44 (6), 1521–1528. doi:10.1007/s00726-013-1475-3
- Lu, C., Quan, G., Su, M., Nimmagadda, A., Chen, W., Pan, M., et al. (2019). Molecular Architecture and Charging Effects Enhance the *In Vitro* and *In Vivo* Performance of Multi-Arm Antimicrobial Agents Based on Star-Shaped Poly(L-lysine). *Adv. Therap.* 2 (12), 1900147. doi:10.1002/adtp.201900147
- Lu, C., Wen, T., Zheng, M., Liu, D., Quan, G., Pan, X., et al. (2020). Poly(Ethylene Glycol) Crosslinked Multi-Armed Poly(L-Lysine) with Encapsulating Capacity and Antimicrobial Activity for the Potential Treatment of Infection-Involved Multifactorial Diseases. *Pharmaceutics* 12 (1), 47–14. doi:10.3390/pharmaceutics12010047
- Malekhaia Häfner, S., and Malmsten, M. (2018). Influence of Self-Assembly on the Performance of Antimicrobial Peptides. *Curr. Opin. Colloid Interf. Sci.* 38, 56–79. doi:10.1016/j.cocis.2018.09.002
- Manabe, T., and Kawasaki, K. (2017). D-form KLKLLLLK-NH₂ Peptide Exerts Higher Antimicrobial Properties Than its L-form Counterpart via an Association with Bacterial Cell wall Components. *Sci. Rep.* 7 (March), 1–10. doi:10.1038/srep43384
- Manzo, G., Scoriapino, M. A., Wadhwani, P., Bürck, J., Montaldo, N. P., Pintus, M., et al. (2015). Enhanced Amphiphilic Profile of a Short β -Stranded Peptide Improves its Antimicrobial Activity. *PLOS ONE* 10 (1), e0116379. doi:10.1371/journal.pone.0116379
- Migoń, D., Jaskiewicz, M., Neubauer, D., Bauer, M., Sikorska, E., Kamysz, E., et al. (2019). Alanine Scanning Studies of the Antimicrobial Peptide Aurein 1.2. *Probiotics Antimicro. Prot.* 11 (3), 1042–1054. doi:10.1007/s12602-018-9501-0
- Mojsoska, B., Zuckermann, R. N., and Jenssen, H. (2015). Structure-Activity Relationship Study of Novel Peptoids that Mimic the Structure of Antimicrobial Peptides. *Antimicrob. Agents Chemother.* 59 (7), 4112–4120. doi:10.1128/AAC.00237-15
- Moret, M. A., and Zebende, G. F. (2007). Amino Acid Hydrophobicity and Accessible Surface Area. *Phys. Rev. E* 75 (1), 011920. doi:10.1103/PhysRevE.75.011920
- Nam, H. Y., Choi, J., Kumar, S. D., Nielsen, J. E., Kyeong, M., Wang, S., et al. (2020). Helicity Modulation Improves the Selectivity of Antimicrobial Peptoids. *ACS Infect. Dis.* 6 (10), 2732–2744. doi:10.1021/acsinfectdis.0c00356
- Namivandi-Zangeneh, R., Sadreahmadi, Z., Dutta, D., Willcox, M., Wong, E. H. H., and Boyer, C. (2019). Synergy between Synthetic Antimicrobial Polymer and Antibiotics: a Promising Platform to Combat Multidrug-Resistant Bacteria. *ACS Infect. Dis.* 5 (8), 1357–1365. doi:10.1021/acsinfectdis.9b00049
- Nguyen, L. T., Haney, E. F., and Vogel, H. J. (2011). The Expanding Scope of Antimicrobial Peptide Structures and Their Modes of Action. *Trends Biotechnol.* 29 (9), 464–472. doi:10.1016/j.tibtech.2011.05.001
- Nguyen, T.-K., Lam, S. J., Ho, K. K. K., Kumar, N., Qiao, G. G., Egan, S., et al. (2017). Rational Design of Single-Chain Polymeric Nanoparticles that Kill Planktonic and Biofilm Bacteria. *ACS Infect. Dis.* 3 (3), 237–248. doi:10.1021/acsinfectdis.6b00203
- Oda, Y., Kanaoka, S., Sato, T., Aoshima, S., and Kuroda, K. (2011). Block versus Random Amphiphilic Copolymers as Antibacterial Agents. *Biomacromolecules* 12 (10), 3581–3591. doi:10.1021/bm200780r
- O'Neill, J. (2016). "Tackling Drug-Resistant Infections Globally: Final Report and Recommendations the Review on Antimicrobial Resistance," in *Review on Antimicrobial Resistance* (London, UK: Government of the United Kingdom). Available at: https://amr-review.org/sites/default/files/160525_Final_paper_with_cover.pdf.
- Ortega, M. Á., Guzmán Merino, A., Fraile-Martínez, O., Recio-Ruiz, J., Pekarek, L., Gujjarro, L. L., et al. (2020). Dendrimers and Dendritic Materials: from Laboratory to Medical Practice in Infectious Diseases. *Pharmaceutics* 12 (9), 874. doi:10.3390/pharmaceutics12090874
- Otvos, L., Flick-Smith, H., Fox, M., Ostorhazy, E., Dawson, R., and Wade, J. (2014). The Designer Proline-Rich Antibacterial Peptide A3-APO Prevents Bacillus Anthracis Mortality by Deactivating Bacterial Toxins. *Ppl* 21 (4), 374–381. doi:10.2174/09298665113206660108
- Otvos, L., Jr., and Otvos, L., Jr (2002). The Short Proline-Rich Antibacterial Peptide Family. *Cell Mol. Life Sci. (Cmls)* 59 (7), 1138–1150. doi:10.1007/s00018-002-8493-8
- Otvos, L., Wade, J. D., Lin, F., Condie, B. A., Hanrieder, J., and Hoffmann, R. (2005). Designer Antibacterial Peptides Kill Fluoroquinolone-Resistant Clinical Isolates. *J. Med. Chem.* 48 (16), 5349–5359. doi:10.1021/jm050347i
- Park, C. B., Kim, H. S., and Kim, S. C. (1998). Mechanism of Action of the Antimicrobial Peptide Buforin II: Buforin II Kills Microorganisms by Penetrating the Cell Membrane and Inhibiting Cellular Functions. *Biochem. Biophys. Res. Commun.* 244 (1), 253–257. doi:10.1006/bbrc.1998.8159

- Patch, J. A., and Barron, A. E. (2003). Helical Peptoid Mimics of Magainin-2 Amide. *J. Am. Chem. Soc.* 125 (40), 12092–12093. doi:10.1021/ja037320d
- Patrzykat, A., Friedrich, C. L., Zhang, L., Mendoza, V., and Hancock, R. E. W. (2002). Sublethal Concentrations of Pleurocidin-Derived Antimicrobial Peptides Inhibit Macromolecular Synthesis in *Escherichia coli*. *Antimicrob. Agents Chemother.* 46 (3), 605–614. doi:10.1128/AAC.46.3.605-614.2002
- Qian, Y., Qi, F., Chen, Q., Zhang, Q., Qiao, Z., Zhang, S., et al. (2018). Surface Modified with a Host Defense Peptide-Mimicking β -Peptide Polymer Kills Bacteria on Contact with High Efficacy. *ACS Appl. Mater. Inter.* 10 (18), 15395–15400. doi:10.1021/acsami.8b01117
- Raheem, N., Kumar, P., Lee, E., Cheng, J. T. J., Hancock, R. E. W., and Straus, S. K. (2020). Insights into the Mechanism of Action of Two Analogues of Aurein 2.2. *Biochim. Biophys. Acta (Bba) - Biomembranes* 1862 (6), 183262. doi:10.1016/j.bbame.2020.183262
- Ramezanzadeh, M., Saeedi, N., Mesbahfar, E., Farrokhi, P., Salimi, F., and Rezaei, A. (2021). Design and Characterization of New Antimicrobial Peptides Derived from Aurein 1.2 with Enhanced Antibacterial Activity. *Biochimie* 181, 42–51. doi:10.1016/j.biochi.2020.11.020
- Rončević, T., Vukičević, D., Ilić, N., Krce, L., Gajski, G., Tonkić, M., et al. (2018). Antibacterial Activity Affected by the Conformational Flexibility in Glycine-Lysine Based α -Helical Antimicrobial Peptides. *J. Med. Chem.* 61 (7), 2924–2936. doi:10.1021/acs.jmedchem.7b01831
- Rothbard, J., Jessop, T., and Wender, P. (2005). Adaptive Translocation: the Role of Hydrogen Bonding and Membrane Potential in the Uptake of Guanidinium-Rich Transporters into Cells. *Adv. Drug Deliv. Rev.* 57 (4), 495–504. doi:10.1016/j.addr.2004.10.003
- Rounds, T., and Straus, S. K. (2020). Lipidation of Antimicrobial Peptides as a Design Strategy for Future Alternatives to Antibiotics. *Ijms* 21 (24), 9692. doi:10.3390/ijms21249692
- Saint Jean, K. D., Henderson, K. D., Chrom, C. L., Abiuso, L. E., Renn, L. M., and Caputo, G. A. (2018). Effects of Hydrophobic Amino Acid Substitutions on Antimicrobial Peptide Behavior. *Probiotics Antimicro. Prot.* 10 (3), 408–419. doi:10.1007/s12602-017-9345-z
- Sass, V., Schneider, T., Wilmes, M., Körner, C., Tossi, A., Novikova, N., et al. (2010). Human β -Defensin 3 Inhibits Cell Wall Biosynthesis in Staphylococci. *Infect. Immun.* 78 (6), 2793–2800. doi:10.1128/IAI.00688-09
- Sha, X., Li, P., Feng, Y., Xia, D., Tian, X., Wang, Z., et al. (2020). Self-Assembled Peptide Nanofibrils Designed to Release Membrane-Lysing Antimicrobial Peptides. *ACS Appl. Bio Mater.* 3 (6), 3648–3655. doi:10.1021/acsabm.0c00281
- Shahmiri, M., Cornell, B., and Mechler, A. (2017). Phenylalanine Residues Act as Membrane Anchors in the Antimicrobial Action of Aurein 1.2. *Biointerphases* 12 (5), 05G605. doi:10.1116/1.4995674
- Shai, Y. (2002). Mode of Action of Membrane Active Antimicrobial Peptides. *Biopolymers* 66 (4), 236–248. doi:10.1002/bip.10260
- Shang, D., Li, X., Sun, Y., Wang, C., Sun, L., Wei, S., et al. (2012). Design of Potent, Non-toxic Antimicrobial Agents Based upon the Structure of the Frog Skin Peptide, Temporin-1CEB from Chinese Brown Frog, *Rana chensinensis*. *Chem. Biol. Drug Des.* 79 (5), 653–662. doi:10.1111/j.1747-0285.2012.01363.x
- Shang, D., Zhang, Q., Dong, W., Liang, H., and Bi, X. (2016). The Effects of LPS on the Activity of Trp-Containing Antimicrobial Peptides against Gram-Negative Bacteria and Endotoxin Neutralization. *Acta Biomater.* 33, 153–165. doi:10.1016/j.actbio.2016.01.019
- Shirbin, S. J., Insua, I., Holden, J. A., Lenzo, J. C., Reynolds, E. C., O'Brien-Simpson, N. M., et al. (2018). Architectural Effects of Star-Shaped "Structurally Nanoengineered Antimicrobial Peptide Polymers" (SNAPPs) on Their Biological Activity. *Adv. Healthc. Mater.* 7 (21), 1800627. doi:10.1002/adhm.201800627
- Siliakus, M. F., van der Oost, J., and Kengen, S. W. M. (2017). Adaptations of Archaeal and Bacterial Membranes to Variations in Temperature, pH and Pressure. *Extremophiles* Springer Jpn. 21 (Issue 4), 651–670. doi:10.1007/s00792-017-0939-x
- Singh, J., Mumtaz, S., Joshi, S., and Mukhopadhyay, K. (2020). In Vitro and Ex Vivo Efficacy of Novel Trp-Arg Rich Analogue of α -MSH against *Staphylococcus aureus*. *ACS Omega* 5 (7), 3258–3270. doi:10.1021/acsomega.9b03307
- Sobczak, M., Dębek, C., Olędzka, E., and Kozłowski, R. (2013). Polymeric Systems of Antimicrobial Peptides-Strategies and Potential Applications. *Molecules* 18 (11), 14122–14137. doi:10.3390/molecules181114122
- Sohlenkamp, C., and Geiger, O. (2015). Bacterial Membrane Lipids: Diversity in Structures and Pathways. *FEMS Microbiol. Rev.* 40 (1), 133–159. doi:10.1093/femsre/fuv008
- Stensvåg, K., Haug, T., Sperstad, S. V., Rekdal, Ø., Indrevoll, B., and Styrvoid, O. B. (2008). Arasin 1, a Proline-Arginine-Rich Antimicrobial Peptide Isolated from the Spider Crab, *Hya Araneus*. *Develop. Comp. Immunol.* 32 (3), 275–285. doi:10.1016/j.dci.2007.06.002
- Stone, T. A., Cole, G. B., Ravamehr-Lake, D., Nguyen, H. Q., Khan, F., Sharpe, S., et al. (2019). Positive Charge Patterning and Hydrophobicity of Membrane-Active Antimicrobial Peptides as Determinants of Activity, Toxicity, and Pharmacokinetic Stability. *J. Med. Chem.* 62 (13), 6276–6286. doi:10.1021/acs.jmedchem.9b00657
- Strøm, M. B., Rekdal, Ø., and Svendsen, J. S. (2002). Antimicrobial Activity of Short Arginine- and Tryptophan-Rich Peptides. *J. Pept. Sci.* 8 (8), 431–437. doi:10.1002/psc.398
- Su, X., Zhou, X., Tan, Z., and Zhou, C. (2017). Highly Efficient Antibacterial Diblock Copolypeptides Based on Lysine and Phenylalanine. *Biopolymers* 107 (11), e23041–8. doi:10.1002/bip.23041
- Subbalakshmi, C., and Sitaram, N. (1998). Mechanism of Antimicrobial Action of Indolicidin. *FEMS Microbiol. Lett.* 160 (1), 91–96. doi:10.1016/S0378-1097(98)00008-1
- Takahashi, H., Palermo, E. F., Yasuhara, K., Caputo, G. A., and Kuroda, K. (2013). Molecular Design, Structures, and Activity of Antimicrobial Peptide-Mimetic Polymers. *Macromol. Biosci.* 13 (10), 1285–1299. doi:10.1002/mabi.201300126
- Tam, J. P., Lu, Y.-A., and Yang, J.-L. (2002). Antimicrobial Dendrimeric Peptides. *Eur. J. Biochem.* 269 (3), 923–932. doi:10.1046/j.0014-2956.2001.02728.x
- Tan, J., Huang, J., Huang, Y., and Chen, Y. (2014). Effects of Single Amino Acid Substitution on the Biophysical Properties and Biological Activities of an Amphipathic α -Helical Antibacterial Peptide against Gram-Negative Bacteria. *Molecules* 19 (8), 10803–10817. doi:10.3390/molecules190810803
- Teixeira, M. C., Carbone, C., Sousa, M. C., Espina, M., Garcia, M. L., Sanchez-Lopez, E., et al. (2020). Nanomedicines for the Delivery of Antimicrobial Peptides (AMPs). *Nanomaterials* 10 (3), 560. doi:10.3390/nano10030560
- Tian, X., Sun, F., Zhou, X.-R., Luo, S.-Z., and Chen, L. (2015). Role of Peptide Self-Assembly in Antimicrobial Peptides. *J. Pept. Sci.* 21 (7), 530–539. doi:10.1002/psc.2788
- Torcatto, I. M., Huang, Y.-H., Franquelim, H. G., Gaspar, D., Craik, D. J., Castanho, M. A. R. B., et al. (2013). Design and Characterization of Novel Antimicrobial Peptides, R-Bp100 and RW-Bp100, with Activity against Gram-Negative and Gram-Positive Bacteria. *Biochim. Biophys. Acta (Bba) - Biomembranes* 1828 (3), 944–955. doi:10.1016/j.bbame.2012.12.002
- Wang, G., Li, X., and Wang, Z. (2016). APD3: the Antimicrobial Peptide Database as a Tool for Research and Education. *Nucleic Acids Res.* 44 (D1), D1087–D1093. doi:10.1093/nar/gkv1278
- Wang, J., Liu, K., Xing, R., and Yan, X. (2016). Peptide Self-Assembly: Thermodynamics and Kinetics. *Chem. Soc. Rev.* 45 (20), 5589–5604. doi:10.1039/C6CS00176A
- Welch, N. G., Li, W., Hossain, M. A., Separovic, F., O'Brien-Simpson, N. M., and Wade, J. D. (2020). (Re)Defining the Proline-Rich Antimicrobial Peptide Family and the Identification of Putative New Members. *Front. Chem.* 8, 607769. doi:10.3389/fchem.2020.607769
- Wimley, W. C. (2010). Describing the Mechanism of Antimicrobial Peptide Action with the Interfacial Activity Model. *ACS Chem. Biol.* 5 (10), 905–917. doi:10.1021/cb1001558
- Wiradharma, N., Liu, S.-Q., and Yang, Y.-Y. (2012). Branched and 4-Arm Starlike α -Helical Peptide Structures with Enhanced Antimicrobial Potency and Selectivity. *Small* 8 (3), 362–366. doi:10.1002/sml.201101672
- Wong, E. H. H., Khin, M. M., Ravikumar, V., Si, Z., Rice, S. A., and Chan-Park, M. B. (2016). Modulating Antimicrobial Activity and Mammalian Cell Biocompatibility with Glucosamine-Functionalized star Polymers. *Macromolecules* 49 (3), 1170–1178. doi:10.1021/acs.biomac.5b01766
- Yang, N., Wang, X., Teng, D., Mao, R., Hao, Y., Feng, X., et al. (2017). Deleting the First Disulphide Bond in an Arenicin Derivative Enhances its Expression in *Pichia pastoris*. *Let. Appl. Microbiol.* 65 (3), 241–248. doi:10.1111/lam.12770
- Yang, S.-T., Kim, J. I., and Shin, S. Y. (2009). Effect of Dimerization of a β -turn Antimicrobial Peptide, PST13-RK, on Antimicrobial Activity and Mammalian Cell Toxicity. *Biotechnol. Lett.* 31 (2), 233–237. doi:10.1007/s10529-008-9848-5

- Yang, Z., He, S., Wu, H., Yin, T., Wang, L., and Shan, A. (2021). Nanostructured Antimicrobial Peptides: Crucial Steps of Overcoming the Bottleneck for Clinics. *Front. Microbiol.* 12. doi:10.3389/fmicb.2021.710199
- Zasloff, M. (2002). Antimicrobial Peptides of Multicellular Organisms. *Nature* 415 (6870), 389–395. doi:10.1038/415389a
- Zelezetsky, I., and Tossi, A. (2006). Alpha-helical Antimicrobial Peptides-Using a Sequence Template to Guide Structure-Activity Relationship Studies. *Biochim. Biophys. Acta (Bba) - Biomembranes* 1758 (9), 1436–1449. doi:10.1016/j.bbame.2006.03.021
- Zhang, L., Falla, T., Wu, M., Fidai, S., Burian, J., Kay, W., et al. (1998). Determinants of Recombinant Production of Antimicrobial Cationic Peptides and Creation of Peptide Variants in Bacteria. *Biochem. Biophysical Res. Commun.* 247 (3), 674–680. doi:10.1006/bbrc.1998.8848
- Zhang, Q., Ma, P., Xie, J., Zhang, S., Xiao, X., Qiao, Z., et al. (2019). Host Defense Peptide Mimicking Poly- β -Peptides with Fast, Potent and Broad Spectrum Antibacterial Activities. *Biomater. Sci.* 7 (5), 2144–2151. doi:10.1039/c9bm00248k
- Zhang, R., Wu, F., Wu, L., Tian, Y., Zhou, B., Zhang, X., et al. (2018). Novel Self-Assembled Micelles Based on Cholesterol-Modified Antimicrobial Peptide (DP7) for Safe and Effective Systemic Administration in Animal Models of Bacterial Infection. *Antimicrob. Agents Chemother.* 62 (11), 1–13. doi:10.1128/AAC.00368-18
- Zhang, S.-K., Song, J.-w., Gong, F., Li, S.-B., Chang, H.-Y., Xie, H.-M., et al. (2016). Design of an α -helical Antimicrobial Peptide with Improved Cell-Selective and Potent Anti-biofilm Activity. *Sci. Rep.* 6 (1), 27394. doi:10.1038/srep27394
- Zhong, C., Liu, T., Gou, S., He, Y., Zhu, N., Zhu, Y., et al. (2019). Design and Synthesis of New N-Terminal Fatty Acid Modified-Antimicrobial Peptide Analogues with Potent *In Vitro* Biological Activity. *Eur. J. Med. Chem.* 182, 111636. doi:10.1016/j.ejmech.2019.111636
- Zhou, C., Qi, X., Li, P., Chen, W. N., Mouad, L., Chang, M. W., et al. (2010). High Potency and Broad-Spectrum Antimicrobial Peptides Synthesized via Ring-Opening Polymerization of α -Aminoacid-N-carboxyanhydrides. *Biomacromolecules* 11 (1), 60–67. doi:10.1021/bm900896h
- Zhu, J., Han, H., Li, F., Wang, X., Yu, J., Chu, C.-C., et al. (2019). Self-assembly of Amino Acid-Based Random Copolymers for Antibacterial Application and Infection Treatment as Nanocarriers. *J. Colloid Interf. Sci.* 540, 634–646. doi:10.1016/j.jcis.2018.12.091
- Zhu, Y., Mohapatra, S., and Weisshaar, J. C. (2019). Rigidification of the *Escherichia coli* Cytoplasm by the Human Antimicrobial Peptide LL-37 Revealed by Superresolution Fluorescence Microscopy. *Proc. Natl. Acad. Sci. USA* 116 (3), 1017–1026. doi:10.1073/pnas.1814924116
- Zou, P., Chen, W.-T., Sun, T., Gao, Y., Li, L.-L., and Wang, H. (2020). Recent Advances: Peptides and Self-Assembled Peptide-Nanosystems for Antimicrobial Therapy and diagnosis. *Biomater. Sci.* 8 (18), 4975–4996. doi:10.1039/d0bm00789g
- Zweytick, D., Deutsch, G., Andrä, J., Blondelle, S. E., Vollmer, E., Jerala, R., et al. (2011). Studies on Lactoferricin-Derived *Escherichia coli* Membrane-Active Peptides Reveal Differences in the Mechanism of N-Acylated versus Nonacylated Peptides. *J. Biol. Chem.* 286 (24), 21266–21276. doi:10.1074/jbc.M110.195412

Conflict of Interest: The authors declare that the research was conducted in the absence of any commercial or financial relationships that could be construed as a potential conflict of interest.

Publisher's Note: All claims expressed in this article are solely those of the authors and do not necessarily represent those of their affiliated organizations, or those of the publisher, the editors and the reviewers. Any product that may be evaluated in this article, or claim that may be made by its manufacturer, is not guaranteed or endorsed by the publisher.

Copyright © 2022 Matthyssen, Li, Holden, Lenzo, Hadjigol and O'Brien-Simpson. This is an open-access article distributed under the terms of the Creative Commons Attribution License (CC BY). The use, distribution or reproduction in other forums is permitted, provided the original author(s) and the copyright owner(s) are credited and that the original publication in this journal is cited, in accordance with accepted academic practice. No use, distribution or reproduction is permitted which does not comply with these terms.



Functional Effects of ARV-1502 Analogs Against Bacterial Hsp70 and Implications for Antimicrobial Activity

Alexandra Brakel^{1,2*}, Lisa Kolano^{1,2}, Carl N. Kraus³, Laszlo Otvos Jr^{3,4} and Ralf Hoffmann^{1,2*}

¹Faculty of Chemistry and Mineralogy, Institute of Bioanalytical Chemistry, Universität Leipzig, Leipzig, Germany, ²Center for Biotechnology and Biomedicine, Universität Leipzig, Leipzig, Germany, ³Aceragen, Inc., Durham, NC, United States, ⁴Institute of Medical Microbiology, Semmelweis University, Budapest, Hungary

OPEN ACCESS

Edited by:

Maria Luisa Mangoni,
Sapienza University of Rome, Italy

Reviewed by:

Berthony Deslouches,
University of Pittsburgh, United States
Francesco Merlino,
University of Naples Federico II, Italy

*Correspondence:

Alexandra Brakel
bioanaly@rz.uni-leipzig.de
Ralf Hoffmann
bioanaly@rz.uni-leipzig.de

Specialty section:

This article was submitted to
Chemical Biology,
a section of the journal
Frontiers in Chemistry

Received: 19 October 2021

Accepted: 11 January 2022

Published: 09 February 2022

Citation:

Brakel A, Kolano L, Kraus CN, Otvos L
and Hoffmann R (2022) Functional
Effects of ARV-1502 Analogs Against
Bacterial Hsp70 and Implications for
Antimicrobial Activity.
Front. Chem. 10:798006.
doi: 10.3389/fchem.2022.798006

The antimicrobial peptide (AMP) ARV-1502 was designed based on naturally occurring short proline-rich AMPs, including pyrrhocoricin and drosocin. Identification of chaperone DnaK as a therapeutic target in *Escherichia coli* triggered intense research on the ligand-DnaK-interactions using fluorescence polarization and X-ray crystallography to reveal the binding motif and characterize the influence of the chaperone on protein refolding activity, especially in stress situations. In continuation of this research, 182 analogs of ARV-1502 were designed by substituting residues involved in antimicrobial activity against Gram-negative pathogens. The peptides synthesized on solid-phase were examined for their binding to *E. coli* and *S. aureus* DnaK providing 15 analogs with improved binding characteristics for at least one DnaK. These 15 analogs were distinguished from the original sequence by their increased hydrophobicity parameters. Additionally, the influence of the entire DnaK chaperone system, including co-chaperones DnaJ and GrpE on refolding and ATPase activity, was investigated. The increasingly hydrophobic peptides showed a stronger inhibitory effect on the refolding activity of *E. coli* chaperones, reducing protein refolding by up to 64%. However, these more hydrophobic peptides had only a minor effect on the ATPase activity. The most dramatic changes on the ATPase activity involved peptides with aspartate substitutions. Interestingly, these peptides resulted in a 59% reduction of the ATPase activity in the *E. coli* chaperone system whereas they stimulated the ATPase activity in the *S. aureus* system up to 220%. Of particular note is the improvement of the antimicrobial activity against *S. aureus* from originally >128 µg/mL to as low as 16 µg/mL. Only a single analog exhibited improved activity over the original value of 8 µg/mL against *E. coli*. Overall, the various moderate-throughput screenings established here allowed identifying (un)favored substitutions on 1) DnaK binding, 2) the ATPase activity of DnaK, 3) the refolding activity of DnaK alone or together with co-chaperones, and 4) the antimicrobial activity against both *E. coli* and *S. aureus*.

Keywords: proline-rich antimicrobial peptide (PrAMP), Chex1-Arg20, 70 kDa heat shock protein DnaK, co-chaperones DnaJ and GrpE, ATPase activity, refolding, *Escherichia coli*, *Staphylococcus aureus*

1 INTRODUCTION

Proline-rich antimicrobial peptides (PrAMP) have been intensively studied with special emphasis on their mode of action, protease stability, and toxicity (Scocchi et al., 2011; Hansen et al., 2012; Li et al., 2014; Böttger et al., 2017). Peptide Chex1-Arg20 (recently termed ARV-1502; Chex-RDPKPRPYLPRPRPPVR-NH₂; Chex denotes 1-amino-cyclohexane carboxylic acid) and its dimer A3-APO were designed based on a sequence comparison of different naturally occurring PrAMPs, such as pyrrhocoricin and drosocin (Otvos et al., 2005; Noto et al., 2008), to obtain analogs with improved preclinical properties against various infections. In diverse studies, ranging from MICs to infection models and finally pharmacokinetics, ARV-1502 proved to be a very promising candidate against infections induced by Enterobacteriaceae (Ostorhazi et al., 2017; Otvos et al., 2018; Brakel et al., 2019). Its binding to the bacterial chaperone DnaK, which was first identified as the lethal target but is currently considered as a secondary, non-lethal, target after the 70S ribosome, was thoroughly investigated (Zahn et al., 2013). ARV-1502 binds *via* residues YLPRP to the hydrophobic pocket of the 27 kDa C-terminal substrate binding domain (SBD) of DnaK influencing its functional activity (Zahn et al., 2013). These residues are also involved in the *in vitro* antimicrobial activity of pyrrhocoricin analogs (Cassone et al., 2008). DnaK belongs to the highly conserved family of 70 kDa heat shock proteins and acts as a molecular chaperone, supporting protein folding, especially in stress conditions (Mayer and Bukau, 2005). DnaK is an ATP-dependent enzyme, with the ATPase activity located in the 42 kDa N-terminal nucleotide binding domain (NBD) (Szabo et al., 1994). The intrinsic ATPase activity of DnaK is low, but it can be accelerated *in vitro* by co-chaperones DnaJ and GrpE (Chang et al., 2008). The rate-limiting step is the release of the ADP generated after hydrolysis of ATP, whereby DnaK transitions from the high (ADP-bound) to the low peptide affinity state (ATP-bound). The nucleotide exchange factor GrpE supports this step initiating a new cycle (Harrison and Kuriyan, 1997; Brehmer et al., 2001), which starts with Hsp40 chaperone transferring a peptide or a protein to the opened SBD of DnaK (Han and Christen, 2003). Since both DnaK and DnaJ prefer hydrophobic protein and peptide sequences, especially sequences containing leucine and phenylalanine, DnaJ is able to pre-select the substrates (Brehmer et al., 2001). In addition, the J-domain of DnaJ stimulates the ATP hydrolysis of DnaK by binding to its NBD (Karzai and McMacken, 1996). Due to the allosteric coupling of NBD and SBD, the C-terminal lid closes initiating a proper folding of the protein. Unlike ATP hydrolysis, protein folding requires the presence of co-chaperones (Mayer and Bukau, 2005). The interaction between the 70 kDa chaperone and its co-chaperones has been extensively studied in recent years using the *E. coli* DnaK system (Li et al., 2016). *E. coli* DnaK exhibits high homology to the 70 kDa chaperones of other organisms including mammals and humans (Winardhi et al., 2018). As the human chaperone Hsp70 is also associated with misfolding diseases (e.g., Huntington's disease) and cancer, it

appears to be a promising pharmaceutical target to inhibit the cellular chaperone machinery (Mosser and Morimoto, 2004; Schlecht et al., 2013). Molecular insights into the substrate-target interactions are very useful for a rational inhibitor design. PrAMPs are excellent DnaK substrates and are additionally interesting drug options due to their good antimicrobial and host defense activities. This study describes the influence of PrAMP ARV-1502 and 182 substituted analogs on the chaperone system of the Gram-negative bacterium *E. coli* and the Gram-positive bacterium *S. aureus* to identify amino acid substitutions affecting the functional properties of different DnaK alleles. Moreover, the relationship between the influence on the protein refolding activity and the antimicrobial activity of the novel peptides was thoroughly examined.

MATERIALS AND METHODS

Reagents

Ammonium heptamolybdate tetrahydrate (>99%), dithiothreitol (DTT, >99%), glycerol (>99.5%), LB-broth, D-luciferin sodium salt (>99%), lysozyme (≥45,000 FIP U/mg), malachite green oxalate, sodium chloride (>99.5%) and sodium dodecyl sulfate (SDS, >99.5%) were purchased from Carl Roth GmbH and Co. KG (Karlsruhe, Germany). Adenosine 5'-triphosphate disodium salt hydrate (ATP, >99%), antifoam Y-30 emulsion, coenzyme A (free acid), disodium hydrogen phosphate (>98%), imidazole (>99.5%), luciferase (from *Photinus pyralis*, recombinant), magnesium acetate tetrahydrate (>99%), magnesium sulfate (>97%), potassium chloride (>99%), potassium dihydrogen phosphate (>98%), sodium acetate (>99%), sulfuric acid (>95%) and thiazolyl blue tetrazolium bromide (MTT; ≥97.5%) were obtained from Sigma Aldrich Chemie GmbH (Taufkirchen, Germany). cOmplete™ Mini EDTA-free protease inhibitor cocktail and DNase I (from bovine pancreas) were purchased from Roche Deutschland Holding GmbH (Mannheim, Germany). Magnesium chloride hexahydrate (>99%) and β-mercaptoethanol were obtained from Fluka (Buchs, Germany). EDTA (>99%), HEPES (>99.5%), and Tris ultrapure (>99.9%) were purchased from AppliChem GmbH (Darmstadt, Germany). Casein (from bovine milk) and guanidinium hydrochloride (>99.9%) were obtained from CalbioChem™ (San Diego, CA, United States). Ammonium persulfate, acrylamide/bis solution (30% w/v), Coomassie Brilliant blue G250, and TEV protease (10 U/μl) were purchased from SERVA electrophoresis GmbH (Heidelberg, Germany). Gibco® DMEM/F-12 medium, Gibco® PBS, Gibco® Penicillin-Streptomycin (10,000 U/mL) and Gibco® Trypsin-EDTA (0.5%) were obtained from Life Technologies GmbH (Darmstadt, Germany). Acetonitrile (ULC-MS grade, >99.97%) and formic acid (ULC-MS grade, >99%) were purchased from Biosolve B.V. (Valkenswaard, Netherlands).

Water (resistance R > 18 mΩ/cm; total organic content <10 ppb) was purified by a PureLab Ultra Analytic system (ELGA Lab Water, Celle, Germany).

Peptide Synthesis

ARV-1502 acetate was obtained from PolyPeptide Laboratories (San Diego, CA, United States) as white powder with a purity of 97.3% according to RP-HPLC. The residual TFA content was 0.05%. The identity was further confirmed by amino acid analysis (Asx, Pro, Val, Leu, Tyr, Lys, and Arg).

The 182 substituted analogs of ARV-1502 were obtained from ABClonal, Inc. (Woburn, United States). These peptides were purified by RP-HPLC using an acetonitrile gradient in the presence of 0.1% TFA. Masses were confirmed by ESI-MS and the purities (>80%) were determined by RP-HPLC recording the absorbance at 214 nm.

Peptides containing a N-terminal 5 (6)-carboxyfluorescein-label were synthesized in-house by Fmoc/^tBu-chemistry on Rink amide resin and purified by RP-HPLC using an acetonitrile gradient in the presence of 0.1% TFA. Masses were confirmed by ESI-MS and the purities (>95%) were determined by RP-HPLC recording the absorbance at 214 nm.

Protein Expression and Purification

DnaK (UniProt-ID P0A6Y8 and P99110), DnaJ (UniProt-ID P08622 and P63971), and GrpE (UniProt-ID P09372 and P99086, downloaded on 26.08.2021), from *Escherichia coli* and *Staphylococcus aureus* were overexpressed in *E. coli* (DE3) Rosetta pLysS after induction with IPTG (Zahn et al., 2013). Briefly, the coding sequences were cloned into a pET 15b vector (GeneScript Biotech BV, Leiden, Netherlands) using restriction enzymes NdeI and NcoI. *E. coli* (DE3) Rosetta pLysS was grown in LB broth containing ampicillin (0.1 g/L), chloramphenicol (34 mg/L), and 0.0075% (v/v) Antifoam Y-30 to reach an optical density of 0.6 recorded at 600 nm on an orbital shaker (180 rpm, 30°C). Expression was induced with IPTG (1 mmol/L). After 4 h, the cells were harvested, resuspended in lysis buffer (20 mmol/L KH₂PO₄/Na₂HPO₄, 0.5 mol/L NaCl, 30 mmol/L imidazole, 5% (v/v) glycerol) containing 2 mmol/L DTT for DnaK or 3 mmol/L DTT for DnaJ expression (pH 8.0), and disrupted by FastPrep-24™ 5G (60 s, 4 m/s, three cycles, MP Biomedicals Germany GmbH, Eschwege, Germany). Proteins were purified using immobilized metal affinity chromatography (IMAC, HisTrap™ HP, GE Healthcare Bio-Sciences AB, Uppsala, Sweden). The N-terminal sequence MGSSHHHHHHSSGENLYFQ was cleaved with TEV protease overnight at room temperature leaving only the sequence GGTHT at the N-terminus of all six proteins. The TEV protease, the cleaved His-tag, and proteins with the remaining His-tag were removed by IMAC. Proteins were stored at -80°C in Tris-HCl (20 mmol/L), KCl (150 mmol/L), MgCl₂ (5 mmol/L), and glycerol (5%, v/v) containing 2 mmol/L DTT (only DnaK) or 3 mmol/L DTT (only DnaJ) at pH 7.5. The purity of all proteins was verified with SDS-PAGE. The corresponding bands were excised, incubated with trypsin (in-gel digest), and the protein confirmed by identifying the tryptic peptides by LC-MS.

Fluorescence Polarization Assays

Dissociation (K_d) and inhibitory constants (K_i) were measured using a previously reported protocol with slight modifications (Krizsan et al., 2015; Kolano et al., 2020). Briefly, black 384-well

plates (flat bottom, Greiner Bio-One GmbH, Frickenhausen, Germany) were blocked with 0.5% (w/v) casein in phosphate buffered saline (PBS; 10 mmol/L Na₂HPO₄, 0.2 mmol/L KH₂PO₄, 137 mmol/L NaCl, 2.7 mmol/L KCl, pH 7.4) containing 0.05% (w/v) Tween® 20 (PBST) at 4°C overnight and washed three times with PBST. K_d values were measured by dissolving the proteins in FP-buffer (20 mmol/L Tris-HCl, 150 mmol/L KCl, 5 mmol/L MgCl₂, 1 mmol/L NaN₃, 2 mmol/L DTT, pH 7.5) and serially diluting them twofold in 23 steps on the plate (20 µL/well). The 5 (6)-carboxyfluorescein-labeled peptide was added (20 µL/well, 40 nmol/L), incubated (2 h, 28°C, dark), and the fluorescence polarization recorded at an excitation wavelength (λ_{ex}) of 485 nm and an emission wavelength (λ_{em}) of 535 nm using a PARADIGM™ microplate reader (Beckman Coulter, Krefeld, Germany). K_i values were determined using a twofold dilution series of unlabeled peptide (20 µL/well) and DnaK (10 µL/well). The plate was incubated at 28°C in the dark for 90 min before the Cf-labeled peptides were added (10 µL/well, 80 nmol/L). After a second incubation (90 min, 28°C), the fluorescence polarization was recorded (λ_{ex} = 485 nm, λ_{em} = 535 nm). Dissociation and inhibitory constants were calculated by fitting the data with a variable slope parameter [$y = \min + (\max - \min)/(1 + (x/K_d)^{-\text{Hill slope}})$] using SigmaPlot 13 (Systat Software Inc., San Jose, CA, United States).

The peptide binding screening with *E. coli* or *S. aureus* DnaK used unlabeled peptide (10 µmol/L for *E. coli*, 70 µmol/L for *S. aureus*; 20 µL/well) pipetted into a 384-well plate and DnaK solutions of 20 µmol/L (*E. coli*) or 64 µmol/L (*S. aureus*; 10 µL/well). The plate was incubated (90 min, 28°C, dark) and Cf-ARV-1502 (80 nmol/L; 10 µL/well) added. After a second incubation (90 min, 28°C, dark), the fluorescence polarization was recorded (λ_{ex} = 485 nm, λ_{em} = 535 nm) on the PARADIGM™ microplate reader. Each peptide was screened in duplicate. Control samples either lacked the unlabeled peptide (maximum) or contained Cf-ARV-1502 in buffer (minimum).

ATPase Activity Assay

ATPase activity of *E. coli* and *S. aureus* chaperones was studied in the presence of an AMP using a 384-well plate colorimetric assay (Chang et al., 2008; Zahn et al., 2013). The peptide screening used a chaperone mix of DnaK, DnaJ, and GrpE (final concentrations of 0.6, 1.0, and 0.9 µmol/L, respectively) dissolved in assay buffer (20 mmol/L Tris-HCl, 150 mmol/L KCl, 5 mmol/L MgCl₂, pH 7.5). The chaperone mix (13.5 µL) was incubated with an aqueous peptide solution (1.5 µL; final concentration 0.3 mmol/L) at 37°C for 30 min in a non-binding 384-well plate (flat bottom, Greiner Bio-One GmbH). Each sample was prepared in triplicates on the same plate. The reaction was started by addition of ATP dissolved in assay buffer (5 µL, 4 mmol/L) and the plate centrifuged (500 × g, 2 min; Allegra™ 21R, Beckmann Coulter, Krefeld, Germany) before incubated (37°C, 2 h). The released phosphate was quantified using an external phosphate dilution series (10–200 µmol/L KH₂PO₄ in assay buffer) prepared on each plate and treated equally as the samples. The reaction was stopped by adding assay buffer (80 µL) to all samples except the phosphate dilution series. Aliquots of all samples (10 µL) were transferred to a clear 384-well plate (flat bottom, Greiner Bio-One

GmbH) and malachite green reagent added (90 μ L; mixture of malachite green in water (0.04%, w/v), ammonium molybdate (2%, w/w) in aqueous sulfuric acid (3.5 mol/L), and water at a ratio of 1:1:3.6, v/v/v). After 15 min, the absorbance was recorded at 620 nm on the PARADIGM™ microplate reader. The phosphate standard curve was fitted by a hyperbolic equation $y = (ax)/(b + x) + c$.

Denatured Luciferase Refolding Assay

Recombinant firefly luciferase (0.5 g/L) was denatured in luciferase buffer (25 mmol/L HEPES (pH 7.2), 50 mmol/L potassium acetate, 5 mmol/L DTT) containing guanidine hydrochloride (6 mol/L) at room temperature for 1 h (Wisén and Gestwicki, 2008). The denatured luciferase was 100fold diluted in luciferase buffer and incubated on ice for 20 min in the dark. Peptides (4 μ L; final concentration 150 μ mol/L) were incubated in a non-binding 384-well plate (flat bottom, Greiner Bio-One GmbH) with chaperone mix (41 μ L; final concentrations: 240 nmol/L DnaK, 48 nmol/L DnaJ and 24 nmol/L GrpE) in refolding buffer [28 mmol/L HEPES (pH 7.6), 120 mmol/L potassium acetate, 12 mmol/L magnesium acetate, 2 mmol/L DTT, 0.5 mmol/L ATP, 8.8 mmol/L creatine phosphate, 35 U/mL creatine kinase) at 37°C for 30 min. The reaction was started by addition of denatured luciferase (5 μ L). The plate was incubated (37°C, 2 h, dark) before 10 μ L of each sample were transferred to a white 384-well plate (Greiner Bio-One GmbH) and diluted with detection buffer (20 μ L; 25 mmol/L HEPES (pH 7.8), 8 mmol/L magnesium sulfate, 12 mmol/L DTT, 0.5 mmol/L ATP, 120 μ mol/L coenzyme A, 100 μ mol/L D-luciferin). After incubation (30°C, 10 min) in the PARADIGM™ microplate reader, the luminescence was recorded using an integration time of 0.5 s.

Antimicrobial Activity

Minimal inhibitory concentrations (MICs) were determined using a liquid broth micro dilution assay in sterile 96-well plates (polystyrene F-bottom, Greiner Bio-One GmbH) and a total volume of 100 μ L per well. Aqueous peptide solutions (10 g/L) were serially twofold diluted in 25% Mueller-Hinton broth 2 (25% MBH2) starting at a peptide concentration of 128–1 μ g/mL (50 μ L per well). Overnight cultures of bacteria, i.e., *E. coli* BW25113 or *S. aureus* DSM 6247, grown in 25% MHB2 were diluted 30-fold in 25% MHB2. After an incubation period of 4 h (37°C, 200 rpm), cells were diluted to 1.5×10^7 cfu/mL, based on a McFarland test, and 50 μ L were added to each well (final concentration of 7.5×10^6 cfu/mL per well). The plates were incubated (37°C, 20 h) and the optical density was determined at 595 nm using the PARADIGM™ microplate reader. The MIC was defined as the lowest peptide concentration preventing visible bacterial growth.

Cytotoxicity

Human embryonic kidney (HEK293) and human hepatoma (HepG2) cells were cultured in Dulbecco's modified Eagle's/Ham's F-12 medium (DMEM/F-12) containing 10% (v/v) fetal bovine serum and 1% (v/v) penicillin/streptomycin. Cells (20,000/well; 200 μ L) were seeded into a 96-well plate

(polystyrene F-bottom, Greiner Bio-One GmbH) and incubated for 24 h (37°C, 5% CO₂). Cells were washed with PBS (100 μ L) and peptide solutions (0.6 g/L in DMEM/F-12) were added. The positive control consisted of a dilution series from 12 to 1.5% (v/v) DMSO and the negative control was 12% (v/v) PBS. After incubation (37°C, 24 h, 5% CO₂) the supernatant was discarded, fresh medium (90 μ L/well) and MTT (10 μ L/well, 5 g/L in PBS) were added and the plate was incubated for 4 h (37°C, 5% CO₂). A solution (100 μ L) of sodium lauryl sulfate [10% (v/v)] in hydrochloric acid (10 mmol/L) was added and the plate was incubated again for 24 h (37°C, 5% CO₂). The absorbance was recorded at 570 nm relative to the reference at 650 nm (PARADIGM™ microplate reader). All samples were corrected for background extinction of the medium. The relative cell viability was calculated using the ratio of the absorbance between treated and untreated cells.

RESULTS

Design of ARV-1502 Derivatives and Protein Expression

ARV-1502 binds with sequence motif YLPRP in a forward binding mode to the conventional substrate binding cleft of DnaK occupying the hydrophobic pocket (Zahn et al., 2013). These are also the residues in pyrrocicrin that cannot be substituted without a loss in antimicrobial activity against Enterobacteriaceae. Previous investigations indicated the importance of Asp³ and Lys⁴ for inhibiting the ATPase activity of DnaK (Cassone et al., 2008). These are also residues that seem to be important for the anti-Gram-negative activity of pyrrocicrin. This project was the first part of a larger research program in which a library was constructed from the residues found responsible for DnaK binding and *in vitro* activity against *E. coli*. In the first phase we had to limit ourselves to approximately 400 residues that could be tested simultaneously with high confidence. All seven residues involved, residues Asp³, Lys⁴, Tyr⁸, Leu⁹, Pro¹⁰, Arg¹¹, and Pro¹² were singly or multiply substituted with Asp (representing negatively charged side-chains), Lys (representing positively charged side-chains), Ser (representing uncharged hydrophilic side-chains), Leu (representing aliphatic side chains or no side chain functionalities at all), and Phe (representing cyclic side chains or the cyclic proline backbone). The idea was to expand the chemical space to properties not present in the original ARV-1502 monomer sequence. Thus, to reduce the number of peptides, the analogs did not include residues with “like” or chemically not different side-chains, such as Phe for Tyr or Phe and Leu for Pro. In total, the different combinations lead to 183 peptide sequences (ARV-1502 and 182 analogs) synthesized on solid phase (Supplementary Table S1). DnaK, DnaJ, and GrpE from *E. coli* and *S. aureus* were expressed in *E. coli* (DE3) Rosetta pLysS and purified via the N-terminal His-tag that was cleaved off afterwards. All proteins were obtained in high quantities and good purities (Supplementary Figure S1).

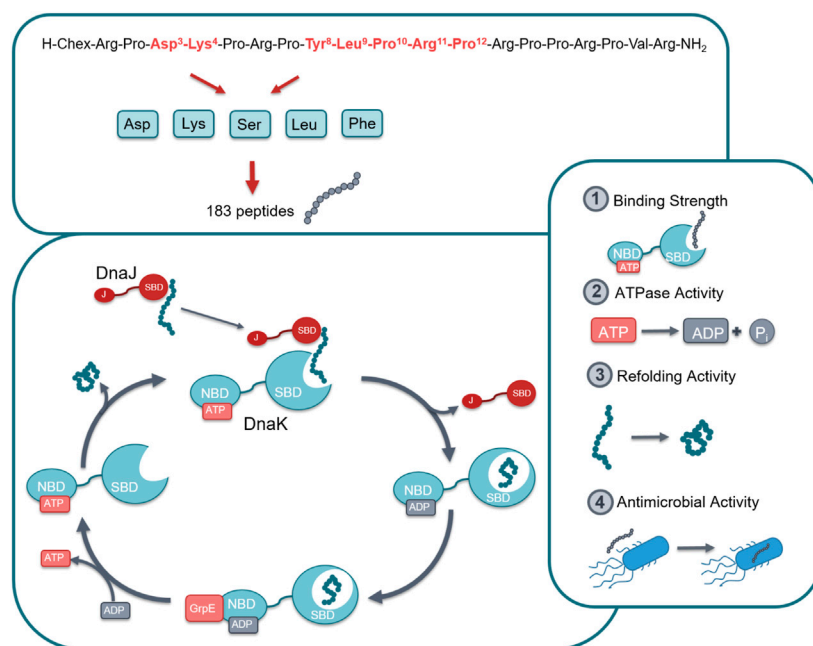


FIGURE 1 | Graphical representation of the studied chaperone system. In total 183 peptides were designed and synthesized by substituting seven different positions in lead structure ARV-1502 (marked in red) by Asp, Lys, Ser, Leu or Phe in different combinations (top). All peptides were studied for their effect on the DnaK/DnaJ/GrpE-chaperone systems of *E. coli* and *S. aureus*, i.e., target binding, ATPase activity, and protein refolding activity as well as the antibacterial activity against one strain of each bacterium. Abbreviations; Chex, 1-Amino cyclohexyl carboxylic acid; SBD, Substrate binding domain; NBD, Nucleotide binding domain; J, J domain; ATP, Adenosine triphosphate; ADP, Adenosine diphosphate.

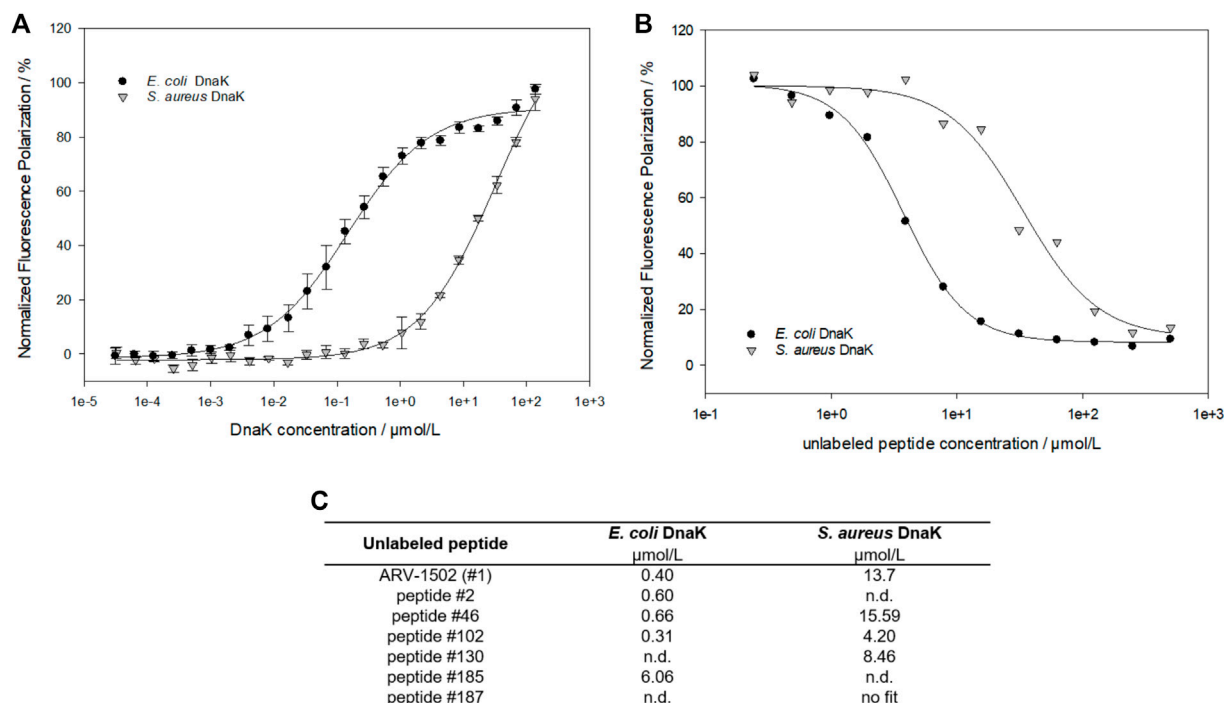
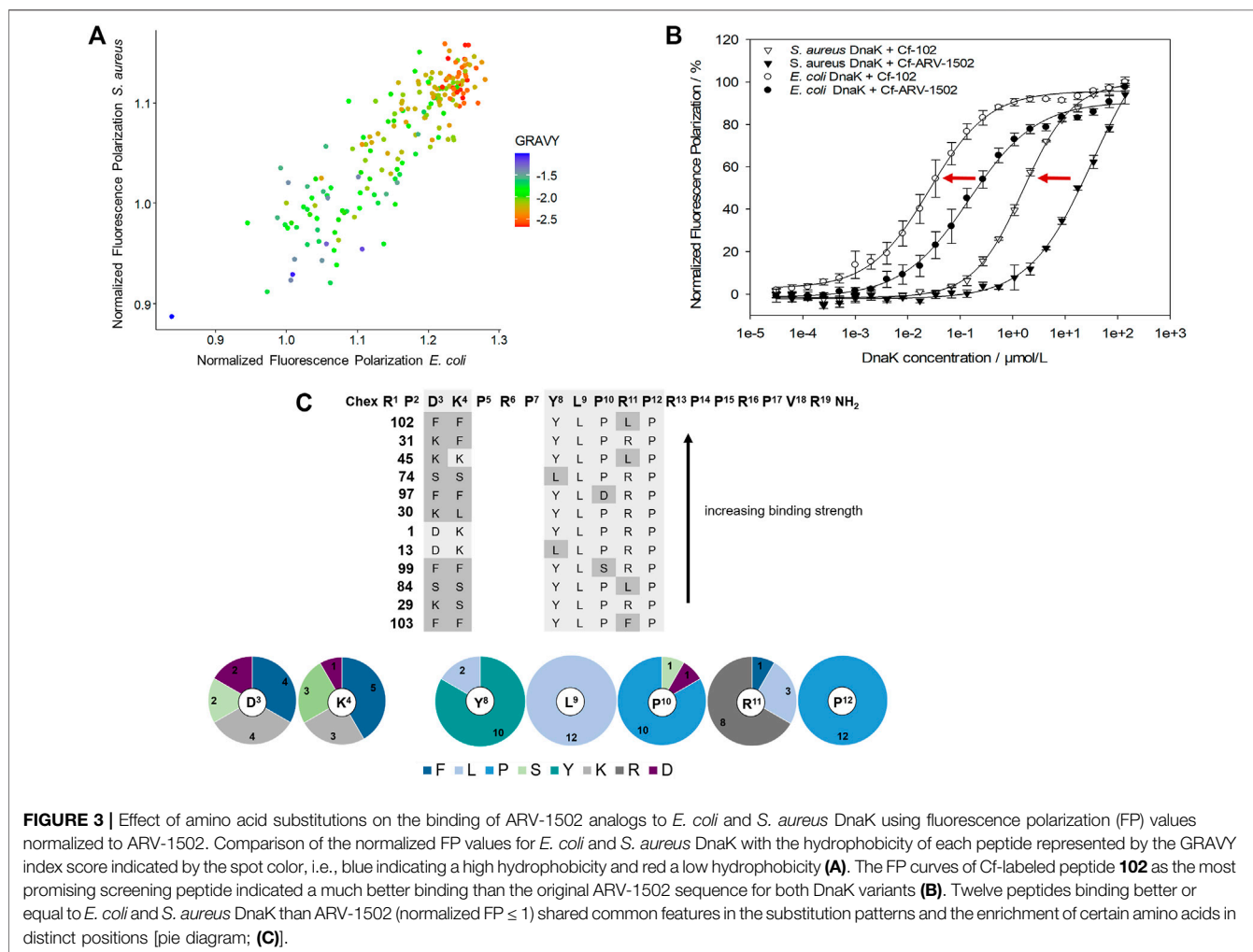


FIGURE 2 | Fluorescence polarization measurements to study the interaction between ARV-1502 or substituted analogs and *E. coli* or *S. aureus* DnaK. Based on the dissociation constants (K_d) determined for Cf-ARV-1502 (**A**), the inhibitory constant (K_i) was measured for ARV-1502 (**B**) and six randomly chosen screening peptides (**C**) confirming a suitable dynamic range for the screening assay.

TABLE 1 | Dissociation constants (K_d) measured for ARV-1502 and the analog **102**. K_d were determined with Cf-labeled peptides and recombinant proteins DnaK, DnaJ and GrpE as *E. coli* and *S. aureus* variant. For the measurement with full chaperone system DnaK, DnaJ and GrpE (ratio 0.6:1.0:0.9) were pre-incubated for 30 min at room temperature. Fluorescence polarization of samples marked with * did not reach the upper plateau. Thus, the K_d is only approximate, albeit, gives a good hint of binding strength.

Peptide	$K_d/\mu\text{mol/L}$							
	<i>E. coli</i>				<i>S. aureus</i>			
	DnaK	DnaJ	GrpE	DnaK/DnaJ/GrpE	DnaK	DnaJ	GrpE	DnaK/DnaJ/GrpE
Cf-ARV-1502	0.2	33.4*	212.8*	3.1	25.12	no fit	138.5*	30.2
Cf-peptide 102	0.03	8.8	21.4*	0.6	1.6	53.2*	118.0*	1.6



The recombinant proteins were properly folded, as confirmed by the data obtained in the functional assays reported below. Thus, all peptides could be studied for their binding to *E. coli* and *S. aureus* chaperone DnaK, their impact on the ATPase activity and the protein refolding activity of DnaK in the absence or presence of co-chaperones DnaJ and GrpE, and

their antibacterial activity against *E. coli* and *S. aureus* strains (Figure 1).

DnaK Binding

A fluorescence polarization (FP) assay using 5 (6)-carboxyfluorescein (Cf)-labeled peptides was applied to study

the binding of screening peptides to *E. coli* and *S. aureus* DnaK (Figure 2). The dissociation constants (K_d) for Cf-ARV-1502 were 0.2 $\mu\text{mol/L}$ for *E. coli* DnaK and 25.1 $\mu\text{mol/L}$ for *S. aureus*, although the sequences of both DnaK variants share ~56% identity and ~72% similarity. The homology is even higher in the substrate binding domains, being ~72% identity and ~82% similarity. While the K_d value to *S. aureus* DnaK was not influenced by the presence of co-chaperones DnaJ and GrpE, the K_d value of *E. coli* DnaK increased 15-fold to 3.1 $\mu\text{mol/L}$ (Table 1).

As the determination of K_d -values for all screening peptides would require high protein quantities and 183 Cf-labeled peptides, a competitive assay was established using Cf-ARV-1502 and unlabeled screening peptides. The DnaK concentrations were adjusted to 5 $\mu\text{mol/L}$ for *E. coli* and 16 $\mu\text{mol/L}$ for *S. aureus*, which was above the K_d at approximately 80% of the maximal plateau level. The assay was first established by determining the inhibitory constants (K_i) of randomly chosen peptides (Figure 2 (c)), which confirmed the trend of weaker binding to *S. aureus* DnaK and provided different K_i -values among the substituted peptides. Based on these K_i -values, a high-throughput screening was established using the above-mentioned concentrations of DnaK and unlabeled peptide concentrations of 5 $\mu\text{mol/L}$ and 35 $\mu\text{mol/L}$ for *E. coli* and *S. aureus* DnaK, respectively. The quality of the experimental set up was evaluated by the Z' factor (Zhang et al., 1999) (Supplementary Table S2). The Z' values were 0.78 or higher indicating a reproducible measure with a large separation band between strongly and weakly binding controls. The obtained FP-values were normalized to the FP-values determined for lead sequence ARV-1502. Despite differences in the K_i -values, substitutions showed similar effects on the binding to *E. coli* and *S. aureus* DnaK with a linear relationship (Figure 3A). Furthermore, the peptide hydrophobicity calculated as GRAVY index score correlated well to the binding strength (Figure 3A). Most hydrophilic peptides, e.g., peptides **108** (Chex-RPDKPRPDKPRPRPVR-NH₂) or **122** (Chex-RPDKPRPKKPRPRPVR-NH₂), bound neither to *E. coli* nor to *S. aureus* DnaK (Figure 3A, red dots), while the second most hydrophobic peptide **102** (Chex-RPFFPRPYLPLPRPVR-NH₂) emerged as a clear leader with 10- and 20-fold lower K_d -values for *E. coli* (30 nmol/L) and *S. aureus* DnaK (1.6 $\mu\text{mol/L}$), respectively, than for lead structure ARV-1502 (Figure 3B, Table 1). Altogether, 42 substituted peptides bound equal or better than ARV-1502 to *S. aureus* DnaK and 12 analogs equal or better to *E. coli* DnaK, as indicated by normalized FP-values below 1 (Figure 3C). In addition to the elevated hydrophobicity, the substituted position was also important for binding, as eight of the ten best binding peptides were modified at residue 3 or 4 (mostly Phe or Lys; e.g. **31**, **45**, or **97**) and the other two peptides at residue eight or 10 (e.g. **13** or **99**), while substitutions at residues 9 and 12 weakened the interactions.

Based on the screening data obtained for DnaK, the binding of Cf-labeled peptides **102** and ARV-1502 to co-chaperones DnaJ and GrpE was also studied (Table 1). For *E. coli*, Cf-ARV-1502

and Cf-**102** bound ~1,000- (150-) and 700- (300-) fold weaker, respectively, to GrpE (DnaJ) than to DnaK with Cf-**102** always binding stronger than Cf-ARV 1502. The differences in binding were less noticeable for the *S. aureus* proteins, as both peptides bound around 100-times weaker to *S. aureus* DnaK than to *E. coli* DnaK but showed similar K_d -values for the co-chaperones of both bacteria (Table 1). Interestingly, the K_d of Cf-ARV-1502 was lower for GrpE than for DnaJ, while the K_d of Cf-**102** was lower for DnaJ. As observed for ARV-1502, the K_d of Cf-**102** was 20-fold higher for the *E. coli* DnaJ/DnaJ/GrpE-system than for DnaK alone, while the K_d was not affected by the *S. aureus* co-chaperones.

ATPase Activity

The impact of ARV-1502 and its analogs on the ATPase activity of DnaK was investigated in 384-well plates using the malachite green absorbance assay, which quantitates phosphate (P_i) cleaved from ATP confirming for example the ATPase activity of DnaK. The established assay allowed a robust and reproducible quantitation of phosphate from 10 to 150 $\mu\text{mol/L}$ and was easy to handle (Supplementary Figure S3) providing the intended high-throughput screening. The ATPase activity determined here for *E. coli* DnaK corresponded very similar to the reported activities, while the ATPase activity of *S. aureus* DnaK, which has not been reported so far to the best of our knowledge, was higher (Supplementary Figure S4).

E. coli and *S. aureus* DnaK incubated with ARV-1502 released more P_i from ATP indicating that the intrinsic ATPase activity was stimulated in both cases (Supplementary Figure S5). For *E. coli* DnaK the ATPase activity increased by ~250% reaching the plateau at ARV-1502 concentrations of 50 $\mu\text{mol/L}$ or higher. The *S. aureus* DnaK was stimulated by only 50% and reached the plateau already at 25 $\mu\text{mol/L}$ ARV-1502. To simulate the cellular conditions more closely, co-chaperones DnaJ and GrpE were added to the assay. Interestingly, the ATPase activity of the *E. coli* DnaK/DnaJ/GrpE-chaperone system was downregulated in the presence of ARV-1502 by ~70%, whereas a stimulatory effect of ~50% was observed for the *S. aureus* system, i.e., at a similar degree as for DnaK alone (Supplementary Figure S5).

The peptide screen relied on high peptide concentrations (0.3 mmol/L) to reduce the effect of different adsorption rates of hydrophobic peptides on surfaces and to observe a strong effect on the ATPase activity of the DnaK/DnaJ/GrpE-chaperone system, mostly at the plateau level. The ATPase activity of the *E. coli* system ranged from 41 to 122% with 52 peptides (28%; e.g., **66**, **117**, or **128**) decreasing the activities below 60% and of the *S. aureus* system from 73 to 218% with 39 peptides (21%; e.g., **10**, **83**, **119**) increasing the activities by more than 160% (Figure 4). Surprisingly, 17 peptides affected the ATPase activities of *E. coli* and *S. aureus* chaperones by less than 20% (e.g., **99**, **106**, or **160**), i.e., observed activities between 80 and 120%. Strikingly, seven of these 17 peptides (41%; **90**, **91**, **99**, **101**, **102**, **105**, and **106**) belonged to best binders for *E. coli* and *S. aureus* DnaK and additional five peptides (**54**, **133**, **160**, **170**, and **172**) to the best binders for *S. aureus* DnaK. The Phe³-Phe⁴ motif appeared to be very important, as it was present in twelve of the 17 peptides (e.g., **91**, **99**, **102**). Peptides showing the strongest effects of the ATPase

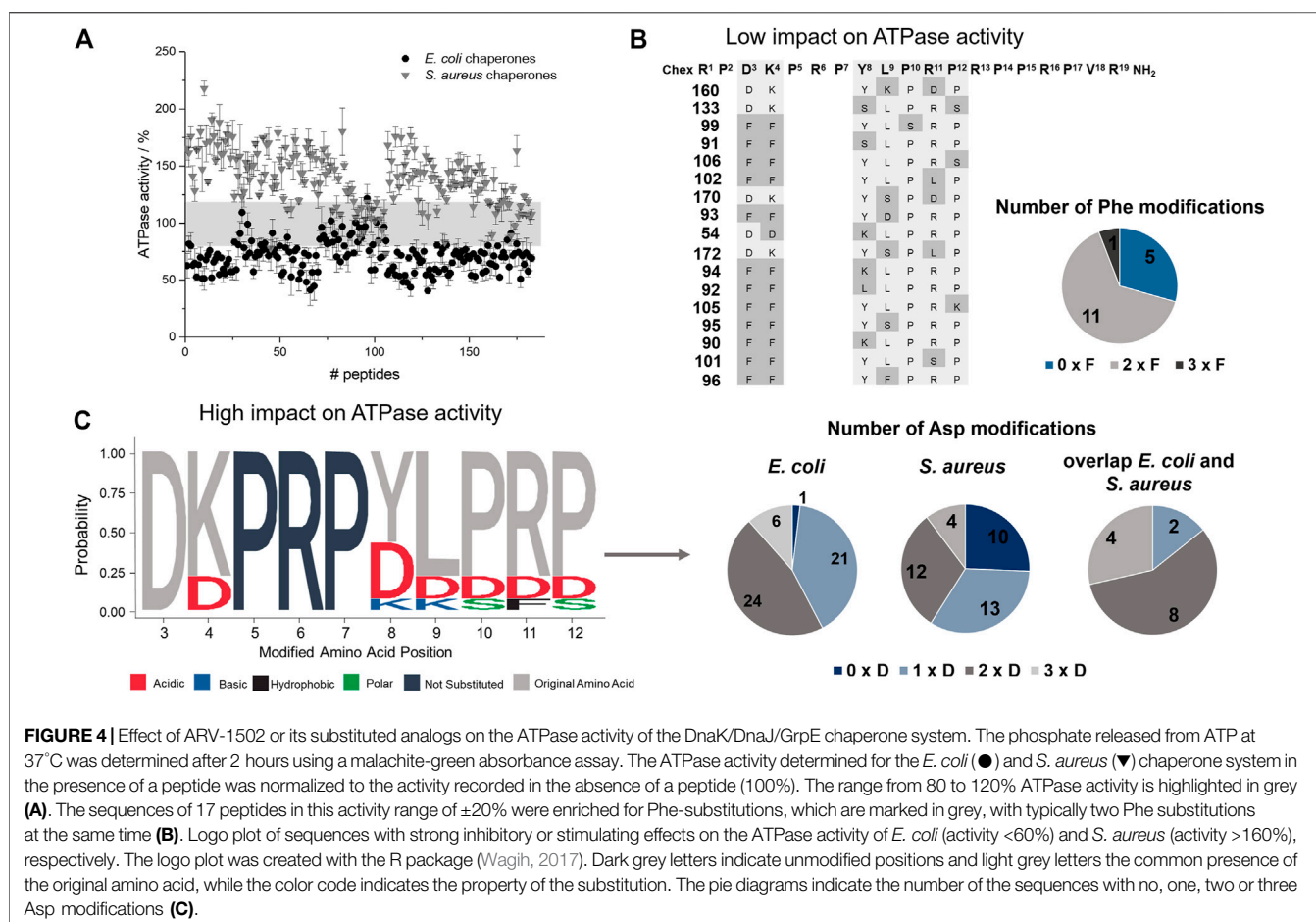


FIGURE 4 | Effect of ARV-1502 or its substituted analogs on the ATPase activity of the DnaK/DnaJ/GrpE chaperone system. The phosphate released from ATP at 37°C was determined after 2 hours using a malachite-green absorbance assay. The ATPase activity determined for the *E. coli* (●) and *S. aureus* (▼) chaperone system in the presence of a peptide was normalized to the activity recorded in the absence of a peptide (100%). The range from 80 to 120% ATPase activity is highlighted in grey (A). The sequences of 17 peptides in this activity range of $\pm 20\%$ were enriched for Phe-substitutions, which are marked in grey, with typically two Phe substitutions at the same time (B). Logo plot of sequences with strong inhibitory or stimulating effects on the ATPase activity of *E. coli* (activity <60%) and *S. aureus* (activity >160%), respectively. The logo plot was created with the R package (Wagih, 2017). Dark grey letters indicate unmodified positions and light grey letters the common presence of the original amino acid, while the color code indicates the property of the substitution. The pie diagrams indicate the number of the sequences with no, one, two or three Asp modifications (C).

activities of *E. coli* (<60%) or *S. aureus* (>160%) contained typically the original Asp³ or Lys⁴, although Asp was also frequently present at position 4. In general, Asp substitutions occurred quite often in these sequences, i.e., 58% of the peptides decreasing the ATPase activity of *E. coli* DnaK by at least 40% and contained at least two Asp residues (e.g., 66, 119, or 128), while 41% of the peptides increasing the ATPase activity of *S. aureus* DnaK by 60% or more had at least two Asp spread on the substituted positions (e.g., 53, 107, or 117). Interestingly, none of these peptides bound to DnaK.

Refolding Activity

The main function of the DnaK chaperone system is the refolding and degradation of denatured or misfolded proteins enabling cell survival after severe stress conditions (Mayer and Bukau, 2005), such as a heat shock. The effect of ARV-1502 analogs on the refolding activity of the DnaK chaperone system was studied in a denatured luciferase refolding assay. When firefly luciferase was denatured with guanidinium hydrochloride, the luminescence intensity of the luciferase assay decreased to 5%. After dilution allowing the protein refolding, the luminescence intensity increased in the absence of a chaperone to only 10% after 2 hours (Supplementary Figure S6). ARV-1502 reduced the refolding activity of the *E. coli* DnaK/DnaJ/GrpE-chaperone

system to ~60% at peptide concentrations $\geq 50 \mu\text{mol/L}$, while the *S. aureus* chaperone system was not affected (Supplementary Figure S7). The peptide screening led to similar results, i.e., an inhibition of the *E. coli* chaperone refolding activity by 22–64%, whereas the *S. aureus* chaperone system was slightly inhibited or slightly activated with activities ranging from 84 to 135%. Although the impact was different, similar trends were observed for the substituted peptides indicating that inhibition of both chaperone systems increased with higher peptide hydrophobicity (GRAVY index; Figure 5). The Phe³-Phe⁴-motif, which improved DnaK-binding without affecting the ATPase activity, was present in 10 of the 20 peptides (e.g., 96, 102, or 105) most strongly inhibiting the *E. coli* chaperone system. Additionally, hydrophobic amino acids phenylalanine and leucine were favored at position 9, i.e., in 60% of the peptides (e.g., 94, 111, 182). A substitution of Tyr⁸ did neither increase nor reduce the inhibitory effect. Generally, the overall peptide hydrophobicity appeared to be more important than the substituted position for the refolding activity.

Antimicrobial Activity and Cytotoxicity

The MIC-values obtained for the Gram-negative strain *E. coli* BW25113 ranged from 4 $\mu\text{g/mL}$ to >128 $\mu\text{g/mL}$ with only peptide 2 being more active than the lead structure ARV-1502 with an

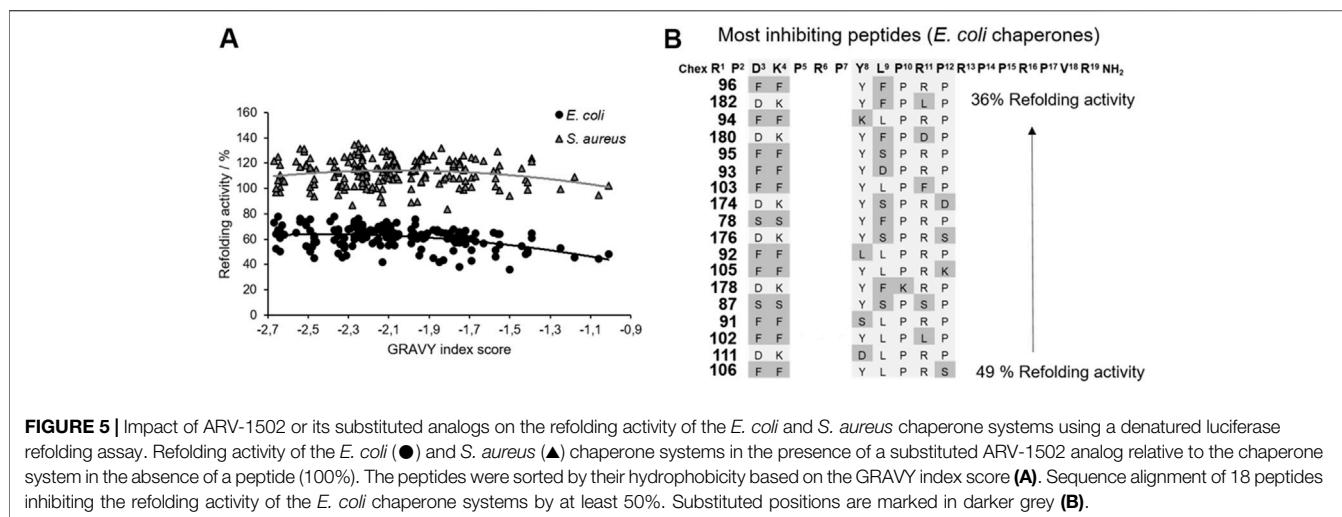


FIGURE 5 | Impact of ARV-1502 or its substituted analogs on the refolding activity of the *E. coli* and *S. aureus* chaperone systems using a denatured luciferase refolding assay. Refolding activity of the *E. coli* (●) and *S. aureus* (▲) chaperone systems in the presence of a substituted ARV-1502 analog relative to the chaperone system in the absence of a peptide (100%). The peptides were sorted by their hydrophobicity based on the GRAVY index score (A). Sequence alignment of 18 peptides inhibiting the refolding activity of the *E. coli* chaperone systems by at least 50%. Substituted positions are marked in darker grey (B).

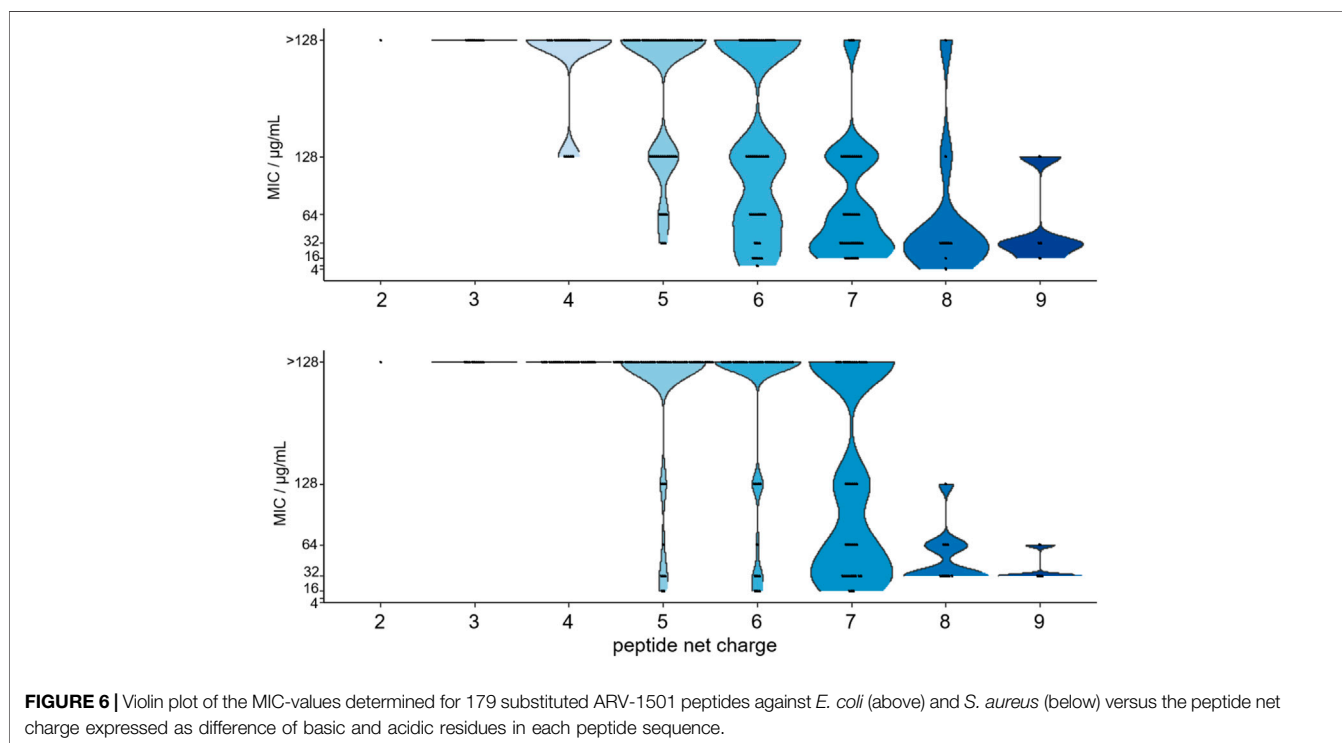


FIGURE 6 | Violin plot of the MIC-values determined for 179 substituted ARV-1501 peptides against *E. coli* (above) and *S. aureus* (below) versus the peptide net charge expressed as difference of basic and acidic residues in each peptide sequence.

MIC of 8 µg/mL determined in parallel. ARV-1502 was inactive against the Gram-positive strain *S. aureus* DSM 6247, but this strain was susceptible to several substituted peptides with the lowest MIC-values at 16 µg/mL. In total 68 and 76% of the tested peptides were inactive (MIC ≥ 128 µg/mL) against *E. coli* and *S. aureus*, respectively, which might relate to changes in the physicochemical properties as a result of some substitutions.

Importantly, the antimicrobial activity was affected by the net charge. Inactive peptides (MIC ≥ 128 µg/mL) had net charges below +5, whereas net charges above +7 resulted mostly in MICs of 32 µg/mL or lower (Figure 6). Particularly, substitutions with Asp strongly decreased the antimicrobial activity. All six

sequences with a single Asp-substitution (Table 2 (a)) as well as 89 and 94% of the peptides, where at least one Asp-substitution was combined with other substitutions, lost the antimicrobial activity against *E. coli* and *S. aureus*, respectively. Reversing the motif Asp³-Lys⁴ to Lys³-Asp⁴ reduced the activity only two-fold to 16 µg/mL for *E. coli* and had no effect for *S. aureus*. Similar to Asp-substitutions, Ser-substitutions at positions Tyr⁸, Pro¹⁰, Arg¹¹, and Pro¹² as well as for 70% or 80% of all peptides carrying multiple substitutions involving serine abolished the antimicrobial activity against *E. coli* or *S. aureus* (Table 2 (a)). Positions Tyr⁸ and Leu⁹ appeared to be most critical, as an exchange of these residues reduced the activity against *E. coli*

TABLE 2 | MIC values measured for *E. coli* BW25113, *S. aureus* DSM 6247 and the knock-out mutant *E. coli* JW0013 Δ dnaK in 25% MHB2. a) Sequences with a single Asp or Ser substitution showed significantly lower antimicrobial activities in *E. coli* BW25113 or *S. aureus* DSM 6247. b) Peptides with similar antibacterial activities against both strains. These peptides were chosen due to their behavior in the other screening (peptide 10: insufficient binding; 45: insufficient binding, but high impact on ATPase activity; 102: best binding).

(a)					
Sequences with a single asp substitution	MIC/ μ g/mL		Sequences with a single Ser substitution	MIC/ μ g/mL	
	<i>E. c.</i>	<i>S. a.</i>		<i>E. c.</i>	<i>S. a.</i>
Chex-RP DK PRPYLPRPRPPRPVR-NH ₂	8	>128	Chex-RP SK PRPYLPRPRPPRPVR-NH ₂	n. d.	128
Chex-RP DD PRPYLPRPRPPRPVR-NH ₂	128	>128	Chex-RP DS PRPYLPRPRPPRPVR-NH ₂	32	>128
Chex-RP DK PRPDLPRPRPPRPVR-NH ₂	>128	>128	Chex-RP DK PRPSLPRPRPPRPVR-NH ₂	128	>128
Chex-RP DK PRPYDPRPRPPRPVR-NH ₂	>128	>128	Chex-RP DK PRPYSRPRPPRPVR-NH ₂	64	>128
Chex-RP DK PRPYLDRPRPPRPVR-NH ₂	>128	>128	Chex-RP DK PRPYLSRPRPPRPVR-NH ₂	128	>128
Chex-RP DK PRPYLPDPRPPRPVR-NH ₂	>128	>128	Chex-RP DK PRPYLPSRPRPPRPVR-NH ₂	>128	>128
Chex-RP DK PRPYLPRDRPPRPVR-NH ₂	>128	>128	Chex-RP DK PRPYLPRSRRPPRPVR-NH ₂	>128	>128
(b)					
#	Peptide Sequence	MIC/ μ g/mL			
		<i>E. coli</i> BW25113		<i>E. coli</i> JW0013 Δ dnaK	
1	Chex-RP DK PRPYLPRPRPPRPVR-NH ₂	8		4-8	
10	Chex-RP DK PRPYDPRPRPPRPVR-NH ₂	32-64		32-64	
45	Chex-RP KK PRPYLPRPRPPRPVR-NH ₂	>128		>128	
102	Chex-RP FF PRPYLPRPRPPRPVR-NH ₂	16		32	

and *S. aureus* significantly for 71 and 80% of these peptides (e.g., **10**, **54**, or **64**), respectively. Less negative effects were observed for substituting the Asp³-Lys⁴ motif in ARV-1502 with Lys or Phe to obtain the Lys³-Lys⁴ or Phe³-Phe⁴ motifs exhibiting good activities. All peptides tested against *S. aureus* with MIC-values $\leq 16 \mu$ g/mL contained the Phe³-Phe⁴-motif (**92**, **94**, **98**, **99**, **102**, **103**, and **105**). Altogether, only peptide **2** of all designed peptides was more active against the Gram-negative *E. coli* strain. Particularly noteworthy is that 32 peptides improved the activity against *S. aureus* by at least three dilution steps (MIC $\leq 32 \mu$ g/mL). When the antimicrobial activity of peptides **1** (ARV-1502), **10**, **45**, and **102** was tested against the Δ dnaK-knock-out-mutant *E. coli* JW0013 (Table 2 (b)), the MIC-values increased or decreased only twofold. The most active peptides ($\leq 16 \mu$ g/mL) were analyzed for possible cytotoxic effects on eukaryotic cells (HEK293 and HepG2) using an MTT-based colorimetric assay and peptide concentrations of 0.6 g/L (Supplementary Figure S8). For 86% of the tested peptides, a lower viability was observed for HepG2. In addition, hydrophobic peptides, such as peptide **105** (Chex-RPFFPRPYLPRKRPPRPVR-NH₂) and **103** (Chex-RPFFPRPYLPFRPPRPVR-NH₂), exhibited a stronger cytotoxic effect, resulting in a minimum viability of 39% ($\pm 5\%$) in HepG2 and 61% ($\pm 6\%$) in HEK293 cells. However, on average, a relative viability of 78% ($\pm 4\%$) was achieved for HepG2 and 91% ($\pm 5\%$) for HEK293 cells.

DISCUSSION

Proteins are involved in almost all biological processes, which demands their correct folding. This is a very complex process requiring cellular chaperone systems. Increased or insufficient activity of chaperones can lead to misfolded proteins, which are

often functionally inactive, or trigger protein aggregation. Human Hsp70 is associated with cancers or neurodegenerative diseases, including Alzheimer's and Parkinson's disease (Wang et al., 2014). Such effects can be exploited *in vitro*, typically using bacterial homologs, often referred to as DnaK, as promising targets. Additionally, DnaK inhibitors might represent a new class of antimicrobial agents. This study investigated the effect of PrAMP ARV-1502 and 182 substituted analogs on different DnaK functions, specifically binding strength, ATPase activity, and refolding activity, also in association with co-chaperones DnaJ and GrpE. In addition to the well-established *E. coli* model system, the corresponding *S. aureus* system was included as a model of Gram-positive bacteria. Despite the high sequence homologies between the chaperones and co-chaperones of both bacteria, the binding domains are different, which may influence their interactions and thus require different inhibitors. All studied peptides were 19 residues long and differed only by a maximum of three substitutions at seven different positions. Nevertheless, major differences and trends were observed in all functional assay types. Substitution with Asp, Lys, Ser, Leu or Phe changed the peptide properties, mainly by the hydrophobicity and net charge, resulting in varying degrees of interference between the different assay types (Figure 7). Not surprisingly, inhibition of DnaK activity correlated well with the antibacterial activity.

DnaK prefers substrate peptides enriched for aliphatic (Leu and Ile) or aromatic amino acids (Phe and Tyr) with leucine being the most important (Rüdiger et al., 1997). Leucine is also essential for the binding of ARV-1502, which binds in a forward binding mode to the central hydrophobic pocket of the substrate binding domain (SBD) (Zahn et al., 2013). The importance of Leu⁹ was confirmed here, as none of the twelve peptides binding best to DnaK was substituted in position 9. However, some peptides

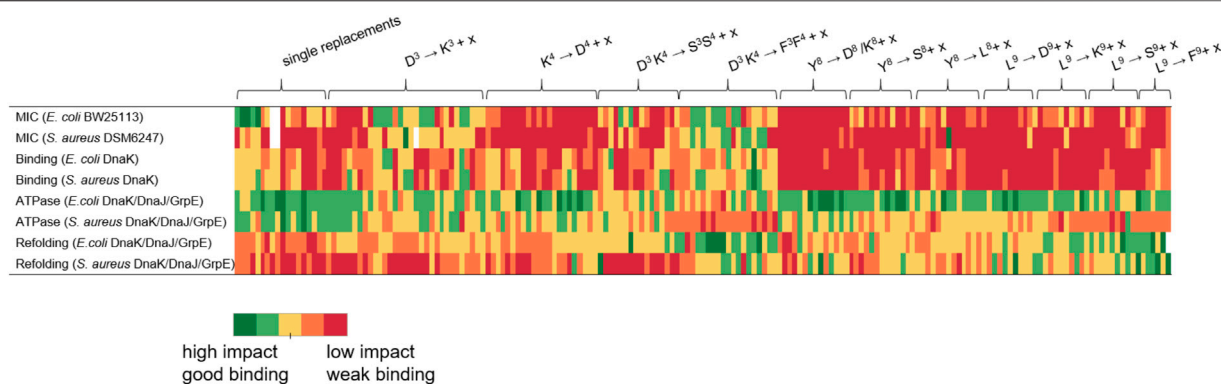


FIGURE 7 | Graphical representation of the influence strength of the studied peptides grouped by substituted amino acids. x represents one of the five substituted amino acids Asp, Lys, Ser, Leu or Phe. Peptides with high impact or good DnaK binding are shown in green and those with low efficacy or poor binding are shown in red. For the assignment of the color scale, the results of the respective tests were divided into five equal groups corresponding to the five color groups used.

contained additional leucines at other positions (e.g., peptides **23**, **45**, or **102**). In general, only few modifications at the binding motif Y^8LPRP^{12} increased the binding strength for both DnaK variants, not even a substitution with the hydrophobic phenylalanine. A likely reason is the limited space in the central pocket, where bulky residues can bind only after reorientation (Mayer et al., 2000; Mayer and Bukau, 2005). Interestingly, the peptide binding best (peptide **102**) contained a Phe^3-Phe^4 motif instead of Asp^3-Lys^4 . This drastic change could possibly lead to a different binding mode enhancing the binding through additional interactions with the SBD. It is particularly noteworthy that the K_d -values determined for *S. aureus* DnaK were much higher than for *E. coli*, although both variants and their SBD share high homologies. Small changes of central hydrophobic pocket, such as the exchange of Phe^{426} to Tyr, might explain the difference. In addition, the SBD of *S. aureus* DnaK has a lower isoelectric point than the corresponding *E. coli* sequence influencing electrostatic interactions (Rüdiger et al., 1997). Stronger DnaK binding of the primarily hydrophobic peptides increased also the inhibition of the DnaK-refolding activity (e.g., peptides **92**, **102**, or **103**). When the SBD is occupied by a peptide, it cannot bind to denatured luciferase and thus cannot promote its refolding to the native state. ARV-1502 added at concentrations of $\geq 50 \mu\text{mol/L}$ reduced the refolding activity of the *E. coli* system to only 60%, while substituted analogs with hydrophobic character reduced it even further to 36% (e.g., peptides **78**, **94**, **96**, or **105**), always reaching the basal refolding level of 10% in the absence of a chaperone. The relevance of hydrophobicity for the binding mode is known from studies on small molecules, e.g., dihydropyrimidines, with EC_{50} -values in the lower micromolar range (Wisén and Gestwicki, 2008; Liebscher et al., 2010). The inhibition reached seems to be limited by the peptide size. However, it should be noted that the inhibitory and stimulatory effects did not only depend on the binding to DnaK but were also influenced by co-chaperones DnaJ and GrpE, important for the transfer and release of DnaK substrates. This was also reported for other inhibitors or activators (Cesa et al., 2013), which are able to induce conformational changes or suppress the chaperone-co-chaperone-interaction (Liebscher et al., 2010). For the *E. coli* chaperone system, the addition of co-chaperones

reversed the effect of ARV-1502 from stimulation to inhibition of the ATPase activity of DnaK along with 15-fold higher K_d -values. Interestingly, the best binding peptides (e.g., peptides **102**, **103**, and **106**) showed the weakest effects on the ATPase activity, whereas peptides that did not bind to DnaK, decreased the ATPase activity by 50% (e.g., peptides **68**, **119**, **128**). Since ARV-1502 bound more weakly to *E. coli* DnaK, DnaJ, and GrpE than peptide **102**, but affected the ATPase activity more strongly, we assume that the binding strength is not the leading parameter for designing inhibitors. The influence of the co-chaperones on the peptide-DnaK binding strength probably affected also the impact on the ATPase and refolding activities. Notably, weakly binding peptides inhibited the ATPase activity of *E. coli* chaperones, but stimulated the corresponding *S. aureus* chaperones. Again, strongly binding peptides did not affect the ATPase activity in either system (e.g., peptides **91**, **99**, or **102**). Considering the antimicrobial activity, only the Asp^3Lys^4 substitution slightly improved the MIC-value for *E. coli*, while substitutions of the original ARV-1502 sequence in the binding motif YLPRP always reduced the activity (peptides **10** to **27** and **107–183**), although peptides **158** (YKKRP) and **178** (YFKRP) were more active against *S. aureus* (MIC = 32 $\mu\text{g/mL}$). In general, substitutions with Asp and Ser were unfavorable, most likely due to poor interactions with the cell wall and the outer cell membrane (Welch et al., 2020). In contrast, the antimicrobial activity against *S. aureus* was significantly improved. This is very encouraging, especially for the Phe^3-Phe^4 -motif present in most highly active sequences (e.g., peptides **90**, **92**, **94**, **102**, and **106**). Again, it can be assumed that the cellular uptake is improved and that slight lytic effects may also occur (Matsuzaki, 2009; Lee et al., 2014). As shown in previous studies, the antimicrobial activity testing with the DnaK knockout mutant confirmed that DnaK is not the primary lethal target for PrAMPs, but rather can be described as a secondary non-lethal target (Krizsan et al., 2014; Knappe et al., 2016). In addition, some peptides were found to inhibit the ATPase and refolding activity of *E. coli* DnaK better than the lead sequence without improving the antimicrobial activity (e.g., peptides **66**, **111**, and **159**). Inhibition of DnaK is particularly harmful for bacteria, especially in stressful situations, leading to cell death (Paek and Walker, 1987). However,

since PrAMPs, such as ARV-1502-like Onc112, bind and act at the 70S ribosome of multiple bacteria and translation goes hand in hand with protein folding, a dual mode of action and binding to two different targets could be beneficial for the antimicrobial activity and reduce the probability of target-related resistances (Kolano et al., 2020).

CONCLUSION

The screening of 182 analogs derived from the lead PrAMP ARV-1502 provided interesting results allowing a better understanding of their effect on the functional activity of *E. coli* and *S. aureus* DnaK and its co-chaperones. Similarities and differences between the Gram-negative and Gram-positive chaperone systems could be identified, which could help to develop antibacterials targeting the bacterial chaperone system or to target the human Hsp70 chaperones to treat chaperone-related diseases including cancer. Substitutions with phenylalanine in ARV-1502 improved the binding to DnaK, inhibition of refolding activity, and antimicrobial activity against *S. aureus*. A stronger influence on the functionality of the chaperone system did not necessarily increase the antimicrobial activity, which confirms that inhibition of the DnaK chaperone system does not kill the bacteria, at least when using the favorable growth conditions applied for determining the MIC-values *in vitro*.

DATA AVAILABILITY STATEMENT

The dataset presented in this study can be found in the **Supplementary Material** (Table S3).

REFERENCES

- Böttger, R., Hoffmann, R., and Knappe, D. (2017). Differential Stability of Therapeutic Peptides with Different Proteolytic Cleavage Sites in Blood, Plasma and Serum. *PLoS ONE* 12, e0178943. doi:10.1371/journal.pone.0178943
- Brakel, A., Volke, D., Kraus, C. N., Otvos, L., and Hoffmann, R. (2019). Quantitation of a Novel Engineered Anti-infective Host Defense Peptide, ARV-1502: Pharmacokinetic Study of Different Doses in Rats and Dogs. *Front. Chem.* 7, 753. doi:10.3389/fchem.2019.00753
- Brehmer, D., Rüdiger, S., Gässler, C. S., Klostermeier, D., Packschies, L., Reinstein, J., et al. (2001). Tuning of Chaperone Activity of Hsp70 Proteins by Modulation of Nucleotide Exchange. *Nat. Struct. Biol.* 8, 427–432. doi:10.1038/87588
- Bukau, B., Mayer, M. P., Schröder, H., Rüdiger, S., Paal, K., and Laufen, T. (2000). Multistep Mechanism of Substrate Binding Determines Chaperone Activity of Hsp70. *Nat. Struct. Biol.* 7, 586–593. doi:10.1038/76819
- Cassone, M., Vogiatzi, P., La Montagna, R., De Olivier Inacio, V., Cudic, P., Wade, J. D., et al. (2008). Scope and Limitations of the Designer Proline-Rich Antibacterial Peptide Dimer, A3-APO, Alone or in Synergy with Conventional Antibiotics. *Peptides* 29, 1878–1886. doi:10.1016/j.peptides.2008.07.016
- Cesa, L. C., Patury, S., Komiyama, T., Ahmad, A., Zuiderweg, E. R. P., and Gestwicki, J. E. (2013). Inhibitors of Difficult Protein-Protein Interactions Identified by High-Throughput Screening of Multiprotein Complexes. *ACS Chem. Biol.* 8, 1988–1997. doi:10.1021/cb400356m

AUTHOR CONTRIBUTIONS

CK and LO designed ARV-1502 analogs. AB and RH conceived and designed the experiments. AB performed the experiments. LK performed MIC experiments for *S. aureus* and has cultivated the cells for cytotoxicity assay. The manuscript was drafted by AB. AB, LK, CK, LO, and RH reviewed and edited the manuscript. All authors critically revised the manuscript, approved the final version, and agreed to be accountable for all aspects of the work.

FUNDING

Support from the National Institutes of Health (grant R41AI142829-01 to CK) and a PhD stipend from Universität Leipzig to AB is gratefully acknowledged.

ACKNOWLEDGMENTS

We thank Susanne Moschütz and Norbert Sträter for providing the *E. coli* DnaK. We acknowledge support from the German Research Foundation (DFG) and Universität Leipzig within the program of Open Access Publishing.

SUPPLEMENTARY MATERIAL

The Supplementary Material for this article can be found online at: <https://www.frontiersin.org/articles/10.3389/fchem.2022.798006/full#supplementary-material>

- Chang, L., Bertelsen, E. B., Wisén, S., Larsen, E. M., Zuiderweg, E. R. P., and Gestwicki, J. E. (2008). High-throughput Screen for Small Molecules that Modulate the ATPase Activity of the Molecular Chaperone DnaK. *Anal. Biochem.* 372, 167–176. doi:10.1016/j.ab.2007.08.020
- Han, W., and Christen, P. (2003). Mechanism of the Targeting Action of DnaJ in the DnaK Molecular Chaperone System. *J. Biol. Chem.* 278, 19038–19043. doi:10.1074/jbc.M300756200
- Hansen, A., Schäfer, I., Knappe, D., Seibel, P., and Hoffmann, R. (2012). Intracellular Toxicity of Proline-Rich Antimicrobial Peptides Shuttled into Mammalian Cells by the Cell-Penetrating Peptide Penetratin. *Antimicrob. Agents Chemother.* 56, 5194–5201. doi:10.1128/AAC.00585-12
- Harrison, C. J., and Kuriyan, J. (1997). Crystal Structure of the Nucleotide Exchange Factor GrpE Bound to the Atpase Domain of the Molecular Chaperone DnaK. *Science* 276, 431–435. doi:10.2210/pdb1dkg/pdb
- Karzai, A. W., and McMacken, R. (1996). A Bipartite Signaling Mechanism Involved in DnaJ-Mediated Activation of the *Escherichia coli* DnaK Protein. *J. Biol. Chem.* 271, 11236–11246. doi:10.1074/jbc.271.19.11236
- Knappe, D., Goldbach, T., Hatfield, M., Palermo, N., Weinert, S., Sträter, N., et al. (2016). Proline-rich Antimicrobial Peptides Optimized for Binding to *Escherichia coli* Chaperone DnaK. *Ppl* 23, 1061–1071. doi:10.2174/0929866523666160719124712
- Kolano, L., Knappe, D., Volke, D., Sträter, N., and Hoffmann, R. (2020). Ribosomal Target-Binding Sites of Antimicrobial Peptides Api137 and Onc112 Are Conserved Among Pathogens Indicating New Lead Structures to Develop

- Novel Broad-Spectrum Antibiotics. *Chembiochem* 21, 2628–2634. doi:10.1002/cbic.202000109
- Krizsan, A., Prah, C., Goldbach, T., Knappe, D., and Hoffmann, R. (2015). Short Proline-Rich Antimicrobial Peptides Inhibit Either the Bacterial 70S Ribosome or the Assembly of its Large 50S Subunit. *Chembiochem* 16, 2304–2308. doi:10.1002/cbic.201500375
- Krizsan, A., Volke, D., Weinert, S., Sträter, N., Knappe, D., and Hoffmann, R. (2014). Insect-Derived Proline-Rich Antimicrobial Peptides Kill Bacteria by Inhibiting Bacterial Protein Translation at the 70 S Ribosome. *Angew. Chem. Int. Ed.* 53, 12236–12239. doi:10.1002/anie.201407145
- Lee, E., Shin, A., Jeong, K.-W., Jin, B., Jnawali, H. N., Shin, S., et al. (2014). Role of Phenylalanine and Valine¹⁰ Residues in the Antimicrobial Activity and Cytotoxicity of Piscidin-1. *PLoS ONE* 9, e114453. doi:10.1371/journal.pone.0114453
- Li, W., Tailhades, J., O'Brien-Simpson, N. M., Separovic, F., Otvos, L., Hossain, M. A., et al. (2014). Proline-rich Antimicrobial Peptides: Potential Therapeutics against Antibiotic-Resistant Bacteria. *Amino Acids* 46, 2287–2294. doi:10.1007/s00726-014-1820-1
- Li, X., Shao, H., R. Taylor, I., and E. Gestwicki, J. (2016). Targeting Allosteric Control Mechanisms in Heat Shock Protein 70 (Hsp70). *Ctmc* 16, 2729–2740. doi:10.2174/1568026616666160413140911
- Liebscher, M., Haupt, K., Yu, C., Jahreis, G., Lücke, C., and Schiene-Fischer, C. (2010). Rational Design of Novel Peptidic DnaK Ligands. *Chem. Eur. J. Chem. Bio.* 11, 1727–1737. doi:10.1002/cbic.201000166
- Matsuzaki, K. (2009). Control of Cell Selectivity of Antimicrobial Peptides. *Biochim. Biophys. Acta (Bba) - Biomembranes* 1788, 1687–1692. doi:10.1016/j.bbamem.2008.09.013
- Mayer, M. P., and Bukau, B. (2005). Hsp70 Chaperones: Cellular Functions and Molecular Mechanism. *Cmls, Cel. Mol. Life Sci.* 62, 670–684. doi:10.1007/s00018-004-4464-6
- Mosser, D. D., and Morimoto, R. I. (2004). Molecular Chaperones and the Stress of Oncogenesis. *Oncogene* 23, 2907–2918. doi:10.1038/sj.onc.1207529
- Noto, P. B., Abbadessa, G., Cassone, M., Mateo, G. D., Agelan, A., Wade, J. D., et al. (2008). Alternative Stabilities of a Proline-Rich Antibacterial Peptide *In Vitro* and *In Vivo*. *Protein Sci.* 17, 1249–1255. doi:10.1110/ps.034330.108
- Ostorhazi, E., Horvath, A., Szabo, D., and Otvos, L. (2017). Transdermally Administered Proline-Arginine-Rich Host Defense Peptides Show Systemic Efficacy in a Lethal Mouse Bacteremia Model. *Amino Acids* 49, 1647–1651. doi:10.1007/s00726-017-2457-7
- Otvos Jr., L., Ostorhazi, E., Szabo, D., Zumbrun, S. D., Miller, L. L., Halasohoris, S. A., et al. (2018). Synergy between Proline-Rich Antimicrobial Peptides and Small Molecule Antibiotics against Selected Gram-Negative Pathogens *In Vitro* and *In Vivo*. *Front. Chem.* 6, 309. doi:10.3389/fchem.2018.00309
- Otvos, L., Wade, J. D., Lin, F., Condie, B. A., Hanrieder, J., and Hoffmann, R. (2005). Designer Antibacterial Peptides Kill Fluoroquinolone-Resistant Clinical Isolates. *J. Med. Chem.* 48, 5349–5359. doi:10.1021/jm050347i
- Paek, K. H., and Walker, G. C. (1987). *Escherichia coli* dnaK Null Mutants Are Inviably at High Temperature. *J. Bacteriol.* 169, 283–290. doi:10.1128/jb.169.1.283-290.1987
- Rudiger, S., Germeroth, L., Schneider-Mergener, J., and Bukau, B. (1997). Substrate Specificity of the DnaK Chaperone Determined by Screening Cellulose-Bound Peptide Libraries. *EMBO J.* 16, 1501–1507. doi:10.1093/emboj/16.7.1501
- Schlecht, R., Scholz, S. R., Dahmen, H., Wegener, A., Sirrenberg, C., Musil, D., et al. (2013). Functional Analysis of Hsp70 Inhibitors. *PLoS ONE*. doi:10.1371/journal.pone.0078443.g001
- Scocchi, M., Tossi, A., and Gennaro, R. (2011). Proline-rich Antimicrobial Peptides: Converging to a Non-lytic Mechanism of Action. *Cell. Mol. Life Sci.* 68, 2317–2330. doi:10.1007/s00018-011-0721-7
- Szabo, A., Langer, T., Schroder, H., Flanagan, J., Bukau, B., and HartlUlrich, F. U. (1994). The ATP Hydrolysis-dependent Reaction Cycle of the *Escherichia coli* Hsp70 System DnaK, DnaJ, and GrpE. *Proc. Natl. Acad. Sci.* 91, 10345–10349. doi:10.1073/pnas.91.22.10345
- Wagih, O. (2017). Ggseqlogo: a Versatile R Package for Drawing Sequence Logos. *Bioinformatics* 33, 3645–3647. doi:10.1093/bioinformatics/btx469
- Wang, T., Echeverría, P. C., and Picard, D. (2014). in “CHAPTER 1. Overview of Molecular Chaperones in Health and Disease,” in *Inhibitors Of Molecular Chaperones as Therapeutic Agents*. Editors T. Machajewski, and Z. Gao (Cambridge: RSC Publ), 1–36.
- Welch, N. G., Li, W., Hossain, M. A., Separovic, F., O'Brien-Simpson, N. M., and Wade, J. D. (2020). (Re)Defining the Proline-Rich Antimicrobial Peptide Family and the Identification of Putative New Members. *Front. Chem.* 8, 607769. doi:10.3389/fchem.2020.607769
- Winardhi, R. S., Tang, Q., You, H., Sheetz, M., and Yan, J. (2018). The Holdase Function of *Escherichia coli* Hsp70 (DnaK) Chaperone. doi:10.1101/305854
- Wisén, S., and Gestwicki, J. E. (2008). Identification of Small Molecules that Modify the Protein Folding Activity of Heat Shock Protein 70. *Anal. Biochem.* 374, 371–377. doi:10.1016/j.ab.2007.12.009
- Zahn, M., Berthold, N., Kieslich, B., Knappe, D., Hoffmann, R., and Sträter, N. (2013). Structural Studies on the Forward and Reverse Binding Modes of Peptides to the Chaperone DnaK. *J. Mol. Biol.* 425, 2463–2479. doi:10.1016/j.jmb.2013.03.041
- Zhang, J.-H., Chung, T. D. Y., and Oldenburg, K. R. (1999). A Simple Statistical Parameter for Use in Evaluation and Validation of High Throughput Screening Assays. *J. Biomol. Screen.* 4, 67–73. doi:10.1177/108705719900400206

Conflict of Interest: CK and LO were employed by Aceragen, Inc.

The remaining authors declare that the research was conducted in the absence of any commercial or financial relationships that could be construed as a potential conflict of interest.

Publisher's Note: All claims expressed in this article are solely those of the authors and do not necessarily represent those of their affiliated organizations, or those of the publisher, the editors and the reviewers. Any product that may be evaluated in this article, or claim that may be made by its manufacturer, is not guaranteed or endorsed by the publisher.

Copyright © 2022 Brakel, Kolano, Kraus, Otvos and Hoffmann. This is an open-access article distributed under the terms of the Creative Commons Attribution License (CC BY). The use, distribution or reproduction in other forums is permitted, provided the original author(s) and the copyright owner(s) are credited and that the original publication in this journal is cited, in accordance with accepted academic practice. No use, distribution or reproduction is permitted which does not comply with these terms.



Recent Progress of Exosome Isolation and Peptide Recognition-Guided Strategies for Exosome Research

Kun Xu^{1,2}, Yulong Jin^{1,2*}, Yongming Li^{1,2}, Yanyan Huang^{1,2} and Rui Zhao^{1,2*}

¹Beijing National Laboratory for Molecular Sciences, CAS Key Laboratory of Analytical Chemistry for Living Biosystems, CAS Research/Education Center for Excellence in Molecular Sciences, Institute of Chemistry, Chinese Academy of Sciences, Beijing, China, ²School of Chemistry, University of Chinese Academy of Sciences, Beijing, China

Exosomes are membrane extracellular vesicles secreted by almost all kinds of cells, which are rich in proteins, lipids, and nucleic acids. As a medium of intercellular communication, exosomes play important roles in biological processes and are closely related to the occurrence, and development of many diseases. The isolation of exosomes and downstream analyses can provide important information to the accurate diagnosis and treatment of diseases. However, exosomes are various in a size range from 30 to 200 nm and exist in complex bio-systems, which provide significant challenges for the isolation and enrichment of exosomes. Different methods have been developed to isolate exosomes, such as the “gold-standard” ultracentrifugation, size-exclusion chromatography, and polymer precipitation. In order to improve the selectivity of isolation, affinity capture strategies based on molecular recognition are becoming attractive. In this review, we introduced the main strategies for exosome isolation and enrichment, and compared their strengths and limitations. Furthermore, combined with the excellent performance of targeted peptides, we summarized the application of peptide recognition in exosome isolation and engineering modification.

OPEN ACCESS

Edited by:

Wenshe Ray Liu,
Texas A&M University, United States

Reviewed by:

Bo Ning,
Tulane University, United States

*Correspondence:

Yulong Jin
jinyulong@iccas.ac.cn
Rui Zhao
zhaorui@iccas.ac.cn

Specialty section:

This article was submitted to
Chemical Biology,
a section of the journal
Frontiers in Chemistry

Received: 27 December 2021

Accepted: 14 February 2022

Published: 24 February 2022

Citation:

Xu K, Jin Y, Li Y, Huang Y and Zhao R
(2022) Recent Progress of Exosome
Isolation and Peptide Recognition-
Guided Strategies for
Exosome Research.
Front. Chem. 10:844124.
doi: 10.3389/fchem.2022.844124

Keywords: exosome, isolation, enrichment, peptide recognition, targeted therapy

INTRODUCTION

Exosomes are nanoscale extracellular vesicles secreted by almost all kinds of eukaryotic cells (Min et al., 2021) or bacteria (Vanaja et al., 2016; Tzipilevich et al., 2017). Unlike the outward blebbing of microvesicles, the biogenesis of exosomes involves a series of complex molecular regulation and substances exchange (Fei et al., 2021; Hao et al., 2021). It is generally believed that exosomes originate from the endosomes formed by the inward budding of plasma membrane (Jeppesen et al., 2019). Exosomes were once considered to be the waste products of cells in the original research. Nowadays, more and more studies have shown that exosomes play important roles in organisms, such as cell-to-cell communication (Ruhland et al., 2020; Schneider et al., 2021), immune response (Kalluri and LeBleu, 2020; Su et al., 2020), cell growth and differentiation (Yin et al., 2021; Zarnowski et al., 2021), as well as molecular transport (Zhu Q. et al., 2021). Crucially, the concentration and phenotype of exosomes have been proved to reflect the state of their parental cells and associate with the occurrence and development of various diseases, such as cancers (Jiang et al., 2021), infectious diseases (Ning et al., 2021; Xie et al., 2021), metabolic, and cardiovascular diseases (Kalluri and LeBleu, 2020). Therefore, developing exosome isolation methods with high efficiency and selectivity will definitely promote the deep understanding of the functions of exosome, as well as the accurate diagnosis and treatment of diseases.

Exosomes are widely existed in complex bio-systems, such as blood (Verweij et al., 2021), urine (Zheng et al., 2020), saliva (Wu et al., 2021), tears (Takeuchi et al., 2020), tissue fluid, and cerebrospinal fluid (Kalluri and LeBleu, 2020). Due to the heterogeneity of budding in the cell membrane, exosomes are not homogeneous vesicles but a series of complex subtypes with a size range from 30 to 200 nm and various functions respectively (Kalluri and Lebleu, 2020; Bordanaba-Florit et al., 2021). Besides, exosomes encapsulate various cargoes, including nucleic acids, proteins, lipids, and metabolites (Kowala et al., 2016; Mathieu et al., 2021). The contents of exosomes could be up- or down-regulated due to cell types or carcinogenesis (Cai et al., 2021). Such heterogeneity makes the isolation and enrichment of exosomes a challenging task.

A variety of exosome isolation protocols have been reported in the past few decades. Currently, ultracentrifugation has become the most accepted methods for exosome isolation (Théry et al., 2006; Yang et al., 2020), nevertheless it is often time-consuming and requires expensive instruments. Ultrafiltration (Liu et al., 2017), size-exclusion chromatography (Xu et al., 2016), and polymer precipitation (Pegtel and Gould, 2019) based on the physical characteristics (such as size and solubility) have been developed to achieve the isolation of exosomes. However, these methods usually capture the vesicles indiscriminately and cannot distinguish exosomes and lipoprotein particles efficiently. In order to improve the specificity, affinity-based capture strategies are emerging to isolate exosomes via the high binding abilities of specific exosomal markers to their corresponding ligands (Benjamin-Davalos et al., 2021). Because of the high specificity and affinity, antibodies are the most frequently used recognition tools (Ning et al., 2021; Park et al., 2021). Except for antibodies, peptides and aptamers have also been selected for exosome isolation (Gao et al., 2018; Chang et al., 2020; Zhu Lin et al., 2021). Through rational design and screening, specific protein-targeting peptides and aptamers can be obtained (Suwatthanarak et al., 2021a; Lin et al., 2021). Thus, highly selective capture and engineering modification of exosomes can be achieved effectively, which provide new strategies for exosome isolation and targeted therapy.

In this review, we introduced the main and novel strategies for exosome separation and enrichment, and discussed their strengths and limitations. Furthermore, we summarized the application of peptide recognition in exosome isolation and engineering modification.

2 ISOLATION AND ENRICHMENT STRATEGIES OF EXOSOMES

Obtaining exosomes with high yield, purity, and quality is the first step for the downstream analyses. However, exosomes are not single-component vesicles and have the complicated heterogeneity, which urgently demand the development of effective approaches for the isolation and enrichment of exosomes with high affinity and selectivity. After decades of efforts, several methods have been established, and successfully applied in exosome isolation from complex biosystems, such as

“gold-standard” ultracentrifugation, size-exclusion chromatography, ultrafiltration, and polymer precipitation. Since these methods are based on the physical characteristics of exosomes, it is difficult to distinguish exosomes and interfering particles efficiently. To improve the selectivity of exosome enrichment, the exosomal markers provide new thoughts to develop affinity-based capture strategies based on the specific binding between such markers, and their corresponding ligands. Through this strategy, exosome subtypes expressing specific proteins can be efficiently isolated and enriched. In this section, we will introduce the conventional and new methods of exosome isolation and enrichment, and compare their advantages and limitations of each method.

2.1 Conventional Isolation and Enrichment Strategies

2.1.1 Ultracentrifugation

Ultracentrifugation is the most widely accepted method for exosome separation, which usually includes differential ultracentrifugation, and gradient ultracentrifugation (Théry et al., 2006; Yang et al., 2020). This method can be employed to isolate exosomes from large scale of samples, such as more than 400 ml. However, the entire process usually takes more than 4 h and is very time-consuming (Shao et al., 2018). During the process of differential ultracentrifugation, cells, cell fragments, and large microvesicles in samples are removed successively under different centrifugal forces of 500, 2000, and 20,000 g (Figure 1A). Exosomes from cell culture medium are subsequently collected under ultracentrifugation conditions in excess of 1,10,000 g (Livshits et al., 2015). Li et al. successfully isolated exosomes from serum of breast cancer patients via differential ultracentrifugation (Li et al., 2018). Due to the high viscosity of serum, high centrifugal force of 1,50,000 g, and longer time of overnight were utilized.

During gradient ultracentrifugation, exosomes can be retained in the density equilibrium region (1.13–1.21 g/cm³) to isolate from other impurities (Melo et al., 2015). Paolini et al. isolated exosomes from serum of patients with multiple myeloma by differential ultracentrifugation, gradient ultracentrifugation, and one-step precipitation kits, and then assessed the presence of residual contaminants. The results showed that exosomes obtained by gradient ultracentrifugation were highly pure. In contrast, exosomes isolated by differential ultracentrifugation or one-step precipitation kits were contaminated by the residual matrix embedding the exosomes. The residual matrix prevented the fusion of the exosomes with plasma membrane, which interfered with the normal functioning of exosomes (Paolini et al., 2016). In general, exosomes can be obtained by gradient ultracentrifugation with higher purity, while differential ultracentrifugation has the advantage of separating large volume of samples at one time. However, it should be noted that high centrifugal force and repeated centrifugation may cause irreversible damage to vesicles.

2.1.2 Size-Exclusion Chromatography

Size-exclusion chromatography (SEC) is a newly adopted method for the isolation of exosomes from complex samples (Suthar et al.,

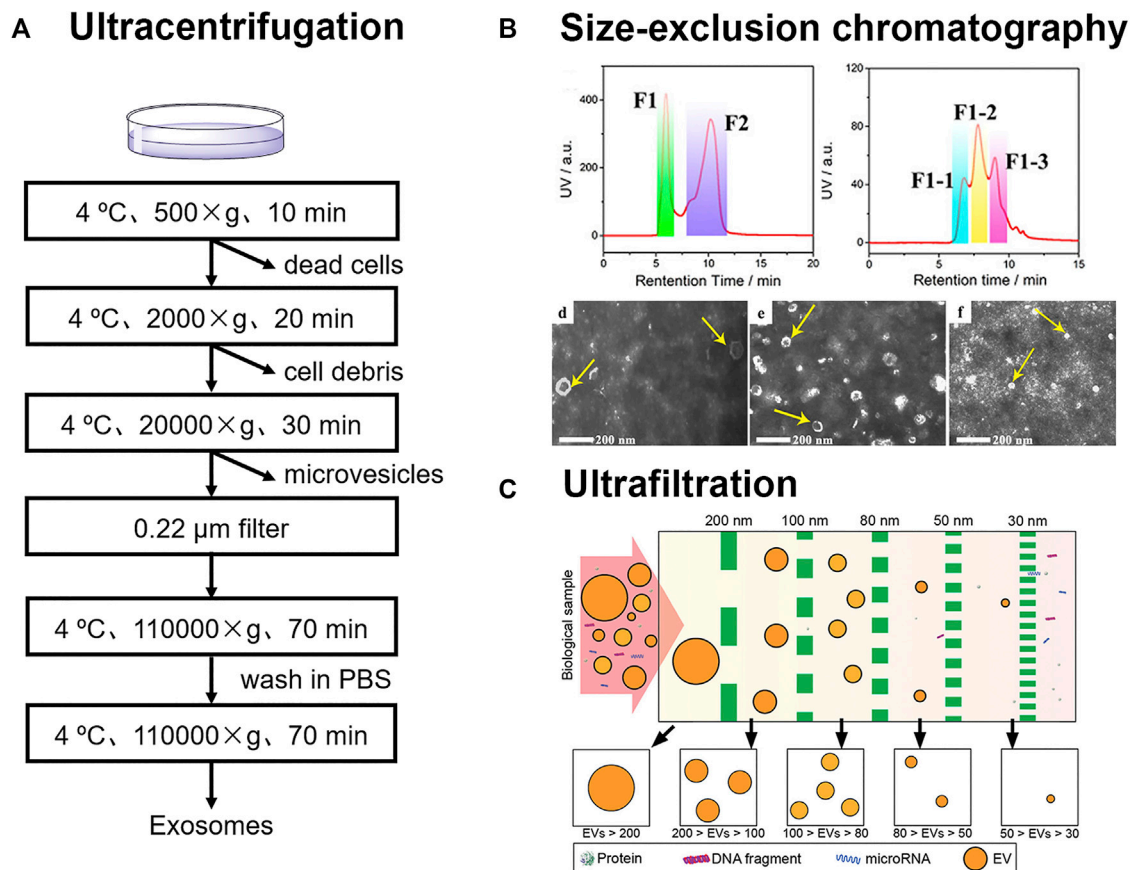


FIGURE 1 | (A) Schematic for differential ultracentrifugation **(B)** Size-exclusion chromatography was employed for the isolation of three exosomes subpopulations from urines. Reprinted with permission from Zheng et al., 2020. Copyright 2020 American Chemical Society. **(C)** Exosomes were sorted into subtypes with different size distribution via ultrafiltration. Reprinted with permission from Liu et al., 2017. Copyright 2017 American Chemical Society.

2020). In SEC columns, the diffusion paths of substances in the gels are different. The small vesicles and molecules in the samples have longer paths in the gels with a longer retention time, while the large vesicles have much shorter paths with a shorter retention time. Specifically, SEC method has good reproducibility and can also be used for quantitative detection of exosomes by fluorescence labeling (Xu et al., 2016).

The selection of gels has a significant effect on the isolation of exosomes. Xu et al. evaluated the separation efficiency of several commercially available SEC matrixes (Sephacryl S-100, Sepharose CL-2B, Sepharose CL-4B, and their combinations) for fluorescence-labeled exosomes from cell culture medium (Xu et al., 2016). The results showed that Sepharose CL-4B SEC column had the best separation efficiency, speed, and peak shape. Exosomes isolated from cell culture medium by this method showed a size range of 50–300 nm and the detection limit was calculated to be 2.9×10^7 particles/mL. Guo et al. recently also investigated Sepharose CL-6B, CL-4B and CL-2B matrixes for exosome enrichments. Sepharose CL-6B was superior to CL-4B and CL-2B in the isolation of exosomes from protein serums (Guo et al., 2021). The exosomes with the size of 200 nm were collected. Since the pore sizes of CL-2B, CL-

4B, and CL-6B are 75, 42, and 24 nm, respectively, exosomes with different sizes require different SEC separation materials.

SEC has also made great contributions in the research of exosome heterogeneity. Zheng et al. developed a two-dimensional SEC method for subtypes analysis of exosomes in urine (Zheng et al., 2020). Exosomes in urine were sorted into three subtypes (L-Exo, M-Exo, and S-Exo) in the 2nd D-SEC (**Figure 1B**). Further, 144 glycoproteins and 44 phosphoproteins from L-Exo, 156 glycoproteins and 46 phosphoproteins from M-Exo, as well as 134 glycoproteins and 10 phosphoproteins from S-Exo were identified by liquid chromatography-tandem mass spectrometry. This confirmed that proteins in three subtypes of exosomes had different glycosylation and phosphorylation levels, which suggested that the corresponding exosomes may play different biological functions.

2.1.3 Ultrafiltration

The size of vesicles is larger than that of biological molecules such as peptides, proteins, and nucleic acids. Vesicles can be intercepted by the membranes of different apertures. Poly (ether sulfone) (Heinemann et al., 2014), polycarbonate (Liu et al., 2017), and anodic aluminum oxide (Chen et al., 2021)

TABLE 1 | Comparison of strategies for exosome isolation and enrichment.

Strategy	Mechanism	Advantages	Limitations	Reference
Differential ultracentrifugation	density	a standard protocol, large sample volume	low yields and specificity, long time (more than 4 h), low purity, needs ultracentrifuge	Shao et al. (2018); Théry et al. (2006)
Gradient ultracentrifugation	density	a standard protocol, high purity	low yields, long time (more than 4 h), more complex operation steps, needs ultracentrifuge	Shao et al. (2018); Paolini et al. (2016)
Size-exclusion chromatography	size	fast and easy preparation, both small and large sample volume	low specificity, relatively high device cost	Zheng et al. (2020); Guo et al. (2021)
Ultrafiltration	size	fast and easy preparation, both small and large sample volume	low specificity, possible loss due to clogging	Liu et al. (2017); Chen et al. (2021)
Polymer precipitation	solubility	easy preparation, high yields, large sample volume	low specificity, long processing time (more than 12 h)	Yang et al. (2020)
Affinity capture	molecular recognition	high purity, suitable for small volume diagnosis	requires high-cost antibody, needs to select exosome markers	Chang et al. (2020); Yang et al. (2020)
Microfluidic technique	multiple principles, including affinity or size	portable and integrable, cost-efficient, fast preparation, high purity	low sample capacity, complex fabrication	Lin et al. (2020)

can be used for the membrane filter. To address the need of sorting different-sized exosomes from the same samples, filters with different apertures can also be used in series (**Figure 1C**; Liu et al., 2017). However, the pore size of the membrane is usually narrow, and it is easy to clog when separating biological samples. It may also cause the deformation of vesicles under pressure.

Ultrafiltration has the advantages of fast, low cost, easy operation, and batch processing. Based on this, ultrafiltration is also feasible to achieve instrument automation. Chen et al. reported an efficient exosome isolation method via the ultrafast-isolation system (EXODUS) for varied biofluids (Chen et al., 2021). Double coupled harmonic oscillations were introduced into a dual-membrane filter configuration for the generation of transverse waves. The nanoporous membrane allowed small molecules and fluids to pass through, while exosomes remained inside the central chamber. EXODUS reduced the entire isolation time for 10 ml of urine to less than 10 min, while the isolation time of ultracentrifugation was more than 3 h. The exosomal transcriptome in 113 urine samples was profiled by the automation of EXODUS. According to the distribution analyses of RNA biotypes, mRNAs (33.1%), long noncoding RNAs (21.9%) and pseudogenes (21.7%) were identified as the most abundant biotypes.

2.1.4 Polymer Precipitation

Polymer-based coprecipitation is also a common strategy in commercial exosome isolation kits, such as ExoQuick™ (System Biosciences, United States), ExoPrep (HansaBioMed, Estonia), and Total Exosome Isolation™ (Invitrogen, United States). Among various hydrophilic polymers, poly-ethylene glycol (PEG) is the widely used as the precipitation reagent. Hydrophilic PEG can interact with water molecules surrounding the exosomes, leading to a hydrophobic micro-environment (Yang et al., 2020). During this process, the solubility of exosomes decreases, and exosomes will precipitate under low-speed centrifugation. These commercial kits own high yields and easy adaptation to different researches. Meanwhile, this method avoids the utility of expensive ultracentrifugation and reduces the damage to vesicles. But it is worth noting that the process of polymer precipitation may also coprecipitate proteins, nucleic

acids, and lipids (Paolini et al., 2016; Shao et al., 2018). Purity is an important factor that could cause interference during downstream analysis. Therefore, it is very important to develop an exosome extraction kit with high purity and high yield. The mechanism, advantages, and limitations of the above-mentioned strategies for exosome isolation and enrichment have been summarized in **Table 1**.

2.2 New Isolation and Enrichment Strategies

Exosomes are widely distributed in complex biological systems, where many interfering particles exist, such as lipoprotein particles, protein aggregates, and microvesicles with similarity in size and structure to exosomes. As shown in **Table 1**, the isolation methods based on the physical properties of exosomes are generally less specific. Therefore, how to effectively distinguish exosomes from interfering particles is a key problem to be solved. Meanwhile, biological samples are often precious and difficult to be obtained, which makes the isolation of exosomes from small-volume samples a great challenge. Therefore, affinity-based capture strategies, microfluidic chips, molecularly imprinted polymer, asymmetric-flow field-flow fractionation, and other technologies are gradually established.

2.2.1 Affinity Capture with Biopolymers

Affinity capture strategy has been attractive in the isolation and enrichment of exosomes. Owing to the high affinity and excellent specificity, antibodies are the most frequently used recognition tools (Lin et al., 2021; Park et al., 2021). It is generally believed that certain transmembrane proteins (such as CD9, CD63, and CD81) are highly expressed on the surface of exosomes. Ning et al. described an assay approach where exosomes were directly captured from COVID-19 patient plasma through the interaction of an antibody with the exosomal surface protein CD81 (Ning et al., 2021). Then liposomes containing reagents for reverse transcriptase were introduced to realize the ultrasensitive detection of SARS-CoV-2 RNA. SARS-CoV-2-positive exosomes were detected early at 1 day post-infection in a non-human primate model. Meanwhile, this approach offered a

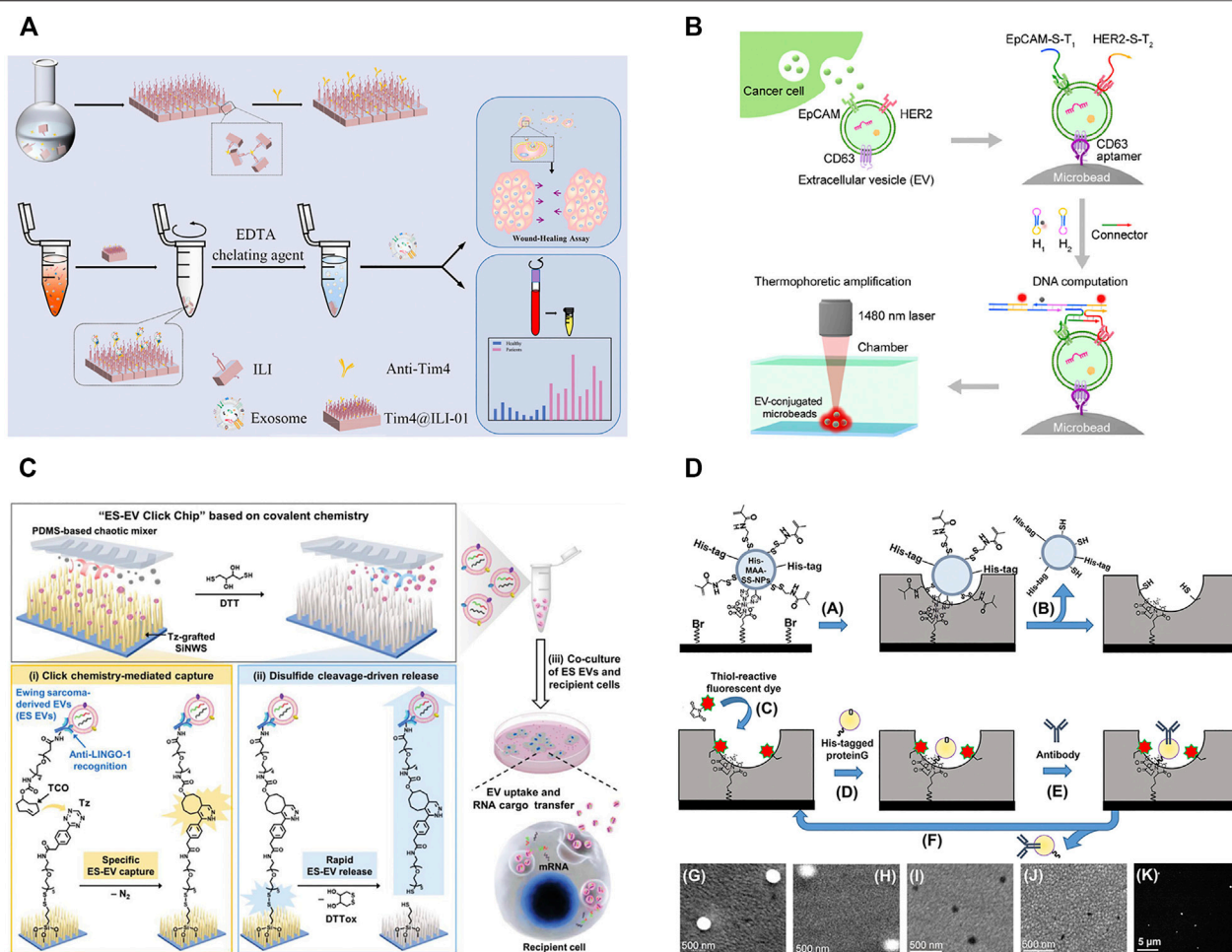


FIGURE 2 | (A) Schematic for synthesis of Tim4@ILI-01 immunoaffinity flake and exosomes enrichment and downstream analysis. Reprinted with permission from Zhang et al., 2021a. Copyright 2021 American Chemical Society. **(B)** Schematic of aptamer-based isolation of extracellular vesicles. Reprinted with permission from Li et al., 2021. Copyright 2021 American Chemical Society. **(C)** Schematic for nanowire-embedded microchip's working mechanism and purification of exosomes. Reprinted with permission from Dong et al., 2020. **(D)** Molecular imprinting-based nanocavities for sensing intact exosomes. Reprinted with permission from Takeuchi et al., 2020. Copyright 2020 American Chemical Society.

powerful tool for the diagnosis of patients with COVID-19. In addition, tumor-derived exosomes have also been identified to contain corresponding tumor biomarkers (Min et al., 2021), such as EpCAM, PD-L1, and EGFR. Li et al. established a strategy for the disease diagnosis based on microbead-assisted flow cytometry. Exosomes were enriched by aldehyde beads and flow cytometry was then performed to detect the disease markers by using corresponding antibodies. Using these strategies, they succeeded in achieving a highly sensitive diagnosis of breast cancer (Li et al., 2018) and invasive nonfunctional pituitary adenomas (Wang et al., 2019).

Although antibodies reveal the high affinity and excellent specificity in exosome isolation, antibodies also have some limitations, such as the complex preparation process, expensive costs, and low stability (Chang et al., 2020). Compared with antibodies, aptamers and peptides show the advantages of easy chemical synthesis, flexible modification, and high stability, which have expanded their applications in

exosome isolation and enrichment (Zhu L. et al., 2021; Chang et al., 2020). Li et al. modified the microbeads with CD63-aptamers and developed a new thermophoretic aptasensor for the separation and detection of exosomes (Figure 2B; Li et al., 2021). In this process, exosomes in the samples were first captured by CD63-aptamers to the surface of microbeads. Then, infrared laser was used for local heating to lead to the directional enrichment of microbeads. Employing this platform, breast cancer patients and healthy donors could be discriminated with a high accuracy of 97%. This strategy was also successfully applied in therapeutic response in metastatic breast cancer (Tian et al., 2021) and the classification of prostate cancer (Liu Chao et al., 2019). Chang et al. reported an CD63-aptamer-based magnetic graphene composites to achieve the convenient capture and efficient enrichment of exosomes from cell culture medium (Chang et al., 2020). The prepared composites were then applied to profile the metabolite composition of MCF-7- and MCF-10A-derived exosomes, and 119 metabolites were identified

in total. Compared with exosomes from MCF-10A, 43, and 42 metabolites were upregulated and downregulated in exosomes from MCF-7.

During the biogenesis of vesicles, phosphatidylserine is regulated by the flippase and distributed in the outer membrane of exosomes (Shao et al., 2018). Therefore, the highly expressed phosphatidylserine can also be used as a target for the isolation of exosomes. TiO_2 is often modified on the surface of magnetic beads to separate exosomes via the non-covalent bond of $\text{Ti-PO}_3\text{-Ti}$ (Pang et al., 2020). In addition, phosphatidylserine can also specifically bind to Tim4 protein and is identified to be Ca^{2+} -dependent. Magnetic beads immobilized with Tim4 can capture exosomes quickly, and intact exosomes can be easily eluted by chelating agent (Xu et al., 2018). Zhang et al. developed a novel Tim4@ILI-01 immunoaffinity flake material for the enrichment of exosomes from serum (Figure 2A; Zhang et al., 2021b). The gene analysis of eluted exosomes showed that the level of the expressed CD44 gene was significantly high in lung adenocarcinoma patients. The captured exosomes significantly induced more migration than the uneducated cells via a wound-healing assay, and the expression of epithelial-mesenchymal transition-related proteins changed significantly during cell migration. Since phosphatidylserine is not unique to exosomes and is also found in other vesicles, such as microvesicles, the specificity of this method remains to be assessed.

2.2.2 Molecular Imprinting Technique

As a kind of artificial antibodies, molecularly imprinted polymers (MIPs) have the unique advantages of high specificity, good chemical stability, tailor-made versatility (BelBruno, 2018). Shape, size, and spatial matching play the indispensable roles in the recognition process of MIPs with exosomes. Yang et al. reported a surface imprinting technology for antibody-free magnetic isolation of small extracellular vesicles (sEVs) (Yang et al., 2021). sEVs bound to the magnetic beads were easily removed by mild ultrasonic treatment, and vesicles could be isolated by the imprinted holes. The MIPs presented a higher capture yield in 20 min, which was 3-fold enrichment of sEVs compared with ultracentrifugation (more than 4 h). CD24 and EpCAM on sEVs were highly overexpressed in phenotype analyses, providing an effective predictive tool for real-time noninvasive monitoring of tumor development in mice. Mori et al. reported a kind of molecular imprinting-based antibody-conjugated nanocavities (Mori et al., 2019). Exosomes in tears were captured to the surface of MIPs by the double recognition of antibody and nano holes. The MIPs were successfully employed to discriminate normal exosomes and prostate cancer patients' exosomes in tear drops. However, when exosomes were used as the templates for exosome imprinting, it was usually difficult to synthesize MIPs with uniform pore sizes. Also, during the polymerization, the integrity and surface properties of exosomes might be destroyed. To overcome these drawbacks, silica nanoparticles have been used to simulate exosomes, aiming to create MIPs with uniform pore sizes (Figure 2D; Takeuchi et al., 2020). The apparent dissociation constant of MIPs to exosomes was calculated to be 2.4×10^{-16} mol/L, which was almost 1000-fold lower than that of commercial immunoassays. Exosomes from tears were successfully captured and used for the noninvasive diagnosis of breast cancer. Even though, the preparation routes of MIPs are still

relatively complex and required multi-step chemical modification (BelBruno, 2018). Meanwhile, the reproducibility and affinity of MIPs need to be improved.

2.2.3 Microfluidic Technique

Conventional exosome separation and purification methods often require a large volume of samples, complicated operation, or long time consuming. Microfluidics as a new technology can manipulate tiny fluids (ranging from a few microlitre to hundreds of microlitres) in microtubes. Microfluidic chip owns unique advantages of fast separation speed, high throughput, and less required samples, which is very suitable for the separation of exosomes from few precious biological samples (Lin et al., 2020; Hassanpour Tamrin et al., 2021).

Antibodies, aptamers, or peptides are often modified in microfluidic channels to increase the specificity of exosome isolation (Xu et al., 2018; Suwatthanarak et al., 2021b; Yu et al., 2021). Furthermore, in order to enhance the opportunities of collisions between exosomes and antibodies, aptamers, or peptides, a variety of micropipe shapes have been rationally designed for exosome enrichment, and such as trapping microchannel (Tayebi et al., 2020), Y-shaped micropillars (Xu et al., 2018), and nanowires (Sun Na et al., 2020). Their combination will help to improve the selectivity and efficiency of exosome isolation. Yu et al. reported a highly integrated exosome separation and detection chip (ExoSD) which was modified with anti-CD63 antibodies (Yu et al., 2021). Exosomes were efficiently isolated from cell culture supernatant and clinical serums of gastric cancer patients (stages I and II). To isolate Ewing sarcoma-derived exosomes, Dong et al. developed a specific purification system by a silicon nanowire-embedded microchip conjugated with antibodies (Figure 2C; Dong et al., 2020). The purified exosomes could be released intactly by disulfide cleavage and internalized once more by recipient cells, transferring their RNA cargoes *in vivo* to exhibit their potential roles in intercellular communication.

In addition, the isolation and analysis of single cell-derived exosomes is still a scientific problem. Zhu et al. designed a microwell array chips to trap a single cell, and antibody-coated glass slide could capture exosomes secreted from the single cell (Zhu F. et al., 2021). The number of exosomes secreted from every single cell was quantified by combining gold nanoparticle-enhanced silver staining, which reflecting the ability of individual cells to secrete exosomes. A very few cells (2–3%) in the cell line secreted exosomes 60 to 80 times faster than the other cells. If these cells were excluded, the total number of exosomes secreted would reduce by 2/3. This strategy would also provide a powerful tool for the research of other precious and rare cells with minimal consumption, such as circulating tumor cells.

2.2.4 Asymmetric-flow field-flow Fractionation

Asymmetric-flow field-flow fractionation (AF4) is a powerful fractionating technique with great flexibility to separate samples in a large size range, such as proteins, virus, liposomes, and various polymers (Kim et al., 2020). Compared with ultracentrifugation and ultrafiltration, AF4 could obtain intact

TABLE 2 | The sequences and targets of exosome-targeting peptides.

Peptide	Sequence	Target	References
CP05	CRHSQMTVTSRL	CD63	Gao et al. (2018)
P238	RSHRLRLH	CD9	Suwatthanarak et al. (2021a); Suwatthanarak et al. (2021b)
Vn96	PSQGGKGRSLSRFSWGALTLGEFLKL	Heat shock protein 70	Ghosh et al. (2014); Bijnisdorp et al. (2017); Bathini et al. (2021)
BP	RPPGFSPFR	Exosome membranes	Saludes et al. (2013); Gori et al. (2020)
PS-specific peptide	FNFRLLKAGAKIRFGRGC	Phosphatidylserine	Liu X. et al. (2021)
EGFR-specific peptide	FALGEA	Epidermal growth factor receptor	Sun Z. et al. (2020)

extracellular vesicles easily without high centrifugal force and pressure (Zhang and Lyden, 2019). By employing AF4, Zhang et al. identified two exosome subtypes (large exosome vesicles, 90–120 nm and small exosome vesicles, 60–80 nm) and discovered an abundance of non-membranous nanoparticles termed “exomeres” (~35 nm) (Zhang et al., 2018). Compared with exosomes, exomeres had unique N-glycosylation, proteins, lipids, DNA, and RNA profiles. These subsets were proved to diverse organ biodistribution, playing distinct biological functions. However, in the current study, AF4 for exosome isolation are usually lengthy duration and limited by the expensive equipment.

2.2.5 Liposome Fusion Technique

Liposomes and exosomes have the similar membrane structures, and the fluidity of the bilayer membrane allows the fusion of liposomes and exosomes. This principle has also been applied to the isolation and content analysis of exosomes (Ning et al., 2021). Liu et al. designed an antibody-modified lipid patch microarray for rapid capture of cancer extracellular vesicles (Liu Hui-Yu et al., 2021). The binding exosomes successfully fused with the lipid layer to trap the contents to the surface of the microarray. The RNA cargo trapped in the lipid patches offered a high potential for the downstream analysis.

3 PEPTIDE RECOGNITION-GUIDED NEW STRATEGIES FOR EXOSOME RESEARCH

Molecular recognition involves almost every link of life process and plays an important role in the growth, development, metabolism, and aging process of life. As a classical molecular recognition tool, antibody has been widely used in the recognition and research of target molecules. Meanwhile, peptides are one of the most crucial biomolecules in life, which are formed by dehydration of various amino acids. Compared with biological macromolecules, peptides have their unique advantages, such as high stability, diverse properties, and easy preparation (He et al., 2017). The rapid development of solid-phase synthesis strategy offers great convenience for the automatic batch synthesis and site-specific chemical modification of peptides (Pedersen et al., 2012).

In recent years, the applications of peptides towards exosome research received more and more concentration. Exosome-anchoring peptides were obtained by the rational design and screening from peptide libraries (Liu Xiangwei et al., 2019). The

sequences and targets of exosome-targeting peptides have been shown in **Table 2**. Exosome-targeting peptides with high binding affinity and selectivity were successfully applied for the efficient separation and enrichment of exosomes. Furthermore, cargo molecules coupled with peptides can be easily modified to exosomes via a non-covalent way, which play a huge role in drug delivery, and treatment of diseases.

3.1 Peptide Recognition-Based Exosome Isolation and Enrichment

To obtain a new exosome-targeting peptide, the highly expressed molecules in exosomes can be selected as the targets, such as transmembrane proteins (CD9, CD63, or CD81), tumor markers, and or phosphatidylserine on biofilms. Gao et al. selected the second extracellular loop of CD63 as a target and obtained a high affinity exosome-targeting peptide CP05 by phage display technology (Gao et al., 2018). CP05 can bind to the surface of exosomes efficiently (binding efficiency up to 88.7%) without changing the original properties of exosomes. When CP05 was fixed on dynabeads, $108.98 \pm 7.82 \mu\text{g}$ of exosomes could be captured efficiently from per milliliter of serum. For another exosomal marker protein CD9, Suwatthanarak et al. designed and synthesized a candidate peptide library in a microporous array, in which the peptide sequences were derived from the CD9 partner protein EWI-2 (Suwatthanarak et al., 2021a). A CD9-targeting peptide P238 was screened out, revealing a dissociation constant of $4.66 \times 10^{-7} \text{ mol/L}$. In order to further explore the binding mechanism of P238 to CD9, a site-by-site alanine substitution of P238 was performed. The results showed that the binding ability decreased significantly after the substitution of arginine, histidine, and serine. This also suggested that electrostatics and polarity played important roles in the binding of P238 to CD9 (Suwatthanarak et al., 2021b).

Besides, tumor-targeting peptides can accurately locate the tumor-derived exosomes from numerous exosomes, and provide a powerful tool for the early diagnosis of tumors. Sun et al. designed an electrochemical sensor, combining EPGR-targeted peptides with Zr-MOFs for the quantification of exosomes from glioblastoma (Sun Zhaowei et al., 2020). The detection range was from 9.5×10^3 – 1.9×10^7 particles/ μL , and the detection limit was 7.83×10^3 particles/ μL . The signals of exosomes from Glioblastoma patients were significantly higher than healthy samples, being consistent with the higher expression of EGFR in Glioblastoma-derived exosomes than normal cells.

Heat shock protein (HSP) is highly expressed in exosomes. When HSP-targeting peptide Vn96 was bind to exosomes, the

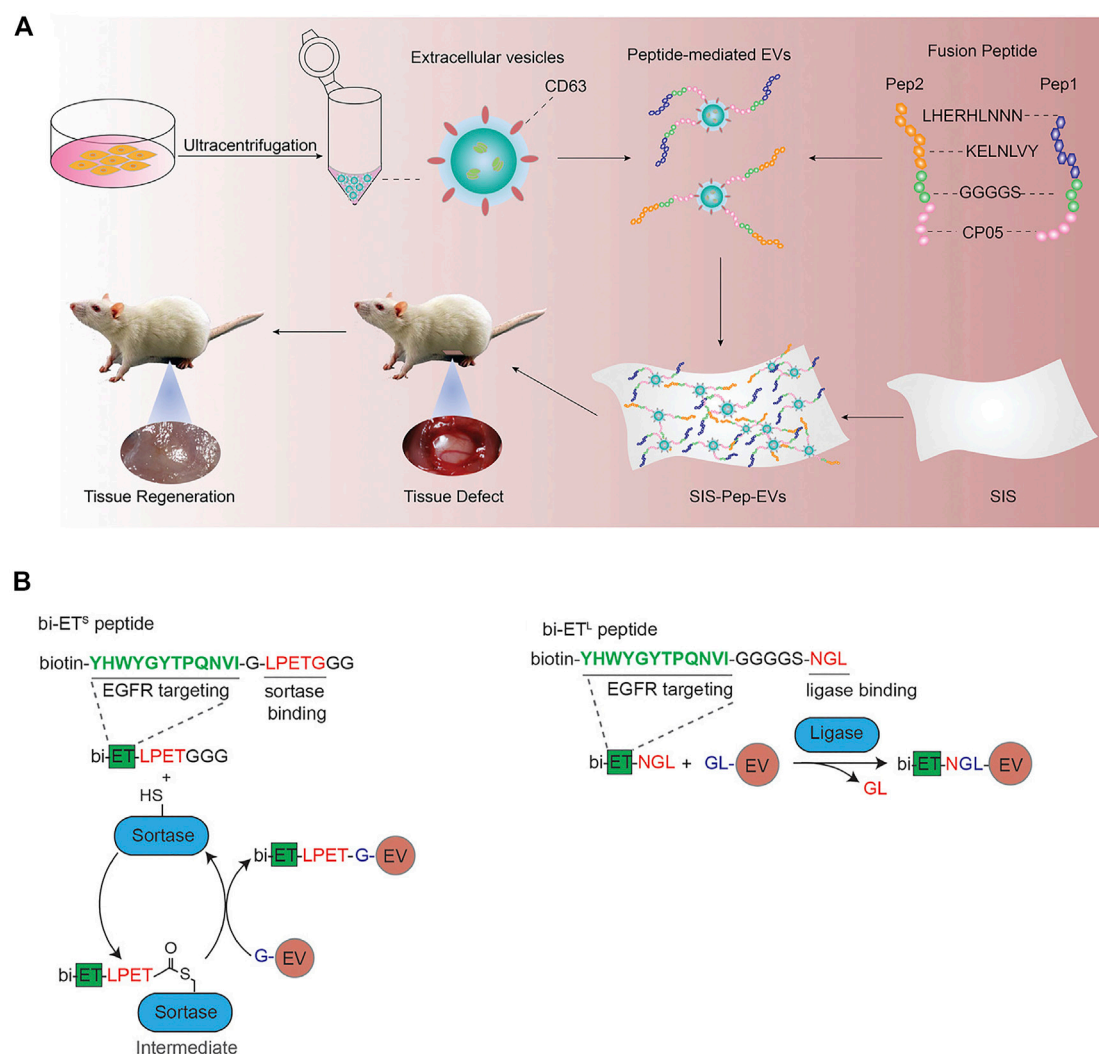


FIGURE 3 | (A) Schematic diagram of the membrane modified by fusion peptide-mediated exosomes. Reprinted with permission from Zhang et al., 2021b. **(B)** Protein ligating enzymes mediate a covalent conjugation of exosomes with peptides. Reprinted with permission from Pham et al., 2021.

hydrophilicity of exosomes might be changed, and reducing the solubility of exosomes (Ghosh et al., 2014). Inspired by this principle, Bijnsdorp et al. designed a new exosome isolation kit to obtain exosomes with low-speed centrifugation (Bijnsdorp et al., 2017). By the excellent binding ability of Vn96, Bathini et al. presented an immunoaffinity chip for the capture of exosomes from the MCF-7 cell culture medium (Bathini et al., 2021). The isolation efficiency obtained was about 90% when 200 μ l MCF-7 cell culture medium was added.

In addition, curvature-targeting peptide (Saludes et al., 2013) and phosphatidylserine-targeting peptide (Liu Xuejiao et al., 2021) have also been reported for exosome isolation and enrichment. Curvature-targeting peptide (BP) rich in positive-charged amino acids (e.g., arginine) can bind to the negative-charged exosome membranes via the electrostatic interaction. Meanwhile, the secondary helical structure can induce the peptides to be embedded in the defect of membranes, thus

increasing the anchoring ability of peptides. Gori et al. designed a microarray platform modified with curvature-targeting peptide to isolate exosomes from serum without pretreatment (Gori et al., 2020). Fluorescence imaging results showed that the captured exosomes ranged a particle size of 50–120 nm and were rich in CD63, CD81, and CD9.

3.2 Peptide-Engineering Exosomes for Targeted Therapy

Since the first clinical trial in the treatment of metastatic melanoma patients (Escudier et al., 2005), exosomes have attracted more and more attention in the field of drug delivery and disease treatment (Meng et al., 2021; Xie et al., 2021). As a platform for drug delivery and disease treatment, exosomes have several significant advantages. Firstly, homing effect is the unique advantage of exosomes compared with liposomes (Zhang et al.,

2017). Tumor-derived exosomes have natural targeting ability to tumor cells. Secondly, the membrane of exosomes protects the contents from release in the circulatory system (Zhu et al., 2020). After exosomes are fused with the target cell membrane, drugs loaded by exosomes can be released efficiently. Thirdly, exosomes secreted by cells are low immunogenic (Kalluri and Lebleu, 2020), such as plant- or milk-derived exosomes.

For drug loading, electroporation is a widely used method, however it can damage the membrane structure of exosomes (Gudbergsson et al., 2019). Different from electroporation, using exosome-targeting peptide as a bridge, the peptide-drug conjugates can be anchored to the surface of exosomes via the non-covalent interaction between the peptides and exosomes in a mild condition, which do not affect the original physiological activity of exosomes.

As described in the previous section, CP05 is an excellent exosome-targeting peptide that can anchor to the exosomal surface protein CD63. Gao et al. constructed a ternary complex with an oligonucleotide drug PMO, a muscle-targeting peptide M12 and an exosome-targeting peptide CP05. By the targeted recognition of CP05, exosomes were successfully loaded PMO and M12. The muscle-targeting peptide functionalized exosomes can accurately deliver oligonucleotide drugs to muscle tissue for the treatment of duchenne muscular dystrophy (Gao et al., 2018). Besides, CP05 was also successfully applied in the treatment of other several diseases, including tumor immunotherapy (Zuo et al., 2020), proliferative retinopathy (Dong et al., 2021), and traumatic optic neuropathy (Wang et al., 2021). CP05 can also work synergistically with other targeted peptides. For example, two collagen-binding peptides (LHERHLNNN and KELNLVY) were combined with CP05 to promote the engineering modification of exosomes derived from umbilical cord mesenchymal stem cells (Figure 3A; Zhang et al., 2021a). The peptide-exosome conjugates could improve tissue regeneration and were successfully used to the treatment of tissue injury.

In addition to these engineering approaches, it has also been reported that peptide can be inserted into exosomal surface proteins by transfection or ligase (Gudbergsson et al., 2019). Pham et al. used protein ligase to introduce EGFR-targeting peptides and HER2-targeting peptides to the surface of

exosomes (Figure 3B; Pham et al., 2021), which could improve the targeting ability of exosomes loaded with paclitaxel and achieve satisfied therapeutic effects.

4 CONCLUSION

With an extensive research interest in exosomes in recent years, a variety of methods based on different principles have been developed by researchers for the isolation and enrichment of exosomes from biofluids. Great progress has been achieved regarding the isolation performance, including yield, purity, quality, and efficiency. However, as summarized above, every method has its inherent merits and shortcomings based on these evaluation index. Therefore, it is wise and highly recommended to select the right isolation method or method combination that well suits the aim of downstream research on exosomes. Despite of the progress, there is much space for growth in this area. The development of novel materials, isolation methods that hold a better performance, as well as integrating them with online analytical instruments will be promising to achieve a more accurate and efficient isolation and analysis of exosomes in the years to come. Furthermore, the screening of exosome-targeting peptides as the affinity materials and developing new methods for the construction of peptide-exosome complex will provide useful tools for the peptide-recognition guided exosome research and applications.

AUTHOR CONTRIBUTIONS

RZ, KX, and YJ conceived the concept. KX wrote the original draft. All authors modified the manuscript and approved the submitted version.

FUNDING

Financial support from the National Natural Science Foundation of China (21974143, 21874141, and 22174145) and Chinese Academy of Sciences (E01Z0112) is gratefully acknowledged.

REFERENCES

- Bathini, S., Pakkiriswami, S., Ouellette, R. J., Ghosh, A., and Packirisamy, M. (2021). Magnetic Particle Based Liquid Biopsy Chip for Isolation of Extracellular Vesicles and Characterization by Gene Amplification. *Biosens. Bioelectron.* 194, 113585. doi:10.1016/j.bios.2021.113585
- BelBruno, J. J. (2018). Molecularly Imprinted Polymers. *Chem. Rev.* 119, 94–119. doi:10.1021/acs.chemrev.8b00171
- Benjamin-Davalos, S., Koroleva, M., Allen, C. L., Ernstoff, M. S., and Shu, S. L. (2021). Co-isolation of Cytokines and Exosomes: Implications for Immunomodulation Studies. *Front. Immunol.* 12, 638111. doi:10.3389/fimmu.2021.638111
- Bijnsdorp, I. V., Maxouri, O., Kardar, A., Schelfhorst, T., Piersma, S. R., Pham, T. V., et al. (2017). Feasibility of Urinary Extracellular Vesicle Proteome Profiling Using a Robust and Simple, Clinically Applicable Isolation Method. *J. Extracellular Vesicles* 6, 1313091. doi:10.1080/20013078.2017.1313091
- Bordanaba-Florit, G., Royo, F., Kruglik, S. G., and Falcón-Pérez, J. M. (2021). Using Single-Vesicle Technologies to Unravel the Heterogeneity of Extracellular Vesicles. *Nat. Protoc.* 16, 3163–3185. doi:10.1038/s41596-021-00551-z
- Cai, T., Zhang, Q., Wu, B., Wang, J., Li, N., Zhang, T., et al. (2021). LncRNA-encoded Microproteins: A New Form of Cargo in Cell Culture-Derived and Circulating Extracellular Vesicles. *J. Extracell. Vesicles* 10, e12123. doi:10.1002/jev2.12123
- Chang, M., Wang, Q., Qin, W., Shi, X., and Xu, G. (2020). Rational Synthesis of Aptamer-Functionalized Polyethylenimine-Modified Magnetic Graphene Oxide Composites for Highly Efficient Enrichment and Comprehensive Metabolomics Analysis of Exosomes. *Anal. Chem.* 92, 15497–15505. doi:10.1021/acs.analchem.0c03374
- Chen, Y., Zhu, Q., Cheng, L., Wang, Y., Li, M., Yang, Q., et al. (2021). Exosome Detection via the Ultrafast-Isolation System: EXODUS. *Nat. Methods* 18, 212–218. doi:10.1038/s41592-020-01034-x
- Dong, J., Zhang, R. Y., Sun, N., Hu, J., Smalley, M. D., Zhou, A., et al. (2020). Coupling Nanostructured Microchips with Covalent Chemistry Enables Purification of Sarcoma-Derived Extracellular Vesicles for Downstream

- Functional Studies. *Adv. Funct. Mater.* 30, 2003237. doi:10.1002/adfm.202003237
- Dong, X., Lei, Y., Yu, Z., Wang, T., Liu, Y., Han, G., et al. (2021). Exosome-mediated Delivery of an Anti-angiogenic Peptide Inhibits Pathological Retinal Angiogenesis. *Theranostics* 11, 5107–5126. doi:10.7150/thno.54755
- Escudier, B., Dorval, T., Chaput, N., André, F., Caby, M.-P., Novault, S., et al. (2005). Vaccination of Metastatic Melanoma Patients with Autologous Dendritic Cell (DC) Derived-Exosomes: Results of Thefirst Phase I Clinical Trial. *J. Transl. Med.* 3, 10. doi:10.1186/1479-5876-3-10
- Fei, X., Li, Z., Yang, D., Kong, X., Lu, X., Shen, Y., et al. (2021). Neddylaton of Coro1a Determines the Fate of Multivesicular Bodies and Biogenesis of Extracellular Vesicles. *J. Extracell. Vesicles* 10, e12153. doi:10.3402/jev.v2i0.2036010.1002/jev.2.12153
- Gao, X., Ran, N., Dong, X., Zuo, B., Yang, R., Zhou, Q., et al. (2018). Anchor Peptide Captures, Targets, and Loads Exosomes of Diverse Origins for Diagnostics and Therapy. *Sci. Transl. Med.* 10, eaat0195. doi:10.1126/scitranslmed.aaw0534
- Ghosh, A., Davey, M., Chute, I. C., Griffiths, S. G., Lewis, S., Chacko, S., et al. (2014). Rapid isolation of extracellular vesicles from cell culture and biological fluids using a synthetic peptide with specific affinity for heat shock proteins. *PLoS One*, 9:e110443. doi:10.1371/journal.pone.0110443
- Gori, A., Romanato, A., Bergamaschi, G., Strada, A., Gagni, P., Frigerio, R., et al. (2020). Membrane-binding Peptides for Extracellular Vesicles On-chip Analysis. *J. Extracellular Vesicles* 9, 1751428. doi:10.1080/20013078.2020.1751428
- Gudbergsson, J. M., Jönsson, K., Simonsen, J. B., and Johnsen, K. B. (2019). Systematic Review of Targeted Extracellular Vesicles for Drug Delivery - Considerations on Methodological and Biological Heterogeneity. *J. Controlled Release* 306, 108–120. doi:10.1016/j.jconrel.2019.06.006
- Guo, J., Wu, C., Lin, X., Zhou, J., Zhang, J., Zheng, W., et al. (2021). Establishment of a Simplified Dichotomic Size-Exclusion Chromatography for Isolating Extracellular Vesicles toward Clinical Applications. *J. Extracell. Vesicles* 10, e12145. doi:10.1002/jev.2.12145
- Hao, Y., Song, H., Zhou, Z., Chen, X., Li, H., Zhang, Y., et al. (2021). Promotion or Inhibition of Extracellular Vesicle Release: Emerging Therapeutic Opportunities. *J. Controlled Release* 340, 136–148. doi:10.1016/j.jconrel.2021.10.019
- Hassanpour Tamrin, S., Sanati Nezhad, A., and Sen, A. (2021). Label-free Isolation of Exosomes Using Microfluidic Technologies. *ACS Nano* 15, 17047–17079. doi:10.1021/acsnano.1c03469
- He, J., Gui, S., Huang, Y., Hu, F., Jin, Y., Yu, Y., et al. (2017). Rapid, Sensitive, and In-Solution Screening of Peptide Probes for Targeted Imaging of Live Cancer Cells Based on Peptide Recognition-Induced Emission. *Chem. Commun.* 53, 11091–11094. doi:10.1039/c7cc06485c
- Heinemann, M. L., Ilmer, M., Silva, L. P., Hawke, D. H., Recio, A., Vorontsova, M. A., et al. (2014). Benchtop Isolation and Characterization of Functional Exosomes by Sequential Filtration. *J. Chromatogr. A* 1371, 125–135. doi:10.1016/j.chroma.2014.10.026
- Jeppesen, D. K., Fenix, A. M., Franklin, J. L., Higginbotham, J. N., Zhang, Q., Zimmerman, L. J., et al. (2019). Reassessment of Exosome Composition. *Cell* 177, 428–445. doi:10.1016/j.cell.2019.02.029
- Jiang, C., Zhang, N., Hu, X., and Wang, H. (2021). Tumor-associated Exosomes Promote Lung Cancer Metastasis through Multiple Mechanisms. *Mol. Cancer* 20, 117. doi:10.1186/s12943-021-01411-w
- Kalluri, R., and LeBleu, V. S. (2020). The Biology, Function, and Biomedical Applications of Exosomes. *Science* 367, 640–655. doi:10.1126/science.aau6977
- Kim, Y. B., Yang, J. S., Lee, G. B., and Moon, M. H. (2020). Evaluation of Exosome Separation from Human Serum by Frit-Inlet Asymmetrical Flow Field-Flow Fractionation and Multiangle Light Scattering. *Analytica Chim. Acta* 1124, 137–145. doi:10.1016/j.aca.2020.05.031
- Kowal, J., Arras, G., Colombo, M., Jouve, M., Morath, J. P., Primdal-Bengtson, B., et al. (2016). Proteomic Comparison Defines Novel Markers to Characterize Heterogeneous Populations of Extracellular Vesicle Subtypes. *Proc. Natl. Acad. Sci. USA* 113, E968–E977. doi:10.1073/pnas.1521230113
- Li, W., Shao, B., Liu, C., Wang, H., Zheng, W., Kong, W., et al. (2018). Noninvasive Diagnosis and Molecular Phenotyping of Breast Cancer through Microbead-Assisted Flow Cytometry Detection of Tumor-Derived Extracellular Vesicles. *Small Methods* 2, 1800122. doi:10.1002/smt.201800122
- Li, Y., Deng, J., Han, Z., Liu, C., Tian, F., Xu, R., et al. (2021). Molecular Identification of Tumor-Derived Extracellular Vesicles Using Thermophoresis-Mediated DNA Computation. *J. Am. Chem. Soc.* 143, 1290–1295. doi:10.1021/jacs.0c12016
- Lin, B., Tian, T., Lu, Y., Liu, D., Huang, M., Zhu, L., et al. (2021). Tracing Tumor-Derived Exosomal PD-L1 by Dual-Aptamer Activated Proximity-Induced Droplet Digital PCR. *Angew. Chem. Int. Ed.* 60, 7582–7586. doi:10.1002/anie.202015628
- Lin, S., Yu, Z., Chen, D., Wang, Z., Miao, J., Li, Q., et al. (2020). Progress in Microfluidics-Based Exosome Separation and Detection Technologies for Diagnostic Applications. *Small* 16, 1903916. doi:10.1002/sml.201903916
- Liu, C., Zhao, J., Tian, F., Cai, L., Zhang, W., Feng, Q., et al. (2019). Low-cost Thermophoretic Profiling of Extracellular-Vesicle Surface Proteins for the Early Detection and Classification of Cancers. *Nat. Biomed. Eng.* 3, 183–193. doi:10.1038/s41551-018-0343-6
- Liu, F., Vermesh, O., Mani, V., Ge, T. J., Madsen, S. J., Sabour, A., et al. (2017). The Exosome Total Isolation Chip. *ACS Nano* 11, 10712–10723. doi:10.1021/acsnano.7b04878
- Liu, H.-Y., Kumar, R., Zhong, C., Gorji, S., Paniushkina, L., Masood, R., et al. (2021). Rapid Capture of Cancer Extracellular Vesicles by Lipid Patch Microarrays. *Adv. Mater.* 33, 2008493. doi:10.1002/adma.202008493
- Liu, X., Wang, Q., Chen, J., Chen, X., and Yang, W. (2021). Ultrasensitive Electrochemiluminescence Biosensor for the Detection of Tumor Exosomes Based on Peptide Recognition and Luminol-AuNPs@g-C3n4 Nanoprobe Signal Amplification. *Talanta* 221, 121379. doi:10.1016/j.talanta.2020.121379
- Liu, X., Yang, X., Sun, W., Wu, Q., Song, Y., Yuan, L., et al. (2019). Systematic Evolution of Ligands by Exosome Enrichment: A Proof-Of-Concept Study for Exosome-Based Targeting Peptide Screening. *Adv. Biosys.* 3, 1800275. doi:10.1002/adbi.201800275
- Livshits, M. A., Khomyakova, E., Evtushenko, E. G., Lazarev, V. N., Kulemin, N. A., Semina, S. E., et al. (2015). Isolation of Exosomes by Differential Centrifugation: Theoretical Analysis of a Commonly Used Protocol. *Sci. Rep.* 5, 17319. doi:10.1038/srep17319
- Mathieu, M., Névo, N., Jouve, M., Valenzuela, J. I., Maurin, M., Verweij, F. J., et al. (2021). Specificities of Exosome versus Small Ectosome Secretion Revealed by Live Intracellular Tracking of CD63 and CD9. *Nat. Commun.* 12, 4389. doi:10.1038/s41467-021-24384-2
- Melo, S. A., Luecke, L. B., Kahlert, C., Fernandez, A. F., Gammon, S. T., Kaye, J., et al. (2015). Glypican-1 Identifies Cancer Exosomes and Detects Early Pancreatic Cancer. *Nature* 523, 177–182. doi:10.1038/nature14581
- Meng, Q. F., Zhao, Y., Dong, C., Liu, L., Pan, Y., Lai, J., et al. (2021). Genetically Programmable Fusion Cellular Vesicles for Cancer Immunotherapy. *Angew. Chem. Int. Edit* 60, 1–8. doi:10.1002/anie.202108342
- Min, L., Wang, B., Bao, H., Li, X., Zhao, L., Meng, J., et al. (2021). Advanced Nanotechnologies for Extracellular Vesicle-Based Liquid Biopsy. *Adv. Sci.* 8, 2102789. doi:10.1002/advs.202102789
- Mori, K., Hirase, M., Morishige, T., Takano, E., Sunayama, H., Kitayama, Y., et al. (2019). A Pretreatment-Free, Polymer-Based Platform Prepared by Molecular Imprinting and Post-Imprinting Modifications for Sensing Intact Exosomes. *Angew. Chem.* 131, 1626–1629. doi:10.1002/ange.201811142
- Ning, B., Huang, Z., Youngquist, B. M., Scott, J. W., Niu, A., Bojanowski, C. M., et al. (2021). Liposome-mediated Detection of SARS-CoV-2 RNA-Positive Extracellular Vesicles in Plasma. *Nat. Nanotechnol.* 16, 1039–1044. doi:10.1038/s41565-021-00939-8
- Pang, Y., Shi, J., Yang, X., Wang, C., Sun, Z., and Xiao, R. (2020). Personalized Detection of Circling Exosomal PD-L1 Based on Fe3O4@TiO2 Isolation and SERS Immunoassay. *Biosens. Bioelectron.* 148, 111800. doi:10.1016/j.bios.2019.111800
- Paolini, L., Zendri, A., Noto, G. D., Busatto, S., Lottini, E., Radeghieri, A., et al. (2016). Residual Matrix from Different Separation Techniques Impacts Exosome Biological Activity. *Sci. Rep.* 6, 23550. doi:10.1038/srep23550
- Park, J., Park, J. S., Huang, C.-H., Jo, A., Cook, K., Wang, R., et al. (2021). An Integrated Magneto-Electrochemical Device for the Rapid Profiling of Tumour Extracellular Vesicles from Blood Plasma. *Nat. Biomed. Eng.* 5, 678–689. doi:10.1038/s41551-021-00752-7

- Pedersen, S. L., Tofteng, A. P., Malik, L., and Jensen, K. J. (2012). Microwave Heating in Solid-phase Peptide Synthesis. *Chem. Soc. Rev.* 41, 1826–1844. doi:10.1039/c1cs15214a
- Pegtel, D. M., and Gould, S. J. (2019). Exosomes. *Annu. Rev. Biochem.* 88, 487–514. doi:10.1146/annurev-biochem-013118-111902
- Pham, T. C., Jayasinghe, M. K., Pham, T. T., Yang, Y., Wei, L., Usman, W. M., et al. (2021). Covalent Conjugation of Extracellular Vesicles with Peptides and Nanobodies for Targeted Therapeutic Delivery. *J. Extracell. Vesicles* 10, e12057. doi:10.1002/jev2.12057
- Ruhland, M. K., Roberts, E. W., Cai, E., Mujal, A. M., Marchuk, K., Beppler, C., et al. (2020). Visualizing Synaptic Transfer of Tumor Antigens Among Dendritic Cells. *Cancer Cell* 37, 786–799. doi:10.1016/j.ccell.2020.05.002
- Saludes, J. P., Morton, L. A., Coulup, S. K., Fiorini, Z., Cook, B. M., Beninson, L., et al. (2013). Multivalency Amplifies the Selection and Affinity of Bradykinin-Derived Peptides for Lipid Nanovesicles. *Mol. Biosyst.* 9, 2005–2009. doi:10.1039/c3mb70109c
- Schneider, E., Winzer, R., Rissiek, A., Ricklefs, I., Meyer-Schwesinger, C., Ricklefs, F. L., et al. (2021). CD73-mediated Adenosine Production by CD8⁺ T Cell-Derived Extracellular Vesicles Constitutes an Intrinsic Mechanism of Immune Suppression. *Nat. Commun.* 12, 5911. doi:10.1038/s41467-021-26134-w
- Shao, H., Im, H., Castro, C. M., Breakefield, X., Weissleder, R., and Lee, H. (2018). New Technologies for Analysis of Extracellular Vesicles. *Chem. Rev.* 118, 1917–1950. doi:10.1021/acs.chemrev.7b00534
- Su, D., Tsai, H. I., Xu, Z., Yan, F., Wu, Y., Xiao, Y., et al. (2020). Exosomal PD-L1 Functions as an Immunosuppressant to Promote Wound Healing. *J. Extracellular Vesicles* 9, 1709262. doi:10.1080/20013078.2019.1709262
- Sun, N., Lee, Y.-T., Zhang, R. Y., Kao, R., Teng, P.-C., Yang, Y., et al. (2020). Purification of HCC-specific Extracellular Vesicles on Nanosubstrates for Early HCC Detection by Digital Scoring. *Nat. Commun.* 11, 4489. doi:10.1038/s41467-020-18311-0
- Sun, Z., Wang, L., Wu, S., Pan, Y., Dong, Y., Zhu, S., et al. (2020). An Electrochemical Biosensor Designed by Using Zr-Based Metal-Organic Frameworks for the Detection of Glioblastoma-Derived Exosomes with Practical Application. *Anal. Chem.* 92, 3819–3826. doi:10.1021/acs.analchem.9b05241
- Suthar, J., Parsons, E. S., Hoogenboom, B. W., Williams, G. R., and Guldin, S. (2020). Acoustic Immunosensing of Exosomes Using a Quartz crystal Microbalance with Dissipation Monitoring. *Anal. Chem.* 92, 4082–4093. doi:10.1021/acs.analchem.9b05736
- Suwatthanarak, T., Tanaka, M., Miyamoto, Y., Miyado, K., and Okochi, M. (2021b). Inhibition of Cancer-Cell Migration by Tetraspanin CD9-Binding Peptide. *Chem. Commun.* 57, 4906–4909. doi:10.1039/d1cc01295a
- Suwatthanarak, T., Thiodorus, I. A., Tanaka, M., Shimada, T., Takeshita, D., Yasui, T., et al. (2021a). Microfluidic-based Capture and Release of Cancer-Derived Exosomes via Peptide-Nanowire Hybrid Interface. *Lab. Chip* 21, 597–607. doi:10.1039/d0lc00899k
- Takeuchi, T., Mori, K., Sunayama, H., Takano, E., Kitayama, Y., Shimizu, T., et al. (2020). Antibody-conjugated Signaling Nanocavities Fabricated by Dynamic Molding for Detecting Cancers Using Small Extracellular Vesicle Markers from Tears. *J. Am. Chem. Soc.* 142, 6617–6624. doi:10.1021/jacs.9b13874
- Tayebi, M., Zhou, Y., Tripathi, P., Chandramohanadas, R., and Ai, Y. (2020). Exosome Purification and Analysis Using a Facile Microfluidic Hydrodynamic Trapping Device. *Anal. Chem.* 92, 10733–10742. doi:10.1021/acs.analchem.0c02006
- Théry, C., Amigorena, S., Raposo, G., and Clayton, A. (2006). Isolation and Characterization of Exosomes from Cell Culture Supernatants and Biological Fluids. *Curr. Protoc. Cell Biol.* Chapter 3. doi:10.1002/0471143030.cb0322s30
- Tian, F., Zhang, S., Liu, C., Han, Z., Liu, Y., Deng, J., et al. (2021). Protein Analysis of Extracellular Vesicles to Monitor and Predict Therapeutic Response in Metastatic Breast Cancer. *Nat. Commun.* 12, 2536. doi:10.1038/s41467-021-22913-7
- Tzipilevich, E., Habusha, M., and Ben-Yehuda, S. (2017). Acquisition of Phage Sensitivity by Bacteria through Exchange of Phage Receptors. *Cell* 168, 186–199. doi:10.1016/j.cell.2016.12.003
- Vanaja, S. K., Russo, A. J., Behl, B., Banerjee, I., Yankova, M., Deshmukh, S. D., et al. (2016). Bacterial Outer Membrane Vesicles Mediate Cytosolic Localization of LPS and Caspase-11 Activation. *Cell* 165, 1106–1119. doi:10.1016/j.cell.2016.04.015
- Verweij, F. J., Balaj, L., Boulanger, C. M., Carter, D. R. F., Compeer, E. B., D'Angelo, G., et al. (2021). The Power of Imaging to Understand Extracellular Vesicle Biology *In Vivo*. *Nat. Methods* 18, 1013–1026. doi:10.1038/s41592-021-01206-3
- Wang, H., Chen, K., Yang, Z., Li, W., Wang, C., Zhang, G., et al. (2019). Diagnosis of Invasive Nonfunctional Pituitary Adenomas by Serum Extracellular Vesicles. *Anal. Chem.* 91, 9580–9589. doi:10.1021/acs.analchem.9b00914
- Wang, T., Li, Y., Guo, M., Dong, X., Liao, M., Du, M., et al. (2021). Exosome-mediated Delivery of the Neuroprotective Peptide PACAP38 Promotes Retinal Ganglion Cell Survival and Axon Regeneration in Rats with Traumatic Optic Neuropathy. *Front. Cell Dev. Biol.* 9, 659783. doi:10.3389/fcell.2021.659783
- Wu, M., Chen, Z., Xie, Q., Xiao, B., Zhou, G., Chen, G., et al. (2021). One-step Quantification of Salivary Exosomes Based on Combined Aptamer Recognition and Quantum Dot Signal Amplification. *Biosens. Bioelectron.* 171, 112733. doi:10.1016/j.bios.2020.112733
- Xie, F., Su, P., Pan, T., Zhou, X., Li, H., Huang, H., et al. (2021). Engineering Extracellular Vesicles Enriched with Palmitoylated ACE2 as COVID-19 Therapy. *Adv. Mater.* 33, 2103471. doi:10.1002/adma.202103471
- Xu, H., Liao, C., Zuo, P., Liu, Z., and Ye, B.-C. (2018). Magnetic-based Microfluidic Device for On-Chip Isolation and Detection of Tumor-Derived Exosomes. *Anal. Chem.* 90, 13451–13458. doi:10.1021/acs.analchem.8b03272
- Xu, R., Fitts, A., Li, X., Fernandes, J., Pochampally, R., Mao, J., et al. (2016). Quantification of Small Extracellular Vesicles by Size Exclusion Chromatography with Fluorescence Detection. *Anal. Chem.* 88, 10390–10394. doi:10.1021/acs.analchem.6b03348
- Yang, D., Zhang, W., Zhang, H., Zhang, F., Chen, L., Ma, L., et al. (2020). Progress, Opportunity, and Perspective on Exosome Isolation - Efforts for Efficient Exosome-Based Theranostics. *Theranostics* 10, 3684–3707. doi:10.7150/thno.41580
- Yang, J., Pan, B., Zeng, F., He, B., Gao, Y., Liu, X., et al. (2021). Magnetic Colloid Antibodies Accelerate Small Extracellular Vesicles Isolation for point-of-care Diagnostics. *Nano Lett.* 21, 2001–2009. doi:10.1021/acs.nanolett.0c04476
- Yin, Y., Chen, H., Wang, Y., Zhang, L., and Wang, X. (2021). Roles of Extracellular Vesicles in the Aging Microenvironment and Age-Related Diseases. *J. Extracell. Vesicles* 10, e12154. doi:10.1002/jev2.12154
- Yu, Z., Lin, S., Xia, F., Liu, Y., Zhang, D., Wang, F., et al. (2021). ExoSD Chips for High-Purity Immunomagnetic Separation and High-Sensitivity Detection of Gastric Cancer Cell-Derived Exosomes. *Biosens. Bioelectron.* 194, 113594. doi:10.1016/j.bios.2021.113594
- Zarnowski, R., Noll, A., Chevrette, M. G., Sanchez, H., Jones, R., Anhalt, H., et al. (2021). Coordination of Fungal Biofilm Development by Extracellular Vesicle Cargo. *Nat. Commun.* 12, 6235. doi:10.1038/s41467-021-26525-z
- Zhang, H., Freitas, D., Kim, H. S., Fabijanic, K., Li, Z., Chen, H., et al. (2018). Identification of Distinct Nanoparticles and Subsets of Extracellular Vesicles by Asymmetric Flow Field-Flow Fractionation. *Nat. Cell Biol.* 20, 332–343. doi:10.1038/s41556-018-0040-4
- Zhang, H., and Lyden, D. (2019). Asymmetric-flow Field-Flow Fractionation Technology for Exosome and Small Extracellular Vesicle Separation and Characterization. *Nat. Protoc.* 14, 1027–1053. doi:10.1038/s41596-019-0126-x
- Zhang, L., Ma, S., Wei, P., Zhao, Y., Mu, Y., Wu, J., et al. (2021a). Small Intestinal Submucosa Membrane Modified by Fusion Peptide-Mediated Extracellular Vesicles to Promote Tissue Regeneration. *Adv. Healthc. Mater.*, 2101298. doi:10.1002/adhm.202101298
- Zhang, L., Wang, H., Zhao, G., Li, N., Wang, X., Li, Y., et al. (2021b). Anti-Tim4 Grafting Strongly Hydrophilic Metal-Organic Frameworks Immunoaffinity Flake for High-Efficiency Capture and Separation of Exosomes. *Anal. Chem.* 93, 6534–6543. doi:10.1021/acs.analchem.1c00528
- Zhang, W., Yu, Z.-L., Wu, M., Ren, J.-G., Xia, H.-F., Sa, G.-L., et al. (2017). Magnetic and Folate Functionalization Enables Rapid Isolation and Enhanced Tumor-Targeting of Cell-Derived Microvesicles. *ACS Nano* 11, 277–290. doi:10.1021/acsnano.6b05630
- Zheng, H., Guan, S., Wang, X., Zhao, J., Gao, M., and Zhang, X. (2020). Deconstruction of Heterogeneity of Size-dependent Exosome Subpopulations from Human Urine by Profiling N-Glycoproteomics and Phosphoproteomics Simultaneously. *Anal. Chem.* 92, 9239–9246. doi:10.1021/acs.analchem.0c01572

- Zhu, D., Duo, Y., Suo, M., Zhao, Y., Xia, L., Zheng, Z., et al. (2020). Tumor-Exocytosed Exosome/Aggregation-Induced Emission Luminogen Hybrid Nanovesicles Facilitate Efficient Tumor Penetration and Photodynamic Therapy. *Angew. Chem. Int. Ed.* 59, 13836–13843. doi:10.1002/anie.202003672
- Zhu, F., Ji, Y., Li, L., Bai, X., Liu, X., Luo, Y., et al. (2021). High-throughput Single-Cell Extracellular Vesicle Secretion Analysis on a Desktop Scanner without Cell Counting. *Anal. Chem.* 93, 13152–13160. doi:10.1021/acs.analchem.1c01446
- Zhu, L., Xu, Y., Wei, X., Lin, H., Huang, M., Lin, B., et al. (2021). Coupling Aptamer-based Protein Tagging with Metabolic Glycan Labeling for *In Situ* Visualization and Biological Function Study of Exosomal Protein-Specific Glycosylation. *Angew. Chem. Int. Ed.* 60, 18111–18115. doi:10.1002/anie.202103696
- Zhu, Q., Cheng, L., Deng, C., Huang, L., Li, J., Wang, Y., et al. (2021). The Genetic Source Tracking of Human Urinary Exosomes. *Proc. Natl. Acad. Sci. U. S. A.* 118, e2108876118. doi:10.1073/pnas.2108876118
- Zuo, B., Qi, H., Lu, Z., Chen, L., Sun, B., Yang, R., et al. (2020). Alarmin-painted Exosomes Elicit Persistent Antitumor Immunity in Large Established Tumors in Mice. *Nat. Commun.* 11, 1790. doi:10.1038/s41467-020-15569-2

Conflict of Interest: The authors declare that the research was conducted in the absence of any commercial or financial relationships that could be construed as a potential conflict of interest.

Publisher's Note: All claims expressed in this article are solely those of the authors and do not necessarily represent those of their affiliated organizations, or those of the publisher, the editors and the reviewers. Any product that may be evaluated in this article, or claim that may be made by its manufacturer, is not guaranteed or endorsed by the publisher.

Copyright © 2022 Xu, Jin, Li, Huang and Zhao. This is an open-access article distributed under the terms of the Creative Commons Attribution License (CC BY). The use, distribution or reproduction in other forums is permitted, provided the original author(s) and the copyright owner(s) are credited and that the original publication in this journal is cited, in accordance with accepted academic practice. No use, distribution or reproduction is permitted which does not comply with these terms.



Post-Translational Modifications of G Protein–Coupled Receptors Revealed by Proteomics and Structural Biology

Bingjie Zhang^{1†}, Shanshan Li^{1†} and Wenqing Shui^{1,2*}

¹iHuman Institute, ShanghaiTech University, Shanghai, China, ²School of Life Science and Technology, ShanghaiTech University, Shanghai, China

OPEN ACCESS

Edited by:

Wenshe Ray Liu,
Texas A&M University,
United States

Reviewed by:

Fei Fang,
Michigan State University,
United States

*Correspondence:

Wenqing Shui
shuiwq@shanghaitech.edu.cn

[†]These authors have contributed
equally to this work

Specialty section:

This article was submitted to
Chemical Biology,
a section of the journal
Frontiers in Chemistry

Received: 26 December 2021

Accepted: 16 February 2022

Published: 10 March 2022

Citation:

Zhang B, Li S and Shui W (2022) Post-
Translational Modifications of G
Protein–Coupled Receptors Revealed
by Proteomics and Structural Biology.
Front. Chem. 10:843502.
doi: 10.3389/fchem.2022.843502

G protein–coupled receptors (GPCRs) are a protein superfamily comprising >800 members that regulate numerous cellular and physiologic responses. GPCRs represent the largest class of therapeutic targets with implications in various diseases. Although advances in GPCR structural and pharmacological research have significantly improved our knowledge of GPCR signaling mechanisms, mapping diverse post-translational modifications (PTMs) of GPCR proteins and understanding their regulatory roles have received much less attention. Mass spectrometry-based proteomics has become the most popular technology for profiling protein PTMs in a systematic manner. Herein we provide an overview of PTM types, locations, crosstalk and dynamic regulation for different GPCRs that are characterized using proteomic and/or biochemical approaches. Our main focus is on glycosylation, phosphorylation, ubiquitination and palmitoylation that are known to modulate receptor folding, biosynthesis, trafficking, dimerization and signaling. Furthermore, we discuss the locations of specific PTM sites in the structure of a given GPCR and its signaling complex to highlight the importance of PTM regulation in the molecular basis of GPCRs, which may shed new light on structure-based drug discovery.

Keywords: G protein coupled receptors, mass spectrometry-based proteomics, Post-translational modification (PTM), phosphorylation, signaling regulation

INTRODUCTION

G protein–coupled receptors (GPCRs), which are seven-transmembrane proteins, constitute the largest family of cell surface receptors in mammalian cells (>800 in human). According to sequence homology, mammalian GPCRs are divided into five major subfamilies: Rhodopsin (Class A), Secretin/Adhesion (Class B), Glutamate (Class C), Frizzled (Class F) and Taste 2 (Class T) (Lagerstrom and Schioth, 2008). GPCR activation results in coupling to G proteins at the plasma membrane and signaling from endosomes after receptor internalization (Thomsen et al., 2016). Dysregulation of GPCR signaling contributes to various human diseases such as obesity, diabetes, depression, Alzheimer's disease and multiple types of cancer (Dorsam and Gutkind, 2007; Hauser et al., 2017; Huang et al., 2017; Zhou and Wild, 2019). Serving as the most successful drug target family, GPCRs currently account for targets of over 34% of FDA approved therapeutics (Kooistra et al., 2021).

Post-translational modifications (PTMs) mediate the abundance and/or activity of vast proteins and thus play a critical role in modulating signal transduction. Through covalently attaching a chemical or protein moiety to specific sites, PTMs increase the functional diversity of proteins and

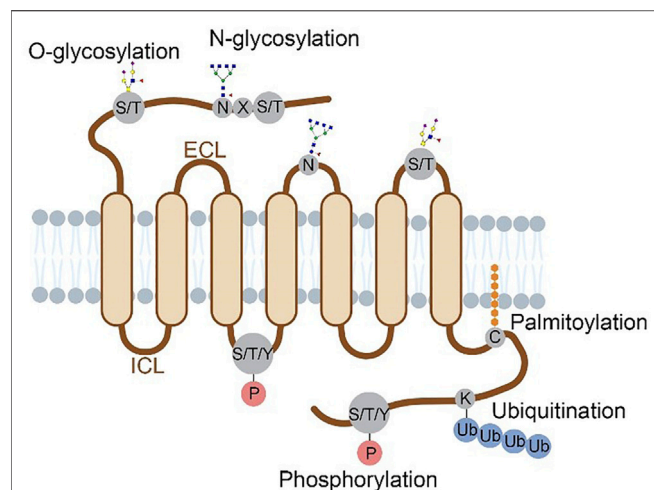


FIGURE 1 | Structural localization of GPCR post-translational modifications overviewed in this review. Four major types of PTMs are distributed on the N-terminus, ECLs, ICLs and C-terminus of a GPCR protein. Glycosylation occurs on the N-terminal and ECL domains, with N-glycosylation at N of the sequence motif N-X-S/T (X≠P) and O-glycosylation at S/T residues. Phosphorylation occurs at S, T or Y residues on the C-terminal and ICL domains. Ubiquitination occurs at K residues and palmitoylation at C residues, both on the C-terminus.

fine-tune signaling cascades (Krishna and Wold, 1993). These modifications including phosphorylation, glycosylation, ubiquitination, palmitoylation, methylation, acetylation and lipidation affect almost all aspects of normal cell biology and pathogenesis. For GPCRs, the most extensively characterized PTMs are glycosylation, phosphorylation, ubiquitination and palmitoylation which control the spatial and temporal dynamics of receptor signaling and physiologic responses (Duarte and Devi, 2020; Patwardhan et al., 2021). Specific PTMs are known to regulate receptor folding, maturation, trafficking, dimerization, and signaling activity (Patwardhan et al., 2021). Disorders of GPCR PTMs, which cause deficient or overabundant signaling responses, are linked to a variety of diseases, such as neurodegenerative disorders (Fang et al., 2020), immune dysfunction (Farzan et al., 1999) and cancer (Chen et al., 2017; Xiao et al., 2017).

The characterized GPCR PTMs occur at different domains of the receptor including N-terminus, extracellular loops (ECLs), intracellular loops (ICLs) and C-terminus. Compared to the seven transmembrane domains, these regions are much more accessible to PTM enzymes. **Figure 1** summarizes the locations of multiple PTM types in the extracellular or cytoplasmic regions of a GPCR protein. Historically, these PTM types were discovered using metabolic labeling with radioactive probes or enzymatic methods, and PTM sites were deduced by site-directed mutagenesis (Prihandoko et al., 2015; Lu and Fang, 2020). More recently, prominent advancements in mass spectrometry (Nguyen et al.)-based proteomics allow for systematic analysis of protein PTM sites and abundances in cultured cells and tissues (Olsen and Mann, 2013; Hansen et al., 2021; Kitata et al., 2021), which facilitates PTM profiling in various GPCR proteins. In this

review, we provide an overview of PTM types, locations, crosstalk and dynamic regulation for different GPCR proteins that are characterized mainly with proteomic approaches. In addition, specific PTMs revealed by structural biology are highlighted to understand the importance of PTMs in regulating the molecular function of GPCRs.

GPCR GLYCOSYLATION

Glycosylation mainly takes place in the endoplasmic reticulum (ER) and Golgi apparatus and serves as a tag to direct the receptor to the plasma membrane (Schjoldager et al., 2020). N- and O-linked glycosylation are prevalently present at the N-terminal or ECL domains of GPCRs, and both modulate receptor maturation, trafficking, ligand binding and cell signaling (Chen et al., 2010; Lackman et al., 2018; Wang et al., 2020). N-glycosylation which links a sugar molecular to the nitrogen of Asn (N) residue in the consensus motif N-X-S/T (X≠P) is the major form of glycosylation found in GPCRs. Traditionally, enzymatic cleavage with PNGase F or Endo H to remove glycans along with site-directed mutagenesis is widely employed to detect N-glycosylation of specific receptors. For instance, three sites of GLP-1R (N63, N82 and N115) and four sites of mGluR7 (N98, N458, N486, N572), all at the N-terminus, were found to be glycosylated using this approach (Chen et al., 2010; Irwin et al., 2012; Park et al., 2020). Combined mutation of 2-3 glycosites caused significant reduction of GLP-1R cell surface expression, indicating that the cooperative function of multiple glycosites (Chen et al., 2010; Irwin et al., 2012).

Although biochemical methods have been effective for mapping glycosylation sites of specific GPCRs in an overexpression system, comprehensive profiling of glycosites and glycan compositions of various receptors *in vivo* remain very difficult because of the structural complexity and varying abundance of glycans. Fortunately, development of new methods for the enrichment and MS analysis of glycopeptides has largely promoted systematic profiling of various glycoproteins including GPCRs. Zielinska *et al.* developed a “filter aided sample preparation” (FASP) method to enrich glycopeptides bound to lectins on top of a filter (Zielinska et al., 2010). After removal of the N-glycans, peptides were analyzed by high-resolution MS to determine their N-glycosites. This work identified 6367 N-glycosites on 2352 proteins in four mouse tissues and plasma, among which many novel glycosites were detected for tissue-specific proteins, such as neurotransmitter receptors and contactins in the brain. Liu *et al.* employed zwitterionic hydrophilic interaction liquid chromatography (ZIC-HILIC) for separating and enriching glycopeptides (Liu et al., 2017). They analyzed intact N-glycopeptides at the proteome scale using a stepped collision energy-based MS method. The MS data were processed with a dedicated search engine pGlyco 2.0 to decode the N-glycosites and N-glycan composition simultaneously. This study generated a large-scale glycoproteome dataset consisting of 10,009 site-specific N-glycans on 1988 glycosites from 955 glycoproteins in five mouse tissues. Of note, the two previous glycoproteomic datasets included a small fraction of glycosylated

GPCRs identified in different mouse tissues (180 N-glycosites mapped to 84 GPCRs by Zielinska *et al.*, and 51 N-glycosites mapped to 26 GPCRs by Liu *et al.*). A similar approach of intact glycopeptide analysis was adopted by Fang *et al.* to map the brain N-glycoproteomic landscape in an AD mouse model (Fang *et al.*, 2020). Interestingly, among the hundreds of up- or down-regulated N-glycopeptides from the AD mouse brain relative to the control, we noticed that 25 N-glycopeptides mapped to 8 GPCRs such as S1P1, Gpr158, mGluR3 showed dysregulated glycosylation occupancy on specific sites.

Apart from the direct glycopeptide enrichment, capturing cell-surface proteins prior to glycopeptide enrichment is another approach to improve the sensitivity of profiling low-abundance N-glycosylation. Through covalently labeling extracellular glycan moieties in live cells, Danzer *et al.* identified N-glycosites of 28 GPCRs in mouse pancreatic β -cells or human islets (Danzer *et al.*, 2012). These glycosylated GPCRs span orphan receptors (e.g., GPR116, GPR158), class A (e.g., ADRA2A, GALR1), class B (e.g., GLP-1R, CRHR1), and class C (e.g., CASR, GABBR2) receptors. For GLP-1R which represents an important therapeutic target of type II diabetes and obesity, glycosylation at both N63 and N115 were detected in this study. Moreover, glycopeptides released from these two sites were reduced by 9-fold in response to glucose and GLP-1 stimulation as measured by quantitative MS analysis, implying the involvement of N-glycosylation of GLP-1R in insulin secretion and blood glucose control.

In regard to mucin-type O-linked glycosylation, up to 20 different GalNAc transferases installs N-acetylgalactosamine to the hydroxyl group of S, T or Y residues in Golgi after protein folding. Different monosaccharides are then added successively to the growing oligosaccharide before the elongated glycans are capped with terminal sialic acids (Patwardhan *et al.*, 2021). Lack of a consensus sequence and enzymatic tools, together with highly complex and heterogeneous glycan structures, makes it more difficult to determine the modification site and glycan composition of O-glycosylation than N-glycosylation (Wilkinson and Saldova, 2020). Although computational prediction implicates over 350 GPCRs could be O-glycosylated, most of them are not experimentally verified (Steentoft *et al.*, 2013). To reduce the complexity of O-glycosylation in cells, Steentoft *et al.* developed a genetic engineering strategy to produce truncated and homogeneous O-glycans by blocking the elongation process. The simplified O-linked glycopeptides were then analyzed with an HCD/ETD hybrid MS method to determine the O-glycosylation sites on various peptides (Steentoft *et al.*, 2011). Applying this strategy to O-glycoproteome profiling of 12 human cell lines generated an expanded map of almost 3,000 glycosites from over 600 O-glycoproteins (Steentoft *et al.*, 2013). From this dataset, we found 35 O-glycosites mapped to 14 GPCRs. For instance, 5 O-glycosites were identified in Frizzled-2 receptor (FZD2) and 3 O-glycosites in adhesion receptor GPR64, all within the N-terminal domain. Recently a new chemoenzymatic method named EXoO was introduced for the selective extraction of O-linked glycopeptides from protein digests. Yang *et al.* exploited an endo-protease OPERATOR to specifically release

O-glycopeptides from proteins conjugated to a solid support before their glycosites were assigned by high-resolution MS/MS analysis (Yang *et al.*, 2018). EXoO was benchmarked with human kidney tissue, T cells, and serum to map a total of 3,055 O-glycosites from 1,060 glycoproteins, which included 23 GPCRs with 39 O-glycosites assigned.

A profound breakthrough in the glycoproteomics field is the recent development of a panel of bioinformatics tools such as Byonic (Bern *et al.*, 2012), GPQuest (Toghi Eshghi *et al.*, 2015), pGlyco3 (Zeng *et al.*, 2021) and StrucGP (Shen *et al.*, 2021) for efficient interpretation of tandem MS data from N-linked or O-linked glycopeptides. These search engines enable accurate identification of the composition and localization of glycans on glycopeptides as well as elucidation of site-specific glycan structures on a proteome-wide scale. Major characteristics of these software tools are summarized in **Table 1**. We envision such bioinformatic advances would facilitate the structural and functional study of GPCR glycosylation.

GPCR Phosphorylation

Phosphorylation is a major regulator of GPCR transduction signaling dynamics in mammalian cells. GPCR phosphorylation mainly mediated by two classes of serine/threonine kinases, namely GPCR kinases and second message kinases (such as protein kinase A and protein kinase C) (Lefkowitz, 1998). A large number of GPCR phosphorylation sites have been reported, mostly using mass spectrometry, phosphor-specific immunoblotting and metabolic labeling approaches (Prihandoko *et al.*, 2015).

The traditional method for detecting GPCR phosphorylation in early studies is through metabolic labeling of cultured cells with the radioactive phosphate (usually ^{32}P orthophosphate) (Fredericks *et al.*, 1996; Prihandoko *et al.*, 2015). Metabolic labeling employed together with receptor-specific immunoprecipitation provides a global assessment of GPCR phosphorylation. However, this approach does not allow precise mapping of phosphorylated residues, which requires mass spectrometry or phosphosite-specific antibodies.

Compared to immunoblotting with site-specific antibodies, MS-based proteomic profiling enables more comprehensive site determination and accurate quantification of protein phosphorylation *in vitro* and *in vivo* (Lawrence *et al.*, 2016; Liu *et al.*, 2018). This powerful technology has been applied to phosphorylation mapping and signaling investigation of numerous GPCRs. In the case of β_2 -adrenergic receptor ($\beta_2\text{AR}$) expressed in HEK293 cells, by performing MS analysis of phosphosite-specific regulation, the authors reported the induction of phosphorylation at 13 sites located at ICL3 or C-terminus by an unbiased agonist (Nobles *et al.*, 2011). Distinct phosphorylation only occurred at S355 and S356 in response to the stimulation with a β -arrestin-biased agonist carvedilol, which was discovered by MS analysis and validated with site-specific antibodies (Nobles *et al.*, 2011). Application of the same strategy has led to decoding 14 phosphorylation sites on M1 muscarinic acetylcholine receptor (M1 mAChR) upon the simulation of acetylcholine (Butcher *et al.*, 2016). Although S228 in ICL3 of M1 mAChR displayed an extremely low level of constitutive

TABLE 1 | Major characteristics of different glycoproteomic search engines.

	Byonic	GPQuest	pGlyco	StrucGP
Open source	no	yes	yes	yes
Graphical interface	yes	yes	yes	yes
Intact N-glycopeptide identification ^a	yes	yes	yes	yes
Intact O-glycopeptide identification ^a	yes	yes	yes	no
Glycan structure ^b	no	no	no	yes
Glycan database ^c	yes	yes	yes	no

^aAble to determine both N-/O-glycosites and glycan composition.^bAble to determine the detailed glycan structures on specific sites.^cDependent on a glycan database or not when searching MS data.

phosphorylation, its modification level was dramatically up-regulated under the stimulation of an orthosteric agonist. A positive allosteric modulator was able to further enhance acetylcholine-induced phosphorylation at S228. The MS-based proteomic approach has also been applied to mapping three endogenous phosphosites of MOP in the mouse brain (Mouledous et al., 2015). Only the phosphorylation of T370 and S375 was enhanced by agonist administration *in vivo*.

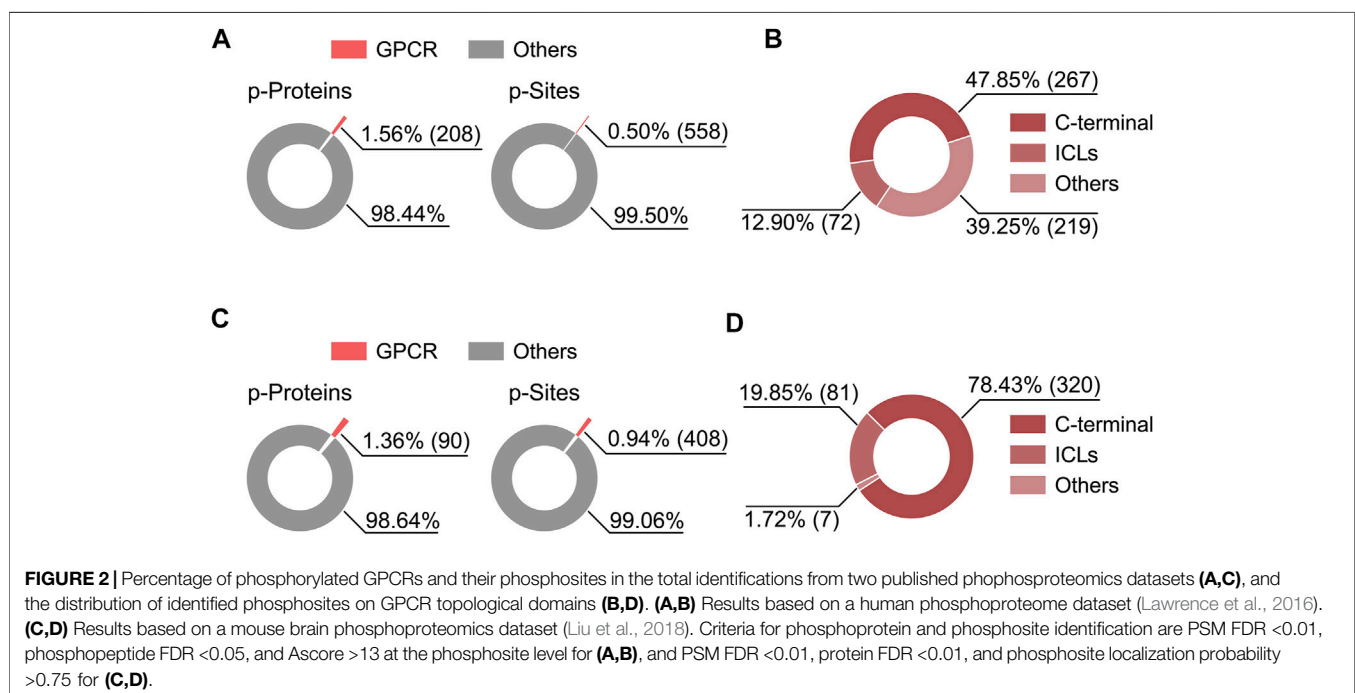
MS-based phosphoproteomics has become the method of choice for the genome-wide study of protein phosphorylation and dynamic cell signaling (Humphrey et al., 2015). Recently, Liu *et al.* employed high-throughput phosphoproteomics to study *in vivo* signaling of kappa opioid receptor (KOR) induced by structurally diverse agonists in five mouse brain regions (Liu et al., 2018). By analyzing this proteomics dataset, we noticed the phosphorylation level at S317 of cannabinoid receptor 1 (CB1) was downregulated upon KOR's aversive agonist administration, suggesting a signaling crosstalk might be present between CB1 and KOR through dynamic regulation

of phosphorylation. We also analyzed the percentage of phosphorylated GPCRs and their phosphosites in total identifications as well as topological localization of identified phosphosites in GPCRs included in this dataset and in a most comprehensive human phosphoproteome database (Christensen et al., 2010; Lawrence et al., 2016) (**Figure 2**). Among the 6766 phosphoproteins reported in the KOR signaling study, a very small fraction (1.36%) was phosphorylated GPCRs (**Figure 2C**), highlighting the challenge of detecting endogenous GPCR phosphorylation in tissues.

Given that the C-terminus of GPCRs often contains multiple serine, threonine and tyrosine residues, the hydrophilic phosphopeptides released from this region are easily overlooked in conventional proteomic workflows. To address this issue, a TMT chemical labeling method was developed to increase the phosphopeptide hydrophobicity so as to render quantitative measurement of the phosphorylated C-terminus of a selected GPCR (Tsai et al., 2019). Using CXCR3 as an example, both its unphosphorylated and single-site phosphorylated form at the C-terminus were detected and quantified under agonist stimulation. This method is anticipated to expand the coverage of GPCR phosphoproteome profiling.

GPCR Ubiquitination

GPCR ubiquitination is an enzymatic process that mediates the covalent conjugation of ubiquitin to a targeted protein. This process is critical for regulating biosynthesis, endocytosis, lysosomal sorting degradation and cellular signaling of GPCRs (Kennedy and Marchese, 2015; Patwardhan et al., 2021). In general, GPCRs are modified at one or multiple intracellular



lysine residues with either monoubiquitin or polyubiquitin chains in an agonist-dependent or -independent manner (Imai et al., 2001; Marchese and Benovic, 2001). Currently, the major strategy adopted for profiling GPCR ubiquitination is target protein immunoprecipitation followed by immunoblotting or MS-based proteomic analysis. Immunoblotting coupled with mutagenesis of targeted lysine residues was performed to infer the ubiquitin-conjugation sites on mGluR7 (Lee et al., 2019). Two lysine residues at the ICL2 and eight lysine residues at the C terminus of mGluR7 were found to be ubiquitinated, which was primarily mediated by Nedde E3 ligase with agonist treatment. Complementary to immunoblotting and mutagenesis, proteomic analysis allows for direct and systematic identification of all putative ubiquitination sites in a specific GPCR. To study the regulation of β_2 AR ubiquitination, Xiao *et al.* performed LC-MS/MS analysis of tryptic digests of the purified receptor with or without agonist stimulation (Xiao and Shenoy, 2011). Lysines at the ICL3 (K263 and K270) and the C-terminus (K348, K372 and K375) of β_2 AR showed agonist-induced ubiquitination, which played a key role in the long-term receptor desensitization through lysosomal degradation. Using the same approach, Zhang *et al.* reported characteristic ubiquitin modifications of specific residues at the ICL3 (K388) and the C-terminus (K484) of parathyroid hormone receptor (PTHr) upon PTH (1–34) stimulation (Zhang et al., 2018). These two ubiquitination sites were then confirmed by site-directed mutagenesis and shown to modulate PTHr trafficking, signaling and function in HEK293 cells.

GPCR Palmitoylation

GPCR palmitoylation involves covalent attachment of palmitate (saturated 16-carbon fatty acid) to one or more cysteine residues of the receptor via a thioester bond (S-palmitate). This modification usually occurs basally at the C-terminus of GPCRs during their biosynthesis, and in some cases, can be induced by agonist stimulation (Qanbar and Bouvier, 2003). GPCR palmitoylation plays an important role in receptor trafficking, localization to cell surface, dimerization and signaling (Qanbar and Bouvier, 2003; Chini and Parenti, 2009). The analysis of GPCR palmitoylation remains challenging due to the hydrophobicity and instability of S-palmitate modified peptides. Recently, bioorthogonal labeling or click chemistry have been increasingly used for GPCR palmitoylation profiling in receptor-overexpressing cell lines (Zuckerman et al., 2011; Adachi et al., 2016). One of these methods is to use alkyne-modified palmitic acid reporters to label proteins in live cells and then apply azide biotin for isolation or immunoblotting of palmitoylated proteins from cell lysates (Ebersole et al., 2014; Kallemeyn et al., 2021). Notably, metabolic labeling or chemical labeling based on acyl-biotin replacement or acyl-polyethylene glycol (PEG) exchange have been developed to achieve sensitive analysis of protein S-palmitoylation sites and abundances on a proteome-wide scale (Yang et al., 2010; Percher et al., 2016). Similar to phosphoproteomics, palmitoylation sites in a number of GPCRs such as FZD5, GPRC5A and mGluR7 were determined in a proteome-wide analysis of human palmitoylated proteins (Yang et al., 2010).

GPCR PTM Crosstalk

Typically, GPCRs are modified at multiple sites by various PTMs to regulate their structure, stability, activity and function. However, these PTMs do not exist in isolation and they can either positively or negatively influence each other. This combinatorial effect of different PTMs at the same or multiple residues is termed PTM crosstalk. PTM crosstalk offers unique mechanisms for GPCR functional regulation. The crosstalk between GPCR phosphorylation and ubiquitination has been extensively studied. For instance, mutation of phosphorylated residues S324 and S325 of CXCR4 inhibited agonist-induced ubiquitination of nearby lysine residues and eventually affected receptor degradation. This was attributed to the impaired recruitment of E3 ubiquitin ligase AIP4 to the cell membrane by the phosphor-deficient mutants (Bhandari et al., 2009). In another work, mutation of phosphorylated residues T387 and T392 of PTHR suppressed β -arrestin recruitment after agonist activation and inhibited subsequent PTHR ubiquitination (Zhang et al., 2018). In fact, it is proposed that most of GPCR agonist-induced ubiquitination requires phosphorylation for direct recruitment of the E3 ligase or adaptor proteins that mediate the interaction or activity of the ubiquitination machinery. However, a comprehensive proteomic map and mechanistic details of interdependent GPCR phosphorylation and ubiquitination remain unavailable.

PTMs Observed in High-Resolution GPCR Structures

Over the last decade, technology breakthroughs in structural biology of membrane proteins have resulted in the determination of over 600 structures of GPCRs in complexes with various ligands and signaling partners. However, PTM moieties are rarely present in these high-resolution structures possibly due to the fact that the majority of PTMs are located in highly flexible regions such as the N- and C-terminus. Nevertheless, in the X-ray free electron laser (XFEL) crystal structure of a rhodopsin-arrestin complex, phosphorylation of two residues T336 and S338 of rhodopsin were observed (Zhou et al., 2017) (**Figure 3A**). The two phosphosites, together with E341, formed an electrostatic interaction network with three positively charged pockets in β -arrestin1 to stabilize the entire complex. Moreover, the authors proposed a phosphorylation code in the receptor C-tail as a common mechanism of mediating arrestin recruitment (Zhou et al., 2017) (**Figure 3D**). More recently, in the cryo-EM structure of β_2 V₂R-G protein- β -arrestin1 megaplex, six GRK2-phosphorylated residues were observed in the subcomplex of β -arrestin1 and vasopressin receptor-2 C-tail (V₂T) (Nguyen et al., 2019) (**Figure 3B**). The presence of multiple phosphosites on the V₂T presumably enhanced the affinity of β_2 V₂R with β -arrestin1 to form the megaplex. The majority of these phosphosites on V₂T made electrostatic interactions with lysine or arginine residues at the N-terminus of β -arrestin1. Through MS analysis of the phosphorylation code on the V₂T, this study revealed that four residues in this domain were basally phosphorylated,

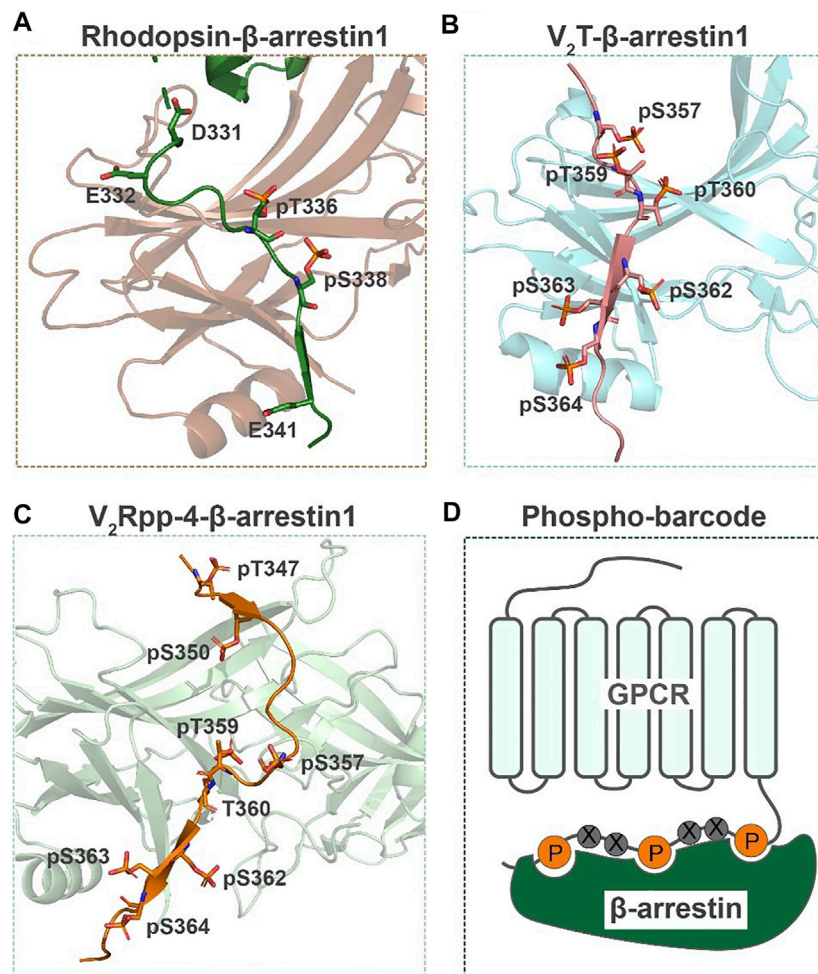


FIGURE 3 | GPCR phosphorylation sites present in crystal or cryo-EM structures. **(A)** The phosphorylated rhodopsin C terminus (green) interacting with β -arrestin1 (brown) in the crystal structure (Zhou et al., 2017). **(B)** Phosphorylated residues on V₂T (pink) interacting with β -arrestin1 (light blue) in the cryo-EM structure (Nguyen et al., 2019). **(C)** Crystal structure of β -arrestin1 (light green) in complex with a V₂R phosphopeptide (orange) (He et al., 2021). **(D)** A model of the GPCR phosphorylation code in a pattern of Px(x)PxxP for β -arrestin recruitment (Zhou et al., 2017).

whereas the other four residues were phosphorylated in response to agonist stimulation. These results indicated that a specific C-terminal phosphorylation pattern of GPCR is required for recruiting and stabilizing the signaling transducer β -arrestin1.

To further elucidate the mechanism of regulating arrestin interaction and function by GPCR phosphorylation codes, He *et al.* determined the structures of arrestin2 in complex with four different phosphopeptides derived from the V₂T (He et al., 2021) (one representative structure shown in **Figure 3C**). These crystal structures in line with NMR analysis and functional characterization suggested that different phosphorylation patterns of a GPCR could not only determine the strength of the phosphor-arrestin interaction, but also induce distinct conformational changes at remote positions of arrestin to ultimately modulate its selective functions.

In addition to phosphorylation, palmitoylation at cysteine residues observed in both structures of rhodopsin and

adrenoceptor β_2 AR (Salom et al., 2006; Cherezov et al., 2007). For instance, in the β_2 AR crystal structure, C341 on the receptor H8 helix was modified with a palmitic acid, which makes hydrophobic interaction with cholesterol to possibly regulate receptor dimerization (Cherezov et al., 2007).

CONCLUSION AND PERSPECTIVE

Diverse PTMs in GPCR proteins provide novel and expansive mechanisms for GPCR functional regulation as well as new opportunities for GPCR-targeted drug development (Patwardhan et al., 2021). With the advancement of MS-based proteomics technology, a number of PTM sites have been mapped to specific receptors stimulated with different ligands, which substantially enhanced our mechanistic understanding of receptor trafficking, activation, internalization and degradation. Most biochemical studies looked into one receptor at a time, identified PTM

residues by MS analysis, and elucidated the function of specific modification sites in GPCRs overexpressed in cell lines. Furthermore, certain PTMs are observed in GPCR structures, providing a molecular basis for *in vitro* PTM regulation of receptor conformation and interaction with signal transducers.

However, GPCR PTM characterization at physiological conditions remains a long-standing challenge due to the low receptor expression and low stoichiometry of most PTMs in primary cells or tissues. Therefore, more sensitive and robust techniques are required for mapping PTM sites on endogenous GPCRs and profiling the spatial and temporal dynamics of GPCR PTMs during disease progression. Revealing the PTM landscape of various GPCRs at pathological conditions would foster our understanding of dysregulated mechanisms in diseases and discovery of new drug targets. It is noteworthy that a growing number of large-scale PTM proteomic studies have documented GPCR modification sites and regulation, but they are lack of functional linkage to specific receptors. More GPCR-oriented proteomic studies need to be designed to uncover new regulatory mechanisms and physiological functions for GPCR PTMs in a systematic manner.

REFERENCES

- Adachi, N., Hess, D. T., McLaughlin, P., and Stamler, J. S. (2016). S-Palmitoylation of a Novel Site in the β_2 -Adrenergic Receptor Associated with a Novel Intracellular Itinerary. *J. Biol. Chem.* 291, 20232–20246. doi:10.1074/jbc.M116.725762
- Bern, M., Kil, Y. J., and Becker, C. (2012). Byonic: Advanced Peptide and Protein Identification Software. *Curr. Protoc. Bioinformatics* 13, 20. doi:10.1002/0471250953.bi1320s40
- Bhandari, D., Robia, S. L., and Marchese, A. (2009). The E3 Ubiquitin Ligase Atrophia Interacting Protein 4 Binds Directly to the Chemokine Receptor CXCR4 via a Novel WW Domain-Mediated Interaction. *Mol. Biol. Cell* 20, 1324–1339. doi:10.1091/mbc.E08-03-0308
- Butcher, A. J., Bradley, S. J., Prihandoko, R., Brooke, S. M., Mogg, A., Bourgognon, J.-M., et al. (2016). An Antibody Biosensor Establishes the Activation of the M1 Muscarinic Acetylcholine Receptor during Learning and Memory. *J. Biol. Chem.* 291, 8862–8875. doi:10.1074/jbc.M115.681726
- Chen, Q., Miller, L. J., and Dong, M. (2010). Role of N-Linked Glycosylation in Biosynthesis, Trafficking, and Function of the Human Glucagon-Like Peptide 1 Receptor. *Am. J. Physiology-Endocrinology Metab.* 299, E62–E68. doi:10.1152/ajpendo.00067.2010
- Chen, S., Zhu, B., Yin, C., Liu, W., Han, C., Chen, B., et al. (2017). Palmitoylation-Dependent Activation of MC1R Prevents Melanomagenesis. *Nature* 549, 399–403. doi:10.1038/nature23887
- Cherezov, V., Rosenbaum, D. M., Hanson, M. A., Rasmussen, S. G. F., Thian, F. S., Kobilka, T. S., et al. (2007). High-Resolution Crystal Structure of an Engineered Human β_2 -Adrenergic G Protein-Coupled Receptor. *Science* 318, 1258–1265. doi:10.1126/science.1150577
- Chini, B., and Parenti, M. (2009). G-Protein-Coupled Receptors, Cholesterol and Palmitoylation: Facts about Fats. *J. Mol. Endocrinol.* 42, 371–379. doi:10.1677/JME-08-0114
- Christensen, G. L., Kelstrup, C. D., Lyngso, C., Sarwar, U., Bøgebo, R., Sheikh, S. P., et al. (2010). Quantitative Phosphoproteomics Dissection of Seven-Transmembrane Receptor Signaling Using Full and Biased Agonists. *Mol. Cell Proteomics* 9, 1540–1553. doi:10.1074/mcp.M900550-MCP200
- Danzer, C., Eckhardt, K., Schmidt, A., Fankhauser, N., Ribrioux, S., Wollscheid, B., et al. (2012). Comprehensive Description of the N-Glycoproteome of Mouse Pancreatic β -Cells and Human Islets. *J. Proteome Res.* 11, 1598–1608. doi:10.1021/pr2007895
- Dorsam, R. T., and Gutkind, J. S. (2007). G-Protein-Coupled Receptors and Cancer. *Nat. Rev. Cancer* 7, 79–94. doi:10.1038/nrc2069

AUTHOR CONTRIBUTIONS

BZ and SL prepared the draft of this review. WS edited and finished the manuscript. All authors contributed to the article and approved the submitted version.

FUNDING

This work was funded by the ShanghaiTech University, the National Program on Key Basic Research Project of China (2018YFA0507004), and National Natural Science Foundation of China (31971362, 32171439).

ACKNOWLEDGMENTS

We specially thank Ronghui Lou from iHuman Institute, ShanghaiTech University for making data analysis and preparing Figure 2.

- Duarte, M. L., and Devi, L. A. (2020). Post-Translational Modifications of Opioid Receptors. *Trends Neurosciences* 43, 417–432. doi:10.1016/j.tins.2020.03.011
- Ebersole, B., Petko, J., and Levenson, R. (2014). Bioorthogonal Click Chemistry to Assay Mu-Opioid Receptor Palmitoylation Using 15-Hexadecynoic Acid and Immunoprecipitation. *Anal. Biochem.* 451, 25–27. doi:10.1016/j.ab.2014.01.008
- Fang, P., Xie, J., Sang, S., Zhang, L., Liu, M., Yang, L., et al. (2020). Multilayered N-Glycoproteome Profiling Reveals Highly Heterogeneous and Dysregulated Protein N-Glycosylation Related to Alzheimer's Disease. *Anal. Chem.* 92, 867–874. doi:10.1021/acs.analchem.9b03555
- Farzan, M., Mirzabekov, T., Kolchinsky, P., Wyatt, R., Cayabyab, M., Gerard, N. P., et al. (1999). Tyrosine Sulfation of the Amino Terminus of CCR5 Facilitates HIV-1 Entry. *Cell* 96, 667–676. doi:10.1016/s0092-8674(00)80577-2
- Fredericks, Z. L., Pitcher, J. A., and Lefkowitz, R. J. (1996). Identification of the G Protein-Coupled Receptor Kinase Phosphorylation Sites in the Human β_2 -Adrenergic Receptor. *J. Biol. Chem.* 271, 13796–13803. doi:10.1074/jbc.271.23.13796
- Hansen, F. M., Tanzer, M. C., Brüning, F., Bludau, I., Stafford, C., Schulman, B. A., et al. (2021). Data-Independent Acquisition Method for Ubiquitinome Analysis Reveals Regulation of Circadian Biology. *Nat. Commun.* 12, 254. doi:10.1038/s41467-020-20509-1
- Hauser, A. S., Attwood, M. M., Rask-Andersen, M., Schiöth, H. B., and Gloriam, D. E. (2017). Trends in GPCR Drug Discovery: New Agents, Targets and Indications. *Nat. Rev. Drug Discov.* 16, 829–842. doi:10.1038/nrd.2017.178
- He, Q.-T., Xiao, P., Huang, S.-M., Jia, Y.-L., Zhu, Z.-L., Lin, J.-Y., et al. (2021). Structural Studies of Phosphorylation-Dependent Interactions between the V2R Receptor and Arrestin-2. *Nat. Commun.* 12, 2396. doi:10.1038/s41467-021-22731-x
- Huang, Y., Todd, N., and Thathiah, A. (2017). The Role of GPCRs in Neurodegenerative Diseases: Avenues for Therapeutic Intervention. *Curr. Opin. Pharmacol.* 32, 96–110. doi:10.1016/j.coph.2017.02.001
- Humphrey, S. J., Azimifar, S. B., and Mann, M. (2015). High-Throughput Phosphoproteomics Reveals *In Vivo* Insulin Signaling Dynamics. *Nat. Biotechnol.* 33, 990–995. doi:10.1038/nbt.3327
- Imai, Y., Soda, M., Inoue, H., Hattori, N., Mizuno, Y., and Takahashi, R. (2001). An Unfolded Putative Transmembrane Polypeptide, Which Can lead to Endoplasmic Reticulum Stress, Is a Substrate of Parkin. *Cell* 105, 891–902. doi:10.1016/s0092-8674(01)00407-x
- Irwin, N., Whitaker, G. M., Lynn, F. C., McIntosh, C. H. S., and Accili, E. A. (2012). Regulation of GIP and GLP1 Receptor Cell Surface Expression by

- N-Glycosylation and Receptor Heteromerization. *PLoS ONE* 7, e32675. doi:10.1371/journal.pone.0032675
- Kallemijn, W. W., Lanyon-Hogg, T., Panyain, N., Goya Grocin, A., Ciepla, P., Morales-Sanfrutos, J., et al. (2021). Proteome-wide Analysis of Protein Lipidation Using Chemical Probes: In-Gel Fluorescence Visualization, Identification and Quantification of N-Myristoylation, N- and S-Acylation, O-Cholesteryl, S-Farnesylation and S-Geranylgeranylation. *Nat. Protoc.* 16, 5083–5122. doi:10.1038/s41596-021-00601-6
- Kennedy, J. E., and Marchese, A. (2015). Regulation of GPCR Trafficking by Ubiquitin. *Prog. Mol. Biol. Transl. Sci.* 132, 15–38. doi:10.1016/bs.pmbts.2015.02.005
- Kitata, R. B., Choong, W.-K., Tsai, C.-F., Lin, P.-Y., Chen, B.-S., Chang, Y.-C., et al. (2021). A Data-independent Acquisition-Based Global Phosphoproteomics System Enables Deep Profiling. *Nat. Commun.* 12, 2539. doi:10.1038/s41467-021-22759-z
- Kooistra, A. J., Mordalski, S., Pándy-Szekeres, G., Esguerra, M., Mamyrbekov, A., Munk, C., et al. (2021). GPCRdb in 2021: Integrating GPCR Sequence, Structure and Function. *Nucleic Acids Res.* 49, D335–D343. doi:10.1093/nar/gkaa1080
- Krishna, R. G., and Wold, F. (1993). Post-Translational Modification of Proteins. *Adv. Enzymol. Relat. Areas Mol. Biol.* 67, 265–298. doi:10.1002/9780470123133.ch3
- Lackman, J. J., Goth, C. K., Halim, A., Vakhrushev, S. Y., Clausen, H., and Petäjä-Repo, U. E. (2018). Site-Specific O-Glycosylation of N-Terminal Serine Residues by Polypeptide GalNAc-Transferase 2 Modulates Human δ -Opioid Receptor Turnover at the Plasma Membrane. *Cell Signal.* 42, 184–193. doi:10.1016/j.cellsig.2017.10.016
- Lagerström, M. C., and Schiöth, H. B. (2008). Structural Diversity of G Protein-Coupled Receptors and Significance for Drug Discovery. *Nat. Rev. Drug Discov.* 7, 339–357. doi:10.1038/nrd2518
- Lawrence, R. T., Searle, B. C., Llovet, A., and Villén, J. (2016). Plug-and-Play Analysis of the Human Phosphoproteome by Targeted High-Resolution Mass Spectrometry. *Nat. Methods* 13, 431–434. doi:10.1038/nmeth.3811
- Lee, S., Park, S., Lee, H., Han, S., Song, J. M., Han, D., et al. (2019). Nedd4 E3 Ligase and Beta-Arrestins Regulate Ubiquitination, Trafficking, and Stability of the mGlu7 Receptor. *Elife* 8, e44502. doi:10.7554/eLife.44502
- Lefkowitz, R. J. (1998). G Protein-Coupled Receptors. III. New Roles for Receptor Kinases and Beta-Arrestins in Receptor Signaling and Desensitization. *J. Biol. Chem.* 273, 18677–18680. doi:10.1074/jbc.273.30.18677
- Liu, J. J., Sharma, K., Zangrandi, L., Chen, C., Humphrey, S. J., Chiu, Y. T., et al. (2018). *In Vivo* Brain GPCR Signaling Elucidated by Phosphoproteomics. *Science* 360 (6395), ea404927. doi:10.1126/science.a404927
- Liu, M.-Q., Zeng, W.-F., Fang, P., Cao, W.-Q., Liu, C., Yan, G.-Q., et al. (2017). pGlyco 2.0 Enables Precision N-Glycoproteomics with Comprehensive Quality Control and One-Step Mass Spectrometry for Intact Glycopeptide Identification. *Nat. Commun.* 8, 438. doi:10.1038/s41467-017-00535-2
- Lu, H., and Fang, C. (2020). Methodology for Detecting Protein Palmitoylation. *Adv. Exp. Med. Biol.* 1248, 425–430. doi:10.1007/978-981-15-3266-5_17
- Marchese, A., and Benovic, J. L. (2001). Agonist-Promoted Ubiquitination of the G Protein-Coupled Receptor CXCR4 Mediates Lysosomal Sorting. *J. Biol. Chem.* 276, 45509–45512. doi:10.1074/jbc.C100527200
- Moulédous, L., Froment, C., Burlet-Schiltz, O., Schulz, S., and Mollereau, C. (2015). Phosphoproteomic Analysis of the Mouse Brain Mu-Opioid (MOP) Receptor. *FEBS Lett.* 589, 2401–2408. doi:10.1016/j.febslet.2015.07.025
- Nguyen, A. H., Thomsen, A. R. B., Cahill, T. J., 3rd, Huang, R., Huang, L.-Y., Marcink, T., et al. (2019). Structure of an Endosomal Signaling GPCR-G Protein- β -Arrestin Megacomplex. *Nat. Struct. Mol. Biol.* 26, 1123–1131. doi:10.1038/s41594-019-0330-y
- Nobles, K. N., Xiao, K., Ahn, S., Shukla, A. K., Lam, C. M., Rajagopal, S., et al. (2011). Distinct Phosphorylation Sites on the Beta(2)-Adrenergic Receptor Establish a Barcode that Encodes Differential Functions of Beta-Arrestin. *Sci. Signal.* 4, ra51. doi:10.1126/scisignal.2001707
- Olsen, J. V., and Mann, M. (2013). Status of Large-Scale Analysis of Post-Translational Modifications by Mass Spectrometry. *Mol. Cell Proteomics* 12, 3444–3452. doi:10.1074/mcp.O113.034181
- Park, D. h., Park, S., Song, J. m., Kang, M., Lee, S., Horak, M., et al. (2020). N-Linked Glycosylation of the mGlu7 Receptor Regulates the Forward Trafficking and Transsynaptic Interaction with Elfn1. *FASEB J.* 34, 14977–14996. doi:10.1096/fj.202001544R
- Patwardhan, A., Cheng, N., and Trejo, J. (2021). Post-Translational Modifications of G Protein-Coupled Receptors Control Cellular Signaling Dynamics in Space and Time. *Pharmacol. Rev.* 73, 120–151. doi:10.1124/pharmrev.120.000082
- Percher, A., Ramakrishnan, S., Thion, E., Yuan, X., Yount, J. S., and Hang, H. C. (2016). Mass-Tag Labeling Reveals Site-Specific and Endogenous Levels of Protein S-Fatty Acylation. *Proc. Natl. Acad. Sci. USA* 113, 4302–4307. doi:10.1073/pnas.1602244113
- Prihandoko, R., Bradley, S. J., Tobin, A. B., and Butcher, A. J. (2015). Determination of GPCR Phosphorylation Status: Establishing a Phosphorylation Barcode. *Curr. Protoc. Pharmacol.* 69, 2.13.1–2.13.26. doi:10.1002/0471141755.ph0213s69
- Qanbar, R., and Bouvier, M. (2003). Role of Palmitoylation/Depalmitoylation Reactions in G-Protein-Coupled Receptor Function. *Pharmacol. Ther.* 97, 1–33. doi:10.1016/s0163-7258(02)00300-5
- Salom, D., Lodowski, D. T., Stenkamp, R. E., Trong, I. L., Golczak, M., Jastrzebska, B., et al. (2006). Crystal Structure of a Photoactivated Deprotonated Intermediate of Rhodopsin. *Proc. Natl. Acad. Sci.* 103, 16123–16128. doi:10.1073/pnas.0608022103
- Schjoldager, K. T., Narimatsu, Y., Joshi, H. J., and Clausen, H. (2020). Global View of Human Protein Glycosylation Pathways and Functions. *Nat. Rev. Mol. Cell Biol.* 21, 729–749. doi:10.1038/s41580-020-00294-x
- Shen, J., Jia, L., Dang, L., Su, Y., Zhang, J., Xu, Y., et al. (2021). StrucGP: De Novo Structural Sequencing of Site-Specific N-Glycan on Glycoproteins Using a Modularization Strategy. *Nat. Methods* 18, 921–929. doi:10.1038/s41592-021-01209-0
- Stentoft, C., Vakhrushev, S. Y., Joshi, H. J., Kong, Y., Vester-Christensen, M. B., Schjoldager, K. T.-B. G., et al. (2013). Precision Mapping of the Human O-GalNAc Glycoproteome through SimpleCell Technology. *Embo J.* 32, 1478–1488. doi:10.1038/emboj.2013.79
- Stentoft, C., Vakhrushev, S. Y., Vester-Christensen, M. B., Schjoldager, K. T.-B. G., Kong, Y., Bennett, E. P., et al. (2011). Mining the O-Glycoproteome Using Zinc-Finger Nuclease-Glycoengineered SimpleCell Lines. *Nat. Methods* 8, 977–982. doi:10.1038/nmeth.1731
- Thomsen, A. R. B., Plouffe, B., Cahill, T. J., 3rd, Shukla, A. K., Tarrasch, J. T., Dosey, A. M., et al. (2016). GPCR-G Protein- β -Arrestin Super-Complex Mediates Sustained G Protein Signaling. *Cell* 166, 907–919. doi:10.1016/j.cell.2016.07.004
- Toghi Eshghi, S., Shah, P., Yang, W., Li, X., and Zhang, H. (2015). GPQuest: A Spectral Library Matching Algorithm for Site-Specific Assignment of Tandem Mass Spectra to Intact N-Glycopeptides. *Anal. Chem.* 87, 5181–5188. doi:10.1021/acs.analchem.5b00024
- Tsai, C.-F., Smith, J. S., Krajewski, K., Zhao, R., Moghieb, A. M., Nicora, C. D., et al. (2019). Tandem Mass Tag Labeling Facilitates Reversed-phase Liquid Chromatography-Mass Spectrometry Analysis of Hydrophilic Phosphopeptides. *Anal. Chem.* 91, 11606–11613. doi:10.1021/acs.analchem.9b01814
- Wang, T., Nakagawa, S., Miyake, T., Setsu, G., Kunisue, S., Goto, K., et al. (2020). Identification and Functional Characterisation of N-Linked Glycosylation of the Orphan G Protein-Coupled Receptor Gpr176. *Scientific Rep.* 10, 4429. doi:10.1038/s41598-020-61370-y
- Wilkinson, H., and Saldova, R. (2020). Current Methods for the Characterization of O-Glycans. *J. Proteome Res.* 19, 3890–3905. doi:10.1021/acs.jproteome.0c00435
- Xiao, K., and Shenoy, S. K. (2011). β 2-Adrenergic Receptor Lysosomal Trafficking Is Regulated by Ubiquitination of Lysyl Residues in Two Distinct Receptor Domains. *J. Biol. Chem.* 286, 12785–12795. doi:10.1074/jbc.M110.203091
- Xiao, X., Tang, J.-J., Peng, C., Wang, Y., Fu, L., Qiu, Z.-P., et al. (2017). Cholesterol Modification of Smoothed Is Required for Hedgehog Signaling. *Mol. Cell* 66, 154–162. doi:10.1016/j.molcel.2017.02.015
- Yang, W., Ao, M., Hu, Y., Li, Q. K., and Zhang, H. (2018). Mapping the O-Glycoproteome Using Site-specific Extraction of O-Linked Glycopeptides (EXoO). *Mol. Syst. Biol.* 14, e8486. doi:10.15252/msb.20188486
- Yang, W., Di Vizio, D., Kirchner, M., Steen, H., and Freeman, M. R. (2010). Proteome Scale Characterization of Human S-Acylated Proteins in Lipid Raft-Enriched and Non-Raft Membranes. *Mol. Cell Proteomics* 9, 54–70. doi:10.1074/mcp.M800448-MCP200
- Zeng, W.-F., Cao, W.-Q., Liu, M.-Q., He, S.-M., and Yang, P.-Y. (2021). Precise, Fast and Comprehensive Analysis of Intact Glycopeptides and Modified

- Glycans with pGlyco3. *Nat. Methods* 18, 1515–1523. doi:10.1038/s41592-021-01306-0
- Zhang, Q., Xiao, K., Liu, H., Song, L., Mcgarvey, J. C., Sneddon, W. B., et al. (2018). Site-Specific Polyubiquitination Differentially Regulates Parathyroid Hormone Receptor-Initiated MAPK Signaling and Cell Proliferation. *J. Biol. Chem.* 293, 5556–5571. doi:10.1074/jbc.RA118.001737
- Zhou, J., and Wild, C. (2019). GPCR Drug Discovery: Emerging Targets, Novel Approaches and Future Trends. *Curr. Top. Med. Chem.* 19, 1363–1364. doi:10.2174/156802661916190828093500
- Zhou, X. E., He, Y., De Waal, P. W., Gao, X., Kang, Y., Van Eps, N., et al. (2017). Identification of Phosphorylation Codes for Arrestin Recruitment by G Protein-Coupled Receptors. *Cell* 170, 457–469. doi:10.1016/j.cell.2017.07.002
- Zielinska, D. F., Gnad, F., Wiśniewski, J. R., and Mann, M. (2010). Precision Mapping of an *In Vivo* N-Glycoproteome Reveals Rigid Topological and Sequence Constraints. *Cell* 141, 897–907. doi:10.1016/j.cell.2010.04.012
- Zuckerman, D. M., Hicks, S. W., Charron, G., Hang, H. C., and Machamer, C. E. (2011). Differential Regulation of Two Palmitoylation Sites in the Cytoplasmic Tail of the β 1-Adrenergic Receptor. *J. Biol. Chem.* 286, 19014–19023. doi:10.1074/jbc.M110.189977
- Conflict of Interest:** The authors declare that the research was conducted in the absence of any commercial or financial relationships that could be construed as a potential conflict of interest.
- Publisher's Note:** All claims expressed in this article are solely those of the authors and do not necessarily represent those of their affiliated organizations, or those of the publisher, the editors and the reviewers. Any product that may be evaluated in this article, or claim that may be made by its manufacturer, is not guaranteed or endorsed by the publisher.

Copyright © 2022 Zhang, Li and Shui. This is an open-access article distributed under the terms of the Creative Commons Attribution License (CC BY). The use, distribution or reproduction in other forums is permitted, provided the original author(s) and the copyright owner(s) are credited and that the original publication in this journal is cited, in accordance with accepted academic practice. No use, distribution or reproduction is permitted which does not comply with these terms.



Label-Free Target Identification Reveals the Anticancer Mechanism of a Rhenium Isonitrile Complex

Junhyeong Yim¹ and Seung Bum Park^{1,2*}

¹Department of Biophysics and Chemical Biology, Seoul National University, Seoul, South Korea, ²CRI Center for Chemical Proteomics, Department of Chemistry, Seoul National University, Seoul, South Korea

OPEN ACCESS

Edited by:

John D. Wade,
University of Melbourne, Australia

Reviewed by:

Wukun Liu,
Nanjing University of Chinese
Medicine, China
Samuel Meier-Menches,
University of Vienna, Austria

*Correspondence:

Seung Bum Park
sbpark@snu.ac.kr

Specialty section:

This article was submitted to
Chemical Biology,
a section of the journal
Frontiers in Chemistry

Received: 07 January 2022

Accepted: 25 February 2022

Published: 14 March 2022

Citation:

Yim J and Park SB (2022) Label-Free
Target Identification Reveals the
Anticancer Mechanism of a Rhenium
Isonitrile Complex.
Front. Chem. 10:850638.
doi: 10.3389/fchem.2022.850638

Elucidation of the molecular mechanism of therapeutic agents and potential candidates is in high demand. Interestingly, rhenium-based complexes have shown a highly selective anticancer effect, only on cancer cells, unlike platinum-based drugs, such as cisplatin and carboplatin. These differences might be attributed to their different molecular targets. We confirmed that the target of tricarbonyl rhenium isonitrile polypyridyl (TRIP) complex is a protein, not DNA, using ICP-MS analysis and identified heat shock protein 60 (HSP60) as its target protein using a label-free target identification method. The subsequent biological evaluation revealed that TRIP directly inhibits the chaperone function of HSP60 and induces the accumulation of misfolded proteins in mitochondria, thereby leading to the activation of mitochondrial unfolded protein response (mtUPR)-mediated JNK2/AP-1/CHOP apoptotic pathway.

Keywords: anticancer agents, label-free target identification, metal-based drug, rhenium isonitrile complex, heat shock protein 60

INTRODUCTION

Cancer, the uncontrolled growth of cells, is the second leading cause of death in the United States (Shewach and Kuchta, 2009; Siegel et al., 2021). Various therapeutic agents have been developed to treat cancers (Thanarajasingam et al., 2018). Before the 1980s, chemotherapy focused on inhibiting the proliferation of cancer cells (Falzone et al., 2018); methotrexate inhibits the enzymes responsible for nucleotide synthesis, including dihydrofolate reductase and thymidylate synthase (Walling, 2006). Similarly, vincristine inhibits tubulin polymerization, leading to mitotic arrest (Bates and Eastman, 2017), and cisplatin crosslinks to DNA (Basu and Krishnamurthy, 2010), all resulting in the prevention of cell division. Unlike other drugs, cisplatin, a platinum-based compound, targets DNA, rather than proteins. Since platinum complex binds to DNA, various platinum analogs (e.g., carboplatin and oxaliplatin) were developed and used for cancer treatment to overcome the cisplatin-induced non-selective cytotoxic effects and resistance to treatments (Go and Adjei, 1999; Cox and Ang, 2009; Riddell and Lippard, 2018). Interestingly, the efficacy and side-effects of oxaliplatin are quite different from those of cisplatin and carboplatin (Machover et al., 1996; Rixe et al., 1996). Hemann and his co-workers revealed that oxaliplatin kills cancer cells by inducing ribosome biogenesis stress instead of DNA damage responses (Bruno et al., 2017). Subsequently, another study showed that oxaliplatin and some derivatives induce nucleolar stress derived from their organic ligands (Sutton et al., 2019), which means that the ligands of platinum-based complexes could alter their target proteins and modes of action. These events were also observed in non-platinum-based anticancer agents. For instance, ruthenium-based complexes target either DNA or proteins depending on their ligands (Ang et al., 2007; Gill et al., 2016). The types of organic ligands in

titanium-based complexes can alter their targets. (Guo et al., 2000; Miller et al., 2020). Therefore, the ligand modification in metal-based complexes can significantly influence their engagement to different targets (Meggers, 2007; Blanck et al., 2012).

Recently developed rhenium-based compounds have shown anticancer effects (Knopf et al., 2017). Wilson and his co-workers produced various rhenium analogs via combinatorial synthesis and selected TRIP as a therapeutic candidate with improved anticancer efficacy (Konkankit et al., 2019a; Konkankit et al., 2019b; King et al., 2019). They ascertained that TRIP induced misfolded protein accumulation, mitochondrial fission, and C/EBP homologous protein (CHOP)-mediated apoptosis. Moreover, using a TRIP-resistant A2780 cell line, they revealed that TRIP resistance might be caused by the overexpression of metallothionein 1E (MT1E) gene, which is related to the detoxification of metal-based compounds (Marker et al., 2020). Even though there are high demands to reveal the exact molecular target of TRIP, the application of conventional target identification methods with affinity-based probes is quite limited since the structural modification of organic ligands in rhenium-based complexes might hamper the activity of its probes or alter the engagement pattern to their targets (Bregman et al., 2006; Feng et al., 2011). To circumvent these challenges, we hypothesized that label-free target identification could be a method of choice for identifying cellular targets of TRIP without structural modification. In this study, we identified and validated HSP60 as the target protein of TRIP *via* label-free target identification. We also revealed the molecular mechanism underlying the cytotoxicity of TRIP.

MATERIALS AND METHODS

Cell Culture

HeLa (human cervical adenocarcinoma cell line), CaSki (human cervical epidermoid carcinoma cell line), A375P (human malignant melanoma), HEK293T (human embryonic kidney cell line), and C8-D1A (murine astrocyte cell line) were obtained from American Type Culture Collection (ATCC). HeLa (ATCC; CCL-2) and CaSki (ATCC; CRL-1550) were cultured in Roswell Park Memorial Institute (RPMI) 1,640 Medium (Gibco; #11875-093) supplemented with heat-inactivated 10% fetal bovine serum (FBS) (Gibco; #16000-044), and 1% penicillin (100 units/mL)/streptomycin (100 µg/mL) solution (Gibco; #15240-062). A375P (ATCC; CRL-3224), HEK293T (ATCC; CRL-3216), and C8-D1A (ATCC; CRL-2541) were cultured in Dulbecco's Modified Eagle's Medium (DMEM) (Gibco; #11995-065) supplemented with heat-inactivated 10% FBS (Gibco; #16000-044), and 1% penicillin/streptomycin solution (Gibco; #15240-062). All types of cells were maintained in 100-mm cell culture dishes in a humidified atmosphere of a 5% CO₂ incubator at 37°C. All cells were cultured every 2 days using trypsin (Gibco; #12605-010).

Cell Viability Assay

5,000 cells of HeLa, CaSki, A375P, and HEK293T were seeded per well at the transparent flat-bottom 96-well plate (Corning;

#3598), and 10,000 cells of C8-D1A were seeded per well at the transparent flat-bottom 96-well plate and sealed with breathable sealing tape (Axygen; BF-400-S). After 24-h incubation, cisplatin (Sigma; P4393), carboplatin (Sigma; C2538), and TRIP were treated for 48 h. After changing the culture medium to 100 µL of fresh culture medium, 10 µL of Ez-cytox solution (Dogen; EZ-BULK150) was added to the 96-well plate. After 2-h incubation, absorbance at 455 nm was measured using a microplate reader (Biotek; Synergy).

Inductively Coupled Plasma-Mass Spectrometry

5,000 cells/ml of HeLa were seeded in a 150-mm cell culture dish (Corning; #430599) and allowed to grow for 48 h. HeLa cells were then treated with 10 µM of either cisplatin (P4393; Sigma) or TRIP for 1, 2, 4, and 8 h. After washing with 1× phospho-buffered saline (PBS, Welgene; ML008-02), HeLa cells harvested by trypsinization (Gibco; #12605-010) were used for either protein or DNA extraction.

To measure metal accumulations in proteins, we re-suspended cells in 300 µL of distilled water (DW) and lysed by freeze and thaw cycle three times in liquid nitrogen. The cell lysates were clarified by centrifugation at 20,000 g, 4°C for 20 min. The concentration of the soluble protein fraction was measured by BCA (bicinchoninic acid) protein assay kit (Thermo; #23225). Cell lysates were digested in concentrated HNO₃ at 160°C for 3 h and rested at room temperature overnight. The digested cell lysates were diluted in DW to make the final concentration of HNO₃ less than 5%. Metal contents, platinum for cisplatin and rhenium for TRIP, were quantified with an ICP-MS (Perkin-Elmer SCIEX; NexION 350D) by measuring the most abundant isotope ¹⁹⁵Pt and the most stable isotope ¹⁸⁵Re, and calculated using a calibration curve from a series of concentrations of Pt and Re standards, respectively. The metal accumulations in proteins were expressed as ng Pt or Re/mg protein.

In order to quantify metal accumulations in DNA, cells were re-suspended in 300 µL of lysis buffer [100 mM NaCl, 25 mM EDTA (Acros; #11843-5000), 0.5% SDS (w/v) (Acros; #230420100), 0.1 mg/ml proteinase K (Merck; #70663-4CN), and 10 mM Tris-HCl, pH 8.0] and incubated at 50°C overnight. A 300 µL of phenol:chloroform:isoamyl alcohol mixture (25:24:1, Sigma; #77617) was added to cell lysates and shaken vigorously. After centrifugation at 13,000 g for 5 min, upper layer containing DNA, out of two layers, was transferred to a new tube. DNase-free dsRNase (Roche; # 11119915001) was added to DNA solution to a final concentration 1 µg/ml and incubated at 37°C for 1 h. Then, 200 µL of 7.5 M ammonium acetate (Merck; # 1.01116.1000) was added to DNA solution, followed by 400 µL of 100% ethanol (Daejung; #4023-4104), and the mixture was incubated at -80°C for 30 min. To precipitate DNA, the solution was centrifuged at 10,000 g for 5 min, and the precipitated DNA pellet was rinsed with 70% ethanol and dried by air. The DNA was dissolved in 50 µL of DW and added 100 µL of 8 mM NaOH solution (Acros; AC124260050). DNA concentration was quantified by measuring the absorbance at 260 nm. DNA was digested in concentrated HNO₃ at 160°C for

3 h and rested at room temperature overnight. Metal contents in DNA were quantified by ICP-MS as same method as measuring metal contents in protein. The metal accumulations in DNA were expressed as ng Pt or Re/mg DNA.

TS-FITGE

Procedures for TS-FITGE were previously described (Park et al., 2017). Briefly, HeLa cells were treated with either vehicle (veh) or 10 μ M of TRIP for 4 h. Veh- or TRIP-treated HeLa cells were heat-denatured for 3 min at various temperature ranges, followed by 25°C for 3 min. The heated cells were washed with 1× PBS (Welgene; ML008-02) and re-suspended in the lysis buffer [PBS containing 0.4% IGEPAL CA-630 (Sigma; I8896) and 1× Protease Inhibitor Cocktail (PIC, Roche; #11873580001)]. Cells were lysed by freeze and thaw cycle three times in liquid nitrogen. The cell lysates were clarified by centrifugation at 20,000 g, 4°C for 20 min. The concentration of the soluble protein fraction was measured by BCA protein assay kit (Thermo; #23225). Then, each 50 μ g of the protein was precipitated by cold acetone at −20°C for 20 min, followed by centrifugation at 20,000 g, 4°C for 7 min. After acetone washing three times, the protein pellet was re-suspended with 10 μ L of conjugation buffer [7 M urea (Acros; #32738), 2 M thiourea (Acros; #13891), 4% (w/v) CHAPS (Sigma; C3023), and 30 mM Tris-HCl, pH 8.0]. Veh- and TRIP-treated proteins were added 1 μ L of 0.4 mM Cy3-*N*-hydroxysuccinimide (NHS) and Cy5-NHS, respectively, and incubated at 4°C for 45 min. The dye-conjugated proteomes were precipitated by cold acetone at −20°C for 20 min, followed by centrifugation at 20,000 g, 4°C for 7 min. After acetone washing three times, the pellets were re-suspended with 50 μ L of re-hydration buffer [7 M urea, 2 M thiourea, 2% (w/v) CHAPS, 40 mM DTT (Millipore; #1.11474.0025), and 1% pH 3–10 IPG buffer (Cytiva; #17-6000-87)]. The same amount of veh- and TRIP-treated samples were mixed and loaded on a pH 3–10, 24-cm Immobiline Drystrip gel (Cytiva; #17-6002-44). The primary dimension was separated by an isoelectric focusing system (Cytiva; Ettan IPGphor 3), and the secondary dimension was separated by a polyacrylamide gel electrophoresis (PAGE) system (Cytiva; Ettan DALTSix). The 2-dimensional (2D) gel was scanned with a fluorescent gel scanner (Azure Biosystems; Sapphire).

In-Gel Digestion and Mass Spectrometry

As previously described, the protein spots from silver-stained gels were excised, de-stained, and digested only with trypsin (Choi et al., 2018). The resulting peptides were identified by peptide sequencing using nanoAcquity UPLC-ESI-Q-TOF mass spectrometry (Waters; SYNAPT G2-Si HDMS). Peptides were eluted with a linear gradient of 5–40% buffer B [ACN/formic acid; 100:0.1 (v/v)] with buffer A [water/formic acid; 100:0.1 (v/v)] over 80 min, and MS scan cycle was composed of one MS scan followed by MS/MS scans of the 10 most abundant ions in each MS scan. The resulting MS data were converted to peaklist files (.pkl) using Protein Lynx Global Server (PLGS) 2.3 data processing software (Waters). Peaklists were searched using a global search engine Mascot (version 2.2.0) with the protein sequence database SwissProt (version 51.6, 257964 entries). The taxonomy filter for 2D-PAGE samples was *Homo sapiens*

(human). The maximum number of one missed cleavage was permitted, and no fixed modifications were considered. As variable modifications, carbamidomethylation of Cys, oxidation of Met, phosphorylation of Ser or Thr, acetylation and formylation of Lys, *N*-terminal pyroglutamylation of Gln and Glu, and acrylamide adduct propionamide of Cys were considered for the identification of protein spots.

Immunoblotting

HeLa cells were harvested and lysed in modified radioimmunoprecipitation assay (RIPA) buffer [150 mM NaCl, 1% IGEPAL CA-630 (Sigma; I8896), 0.5% deoxycholate (Sigma; #30970), 5 mM NaF (Sigma; S7920), 2 mM Na₃VO₄ (Sigma; #450243), 1× PIC (Roche; #11873580001), and 50 mM Tris-HCl, pH 7.8] for 20 min on ice, and the cell lysates were clarified by centrifugation at 20,000 g, 4°C for 20 min. The concentration of the soluble protein fraction was measured by BCA protein assay kit (Thermo; #23225). Proteome was added with 5× SDS (Biosesang; SF 2002-110-00) and heated at 95°C for 5 min.

Equal amounts of the proteome were analyzed by SDS-PAGE and transferred to PVDF membranes (Bio-Rad; BR162-0177). The membranes were blocked with 2% bovine serum albumin (BSA, MP Biomedicals; #0216006980) in Tris-buffered saline containing 0.1% Tween-20 (TBS-T, Sigma; P9416) at room temperature for 1 h. To detect the desired proteins, the membranes were incubated overnight at 4°C with primary antibodies—1:1,000 dilution of HSP60 (Santa Cruz; sc-1052), eIF2 α (Santa Cruz; sc-133132), p-eIF2 α (phospho S51, Abcam; ab32157), ATF4 (CST; #11815), JNK (CST; #9252S), p-JNK (CST; #9251S), CHOP (CST; #2895); 1:2,000 dilution of GAPDH (CST; #2118), and β -actin (CST; #4970). After washing with TBS-T, the resulting membranes were exposed to HRP-conjugated secondary antibody at room temperature for 1 h—1:5,000 dilution of anti-rabbit (CST; #7074), anti-mouse (CST; #7076), and anti-goat (Santa Cruz; sc-2033). After washing with TBS-T, the membranes were incubated with enhanced chemiluminescence (ECL) prime kit (Cytiva; RPN2232). Chemiluminescent signals from desired proteins were detected using ChemiDoc (Bio-Rad).

Cellular Thermal Shift Assay

HeLa cells were treated with either vehicle or 10 μ M of TRIP for 4 h. Veh- or TRIP-treated HeLa cells were heat-denatured for 3 min at various temperature ranges, followed by 25°C for 3 min. The heated cells were washed with 1× PBS (Welgene; ML008-02) and re-suspended in the lysis buffer [PBS containing 0.4% IGEPAL CA-630 (Sigma; I8896) and 1× PIC (Roche; #11873580001)]. Cells were lysed by freeze and thaw cycle three times in liquid nitrogen. The cell lysates were clarified by centrifugation at 20,000 g, 4°C for 20 min. The soluble protein fraction was added with 5× SDS (Biosesang; SF 2002-110-00), heated at 95°C for 5 min, and subjected to immunoblotting.

Preparation of Recombinant HSP60

HSP60 with C-term His-tag plasmid (Sino Biological; HG11322-CH) was transferred to BL21 (DE3) competent *E. coli* (Enzynomics; CP110). The BL21 cells were grown in 250 ml of LB broth

(Biosesang; LR3004-250-02) at 37°C with shaking until OD₆₀₀ reached 0.6. The cultures were then induced with the final concentration 0.4 mM IPTG (Sigma; I5502) at 37°C for 4 h. Cells were harvested by centrifugation at 5,000 g, 4°C for 10 min, and re-suspended by the protein buffer (150 mM NaCl, 1 mM DTT (Millipore; #1.11474.0025), and 10 mM Tris-HCl, pH 8.0) containing 1× PIC (Roche; #11873580001). Cells were lysed by sono-smasher (Ulsso Hitech; ULH-700S) and clarified by centrifugation at 13,000 g, 4°C for 30 min. Cell lysates were incubated with Ni-NTA agarose (Qiagen; #30210) at 4°C for 1 h and purified by various concentrations of imidazole (Sigma; I5513) in the protein buffer. Imidazole was removed by buffer exchange with 10K Amicon (Millipore, UFC501096), and the concentration of purified HSP60 was measured by BCA protein assay kit (Thermo; #23225). The purity of HSP60 was determined by SDS-PAGE with the final purity over 90% in Coomassie staining (Abcam; ab119211).

Surface Plasmon Resonance Assay

SPR experiments were performed using a real-time biomolecular interaction analysis system (Cytiva; Biacore T100). Recombinant HSP60 proteins were immobilized to a CM5 sensor chip (Cytiva; BR100012) with amine coupling kit (Cytiva; BR100050) in 1× PBS (Wegene; ML008-02) containing 0.005% Tween 20 (Sigma; P9416) at pH 4.0 acetate buffer (Cytiva; BR100349). Final immobilization level of HSP60 reached 1,881 RU. To monitor the biophysical interaction between HSP60 and TRIP, we injected various concentrations of TRIP in the running buffer [PBS (pH 7.4) containing 0.005% Tween 20] for 60 s with a flow rate of 30 µL/min. The dissociation event of TRIP from HSP60 was monitored by injecting the running buffer for 300 s at 25°C. Data were analyzed to calculate kinetic parameters by fitting sensorgrams with the one-on-one binding model using Biacore T100 Evaluation software (Cytiva).

Differential Scanning Fluorimetry Assay

DSF experiments were carried out in Step One Real-Time PCR system (Applied Biosystems; #4376357). 4 µM of the recombinant HSP60 proteins was incubated with 5,000× Sypro-Orange (Sigma; S5692) in the absence or presence of TRIP for 1 h, followed by heat scanning from 25°C to 95°C in an increment of 1% continuous temperature. Normalized and first derivative reporter data were analyzed.

Heat Shock Protein 60/Heat Shock Protein 10 Refolding Assay

The refolding activity of HSP60 was measured by a human HSP60/HSP10 protein refolding kit (R&D Systems; K-300) according to the manufacturer's protocol. Briefly, luciferase protein was denatured by heat shock at 45°C for 7 min on C1000 Touch Thermal Cycler (Bio-Rad; #1841000) and incubated with the HSP60/HSP10 complex in the absence or presence of various concentrations of either TRIP or epolactaene *t*-butyl ester (ETB), a known HSP60 inhibitor, at 30°C for 1.5, 3, and 6 h on C1000 Touch Thermal Cycler. After that, the refolded luciferase protein was mixed with luciferin to measure the chaperone activity of HSP60 on the basis of luminescence

signals. The luminescence signals were measured using a microplate reader (Biotek; Synergy HTX).

siRNA Transfection

For HSP60 knockdown experiments, a short interfering RNA (siRNA) duplex against HSP60 was used (Bioneer; #3329). siRNA oligonucleotides were transfected in HeLa cells for 2 days using Lipofectamine RNAiMAX (Thermo; #15338100) and Opti-MEM (Gibco, #31985070) based on manufacturer's instructions. For the experiments to assess the activity change of TRIP after gene knockdown, cells were transfected with siRNA for 2 days and treated with either cisplatin or TRIP for another 2 days, followed by a cell viability assay.

SiRNA Oligonucleotide sequences for HSP60 are as follows:

SiHSP60-1 sense 5'- GUG UUG AAG GAU CUU UGA UTT -3'

antisense 5'- AUC AAA GAU CCU UCA ACA CTT -3'

SiHSP60-2 sense 5'- GAA GUU UGA UCG AGG CUA UTT -3'

antisense 5'- AUA GCC UCG AUC AAA CUU CTT -3'

SiHSP60-3 sense 5'- CAG UGU ACU GCU UUC AAU UTT -3'

antisense 5'- AGU UGA AAG CAG UAC ACU GTT -3'

Flow Cytometry Analysis

HeLa cells were treated with each compound for the designated time and dose, or transfected with siRNAs using Lipofectamine RNAiMAX (Thermo; #15338100). The cells were trypsinized and re-suspended in PBS containing 2% FBS (Gibco; #16000-044). To measure mitochondrial reactive oxygen species (ROS) and polarization, we stained the same number of re-suspended cells with either 2.5 µM of mitoSOX (Invitrogen; M36008) or 500 nM of TMRE (tetramethylrhodamine ethyl ester) (Invitrogen; T669) at 37°C for 1 h. To measure apoptosis, we also stained the same number of re-suspended cells with Annexin V-FITC Apoptosis Staining and Detection Kit (Abcam; ab14085) according to the manufacturer's protocol. The stained cells were subjected to flow cytometry analysis using FACSaria II (BD).

Reporter Gene Assay

HeLa cells were seeded 10,000 cells per well at a white 96-well plate (Falcon; #353296). HeLa cells were transfected with a 1 to 1 ratio of 3× AP1pGL3 (Addgene; #40342) and pRL-TK (Promega; E2241) mixture using LTX plus (Invitrogen; #15338100) and Opti-MEM (Gibco, #31985070) according to the manufacturer's protocol and incubated for 24 h. The transfected cells were treated with 10 µM of cisplatin (Sigma; P4393), 10, 20, 40 µM of TRIP, or 200 nM of thapsigargin (Sigma; T9033) for 24 h. To measure the AP-1 activation, cells were washed with 1× PBS (Wegene; ML008-02) and lysed with 20 µL of 1× passive lysis buffer for 15 min. Luciferase signals were measured by dual-luciferase reporter assay system (Promega; E1980) using a microplate reader (Biotek; Synergy HTX). Expression levels of AP-1 were normalized by the Renilla luciferase signal.

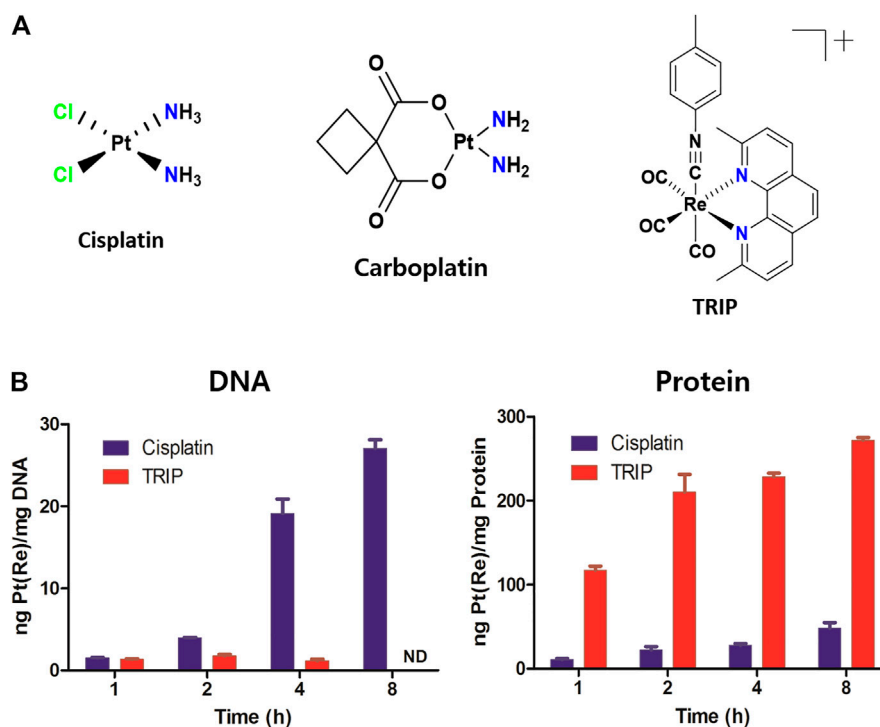


FIGURE 1 | Each metal-based anticancer agent showed distinct accumulation in DNA and proteins. **(A)** Chemical structures of metal-based anticancer agents. **(B)** HeLa human cervical cancer cells were treated with either cisplatin or TRIP for 1, 2, 4, and 8 h. Platinum and rhenium were quantitatively measured by ICP-MS for cisplatin and TRIP, respectively.

Mitochondrial Monitoring in Live Cell

25,000 cells of HeLa were seeded per well on an 8-well chamber (Nunc; #155409). To monitor mitochondrial fission, we stained the mitochondria of HeLa cells with 100 nM of Mito-tracker deep red (Invitrogen; M22426) and the nuclei of HeLa cells with 4 nM of Hoechst 33342 (Thermo; #62249) for 30 min. The stained cells were pre-treated with 50 μ M of Mdivi-1 (Sigma; M0199) for 1 h, followed by 10 μ M of TRIP treatment. HeLa cells were monitored in a humidified atmosphere of 5% CO₂ at 37°C using a high-resolution microscope (Cytiva; Delta Vision).

Statistical Analysis

Statistical analyses of all experiments were performed with Student's t-test using Graph Pad Prism (GraphPad). Data are represented as mean \pm SD (standard deviation), as indicated in the individual figure legends. The *p*-value is stated in the legend of each figure.

RESULT AND DISCUSSION

Tricarbonyl Rhenium Isonitrile Polypyridyl Induces Selective Death of Cancer Cells *via* Working on Protein, not DNA

Although anticancer therapeutic agents focus on inhibiting the aberrant proliferation of cancer cells, they unintentionally affect the fast-growing normal cells as well, resulting in anemia (Groopman and

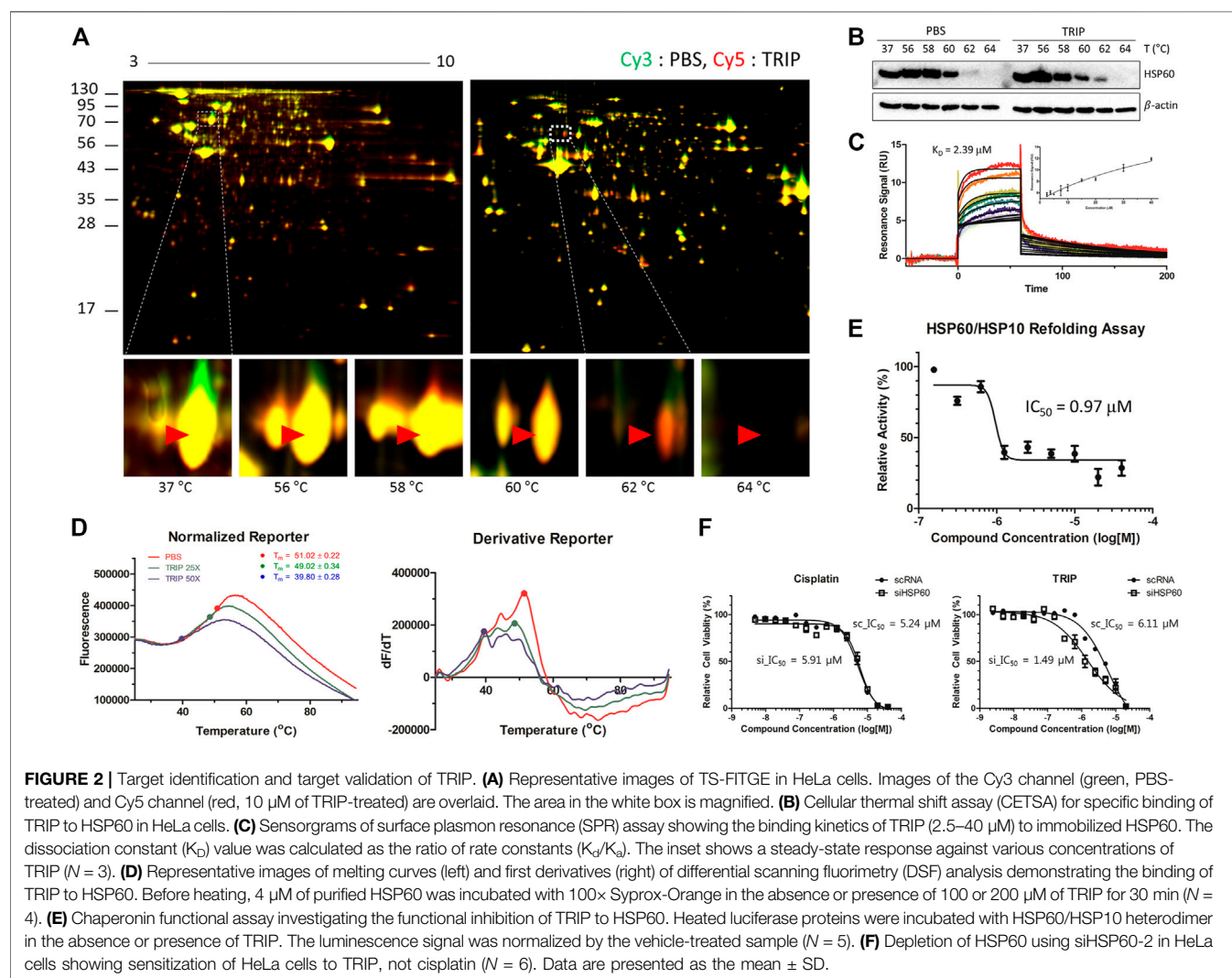
Itri, 1999), alopecia (Chon et al., 2012), and fertility problems (Blumenfeld, 2012). Interestingly, the growth inhibition assay ascertained that although cisplatin and carboplatin kill all cell lines, TRIP selectively kills cancer cells, not normal cells (Figure 1A, Supplementary Figure S1, Table 1), indicating that the mechanism of TRIP might be different from that of platinum-based drugs. It was hypothesized that the non-selective cytotoxicity of platinum-based compounds might be correlated with the efficiency of their cellular uptake and platinum-DNA adduct formation (Dasari and Tchounwou, 2014). To verify whether TRIP generates metal-DNA adducts like cisplatin, we conducted ICP-MS (inductively coupled plasma-mass spectrometry) analysis. HeLa human cervical cancer cells were treated with 10 μ M of either cisplatin or TRIP for 1, 2, 4, and 8 h. The accumulation of metal (platinum for cisplatin and rhenium for TRIP) was quantitatively compared between proteins and DNA. Cisplatin treatment induced the DNA platination in a time-dependent manner, as expected. However, TRIP treatment induced the time-dependent accumulation of rhenium only in proteins, not in DNA (Figure 1B), which implies that, unlike platinum-based drugs, TRIP induced cancer-selective cytotoxicity by targeting proteins, not DNA.

TS-FITGE Identifies Heat Shock Protein 60 as the Target Protein of TRIP

Platinum analogs contain various organic ligands to overcome the non-selective cytotoxicity of cisplatin (Go and Adjei, 1999;

TABLE 1 | IC₅₀ values of cisplatin, carboplatin, and TRIP in cancer and non-cancer cell lines. Cell lines were treated with each compound for 2 days; then, a colorimetric MTT metabolic activity assay was conducted to determine cell viability. Data are presented as the mean \pm SD ($n = 3$). (a, b) cervical cancer; (c) skin melanoma; (d) embryonic kidney fibroblasts; (e) normal astrocyte.

Compound	IC ₅₀ (μ M)				
	HeLa _(a)	Caski _(b)	A375P _(c)	HEK293T _(d)	C8-D1A _(e)
Cisplatin	9.20 \pm 0.38	7.89 \pm 0.26	8.35 \pm 0.37	8.33 \pm 0.30	10.19 \pm 0.23
Carboplatin	40.48 \pm 2.62	22.73 \pm 0.20	23.04 \pm 0.85	49.64 \pm 6.99	23.66 \pm 0.21
TRIP	5.30 \pm 0.51	5.00 \pm 0.86	4.83 \pm 0.24	> 100	> 100



Cox and Ang, 2009; Riddell and Lippard, 2018). However, since the structural changes in ligands of metal-based complexes can perturb their target engagement (Bruno et al., 2017; Sutton et al., 2019), identifying target proteins without structural changes in metal-based complexes, especially their ligands, would be critical. Therefore, we decided to pursue a label-free target identification for metal-based complexes to overcome specificity. Since TRIP acts on proteins, we conducted a label-free target protein identification that we have developed, namely thermal stability

shift-based fluorescence differences in two-dimensional gel electrophoresis (TS-FITGE) (Park et al., 2017). Briefly, HeLa cells were heat-denatured for 3 min at various temperature ranges in the absence or presence of TRIP. Thereafter, the heat-treated cells were lysed, and soluble protein fractions from vehicle- and TRIP-treated conditions were labeled with Cy3 and Cy5 dyes, respectively. Cy3- and Cy5-labeled proteomes from the same temperature point were mixed and analyzed by 2-dimensional gel electrophoresis. Based on color-based image

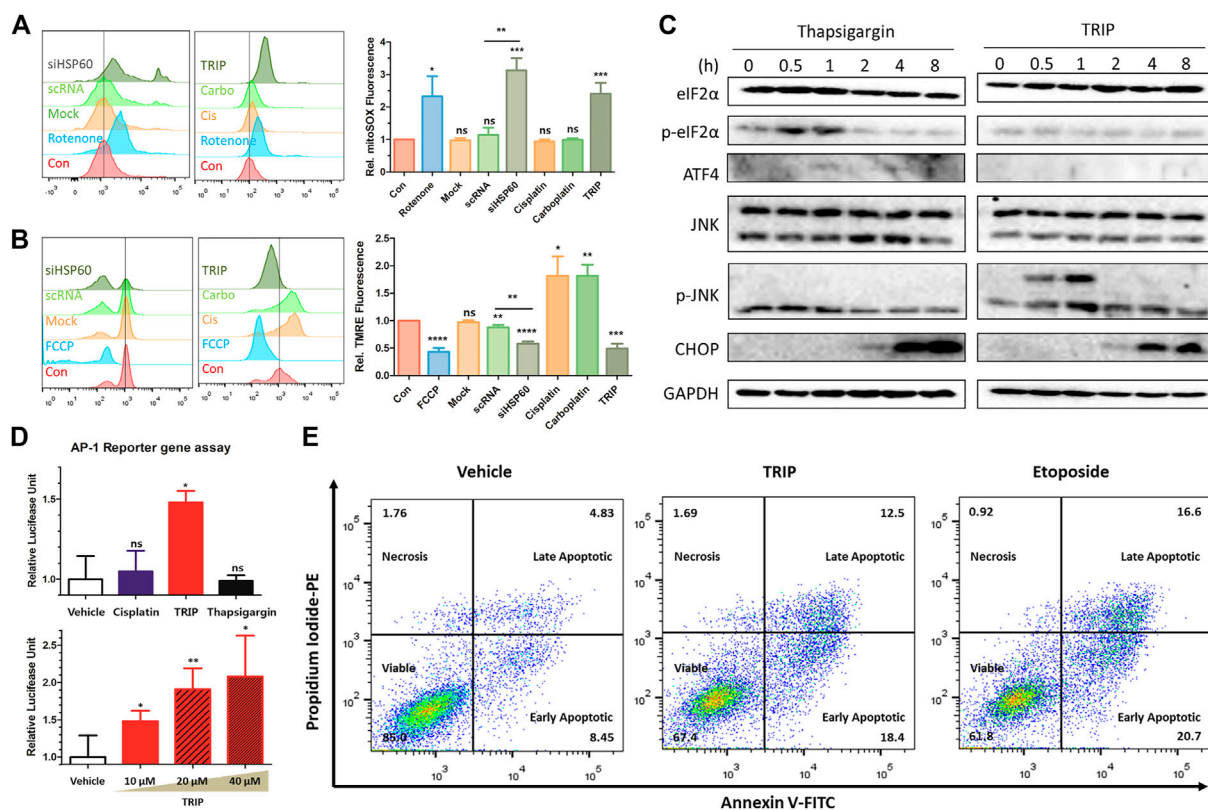


FIGURE 3 | TRIP induced mitochondrial stress-mediated p-JNK/AP-1/CHOP apoptosis. **(A,B)** Flow cytometry data investigating **(A)** an increase of mitochondrial reactive oxygen species (ROS) and **(B)** mitochondrial depolarization upon either TRIP treatment or depletion of HSP60 using siRNA in HeLa cells ($N = 3$). HeLa cells were treated with 10 μM of TRIP for 8 h or transfected with siRNA for 48 h. **(C)** Immunoblot data showing CHOP activation via different signaling pathways in HeLa cells. HeLa cells were treated with either 200 nM of thapsigargin or 10 μM of TRIP at various time points. **(D)** TRIP-mediated AP-1 activation in HeLa cells. 10 μM of each compound was treated for 24 h (upper), and 10, 20, and 40 μM of TRIP were treated for 24 h (lower). Luciferase signal was normalized by the vehicle-treated sample ($N = 6$). Statistical analysis was performed compared to the vehicle group. **(E)** Flow cytometry data showing the alteration in the number of apoptotic cells upon treatment with either TRIP or etoposide in HeLa cells. HeLa cells were treated with either 10 μM of TRIP for 24 h or 50 μM of etoposide for 24 h. Data are presented as the mean \pm SD (ns, not significant, $p > 0.05$; *, $p < 0.05$; **, $p < 0.01$; ***, $p < 0.001$; ****, $p < 0.0001$).

analysis of each gel, we selected a total of nine protein spots with thermal stability shift, including heat-sensitive green and heat-resistant red spots in the presence of TRIP (**Supplementary Figure S2, Supplementary Table S1**). Among the potential target proteins identified from these spots, we focused on HSP60 (Bukau and Horwich, 1998), a mitochondrial chaperone protein, since we knew that TRIP treatment causes changes in mitochondrial morphology (King et al., 2019). TS-FITGE analysis of the HSP60 spot showed a distinct thermal-stabilized red spot in the 62°C gel (**Figure 2A**). Cellular thermal shift assay (CETSA) with HSP60-specific antibody further confirmed the thermal stabilization of HSP60 upon TRIP treatment, compared to vehicle, which was consistent with TS-FITGE results (**Figure 2B**).

To validate the direct binding of TRIP to HSP60, we conducted surface plasmon resonance (SPR) and differential scanning fluorimetry (DSF) analyses. SPR analysis clearly showed a dose-dependent response of the conventional one-on-one binding pattern with a K_D value of 2.39 μM (**Figure 2C**). DSF analysis also showed the melting temperature (T_m) shift

from 51°C to 39.8°C in the presence of TRIP (**Figure 2D, Supplementary Figure S3**). However, the increased heat sensitivity in DSF was somewhat opposite to TRIP-induced heat resistance of HSP60 observed in TS-FITGE and CETSA experiments. This discrepancy in the thermal stability of HSP60 might be caused by the different states of HSP60 in each experimental setting; TS-FITGE and CETSA were performed in live cells, while DSF was measured with a purified protein. In the cellular system, HSP60 is known to form a heterodimer with heat shock protein 10 (HSP10); however, when purified, HSP60 oligomerizes with itself through protein-protein interactions with a T_m value of over 50°C, which can in turn be blocked by HSP60 binders (Shao et al., 2020). When HSP60 disassociates from the oligomer to its monomers, the T_m value decreases to 40°C, as observed in DSF analysis in the presence of TRIP. Next, we examined whether the chaperone function of HSP60 can be affected by TRIP. Luciferase protein was denatured by 7-min heat shock at 45°C and incubated with the HSP60/HSP10 complex in the absence or presence of either TRIP or epolactaene *t*-butyl ester (ETB), a known HSP60 inhibitor

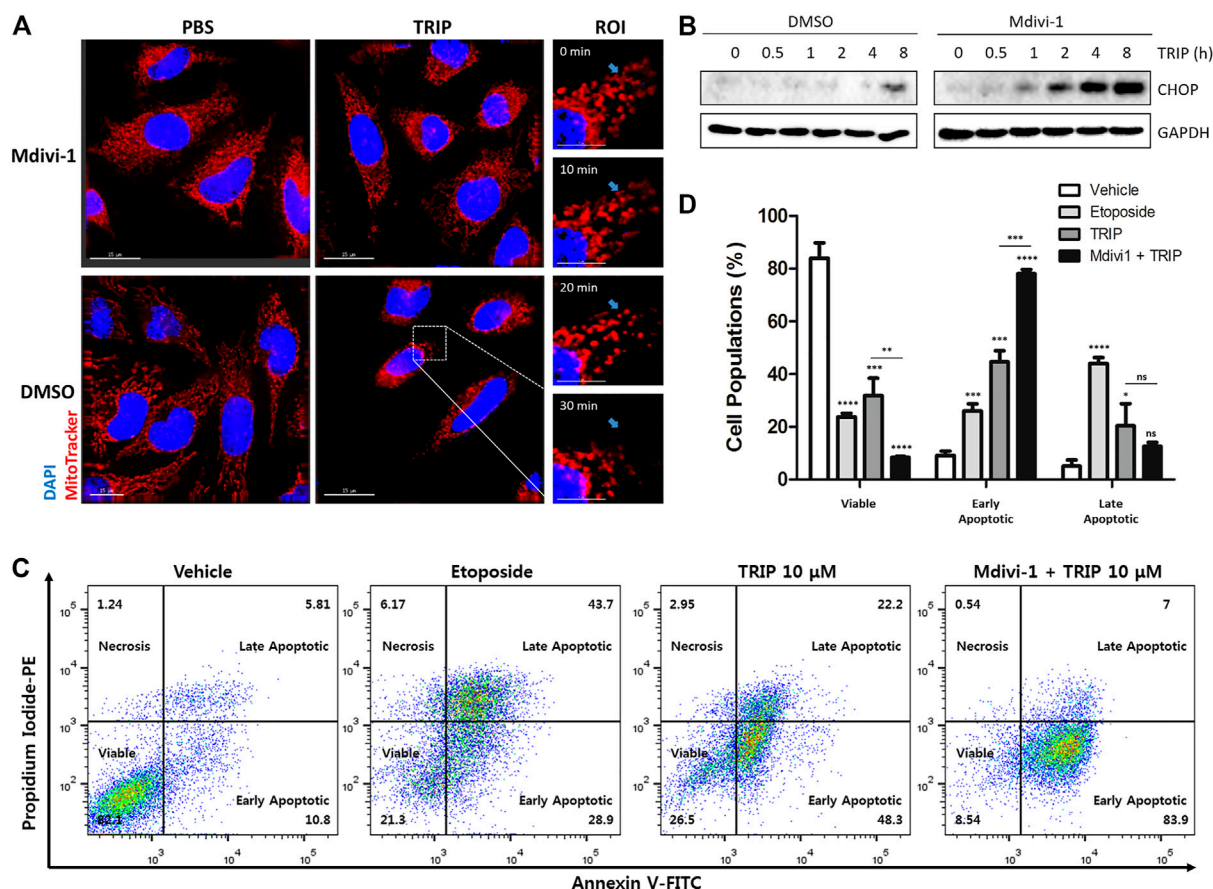


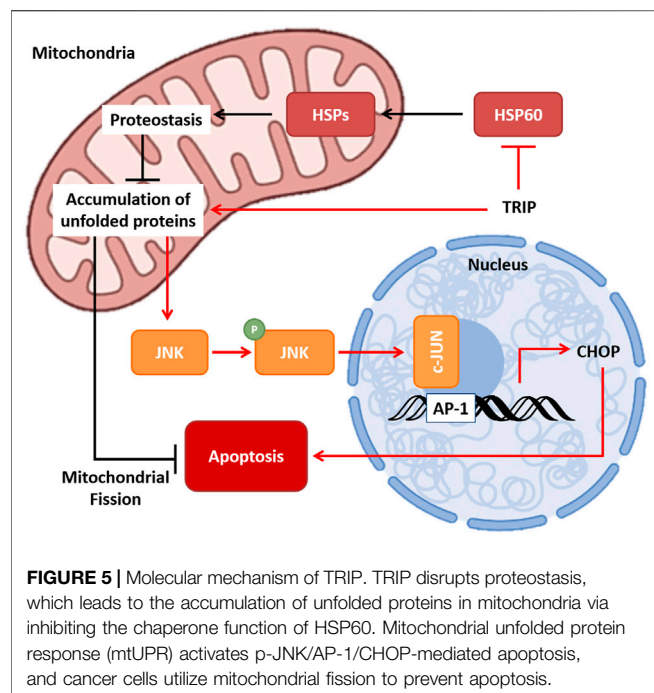
FIGURE 4 | Cancer cells utilize mitochondrial fission to reduce mitochondrial stress. **(A)** Immunofluorescence images showing mitochondrial fission induced by TRIP and perturbed by Mdivi-1 in HeLa cells. **(B)** Immunoblot data in HeLa cells demonstrating CHOP activation enhanced by 50 μ M of Mdivi-1 co-treatment with TRIP. **(C)** Flow cytometry data showing CHOP-mediated apoptosis reinforced by 50 μ M of Mdivi-1 co-treatment with TRIP in HeLa cells. **(D)** Quantitative data pertaining to **(C)** ($N = 3$). Data are presented as the mean \pm SD (ns, not significant, $p > 0.05$; *, $p < 0.05$; **, $p < 0.01$; ***, $p < 0.001$; ****, $p < 0.0001$). R.O.I., region of interest.

(Nagumo et al., 2005), for 1.5, 3, and 6 h. Thereafter, the refolded luciferase protein was mixed with luciferin to measure the chaperone activity of HSP60 on the basis of luminescence signals. As shown in **Figure 2E**, TRIP inhibited the chaperone activity of HSP60 with an IC_{50} value of 0.97 μ M (**Supplementary Figure S4**). Finally, we examined whether the cytotoxic activity of TRIP can be sensitized by siRNA-based knockdown of HSP60 to validate the target specificity of TRIP toward HSP60. Compared to scRNA-treatment, the knockdown of HSP60 significantly sensitized cells to TRIP treatment, although there was no difference in the case of cisplatin (**Figure 2F**, **Supplementary Figure S5**). Collectively, our data suggested that TRIP kills cancer cells selectively by inhibiting the chaperone function of HSP60.

Tricarbonyl Rhenium Isonitrile Polypyridyl Induced Mitochondrial Stress-Mediated p-JNK/AP-1/CHOP Apoptosis

TRIP-mediated inhibition of the chaperone function of HSP60 results in the loss of protein homeostasis (proteostasis) and the

accumulation of unfolded proteins in mitochondria, with the latter inducing mitochondrial dysfunction and JNK signaling (Mottis et al., 2014; Joy et al., 2021). To quantify mitochondrial stress, we measured the level of reactive oxidative stress (ROS) in mitochondria and their polarization using flow cytometry (Suzuki-Karasaki et al., 2014). Both TRIP treatment and HSP60 knockdown increased mitochondrial ROS levels and induced mitochondrial depolarization (**Figures 3A,B**). Unfolded protein responses (UPR) in cellular organelles, including endoplasmic reticulum (ER) and mitochondria, induce CHOP-mediated apoptosis in various pathways. For instance, ER-stress inducers (i.e., thapsigargin) activate CHOP via p-eIF2 α /ATF4 signaling (Rozpedek et al., 2016), and mitochondrial stress inducers (i.e., alkannin) activate CHOP through p-JNK/AP-1 signaling (Aldridge et al., 2007; Horibe and Hoogenraad, 2007; Mottis et al., 2014; Qureshi et al., 2017; Zheng et al., 2020). To validate the specific organelle-derived CHOP activation, we treated HeLa cells with either thapsigargin or TRIP, and observed the subsequent signaling pathways at various time points. Although CHOP activation was observed after 2 h in both conditions, thapsigargin and TRIP activated the



p-eIF2 α /ATF4 and p-JNK2 signaling pathways, respectively, within 1 h (Figure 3C). AP-1 reporter gene assay confirmed that only TRIP activated p-JNK/AP-1 signaling as a mitochondrial stress inducer, unlike cisplatin or thapsigargin (Figure 3D). To validate p-JNK/AP-1/CHOP-mediated apoptosis, we treated HeLa cells with TRIP or etoposide—an apoptosis inducer by modulating the function of topoisomerase II. Flow cytometry confirmed that both TRIP and etoposide kill HeLa cells via apoptosis, not necrosis (Figure 3E, Supplementary Figure S6). Furthermore, the time- and dose-dependent TRIP treatment significantly increased the number of cells that entered early and late apoptosis compared to vehicle treatment (Supplementary Figure S7).

Cancer Cells Utilized Mitochondrial Fission to Reduce Mitochondrial Stress

TRIP treatment induces mitochondrial fission that can be blocked by Mdivi-1, an inhibitor for dynamin-related protein 1 (Drp1)—a crucial mediator of mitochondrial fission (King et al., 2019). As shown in Figure 4A, our immunofluorescence images suggested that TRIP treatment induces mitochondrial fission in a time-dependent manner, which in turn could be blocked by Mdivi-1 treatment. Therefore, to examine whether TRIP-induced mitochondrial fission triggers CHOP-mediated apoptosis or relieves mitochondrial stress, we treated HeLa cells with TRIP in the absence or presence of Mdivi-1 at various time points. Interestingly, Mdivi-1 accelerated TRIP-induced CHOP activation, but Mdivi-1 did not boost thapsigargin-induced CHOP activation (Figure 4B, Supplementary Figure S8), indicating that cancer cells utilize mitochondrial fission to reduce mitochondrial stress.

To validate this observation, we conducted flow cytometry analysis. Compared to the TRIP-only treatment, the co-treatment of TRIP with Mdivi-1 increased early apoptotic cells by approximately two-fold without significant changes in the late apoptotic cells (Figures 4C,D), confirming the acceleration of TRIP-mediated apoptotic cell death by inhibiting mitochondrial fission. When the TRIP-treatment time was extended to 48 h, Mdivi-1 significantly increased the late apoptotic cell death (Supplementary Figure S9). However, Mdivi-1 did not influence the portion of late apoptotic cells in the case of etoposide-mediated cell death via DNA double-strand break, which is orthogonal to TRIP-mediated apoptotic cell death via the accumulation of unfolded proteins in mitochondria (Supplementary Figure S10).

CONCLUSION

In this study, based on ICP-MS analysis, we revealed that TRIP targets protein, not DNA. Furthermore, we identified HSP60 as the target protein of TRIP by a label-free target identification method, TS-FITGE. We also confirmed that TRIP directly binds to HSP60 and inhibits its chaperone function, eventually leading to cancer-specific cell death. Inhibition of the chaperone function of HSP60 disrupts cellular proteostasis and causes the accumulation of unfolded proteins in mitochondria. The resulting mtUPR activates the p-JNK2/AP-1/CHOP-mediated apoptotic pathway, exacerbated by inhibiting mitochondrial fission (Figure 5). Collectively, our study revealed how a rhenium-based compound could selectively induce apoptosis of cancer cells at the molecular level and demonstrated label-free target identification as a potential and indispensable tool for unveiling the molecular mechanism of metal-based drugs.

DATA AVAILABILITY STATEMENT

The original contributions presented in the study are included in the article/Supplementary Material, further inquiries can be directed to the corresponding author.

AUTHOR CONTRIBUTIONS

JY and SP designed the study, prepared the figures, and wrote the manuscript. JY performed the molecular biology work. Both authors critically reviewed the manuscript.

FUNDING

This work was supported by the Creative Research Initiative Grant (2014R1A3A2030423) and the Bio & Medical Technology Development Program (2012M3A9C4048780) through the

National Research Foundation of Korea (NRF) funded by the Korean Government (Ministry of Science & ICT).

ACKNOWLEDGMENTS

We appreciate Justin J. Wilson, Sierra Marker, and A. Paden King at Cornell University for kindly providing TRIP. We gratefully acknowledged the National Center for Inter-university Research

Facilities (NCIRF) for technical support of ICP-MS and flow cytometry analysis. Figures were created with BioRender.com.

SUPPLEMENTARY MATERIAL

The Supplementary Material for this article can be found online at: <https://www.frontiersin.org/articles/10.3389/fchem.2022.850638/full#supplementary-material>

REFERENCES

- Aldridge, J. E., Horibe, T., and Hoogenraad, N. J. (2007). Discovery of Genes Activated by the Mitochondrial Unfolded Protein Response (mtUPR) and Cognate Promoter Elements. *PLoS One* 2, e874. doi:10.1371/journal.pone.0000874
- Ang, W. H., De Luca, A., Chapuis-Bernasconi, C., Juillerat-Jeanneret, L., Lo Bello, M., and Dyson, P. J. (2007). Organometallic Ruthenium Inhibitors of Glutathione-S-Transferase P1-1 as Anticancer Drugs. *ChemMedChem* 2, 1799–1806. doi:10.1002/cmdc.200700209
- Basu, A., and Krishnamurthy, S. (2010). Cellular Responses to Cisplatin-Induced DNA Damage. *J. Nucleic Acids* 2010, 1–16. doi:10.4061/2010/201367
- Bates, D., and Eastman, A. (2017). Microtubule Destabilising Agents: Far More Than Just Antimitotic Anticancer Drugs. *Br. J. Clin. Pharmacol.* 83, 255–268. doi:10.1111/bcp.13126
- Blanck, S., Maksimoska, J., Baumeister, J., Harms, K., Marmorstein, R., and Meggers, E. (2012). The Art of Filling Protein Pockets Efficiently with Octahedral Metal Complexes. *Angew. Chem. Int. Ed.* 51, 5244–5246. doi:10.1002/anie.201108865
- Blumenfeld, Z. (2012). Chemotherapy and Fertility. *Best Pract. Res. Clin. Obstet. Gynaecol.* 26, 379–390. doi:10.1016/j.bpobgyn.2011.11.008
- Bregman, H., Carroll, P. J., and Meggers, E. (2006). Rapid Access to Unexplored Chemical Space by Ligand Scanning Around a Ruthenium center: Discovery of Potent and Selective Protein Kinase Inhibitors. *J. Am. Chem. Soc.* 128, 877–884. doi:10.1021/ja055523r
- Bruno, P. M., Liu, Y., Park, G. Y., Murai, J., Koch, C. E., Eisen, T. J., et al. (2017). A Subset of Platinum-Containing Chemotherapeutic Agents Kills Cells by Inducing Ribosome Biogenesis Stress. *Nat. Med.* 23, 461–471. doi:10.1038/nm.4291
- Bukau, B., and Horwich, A. L. (1998). The Hsp70 and Hsp60 Chaperone Machines. *Cell* 92, 351–366. doi:10.1016/s0092-8674(00)80928-9
- Choi, J.-E., Lee, J.-J., Kang, W., Kim, H. J., Cho, J.-H., Han, P.-L., et al. (2018). Proteomic Analysis of Hippocampus in a Mouse Model of Depression Reveals Neuroprotective Function of Ubiquitin C-Terminal Hydrolase L1 (UCH-L1) via Stress-Induced Cysteine Oxidative Modifications. *Mol. Cell Proteomics* 17, 1803–1823. doi:10.1074/mcp.RA118.000835
- Chon, S. Y., Champion, R. W., Geddes, E. R., and Rashid, R. M. (2012). Chemotherapy-induced Alopecia. *J. Am. Acad. Dermatol.* 67, e37–e47. doi:10.1016/j.jaad.2011.02.026
- Cox, J. D., and Ang, K. K. (2009). *Radiation Oncology E-Book: Rationale, Technique, Results*. London: Elsevier Health Sciences/Elsevier Health Sciences, 560–605.
- Dasari, S., and Bernard Tchounwou, P. (2014). Cisplatin in Cancer Therapy: Molecular Mechanisms of Action. *Eur. J. Pharmacol.* 740, 364–378. doi:10.1016/j.ejphar.2014.07.025
- Falzone, L., Salomone, S., and Libra, M. (2018). Evolution of Cancer Pharmacological Treatments at the Turn of the Third Millennium. *Front. Pharmacol.* 9, 1300. doi:10.3389/fphar.2018.01300
- Feng, L., Geisselbrecht, Y., Blanck, S., Wilbuer, A., Atilla-Gokcumen, G. E., Filippakopoulos, P., et al. (2011). Structurally Sophisticated Octahedral Metal Complexes as Highly Selective Protein Kinase Inhibitors. *J. Am. Chem. Soc.* 133, 5976–5986. doi:10.1021/ja1112996
- Gill, M. R., Harun, S. N., Halder, S., Boghazian, R. A., Ramadan, K., Ahmad, H., et al. (2016). A Ruthenium Polypyridyl Intercalator Stalls DNA Replication forks, Radiosensitizes Human Cancer Cells and Is Enhanced by Chk1 Inhibition. *Sci. Rep.* 6, 31973. doi:10.1038/srep31973
- Go, R. S., and Adjei, A. A. (1999). Review of the Comparative Pharmacology and Clinical Activity of Cisplatin and Carboplatin. *Jco* 17, 409. doi:10.1200/JCO.1999.17.1.409
- Groopman, J. E., and Itri, L. M. (1999). Chemotherapy-induced Anemia in Adults: Incidence and Treatment. *JNCI J. Natl. Cancer Inst.* 91, 1616–1634. doi:10.1093/jnci/91.19.1616
- Guo, M., Sun, H., Mcardle, H. J., Gambling, L., and Sadler, P. J. (2000). TiIV Uptake and Release by Human Serum Transferrin and Recognition of TiIV-Transferrin by Cancer Cells: Understanding the Mechanism of Action of the Anticancer Drug Titanocene Dichloride. *Biochemistry* 39, 10023–10033. doi:10.1021/bi000798z
- Horibe, T., and Hoogenraad, N. J. (2007). The Chop Gene Contains an Element for the Positive Regulation of the Mitochondrial Unfolded Protein Response. *PLoS One* 2, e835. doi:10.1371/journal.pone.0000835
- Joy, J., Barrio, L., Santos-Tapia, C., Romão, D., Giakoumakis, N. N., Clemente-Ruiz, M., et al. (2021). Proteostasis Failure and Mitochondrial Dysfunction Leads to Aneuploidy-Induced Senescence. *Dev. Cel* 56, 2043–2058. doi:10.1016/j.devcel.2021.06.009
- King, A. P., Marker, S. C., Swanda, R. V., Woods, J. J., Qian, S. B., and Wilson, J. J. (2019). A Rhenium Isonitrile Complex Induces Unfolded Protein Response-Mediated Apoptosis in Cancer Cells. *Chem. Eur. J.* 25, 9206–9210. doi:10.1002/chem.201902223
- Knopf, K. M., Murphy, B. L., Macmillan, S. N., Baskin, J. M., Barr, M. P., Boros, E., et al. (2017). *In Vitro* Anticancer Activity and *In Vivo* Biodistribution of Rhenium(I) Tricarbonyl Aqua Complexes. *J. Am. Chem. Soc.* 139, 14302–14314. doi:10.1021/jacs.7b08640
- Konkankit, C. C., King, A. P., Knopf, K. M., Southard, T. L., and Wilson, J. J. (2019a). *In Vivo* Anticancer Activity of a Rhenium(I) Tricarbonyl Complex. *ACS Med. Chem. Lett.* 10, 822–827. doi:10.1021/acsmchemlett.9b00128
- Konkankit, C. C., Vaughn, B. A., Macmillan, S. N., Boros, E., and Wilson, J. J. (2019b). Combinatorial Synthesis to Identify a Potent, Necrosis-Inducing Rhenium Anticancer Agent. *Inorg. Chem.* 58, 3895–3909. doi:10.1021/acs.inorgchem.8b03552
- Machover, D., Diaz-Rubio, E., De Gramont, A., Schilf, A., Gastiaburu, J.-J., Brienza, S., et al. (1996). Two Consecutive Phase II Studies of Oxaliplatin (L-OHP) for Treatment of Patients with Advanced Colorectal Carcinoma Who Were Resistant to Previous Treatment with Fluoropyrimidines. *Ann. Oncol.* 7, 95–98. doi:10.1093/oxfordjournals.annonc.a010489
- Marker, S. C., King, A. P., Swanda, R. V., Vaughn, B., Boros, E., Qian, S. B., et al. (2020). Exploring Ovarian Cancer Cell Resistance to Rhenium Anticancer Complexes. *Angew. Chem. Int. Ed.* 59, 13391–13400. doi:10.1002/anie.202004883
- Meggers, E. (2007). Exploring Biologically Relevant Chemical Space with Metal Complexes. *Curr. Opin. Chem. Biol.* 11, 287–292. doi:10.1016/j.cbpa.2007.05.013
- Miller, M., Mellul, A., Braun, M., Sherill-Rofe, D., Cohen, E., Shpilt, Z., et al. (2020). Titanium Tackles the Endoplasmic Reticulum: A First Genomic Study on a Titanium Anticancer Metallo-drug. *iScience* 23, 101262. doi:10.1016/j.isci.2020.101262
- Mottis, A., Jovaisaite, V., and Auwerx, J. (2014). The Mitochondrial Unfolded Protein Response in Mammalian Physiology. *Mamm. Genome* 25, 424–433. doi:10.1007/s00335-014-9525-z
- Nagumo, Y., Kakeya, H., Shoji, M., Hayashi, Y., Dohmae, N., and Osada, H. (2005). Epolactaene Binds Human Hsp60 Cys442 Resulting in the Inhibition of Chaperone Activity. *Biochem. J.* 387, 835–840. doi:10.1042/BJ20041355

- Park, H., Ha, J., Koo, J. Y., Park, J., and Park, S. B. (2017). Label-free Target Identification Using In-Gel Fluorescence Difference via thermal Stability Shift. *Chem. Sci.* 8, 1127–1133. doi:10.1039/c6sc03238a
- Qureshi, M. A., Haynes, C. M., and Pellegrino, M. W. (2017). The Mitochondrial Unfolded Protein Response: Signaling from the Powerhouse. *J. Biol. Chem.* 292, 13500–13506. doi:10.1074/jbc.R117.791061
- Riddell, I. A., and Lippard, S. J. (2018). *1. Cisplatin and Oxaliplatin: Our Current Understanding of Their actionsMetallo-Drugs: Development and Action of Anticancer Agents*. Berlin: De Gruyter, 1–42.
- Rixe, O., Ortuzar, W., Alvarez, M., Parker, R., Reed, E., Paull, K., et al. (1996). Oxaliplatin, Tetraplatin, Cisplatin, and Carboplatin: Spectrum of Activity in Drug-Resistant Cell Lines and in the Cell Lines of the National Cancer Institute's Anticancer Drug Screen Panel. *Biochem. Pharmacol.* 52, 1855–1865. doi:10.1016/s0006-2952(97)81490-6
- Rozpedek, W., Pytel, D., Mucha, B., Leszczynska, H., Diehl, J. A., and Majsterek, I. (2016). The Role of the PERK/eIF2 α /ATF4/CHOP Signaling Pathway in Tumor Progression during Endoplasmic Reticulum Stress. *Cmm* 16, 533–544. doi:10.2174/1566524016666160523143937
- Shao, H., Oltion, K., Wu, T., and Gestwicki, J. E. (2020). Differential Scanning Fluorimetry (DSF) Screen to Identify Inhibitors of Hsp60 Protein-Protein Interactions. *Org. Biomol. Chem.* 18, 4157–4163. doi:10.1039/D0OB00928H
- Shewach, D. S., and Kuchta, R. D. (2009). Introduction to Cancer Chemotherapeutics. *Chem. Rev.* 109, 2859–2861. doi:10.1021/cr900208x
- Siegel, R. L., Miller, K. D., Fuchs, H. E., and Jemal, A. (2021). Cancer Statistics, 2021. *CA A. Cancer J. Clin.* 71, 7–33. doi:10.3322/caac.21654
- Sutton, E. C., Mcdevitt, C. E., Prochnau, J. Y., Yglesias, M. V., Mroz, A. M., Yang, M. C., et al. (2019). Nucleolar Stress Induction by Oxaliplatin and Derivatives. *J. Am. Chem. Soc.* 141, 18411–18415. doi:10.1021/jacs.9b10319
- Suzuki-Karasaki, M., Ochiai, T., and Suzuki-Karasaki, Y. (2014). Crosstalk between Mitochondrial ROS and Depolarization in the Potentiation of TRAIL-Induced Apoptosis in Human Tumor Cells. *Int. J. Oncol.* 44, 616–628. doi:10.3892/ijo.2013.2215
- Thanarajasingam, G., Minasian, L. M., Baron, F., Cavalli, F., De Claro, R. A., Dueck, A. C., et al. (2018). Beyond Maximum Grade: Modernising the Assessment and Reporting of Adverse Events in Haematological Malignancies. *Lancet Haematol.* 5, e563–e598. doi:10.1016/S2352-3026(18)30051-6
- Walling, J. (2006). From Methotrexate to Pemetrexed and beyond. A Review of the Pharmacodynamic and Clinical Properties of Antifolates. *Invest. New Drugs* 24, 37–77. doi:10.1007/s10637-005-4541-1
- Zheng, Q., Li, Q., Zhao, G., Zhang, J., Yuan, H., Gong, D., et al. (2020). Alkannin Induces Cytotoxic Autophagy and Apoptosis by Promoting ROS-Mediated Mitochondrial Dysfunction and Activation of JNK Pathway. *Biochem. Pharmacol.* 180, 114167. doi:10.1016/j.bcp.2020.114167

Conflict of Interest: The authors declare that the research was conducted in the absence of any commercial or financial relationships that could be construed as a potential conflict of interest.

Publisher's Note: All claims expressed in this article are solely those of the authors and do not necessarily represent those of their affiliated organizations, or those of the publisher, the editors and the reviewers. Any product that may be evaluated in this article, or claim that may be made by its manufacturer, is not guaranteed or endorsed by the publisher.

Copyright © 2022 Yim and Park. This is an open-access article distributed under the terms of the Creative Commons Attribution License (CC BY). The use, distribution or reproduction in other forums is permitted, provided the original author(s) and the copyright owner(s) are credited and that the original publication in this journal is cited, in accordance with accepted academic practice. No use, distribution or reproduction is permitted which does not comply with these terms.



An Efficient Approach for the Design and Synthesis of Antimicrobial Peptide-Peptide Nucleic Acid Conjugates

Nitin A. Patil^{1*}, Varsha J. Thombare², Rong Li¹, Xiaoji He¹, Jing Lu^{1,2}, Heidi H. Yu¹, Hasini Wickremasinghe¹, Kavya Pamulapati¹, Mohammad A. K. Azad¹, Tony Velkov², Kade D. Roberts¹ and Jian Li¹

¹Infection and Immunity Program and Department of Microbiology, Biomedicine Discovery Institute, Monash University, Melbourne, VIC, Australia, ²Department of Biochemistry and Pharmacology, The University of Melbourne, Melbourne, VIC, Australia

OPEN ACCESS

Edited by:

Olga Avrutina,
Darmstadt University of Technology,
Germany

Reviewed by:

Rongsheng (Ross) Wang, Temple
University, United States
Michele Saviano,
National Research Council, Italy

*Correspondence:

Nitin A. Patil
nitin.patil@monash.edu

Specialty section:

This article was submitted to
Chemical Biology,
a section of the journal
Frontiers in Chemistry

Received: 24 December 2021

Accepted: 16 February 2022

Published: 15 March 2022

Citation:

Patil NA, Thombare VJ, Li R, He X,
Lu J, Yu HH, Wickremasinghe H,
Pamulapati K, Azad MAK, Velkov T,
Roberts KD and Li J (2022) An Efficient
Approach for the Design and Synthesis
of Antimicrobial Peptide-Peptide
Nucleic Acid Conjugates.
Front. Chem. 10:843163.
doi: 10.3389/fchem.2022.843163

Peptide-Peptide Nucleic Acid (PNA) conjugates targeting essential bacterial genes have shown significant potential in developing novel antisense antimicrobials. The majority of efforts in this area are focused on identifying different PNA targets and the selection of peptides to deliver the peptide-PNA conjugates to Gram-negative bacteria. Notably, the selection of a linkage strategy to form peptide-PNA conjugate plays an important role in the effective delivery of PNAs. Recently, a unique Cysteine- 2-Cyanoisonicotinamide (Cys-CINA) click chemistry has been employed for the synthesis of cyclic peptides. Considering the high selectivity of this chemistry, we investigated the efficiency of Cys-CINA conjugation to synthesize novel antimicrobial peptide-PNA conjugates. The PNA targeting acyl carrier protein gene (*acpP*), when conjugated to the membrane-active antimicrobial peptides (polymyxin), showed improvement in antimicrobial activity against multidrug-resistant Gram-negative *Acinetobacter baumannii*. Thus, indicating that the Cys-CINA conjugation is an effective strategy to link the antisense oligonucleotides with antimicrobial peptides. Therefore, the Cys-CINA conjugation opens an exciting prospect for antimicrobial drug development.

Keywords: antisense oligonucleotides, peptide nucleic acids, antimicrobial agents, cell-penetrating peptides, conjugation

INTRODUCTION

Antimicrobial resistance is now considered one of the greatest threats to global health and the economy. The World Health Organization (WHO) identified multidrug-resistant (MDR) Gram-negative pathogens such as *Pseudomonas aeruginosa*, *Acinetobacter baumannii*, *Enterobacteriales* as the top priority for the development of new antibiotics (WHO, 2017). This situation has been made even more problematic by the lack of development of new effective antibiotic drug therapies targeting these multi-drug resistant (MDR) bacteria. Therefore, there is an urgent requirement for the development of antibiotics with novel modes of action (Andersson et al., 2016; WHO, 2017). To this end, antisense antibiotics such as Peptide Nucleic Acids (PNAs) can be used to target essential genes in bacteria, resulting in translational gene silencing and bactericidal effects (Good et al., 2001; Ghosal and Nielsen, 2012). PNAs are artificial DNA mimics with tertiary amide linked nucleobases

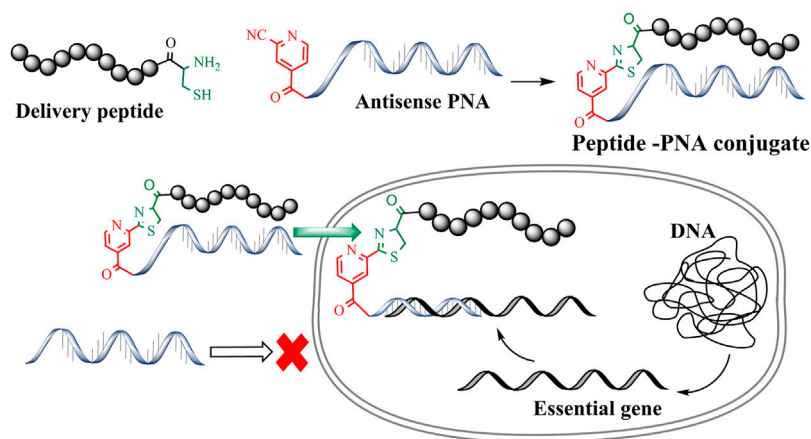


FIGURE 1 | CINA mediated conjugation to generate peptide-PNA antisense conjugates.

and aminoethylglycine (*aeg*) repeating units (Nielsen et al., 1991; Egholm et al., 1993; Wittung et al., 1996; Good and Nielsen, 1998; Nielsen, 2001). This unique combination of amide linkage and carbonyl methylene linked nucleobases provides thermal and hydrolytic (enzymatic degradation) stability. Furthermore, PNAs are easy to synthesize and exhibit improved binding affinity towards complementary DNA/RNA sequences. The last decade has seen a rapid surge in the development of PNA-based therapeutics and biochemical tools (Siddiquee et al., 2015; Gupta et al., 2017). However, the charge-neutral amide backbone in PNA can result in poor cell permeability that leads to poor antibacterial activity (Koppelhus and Nielsen, 2003). Conjugation of PNAs with cell-penetrating peptides (CPP) is a widely used approach to improve the cellular permeability of antisense PNAs (McAllister et al., 2006; Gupta et al., 2016). Importantly, CPP mediated intracellular delivery of oligonucleotides has been effectively used to target essential bacterial genes and develop novel antimicrobial peptide-PNA conjugates (Figure 1) (Good et al., 2001; Ghosal et al., 2013). Along these lines, peptide-mediated cell penetration was shown to be effective for the delivery of antisense PNA targeting top-priority *Acinetobacter baumannii* (Rose et al., 2019).

A number of conjugation strategies have been explored to link PNA with CPPs, including disulfide (Turner et al., 2006), thio-maleimide (Ede et al., 1994) and triazole (McKay and Finn, 2014). However, these strategies are often limited to simple and linear CPPs. Importantly, conjugation of PNAs with structurally complex peptides such as the polymyxins (Velkov et al., 2013) and cathelicidin (Dürr et al., 2006) remains an unexplored terrain (Soudah et al., 2019). Moreover, peptide conjugations through traditional disulfide and maleimide linkages require orthogonal protecting groups as well as a multistep synthesis strategy (Patil, 2021). Previously, we developed a methodology for cysteine-cyanobenzothiazole (Cys-CBT) mediated peptide-PNA conjugation that enables facile synthesis and improved intracellular stability as compared to other strategies (Patil et al., 2019). However, commercially available 2-cyanobenzothiazole is expensive and requires additional

synthetic steps before being employed for the solid-phase synthesis of peptides or PNAs. In our hands, succinoyl-2-cyanobenzothiazole moiety increased the hydrophobicity of peptide and PNA analogues, resulting in conjugates with poor aqueous solubility (Patil et al., 2019; Patil et al., 2021). To overcome the high-cost and hydrophobicity limitations of the previously developed Cys-CBT conjugation method, we have exploited the low-cost commercially available 2-cyanoisonicotinamide (CINA) group (Patil et al., 2021). This conjugation strategy involves reaction between an *N*-terminal cysteine residue and the nitrile group of cyanoisonicotinic acid which forms a thiazole ring (Figure 1). The resulting linkage is less hydrophobic due to the presence of smaller heterocyclic moiety. As an improved strategy, Cys-CINA conjugation utilizes a relatively water-soluble, readily available CINA moiety and retains all the other biological advantages of Cys-CBT linkage. We have previously utilized this chemo-selective chemistry for peptide macrocyclization (Patil et al., 2021). In the present work we explore the utility of the Cys-CINA conjugation strategy for the generation of novel antimicrobial peptide-PNA conjugates.

MATERIALS AND METHODS

Materials

Piperidine, Trifluoroacetic acid (TFA) and 1H-Benzotriazolium-1-[bis(dimethylamino)methylene]-5-chloro-hexafluorophosphate-(1-),3-oxide (HCTU) were obtained from Auspep (Melbourne, Australia), and Fmoc-8-amino-3,6-dioxaoctanoic acid (PEG), Fmoc-amino acids were obtained from Chem-Impex International (United States). PNA monomers Fmoc-A (Bhoc)-OH, Fmoc-C(Bhoc)-OH, Fmoc-T (Bhoc)-OH, Fmoc-G (Bhoc)-OH were obtained from PANGENE Inc. (Daejeon, Republic of Korea). Dimethylformamide (DMF), methanol (MeOH), diethyl ether, dichloromethane (DCM), hydrochloric acid (HCl) and acetonitrile were obtained from Merck (Melbourne, Australia). LC-MS grade water and acetonitrile were obtained from Fisher

TABLE 1 | Peptide-PNA conjugates sequences.

Conjugate ^c	Peptide ^c and AA Sequence	PNA ^c and nucleobase Sequence	Conjugation Yields
LASP-058	LASP-054 H-Arg-Acp-Arg-Arg-Acp-Arg-Arg-Acp-Arg-Arg-Acp-Arg-PEG-Lys (CINA)-NH ₂	LASP-050 Cys-PEG-Cyt-Thy-Cyt-Adc-Thy-Adc-Cyt-Thy-Cyt-Thy-Thy-Gua-Lys-NH ₂	95%
LASP-059	LASP-026 CINA-PEG-OctGly-Dab-Thr-Dab-Dab ^b -Dab-D-Phe-Leu-Dab-Dab-Thr ^b	LASP-050 Cys-PEG-Cyt-Thy-Cyt-Adc-Thy-Adc-Cyt-Thy-Cyt-Thy-Thy-Gua-Lys-NH ₂	96%
LASP-084	LASP-077 CINA-PEG-Gly-Lys-Pro-Arg-Pro-Tyr-Ser-Pro-Arg-Pro-Thr-Ser-His-Pro-Arg-Pro-Ile-Arg-Arg-NH ₂	LASP-050 Cys-PEG-Cyt-Thy-Cyt-Adc-Thy-Adc-Cyt-Thy-Cyt-Thy-Thy-Gua-Lys-NH ₂	90%
LASP-086	LASP-078 CINA-PEG-Val-Cys ^c -Lys-Arg-trp-Lys-Lys-Trp-Lys-Arg-Lys-Trp-Lys-Lys-Trp-Cys ^d -Val-NH ₂	LASP-050 Cys-PEG-Cyt-Thy-Cyt-Adc-Thy-Adc-Cyt-Thy-Cyt-Thy-Thy-Gua-Lys-NH ₂	87% ^a
LASP-088	LASP-078 CINA-PEG-Val-Cys ^d -Lys-Arg-trp-Lys-Lys-Trp-Lys-Arg-Lys-Trp-Lys-Lys-Trp-Cys ^d -Val-NH ₂	LASP-050 Cys-PEG-Cyt-Thy-Cyt-Adc-Thy-Adc-Cyt-Thy-Cyt-Thy-Thy-Gua-Lys-NH ₂	92%
LASP-130	LASP-072 Cys-PEG-OctGly-Dab-Thr-Dab-Dab ^b -Dab-D-Phe-Leu-Dab-Dab-Thr ^b	LASP-095 CINA-PEG-Cyt-Gua-Adc-Thy-Cyt-Adc-Thy-Thy-Cyt-Adc-Adc-Adc-Lys-NH ₂	94%
LASP-131	LASP-072 Cys-PEG-OctGly-Dab-Thr-Dab-Dab ^b -Dab-D-Phe-Leu-Dab-Dab-Thr ^b	LASP-096 CINA-PEG-Thy-Cyt-Cyt-Adc-Thy-Thy-Adc-Thy-Thy-Gau-Lys-NH ₂	98%
LASP-132	LASP-072 Cys-PEG-OctGly-Dab-Thr-Dab-Dab ^b -Dab-D-Phe-Leu-Dab-Dab-Thr ^b	LASP-072 Cys-PEG-OctGly-Dab-Thr-Dab-Dab ^b -Dab-D-Phe-Leu-Dab-Dab-Thr ^b	98%
LASP-133	LASP-097 CINA-PEG-Cyt-Thy-Cyt-Adc-Thy-Adc-Cyt-Thy-Cyt-Thy-Lys-NH ₂	LASP-119 CINA-PEG-Thy-Thy-Thy-Cyt-Thy-Cyt-Gua-Thy-Cyt-Adc-Lys-NH ₂	96%

^aConjugated and cross-linked yield.^bDab side-chain and C-terminal cyclization.^cSide-chain cross-linked with a butylene bridge.^dLinked with a disulfide bridge.

Chemicals (Melbourne, Australia). 2-Chlorotrityl-Resin and Rink amide resin were obtained from Chempep Inc. Wellington, United States. Triisopropylsilane (TIPS), 2,2'-(Ethylenedioxy) diethanethiol (DODT), diphenylphosphorylazide (DPPA), 2,2'-dithiodipyridine (DPDS), N,N'-Diisopropylcarbodiimide (DIC), and diisopropylethylamine (DIPEA), N-Methylpyrrolidone (NMP), propidium iodide and phenazine methosulfate were obtained from Sigma-Aldrich (Castle Hill, Australia). Dulbecco's modified eagle medium (DMEM) was purchased from Gibco (Thermo Fisher Scientific, Waltham, MA, United States). Fetal bovine serum (FBS) was from Bovogen Biologicals (Victoria, Australia) and XTT staining reagent was obtained from Santa Cruz Biotechnology (Dallas, TX, United States).

PNA Synthesis

All PNAs (Table 1) were synthesized using standard Fmoc chemistry. The PNA was synthesized on Rink amide resin (100–200, 0.25 mmol/g) 100 μmol scale. The Fmoc deprotection was conducted twice using piperidine 20% in DMF at room temperature for 3 min. The coupling of PNA monomers was performed using 3 molar equivalents of Fmoc-protected

PNA(Bhoc)-OH monomers and HCTU dissolved in NMP, *in situ* activation using 6 molar equivalents of DIPEA for 30 min at room temperature. Following final PNA monomer coupling and deprotection, an 8-amino-3,6-dioxaoctanoic acyl (PEG) spacer and cysteine residue was coupled at the N-terminus (5'-end). All synthesized PNAs were cleaved from the solid support with a solution of TFA: H₂O: TIPS (95:2.5:2.5, v/v/v). The N-terminal cysteine containing PNA (abbreviated below as Cys-PNA) was cleaved with an optimized solution of TFA: H₂O: TIPS (95:2.5:2.5, v/v/v; 20 equivalent cysteamine) for 1.5 h. The TFA solution was filtered and evaporated under a nitrogen stream, and the PNA was precipitated in ice-cold diethyl ether; the PNA pellet was then washed twice with diethyl ether (40 ml). The crude PNA was analyzed with LC-MS (Method C) and purified by RP-HPLC method A. The fractions from RP-HPLC were combined and lyophilized for 2 days to give the purified peptides as their corresponding TFA salt. The purity of the PNA was confirmed by LC-MS analysis method D.

General Peptide Synthesis

All the peptides were synthesized using either Rink amide resin (100-200 mesh 0.61 mmol/g) or 2-Chlorotrityl Resin (0.1 mmol)

(100–200 mesh, 0.71 mmol/g). The first amino acid on 2-Chlorotrityl Resin was loaded using 6 molar equivalents solution of respective Fmoc-amino acid in DMF. The rest of the amino acid sequence was built on a Prelude automated peptide synthesizer (Protein Technologies) using standard Fmoc solid-phase peptide chemistry. All coupling of the Fmoc-amino acids were performed using the default instrument protocol: 3 molar equivalents (relative to resin loading) of the Fmoc amino acid, 3 molar equivalents HCTU and 6 molar equivalents of DIPEA in DMF for 50 min at room temperature. Fmoc deprotection was performed using the default instrument protocol: 20% piperidine in DMF (1 × 5 min, 1 × 10 min) at room temperature. The crude peptide was taken up in 15 ml of TFA cleavage cocktail solution (2.5% DODT, 5% TIPS, 92.5% TFA) and stirred at room temperature for 90 min. TFA solution was filtered and evaporated under a nitrogen stream, then 40 ml of diethyl ether was added into residual TFA to precipitate the peptide. The peptide precipitate was collected by centrifugation and washed 2 times with diethyl ether (40 ml), then air-dried to give the crude peptide as a pale-yellow solid. The crude PNA was analyzed with LC-MS (Method C) and purified by RP-HPLC method A. The fractions from RP-HPLC were combined and lyophilized for 2 days to give the purified peptides as their corresponding TFA salt. The purity of the peptides was confirmed by LC-MS analysis method D.

General Peptide-PNA Conjugation

The PNA (0.01 mmol) was dissolved in 3 ml of 10 mM TCEP PBS buffer. In a different vial, the crude peptide (0.012 mmol) was dissolved 2 ml of 10 mM TCEP PBS buffer, and then both solutions were mixed, and pH was adjusted between 7.4 and 8 (pH paper) with 1 M NaOH. The reaction mixture was stirred for 1–4 h and monitored by LC-MS. The crude was purified by RP-HPLC (method B). The fractions from RP-HPLC were analyzed by LC-MS (method C), combined and lyophilized for 2 days to give the purified peptide-PNA conjugates as its corresponding formic acid salt. The purity of the peptides was confirmed by LC-MS analysis method D.

“One-Pot” Method for the Synthesis of LASP-086

The PNA (LASP-050, 0.005 mmol) was dissolved in 3 ml of 10 mM TCEP PBS buffer. In a different vial, the crude peptide (LASP-078, 0.005 mmol) was dissolved 2 ml of 10 mM TCEP PBS buffer, and then both solutions were mixed, and pH was adjusted between 7.4 and 8 (pH paper) with 1 M NaOH. The progress of the reaction was monitored every hour by LC-MS analysis (method D). Once PNA (LASP-050) was consumed (3 h), the reaction mixture was diluted up to a ~2 mg/ml concentration (estimated concentration of intermediate), and a solution of 1,4-dibromobutene (1 equivalent) in acetonitrile was added dropwise. The reaction was monitored by LC-MS every hour (4 h). The reaction mixture was purified by RP-HPLC (method B) to obtain LASP-086. The crude was purified by RP-HPLC (method B). The fractions from RP-HPLC were analyzed by LC-MS (method C),

combined and lyophilized for 2 days to give the purified peptide-PNA conjugate as its corresponding formic acid salt. The purity of the peptides was confirmed by LC-MS analysis method D.

Synthesis of LASP-088

The PNA (LASP-050, 0.005 mmol) was dissolved in 3 ml of 10 mM TCEP PBS buffer. In a different vial, the crude peptide (LASP-078, 0.005 mmol) was dissolved 2 ml of 10 mM TCEP PBS buffer, and then both solutions were mixed, and pH was adjusted between 7.4 and 8 (pH paper) with 1 M NaOH. The progress of the reaction was monitored every hour by LC-MS. Once PNA (LASP-050) was consumed (3 h), The reaction mixture was purified by RP-HPLC (method B). The fractions from RP-HPLC were analyzed by LC-MS analysis (method C), combined and lyophilized for 2 days to give the purified peptide-PNA conjugate LASP-085 as its corresponding formic acid salt. The purified LASP-085 was dissolved (0.5 mg/ml) in PBS buffer at pH 7.4, and a solution of DPDS (0.5 equivalent) in acetonitrile was added. The reaction mixture was purified by purification method B to obtain LASP-088. The crude was purified by RP-HPLC (method B). The fractions from RP-HPLC were analyzed by LC-MS analysis (method C), combined, and lyophilized for 2 days to give the purified peptide-PNA conjugate as its corresponding formic acid salt. The purity of the peptides was confirmed by LC-MS analysis method D.

RP-HPLC Purification Method A

RP-HPLC purification on Shimadzu LC system with a “Prominence” diode array detector (214 nm). A Phenomenex Axia column (Luna C8 (2), 250 × 21.2 mm i.d., 100 Å, 10 µm) was employed with a gradient of 0–60% buffer B over 60 min at a flow rate of 15 ml/min; buffer A was 0.1% TFA/water, and buffer B was 0.1% TFA/acetonitrile.

RP-HPLC Purification Method B

RP-HPLC purification on a Shimadzu LC system with a “Prominence” diode array detector (214 nm). A Water column (XBridge Peptide BEH C18, 300Å, 150 × 19 mm i.d.) was employed with a gradient of 0–60% buffer B over 60 min at a flow rate of 15 ml/min; buffer A was 0.1% formic acid/water, and buffer B was 0.1% formic acid/acetonitrile.

LC-MS Analysis Method C

The collected fractions were analyzed by Shimadzu LC-MS -2020 instrument. Solvent A was 0.05% TFA/water, and Solvent B was 0.05% TFA/acetonitrile. A Phenomenex column (Luna C8 (2), 100 × 2.0 mm ID) was used, eluting with a gradient of 0–60% solvent B over 10 min at a flow rate of 0.2 ml/min. Mass spectra were acquired in the positive ion mode with a scan range of 200–2,000 m/z.

LC-MS Analysis Method D

The final purity of peptides, PNA and peptide-PNA conjugates was confirmed by LC-MS. Solvent A was 0.05% TFA/water, and Solvent B was 0.05% TFA/acetonitrile. A Phenomenex column (Luna C8 (2), 100 × 2.0 mm ID) was used, eluting with a gradient

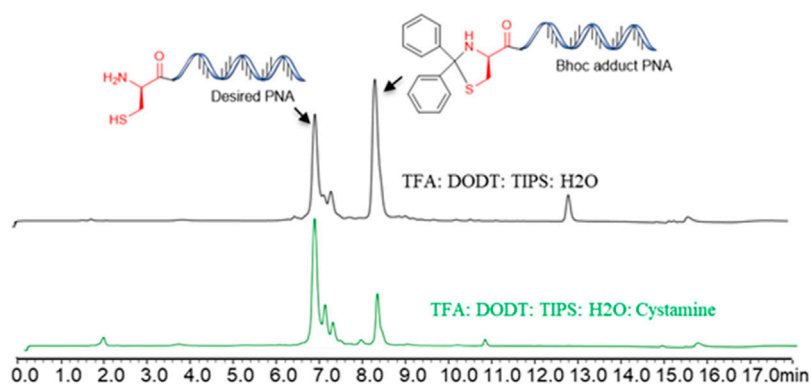
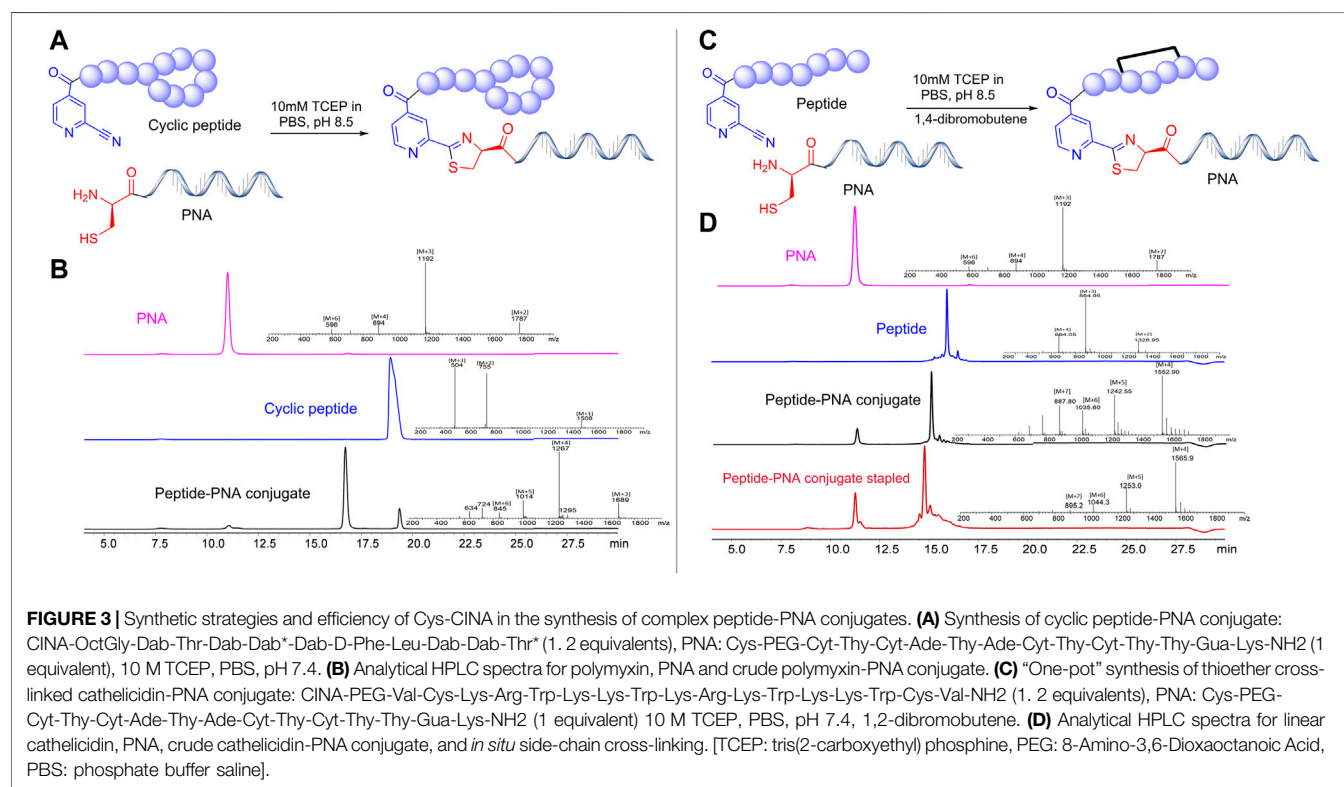


FIGURE 2 | The benzhydryloxy carbonyl (Bhoc) adduct during the Trifluoroacetic acid (TFA) cleavage of PNA and optimisation of cleavage protocol.



of 0–60% solvent B over 30 min at a flow rate of 0.2 ml/min. Mass spectras were acquired in the positive ion mode with a scan range of 200–2,000 m/z.

Antimicrobial Activity

According to the EUCAST guidelines (Eucast, E.C.O.a.S.T., 2021), the inoculum was standardized in sterile saline to the density of a McFarland 0.50 ± 0.02 standard, corresponding to $\sim 10^8$ CFU/ml of each isolate. The freshly prepared bacterial suspension was evenly inoculated onto agar plates and disks containing 40 μ M of peptide-PNA conjugates were applied within 15 min. The diameter of inhibition zones was measured

after incubation for 18 h at 37°C. Polymyxin B (40 μ M/disk) was employed as the control.

Membrane Disorganization Measured With Flow Cytometry

Flow cytometry was employed to examine the membrane disorganization in *A. baumannii* 5075R and 5075D following treatments of LASP-072, LASP-097, LASP-132 (0.040 mM, 1, 24 h) (Zhu et al., 2020; Wickremasinghe et al., 2021). Samples were assessed with an ACEA NovoCyte® high-performance benchtop flow cytometer (ACEA Biosciences, Santa Clara, CA,

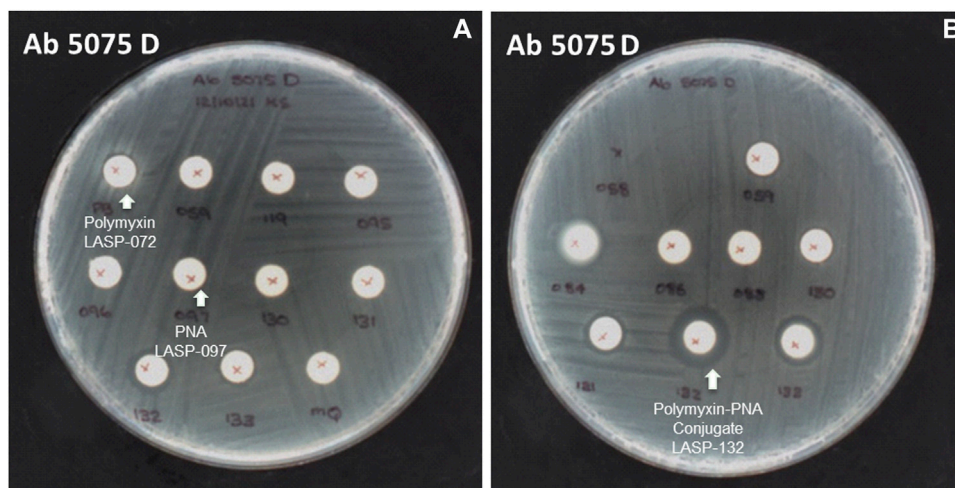


FIGURE 4 | The inhibition zone of peptides, PNA, and peptide-PNA conjugates against *A. baumannii* 5075D (A) polymyxin and PNA No zones of inhibition observed, (B) polymyxin-acpP PNA conjugate zone of inhibition observed.

United States) using blue (BL) and violet (VL) laser detection channels. The percentage of bacterial cells with damaged membranes was determined using propidium iodide (PI, Ex/Em 488/660–690 nm).

In vitro Toxicity

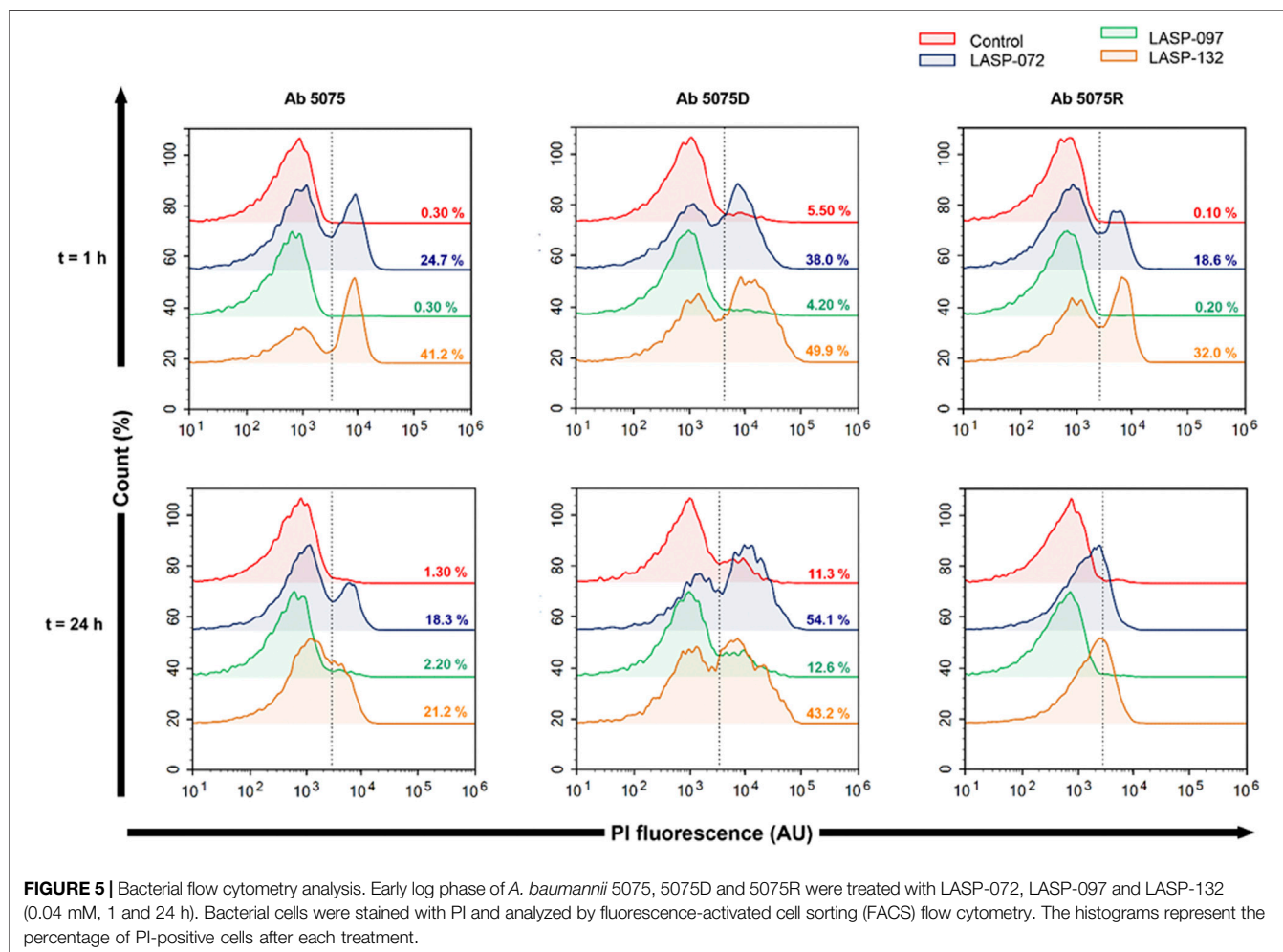
Human lung epithelial cells (A549) were obtained from the American Type Culture Collection (ATCC) and maintained in DMEM supplemented with 10% FBS in an incubator containing 5% CO₂ at 37°C. Cells were plated in 96-well plates at 10⁴ per well for 24 h, then were incubated with LASP-072, LASP-097, LASP-132 (0.04 mM) for another 24 h (Ahmed et al., 2017). The viability (%) of A549 cells was measured with XTT staining (200 µg/ml) combined with phenazine methosulfate (25 µM) in the same culture medium for 2 h at 37°C (De Oliveira Alves et al., 2017). The absorbance was measured at 475 nm using an Infinite M200 plate reader (Tecan group Ltd., Zürich, Switzerland). Cell viability (%) was calculated by the ratio of the background subtracted absorbance of treatments compared with the mean absorbance of untreated controls (Riss et al., 2016).

RESULTS AND DISCUSSION

All PNAs were synthesized using Fmoc/Bhoc protected PNA building blocks by standard solid-phase synthesis (SPPS) protocol (Table 1). In our initial attempt to cleave the *N*-terminal cysteine containing PNA (Cys-PNA) from rink amide resin, we observed the formation of a Bhoc-adduct as a major product (characterized by a 166 Dalton higher mass), resulting in a significant loss in the yield of the desired PNA (Figure 2, purified yield only 5%) (Goodwin et al., 1998). The benzhydryloxycarbonyl (Bhoc) protecting group generates “benzhydryl cation” during the trifluoroacetic acid (TFA) cleavage. This benzhydryl cation reacts with the 1,2-aminiothiol moiety of *N*-terminal cysteine and produces a

Bhoc-adduct. Previously, Goodwin et al. (1998) utilized the *S*-*t*-butylmercapto group as an orthogonal protecting group strategy to synthesize Cys-PNAs. The use of *S*-*t*-butylmercapto protected *N*-terminal cysteine residue prevented the Bhoc adduct formation. However, additional deprotection and purification steps were needed to obtain the desired Cys-PNA. Notably, the reported strategy is time-consuming and may present a bottleneck for structure-function studies involving large peptide-PNA libraries. Therefore, we optimized the cleavage conditions that improved the Cys-PNA yields with minimum steps. Initially, we investigated four cleavage solutions, each with different scavengers (4-Methoxythiophenol, 4-Mercaptophenol, Cysteine, and Cysteamine) that preferentially react with “benzhydryl cation”. The LC-MS analysis suggested that cysteamine exhibited a better ability to scavenge the “benzhydryl cation” (Supplementary Figure S2). We then optimized the concentration of cysteamine and revealed that 2 equivalents of cysteamine per Bhoc group was essential to avoid the formation of the Bhoc adduct. The optimized cleavage conditions significantly improved the yields of the Cys-PNA (LASP-050, 55%).

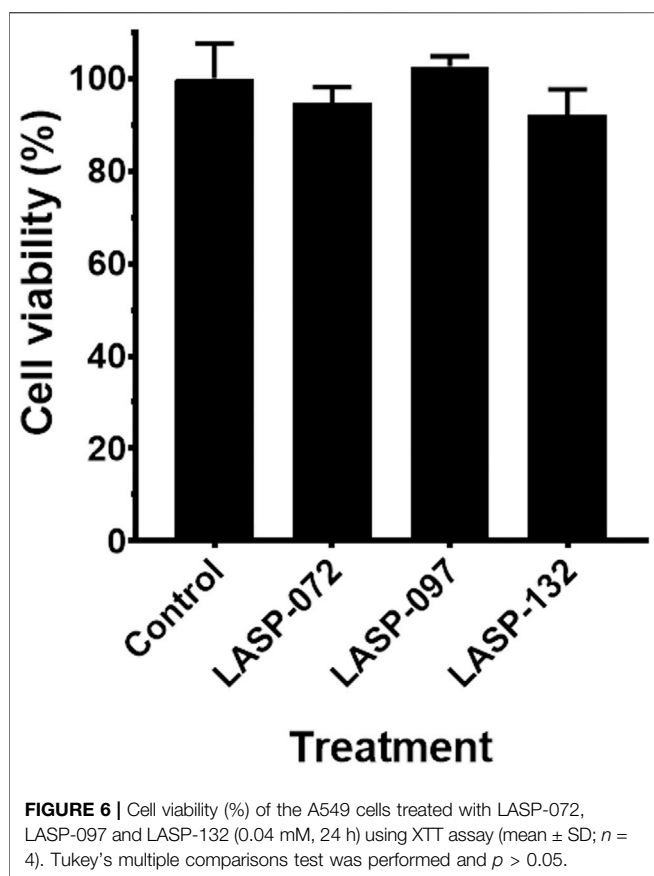
Once a large scale Cys-PNA (LASP-050, Supplementary Figure S1) was accomplished, we synthesized 5 structurally diverse peptides with the CINA moiety using standard SPPS protocol. The synthesis of cyclic peptide-PNA conjugates involves critical steps such as handling orthogonally protected cyclic peptides with labor-intensive synthesis and multiple purifications (Alam et al., 2011; Shinbara et al., 2020). Thus, the synthesis of cyclic peptide-PNA conjugates presents significant challenges. To investigate the efficiency of CINA-conjugation, we synthesized a polymyxin analogue (LASP-026, Table 1, Supplementary Figure S3) with a CINA moiety. The presence of *N*-terminal CINA moiety did not affect the yields of polymyxin analogue. The CINA-peptide LASP-026 and Cys-PNA LASP-050 (Figure 3A) were then used to optimize conjugation conditions. We observed that the Cys-PNA



(LASP-50) was completely conjugated to the polymyxin peptide (LASP-026) within 2 h (Figure 3B). The use of aqueous buffers for the conjugation reaction enabled direct purification. Since the thiazolidine ring is not stable in 0.1% TFA buffers (Morewood and Nitsche, 2021), the peptide-PNA conjugate (LASP-059) was purified using a less acidic formic acid buffer (Nitsche et al., 2019). The optimized Cys-CINA conjugation method was applied to synthesize all other peptide-PNA conjugates (Table 1). Subsequently, we investigated the effect of the position of the CINA group and peptide length on the efficiency of conjugation reaction using LASP-054 and LASP-077 (Table 1, Supplementary Figures S4, S5). A lysine-side-chain anchored CINA peptide RXR (Popella et al., 2021) and an antimicrobial peptide “drosocin” containing 19 amino acids were selected as templates (Hansen et al., 2016). The conjugation reactions were completed within 4 h, and both peptide-PNA conjugates, LASP-058 (95%) and LASP-084 (90%), were obtained with high yields. The CINA group is highly selective towards N-terminal cysteine and enables the orthogonal disulfide bond formation or thioether cross-linking with intra-chain free thiols. We explored this selectivity of Cys-CINA chemistry and synthesized the disulfide-linked cathelicidin-PNA conjugate (LASP-088) in two steps. Interestingly, the conjugation buffer

contains TCEP as a reducing agent, which provides an opportunity to explore the facile formation of thioether bonds using halogenated cross-linking agents such as 1,4-dibromobutene (Heinis et al., 2009; Fadzen et al., 2017). Hence, we utilized this key attribute of the Cys-CINA approach and developed a “one-pot” protocol for the conjugation and side-chain cross-linking. A cathelicidin analogue was an ideal template for investigating this strategy (Mwangi et al., 2019). The linear peptide (LASP-078, Supplementary Figure S6) was quantitatively converted to conjugate intermediate within 3 h (Figure 3C). Excitingly, *in situ* formation of thioether linkage between 1,4-dibromobutene and the free thiols of non-terminal cysteines yielded LASP-086 as a major product (Figure 3D). Notably, Cys-CINA conjugation reactions were efficiently conducted in an aqueous buffer, which allowed facile handling and purification of the conjugates.

The selected peptide sequences are known for their antimicrobial activity (Le et al., 2017). Therefore, we evaluated the antimicrobial activity of synthesized peptide-PNA conjugates using the Disc Diffusion Assay (DDA) against a panel of MDR Gram-negative bacteria consisting of *P. aeruginosa*, *A. baumannii*, *K. pneumoniae*, *E. coli*, including the isolates highly polymyxin-resistant *A. baumannii* 5075R, and



A. baumannii 5075D (Figure 4 and Supplementary Table S1). No zone of bacterial growth inhibition was observed in the presence of conjugates LASP-058, LASP-086, and controls (unconjugated peptide and PNAs). However, conjugates LASP-084 and LASP-088 showed a zone of inhibition (diameter of 8 mm) against *E. coli* DH5 α , *A. baumannii* 5075, and *A. baumannii* 5075D. Interestingly, *A. baumannii* 5075, which exhibits a polymyxin-dependent resistance phenotype, showed greater bacterial growth in the presence of LASP-084. The polymyxin-PNA conjugate LASP-059, showed better antimicrobial activity compared to LASP-058, 084, 088, with the diameters of inhibition zones ranging between 7 and 10 mm (Supplementary Table S1). These experiments suggested that polymyxin peptides can be an effective carrier for antimicrobial PNA. Therefore, we further synthesized 10-mer PNAs targeting four bacterial essential genes *anti-rpoA* LASP-095 (Abushahba et al., 2016), *anti-murA* LASP-096 (Goh et al., 2009; Mondhe et al., 2014), *anti-acpP* LASP-097 (Hansen et al., 2016), and *anti-rpoD* LASP-119 (Bai et al., 2012; Alajlouni and Seleem, 2013). During the synthesis of the next set of peptide-PNA conjugates, we switched the direction of the conjugation handles to investigate the impact on the efficiency of conjugation. Here, PNAs were synthesized with an *N*-terminal CINA moiety (LASP-095, 096, 097 and 119, Table 1) and a polymyxin analogue (LASP-072, Table 1) was synthesized containing an *N*-terminal cysteine residue (Supplementary Figure S3). Pleasingly, the alteration of the

conjugating handle did not affect the efficiency of the Cys-CINA conjugation (90–98%, Table 1). The synthesized peptide-PNA conjugates LASP-130, -131, -132 and -133 showed zones of inhibition in bacterial growth (diameter in the range of 11–14 mm). Importantly, all conjugates (LASP-130 to 133, Supplementary Table S1, Supplementary Figures S7–S13) showed antimicrobial activity against *A. baumannii* 5075R and *A. baumannii* 5075D without any observed dependent phenotype (Figure 4). Excitingly, LASP-132 showed a maximum zone of inhibition, indicating the potential promise of polymyxin *anti-acpP* PNA conjugates for the development of new antimicrobial agents.

Intrigued by the activity of LASP-132 against polymyxin-resistant *A. baumannii* isolates (5075R with LPS phosphoethanolamine modification, and LPS loss polymyxin-dependent resistant isolate 5075D), we investigated the potential mode of action of our PNA conjugates using flow cytometry (Figure 5). The increase in proportions of PI-positive cells (%) was observed following the treatment with LASP-072 and LASP-132 for all the isolates tested at 1 h; whereas these proportions were minimal in untreated controls at the same time-point. Our results show the membrane damage in polymyxin-resistant *A. baumannii* 5075R and 5075D by LASP-072 and LASP-132, indicating re-sensitization of the polymyxin-resistant bacteria to PNAs. Our finding also highlights the outer membrane as a potential target for LASP-132 besides its intracellular antisense activity (Bergen et al., 2006; Rasmussen et al., 2007). Importantly, the proportions of PI-positive bacterial cells (%) after the treatment of LASP-132 was higher (11.9%–16.5%) compared to that by LASP-072 at 1 h, indicating a higher capacity of membrane disorganization activity of the former. The membrane damage activity of LASP-132 is well correlated with the antimicrobial activity, where a larger zone of inhibition was observed for LASP-132 compared to that of LASP-072 (Figure 4). Interestingly, membrane damage activity of LASP-132 was decreased at 24 h; in particular, no distinct population of PI-positive cells was observed in *A. baumannii* 5075R, possibly due to the remodelling of the bacterial outer membrane at 24 h (Zhu et al., 2020). We also investigated the *in vitro* toxicity of LASP-072, LASP-097, and LASP-132 in human lung epithelial A549 cells (Figure 6) (Ahmed et al., 2017; Mea et al., 2020). Interestingly, the antibacterial LASP-072 and LASP-132 caused <10% death of A549 cells and no significant difference was observed with the untreated control samples. Our cell culture results indicate the relatively low toxicity of both compounds. Overall, our findings suggest that LASP-132 is a promising hit for further development of PNA-peptide conjugates against MDR *A. baumannii*, including those resistant to the last-line polymyxins.

CONCLUSION

We successfully developed an efficient and biocompatible strategy to conjugate complex peptides with PNAs using the 2-cyanoisonicotinamide moiety. This method utilizes economic and commercially available 2-cyanoisonicotinic acid that can

be directly introduced to peptide and PNA by SPPS. We also developed a new cleavage protocol to enhance the yields of N-terminal cysteine containing PNAs. Importantly, the compatibility of Cys-CINA conjugation with chemically diverse peptides, including cyclic and cysteine-rich peptides, allows scalable and cost-effective syntheses of complex peptide-PNA analogues. Further, we developed the “one-pot” conjugation and side-chain cross-linking protocol for the cysteine-rich peptide. The Cys-CINA conjugation strategy offers a versatile, high yielding and efficient approach for synthesizing peptide-PNA conjugates that will advance the current oligonucleotide-based chemical biology research. Finally, this study identified a polymyxin-PNA conjugate (LASP-132) as a promising antimicrobial agent against MDR *A. baumannii*. The LASP-132 serves as a template for the future development of peptide-PNA antibiotics underway in our laboratory.

DATA AVAILABILITY STATEMENT

The original contributions presented in the study are included in the article/**Supplementary Material**, further inquiries can be directed to the corresponding author.

REFERENCES

- Abushahba, M. F. N., Mohammad, H., Thangamani, S., Hussein, A. A. A., and Seleem, M. N. (2016). Impact of Different Cell Penetrating Peptides on the Efficacy of Antisense Therapeutics for Targeting Intracellular Pathogens. *Sci. Rep.* 6, 20832–20843. doi:10.1038/srep20832
- Ahmed, M. U., Velkov, T., Lin, Y. W., Yun, B., Nowell, C. J., Zhou, F., et al. (2017). Potential Toxicity of Polymyxins in Human Lung Epithelial Cells. *Antimicrob. Agents Chemother.* 61, e02690. doi:10.1128/AAC.02690-16
- Alajlouni, R. A., and Seleem, M. N. (2013). Targeting listeria Monocytogenes rpoA and rpoD Genes Using Peptide Nucleic Acids. *Nucleic Acid Ther.* 23, 363–367. doi:10.1089/nat.2013.0426
- Alam, M. R., Ming, X., Fisher, M., Lackey, J. G., Rajeev, K. G., Manoharan, M., et al. (2011). Multivalent Cyclic RGD Conjugates for Targeted Delivery of Small Interfering RNA. *Bioconjug. Chem.* 22, 1673–1681. doi:10.1021/bc200235q
- Andersson, D. I., Hughes, D., and Kubicek-Sutherland, J. Z. (2016). Mechanisms and Consequences of Bacterial Resistance to Antimicrobial Peptides. *Drug Resist. Updates* 26, 43–57. doi:10.1016/j.drug.2016.04.002
- Bai, H., You, Y., Yan, H., Meng, J., Xue, X., Hou, Z., et al. (2012). Antisense Inhibition of Gene Expression and Growth in Gram-Negative Bacteria by Cell-Penetrating Peptide Conjugates of Peptide Nucleic Acids Targeted to rpoD Gene. *Biomaterials* 33, 659–667. doi:10.1016/j.biomaterials.2011.09.075
- Bergen, P. J., Li, J., Rayner, C. R., and Nation, R. L. (2006). Colistin Methanesulfonate Is an Inactive Prodrug of Colistin against *Pseudomonas aeruginosa*. *Antimicrob. Agents Chemother.* 50, 1953–1958. doi:10.1128/aac.00035-06
- De Oliveira Alves, N., Vessoni, A. T., Quinet, A., Fortunato, R. S., Kajitani, G. S., Peixoto, M. S., et al. (2017). Biomass Burning in the Amazon Region Causes DNA Damage and Cell Death in Human Lung Cells. *Sci. Rep.* 7, 10937–10949. doi:10.1038/s41598-017-11024-3
- Dürr, U. H. N., Sudheendra, U. S., and Ramamoorthy, A. (2006). LL-37, the Only Human Member of the Cathelicidin Family of Antimicrobial Peptides. *Biochim. Biophys. Acta (Bba) - Biomembranes* 1758, 1408–1425. doi:10.1016/j.bbmem.2006.03.030
- Ede, N. J., Tregear, G. W., and Haralambidis, J. (1994). Routine Preparation of Thiol Oligonucleotides: Application to the Synthesis of

AUTHOR CONTRIBUTIONS

NP conceived the idea, designed the experiments and supervised the project. VT, RL, and XH performed chemical syntheses. HY, HW, and JL performed Disk Diffusion Assays. KP and MA performed flow cytometry and toxicity experiments. VT wrote the first draft of the manuscript. JL provided insightful advice on biological studies. All authors contributed to manuscript writing.

FUNDING

NP was supported by the Australian National Health and Medical Research Council's Early Career Fellowship (Grant ID: APP1158171). JL was supported by the Australian National Health and Medical Research Council's Principal Research Fellowship (Grant ID: APP1157909).

SUPPLEMENTARY MATERIAL

The Supplementary Material for this article can be found online at: <https://www.frontiersin.org/articles/10.3389/fchem.2022.843163/full#supplementary-material>

- Oligonucleotide-Peptide Hybrids. *Bioconjug. Chem.* 5, 373–378. doi:10.1021/bc00028a016
- Egholm, M., Buchardt, O., Christensen, L., Behrens, C., Freier, S. M., Driver, D. A., et al. (1993). PNA Hybridizes to Complementary Oligonucleotides Obeying the Watson-Crick Hydrogen-Bonding Rules. *Nature* 365, 566–568. doi:10.1038/365566a0
- Eucast, E.C.O.a.S.T. (2021). *Disk Diffusion Method for Antimicrobial Susceptibility Testing*. Version 9.0. Växjö, Sweden: The European Committee on Antimicrobial Susceptibility Testing.
- Fadzen, C. M., Wolfe, J. M., Cho, C.-F., Chiocca, E. A., Lawler, S. E., and Pentelute, B. L. (2017). Perfluoroarene-Based Peptide Macrocycles to Enhance Penetration across the Blood-Brain Barrier. *J. Am. Chem. Soc.* 139, 15628–15631. doi:10.1021/jacs.7b09790
- Ghosal, A., and Nielsen, P. E. (2012). Potent Antibacterial Antisense Peptide-Peptide Nucleic Acid Conjugates Against *Pseudomonas Aeruginosa*. *Nucleic Acid Ther.* 22, 323–334. doi:10.1089/nat.2012.0370
- Ghosal, A., Vitali, A., Stach, J. E. M., and Nielsen, P. E. (2013). Role of SbmA in the Uptake of Peptide Nucleic Acid (PNA)-peptide Conjugates in *E. coli*. *ACS Chem. Biol.* 8, 360–367. doi:10.1021/cb300434e
- Goh, S., Boberek, J. M., Nakashima, N., Stach, J., and Good, L. (2009). Concurrent Growth Rate and Transcript Analyses Reveal Essential Gene Stringency in *Escherichia coli*. *PLoS ONE* 4, e6061. doi:10.1371/journal.pone.0006061
- Good, L., Awasthi, S. K., Dryselius, R., Larsson, O., and Nielsen, P. E. (2001). Bactericidal Antisense Effects of Peptide-PNA Conjugates. *Nat. Biotechnol.* 19, 360–364. doi:10.1038/86753
- Good, L., and Nielsen, P. E. (1998). Antisense Inhibition of Gene Expression in Bacteria by PNA Targeted to mRNA. *Nat. Biotechnol.* 16, 355–358. doi:10.1038/nbt0498-355
- Goodwin, T. E., Holland, R. D., Lay, J. O., Jr., and Raney, K. D. (1998). A Simple Procedure for Solid-phase Synthesis of Peptide Nucleic Acids with N-Terminal Cysteine. *Bioorg. Med. Chem. Lett.* 8, 2231–2234. doi:10.1016/s0960-894x(98)00400-4
- Gupta, A., Bahal, R., Gupta, M., Glazer, P. M., and Saltzman, W. M. (2016). Nanotechnology for Delivery of Peptide Nucleic Acids (PNAs). *J. Controlled Release* 240, 302–311. doi:10.1016/j.jconrel.2016.01.005
- Gupta, A., Mishra, A., and Puri, N. (2017). Peptide Nucleic Acids: Advanced Tools for Biomedical Applications. *J. Biotechnol.* 259, 148–159. doi:10.1016/j.jbiotec.2017.07.026

- Hansen, A. M., Bonke, G., Larsen, C. J., Yavari, N., Nielsen, P. E., and Franzyk, H. (2016). Antibacterial Peptide Nucleic Acid-Antimicrobial Peptide (PNA-AMP) Conjugates: Antisense Targeting of Fatty Acid Biosynthesis. *Bioconjug. Chem.* 27, 863–867. doi:10.1021/acs.bioconjchem.6b00013
- Heinis, C., Rutherford, T., Freund, S., and Winter, G. (2009). Phage-encoded Combinatorial Chemical Libraries Based on Bicyclic Peptides. *Nat. Chem. Biol.* 5, 502–507. doi:10.1038/nchembio.184
- Koppelhus, U., and Nielsen, P. E. (2003). Cellular Delivery of Peptide Nucleic Acid (PNA). *Adv. Drug Deliv. Rev.* 55, 267–280. doi:10.1016/s0169-409x(02)00182-5
- Le, C. F., Fang, C. M., and Sekaran, S. D. (2017). Intracellular Targeting Mechanisms by Antimicrobial Peptides. *Antimicrob. Agents Chemother.* 61, e02340–02316. doi:10.1128/AAC.02340-16
- Mcallister, K. A., Peery, R. B., and Zhao, G. (2006). Acyl Carrier Protein Synthases from Gram-Negative, Gram-Positive, and Atypical Bacterial Species: Biochemical and Structural Properties and Physiological Implications. *J. Bacteriol.* 188, 4737–4748. doi:10.1128/jb.01917-05
- Mckay, C. S., and Finn, M. G. (2014). Click Chemistry in Complex Mixtures: Bioorthogonal Bioconjugation. *Chem. Biol.* 21, 1075–1101. doi:10.1016/j.chembiol.2014.09.002
- Mea, H. J., Madhavan, P., Palanisamy, N. K., Yong, P., and Wong, E. H. (2020). *In Vitro* host Immune Response against *Acinetobacter Baumannii* Infection Using A549 Cell Line. *Int. J. Infect. Dis.* 101, 128–129. doi:10.1016/j.ijid.2020.09.352
- Mondhe, M., Chessher, A., Goh, S., Good, L., and Stach, J. E. M. (2014). Species-selective Killing of Bacteria by Antimicrobial Peptide-PNAs. *PLOS ONE* 9, e89082. doi:10.1371/journal.pone.0089082
- Morewood, R., and Nitsche, C. (2021). A Biocompatible Stapling Reaction for *In Situ* Generation of Constrained Peptides. *Chem. Sci.* 12, 669–674. doi:10.1039/d0sc05125j
- Mwangi, J., Yin, Y., Wang, G., Yang, M., Li, Y., Zhang, Z., et al. (2019). The Antimicrobial Peptide ZY4 Combats Multidrug-resistant *Pseudomonas aeruginosa* and *Acinetobacter Baumannii* Infection. *Proc. Natl. Acad. Sci. USA* 116, 26516–26522. doi:10.1073/pnas.1909585117
- Nielsen, P. E., Egholm, M., Berg, R. H., and Buchardt, O. (1991). Sequence-selective Recognition of DNA by Strand Displacement with a Thymine-Substituted Polyamide. *Science* 254, 1497–1500. doi:10.1126/science.1962210
- Nielsen, P. E. (2001). Targeting Double Stranded DNA with Peptide Nucleic Acid (PNA). *Cmc* 8, 545–550. doi:10.2174/0929867003373373
- Nitsche, C., Onagi, H., Quek, J.-P., Otting, G., Luo, D., and Huber, T. (2019). Biocompatible Macrocyclization between Cysteine and 2-cyanopyridine Generates Stable Peptide Inhibitors. *Org. Lett.* 21, 4709–4712. doi:10.1021/acs.orglett.9b01545
- Patil, N. A. (2022). Conjugation Approaches for Peptide-Mediated Delivery of Oligonucleotides Therapeutics. *Aust. J. Chem.* 75, 24–33. doi:10.1071/CH21131
- Patil, N. A., Karas, J. A., Turner, B. J., and Shabanpoor, F. (2019). Thiol-Cyanobenzothiazole Ligation for the Efficient Preparation of Peptide-PNA Conjugates. *Bioconjug. Chem.* 30, 793–799. doi:10.1021/acs.bioconjchem.8b00908
- Patil, N. A., Quek, J.-P., Schroeder, B., Morewood, R., Rademann, J., Luo, D., et al. (2021). 2-Cyanoisonicotinamide Conjugation: A Facile Approach to Generate Potent Peptide Inhibitors of the Zika Virus Protease. *ACS Med. Chem. Lett.* 12, 732–737. doi:10.1021/acsmedchemlett.0c00657
- Popella, L., Jung, J., Popova, K., Durica-Mitić, S., Barquist, L., and Vogel, J. (2021). Global RNA Profiles Show Target Selectivity and Physiological Effects of Peptide-Delivered Antisense Antibiotics. *Nucleic Acids Res.* 49, 4705–4724. doi:10.1093/nar/gkab242
- Rasmussen, L. C. V., Sperling-Petersen, H. U., and Mortensen, K. K. (2007). Hitting Bacteria at the Heart of the central Dogma: Sequence-specific Inhibition. *Microb. Cel Fact* 6, 24. doi:10.1186/1475-2859-6-24
- Riss, T. L., Moravec, R. A., Niles, A. L., Duellman, S., Benink, H. A., Worzella, T. J., et al. (2016). *Cell Viability Assays. Assay Guidance Manual [Internet]*, 2004. Bethesda (MD): Eli Lilly & Company and the National Center for Advancing Translational Sciences.;
- Rose, M., Lapuebla, A., Landman, D., and Quale, J. (2019). *In Vitro* and *In Vivo* Activity of a Novel Antisense Peptide Nucleic Acid Compound against Multidrug-Resistant *Acinetobacter Baumannii*. *Microb. Drug Resist.* 25, 961–965. doi:10.1089/mdr.2018.0179
- Shinbara, K., Liu, W., van Neer, R. H. P., Katoh, T., Suga, H., and Suga, H. (2020). Methodologies for Backbone Macrocyclic Peptide Synthesis Compatible with Screening Technologies. *Front. Chem.* 8, 447. doi:10.3389/fchem.2020.00447
- Siddiquee, S., Rovina, K., and Azriah, A. (2015). A Review of Peptide Nucleic Acid. *Adv. Tech. Biol. Med.* 3, 1–10. doi:10.4172/2379-1764.1000131
- Soudah, T., Khawaled, S., Aqeilan, R. I., and Yavin, E. (2019). AntimiR-155 Cyclic Peptide-PNA Conjugate: Synthesis, Cellular Uptake, and Biological Activity. *ACS Omega* 4, 13954–13961. doi:10.1021/acsomega.9b01697
- Turner, J. J., Williams, D., Owen, D., and Gait, M. J. (2006). Disulfide Conjugation of Peptides to Oligonucleotides and Their Analogs. *Curr. Protoc. Nucleic Acid Chem.* Chapter 4, Unit 4.28. doi:10.1002/0471142700.nc0428s24
- Velkov, T., Roberts, K. D., Nation, R. L., Thompson, P. E., and Li, J. (2013). Pharmacology of Polymyxins: New Insights into an 'old' Class of Antibiotics. *Future Microbiol.* 8, 711–724. doi:10.2217/fmb.13.39
- WHO (2017). *Prioritization of Pathogens to Guide Discovery, Research and Development of New Antibiotics for Drug-Resistant Bacterial Infections, Including Tuberculosis*. Geneva: World Health Organization.;
- Wickremasinghe, H., Yu, H. H., Azad, M. A. K., Zhao, J., Bergen, P. J., Velkov, T., et al. (2021). Clinically Relevant Concentrations of Polymyxin B and Meropenem Synergistically Kill Multidrug-Resistant *Pseudomonas aeruginosa* and Minimize Biofilm Formation. *Antibiotics* 10, 405–423. doi:10.3390/antibiotics10040405
- Wittung, P., Nielsen, P., and Nördén, B. (1996). Direct Observation of Strand Invasion by Peptide Nucleic Acid (PNA) into Double-Stranded DNA. *J. Am. Chem. Soc.* 118, 7049–7054. doi:10.1021/ja960521f
- Zhu, Y., Lu, J., Han, M. L., Jiang, X., Azad, M. A. K., Patil, N. A., et al. (2020). Polymyxins Bind to the Cell Surface of Unculturable *Acinetobacter Baumannii* and Cause Unique Dependent Resistance. *Adv. Sci.* 7, 2000704–2000716. doi:10.1002/adv.20200704

Conflict of Interest: The authors declare that the research was conducted in the absence of any commercial or financial relationships that could be construed as a potential conflict of interest.

Publisher's Note: All claims expressed in this article are solely those of the authors and do not necessarily represent those of their affiliated organizations, or those of the publisher, the editors and the reviewers. Any product that may be evaluated in this article, or claim that may be made by its manufacturer, is not guaranteed or endorsed by the publisher.

Copyright © 2022 Patil, Thombare, Li, He, Lu, Yu, Wickremasinghe, Pamulapati, Azad, Velkov, Roberts and Li. This is an open-access article distributed under the terms of the Creative Commons Attribution License (CC BY). The use, distribution or reproduction in other forums is permitted, provided the original author(s) and the copyright owner(s) are credited and that the original publication in this journal is cited, in accordance with accepted academic practice. No use, distribution or reproduction is permitted which does not comply with these terms.



Mucin-Type O-Glycosylation Proximal to β -Secretase Cleavage Site Affects APP Processing and Aggregation Fate

YashoNandini Singh¹, Deepika Regmi¹, David Ormaza¹, Ramya Ayyalasomayajula¹, Nancy Vela¹, Gustavo Mundim¹, Deguo Du¹, Dmitriy Minond² and Maré Cudic^{1*}

¹Department of Chemistry and Biochemistry, Charles E. Schmidt College of Science, Florida Atlantic University, Boca Raton, FL, United States, ²College of Pharmacy and Rumbaugh-Goodwin Institute for Cancer Research, Nova Southeastern University, Fort Lauderdale, FL, United States

OPEN ACCESS

Edited by:

John D. Wade,
University of Melbourne, Australia

Reviewed by:

Matthew Robert Pratt,
University of Southern California,
United States
Yangmei Li,
University of South Carolina,
United States

*Correspondence:

Maré Cudic
mcudic@fau.edu

Specialty section:

This article was submitted to
Chemical Biology,
a section of the journal
Frontiers in Chemistry

Received: 21 January 2022

Accepted: 07 March 2022

Published: 08 April 2022

Citation:

Singh Y, Regmi D, Ormaza D, Ayyalasomayajula R, Vela N, Mundim G, Du D, Minond D and Cudic M (2022) Mucin-Type O-Glycosylation Proximal to β -Secretase Cleavage Site Affects APP Processing and Aggregation Fate. *Front. Chem.* 10:859822. doi: 10.3389/fchem.2022.859822

The amyloid- β precursor protein (APP) undergoes proteolysis by β - and γ -secretases to form amyloid- β peptides (A β), which is a hallmark of Alzheimer's disease (AD). Recent findings suggest a possible role of O-glycosylation on APP's proteolytic processing and subsequent fate for AD-related pathology. We have previously reported that Tyr⁶⁸¹-O-glycosylation and the Swedish mutation accelerate cleavage of APP model glycopeptides by β -secretase (amyloidogenic pathway) more than α -secretase (non-amyloidogenic pathway). Therefore, to further our studies, we have synthesized additional native and Swedish-mutated (glyco)peptides with O-GalNAc moiety on Thr⁶⁶³ and/or Ser⁶⁶⁷ to explore the role of glycosylation on conformation, secretase activity, and aggregation kinetics of A β 40. Our results show that conformation is strongly dependent on external conditions such as buffer ions and solvent polarity as well as internal modifications of (glyco)peptides such as length, O-glycosylation, and Swedish mutation. Furthermore, the level of β -secretase activity significantly increases for the glycopeptides containing the Swedish mutation compared to their nonglycosylated and native counterparts. Lastly, the glycopeptides impact the kinetics of A β 40 aggregation by significantly increasing the lag phase and delaying aggregation onset, however, this effect is less pronounced for its Swedish-mutated counterparts. In conclusion, our results confirm that the Swedish mutation and/or O-glycosylation can render APP model glycopeptides more susceptible to cleavage by β -secretase. In addition, this study sheds new light on the possible role of glycosylation and/or glycan density on the rate of A β 40 aggregation.

Keywords: Alzheimer's disease, circular dichroism, proteolysis, aggregation kinetics, APP O-glycopeptides

INTRODUCTION

Alzheimer disease (AD) is one of the most common neurodegenerative disorders linked to aging (van Cauwenberghe et al., 2016; Alzheimer's Association, 2020). It has a profound effect on the economy, health-care system, and the society, and is projected to increase even further as the population ages (Hurd et al., 2013). Genetic, biochemical, and behavioral research suggest that physiologic generation of the A β -forming fibrils stems from the proteolytic processing of the amyloid precursor protein (APP), a type 1 transmembrane glycoprotein, by β -secretase (BACE-1) (Hardy and Higgins, 1992; O'Brien and Wong, 2011; Selkoe and Hardy, 2016). This pathway co-exists with the

nonamyloidogenic pathway, that is, initiated by α -secretase within the A β domain and precludes A β formation.

Despite the ongoing debates about the validity of amyloid cascade hypothesis, targeting amyloidogenic processing of APP is still considered a valid strategy to develop disease-modifying AD therapies (Zhao et al., 2020). New evidence continues to emerge to support the idea that deficiencies in APP trafficking and clearance of A β peptides is the initiating event of AD pathogenic processes (Tan and Gleeson, 2019; Zhao et al., 2020). Knowing the importance of protein glycosylation in mediating a plethora of biological functions (Krištić and Lauc, 2017; Akasaka-Manya and Manya, 2020) and considering the fact that most known AD-related molecules are either modified with glycans or play a role in glycan regulation, glycobiology may represent an interesting new insight into the understanding of AD, and a potential for new therapeutic approaches (Haukedal and Freude, 2021). The altered glycan profile of APP in the brain and cerebrospinal fluid (CSF) of AD patients versus healthy controls (Pahlsson et al., 1992; Chun et al., 2017; Boix et al., 2020; Moran et al., 2021) has been reported. Particularly, changes in O-glycosylation have been related to differences in APP processing and A β generation (Kitazume et al., 2010; Akasaka-Manya et al., 2017; Liu et al., 2017). APP695 is modified by a number of O-glycosylation moieties in several sites, both for mucin-linked O-glycans (O-GalNAc or N-acetylgalactosamine) and O-GlcNAc (N-acetylglucosamine) as observed in Chinese hamster ovary cells (CHO) and human CSF (Perdivara et al., 2009; Halim et al., 2011). O-GlcNAcylation has been shown to influence APP cleavage by increasing the nonamyloidogenic processing by α -secretase and reducing the secretion of A β *in vitro* and *in vivo* (Jacobsen and Iverfeldt, 2011; Yuzwa and Vocadlo, 2014; Chun et al., 2015, 2017). O-GalNAcylation is more abundant on APP, with extended and/or sialylated O-glycans occupying the region close to the β -secretase cleavage site (M⁶⁷¹~D⁶⁷²) of APP (Shi et al., 2021), suggesting its possible role in APP ectodomain shedding and A β production (Akasaka-Manya et al., 2017; Nakamura and Kurosaka, 2019). Two O-glycosylation sites, Thr⁶⁶³ and Ser⁶⁶⁷, located at the N-terminal side of β -secretase cleavage site have been reported to contain α -linked terminal GalNAc structure (Shi et al., 2021). Glycosylation on this region has been found to suppress the APP processing (Chun et al., 2015; Akasaka-Manya et al., 2017). In addition, a recent study has shown that the unique Tyr-O-glycosylation induces A β 42 to form less stable fibrils, that are more susceptible towards degradation by extracellular degradation enzymes (Liu et al., 2021). The sialic acid-capped glycans, as found in the CSF samples, would likely further promote inhibition of formation of the typical β sheet-derived fibrils (Liu et al., 2021). We have previously demonstrated that a simple O-GalNAc modification on the Tyr⁶⁸¹ residue of A β can induce a conformational change, provide protection from β -secretase, and slightly improve the nonamyloidogenic processing by α -secretase (Singh et al., 2021). However, in the presence of the Swedish mutation, the amyloidogenic processing by β -secretase was drastically increased (Singh et al., 2021). To date, a stimulating and inhibiting effects of glycosylation on enzyme activity have been reported (Goettig, 2016; Goth et al.,

2018). Thus, a better understanding of the role of O-glycosylation on the balance between production and clearance of A β peptides is necessary to decipher the role of O-glycosylation in the initiating events of AD pathogenic processes.

In this study, we synthesized APP model (glyco)peptides containing the A β -(1-9) fragment, with extended N-terminal domain to incorporate the β -secretase cleavage site with or without the Swedish mutation (Lys⁶⁷⁰Asn/Met⁶⁷¹Leu) and Thr⁶⁶³and/or Ser⁶⁶⁷ O-glycosites, respectively. These analogues were characterized for their secondary structure content using CD spectroscopy. The roles of O-glycosylation and/or Swedish mutation on proteolytic processing by β -secretase and the aggregation kinetics of A β 40 in the absence and presence of APP (glyco)peptides were explored, respectively. Our results demonstrate a unique role of mucin-type O-glycosylation on APP's secondary structure, proteolytic cleavage, and aggregation properties and offer an important insight into glycosylation driven changes of the intrinsic properties of APP derived peptides.

METHODS

Materials

Tentagel S RAM resin was obtained from Advanced ChemTech (Louisville, KY). Fmoc-protected amino acids, and coupling reagents, 1-hydroxybenzotriazole (HOBt) and 2-(6-chloro-1H-benzotriazol-1-yl)-1,1,3,3-tetramethylammonium hexafluorophosphate (HCTU), for peptide synthesis, were purchased from Chem-Impex (Wood Dale, IL). N, N'-Diisopropylethylamine (DIPEA) was purchased from Acros Organics (Thermo Fisher Scientific, Waltham, MA). Trifluoroacetic acid (TFA), thioanisole, and all solvents (DCM, DMF, acetonitrile, and water) were of HPLC grade and purchased from Fisher Scientific (Atlanta, GA) or Sigma-Aldrich (St. Louis, MO). PBS buffer was prepared using sodium phosphate (mono- and dibasic) from Fisher Scientific (Pittsburg, PA). The O-glycosylated GalNAc building blocks of Ser 1 and Thr 2 for glycopeptide synthesis were prepared as published previously by our group (Singh et al., 2020; Beckwith et al., 2021). Recombinant human BACE-1 (rhBACE-1) and BACE-1 fluorogenic peptide substrate IV (MCA-Ser-Glu-Val-Asn-Leu-Asp-Ala-Glu-Phe-Arg-Lys(DPN)-Arg-Arg-NH₂) were from R&D Systems (catalog #ES004 and #931-AS, respectively).

Synthesis of APP (Glyco)peptides

All peptide analogs of APP were synthesized using standard Fmoc chemistry and solid-phase peptide synthesis (SPPS) on a PS3 automated peptide synthesizer (Protein Technologies Inc., Tucson, AZ). The amino acid couplings on the synthesizer were done using a 4-fold excess of amino acids, HOBt, and HCTU, in the presence of 0.4 MN-methylmorpholine (NMM) in DMF. The Fmoc protecting group was removed using 20% piperidine in DMF. For glycopeptides, at the desired site of glycosylation, the Fmoc-protected pentafluorophenyl ester of Ser-O-GalNAc 1) and/or Thr-O-GalNAc 2) was coupled manually using a 1.5-fold excess, in the presence of DIPEA

(pH 8) for 16 h. After coupling was confirmed using the ninhydrin test, the remainder of the peptide's amino acid sequence was completed on the PS3. All the (glyco)peptides were cleaved from the resin using a TFA/thioanisole/water mixture in 95:2.5:2.5 ratio for 3 h, followed by precipitation in cold methyl-*tert*-butyl-ether (MTBE) to precipitate the crude (glyco)peptide. For glycopeptides, the acetylated crude was deprotected using 0.01 M NaOH solution for 15 min to remove all the *O*-acetyl groups on the glycan moiety attached to the peptide sequence. Lastly, the crude was lyophilized to yield the final crude deacetylated glycopeptide or its nonglycosylated counterpart.

Purification and Characterization of APP (Glyco)peptides

Purification of all (glyco)peptides and their corresponding analyses were performed on a 1,260 Agilent Infinity system. The analytical RP-HPLC method uses a Phenomenex Aeris Peptide C18 column (150 mm × 4.6 mm, 3.6 μ m, 100 Å) at 0.8 ml/min flow rate or a Vydac Denali C18 column (250 mm × 4.6 mm, 5 μ m, 120 Å) at 1 ml/min flow rate, with 0.1% TFA in water (A) and 0.1% TFA in acetonitrile (B) as the eluents. The elution gradient for analytical RP-HPLC purification was 0–60% B over 30 min. The preparative RP-HPLC method uses the Grace Vydac monomeric C18 column (250 mm × 22 mm, 15–20 μ m, 300 Å) at 10 ml/min flow rate, with 0.1% TFA in water (A) and 0.1% TFA in acetonitrile (B) as the eluents. The elution gradient for preparative RP-HPLC purification was 0–50% over 110 min. The (glyco)peptides were detected at 214 nm by using a UV-Vis detector (Agilent 1,260 Infinity DAD). Purified (glyco)peptides were characterized by matrix-assisted laser desorption/ionization time-of-flight mass spectrometry (MALDI-TOF MS) with a Voyager-DE STR system or a Bruker Microflex system, using α -cyano-4-hydroxycinnamic acid as matrix.

Conformational Analysis of APP (Glyco)peptides

All (glyco)peptides were analyzed for their secondary structure using circular dichroism (CD) spectroscopy on a Jasco-810 spectropolarimeter (Jasco, Easton, MD) in three solvent systems: water, 10 mM sodium phosphate buffer (pH 7.4), and 50% trifluoroethanol (TFE) in water (v/v) mixture. The CD spectra were recorded using a quartz cell of 1 mm optical path length over a wavelength range of 180–25 nm with a scanning speed of 100 nm/min and a response time of 4 s at 25°C. A concentration of 0.065 mg/ml, determined using the analytical RP-HPLC method, gave the lowest signal-to-noise ratio for all (glyco)peptides. All spectra were baseline-corrected to account for the signal contribution from solvent and then converted into molar ellipticity (deg cm² dmol^{−1}) (Sreerama and Woody, 2000). Lastly, the percentages of all secondary structures were determined using the BeStSel method (Micsonai et al., 2018; Singh et al., 2021).

Proteolytic Activity and Analysis of APP (Glyco)peptides With BACE-1

All APP-based substrates were prepared as 10 mM stocks in DMSO. Before proteolysis, the activity of BACE-1 was verified by the reaction with the fluorogenic BACE-1 substrate Mca-SEVNLDAEFRK(Dnp)RR-NH₂ (Koike et al., 1999) as per the manufacturer's instructions. For the proteolysis assay, APP-based substrates were diluted in BACE-1 activity buffer (0.1 M sodium acetate, pH 4.0) to the final assay concentration of 100 μ M. BACE-1 was diluted to 50 nM final concentration. Reactions were incubated for 24 h at 37°C in the dark. After the incubation period, the enzyme cleavage solutions containing APP-based substrates and BACE-1 were analyzed using the analytical RP-HPLC method on the Aeris C18 column with 0.1% TFA in water (A) and 0.1% TFA in acetonitrile (B) as eluents and 0–60% B as the elution gradient over 30 min with a flow rate of 0.8 ml/min, and detection at 214 nm or the Vydac Denali C18 column with 0.1% TFA in water (A) and 0.1% TFA in acetonitrile (B) as eluents and 0–60% B as the elution gradient over 30 min with a flow rate of 1 ml/min, and detection at 214 nm. The identity of intact and cleaved (*N*- and *C*-terminal) fragments of (glyco)peptides in the absence and presence of BACE-1 (β -secretase) was confirmed by MALDI-TOF and their percentages were evaluated by the integration of the RP-HPLC peaks (averaged from two injections).

Preparation of A β 40 Peptide for Aggregation Kinetics Assay With APP (Glyco)peptides

A β 40 peptide was synthesized on a PS3 solid phase peptide synthesizer (Protein Technologies Inc., Woburn, MA) using the standard Fmoc strategy. The resulting crude peptide was purified by reversed-phase high-performance liquid chromatography (RP-HPLC) using a C18 column and characterized by matrix-assisted laser desorption/ionization (MALDI) mass spectrometry. The peptide was monomerized as described previously before use (Liu et al., 2018). Lyophilized peptide powder was dissolved in aqueous NaOH solution (2 mM), and the pH was adjusted to ~11 by using 100 mM NaOH solution. The solution was sonicated for 1 h in an ice–water bath and then filtered through a 0.22 μ m filter (Millipore) and kept on ice before use. The concentration of the peptide solution was determined by using the tyrosine UV absorbance at 280 nm (ϵ = 1280 M^{−1} cm^{−1}).

Aggregation Kinetics Assay of A β 40 With APP (Glyco)peptides

The aggregation kinetics of A β 40 in the absence and presence of APP (glyco)peptides was performed using ThT binding assay. The monomerized A β 40 peptide solution was diluted to a final concentration of 10 μ M in 50 mM phosphate buffer (pH 7.4) and 20 μ M ThT dye. For the co-incubation assays with APP (glyco)peptides, APP stock solutions of 120 μ M were added to the prepared A β 40 for final (glyco) peptide concentrations of

10 μ M or 50 μ M and A β 40 concentration of 10 μ M in 50 mM phosphate buffer (pH 7.4) with 20 μ M ThT dye. 100 μ L of each prepared solution was run in triplicate of a 96-well microplate (Costar black, clear bottom). The plate was sealed with a microplate cover and loaded into a Gemini SpectraMax EM fluorescence plate reader (Molecular Devices, Sunnyvale, CA) and incubated at 37°C. The ThT fluorescence was measured from the bottom of the plate at 10 min intervals, with 5 s of shaking, and with an excitation and emission wavelengths of 440 and 480 nm, respectively. Error bars of triplicate samples are shown for the particular data points.

AFM Analysis of A β 40 With APP (Glyco)peptides

AFM was employed to monitor the morphological changes of A β 40 incubated in the absence and presence of tyrosine glycosylated (**14** and **16**) and nonglycosylated APP analogues (**13** and **15**). Aliquots (15 μ L) of A β 40 solutions were collected directly from the aggregation kinetics assay and spotted onto the surface of the freshly cleaved mica surface (5 mm \times 5 mm) on solid support at room temperature. Before the measurement, the samples were covered and dried in a vacuum desiccator overnight. The AFM images were acquired in tapping mode with an area of 4 μ m², using AFM workshop TT-2 (Hilton Head Island, SC) with MikroMash NSC 15/Al BS silicon cantilevers (MikroMash, Watsonville, CA). The AFM images were further visualized and analyzed using the Gwyddion software.

RESULTS AND DISCUSSION

APP-Based (Glyco)peptide Synthesis and Characterization

The short APP (glyco) peptide fragments, part of the APP 661–680 region, were prepared. The amino acid sequence included A β -(1–9) DAEFRHDSG at the C-terminal end and either EISEVKM or EISEVNL (NL = Swedish mutation) at the N-terminus to incorporate the β -secretase (BACE-1) cleavage site (M ~ D or L ~ D). Further extension of the backbone with the additional four amino acids (IKTE), furnished a platform for site-specific O-glycosylation of Thr⁶⁶³ and Ser⁶⁶⁷ residues that may impact APP's proteolytic processing due to their proximity to the BACE-1 cleavage site (Goth et al., 2018; Nakamura and Kurosaka, 2019). Hence, APP glycopeptides bearing “mucin-type” O-glycosylation, α -N-acetylgalactosamine (GalNAc), on Thr⁶⁶³ and/or Ser⁶⁶⁷ and their nonglycosylated counterparts were prepared using standard Fmoc-based automated solid-phase peptide chemistry (Scheme 1). For glycopeptides, the building block approach was used for the incorporation of O-glycosylated Ser **1** and/or Thr **2** in the sequence. The organic synthesis of the building blocks was achieved using our previously published protocols (Singh et al., 2020; Beckwith et al., 2021). The purity of the Ser/Thr building blocks **1** and **2**, respectively, were confirmed by RP-HPLC and MALDI-TOF mass spectrometry.

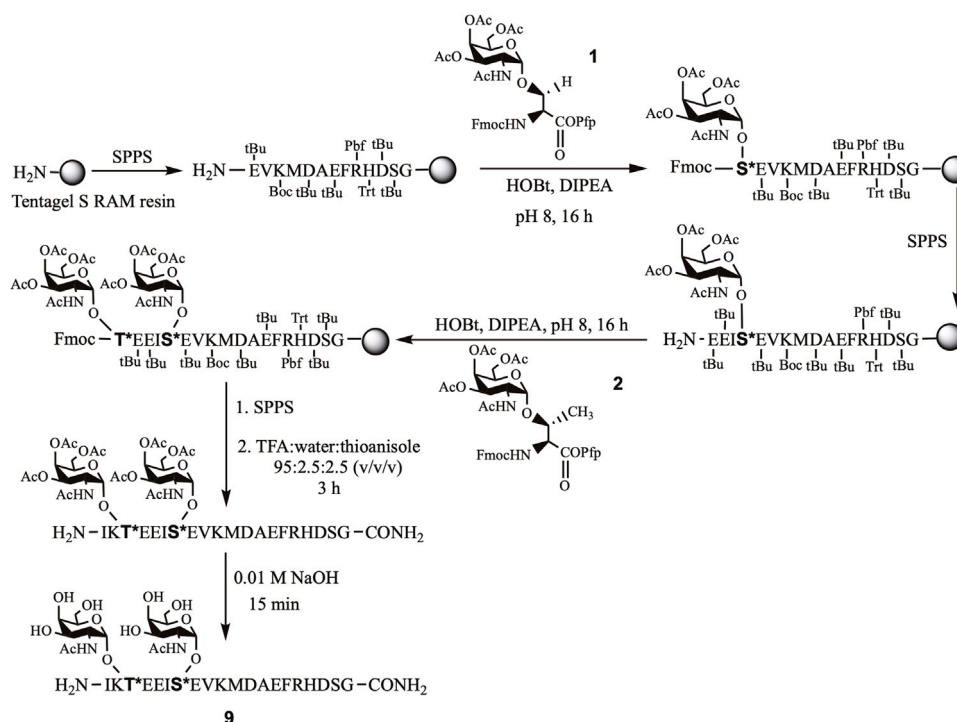
NMR spectra ascertained the α -linkage (Singh et al., 2020; Beckwith et al., 2021).

Automated solid-phase peptide synthesis (SPPS) approach on Tentagel S RAM resin was used to assemble the APP (glyco) peptides. For glycopeptides, the O-glycosylated Ser/Thr building blocks one and two, respectively, were manually coupled at the desired site of glycosylation, Thr⁶⁶³ and/or Ser⁶⁶⁷, of the growing peptide chain. After completion of the (glyco)peptide sequence, the resin was treated with trifluoroacetic acid (TFA), with water and thioanisole as scavengers. The crude acetylated glycopeptides were further deprotected under basic conditions to remove acetyl groups from the glycan moiety and obtain final deacetylated glycopeptides (**4**, **6**, **8**, **9**, **11**, and **12**). The corresponding nonglycosylated peptides (**3**, **5**, **7**, and **10**) were also prepared as above except for introducing usual Fmoc-Thr(tBu)/Ser(tBu)-OH amino acids, instead of their O-glycosylated analogs (Scheme 1). (Glyco)peptides **3–12** were obtained in high purity, as indicated by their RP-HPLC elution profiles and MALDI-TOF MS analysis (Table 1 and Supplementary Material S2–S11). As expected, the RP-HPLC analysis revealed difference in retention time (t_R) between the Swedish-mutated peptide analogs and their native pairs. The Swedish-mutated (glyco)peptides **5**, **6**, **10–12** exhibited a 1.5 min (on average) longer t_R compared to their native counterparts **3**, **4**, **7–9**, respectively, due to increased hydrophobicity of the peptide sequence (Table 1) (Mant et al., 1989; Singh et al., 2021). In contrast, the addition of the GalNAc moiety at either Ser⁶⁶⁷ (**4** and **6**) or Thr⁶⁶³ (**8** and **11**) residue resulted in a decrease in the t_R by 0.4 min (on average) compared to their nonglycosylated counterparts **3**, **5**, **7**, and **10**, respectively, due to increased hydrophilicity of the glycopeptide sequences (Table 1) (Singh et al., 2021). The attachment of GalNAc moiety at both glycosylation sites (**12**), further decreased the t_R by 0.5 min compared to its monoglycosylated counterpart **11** (t_R = 18.9 min, Table 1).

Conformational Properties of APP (Glyco)peptides

To study the role of O-glycosylation on the conformation of APP glycopeptides, circular dichroism (CD) spectroscopy was used to probe the secondary structure in three different solvents, water, sodium phosphate buffer (10 mM, pH 7.4), and 50% trifluoroethanol (TFE) in water (v/v) (Figure 1). The spectra were further analysed for secondary structure estimations by Beta Structure Selection (BeStSel) method, specifically designed for the analysis of beta sheet-rich proteins (Table 2) (Micsonai et al., 2015, 2018).

In water, the addition of N-terminal fragment, EISEVKM (native) or EISEVNL (Swedish-mutated), to A β -(1–9) in **3** and **5**, respectively, exhibited characteristics of β -sheet structure that closely resembled the CD spectra of other A β variants in water (J. and G., 1991; Juszczak et al., 2005; Lambermon et al., 2005). However, further extension of the N-terminal fragment with the additional four amino acids (IKTE) in native **7** and Swedish-mutated **10**, respectively, increased the overall hydrophilicity of A β -(1–9) and caused a conformation shift from β -sheet to random coil (Figure 1A). This agrees with our previous work



SCHEME 1 | Stepwise synthesis of APP glycopeptide, APP⁶⁶¹⁻⁶⁸⁰-T*, S* (**9**).

TABLE 1 | Characterization of APP (glyco)peptides **3–16** by analytical RP-HPLC and MALDI-MS^a.

APP (Glyco)peptides	Sequence	RP-HPLC	MALDI-TOF MS (M+H) ⁺	
		t _R (min)	Calculated (Da)	Observed (Da)
APP ⁶⁶⁵⁻⁶⁸⁰ (3)	EISEVKM~DAEFRHDSG	14.0	1848.98	1849.10
APP ⁶⁶⁵⁻⁶⁸⁰ -S* (4)	EIS*EVKM~DAEFRHDSG	13.6	2051.98	2051.68
APP ⁶⁶⁵⁻⁶⁸⁰ (NL) (5)	EISEVNL~DAEFRHDSG	15.6	1816.88	1816.83
APP ⁶⁶⁵⁻⁶⁸⁰ (NL)-S* (6)	EIS*EVNL~DAEFRHDSG	15.0	2019.88	2018.54
APP ⁶⁶¹⁻⁶⁸⁰ (7)	IKTEEISEVKM~DAEFRHDSG	14.6	2,320.54	2,320.19
APP ⁶⁶¹⁻⁶⁸⁰ -T* (8)	IKT*EEISEVKM~DAEFRHDSG	14.4	2,523.54	2,527.26
APP ⁶⁶¹⁻⁶⁸⁰ -T*, S* (9)	IKT*EEIS*EVKM~DAEFRHDSG	16.9b	2,726.54	2,728.80
APP ⁶⁶¹⁻⁶⁸⁰ (NL) (10)	IKTEEISEVNL~DAEFRHDSG	16.0	2,288.43	2,290.09
APP ⁶⁶¹⁻⁶⁸⁰ (NL)-T* (11)	IKT*EEISEVNL~DAEFRHDSG	15.6/18.9 ^b	2,491.43	2,491.32
APP ⁶⁶¹⁻⁶⁸⁰ (NL)-T*, S* (12)	IKT*EEIS*EVNL~DAEFRHDSG	18.4 ^b	2,694.43	2,696.55
APP ⁶⁶¹⁻⁶⁹⁴ (13) ^c	IKTEEISEVKM~DAEFRHDSGYEVHHQK~LVFFAED	17.6	4,062.09	4,062.27
APP ⁶⁶¹⁻⁶⁹⁴ -Y* (14) ^c	IKTEEISEVKM~DAEFRHDSGY*EVHHQK~LVFFAED	17.1	4,265.14	4,265.41
APP ⁶⁶¹⁻⁶⁹⁴ (NL) (15) ^c	IKTEEISEVNL~DAEFRHDSGYEVHHQK~LVFFAED	18.2	4,030.02	4,029.37
APP ⁶⁶¹⁻⁶⁹⁴ (NL)-Y* (16) ^c	IKTEEISEVNL~DAEFRHDSGY*EVHHQK~LVFFAED	17.8	4,231.99	4,232.71

^aT*/S*/Y* = Thr⁶⁶³/Ser⁶⁶⁷/Tyr⁶⁸¹ O-linked GalNAc, NL, swedish mutation, M~D and L~D = β -secretase cleavage site and K~L = α -secretase cleavage site. RP-HPLC, conditions and MALDI-TOF MS, analyses are described in the **Supplementary Material S2–S9**. Retention times (t_R) are given in minutes.

^bRP-HPLC, conditions and MALDI-TOF MS, analyses are described in the **Supplementary Material S9–S11**.

^cReported in Singh et al., 2021.

where addition of the N-terminal fragment, IKTEEISEVKM (native), to β -sheet-forming A β -(1–23) peptide in **13**, was also largely disordered (Singh et al., 2021). Deconvolution of the spectra revealed that native peptide **3** had the highest amount of β -structure (85.2%, anti-parallel β -sheet, parallel β -sheet, and β -turn), with the majority being anti-parallel β -sheet (59.9%), and the remaining being α -helix (14.8%) (Table 2). The presence of

the Swedish double-mutation in **5**, resulted in an increase in α -helix and decrease in the β -structure amounts (34.5 and 57.8%, respectively). The distribution of α -helix and β -structure content in five is similar to the Swedish-mutated A β -(1–23) peptide **15**, (Juszczyk et al., 2005; Singh et al., 2021). CD spectra clearly indicates that regardless of the Swedish mutation, addition of the N-terminal fragment, IKTEEISEVKM or IKTEEISEVNL, to

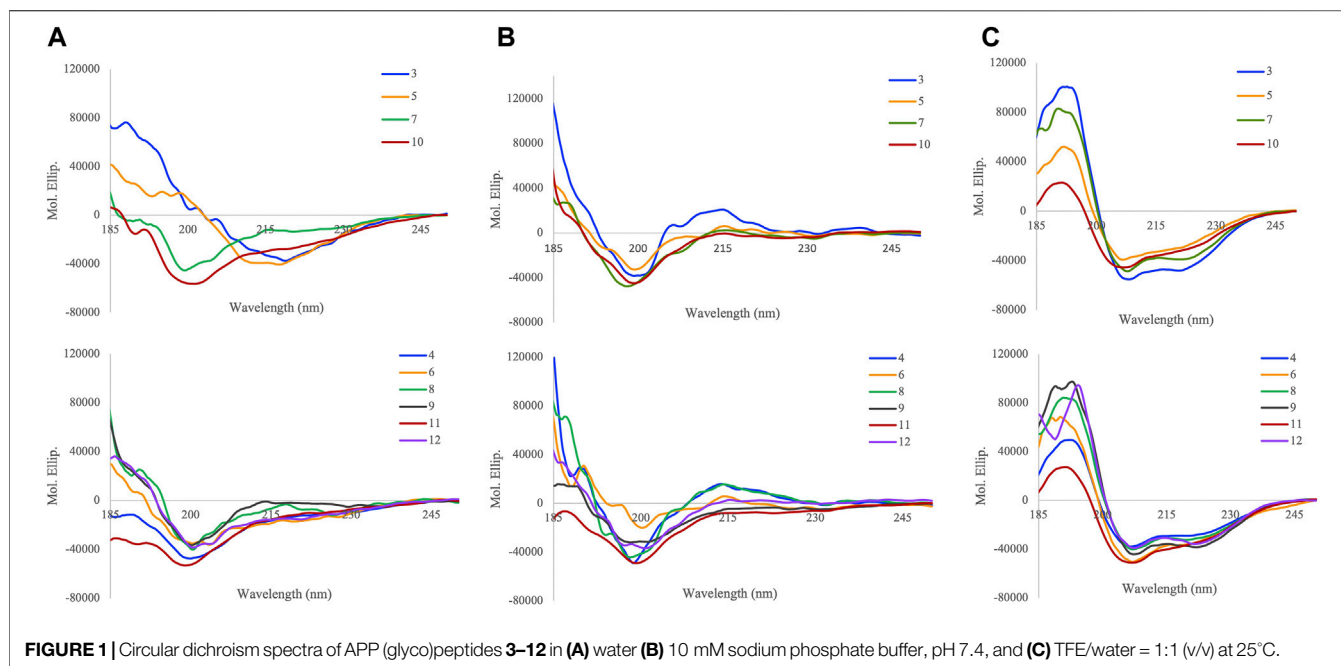


FIGURE 1 | Circular dichroism spectra of APP (glyco)peptides 3–12 in (A) water (B) 10 mM sodium phosphate buffer, pH 7.4, and (C) TFE/water = 1:1 (v/v) at 25°C.

A β -(1–9) significantly increased the percentage of random coil in 7 and 10 (85.1 and 90.7%, respectively). Site-specific O-glycosylation of Ser⁶⁶⁷ in glycopeptides 4 and 6 caused their structure to be largely disordered (87.1% and 41.4%, respectively) with complete loss of parallel β -sheets compared to their nonglycosylated counterparts 3 and 5, respectively (Figure 1A). This effect was more pronounced for the native glycopeptide 4 where β -structure along with α -helix was significantly reduced (12.9% and 0%, respectively). On the other hand, the Swedish-mutated glycopeptide 6 was less prone to change in its β -structure and α -helix amounts (39.4% and 19.2%, respectively) (Table 2). Also, the site-specific O-glycosylation of Thr⁶⁶³ in glycopeptides 8 and 11 did not significantly change the secondary conformation compared to their nonglycosylated counterparts 7 and 10, respectively, that were already largely disordered in water (85–90%). Hence, we were able to confirm that the addition of a single GalNAc moiety in APP 661–694 derived glycopeptides is able to break ordered secondary structures and cause it to be disordered in water (Singh et al., 2021). Interestingly, by increasing the glycan valency in glycopeptides 9 and 12, the amount β -structure increased (64.8 and 55.0%, respectively) and random coil decreased (22.4 and 27.0%, respectively). Therefore, glycan valency is an important determinant of the secondary structure of APP glycopeptides in water.

To evaluate secondary structure in a more physiologically relevant buffer setting, the CD spectra of (glyco)peptides were recorded in sodium phosphate buffer of low ionic strength (10 mM, pH 7.4). As expected, the (glyco)peptides indicated the presence of an unfolded state and were partially disordered with some β -structure properties. Deconvolution of the spectra revealed a prominent presence of random coil

(25–77%) and antiparallel β -sheet (17–48%), followed by β -turn (7–34%), and lastly, α -helix (0–10%) (Figure 1B and Table 2) (Hortschansky et al., 2005; Tew et al., 2008; Singh et al., 2021). The Swedish-mutated diglycosylated peptide 12 showed the highest amount of antiparallel β -sheet (47.9%) whereas its monoglycosylated counterpart 11 had the highest amount of random coil (76.8%) in this solvent system. Notable, in the absence of parallel β -sheets, the ratio of the remaining structural elements varied depending on the modifications (Swedish mutation and/or glycosylation) incorporated into the peptide sequences (Figure 1B and Table 2). These findings are in agreement with the previously reported CD data for A β peptides of different length; the A β -(1–42) peptide exhibited slightly higher α -helix and random coil content compared to A β -(1–16) peptide that has higher β -sheet and β -turn content (Tew et al., 2008). Likewise, our previously reported (glyco)peptides containing longer A β -(1–23) fragment (13–16) showed higher α -helix and random coil, and lower antiparallel β -sheet content, in sodium phosphate buffer (Singh et al., 2021) compared to (glyco)peptides analysed in this study that contain shorter A β -(1–9) fragment (3–12). Hence, A β occurs in various isoforms that differ by the number of residues at the C-terminal end of the peptides, which impacts the secondary structural preferences of the peptides in solution.

APP is an integral membrane protein whose behaviour can be modified by molecules such as trifluoroethanol (TFE) that partition the membrane-water interface and change the physiochemical properties of the lipid bilayer (Barry and Gawrisch, 1994; Özdirekcan et al., 2008). We have previously investigated the effects of TFE on a molecular level using CD spectroscopy to obtain an account of the α -helix-forming potential of model (glyco)peptides 13–16 containing the

TABLE 2 | Summary of the secondary content (%) present in APP (glyco)peptides **3–12** determined by BeStSel for CD spectra obtained in (A) water (B) 10 mM sodium phosphate buffer, pH 7.4, and (C) TFE/water = 1:1 (v/v)^a.

APP (glyco)peptides	α -H (%)	β -AP (%)	β -P (%)	β -T (%)	RC (%)
(A)					
APP ⁶⁶⁵⁻⁶⁸⁰ (3)	14.8	59.9	18.1	7.2	0.0
APP ⁶⁶⁵⁻⁶⁸⁰ -S* (4)	0.0	0.0	0.0	12.9	87.1
APP ⁶⁶⁵⁻⁶⁸⁰ (NL) (5)	34.5	21.9	35.9	0.0	7.7
APP ⁶⁶⁵⁻⁶⁸⁰ (NL)-S* (6)	19.2	30.8	0.0	8.6	41.4
APP ⁶⁶¹⁻⁶⁸⁰ (7)	0.0	8.3	0.0	6.6	85.1
APP ⁶⁶¹⁻⁶⁸⁰ -T* (8)	1.4	5.4	0.0	5.7	87.4
APP ⁶⁶¹⁻⁶⁸⁰ -T*, S* (9)	12.8	48.2	0.0	16.6	22.4
APP ⁶⁶¹⁻⁶⁸⁰ (NL) (10)	0.0	9.3	0.0	0.0	90.7
APP ⁶⁶¹⁻⁶⁸⁰ (NL)-T* (11)	0.0	0.0	0.0	12.5	87.5
APP ⁶⁶¹⁻⁶⁸⁰ (NL)-T*, S* (12)	18.0	45.8	0.0	9.2	27.0
(B)					
APP ⁶⁶⁵⁻⁶⁸⁰ (3)	6.1	39.8	0.0	19.8	34.3
APP ⁶⁶⁵⁻⁶⁸⁰ -S* (4)	9.3	33.6	0.0	14.9	42.2
APP ⁶⁶⁵⁻⁶⁸⁰ (NL) (5)	6.7	34.6	0.0	23.2	35.6
APP ⁶⁶⁵⁻⁶⁸⁰ (NL)-S* (6)	0.0	41.3	0.0	33.5	25.3
APP ⁶⁶¹⁻⁶⁸⁰ (7)	8.4	36.1	0.0	15.7	39.8
APP ⁶⁶¹⁻⁶⁸⁰ -T* (8)	8.8	42.6	0.0	18.3	30.4
APP ⁶⁶¹⁻⁶⁸⁰ -T*, S* (9)	9.5	24.6	0.0	17.1	48.7
APP ⁶⁶¹⁻⁶⁸⁰ (NL) (10)	0.0	34.4	0.0	15.0	50.6
APP ⁶⁶¹⁻⁶⁸⁰ (NL)-T* (11)	0.0	16.6	0.0	6.6	76.8
APP ⁶⁶¹⁻⁶⁸⁰ (NL)-T*, S* (12)	3.6	47.9	0.0	17.2	31.2
(C)					
APP ⁶⁶⁵⁻⁶⁸⁰ (3)	66.2	2.7	12.6	0.9	17.6
APP ⁶⁶⁵⁻⁶⁸⁰ -S* (4)	52.2	0.0	0.0	2.9	44.9
APP ⁶⁶⁵⁻⁶⁸⁰ (NL) (5)	59.9	3.5	3.2	0.0	33.3
APP ⁶⁶⁵⁻⁶⁸⁰ (NL)-S* (6)	66.7	0.0	0.7	0.0	32.6
APP ⁶⁶¹⁻⁶⁸⁰ (7)	88.7	0.0	0.0	3.2	8.1
APP ⁶⁶¹⁻⁶⁸⁰ -T* (8)	85.7	0.0	0.0	6.0	8.3
APP ⁶⁶¹⁻⁶⁸⁰ -T*, S* (9)	94.4	0.0	0.0	5.6	0.0
APP ⁶⁶¹⁻⁶⁸⁰ (NL) (10)	36.8	9.7	7.5	0.0	46.0
APP ⁶⁶¹⁻⁶⁸⁰ (NL)-T* (11)	40.3	6.1	4.7	0.0	48.9
APP ⁶⁶¹⁻⁶⁸⁰ (NL)-T*, S* (12)	86.2	0.0	3.1	6.5	4.3

^aThe content is divided into α -helix (α -H), anti-parallel β -sheet (β -AP), parallel β -sheet (β -P), β -turn (β -T), and random coil (RC).

Tyr⁶⁸¹ O-linked glycosylation in A β -(1–23) region of APP (Singh et al., 2021). Upon addition of TFE into water (1:1, v/v), the (glyco)peptides showed a significant increase in α -helix and random coil content and decrease in β -structure content (Figure 1C). Upon further analysis, shorter native peptide **3** had slightly higher α -helix content (66.2%) than its Swedish-mutated counterpart **5** (59.9%), however, this difference was larger between the longer native peptide **7** (88.7%) and its Swedish-mutated counterpart **10** (36.8%) (Table 2). Regardless of the length of A β fragment, the Swedish mutation significantly reduced the amount of α -helix and increased β -sheet and random coil secondary structure elements in this solvent system. Similarly, site-specific O-glycosylation of Thr⁶⁶³ and Tyr⁶⁸¹ (Singh et al., 2021) slightly decreased the α -helix and increased the random coil content in native glycopeptides, **8** and **14** respectively, whereas it increased α -helix and decreased random coil content in Swedish-mutated glycopeptides, **11** and **16** respectively, with this effect being more pronounced for **16**. Lastly, regardless of the Swedish mutation, the attachment of two GalNAc moieties on Thr⁶⁶³ and Ser⁶⁶⁷ within the peptide sequence drastically increased the α -helix

content in **9** and **12** (94.4% and 86.2%, respectively), in this solvent system. These findings suggest that in membrane-mimicking conditions, excess O-glycosylation can hamper the effects of the Swedish mutation on secondary structure and prompt it to become largely α -helical.

BACE-1 Activity of APP (Glyco)peptides

Glycosylation can alter substrate recognition and impact enzyme activity in either a positive (enhancing) or negative (inhibiting) manner (Goettig, 2016; Goth et al., 2018). The mucin-type O-linked glycosylation of a protein may not only affect its conformation but also affect its transport and localization in the cell (Matsuura et al., 1989; Chen et al., 2002). Proteases are highly regulated by post-translational modifications and drive fate, localization, and activity of many proteins (Bond, 2019). Certain mutations can also affect the subcellular localization of the cleavage event by crucial proteases and mediate a different cellular mechanism for the protein (Haass et al., 1995). We have previously reported that the Swedish mutation is an important criterion for enhancing both ADAM10 (α -secretase) and BACE1 (β -secretase) cleavage rates of A β -(1–23) model (glyco)peptides

TABLE 3 | Proteolytic cleavage of APP (glyco)peptides **3–12** upon treatment with BACE-1 enzyme (KM-D/NL-D cleavage site)^a.

APP (glyco)peptides	BACE-1 activity	
	Recovered (%)	Cleaved (%)
APP ⁶⁶⁵⁻⁶⁸⁰ (3)	95.5	4.48
APP ⁶⁶⁵⁻⁶⁸⁰ -S* (4)	98.6	1.40
APP ⁶⁶⁵⁻⁶⁸⁰ (NL) (5)	3.82	96.2
APP ⁶⁶⁵⁻⁶⁸⁰ (NL)-S* (6)	7.02	93.0
APP ⁶⁶¹⁻⁶⁸⁰ (7)	96.6	3.40
APP ⁶⁶¹⁻⁶⁸⁰ -T* (8)	91.5	8.46
APP ⁶⁶¹⁻⁶⁸⁰ -T*, S* (9)	95.9	4.12
APP ⁶⁶¹⁻⁶⁸⁰ (NL) (10)	20.3	79.7
APP ⁶⁶¹⁻⁶⁸⁰ (NL)-T* (11)	1.90	98.1
APP ⁶⁶¹⁻⁶⁸⁰ (NL)-T*, S* (12)	3.90	96.1
APP ⁶⁶¹⁻⁶⁹⁴ (13)	100 ^b	0.0 ^b
APP ⁶⁶¹⁻⁶⁹⁴ -Y* (14)	100 ^b	0.0 ^b
APP ⁶⁶¹⁻⁶⁹⁴ (NL) (15)	86.8 ^b	13.1 ^b
APP ⁶⁶¹⁻⁶⁹⁴ (NL)-Y* (16)	57.4 ^b	42.4 ^b

^aThe values were calculated as described in the Methods with SD <5% and identity of the fragments was determined by RP-HPLC, analysis and confirmed by MALDI-TOF (see the **Supplementary Material S20–S32**).

^bReported in Singh et al., 2021.

13–16, where site-specific mucin-type O-linked glycosylation of Tyr⁶⁸¹ residue in **16** further increased BACE-1 driven amyloid pathway (Singh et al., 2021). Therefore, similar enzyme cleavage assays with BACE-1 were set up to explore the effect of the Swedish mutation, length of the amino acid sequence, glycan position and valency on the proteolytic susceptibility of **3–12**. BACE1 produced two fragments upon cleavage of (glyco) peptides, for which yields were determined after 24 h treatment. The yields of intact peptide and fragments were evaluated by the RP-HPLC peaks integration (**Table 3**, and the **Supplementary Material S20–S32**).

Regardless of glycosylation, the native A β -(1–9) model (glyco) peptides **3** and **4** showed almost full recovery after incubation with BACE-1 (95.5% and 98.6%, respectively). The extension of the native (glyco)peptide sequence at the N-terminus with IKTEEISEVKM in **7** and **8** also resulted in a very low BACE-1 proteolysis, 3.4% and 8.5%, respectively. Increasing the glycan valency to two, in native glycopeptide **9**, did not significantly alter cleavage rates (95.9% recovery). It became evident that the presence of the Swedish mutation in five was a driving force for the near complete cleavage of the peptide (96.2%). Interestingly, the extension of the peptide sequence at the N-terminus with IKTEEISEVNL in **10** showed a lower amount of the peptide cleaved (79.7%) in comparison to shorter peptide fragment **5**. Thus, a longer N-terminal fragment flanking the A β region can hamper its proteolytic susceptibility and result in slower cleavage rates by BACE-1. Glycosylation had a more significant effect on the sequence carrying the Swedish mutation, where regardless of the N-terminal fragment length, glycan position and valency, BACE-1 treatment resulted in 93–98% cleaved products for glycopeptides **6** and **11–12**. This agrees with our previous findings that apart from the Swedish mutation, the presence of O-glycosylation can drive BACE-1 cleavage rates and result in increased A β production (Singh et al., 2021).

Other key aspects affecting BACE-1 cleavage rates in the presence of the Swedish mutation were the length of the C-terminal A β fragment and the glycan position relative to the cleavage site. For example, **16** contains A β -(1–23) C-terminal fragment and is cleaved to a much lesser extent (42.4%) by BACE-1 than **11** that contains A β -(1–9) C-terminal fragment (98.1%). Moreover, the relative position of the GalNAc moiety on Thr⁶⁶³ and Tyr⁶⁸¹ in **11** and **16**, respectively, can also influence enzymatic activity. Even though **16** is cleaved to a lesser extent than **11** by BACE-1, the ~3-fold increase in cleaved products compared to its non-glycosylated counterpart **15** is observed. This further points to a stronger effect of Tyr⁶⁸¹ O-glycosylation on the C-terminal A β fragment in accelerating BACE-1 activity. Therefore, we can postulate that in the presence of the Swedish mutation, excess O-glycosylation proximal to BACE-1 cleavage site can significantly increase the cleavage propensity of the peptides for the amyloid pathway, with this effect being more pronounced when the glycosylation is on the C-terminal A β side of the cleavage site.

The subcellular localization of BACE-1 cleavage of Swedish-mutated APP differs greatly from that for native APP, where the former is localized to a post Golgi compartment for A β generation and outcompetes anti-amyloidogenic processing by α -secretases (Haass et al., 1995; Thinakaran et al., 1996). However, little is known regarding the regulatory role of mucin-type O-linked glycosylation of APP on BACE-1 activity, and these results are particularly interesting, since A β peptides in CSF of AD patients are heavily glycosylated by mucin-type O-linked glycans (Halim et al., 2011). Thus, we can speculate that both Swedish mutation and mucin-type O-linked glycosylation increase APP processing because the former provides a better cleavage site for BACE-1, and the latter changes the conformation and increases the sensitivity of the protein to BACE-1.

Aggregation Kinetics of APP (Glyco)peptides on A β 40 Fibrillogenesis

We adopted the widely used thioflavin T (ThT) assay (Xue et al., 2017) to investigate how O-glycosylation impacts the kinetics of fiber formation of A β 40, a model peptide for studying the dynamics of protein aggregation. The aggregation kinetic profile of A β 40 peptide (10 μ M) exhibited a typical sigmoidal curve with three different regions: a lag phase associated with nucleation, a rapid growth phase for elongation and polymerization by fibrils, and a final saturation phase dominated with mature fibrils (**Figure 2**, **Supplementary Material S33–S40**). At the conditions used in this study, it has been shown that A β amyloidogenesis proceeds by a nucleation-dependent polymerization mechanism that involves key soluble oligomeric intermediates (Du et al., 2011; Elbassal et al., 2017). The half time (t_{50}) of the growth phase of the A β 40 amyloidogenesis was approximately 8 h (**Figure 2**, **Supplementary Material S33–S40**), where t_{50} is defined as the time at which the fluorescence intensity reaches the midpoint between the pre- and post-aggregation baselines.

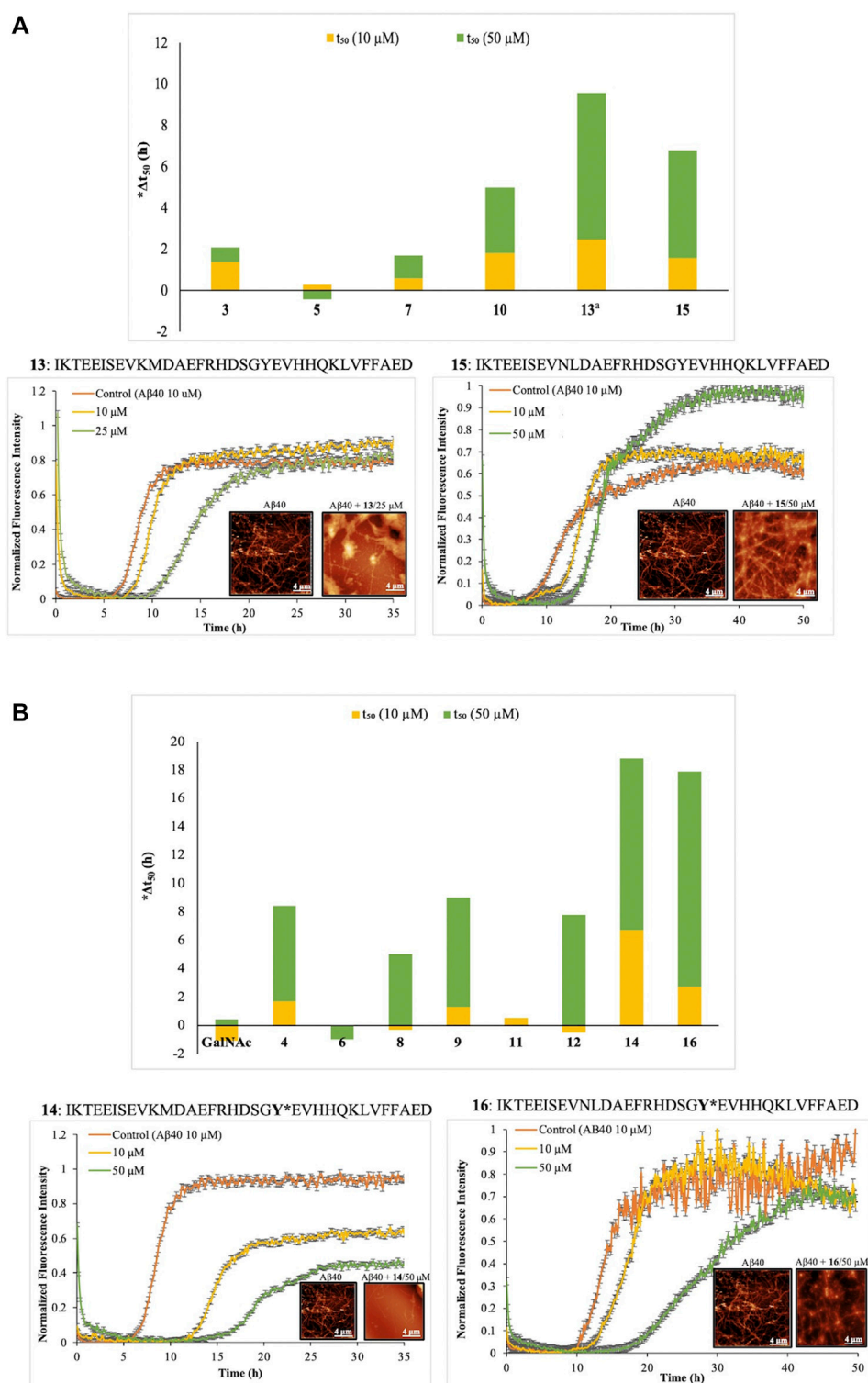


FIGURE 2 | Effect of APP peptides **3, 5, 7, 10, 13**, and **15** (A) and glycopeptides **4, 6, 8, 9, 11, 12, 14, 16** (B) on the aggregation kinetics of Aβ40 (10 μM) using ThT fluorescence assay in phosphate buffer (50 mM, pH 7.4) at 37°C. The concentration of (glyco)peptides was 10 and 50 μM. Peptide 13 was run at 10 and 25 μM. *Aggregation half-time (Δt_{50}) = APP (glyco)peptide t_{50} – Aβ40 t_{50} . The t_{50} values are means of triplicate kinetics results. Alongside are tapping mode atomic force microscopy images of Aβ40 fibril growth upon 24 h incubation with nonglycosylated peptides, **13** and **15** (A) and Tyr-O-glycopeptides, **14** and **16** (B).

Although recent studies have implicated small soluble oligomers, as the main culprits of A β toxicity and AD pathogenesis (Yang et al., 2017), very little is known about the exact mechanism of oligomeric assembly and the conformation of peptides in this early event of A β aggregation. In the presence of APP (glyco) peptides 3–16 at two concentrations (10 and 50 μ M), the kinetics of aggregation of A β 40 was described by a sigmoidal curve, with a lag phase that varied depending on the internal modifications of the (glyco)peptides such as the Swedish mutation, site-specific O-glycosylation, glycan valency and/or sequence length. The curves reached a plateau after approximately 24 h (Supplementary Material S33–S40). The nonglycosylated peptides 3, 5, and 7 displayed no marked effect either on the lag phase ($\Delta t_{50} < 2$ h, Figure 2A) or the final ThT fluorescence intensity in comparison to control A β 40 peptide alone (Supplementary Figures S1A–S3A, Supplementary Material S33–S35). Interestingly, we observed a slight delay in the aggregation process by the Swedish-mutated peptide 10 ($\Delta t_{50} = 3.2$ h at 50 μ M, Figure 2A, Supplementary Figure S4A, Supplementary Material S36) with extended N-terminal domain. Increasing the C-terminal domain sequence in 13 and 15, to include A β -(1–23) fragment, led to a much larger effect on the lag phase (Supplementary Figures S5A, S6A, Supplementary Material S38–S39), with $\Delta t_{50} = 7.1$ h for 13 (25 μ M) and $\Delta t_{50} = 5.2$ h for 15 (50 μ M) (Figure 2A), indicating an inhibitory effect on A β 40 aggregation. Notably, we observed a complete saturation of the ThT signal for native peptide 13 at higher concentration (50 μ M) (Supplementary Figures S5A,B, Supplementary Material S38). Hence, the aggregation of A β 40 in the presence of nonglycosylated peptides 3, 5, 7, 10, 13, or 15 displayed a longer lag phase when the length of the A β fragment was increased. The effect of the Swedish mutation was less clear and varied regardless of peptide length.

To evaluate A β 40 aggregation in the presence of glycopeptides, we first performed kinetics with the free GalNAc sugar (10 and 50 μ M) that showed minimal difference in Δt_{50} values ($\Delta t_{50} < 0.5$ h, Figure 2B). The presence of a single GalNAc moiety on Ser⁶⁶⁷ in native glycopeptide four increased the lag phase substantially ($\Delta t_{50} = 6.7$ h at 50 μ M, Figure 2B, and Supplementary Figure S1B in the Supplementary Material S33) and delayed A β 40 aggregation much more compared to its non-glycosylated counterpart 3. Extension of the N-terminal domain sequence in native glycopeptide eight by IKTE, slightly decreased the Δt_{50} value ($\Delta t_{50} = 5$ h at 50 μ M, Figure 2B, and Supplementary Figure S3B in the Supplementary Material S35) compared to four. However, increasing the glycan valency in nine resulted in gain in inhibition of A β 40 aggregation and further increase of the lag phase ($\Delta t_{50} = 7.7$ h at 50 μ M, Figure 2B, Supplementary Figure S3C, Supplementary Material S36). Regardless of the length of the N-terminal domain sequence, the presence of the Swedish mutation in 6 and 11 completely suppressed the inhibitory effect of O-glycosylation on A β 40 aggregation exhibited by 8 ($\Delta t_{50} = 0$ h at 50 μ M, Figure 2B, and Supplementary Figure S2B, S4B in the Supplementary Material S34,S37). A drastic increase in the Δt_{50} value for diglycosylated and Swedish mutated peptide 12 ($\Delta t_{50} = 7.8$ h

at 50 μ M, Figure 2B, and Supplementary Figure S4C in the Supplementary Material S37) clearly indicated that O-glycosylation at multiple sites of attachment can overcome the effect of the Swedish mutation and cause A β 40 to aggregate at slower rates. Consistent with their nonglycosylated versions 13 and 15, the extension of the A β fragment and site-specific O-glycosylation of Tyr⁶⁸¹ in 14 and 16 showed the largest difference in lag phase and strongest inhibition of A β 40 aggregation profile, with $\Delta t_{50} = 12.1$ h for 14 (50 μ M) and $\Delta t_{50} = 15.2$ h for 16 (50 μ M) (Figure 2B, and Supplementary Figures S5C, S6B in the Supplementary Material S39–S40). Along with having a prolonged lag phase, 14 also reduces the final ThT fluorescence intensity dramatically (~50%), suggesting a significant interference in A β 40 aggregation. Therefore, our results suggest that O-glycosylation inhibits A β 40 aggregation in a concentration-dependent manner, and this effect is more pronounced when the glycopeptides contain the longer A β -(1–23) fragment and GalNAc modification on Tyr⁶⁸¹ (14 and 16). It is also important to mention that by reducing the length of the A β fragment to A β -(1–9), we were able to detect the key differences between the Swedish-mutated (6 and 11) and mono-/diglycosylated analogues (4, 8, 9, and 12) on A β 40 aggregation kinetics.

The morphology of the tyrosine (glyco) peptide aggregates (13–16) co-incubated with A β 40 was examined using atomic force microscopy (AFM). In the absence of (glyco)peptides, A β 40 forms a dense meshwork of amyloid fibrils (Figure 2). In the presence of native peptide 13 (25 μ M) lower density of A β 40 fibrils is observed (Figure 2A). Similarly, addition of glycosylated counterpart 14 (50 μ M), resulted in less fibrils formed, and the ones formed were shorter in size (Figure 2B). This is consistent with the ThT kinetics data for 13 and 14 at 25 and 50 μ M, respectively. The addition of the Swedish-mutated peptide 15 (50 μ M) to A β 40 resulted in the fibrillar morphology similar to that of A β 40 alone (Figure 2A). However, its glycosylated counterpart 16 was able to partially inhibit the fibril formation, resulting in thinly dispersed and less dense A β 40 fibril (Figure 2B). Thus, as observed in ThT kinetics, the aggregation of A β 40 can be delayed by 15 and 16 (50 μ M), however, the inhibitory potency is not enough to prevent fibril formation under the current conditions.

Our work parallels and directly complements the study by Liu et al., 2021 that shows A β 42 peptides bearing Tyr⁶⁸¹ O-glycosylation significantly affect both the aggregation and degradation of A β 42. Furthermore, similar inhibiting activity of A β 40 and A β 42 fibrillogenesis by glycation (Emendato et al., 2018; Milordini et al., 2020) and addition of polysaccharides, such as chitosan (Liu et al., 2015; Hao et al., 2017) and heparin sulfate (Wang et al., 2021) was reported.

CONCLUSION

In summary, the dynamical interplay between O-glycosylation and aggregation affected the structure of peptides and slowed down the aggregation process. The presence of the Swedish mutation led to an increased amount of β -structure in

physiological conditions, with the β -secretase activity being drastically increased, and the aggregation process remaining largely unaffected. However, this effect of the Swedish mutation on the (glyco)peptides was overcome by increasing the number of glycosylation sites near the β -secretase cleavage site, increasing the C-terminal domain (A β) sequence relative to the β -secretase cleavage site, and/or having Tyr⁶⁸¹ glycosylated in the A β domain, resulting in glycosylation strongly inhibiting the aggregation process of A β 40. Therefore, our studies demonstrate that O-glycosylation typically supports the non-amyloidogenic processing of APP, however, in FAD cases, it can incline towards the amyloidogenic processing of APP, where its fate lies upon the abundance and position of O-glycans relative to the β -secretase cleavage site.

DATA AVAILABILITY STATEMENT

The original contributions presented in the study are included in the article/**Supplementary Material**, further inquiries can be directed to the corresponding author.

AUTHOR CONTRIBUTIONS

YS and MC wrote the manuscript. YS, DO, and RA conducted the synthesis of the glycosylated Thr/Ser building blocks. Synthesis of glycopeptides was done by YS, NV, GM and

DO. The CD analysis was done by YS and NV. Proteolytic cleavage assay was done by DM and samples analyzed by YS, GM, and NV. Aggregation kinetics assays and AFM images acquired and analyzed by DR and DD. The senior authorship is shared by DM, DD, and MC.

FUNDING

This research was supported by the National Institute of Health (NIH) Grants R15CA242351 to MC, R15CA249788 to DM, and R15GM116006 to DD, the Alzheimer's Association AARG-17-531423 to DD, and Palm Health Foundation and Stiles-Nicholson Brain Institute to MC.

ACKNOWLEDGMENTS

The authors are thankful to Dr. Vivian Merk (FAU) and her lab for their atomic force microscopy system that was used in this study.

SUPPLEMENTARY MATERIAL

The Supplementary Material for this article can be found online at: <https://www.frontiersin.org/articles/10.3389/fchem.2022.859822/full#supplementary-material>

REFERENCES

- Akasaka-Many, K., Kawamura, M., Tsumoto, H., Saito, Y., Tachida, Y., Kitazume, S., et al. (2017). Excess APP-O-Glycosylation by GalNAc-T6 Decreases A β Production. *J. Biochem.* 161, 99–111. doi:10.1093/jb/mvw056
- Akasaka-Many, K., and Many, H. (2020). The Role of APP O-Glycosylation in Alzheimer's Disease. *Biomolecules* 10, 1569. doi:10.3390/biom10111569
- Alzheimer's Association (2020). 2020 Alzheimer's Disease Facts and Figures. *Alzheimers Dement* 16, 391–460. doi:10.1002/alz.12068
- Barry, J. A., and Gawrisch, K. (1994). Direct NMR Evidence for Ethanol Binding to the Lipid-Water Interface of Phospholipid Bilayers. *Biochemistry* 33, 8082–8088. doi:10.1021/bi00192a013
- Beckwith, D. M., FitzGerald, F. G., Rodriguez Benavente, M. C., Mercer, E. R., Ludwig, A.-K., Michalak, M., et al. (2021). Calorimetric Analysis of the Interplay between Synthetic Tn Antigen-Presenting MUC1 Glycopeptides and Human Macrophage Galactose-type Lectin. *Biochemistry* 60, 547–558. doi:10.1021/acs.biochem.0c00942
- Boix, C. P., Lopez-Font, I., Cuchillo-Ibañez, I., and Sáez-Valero, J. (2020). Amyloid Precursor Protein Glycosylation Is Altered in the Brain of Patients with Alzheimer's Disease. *Alz Res. Ther.* 12, 96. doi:10.1186/s13195-020-00664-9
- Bond, J. S. (2019). Proteases: History, Discovery, and Roles in Health and Disease. *J. Biol. Chem.* 294, 1643–1651. doi:10.1074/jbc.TM118.004156
- Chen, P.-Y., Lin, C.-C., Chang, Y.-T., Lin, S.-C., and Chan, S. I. (2002). One O-Linked Sugar Can Affect the Coil-To- β Structural Transition of the Prion Peptide. *Proc. Natl. Acad. Sci. U.S.A.* 99, 12633–12638. doi:10.1073/pnas.192137799
- Chun, Y. S., Kwon, O.-H., and Chung, S. (2017). O-GlcNAcylation of Amyloid- β Precursor Protein at Threonine 576 Residue Regulates Trafficking and Processing. *Biochem. Biophysical Res. Commun.* 490, 486–491. doi:10.1016/j.bbrc.2017.06.067
- Chun, Y. S., Kwon, O.-H., Oh, H. G., Kim, T.-W., McIntire, L. B., Park, M. K., et al. (2015). Threonine 576 Residue of Amyloid- β Precursor Protein Regulates its Trafficking and Processing. *Biochem. Biophysical Res. Commun.* 467, 955–960. doi:10.1016/j.bbrc.2015.10.037
- Du, D., Murray, A. N., Cohen, E., Kim, H.-E., Simkovsky, R., Dillin, A., et al. (2011). A Kinetic Aggregation Assay Allowing Selective and Sensitive Amyloid- β Quantification in Cells and Tissues. *Biochemistry* 50, 1607–1617. doi:10.1021/bi1013744
- Elbassal, E. A., Morris, C., Kent, T. W., Lantz, R., Ojha, B., Wojcikiewicz, E. P., et al. (2017). Gold Nanoparticles as a Probe for Amyloid- β Oligomer and Amyloid Formation. *J. Phys. Chem. C* 121, 20007–20015. doi:10.1021/acs.jpcc.7b05169
- Emendato, A., Milordini, G., Zacco, E., Sicorello, A., Dal Piaz, F., Guerrini, R., et al. (2018). Glycation Affects Fibril Formation of A β Peptides. *J. Biol. Chem.* 293, 13100–13111. doi:10.1074/jbc.RA118.002275
- Goettig, P. (2016). Effects of Glycosylation on the Enzymatic Activity and Mechanisms of Proteases. *Ijms* 17, 1969–1993. doi:10.3390/ijms17121969
- Goth, C. K., Vakhrushev, S. Y., Joshi, H. J., Clausen, H., and Schjoldager, K. T. (2018). Fine-tuning Limited Proteolysis: A Major Role for Regulated Site-specific O -Glycosylation. *Trends Biochem. Sci.* 43, 269–284. doi:10.1016/j.tibs.2018.02.005
- Haass, C., Lemere, C. A., Capell, A., Citron, M., Seubert, P., Schenk, D., et al. (1995). The Swedish Mutation Causes Early-Onset Alzheimer's Disease by β -secretase Cleavage within the Secretory Pathway. *Nat. Med.* 1, 1291–1296. doi:10.1038/nm1295-1291
- Halim, A., Brinkmalm, G., Rüetschi, U., Westman-Brinkmalm, A., Portelius, E., Zetterberg, H., et al. (2011). Site-specific Characterization of Threonine, Serine, and Tyrosine Glycosylations of Amyloid Precursor Protein/amyloid β -peptides in Human Cerebrospinal Fluid. *Proc. Natl. Acad. Sci. U.S.A.* 108, 11848–11853. doi:10.1073/pnas.1102664108

- Hao, C., Wang, W., Wang, S., Zhang, L., and Guo, Y. (2017). An Overview of the Protective Effects of Chitosan and Acetylated Chitosan Oligosaccharides against Neuronal Disorders. *Mar. Drugs* 15, 89. doi:10.3390/md15040089
- Hardy, J. A., and Higgins, G. A. (1992). Alzheimer's Disease: The Amyloid Cascade Hypothesis. *Science* 256, 184–185. doi:10.1126/science.1566067
- Haukedal, H., and Freude, K. K. (2021). Implications of Glycosylation in Alzheimer's Disease. *Front. Neurosci.* 14, 1432. doi:10.3389/fnins.2020.625348
- Hortschansky, P., Schroeckh, V., Christopeit, T., Zandomenighi, G., and Fändrich, M. (2005). The Aggregation Kinetics of Alzheimer's β -amyloid Peptide Is Controlled by Stochastic Nucleation. *Protein Sci. : A Publication Protein Soc.* 14, 1753–1759. doi:10.1110/ps.041266605
- Hurd, M. D., Martorell, P., Delavande, A., Mullen, K. J., and Langa, K. M. (2013). Monetary Costs of Dementia in the United States. *N. Engl. J. Med.* 368, 1326–1334. doi:10.1056/NEJMsa1204629
- Jacobsen, K. T., and Iverfeldt, K. (2011). O-GlcNAcylation Increases Non-amyloidogenic Processing of the Amyloid- β Precursor Protein (APP). *Biochem. Biophysical Res. Commun.* 404, 882–886. doi:10.1016/j.bbrc.2010.12.080
- Juszczyk, P., Kołodziejczyk, A. S., and Grzonka, Z. (2005). Circular Dichroism and Aggregation Studies of Amyloid Beta (11–8) Fragment and its Variants. *Acta Biochim. Pol.* 52, 425–431. doi:10.18388/abp.2005_3455
- Kitazume, S., Tachida, Y., Kato, M., Yamaguchi, Y., Honda, T., Hashimoto, Y., et al. (2010). Brain Endothelial Cells Produce Amyloid β from Amyloid Precursor Protein 770 and Preferentially Secrete the O-Glycosylated Form. *J. Biol. Chem.* 285, 40097–40103. doi:10.1074/jbc.M110.144626
- Koike, H., Seki, H., Kouchi, Z., Ito, M., Kinouchi, T., Tomioka, S., et al. (1999). Thimet Oligopeptidase Cleaves the Full-Length Alzheimer Amyloid Precursor Protein at a β -Secretase Cleavage Site in COS Cells. *J. Biochem.* 126, 235–242. doi:10.1093/oxfordjournals.jbchem.a022428
- Krištić, J., and Lauc, G. (2017). "Ubiquitous Importance of Protein Glycosylation," in *High-Throughput Glycomics and Glycoproteomics: Methods and Protocols*. Editors G. Lauc and M. Wührer (New York, NY: Springer New York), 1–12. doi:10.1007/978-1-4939-6493-2_1
- Lambermon, M. H. L., Rappaport, R. V., and McLaurin, J. (2005). Biophysical Characterization of Longer Forms of Amyloid Beta Peptides: Possible Contribution to Flocculent Plaque Formation. *J. Neurochem.* 95, 1667–1676. doi:10.1111/j.1471-4159.2005.03497.x
- Liu, D., Wei, Q., Xia, W., He, C., Zhang, Q., Huang, L., et al. (2021). O-glycosylation Induces Amyloid- β to Form New Fibril Polymorphs Vulnerable for Degradation. *J. Am. Chem. Soc.* 143, 20216–20223. doi:10.1021/jacs.1c08607
- Liu, F., Xu, K., Xu, Z., de las Rivas, M., Wang, C., Li, X., et al. (2017). The Small Molecule Luteolin Inhibits N-Acetyl- α -Galactosaminyltransferases and Reduces Mucin-type O-Glycosylation of Amyloid Precursor Protein. *J. Biol. Chem.* 292, 21304–21319. doi:10.1074/jbc.M117.814202
- Liu, H., Morris, C., Lantz, R., Kent, T. W., Elbassal, E. A., Wojcikiewicz, E. P., et al. (2018). Residue-Specific Dynamics and Local Environmental Changes in A β 40 Oligomer and Fibril Formation. *Angew. Chem. Int. Ed.* 57, 8017–8021. doi:10.1002/anie.201802490
- Liu, H., Ojha, B., Morris, C., Jiang, M., Wojcikiewicz, E. P., Rao, P. P. N., et al. (2015). Positively Charged Chitosan and N-Trimethyl Chitosan Inhibit A β 40 Fibrillogenesis. *Biomacromolecules* 16, 2363–2373. doi:10.1021/acs.biomac.5b00603
- Mant, C. T., Zhou, N. E., and Hodges, R. S. (1989). Correlation of Protein Retention Times in Reversed-phase Chromatography with Polypeptide Chain Length and Hydrophobicity. *J. Chromatogr. A* 476, 363–375. doi:10.1016/S0021-9673(01)93882-8
- Matsuura, H., Greene, T., and Hakomori, S. (1989). An α -N-Acetylgalactosaminylation at the Threonine Residue of a Defined Peptide Sequence Creates the Oncofetal Peptide Epitope in Human Fibronectin. *J. Biol. Chem.* 264, 10472–10476. doi:10.1016/S0021-9258(18)81645-3
- Miconai, A., Wien, F., Buljaki, E., Kun, J., Moussong, E., Lee, Y.-H., et al. (2018). BeStSel: A Web Server for Accurate Protein Secondary Structure Prediction and Fold Recognition from the Circular Dichroism Spectra. *Nucleic Acids Res.* 46, W315–W322. doi:10.1093/nar/gky497
- Miconai, A., Wien, F., Kerna, L., Lee, Y.-H., Goto, Y., Réfrégiers, M., et al. (2015). Accurate Secondary Structure Prediction and Fold Recognition for Circular Dichroism Spectroscopy. *Proc. Natl. Acad. Sci. U.S.A.* 112, E3095–E3103. doi:10.1073/pnas.1500851112
- Milordini, G., Zacco, E., Percival, M., Puglisi, R., Dal Piaz, F., Temussi, P., et al. (2020). The Role of Glycation on the Aggregation Properties of IAPP. *Front. Mol. Biosci.* 7, 104. doi:10.3389/fmolb.2020.00104
- Moran, F. P., Daniel, S. M., Chen, R., Michaela, Y., Shai, Z., Ehud, G., et al. (2021). Interplay between Protein Glycosylation Pathways in Alzheimer's Disease. *Sci. Adv.* 3, e1601576. doi:10.1126/sciadv.1601576
- Nakamura, N., and Kurosaka, A. (2019). Mucin-type Glycosylation as a Regulatory Factor of Amyloid Precursor Protein Processing. *J. Biochem.* 165, 205–208. doi:10.1093/jb/mvy121
- O'Brien, R. J., and Wong, P. C. (2011). Amyloid Precursor Protein Processing and Alzheimer's Disease. *Annu. Rev. Neurosci.* 34, 185–204. doi:10.1146/annurev-neuro-061010-113613
- Özdirekcan, S., Nyholm, T. K. M., Raja, M., Rijkers, D. T. S., Liskamp, R. M. J., and Killian, J. A. (2008). Influence of Trifluoroethanol on Membrane Interfacial Anchoring Interactions of Transmembrane α -Helical Peptides. *Biophysical J.* 94, 1315–1325. doi:10.1529/biophysj.106.101782
- Påhlsson, P., Shakin-Eshleman, S. H., and Spitalnik, S. L. (1992). N-linked Glycosylation of β -amyloid Precursor Protein. *Biochem. Biophysical Res. Commun.* 189, 1667–1673. doi:10.1016/0006-291X(92)90269-Q
- Perdivara, I., Petrovich, R., Allinquant, B., Deterding, L. J., Tomer, K. B., and Przybylski, M. (2009). Elucidation of O-Glycosylation Structures of the β -Amyloid Precursor Protein by Liquid Chromatography–Mass Spectrometry Using Electron Transfer Dissociation and Collision Induced Dissociation. *J. Proteome Res.* 8, 3786. doi:10.1021/pr9001096
- Selkoe, D. J., and Hardy, J. (2016). The Amyloid Hypothesis of Alzheimer's Disease at 25 Years. *EMBO Mol. Med.* 8, 595–608. doi:10.15252/emmm.201606210
- Shi, J., Ku, X., Zou, X., Hou, J., Yan, W., and Zhang, Y. (2021). Comprehensive Analysis of O-Glycosylation of Amyloid Precursor Protein (APP) Using Targeted and Multi-Fragmentation MS Strategy. *Biochim. Biophys. Acta (Bba) - Gen. Subjects* 1865, 129954. doi:10.1016/j.bbagen.2021.129954
- Singh, Y., Ormazá, D., Massetti, A., Minond, D., and Cudic, M. (2021). Tyrosine O-GalNAc Alters the Conformation and Proteolytic Susceptibility of APP Model Glycopeptides. *ACS Chem. Neurosci.* 12, 2974–2980. doi:10.1021/acscchemneuro.1c00387
- Singh, Y., Rodríguez Benavente, M. C., Al-Hunuti, M. H., Beckwith, D., Ayyalasomayajula, R., Patino, E., et al. (2020). Positional Scanning MUC1 Glycopeptide Library Reveals the Importance of PDTR Epitope Glycosylation for Lectin Binding. *J. Org. Chem.* 85, 1434–1445. doi:10.1021/acs.joc.9b02396
- Sreerama, N., and Woody, R. W. (2000). Estimation of Protein Secondary Structure from Circular Dichroism Spectra: Comparison of CONTIN, SELCON, and CDSSTR Methods with an Expanded Reference Set. *Anal. Biochem.* 287, 252–260. doi:10.1006/abio.2000.4880
- Tan, J. Z. A., and Gleeson, P. A. (2019). The Role of Membrane Trafficking in the Processing of Amyloid Precursor Protein and Production of Amyloid Peptides in Alzheimer's Disease. *Biochim. Biophys. Acta (Bba) - Biomembranes* 1861, 697–712. doi:10.1016/j.bbamem.2018.11.013
- Tew, D. J., Bottomley, S. P., Smith, D. P., Ciccostoto, G. D., Babon, J., Hinds, M. G., et al. (2008). Stabilization of Neurotoxic Soluble β -Sheet-Rich Conformations of the Alzheimer's Disease Amyloid- β Peptide. *Biophysical J.* 94, 2752–2766. doi:10.1529/biophysj.107.119909
- Thinakaran, G., Teplow, D. B., Siman, R., Greenberg, B., and Sisodia, S. S. (1996). Metabolism of the "Swedish" Amyloid Precursor Protein Variant in Neuro2a (N2a) Cells. *J. Biol. Chem.* 271, 9390–9397. doi:10.1074/jbc.271.16.9390
- Van Cauwenberghe, C., Van Broeckhoven, C., and Sleegers, K. (2016). The Genetic Landscape of Alzheimer Disease: Clinical Implications and Perspectives. *Genet. Med.* 18, 421–430. doi:10.1038/gim.2015.117
- Wang, P., Zhao, J., Hossaini Nasr, S., Otieno, S. A., Zhang, F., Qiang, W., et al. (2021). Probing Amyloid β Interactions with Synthetic Heparan Sulfate Oligosaccharides. *ACS Chem. Biol.* 16, 1894–1899. doi:10.1021/acscchembio.0c00904
- Xue, C., Lin, T. Y., Chang, D., and Guo, Z. (2017). Thioflavin T as an Amyloid Dye: Fibril Quantification, Optimal Concentration and Effect on Aggregation. *R. Soc. Open Sci.* 4, 160696. doi:10.1098/rsos.160696
- Yang, T., Li, S., Xu, H., Walsh, D. M., and Selkoe, D. J. (2017). Large Soluble Oligomers of Amyloid β -Protein from Alzheimer Brain Are Far Less Neuroactive Than the Smaller Oligomers to Which They Dissociate. *J. Neurosci.* 37, 152–163. doi:10.1523/JNEUROSCI.1698-16.2016

- Yuzwa, S. A., and Vocadlo, D. J. (2014). O-GlcNAc and Neurodegeneration: Biochemical Mechanisms and Potential Roles in Alzheimer's Disease and beyond. *Chem. Soc. Rev.* 43, 6839–6858. doi:10.1039/C4CS00038B
- Zhao, J., Liu, X., Xia, W., Zhang, Y., and Wang, C. (2020). Targeting Amyloidogenic Processing of APP in Alzheimer's Disease. *Front. Mol. Neurosci.* 13, 137. doi:10.3389/fnmol.2020.00137

Conflict of Interest: The authors declare that the research was conducted in the absence of any commercial or financial relationships that could be construed as a potential conflict of interest.

Publisher's Note: All claims expressed in this article are solely those of the authors and do not necessarily represent those of their affiliated

organizations, or those of the publisher, the editors and the reviewers. Any product that may be evaluated in this article, or claim that may be made by its manufacturer, is not guaranteed or endorsed by the publisher.

Copyright © 2022 Singh, Regmi, Ormaza, Ayyalasomayajula, Vela, Mundim, Du, Minond and Cudic. This is an open-access article distributed under the terms of the Creative Commons Attribution License (CC BY). The use, distribution or reproduction in other forums is permitted, provided the original author(s) and the copyright owner(s) are credited and that the original publication in this journal is cited, in accordance with accepted academic practice. No use, distribution or reproduction is permitted which does not comply with these terms.



The Cytochrome P450 OxyA from the Kistamicin Biosynthesis Cyclization Cascade is Highly Sensitive to Oxidative Damage

OPEN ACCESS

Edited by:

John D. Wade,
University of Melbourne, Australia

Reviewed by:

Sam P. De Visser,
The University of Manchester,
United Kingdom
Lionel Cheruzel,
San Jose State University,
United States
Giovanna Di Nardo,
University of Turin, Italy

*Correspondence:

Max J. Cryle
max.cryle@monash.edu

[†]These authors have contributed
equally to this work

Specialty section:

This article was submitted to
Chemical Biology,
a section of the journal
Frontiers in Chemistry

Received: 02 February 2022

Accepted: 01 March 2022

Published: 08 April 2022

Citation:

Greule A, Izoré T, Machell D,
Hansen MH, Schoppet M, De Voss JJ,
Charkoudian LK, Schittenhelm RB,
Harmer JR and Cryle MJ (2022) The
Cytochrome P450 OxyA from the
Kistamicin Biosynthesis Cyclization
Cascade is Highly Sensitive to
Oxidative Damage.
Front. Chem. 10:868240.
doi: 10.3389/fchem.2022.868240

Anja Greule^{1,2†}, Thierry Izoré^{1,2†}, Daniel Machell^{1,2,3}, Mathias H. Hansen^{1,2,3},
Melanie Schoppet^{1,2}, James J. De Voss⁴, Louise K. Charkoudian⁵, Ralf B. Schittenhelm^{1,6},
Jeffrey R. Harmer⁷ and Max J. Cryle^{1,2,3*}

¹Department of Biochemistry and Molecular Biology, The Monash Biomedicine Discovery Institute, Monash University, Clayton, VIC, Australia, ²EMBL Australia, Monash University, Clayton, VIC, Australia, ³ARC Centre of Excellence for Innovations in Peptide and Protein Science, Clayton, VIC, Australia, ⁴Department of Chemistry, The University of Queensland, St Lucia, QLD, Australia, ⁵Department of Chemistry, Haverford College, Haverford, PA, United States, ⁶Monash Proteomics and Metabolomics Facility, Monash University, Clayton, VIC, Australia, ⁷Centre for Advanced Imaging, The University of Queensland, St Lucia, QLD, Australia

Cytochrome P450 enzymes (P450s) are a superfamily of monooxygenases that utilize a cysteine thiolate–ligated heme moiety to perform a wide range of demanding oxidative transformations. Given the oxidative power of the active intermediate formed within P450s during their active cycle, it is remarkable that these enzymes can avoid auto-oxidation and retain the axial cysteine ligand in the deprotonated—and thus highly acidic—thiolate form. While little is known about the process of heme incorporation during P450 folding, there is an overwhelming preference for one heme orientation within the P450 active site. Indeed, very few structures to date contain an alternate heme orientation, of which two are OxyA homologs from glycopeptide antibiotic (GPA) biosynthesis. Given the apparent preference for the unusual heme orientation shown by OxyA enzymes, we investigated the OxyA homolog from kistamicin biosynthesis (OxyA_{kis}), which is an atypical GPA. We determined that OxyA_{kis} is highly sensitive to oxidative damage by peroxide, with both UV and EPR measurements showing rapid bleaching of the heme signal. We determined the structure of OxyA_{kis} and found a mixed population of heme orientations present in this enzyme. Our analysis further revealed the possible modification of the heme moiety, which was only present in samples where the alternate heme orientation was present in the protein. These results suggest that the typical heme orientation in cytochrome P450s can help prevent potential damage to the heme—and hence deactivation of the enzyme—during P450 catalysis. It also suggests that some P450 enzymes involved in GPA biosynthesis may be especially prone to oxidative damage due to the heme orientation found in their active sites.

Keywords: cytochrome P450, glycopeptide antibiotic biosynthesis, kistamicin, heme, biosynthesis

INTRODUCTION

The glycopeptide antibiotics (GPAs) are a complex class of non-ribosomal peptides with a range of antibiotic activity against gram-positive bacteria (Greule and Cryle, 2020). These (typically) heptapeptides contain a high proportion of amino acids with aromatic side chains and are particularly rich in non-proteinogenic phenylglycine (4-hydroxyphenylglycine (Hpg) and 3,5-dihydroxyphenylglycine (Dpg)) residues (**Figure 1A**) (Al Toma et al., 2015). In addition, these peptides also bear a number (2–4) of aryl and/or phenolic crosslinks between the side chains of aromatic residues, which serve to rigidify their structures and which are, in turn, essential for their antibiotic

activity (Zhao et al., 2021). While most GPAs are known to inhibit bacterial cell wall division through complex formation with the D-Ala–D-Ala terminus of the cell wall precursor Lipid II (such as the clinically relevant compounds vancomycin and teicoplanin, known as type I–IV GPAs), a subgroup of GPAs containing the compounds complestatin (Chiu et al., 2001), kistamicin (Greule et al., 2019), and corbomycin (Culp et al., 2020) (known as type-V GPAs) display altered peptide structures that include a crosslinked tryptophan residue (**Figure 1A**). These GPAs have recently been demonstrated to exhibit a different type of antibiotic activity by inhibiting the activity of autolysins, peptidoglycan hydrolases responsible for cell wall remodeling during bacterial growth (Culp et al., 2020). Given this novel mode

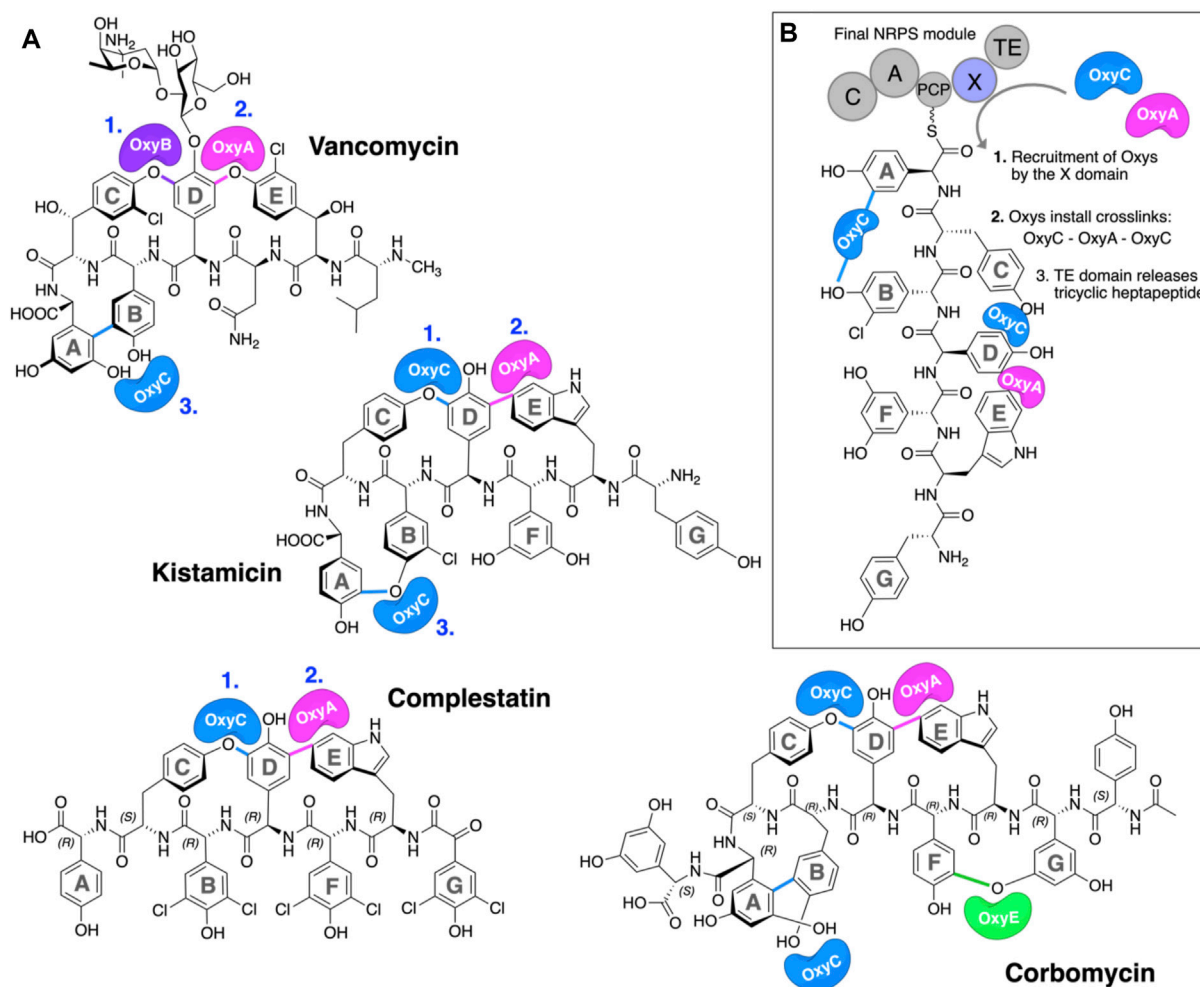


FIGURE 1 | P450-mediated oxidative crosslinking during glycopeptide antibiotic biosynthesis. **(A)** Structure of vancomycin showing the P450-mediated oxidative crosslinking cascade—(OxyB: C–O–D, OxyA: D–O–E, and OxyC: AB) and Type V GPAs (i) kistamicin, whose biosynthesis exploits a bifunctional OxyC enzyme and an OxyA enzyme (OxyC: C–O–D, OxyA: DE, and OxyC: A–O–B); complestatin, whose biosynthesis exploits an OxyC enzyme and an OxyA enzyme (OxyC: C–O–D, and OxyA); and corbomycin, whose biosynthesis exploits a bifunctional OxyC enzyme, an OxyE enzyme, and an OxyA enzyme (tentatively OxyC: C–O–D, OxyE: F–O–G, OxyA: DE, and OxyC: A–O–B, exact timing has not been elucidated). The timing of the Oxy catalyzed crosslinks is indicated by blue numbers when known. **(B)**, boxed] Side chain crosslinking reactions performed during glycopeptide antibiotic biosynthesis take place on the final non-ribosomal peptide synthetase (NRPS) module, while the heptapeptide is connected to a peptidyl carrier protein (PCP); this process requires the essential interaction of the Oxy enzymes with the X-domain (Oxy-recruitment domain), which is unique to GPA biosynthesis. Aromatic rings of the heptapeptide are labeled A–G. Abbreviations: A, adenylation domain; C, condensation domain; Oxy, cytochrome P450 enzyme; PCP, peptidyl carrier protein; TE, thioesterase domain; X, Oxy-recruitment domain.

of activity, such GPAs are of great interest to investigate, both in terms of their structure/activity relationships and their biosynthesis.

Because of their important roles in medicine and as their commercial production remains through the fermentation of producer strains, GPA biosynthesis has been closely investigated (Greule and Cryle, 2020). At the heart of the biosynthesis is a non-ribosomal peptide synthetase (NRPS) assembly line that synthesizes the peptide backbone of GPAs in a stepwise manner (Süssmuth and Mainz, 2017). NRPS biosynthesis centers around groups of repeating catalytic domains—termed modules—that typically serve to introduce a single amino acid into the final peptide. Unlike ribosomal peptide synthesis, NRPS assembly lines directly encode the peptide sequence to be synthesized within the enzymatic domains of the machinery itself. Central to NRPS-mediated biosynthesis is the role of peptidyl carrier proteins (PCPs), which serve as the attachment point for all biosynthetic intermediates during peptide assembly (Izoré and Cryle, 2018). These intermediates are tethered to the PCP domains as thioesters *via* the 4-phosphopantethine (PPant) posttranslational modification found on all such carrier proteins (Süssmuth and Mainz, 2017). Generation of amino acyl-bound PCPs is performed by adenylation (A) domains in a two-step process, first commencing with the selection and activation of the specific amino acid monomer required at the specific stage of NRPS-mediated biosynthesis with consumption of ATP. Having formed a reactive mixed anhydride with AMP, the amino acid is then loaded onto the PCP *via* the attack of this reactive anhydride by the thiol terminus of the PPant arm of the neighboring PCP. From here, aminoacyl-bound PCPs can undergo further modifications *in trans* by a range of enzymes (including halogenases and hydroxylases) (Uhlmann et al., 2013; Kittilä et al., 2017; Kaniusaite et al., 2019) prior to their incorporation into the peptide, which is mediated by condensation (C) domains. In this step, the amino group of the downstream (acceptor) aminoacyl-PCP attacks the thioester of the upstream (donor) amino acid/peptide, leading to peptide bond formation with concomitant transfer of the upstream group onto the downstream aminoacyl-PCP. Such peptidyl-PCP substrates can themselves serve as substrates for additional domains, most commonly seen with epimerization (E) domains, which serve to alter the stereochemistry of the C-terminal residue of the PCP-bound peptide from the (L) to the (D) form.

Once peptide assembly is complete, peptide cleavage from the NRPS usually occurs next in a process that is mostly mediated by thioesterase (TE) domains and that can serve to introduce further modification into these peptides (e.g., through cyclization). In this regard, GPAs represent a unique divergence from this typical NRPS biosynthesis route, for it is at this point in their biosynthesis that the insertion of the side chain crosslinks within the peptide is performed (**Figure 1B**). (Peschke et al., 2017) This process is mediated by the activities of several cytochrome P450 (P450) monooxygenases—termed Oxy_s—which act upon the PCP-bound peptide in the terminal module of the NRPS (Zerbe et al., 2004; Haslinger et al., 2015; Peschke et al., 2016a; Peschke et al., 2016b).

P450s are a superfamily of powerful oxidative hemoproteins that are widely distributed in nature and play diverse roles in biosynthetic processes in bacteria and fungi (Greule et al., 2018). Their prevalence in biosynthesis pathways stems from their unprecedented ability to regio- and stereo-selectively modify nonactivated C–H bonds in complex substrates. Their selectivity and specificity make them premiere biocatalysts, while their range of oxidative transformations is extensive—beyond the archetypal hydroxylation of C–H moieties. P450s are also known to catalyze epoxidation, heteroatom oxidation and aryl crosslinking (as seen in GPAs), among others (Greule et al., 2018). This reactive repertoire stems from their ability to generate a highly electrophilic oxidant—an iron (IV) oxo porphyrin cation radical, termed compound I—(Rittle and Green, 2010) through a complex, step-wise active cycle requiring molecular oxygen and two electrons, themselves delivered sequentially by redox partner enzymes (**Figure 2**). Within the P450 itself, the ligation of the heme iron—*via* a thiolate (i.e., deprotonated) cysteine side chain—is crucial for their ability to generate this extremely powerful oxidizing species (Green, 2009; Yosca et al., 2013), with modification of this cysteine side chain known to prevent the activity of such enzymes (Albertolle et al., 2017). Furthermore, P450s are carefully tuned to avoid autooxidation, especially given the number of Tyr residues found within these enzymes (Yosca et al., 2013). One ongoing area of research in understanding P450 mechanism is the characterization of the pathways of oxidation outside of the canonical C–H hydroxylation reaction, with epoxidation, sulfoxidation, and aromatic crosslinking showing the potential for alternate oxidation pathways. The mechanism through which the P450 (Oxy) enzymes perform the aromatic crosslinking in GPA biosynthesis has been investigated through several techniques (Geib et al., 2008; Holding and Spencer, 2008; Ali et al., 2020; Forneris et al., 2020), with the mechanism suggested to occur *via* two sequential 1-electron oxidation steps as opposed to a typical P450-mediated two-electron oxidation (Ali et al., 2020). The role of the readily abstractable phenolic/indolic protons appears highly important for this process (Forneris et al., 2020), while simultaneously raising the question of autooxidation of active site tyrosine residues in such P450 enzymes (Yosca et al., 2013).

Within GPA biosynthesis, P450s function in a specific, stepwise manner to install the essential side-chain crosslinks in the core peptide in a process that typically requires one Oxy enzyme per crosslink to be installed (Haslinger et al., 2015; Peschke et al., 2016a; Peschke et al., 2016b; Greule and Cryle, 2020). The recruitment of Oxy enzymes to the PCP-bound peptide substrate in these pathways is reliant on interactions of these P450s with the so-called X-domain, a C-type domain unique to the final module of GPA assembly lines (Haslinger et al., 2015; Greule et al., 2019). This interaction is required for the activity of almost all Oxy enzymes, and the discovery of this X/Oxy interaction was crucial to subsequent investigations that sought the reconstitution of GPA peptide crosslinking pathways *in vitro* (Zhao et al., 2021). While experiments studying the process of Oxy-mediated cyclization of peptide *in vitro* have provided a great deal of knowledge regarding the selectivity of this

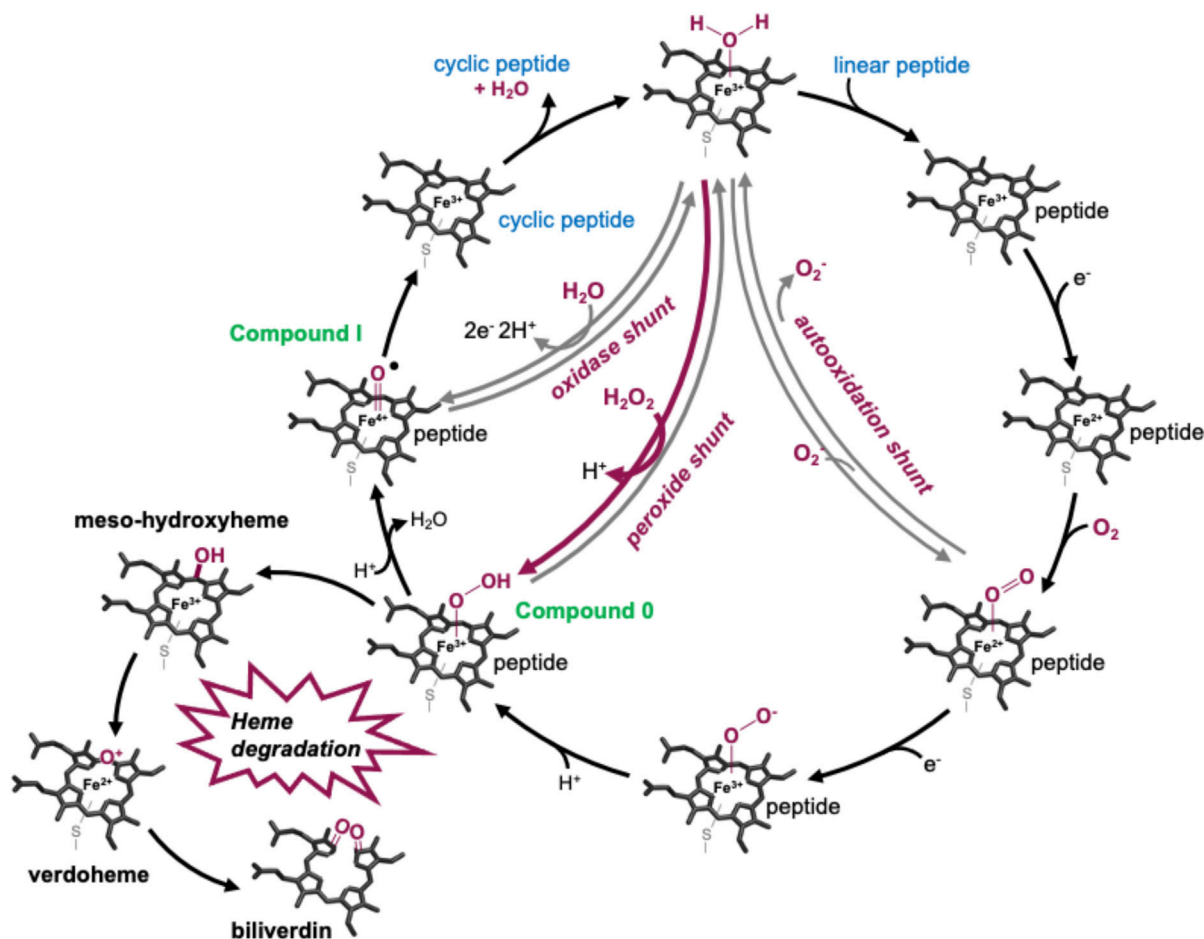


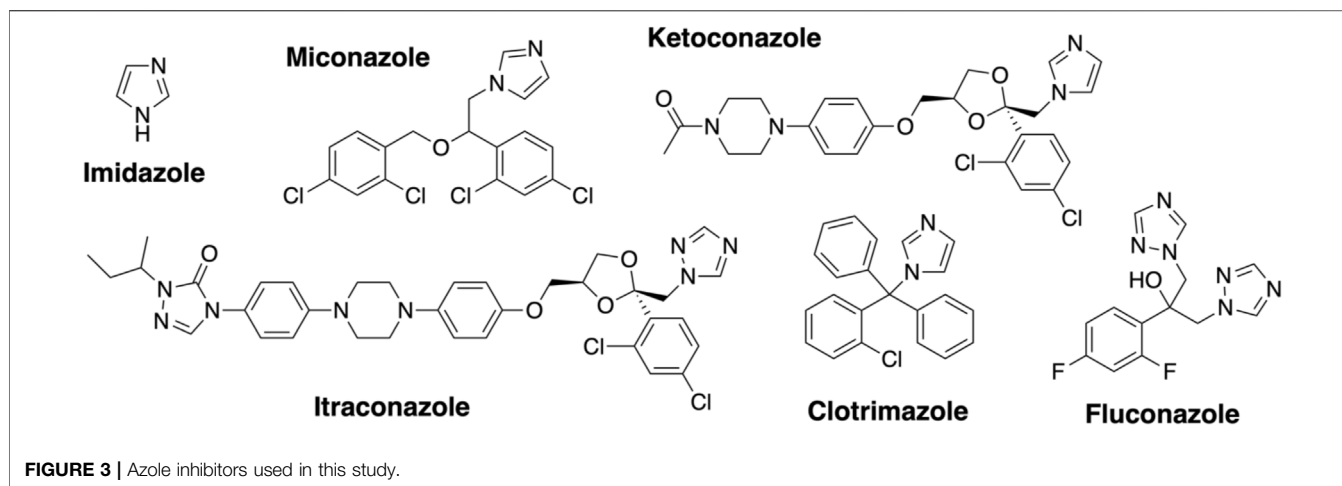
FIGURE 2 | P450-active cycle exemplified for GPA crosslinking together with the heme oxygenase degradation pathway.

process for altered peptide sequences, challenges due to the complexity of the assay, hydrophobic nature of the peptides, and specific nature of the P450 catalysts have made these highly challenging to perform, in turn limiting the scale of the peptide products that can be isolated for further study (Forneris and Seyedsayamdost, 2018; Tailhades et al., 2020; Zhao et al., 2021). In this regard, one glaring omission from *in vitro* experiments into the GPA cyclization cascade is the successful incorporation of the 4-Hpg/Trp crosslink found in Type V GPAs. This limits both the ability to study the selectivity and mechanism of the OxyA enzymes responsible and further the access to homologs of these interesting GPAs *via* biomimetic synthesis. A previous study of the peptide crosslinking cascade in the Type V GPA kistamicin, while revealing important details around the conservation of the Oxy/X interface and dual cyclization activity of the OxyC enzyme in this system, was still unable to reconstitute OxyA activity despite showing good levels of activity for OxyC (Greule et al., 2019). Given that apparent oxidative damage occurs to the Oxy enzymes during *in vitro* reconstitution experiments (and can be averted in some cases through the inclusion of small molecules to reverse this damage) (Tailhades et al., 2019), we undertook here to assess the

susceptibility of OxyA enzymes from Type V GPA biosynthesis to oxidative damage. Our results show that these types of OxyA enzymes are highly prone to oxidative damage by peroxide (a product of non-productive P450 activation) and that the incorporation of the heme moiety in these P450 enzymes appears connected to the presence of such damage. Furthermore, we show that OxyA activity can be reconstituted against small PCP-bound peptide substrates, indicating that the biomimetic synthesis of type V GPAs could well be in reach, provided these reactions are carefully controlled to avoid the generation of unwanted oxidizing species.

EXPERIMENTAL

Site-directed mutagenesis of OxyA_{kis}. To generate the Tyr₉₉ to Phe mutant of OxyA_{kis}, the plasmid pET28a-OxyA_{kis} (6,461 bp) was amplified by PCR using the primer pair ATGGTTGCTCCAGCT TtCTCCGTTCCGCCGGATGC (forward) and TTGCATCCGGCG AACGGAGaAAGCTGGAGCAACC (reverse). The methylated template DNA was digested by *DpnI* restriction endonuclease (NEB), and the linear PCR product was used to transform



chemically competent *E. coli* NEB alpha cells. Positive clones were selected on kanamycin plates, and the desired mutation was verified by DNA sequencing of the isolated, purified plasmid.

Expression and purification of proteins. P450 enzymes. The cloning, expression, and purification of OxyA_{kis}, Y99F OxyA_{kis}, and OxyC_{kis} were described previously (Greule et al., 2019). In brief, for all proteins, 10 L ZYM-50524 autoinduction media was inoculated with 1% (v/v) *E. coli* Arctic Express preculture, supplemented with 50 mg L⁻¹ kanamycin and 0.1 g L⁻¹ of the heme-precursor δ -aminolevulinic acid and incubated for 6 h at 37°C before reducing the temperature to 16°C and allowing the culture to incubate for a further 72 h. The cells were expressed at 120 rpm or 80 rpm shaking. After cell disruption *via* sonication, the P450 enzymes were purified by a combination of Ni-NTA affinity, anion ion exchange, and size exclusion chromatography using an ÄKTA purifier system (GE Healthcare) before being flash-cooled in liquid nitrogen and stored at -80°C.

PCP-X construct. The PCP-X construct from the kistamicin NRPS was expressed and purified as previously reported (Greule et al., 2019).

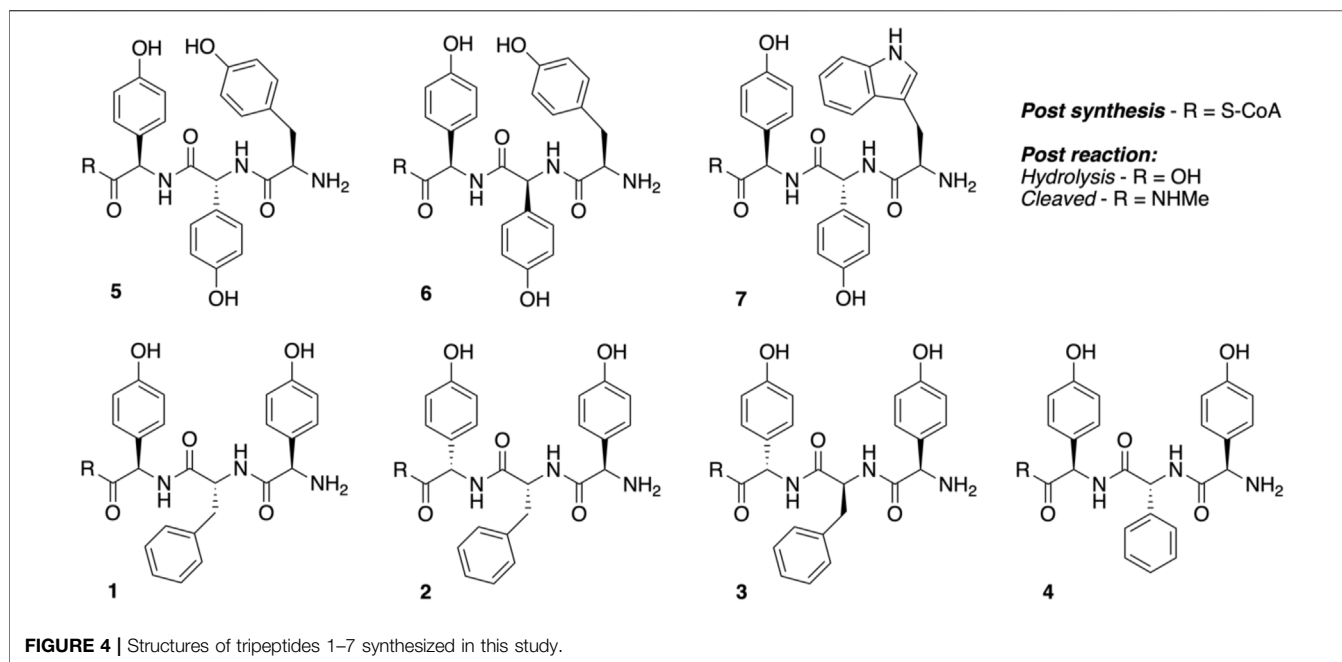
Verification of OxyA_{kis} Y99F mutation by protein mass spectrometry. OxyA_{kis} Y99F was subjected to a tryptic digest and peptide fragments analyzed by a nano LC system (Agilent 1200 series nano) using a Zorbax 300SB-C18 (75 μ m \times 15 cm, nanoViper, C18, 3 μ m, Agilent Technologies) with a trap column Acclaim PepMap 100 (100 μ m \times 2 cm, nanoViper, C18, 5 μ m, 100 Å; Thermo Scientific). The protein masses were detected on a mass spectrometer MicroTOFq (Bruker Daltonics), and peptide fragments were analyzed by MASCOT V2.4 (Matrix Science); SI **Supplementary Figure S4**.

Spectroscopic analysis of P450 enzymes after reduction and CO complexation. Reduced, CO-bound spectra of Y99F OxyA_{kis} were obtained using a Jasco V-750 spectrophotometer at 30°C. The enzymes were diluted to 2.5 μ M in Tris-HCl (50 mM, pH 7.4), reduced using 10 μ L of a saturated solution of sodium dithionite (Sigma) and CO generated by the addition of a small quantity of solid sodium boranocarbonate (Dalton Pharma Services). The UV/Vis spectra were then measured between 390 and 900 nm.

Assessing peroxide-mediated damage of P450 enzymes. Oxy enzymes were diluted to 1 μ M (data shown in Figures 6, 7) or 4 μ M (data shown in Figure 7) in 50 mM Tris-HCl (pH 7.4) in a final volume of 500 μ L. Different concentrations of H₂O₂ (0.4–40 mM) or a saturated *m*-CPBA solution were then added, and the UV/Vis spectra were measured between 390 and 900 nm after various time points using a Jasco V-750 spectrophotometer at 30°C.

Azole inhibitor binding to the Oxy enzymes using UV-Visible spectroscopy. Imidazole (Sigma) was dissolved in water (10 mM stock). Clotrimazole, ketoconazole, fluconazole, miconazole, and itraconazole (Abblis Chemicals LLC, **Figure 3**) were freshly dissolved in DMSO (0.1–10 mM stock solutions). OxyA_{kis} and OxyC_{kis} were diluted to 2.5 μ M in 2 mL Tris-HCl (50 mM) at pH 8 and split into two cuvettes. The spectra were obtained using a dual Jasco V-750 spectrophotometer at 30°C. Different concentrations of the azole compound were added to one cuvette, while in the second cuvette, the same volume of DMSO was added to the protein solution. The spectra were measured between 350 and 600 nm after an equilibration period of 2 min. The absorbance difference ΔA between A_{\max} and A_{\min} was extrapolated and plotted against the azole concentration ($\Delta A = A_{\max} - A_{\min}$); see SI **Supplementary Figure S1**. The maximal amplitudes (ΔA_{\max}) and dissociation constants (K_d) were determined as reported for OxyB_{tei} and OxyA_{tei}.

Electron paramagnetic resonance (EPR) spectroscopy. CW EPR experiments were carried out on a Bruker Elexsys E500 spectrometer equipped with an ElexSys Super High Sensitivity Probehead and an LHe Oxford Instruments cryostat. The magnetic field was calibrated with 2,2-diphenyl-1-picrylhydrazyl ($g = 2.0036$), and measurements were carried out at 7.5 K using a modulation amplitude of 0.5 mT, modulation frequency of 100 kHz, and nonsaturating microwave power of 2 mW (20 dB of 200 W). Simulation of the low-spin P450 signals was carried out with the XShoppe (Hanson et al., 2004). The enzyme (200 μ L/200 μ M in an Eppendorf tube) was treated with 20 μ L of 0.3% H₂O₂ and allowed to react for a specified time before 50 μ L of the



solution was transferred to a quartz EPR tube and flash-frozen in liquid N₂ for CW EPR measurements.

Crystallization, data collection, and structure determination of OxyA_{kis}. The OxyA protein in Tris-HCl (50 mM, pH 7.8) NaCl (200 mM) (15 mg/ml) was crystallized using a sitting-drop vapor diffusion method. Initial screening was performed at the Monash Molecular Crystallization Facility (MMCF), with subsequent optimization performed manually in 48-well sitting-drop plates. The complex was crystallized using a sitting-drop vapor diffusion method by mixing 1 μ L protein with 1 μ L of an optimized reservoir solution containing 0.1 M MMT buffer (molar ratios 1:2:2—DL-malic acid: MES: Tris base pH 6) and 25% PEG 1500. Red crystals formed after 1 week at 20°C. The crystals were cryoprotected by transfer in a drop made of the reservoir solution supplemented with glycerol (30% final concentration, v/v). The crystals were collected in cryoloops and flash-frozen in liquid nitrogen. Data were collected at the Australian Synchrotron (Clayton, Victoria, Australia) on beamline MX1 at 100K. Data processing was performed using XDS (Kabsch, 2010) and AIMLESS as implemented in CCP4 (Collaborative Computational Project Number 4, 1994). The phases were obtained in a molecular replacement experiment using a PHENIX in-built Phaser module (Adams et al., 2010) and with a model generated by PHYPRE (Kelley et al., 2015). The structure was built and refined using COOT (Emsley and Cowtan, 2004) for model building and PHENIX-refine for refinement. All graphics were generated using Pymol (Schrödinger LLC). The sequence alignments were generated using Clustal Omega (Sievers et al., 2011). Data are shown in SI **Supplementary Table S1**.

Soaking of OxyA_{kis} crystals with imidazole. Imidazole was freshly dissolved in DMSO with a final concentration of 10 mM and further diluted to 2 mM in the mother liquor condition +

glycerol. OxyA_{kis} crystals were prepared as previously indicated and soaked/cryoprotected in the solution containing the inhibitor. Data collection was performed as described previously.

Peptidyl synthesis and turnover. Seven tripeptide CoA thioesters (1–7, R = S-CoA; **Figure 4**) were synthesized using the previously reported method for phenylglycine-containing peptides (Brieke and Cryle, 2014; Tailhades et al., 2018) before being enzymatically loaded by the phosphopantetheinyl transferase Sfp (R4-4 mutant) (Sunbul et al., 2009) onto the carrier protein domain of a PCP-X di-domain from the kistamicin NRPS. Turnover of these peptidyl-PCP-X substrates by both OxyA_{kis} and OxyC_{kis} was performed as previously reported (Greule et al., 2019), with the thioester-tethered peptide products liberated as methylamide species (R = NHMe) *via* the addition of methylamine prior to solid-phase extraction and HRMS analysis.

High-resolution mass spectrometry (HRMS) analysis. All high-resolution mass spectrometry measurements were performed on a QExactive Plus mass spectrometer (Thermo Scientific) coupled to a Dionex UltiMate 3,000 RSLCnano system equipped with a Dionex UltiMate 3000 RS autosampler, an Acclaim PepMap RSLC analytical column (75 μ m \times 50 cm, nanoViper, C18, 2 μ m, 100 Å; Thermo Scientific), and an Acclaim PepMap 100 trap column (100 μ m \times 2 cm, nanoViper, C18, 5 μ m, 100 Å; Thermo Scientific). The samples were separated by increasing concentrations of 80% acetonitrile/0.1% formic acid at a flow of 250 nL/min over 30 min. The instrument was operated in alternating data-dependent acquisition (DDA) and parallel reaction monitoring (PRM) cycles, such that for each ms1 precursor scan, five ms2 scans preceded several targeted PRM scans to ensure fragmentation of predefined, sample-dependent m/z precursors. Each survey ms1 scan (250–1,200 m/z) was acquired with a resolution of 70,000 and a normalized AGC (automatic gain control) target of 1e6. Dynamic exclusion was

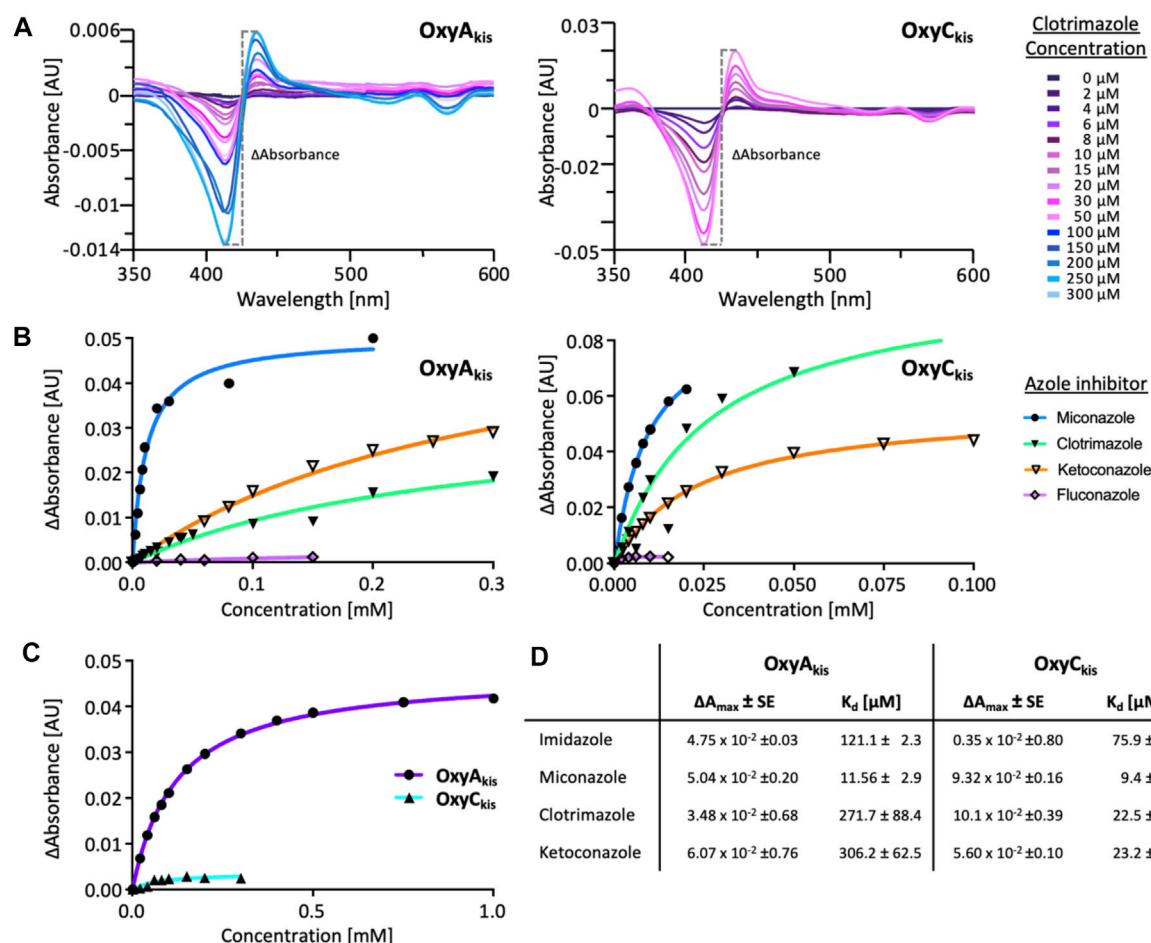


FIGURE 5 | UV-Visible spectroscopic binding studies of OxyA_{kis} and OxyC_{kis} with azole inhibitors. **(A)** Example for the spectral response of OxyA_{kis} (left) and OxyC_{kis} (right) upon different concentrations of clotrimazole. **(B)** Amplitudes of the binding of various azole inhibitors to OxyA_{kis} (left), OxyC_{kis} (right), and imidazole **(C)**. Inhibitors tested: imidazole, miconazole, clotrimazole, ketoconazole, fluconazole, and itraconazole. **(D)** Summary of azole binding to OxyA_{kis} and OxyC_{kis}. ΔA_{max} and K_D derived from the one-site binding model. SE, standard error of the regression.

set to 10 s after one occurrence. The five most intense ions were selected for HCD fragmentation (fixed collision energy mode, 24 HCD collision energy) with a resolution of 17,500 and a normalized AGC target of 1e5. Subsequent targeted PRM scans were acquired with essentially identical settings. The raw data files were analyzed with QualBrowser (XCalibur 3.0.63, Thermo Scientific) to view the spectra and generate extracted ion chromatograms.

RESULTS AND DISCUSSION

Assessing the Heme Environment of the Kistamicin Oxy Enzymes

Given that we had observed a significant difference in activity between the OxyC and OxyA enzymes from kistamicin biosynthesis (OxyC_{kis} and OxyA_{kis}), we first undertook an analysis of the Oxy active sites using the binding of various azole inhibitors to probe the accessibility of the heme iron for

these different structures (Figures 3, 5; Supplementary Figure S1). For the small inhibitor imidazole, OxyA_{kis} showed significant direct binding to the heme iron that was not observed for OxyC_{kis}, which resulted in an order of magnitude increase in the different absorption spectra observed with OxyA_{kis}, despite the affinity being lower for OxyA_{kis} (OxyA_{kis} K_D = 120 μM vs. OxyC_{kis} = 84 μM). In general, OxyC_{kis} displayed higher affinity to all inhibitors than OxyA_{kis}, although these values were lower for both enzymes than those reported for the comparable teicoplanin enzymes OxyA_{tei} and OxyB_{tei} (Haslinger et al., 2014; Haslinger and Cryle, 2016). These data indicate that the heme environment of OxyA_{kis} is significantly different compared to other Oxy enzymes analyzed to date.

OxyA_{kis} is Highly Sensitive to Hydrogen Peroxide

To date, OxyA_{kis} activity had not been observed *in vitro* despite the enzyme showing the requisite 450-nm spectrum upon

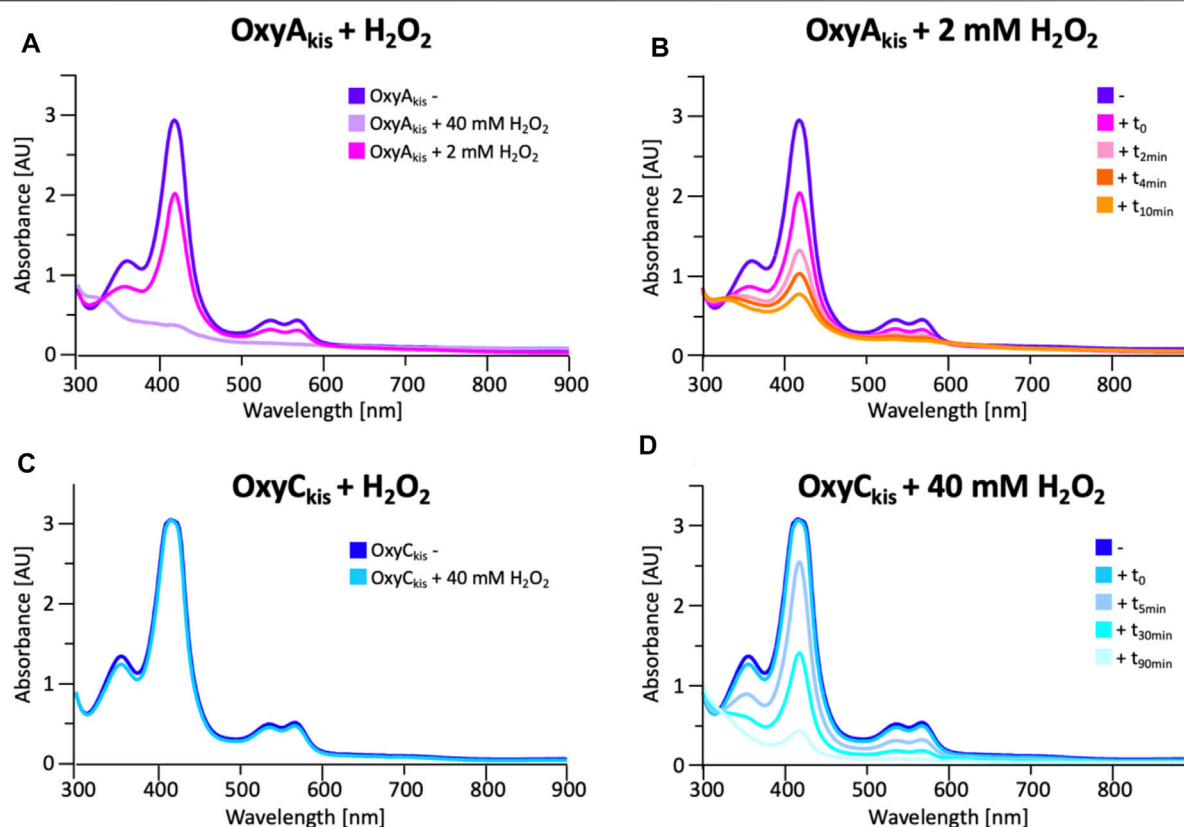


FIGURE 6 | Initial assessment of the effect of hydrogen peroxide addition to the UV/Visible spectra of OxyA_{kis} and OxyC_{kis}. **(A)** UV/Vis spectra of OxyA_{kis} after addition of varying amounts of hydrogen peroxide (t₀). UV/Visible spectra shown from 300 to 900 nm **(B)** Effect over time of addition of 2 mM hydrogen peroxide on the UV/Vis spectra of OxyA_{kis} (300–900 nm). **(C)** UV/Vis spectra of OxyC_{kis} after addition of 40 mM hydrogen peroxide (t₀). UV/Visible spectra shown from 300 to 900 nm **(D)** Effect over time of addition of 40 mM hydrogen peroxide (20x that used with OxyA_{kis}) on the UV/Vis spectra of OxyC_{kis} (300–900 nm).

reduction and CO complex formation, which indicates that the enzyme is expressed in a catalytically competent form. Given that the reconstitution system used with such Oxy enzymes is not natural to the kistamicin producer, we were curious whether this could be causing enzyme inactivation through oxidative damage. Indeed, recent optimization of the GPA cyclization cascade *in vitro* has shown the importance of protecting these P450 enzymes from inactivation over long reactions, presumably caused by oxidative damage (Tailhades et al., 2019). To analyze the sensitivity of both OxyA_{kis} and OxyC_{kis} (that has been shown to be catalytically competent), hydrogen peroxide (H₂O₂) was titrated into solutions of both enzymes, and the resultant damage of the proteins was monitored by a decrease in the absorbance of the 418-nm heme Soret absorbance peak by UV/Vis absorbance spectroscopy (Figure 6).

These experiments showed that there was an obvious difference between these two P450 enzymes. While the addition of a solution of 40 mM hydrogen peroxide led to no obvious change within OxyC_{kis}, the heme signal in the OxyA_{kis} sample is lost almost instantaneously (Figure 6). The use of solutions with a much lower concentration of hydrogen peroxide still led to rapid bleaching of the heme absorption in OxyA_{kis}, with almost no absorbance observed after 10 min

(Figure 7A). OxyC_{kis} is clearly much more stable than OxyA_{kis} to oxidative reagents, as even the use of 20-fold more hydrogen peroxide leads to slower heme bleaching (Figure 7B). The addition of *m*-CPBA does not have such a drastic effect on the Oxy enzymes, with both proteins showing comparable decrease of absorbance (Figures 7C, D). This degradation also displays a different trend to that observed with hydrogen peroxide for the immediate reduction in absorbance upon *m*-CPBA addition does not continue over time. A closer investigation of the UV/Vis spectra of the P450s after hydrogen peroxide treatment also reveals differences between OxyA_{kis} and OxyC_{kis} in the absorption range between 500 and 700 nm. While the β/α bands at 539 and 566 nm of the H₂O₂-treated samples decline in the spectra of both enzymes upon peroxide addition, the spectrum of OxyA_{kis} shows an increase in absorbance between 600 and 700 nm (Figure 8, indicated by an arrow), that is not present in OxyC_{kis}. Such an increase is reminiscent of the absorption spectra of the verdoheme intermediate formed by the heme-degrading enzyme heme oxygenase, and although the absorption shoulder present in the OxyA_{kis} spectra is not as significant as in the case of heme oxygenase, this could be due to the instability of such heme

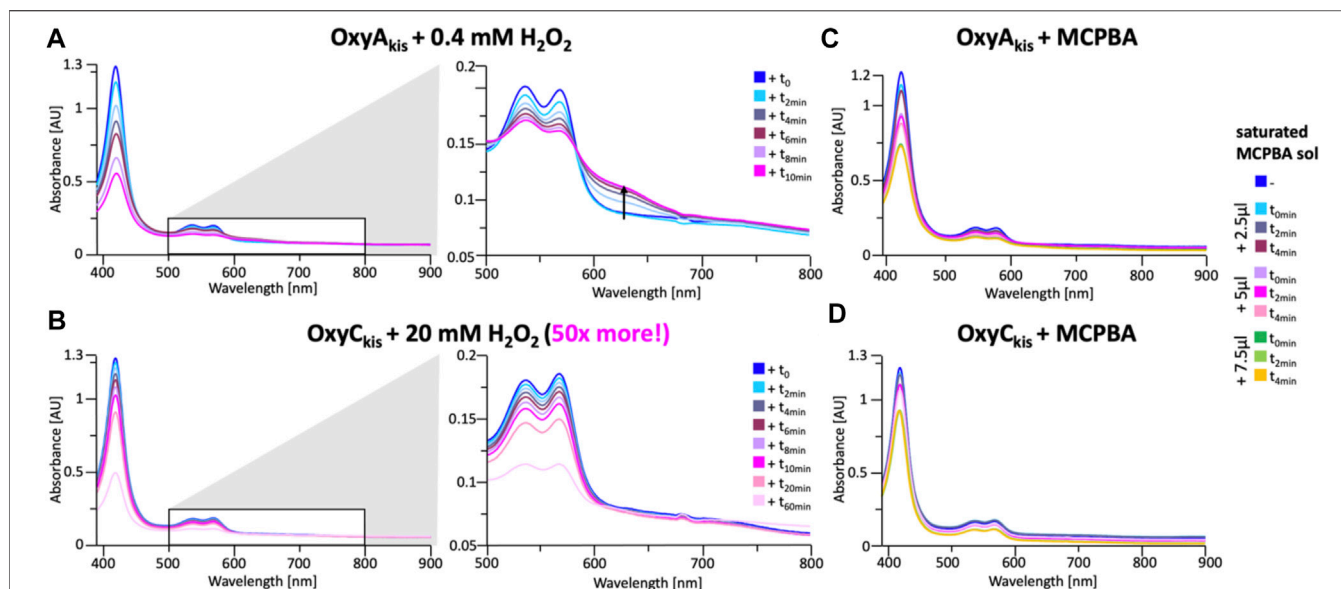


FIGURE 7 | Time-dependent UV/Visible spectra of OxyA_{kis} and OxyC_{kis} after addition of hydrogen peroxide and *m*-CPBA. **(A)** UV/Vis spectra of OxyA_{kis} after addition of 0.4 mM hydrogen peroxide at different time points. UV/Visible spectra shown from 390 to 900 nm (left panel) and a zoomed view of 500–800 nm (center panel). The shoulder in absorbance between 600 and 700 nm is indicated by an arrow. **(B)** UV/Vis spectra of OxyC_{kis} after addition of 20 mM hydrogen peroxide (50 times more than OxyA_{kis}) at different time points. UV/visible spectra shown from 390 to 900 nm (left panel) and a zoomed view of 500–800 nm (center panel). It is to be noted that no shoulder in the absorbance signal is present. UV/Vis spectra of **(C)** OxyA_{kis} and **(D)** OxyC_{kis} after addition of a saturated *m*-CPBA solution.

species under aerobic conditions (Matsui et al., 2005; Uchida et al., 2017). It is curious that this absorbance shoulder is not present in the *m*-CPBA-treated solutions.

To determine whether these responses to peroxide treatment are general for these types of P450s from the biosynthesis of type-V GPAs, the complestatin Oxy homologs ComI (OxyA_{com}) and ComJ (OxyC_{com}) were also treated with hydrogen peroxide and their spectra analyzed (Figure 8; SI Supplementary Figure S2 and Supplementary Figure S3). (Chiu et al., 2001; Mollo et al., 2017) Measurement of OxyC_{com} was challenging because of gas evolution in the cuvette, which shows that this P450 displays significant catalase activity; this enzyme also appears to be very stable to peroxide treatment. Treatment of OxyA_{com} with peroxide shows a similar trend of increased sensitivity to oxidative heme bleaching compared to OxyC_{com}, although it is significantly more stable than OxyA_{kis}. Neither of the complestatin P450s showed increase in the absorbance between 600 and 700 nm, which showed that the damage occurring in the OxyA_{kis} enzyme was unusual and, thus, worthy of further investigation, given the possible parallels to heme oxygenase chemistry in this case.

EPR Measurements of OxyA_{kis} and OxyC_{kis} During Peroxide Treatment.

To shed further light on the mechanism of heme damage occurring in the treatment of OxyA_{kis} and OxyC_{kis} with hydrogen peroxide, we performed continuous wave (CW) electron paramagnetic resonance (EPR) spectroscopic experiments on these enzymes both before and after treatment with varying amounts of peroxide (Figure 9). Before treatment, both enzymes exhibit a

low-spin (LS, $S = \frac{1}{2}$) EPR signal characteristic of the Fe³⁺ ion of heme (Harbort et al., 2017). Upon addition of 20 µL of 0.3% H₂O₂ to 200 µL of 200 µM protein, OxyA_{kis} completely loses its LS heme signal in less than 2 min, and a large signal appears at 156 mT ($g = 4.27$), indicating that the iron has been removed from the heme and is now in a high-spin state ($S = 5/2$). By comparison—and even after 10 min of H₂O₂ exposure—OxyC_{kis} retains the same EPR signal as prior to peroxide addition, together with the same intensity (concentration of LS centers) within experimental error (~10%). Furthermore, after 20 min, this LS EPR signal from the Fe³⁺ heme is reduced by only ~50% (data not shown), showing yet again the increased stability of OxyC_{kis} to hydrogen peroxide when compared to the behavior of OxyA_{kis}.

While these experiments did not provide supporting evidence for a distinct oxidized heme intermediate, they did indicate that the loss of heme from these proteins was *via* oxidative damage. Given that the intermediates involved in this oxidative process were clearly unstable, we next turned to high-resolution X-ray crystallography to assess the OxyA_{kis} active site and determine whether features in the heme environment could be implicated in the relative instability of this P450.

Structural Characterization of OxyA_{kis}

To elucidate the structural implications of P450 inactivation *via* oxidative damage, we turned to X-ray crystallography. Prior to this study, we solved the structure of OxyA_{kis} in the complex with the NRPS recruitment X-domain from the last module of kistamicin NRPS to a resolution of 2.6 Å (Greule et al., 2019). This complex showed that the overall structure of OxyA_{kis} corresponded well to that reported for other Oxy enzymes and

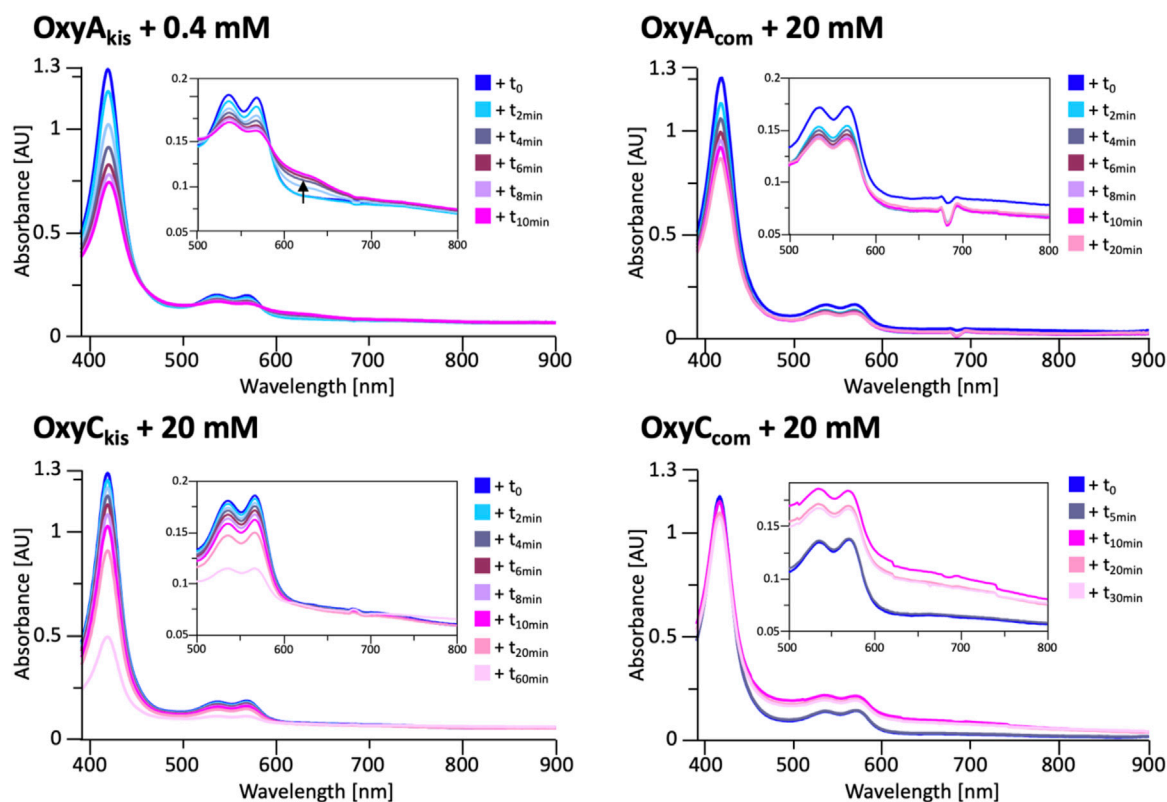


FIGURE 8 | UV/Vis spectra measurement of OxyA_{kis} and OxyC_{kis} and the complestatin homologs OxyA_{com} and OxyC_{com} after addition of hydrogen peroxide. The inset in each panel shows the absorption region between 500 and 800 nm, revealing that the unusual shoulder between 600 and 700 nm is only observed in the case of OxyA_{kis}.

that the interface between the Oxy enzymes and X-domain was conserved to that reported in related systems. However, the resolution of this complex was insufficient to obtain a detailed understanding of the heme environment of this P450. Thus, we sought to crystallize OxyA_{kis} alone, and we were able to identify conditions in which the P450 would crystallize and diffract to high resolution (1.6 Å, **Figure 10A**, SI **Supplementary Table S1**).

With OxyA_{kis} no longer in complex with the X-domain, we observed some changes to the flexible regions of the P450, noting that the loop connecting the F and G helices could no longer be resolved due to lack of clear density and suggesting that this loop is stabilized in the complex. Additional gaps in the structure of mobile sites surrounding the heme and active site were present, suggesting that these regions are disordered without the bound substrate, which is in keeping with results from many structurally characterized P450s. Despite these minor differences, the overall fold of OxyA_{kis} remained largely identical to the structure previously solved in complex with the X-domain (RMSD = 0.47 Å, **Figure 10B**) (Greule et al., 2019).

With the general fold essentially unchanged, we performed a detailed analysis of the active site of this P450, which revealed a mixed population of heme orientations as seen in the Fo–Fc difference map electron density at the substituent vinyl and methyl groups (**Figures 11A,B**). With few reported exceptions, P450s incorporate the heme moiety, such that the β -position of

the heme is placed under the central I-helix, which means that the vinyl and methyl groups at positions 4/5 of the heme also reside under the I-helix (Rudolf et al., 2017). Much less common are examples of P450s in which the heme is inserted in a “flipped” orientation, meaning that the δ -position of the heme (and neighboring 1-methyl and 2-vinyl groups) is placed under the I-helix: examples of P450s displaying this heme orientation include CYP154A1 (PDB ID:1ODO) (Podust et al., 2004), SgvP (4MM0) (Li et al., 2017), CYP105P2 (5IT1) (Lee et al., 2016), StaF (PDB ID: 5EX8) (Ulrich et al., 2016), and OxyA_{tei} (PDB ID: 5HH3) (Haslinger and Cryle, 2016). In this context, CYP121A1 (PDB ID: 1N40) is the only example of a P450 showing a 50:50 mixture of the heme orientations within the active site (Leys et al., 2003). The reasons and mechanism responsible for this distinct preference of one heme orientation within P450s are not yet understood, and it is unclear whether the alternate heme orientation influences the catalytic activity of these enzymes. Two of the P450s with variant heme orientations are OxyA homologs from glycopeptide antibiotic (GPA) biosynthesis that catalyze oxidative phenolic coupling (OxyA_{tei} from teicoplanin biosynthesis and StaF from A47934 biosynthesis) (Haslinger and Cryle, 2016; Ulrich et al., 2016), while CYP121A1 catalyzes the related process of aryl crosslinking in mycrocyclosin. Given that P450s from GPA biosynthesis are overrepresented in the structurally characterized P450s bearing

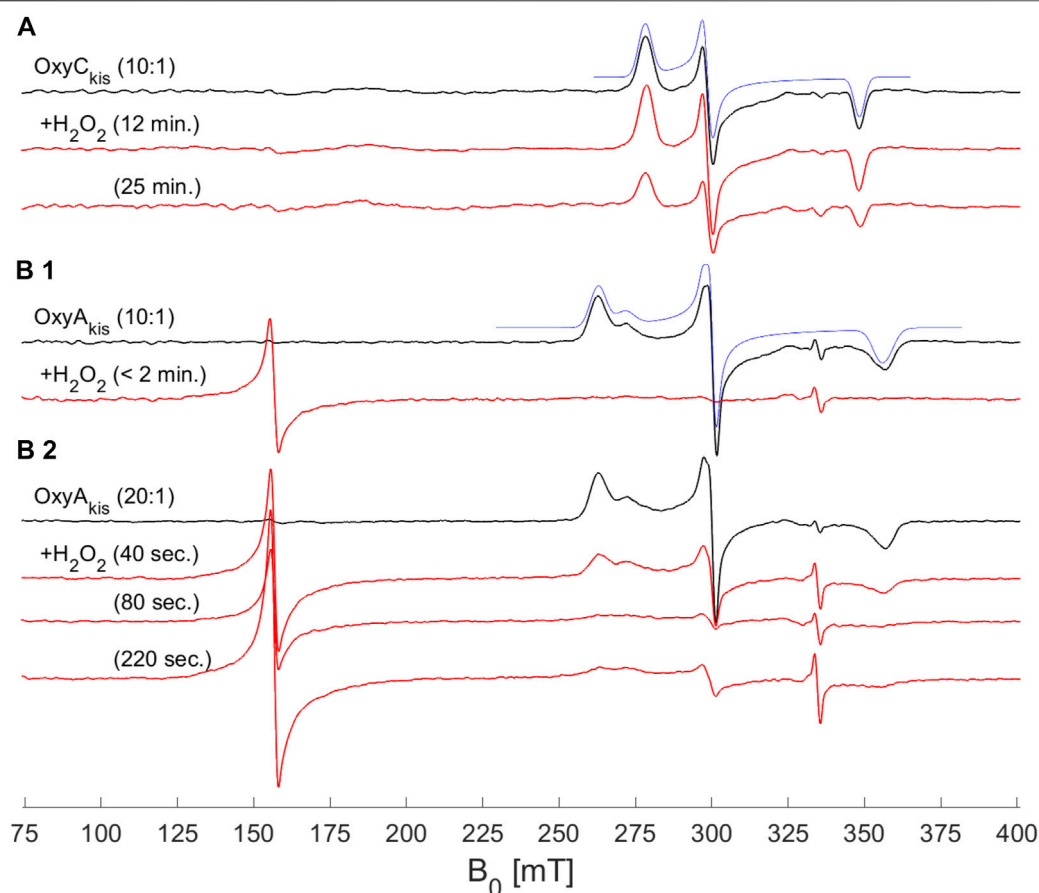


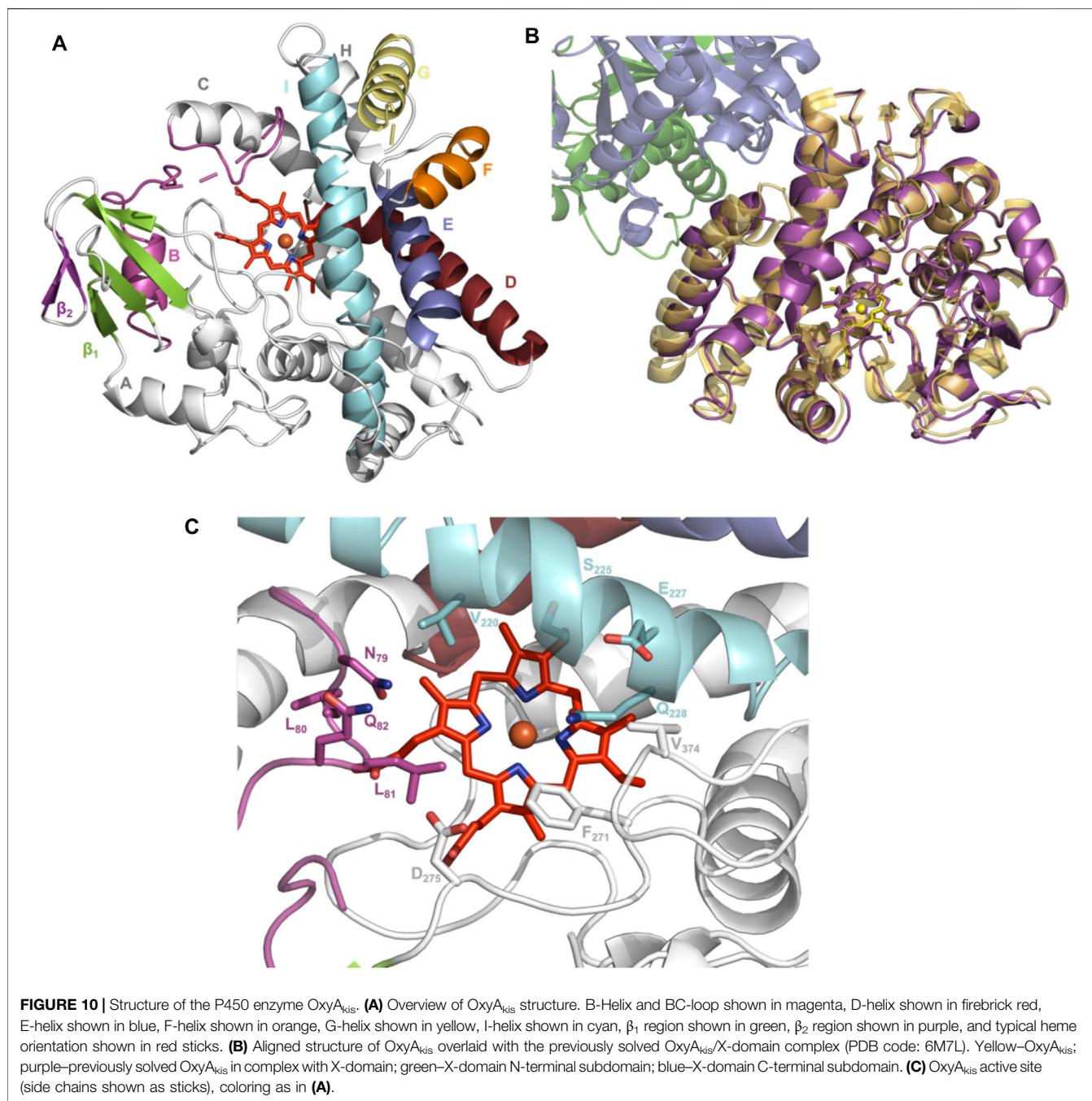
FIGURE 9 | EPR spectra of OxyA_{kis} and OxyC_{kis} after addition of hydrogen peroxide. (X-band (9.383 GHz) CW EPR spectra measured at 7.5 K on OxyA_{kis} and OxyC_{kis} (concentration 200 μ M, black lines) before and after addition of a 0.3% hydrogen peroxide solution for the indicated reaction times (red lines). **(A)** OxyC_{kis} after addition of H₂O₂ at a 10:1 volume ratio (protein:H₂O₂). **(B1)** OxyA_{kis} after addition of H₂O₂ at a 10:1 volume ratio. **(B2)** OxyA_{kis} after addition of H₂O₂ at a 20:1 volume ratio (protein:H₂O₂). The low-spin OxyC_{kis} spectrum is simulated with a single paramagnetic component (blue line) with g-values of $g = (2.410, 2.245, \text{ and } 1.924)$ and the low-spin OxyA_{kis} spectrum with a two-component model, $g_A = (2.551, 2.232, \text{ and } 1.879)$ (77%) and $g_B = (2.469, 2.249, \text{ and } 1.893)$ (23%) (blue line). Several EPR components are often observed in the resting state of P450s, and this is attributed to different conformations of coordinated water/residue side chains in the active site. The large signal at ~ 156 mT in the OxyA_{kis} data is assigned to non-heme iron. The small sharp signal at 335 mT is from an unassigned organic radical.

the alternate heme conformation, we explored various ratios of the heme orientations that could model occupancies (2:1 ratio) of a flipped heme ligand in the structure of OxyA_{kis}.

However, even once the density of the methyl/vinyl groups was well-explained by a mixture of heme orientations; there was still evidence for additional density at the side of the heme immediately below the I-helix (β -position, **Figure 11C**). Given that heme oxygenase chemistry exploits the hydroxylation of heme during its degradation, it is tempting to speculate that this density may represent hydroxylation of the heme (albeit, here the hydroxyl group would be located at a different position of the heme (β versus α position in the heme oxygenase reaction)). To explore the possibility of radiation damage to the heme due to long data collection causing this modification, we collected several datasets using an attenuated beam. Even with a beam attenuation of 95% and collecting data in small wedges to reduce possible damage, this dataset still showed density in

the difference map for modification at the β -position of the heme (**SI Supplementary Table S1**).

With a possible correlation of the orientation of the heme moiety within the OxyA_{kis} active site with this unusual density, we next sought to determine if this was dependent on the orientation of the inserted heme. To carry out this, we crystallized OxyA_{kis} from additional expression batches and observed that the orientations of the heme ligand occupied were batch-specific. Furthermore, we identified a batch in which all proteins contained entirely the typical P450 heme conformation, from which we then solved a structure to a resolution of 1.8 Å (**SI Supplementary Table S1**). This structure was essentially identical to that of the isolated OxyA_{kis} structure we had solved initially (RMSD = 0.68) with the heme present in the active site in the typical orientation seen with most P450s, revealing that the orientation of the heme does not otherwise impact the fold of the P450s. A closer investigation of the heme moiety in this structure revealed no additional density present at the β -position, supporting a correlation between the



additional density on the heme moiety and orientation of the heme itself.

Improved OxyA_{kis} Stability is Enabled by Tyr99 to Phe Mutation

GPA crosslinking is implicated to occur *via* two 1-electron oxidation steps, which generate intermediate phenolic/indolic radical species (Ali et al., 2020). Given this, the potential for autooxidation of Tyr residues close to the P450 active site appears to be a particular challenge for this subclass of P450 enzymes to

overcome. Having seen the extreme sensitivity of OxyA_{kis} for oxidative damage, we inspected the P450 active site for Tyr residues close to the heme to ascertain whether such residues could be playing a role in this sensitivity. The tyrosine residue at position 99 (position 119 in the His-tagged OxyA_{kis} protein) is oriented in such a way that the phenol moiety is very close to the site of additional density present in the OxyA_{kis} structure (distance from the phenol to the site of damage is 3.7 Å). This residue also appears to coordinate a water molecule [2.4 Å; 4 Å from the β -position; 2.7 Å to another molecule (water 202)]. Given this positioning, we performed the sequence alignment of

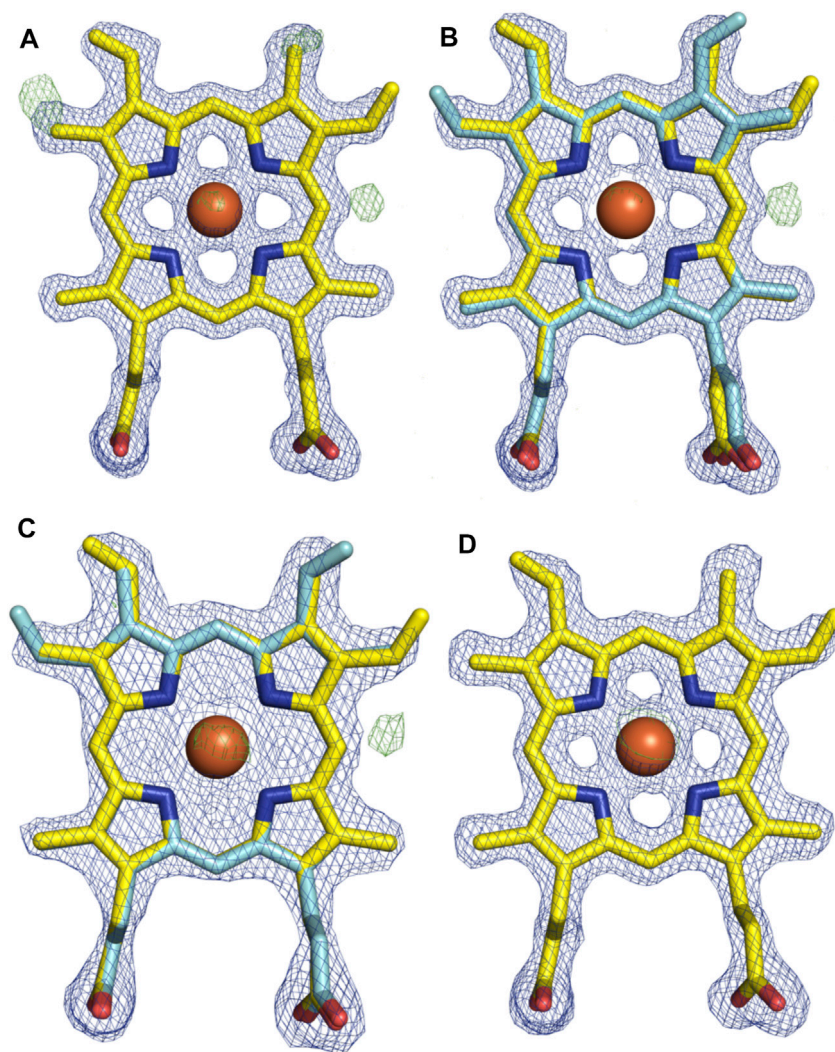
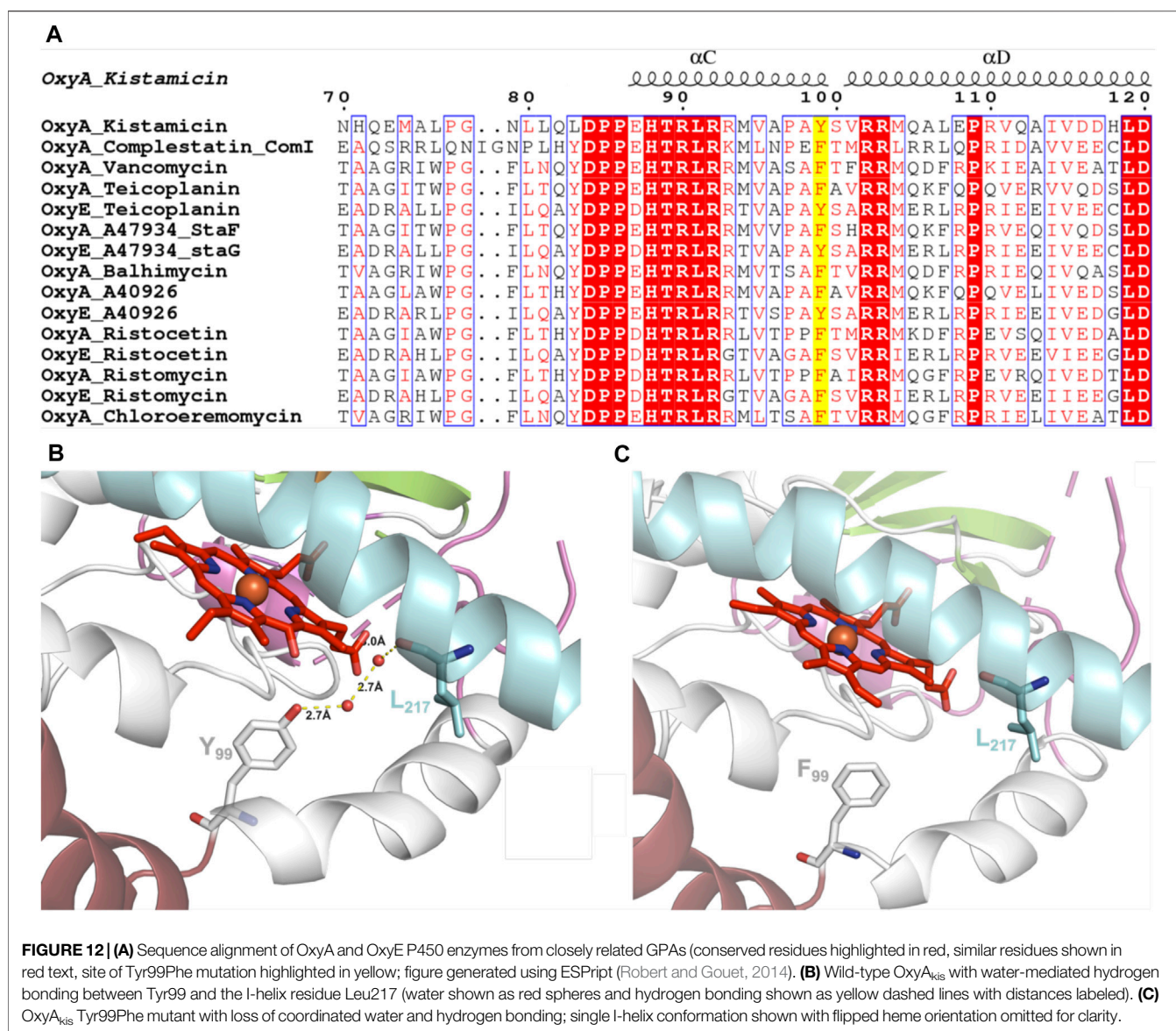


FIGURE 11 | Comparison of the electron density around the heme moiety in OxyA_{kis} structure refinement using differing ratios of typical and “flipped” heme orientations. Electron density map (blue mesh; $+1.5\sigma$ 2mFo-DFc) and difference map (green mesh; $+3\sigma$ mFo-DFc) after refinement of fitted heme ligands. **(A)** Initial data set modeled with 100% typical heme orientation (yellow sticks). **(B)** Initial data set modeled with typical and flipped heme ligand fitted at a 2:1 ratio (0.67 and 0.33 occupancy). **(C)** Low-dose X-ray data collection modeled with typical and flipped orientation at the same ratio as above. **(D)** Subsequent protein batch with typical heme orientation fitted. Yellow—carbon atom, typical heme orientation; cyan—carbon atom, flipped conformation; orange—carbon atom, flipped conformation and modified heme; red—oxygen atom; blue—nitrogen atom; orange sphere—iron atom.

multiple Oxy enzymes from different GPA pathways, which revealed that in most Oxy enzymes, the Tyr99 position is typically occupied by a phenylalanine residue instead (**Figure 12A**). Indeed, the presence of a tyrosine residue at this position is only observed in the OxyA_{kis} and in a group of closely related OxyE enzymes (OxyE_{dbv} from A40926 biosynthesis, OxyE_{tei} from teicoplanin biosynthesis, and OxyE_{sta} from A47934 biosynthesis), which are responsible for the installation of the additional F–O–G ring observed in teicoplanin-like GPAs (Cryle et al., 2011; Peschke et al., 2016c). However, in the structure of the only OxyE homolog to be crystallized, OxyE_{tei}, different I-helix residues alter the environment of the equivalent Y99 residue, with Asn223 in OxyE_{tei} in hydrogen bonding distance to this phenol moiety

(2.5 Å) compared to the equivalent residue in OxyA_{kis} (Val221, 4.1 Å from the phenol moiety) (Cryle et al., 2011).

As the phenol group present in Tyr99 appeared to be appropriately positioned to play a role in potential oxidative heme damage in the catalytic site of OxyA_{kis}, we next cloned a mutant in which Tyr99 was mutated into Phe by site-directed mutagenesis. Verification of the mutation by DNA sequencing and protein mass spectrometry following the expression and purification of the mutant protein indicated that the mutation was present in this protein (SI **Supplementary Figure S4**). The reduced, CO-bound spectra of the OxyA_{kis}-Y99F mutant enzyme showed that the heme environment of the mutant was preserved and that the enzyme was catalytically competent, with a high proportion of the 450 versus 420 nm species present (**Figure 13**).



The addition of H₂O₂ revealed that the mutant enzyme was slightly more stable to oxidative damage than the wild-type enzyme, although the mutant still exhibits the shoulder between 600 and 700 nm and is more sensitive to oxidizing agents than OxyC_{kis} (Figure 7).

To examine this mutant further, OxyA_{kis}-Y₉₉F was crystallized under the same conditions used for the native OxyA_{kis}. These crystals, which are diffracted to a resolution of 1.8 Å (Figure 12B, SI Supplementary Table S1), showed a mixed population of heme orientations in the enzyme active site (6:1 normal orientation/flipped orientation). Interestingly, no additional density has been observed at the β-position of the heme moiety as had been previously observed with the WT crystals. We observed weak and somewhat distorted electron density for the mutated phenylalanine residue itself, suggesting that the side chain exists in multiple conformations in the structure (SI Supplementary Figure S5). Furthermore, it appears that

residues 223–228 of the I-helix now adopt two conformations above the heme moiety. In the wild-type structure, a network of hydrogen bonding is observed between the Tyr99 phenol moiety and amide backbone of the I-helix residue Leu217, mediated via two water molecules (Figure 12C). The Tyr99Phe mutation results in the loss of this H-bond network (Figure 12D), which we then attribute to the differences seen in the structure by permitting both the increase in flexibility of the Phe99 side chain and further the second conformation adopted by the I-helix. While unusual, the CO spectra of the mutant shows that it retains the heme thiolate ligand, suggesting that this alternate conformation of the I-helix does not appear to dramatically influence the incorporation of the heme moiety.

Tripeptide Cyclization Using OxyA_{kis}

Having seen that OxyA_{kis} is, indeed, highly susceptible to oxidative damage, we finally sought to reconstitute activity

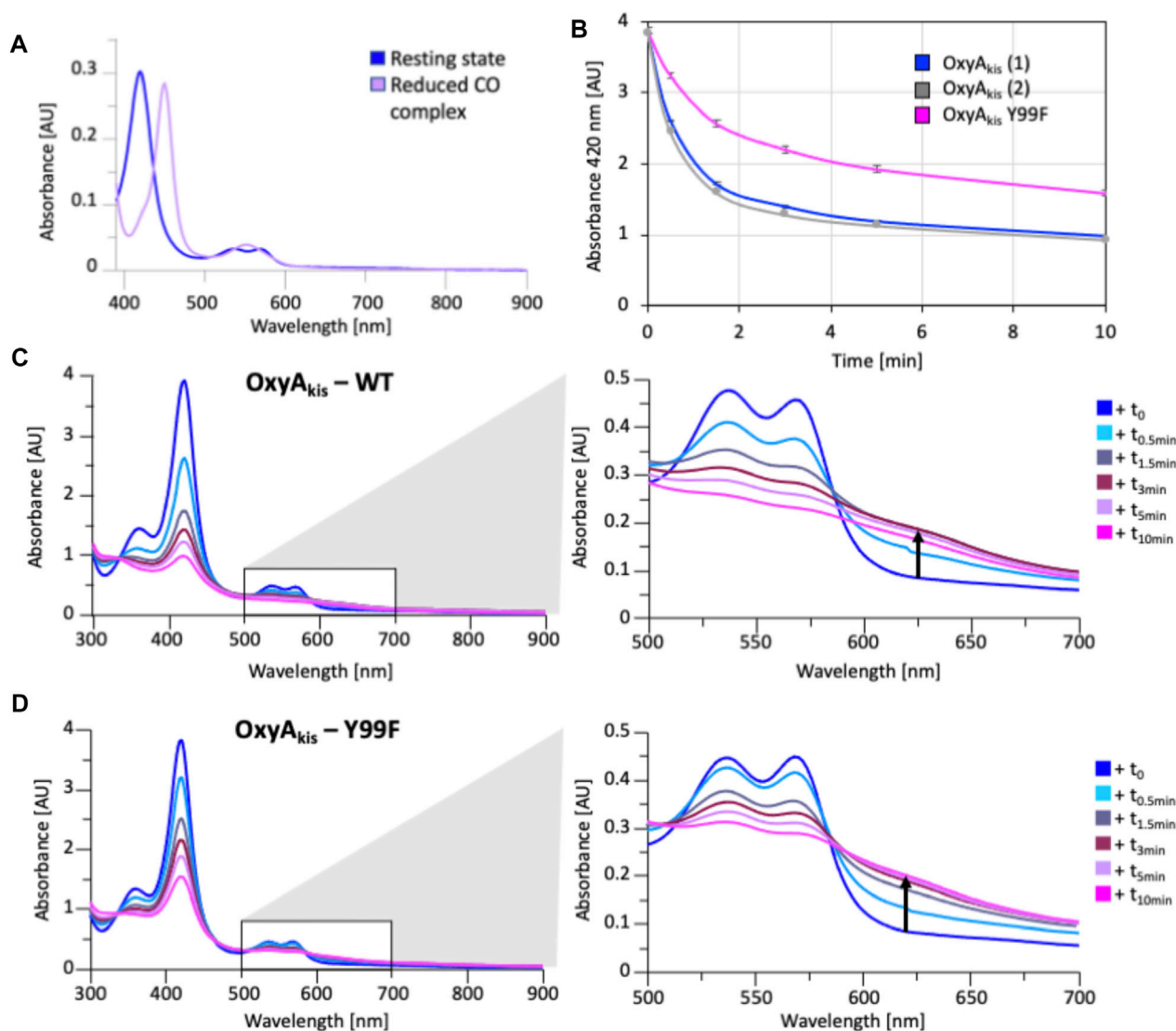


FIGURE 13 | Characterization of OxyA_{kis} Tyr₉₉Phe mutant. **(A)** UV/Vis spectra showing the conversion of the resting state spectra (blue) into the reduced CO difference spectra (mauve); the shift to 450 nm indicates the catalytic competence of the P450. **(B)** Rate of bleaching of the heme Soret peak (420 nm) of OxyA_{kis} upon peroxide addition of expression batches 1 (blue) and 2 (gray) of the WT proteins plus the Y₉₉F mutant (pink). **(C)** UV/Vis spectra of OxyA_{kis} after addition of 0.4 mM hydrogen peroxide at different time points. UV/visible spectra shown from 390 to 900 nm (left panel) and a zoomed view of 500–800 nm (center panel). The shoulder in absorbance between 600 and 700 nm is indicated by an arrow. **(D)** UV/Vis spectra of the OxyA_{kis} Y₉₉F mutant after addition of 0.4 mM hydrogen peroxide at different time points. UV/visible spectra shown from 390 to 900 nm (left panel) and a zoomed view of 500–800 nm (center panel). The shoulder in absorbance between 600 and 700 nm is indicated by an arrow.

from this enzyme in a manner that would provide greater probability for success. The natural peptide substrate of OxyA_{kis} is both hydrophobic and requires prior OxyC_{kis} activity to insert the C–O–D ring, so we turned to the approach first pioneered by Robinson et al., in their studies with OxyB_{van} and sought to directly cyclize minimal PCP-X-bound tripeptides (Woithe et al., 2007; Woithe et al., 2008), given that our experiments with multienzyme cascades and complex peptide substrates had previously failed. To this end, we synthesized a panel of seven tripeptide CoAs based on common residues found in Oxy-

mediated crosslinks (Hpg, Tyr, and Trp) in positions 1 and 3 of the peptide together with variable residues in position 2 (Phe, Phg, and Hpg) of these peptides (1–7); the effect of altering the stereochemistry of positions 2 and 3 in the peptide was also explored. Following their synthesis and enzymatic loading onto a PCP-X_{kis} construct using the promiscuous transferase Sfp, we next subjected these seven peptides to enzymatic turnover by both OxyC_{kis} and OxyA_{kis} (Table 1). As had been anticipated based on previous results, OxyC_{kis} displayed high (>70%, 5, 6) and moderate turnover (>25%, 1, 7) of four peptides, with only trace modification of

TABLE 1 | Structure of tripeptide substrates **1–7** and the results of cyclization assays performed using the kistamicin, OxyC, and OxyA enzymes.

Peptide	AA ₁ residue (N) identity	AA ₂ residue identity	AA ₃ residue (C) identity	OxyC _{kis} cyclization ^b	OxyA _{kis} cyclization ^b
1	(D)-Hpg	(D)-Phe	(D)-Hpg	31%	8%
2	(D)-Hpg	(D)-Phe	(L)-Hpg	Trace	—
3	(D)-Hpg	(L)-Phe	(L)-Hpg	Trace	—
4	(D)-Hpg	(D)-Phg	(D)-Hpg	Trace	—
5	(D)-Tyr	(D)-Hpg	(D)-Hpg	85%	46%
6	(D)-Tyr	(L)-Hpg	(D)-Hpg	71%	35%
7^a	(D)-Trp	(D)-Hpg)-Hpg	30%	—	—

^aNatural kistamicin mimic [residue 2 altered from (D)-Dpg to (D)-Hpg due to lack of commercial availability].

^bProportion of the cyclized peptide based on the HRMS analyses; percentage calculated by dividing the peak area of the cyclic peptide product by the total peak area of (starting material plus product). Hydrolysis of the peptide product was low (<5% in all cases); hence, only the methylamide products generated through methylamine workup of the turnover reactions are included here.

the remaining peptides (**2, 3, 4**). In comparison, OxyA_{kis} (new batch, single anticipated heme geometry present) displayed no activity toward four of the peptides, including the Trp-containing peptide. Gratifyingly, however, cyclization activity was observed to low levels with **1** and moderate levels with peptides **5** and **6**. These peptides mimic the stereochemistry of the residues involved in the natural ring formed by OxyA_{kis} and further show that while the natural Trp residue is not accepted (possibly due to lack of steric restraint in these tripeptides as would be seen in the biosynthetic monocyclic heptapeptide), OxyA_{kis} can instead install aromatic crosslinks between phenol-containing aromatic side chains. This supports the versatility of such P450 enzymes for aromatic crosslinking between a range of possible side chains (demonstrated in the OxyC_{corb} cyclization of Tyr-Hpg instead of Hpg-Hpg in the final OxyC-mediated crosslink) (Culp et al., 2020), which can also lead to different crosslinked species in these peptides (as seen with OxyC_{kis}-mediated insertion of both phenolic and aryl crosslinks) (Greule et al., 2019). Such versatility helps explain why the OxyA and OxyE enzymes found in the corbomycin gene cluster can install different crosslinks (an aryl Trp-Hpg vs. phenolic Dpg-Hpg crosslink, respectively) despite the sequence similarity they display. These results demonstrate that the reconstitution of type V GPA OxyA enzymes *in vitro* is feasible—albeit challenging—and that this could be investigated for chemically synthesized monocyclic peptide substrates in future experiments. Furthermore, they indicate that the roles for such P450s in engineered complex peptide crosslinking pathways could well be more flexible than has perhaps seemed likely to date, opening further opportunities to exploit such enzymes as diverse biocatalysts.

CONCLUSION

Structural and biochemical analysis of OxyA_{kis} has shown that this P450 enzyme is highly prone to oxidation and can display an atypical heme orientation in different protein batches. Crystallographic experiments revealed additional unexplained density adjacent to the heme moiety in structures where this alternate heme conformation was

present, suggesting that P450s may prefer their typical heme orientation to avoid potential oxidative damage. Turnover experiments with OxyA_{kis} have shown that it is possible to reconstitute peptide crosslinking activity from this enzyme, although it remains highly sensitive to oxidation and unsuitable for inclusion in multienzyme cascades. This is a challenge that needs to be overcome to explore both the selectivity of this central Type V GPA crosslinking enzyme and exploit this crosslinking for the generation of diverse crosslinked GPA peptides *in vitro*. Given that GPA homologs are known to exhibit significantly different activity on reconstitution, this suggests that further examples of OxyA enzymes from Type V systems should be sought and analyzed to identify candidates for future research concerning the GPA cyclization cascade.

DATA AVAILABILITY STATEMENT

The datasets presented in this study can be found in online repositories. The names of the repository/repositories and accession number(s) can be found at <http://www.wwpdb.org/>, 7TTA, 7TTB, 7TTO, 7TTP, 7TTQ; <http://www.proteomexchange.org/>, PXD030867.

AUTHOR CONTRIBUTIONS

AG, TI, and MC conceived and designed the research project. AG prepared the constructs, purified the protein, conducted the spectroscopic experiments, performed the enzyme turnovers, and analyzed the data. TI conducted and initially analyzed the protein diffraction experiments. LC cloned the complestatin Oxy enzymes. DM and MH performed final structural refinement and analysis. JH conducted and analyzed the EPR experiments. MS synthesized and purified the tripeptide CoA substrates. RS performed and analyzed the HRMS experiments. JD and LC contributed to analysis and discussion. The manuscript was written through contributions of all the authors. All the authors have given approval to the final version of the manuscript.

FUNDING

This work was supported by the Research Corporation for Scientific Advancement Cottrell Scholars Award #24350 Research Corporation for Scientific Advancement Cottrell Scholars Award #24350 (to LC), Monash University, EMBL Australia, and the National Health and Medical Research Council (APP1140619 to (MC)) and further supported under the Australian Research Council's Discovery Projects funding scheme (project number DPI70102220) to MC and JD. This research was conducted by the Australian Research Council Center of Excellence for Innovations in Peptide and Protein Science (CE200100012) and funded by the Australian Government. This study used BPA-enabled (Bioplatforms Australia)/NCRIS-enabled (National Collaborative Research Infrastructure Strategy) infrastructure located at the Monash Proteomics and Metabolomics Facility.

REFERENCES

- Adams, P. D., Afonine, P. V., Bunkóczi, G., Chen, V. B., Davis, I. W., Echols, N., et al. (2010). PHENIX: a Comprehensive Python-Based System for Macromolecular Structure Solution. *Acta Crystallogr. D Biol. Cryst.* 66, 213–221. doi:10.1107/s0907444909052925
- Al Toma, R. S., Brieke, C., Cryle, M. J., and Süssmuth, R. D. (2015). Structural Aspects of Phenylglycines, Their Biosynthesis and Occurrence in Peptide Natural Products. *Nat. Prod. Rep.* 32, 1207–1235. doi:10.1039/c5np00025d
- Albertolle, M. E., Kim, D., Nagy, L. D., Yun, C.-H., Pozzi, A., Savas, Ü., et al. (2017). Heme-thiolate Sulfenylation of Human Cytochrome P450 4A11 Functions as a Redox Switch for Catalytic Inhibition. *J. Biol. Chem.* 292, 11230–11242. doi:10.1074/jbc.m117.792200
- Ali, H. S., Henchman, R. H., and de Visser, S. P. (2020). Cross-linking of Aromatic Phenolate Groups by Cytochrome P450 Enzymes: a Model for the Biosynthesis of Vancomycin by OxyB. *Org. Biomol. Chem.* 18, 4610–4618. doi:10.1039/d0ob01023e
- Brieke, C., and Cryle, M. J. (2014). A Facile Fmoc Solid Phase Synthesis Strategy to Access Epimerization-Prone Biosynthetic Intermediates of Glycopeptide Antibiotics. *Org. Lett.* 16, 2454–2457. doi:10.1021/ol500840f
- Chiu, H.-T., Hubbard, B. K., Shah, A. N., Eide, J., Fredenburg, R. A., Walsh, C. T., et al. (2001). Molecular Cloning and Sequence Analysis of the Complestatin Biosynthetic Gene Cluster. *Proc. Natl. Acad. Sci.* 98, 8548–8553. doi:10.1073/pnas.151246498
- Collaborative Computational Project Number 4 (1994). The CCP4 Suite: Programs for Protein Crystallography. *Acta Crystallogr. D Biol. Crystallogr.* 50, 760–763. doi:10.1107/S0907444994003112
- Cryle, M. J., Staaden, J., and Schlichting, I. (2011). Structural Characterization of CYP165D3, a Cytochrome P450 Involved in Phenolic Coupling in Teicoplanin Biosynthesis. *Arch. Biochem. Biophys.* 507, 163–173. doi:10.1016/j.abb.2010.10.017
- Culp, E. J., Waglechner, N., Wang, W., Fiebig-Comyn, A. A., Hsu, Y.-P., Koteva, K., et al. (2020). Evolution-guided Discovery of Antibiotics that Inhibit Peptidoglycan Remodelling. *Nature* 578, 582–587. doi:10.1038/s41586-020-1990-9
- Emsley, P., and Cowtan, K. (2004). Coot: Model-Building Tools for Molecular Graphics. *Acta Crystallogr. D Biol. Cryst.* 60, 2126–2132. doi:10.1107/s0907444904019158
- Forneris, C. C., Nguy, A. K. L., and Seyedsayamdost, M. R. (2020). Mapping and Exploiting the Promiscuity of OxyB toward the Biocatalytic Production of Vancomycin Aglycone Variants. *ACS Catal.* 10, 9287–9298. doi:10.1021/acscatal.0c01719
- Forneris, C. C., and Seyedsayamdost, M. R. (2018). *In Vitro* Reconstitution of OxyC Activity Enables Total Chemoenzymatic Syntheses of Vancomycin Aglycone Variants. *Angew. Chem. Int. Ed.* 57, 8048–8052. doi:10.1002/anie.201802856

ACKNOWLEDGMENTS

We would also like to thank the Monash Macromolecular crystallization facility, D. Maksel, and G. Kong for assistance with crystal screening experiments; the MX1 beamline scientists, especially T. Caradoc-Davies at the Australian Synchrotron for their support during data collection; the Monash Proteomics and Metabolomics Facility and D. Steer for MS analysis.

SUPPLEMENTARY MATERIAL

The Supplementary Material for this article can be found online at: <https://www.frontiersin.org/articles/10.3389/fchem.2022.868240/full#supplementary-material>

- Geib, N., Woihte, K., Zerbe, K., Li, D. B., and Robinson, J. A. (2008). New Insights into the First Oxidative Phenol Coupling Reaction during Vancomycin Biosynthesis. *Bioorg. Med. Chem. Lett.* 18, 3081–3084. doi:10.1016/j.bmcl.2007.11.093
- Green, M. T. (2009). CH Bond Activation in Heme Proteins: the Role of Thiolate Ligation in Cytochrome P450. *Curr. Opin. Chem. Biol.* 13, 84–88. doi:10.1016/j.cbpa.2009.02.028
- Greule, A., and Cryle, M. J. (2020). Hung-wen Liu & Tadhg Begley. *Compr. Nat. Prod.* 2, 12247–12283. Elsevier.
- Greule, A., Izoré, T., Iftime, D., Tailhades, J., Schoppet, M., Zhao, Y., et al. (2019). Kistamicin Biosynthesis Reveals the Biosynthetic Requirements for Production of Highly Crosslinked Glycopeptide Antibiotics. *Nat. Commun.* 10, 2613. doi:10.1038/s41467-019-10384-w
- Greule, A., Stok, J. E., De Voss, J. J., and Cryle, M. J. (2018). Unrivalled Diversity: the many Roles and Reactions of Bacterial Cytochromes P450 in Secondary Metabolism. *Nat. Prod. Rep.* 35, 757–791. doi:10.1039/c7np00063d
- Hanson, G. R., Gates, K. E., Noble, C. J., Griffin, M., Mitchell, A., and Benson, S. (2004). XSophe-Sophe-XeprView . A Computer Simulation Software Suite (V. 1.1.3) for the Analysis of Continuous Wave EPR Spectra. *J. Inorg. Biochem.* 98, 903–916. doi:10.1016/j.jinorgbio.2004.02.003
- Harbort, J. S., De Voss, J. J., Stok, J. E., Bell, S. G., and Harmer, J. R. (2017). “CW and Pulse EPR of Cytochrome P450 to Determine Structure and Function,” in *Future Directions in Metalloprotein and Metalloenzyme Research*. Editors G. Hanson and L. Berliner (Springer International Publishing), 103–142. doi:10.1007/978-3-319-59100-1_5
- Haslinger, K., and Cryle, M. J. (2016). Structure of OxyAtei: Completing Our Picture of the Glycopeptide Antibiotic Producing Cytochrome P450 cascade. *Febs Lett.* 590, 571–581. doi:10.1002/1873-3468.12081
- Haslinger, K., Maximowitsch, E., Brieke, C., Koch, A., and Cryle, M. J. (2014). Cytochrome P450 OxyBteiCatalyzes the First Phenolic Coupling Step in Teicoplanin Biosynthesis. *ChemBioChem* 15, 2719–2728. doi:10.1002/cbic.201402441
- Haslinger, K., Peschke, M., Brieke, C., Maximowitsch, E., and Cryle, M. J. (2015). X-domain of Peptide Synthetases Recruits Oxygenases Crucial for Glycopeptide Biosynthesis. *Nature* 521, 105–109. doi:10.1038/nature14141
- Holding, A. N., and Spencer, J. B. (2008). Investigation into the Mechanism of Phenolic Couplings during the Biosynthesis of Glycopeptide Antibiotics. *ChemBioChem* 9, 2209–2214. doi:10.1002/cbic.200800303
- Izoré, T., and Cryle, M. J. (2018). The many Faces and Important Roles of Protein-Protein Interactions during Non-ribosomal Peptide Synthesis. *Nat. Prod. Rep.* 35, 1120–1139. doi:10.1039/c8np00038g
- Kabsch, W. (2010). Integration, Scaling, Space-Group Assignment and post-refinement. *Acta Crystallogr. D Biol. Cryst.* 66, 133–144. doi:10.1107/s0907444909047374
- Kanisaite, M., Goode, R. J. A., Schittenhelm, R. B., Makris, T. M., and Cryle, M. J. (2019). The Diiron Monooxygenase CmlA from Chloramphenicol Biosynthesis Allows Reconstitution of β -Hydroxylation during

- Glycopeptide Antibiotic Biosynthesis. *ACS Chem. Biol.* 14, 2932–2941. doi:10.1021/acscchembio.9b00862
- Kelley, L. A., Mezulis, S., Yates, C. M., Wass, M. N., and Sternberg, M. J. E. (2015). The Phyre2 Web portal for Protein Modeling, Prediction and Analysis. *Nat. Protoc.* 10, 845–858. doi:10.1038/nprot.2015.053
- Kittilä, T., Kittel, C., Tailhades, J., Butz, D., Schoppet, M., Büttner, A., et al. (2017). Halogenation of Glycopeptide Antibiotics Occurs at the Amino Acid Level during Non-ribosomal Peptide Synthesis. *Chem. Sci.* 8, 5992–6004. doi:10.1039/c7sc00460e
- Lee, C., Lee, J.-H., Rimal, H., Park, H., Lee, J., and Oh, T.-J. (2016). Crystal Structure of Cytochrome P450 (CYP105P2) from *Streptomyces Peucetius* and its Conformational Changes in Response to Substrate Binding. *Ijms* 17, 813. doi:10.3390/ijms17060813
- Leys, D., Mowat, C. G., McLean, K. J., Richmond, A., Chapman, S. K., Walkinshaw, M. D., et al. (2003). Atomic Structure of *Mycobacterium tuberculosis* CYP121 to 1.06 Å Reveals Novel Features of Cytochrome P450. *J. Biol. Chem.* 278, 5141–5147. doi:10.1074/jbc.m209928200
- Li, Q., Chen, Y., Zhang, G., and Zhang, H. (2017). Structural Analysis of SgvP Involved in Carbon-Sulfur Bond Formation during Griseoviridin Biosynthesis. *FEBS Lett.* 591, 1295–1304. doi:10.1002/1873-3468.12643
- Matsui, T., Nakajima, A., Fujii, H., Matera, K. M., Migita, C. T., Yoshida, T., et al. (2005). O₂- and H₂O₂-dependent Verdoheme Degradation by Heme Oxygenase. *J. Biol. Chem.* 280, 36833–36840. doi:10.1074/jbc.m503529200
- Mollo, A., von Krusenstiern, A. N., Bulos, J. A., Ulrich, V., Åkerfeldt, K. S., Cryle, M. J., et al. (2017). P450 Monooxygenase ComJ Catalyses Side Chain Phenolic Cross-Coupling during Complestatin Biosynthesis. *RSC Adv.* 7, 35376–35384. doi:10.1039/c7ra06518c
- Peschke, M., Brieke, C., and Cryle, M. J. (2016). F-O-G Ring Formation in Glycopeptide Antibiotic Biosynthesis Is Catalysed by OxyE. *Sci. Rep.* 6, 35584. doi:10.1038/srep35584
- Peschke, M., Brieke, C., Heimes, M., and Cryle, M. J. (2017). The Thioesterase Domain in Glycopeptide Antibiotic Biosynthesis Is Selective for Cross-Linked Aglycones. *ACS Chem. Biol.* doi:10.1021/acscchembio.7b00943
- Peschke, M., Gonsior, M., Süssmuth, R. D., and Cryle, M. J. (2016). Understanding the Crucial Interactions between Cytochrome P450s and Non-ribosomal Peptide Synthetases during Glycopeptide Antibiotic Biosynthesis. *Curr. Opin. Struct. Biol.* 41, 46–53. doi:10.1016/j.sbi.2016.05.018
- Peschke, M., Haslinger, K., Brieke, C., Reinstein, J., and Cryle, M. J. (2016). Regulation of the P450 Oxygenation cascade Involved in Glycopeptide Antibiotic Biosynthesis. *J. Am. Chem. Soc.* 138, 6746–6753. doi:10.1021/jacs.6b00307
- Podust, L. M., et al. (2004). Comparison of the 1.85 Å Structure of CYP154A1 from *Streptomyces Coelicolor* A3(2) with the Closely Related CYP154C1 and CYPs from Antibiotic Biosynthetic Pathways. *Protein Sci.* 13, 255–268. doi:10.1110/ps.03384804
- Rittle, J., and Green, M. T. (2010). Cytochrome P450 Compound I: Capture, Characterization, and C-H Bond Activation Kinetics. *Science* 330, 933–937. doi:10.1126/science.1193478
- Robert, X., and Gouet, P. (2014). Deciphering Key Features in Protein Structures with the New ENDscript Server. *Nucleic Acids Res.* 42, W320–W324. doi:10.1093/nar/gku316
- Rudolf, J. D., Chang, C.-Y., Ma, M., and Shen, B. (2017). Cytochromes P450 for Natural Product Biosynthesis in *Streptomyces*: Sequence, Structure, and Function. *Nat. Prod. Rep.* 34, 1141–1172. doi:10.1039/c7np00034k
- Sievers, F., Wilm, A., Dineen, D., Gibson, T. J., Karplus, K., Li, W., et al. (2011). Fast, Scalable Generation of High-Quality Protein Multiple Sequence Alignments Using Clustal Omega. *Mol. Syst. Biol.* 7, 539. doi:10.1038/msb.2011.75
- Sunbul, M., Marshall, N. J., Zou, Y., Zhang, K., and Yin, J. (2009). Catalytic Turnover-Based Phage Selection for Engineering the Substrate Specificity of Sfp Phosphopantetheinyl Transferase. *J. Mol. Biol.* 387, 883–898. doi:10.1016/j.jmb.2009.02.010
- Süssmuth, R. D., and Mainz, A. (2017). Nonribosomal Peptide Synthesis-Principles and Prospects. *Angew. Chem. Int. Ed.* 56, 3770–3821. doi:10.1002/anie.201609079
- Tailhades, J., Schoppet, M., Greule, A., Peschke, M., Brieke, C., and Cryle, M. J. (2018). A Route to Diastereomerically Pure Phenylglycine Thioester Peptides: Crucial Intermediates for Investigating Glycopeptide Antibiotic Biosynthesis. *Chem. Commun.* 54, 2146–2149. doi:10.1039/c7cc09409d
- Tailhades, J., Zhao, Y., Ho, Y. T. C., Greule, A., Ahmed, I., Schoppet, M., et al. (2020). A Chemoenzymatic Approach to the Synthesis of Glycopeptide Antibiotic Analogues. *Angew. Chem. Int. Ed.* 59, 10899–10903. doi:10.1002/anie.202003726
- Tailhades, J., Zhao, Y., Schoppet, M., Greule, A., Goode, R. J. A., Schittenhelm, R. B., et al. (2019). Enzymatic Cascade to Evaluate the Tricyclization of Glycopeptide Antibiotic Precursor Peptides as a Prequel to Biosynthetic Redesign. *Org. Lett.* 21, 8635–8640. doi:10.1021/acs.orglett.9b03245
- Uchida, T., Sekine, Y., Dojun, N., Lewis-Ballester, A., Ishigami, I., Matsui, T., et al. (2017). Reaction Intermediates in the Heme Degradation Reaction by HtZ from *Vibrio cholerae*. *Dalton Trans.* 46, 8104–8109. doi:10.1039/c7dt01562c
- Uhlmann, S., Süssmuth, R. D., and Cryle, M. J. (2013). Cytochrome P450_{sky} Interacts Directly with the Nonribosomal Peptide Synthetase to Generate Three Amino Acid Precursors in Skyllamycin Biosynthesis. *ACS Chem. Biol.* 8, 2586–2596. doi:10.1021/cb400555e
- Ulrich, V., Brieke, C., and Cryle, M. J. (2016). Biochemical and Structural Characterisation of the Second Oxidative Crosslinking Step during the Biosynthesis of the Glycopeptide Antibiotic A47934. *Beilstein J. Org. Chem.* 12, 2849–2864. doi:10.3762/bjoc.12.284
- Woithe, K., Geib, N., Meyer, O., Wörtz, T., Zerbe, K., and Robinson, J. A. (2008). Exploring the Substrate Specificity of OxyB, a Phenol Coupling P450 Enzyme Involved in Vancomycin Biosynthesis. *Org. Biomol. Chem.* 6, 2861–2867. doi:10.1039/b805956j
- Woithe, K., Geib, N., Zerbe, K., Li, D. B., Heck, M., Fournier-Rousset, S., et al. (2007). Oxidative Phenol Coupling Reactions Catalyzed by OxyB: A Cytochrome P450 from the Vancomycin Producing Organism. Implications for Vancomycin Biosynthesis. *J. Am. Chem. Soc.* 129, 6887–6895. doi:10.1021/ja071038f
- Yosca, T. H., Rittle, J., Krest, C. M., Onderko, E. L., Silakov, A., Calixto, J. C., et al. (2013). Iron(IV)hydroxide P K_a and the Role of Thiolate Ligation in C-H Bond Activation by Cytochrome P450. *Science* 342, 825–829. doi:10.1126/science.1244373
- Zerbe, K., Woithe, K., Li, D. B., Vitali, F., Bigler, L., and Robinson, J. A. (2004). An Oxidative Phenol Coupling Reaction Catalyzed by OxyB, a Cytochrome P450 from the Vancomycin-Producing Microorganism. *Angew. Chem. Int. Ed.* 43, 6709–6713. doi:10.1002/anie.200461278
- Zhao, Y., Ho, Y. T. C., Tailhades, J., and Cryle, M. (2021). Understanding the Glycopeptide Antibiotic Crosslinking Cascade: *In Vitro* Approaches Reveal the Details of a Complex Biosynthesis Pathway. *ChemBioChem* 22, 43–51. doi:10.1002/cbic.202000309

Conflict of Interest: The authors declare that the research was conducted in the absence of any commercial or financial relationships that could be construed as a potential conflict of interest.

Publisher's Note: All claims expressed in this article are solely those of the authors and do not necessarily represent those of their affiliated organizations, or those of the publisher, the editors, and the reviewers. Any product that may be evaluated in this article, or claim that may be made by its manufacturer, is not guaranteed or endorsed by the publisher.

Copyright © 2022 Greule, Izoré, Machell, Hansen, Schoppet, De Voss, Charkoudian, Schittenhelm, Harmer and Cryle. This is an open-access article distributed under the terms of the Creative Commons Attribution License (CC BY). The use, distribution or reproduction in other forums is permitted, provided the original author(s) and the copyright owner(s) are credited and that the original publication in this journal is cited, in accordance with accepted academic practice. No use, distribution or reproduction is permitted which does not comply with these terms.



Signaling Pathway and Small-Molecule Drug Discovery of FGFR: A Comprehensive Review

Jia Zheng[†], Wei Zhang[†], Linfeng Li[†], Yi He, Yue Wei, Yongjun Dang, Shenyue Nie^{*} and Zufeng Guo^{*}

Center for Novel Target and Therapeutic Intervention, Institute of Life Sciences, Chongqing Medical University, Chongqing, China

OPEN ACCESS

Edited by:

John D. Wade,
University of Melbourne, Australia

Reviewed by:

Ahmed Elkamhawy,
Mansoura University, Egypt
Chiara Borsari,
University of Basel, Switzerland

*Correspondence:

Shenyue Nie
nieshenyue@cqmu.edu.cn
Zufeng Guo
zfguo@cqmu.edu.cn

[†]These authors have contributed
equally to this work

Specialty section:

This article was submitted to
Chemical Biology,
a section of the journal
Frontiers in Chemistry

Received: 24 January 2022

Accepted: 28 March 2022

Published: 14 April 2022

Citation:

Zheng J, Zhang W, Li L, He Y, Wei Y,
Dang Y, Nie S and Guo Z (2022)
Signaling Pathway and Small-Molecule
Drug Discovery of FGFR: A
Comprehensive Review.
Front. Chem. 10:860985.
doi: 10.3389/fchem.2022.860985

Targeted therapy is a groundbreaking innovation for cancer treatment. Among the receptor tyrosine kinases, the fibroblast growth factor receptors (FGFRs) garnered substantial attention as promising therapeutic targets due to their fundamental biological functions and frequently observed abnormality in tumors. In the past 2 decades, several generations of FGFR kinase inhibitors have been developed. This review starts by introducing the biological basis of FGF/FGFR signaling. It then gives a detailed description of different types of small-molecule FGFR inhibitors according to modes of action, followed by a systematic overview of small-molecule-based therapies of different modalities. It ends with our perspectives for the development of novel FGFR inhibitors.

Keywords: FGFR, tyrosine kinase, small-molecule inhibitors, targeted therapy, cancer

1 INTRODUCTION

Currently, one of the most important modalities for cancer treatment is the targeted therapy which hampers the growth of cancer cells by chemical intervention against specific target biomolecules known to be essential for tumorigenesis and proliferation. A number of protein kinases in the human body are associated with cancer initiation and progression, and small molecules that inhibit these kinases have thus far gained notable achievement manifested by ~70 FDA-approved small molecule kinase inhibitor drugs for the treatment of a variety of malignancies (Ayala-Aguilera et al., 2022). FGFRs are a family of receptor tyrosine kinases that have been successfully targeted by three approved small-molecule inhibitors. Due to their functional versatility and frequent alterations in different cancers, FGFRs are considered to be a promising target, and more inhibitors are expected to be translated from bench to bedside in the near future.

Small-molecule FGFR inhibitors have been reviewed by others in the past several years, but these papers mainly focused on small molecules targeting the kinase domain. Herein, we make a systematic and comprehensive description on FGF/FGFR signaling, their role in cancer development, and drug resistance. We also update the development of different modalities targeting FGF-FGFR axis with a detailed discussion of their advantages and future trend.

2 FIBROBLAST GROWTH FACTORS

The mammalian fibroblast growth factors (FGFs) are a family of 23 proteins, which exert a wide variety of biological effects on different types of cells. Based on their sequence homology and mode of action, these proteins are classified as secreted FGFs and intracellular FGFs (iFGFs). The iFGFs

(FGF11-14) are non-signaling factors that do not bind to any cell surface receptor. Instead, they function as cofactors for voltage-gated sodium channels (Goldfarb et al., 2007). In contrast, all secreted FGFs signal to a class of receptor tyrosine kinases named fibroblast growth factor receptors (FGFRs). In general, secreted FGFs are produced intracellularly and secreted to extracellular matrix (ECM) and eventually bind to FGFRs to initiate signal transduction.

Depending on how far they can travel, secreted FGFs are further classified into two subfamilies: canonical FGFs and endocrine FGFs. In the ECM, canonical FGFs (FGF1-10, 16-18, 20, and 22) interact with copious cofactors named heparan sulfate proteoglycans (HSPGs), which limit diffusion of FGFs and regulate their specificity toward FGFRs (Ornitz, 2000; Matsuo et al., 2013). Hence, canonical FGFs function as autocrine or paracrine factors, traveling merely a short distance before binding to the FGFRs on the cells of their origin or adjacent cells (Belov et al., 2013). The binding of canonical FGFs to FGFRs triggers a series of cellular processes related to cellular survival, metabolism, proliferation and differentiation, and consequently mediates organogenesis, tissue metabolism, repair, regeneration and inflammatory response (Belov et al., 2013; Powers et al., 2000; N.; Wang et al., 2018).

Due to the reduced affinity for HSPGs, endocrine FGFs (FGF15/19, 21 and 23) often permeate through the HSPGs-rich extracellular matrix into the circulatory system, and subsequently reach all parts of the body like endocrine hormones (Fernandes-Freitas et al., 2015). Instead of HSPGs, endocrine FGFs require members of Klotho family, including α Klotho, β Klotho, and Klotho-LPH related protein (KLPH), to generate FGF-FGFR-Klotho ternary complex (Angelin et al., 2012; Ding et al., 2012). As a result of their hormone-like features, endocrine FGFs play important roles in the metabolism of bile acid, glucose and lipid in addition to the canonical FGF functions.

Therefore, dysregulation of expression, secretion, and degradation of FGFs lead to aberrations in the metabolism, organogenesis (Dorey et al., 2010; Yu et al., 2017), wound healing (Müller et al., 2012), and are responsible for many cancers (Brooks et al., 2012).

3 FIBROBLAST GROWTH FACTOR RECEPTORS

The human fibroblast growth factor receptors belong to receptor tyrosine kinases (RTKs), consisting of FGFR1, FGFR2, FGFR3, FGFR4, and FGFR5. Although FGFR1-4 are encoded by four distinct genes, they share great sequence homology with an identity of 56–71%. The FGFR5, also called FGFR-like 1 (FGFRL1), possesses structural similarity with FGFR1-4 but lacks an intracellular kinase domain (Wiedemann et al., 2000). Activated FGFRs participate in multiple cell processes through intervening several signaling pathways.

3.1 Structure of FGFR

FGFRs are single-pass transmembrane proteins containing approximately 800 amino acids, which are composed of

several domains: an extracellular ligand binding domain, a transmembrane domain, and an intracellular domain with kinase activity (**Figure 1**).

The extracellular ligand binding domain of FGFRs is composed of three immunoglobulin-like subdomains (IgI, IgII and IgIII) and an acidic-residues-rich sequence termed acid box (Itoh et al., 2004). IgI and acid box have been demonstrated to play a key role in autoinhibition of FGFRs in the absence of FGFs (Sanchez-Heras et al., 2006). IgII and IgIII form the FGF-binding pocket, thus are responsible for the binding specificity between FGFRs and FGFs. There are two isoforms of IgIII (b/c) in FGFR1-3 that result from alternative splicing, while this is not observed for FGFR4.

The single-pass transmembrane domain (TM) is embedded in the cell membrane, functioning as an anchor of FGFR. The TM also supports the dimerization of cytoplasmic kinase domains of two FGFRs which leads to activation of FGFR (Itoh et al., 2004).

The intracellular tyrosine kinase domain of FGFR1-4 (~300 amino acids) is the most extensively investigated part, which possesses a classical kinase architecture (**Figure 2**) (Itoh et al., 2004; Mohammadi, Schlessinger, et al., 1996; Sanchez-Heras et al., 2006). The small N-terminal lobe (N-lobe, ~100 amino acids) is composed of a five-stranded anti-parallel β -sheet (β 1- β 5) and an α C-helix that resides between β 3 and β 4 in sequence and flanks the β -sheet spatially. A highly-flexible glycine-rich loop between β 1 and β 2 termed P-loop is able to swing downward in the presence of ATP to create the nucleotide binding site (Guimarães et al., 2011). In contrast, seven α -helices (α D, α E, α EF, α F, α G, α H and α I) gather to form the main part of the larger C-terminal lobe (C-lobe, ~200 amino acids).

The N-lobe and C-lobe are connected by a hinge region containing conserved residues which could offer critical contacts with the adenine moiety of an ATP molecule. In addition, a triad of residues around the hinge region (e.g., N549, E565, and K641 in FGFR2) acts as the “molecular brake” of FGFRs to regulate their autoinhibition (Chen et al., 2007). The C-lobe also contains two long loops and some short strands at the interface of the two lobes, all of which contribute to the exquisite machinery for the activation and functioning of the kinase.

In between β 8 and α EF, 20–30 amino acids round up to form the activation loop (A-loop), which encompasses tyrosine phosphorylation sites (Webster et al., 1996). At the beginning of the A-loop, an Asp-Phe-Gly triad constitutes the highly conserved DFG-motif, which is indicative of the active/inactive states of kinase. Located between α E and β 7 is another important loop named catalytic loop, which contains the His-Arg-Asp (HRD) motif. The Asp of HRD-motif interacts with the hydroxyl group of the substrate tyrosine and therefore contributes to the phosphorylation (Vijayan et al., 2015).

3.2 FGF/FGFR Signaling

3.2.1 Activation of FGFRs

Once FGFs bind to the extracellular domains of FGFRs, the dimerization of transmembrane and intracellular domains takes place along with a series of conformational changes that lead to trans-phosphorylation of dimerized kinase domains for activation.

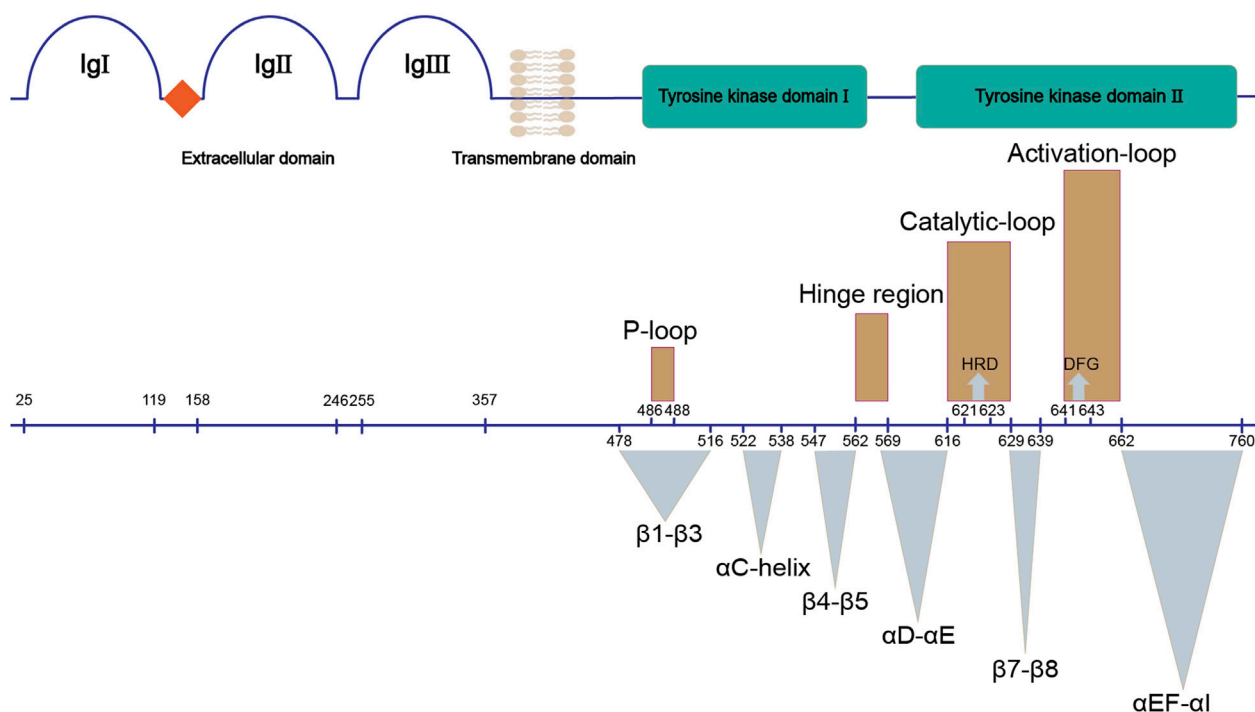


FIGURE 1 | Structure of FGFR. The upper panel shows the main domains of FGFR; the bottom panel demonstrates their corresponding sequences (UniProtKB: P11362). Three dimensional structures (brown) and functional regions (cyan) involved in the kinase domain of FGFR are marked.

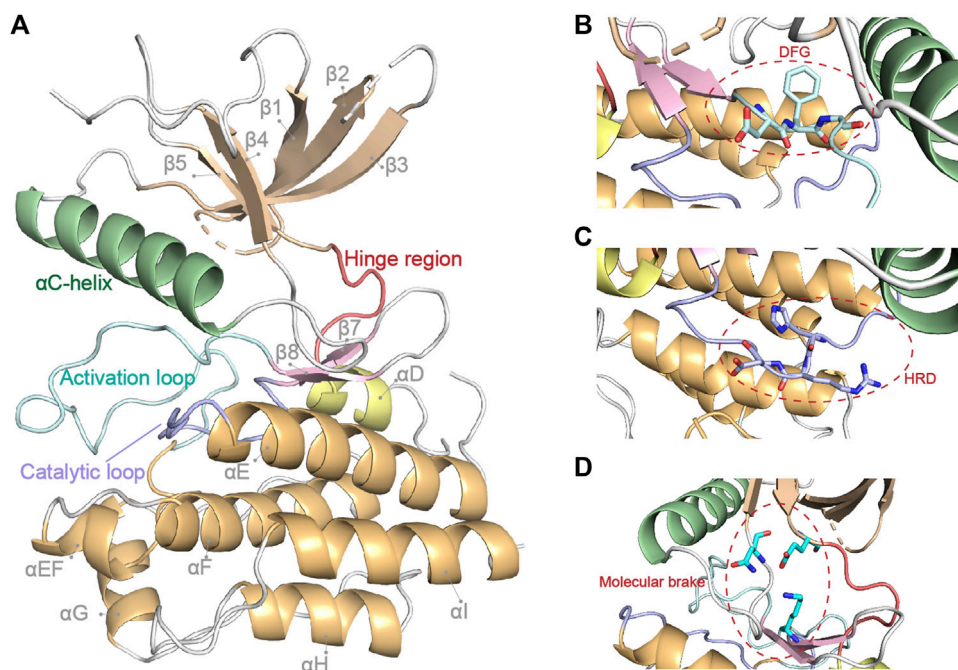


FIGURE 2 | FGFR1 kinase domain structure (PDB: 4UWY). Basic secondary structures and critical regions described in this review are highlighted in (A). The critical DFG, HRD motif and molecular brake are highlighted by close-up in (B–D), respectively.

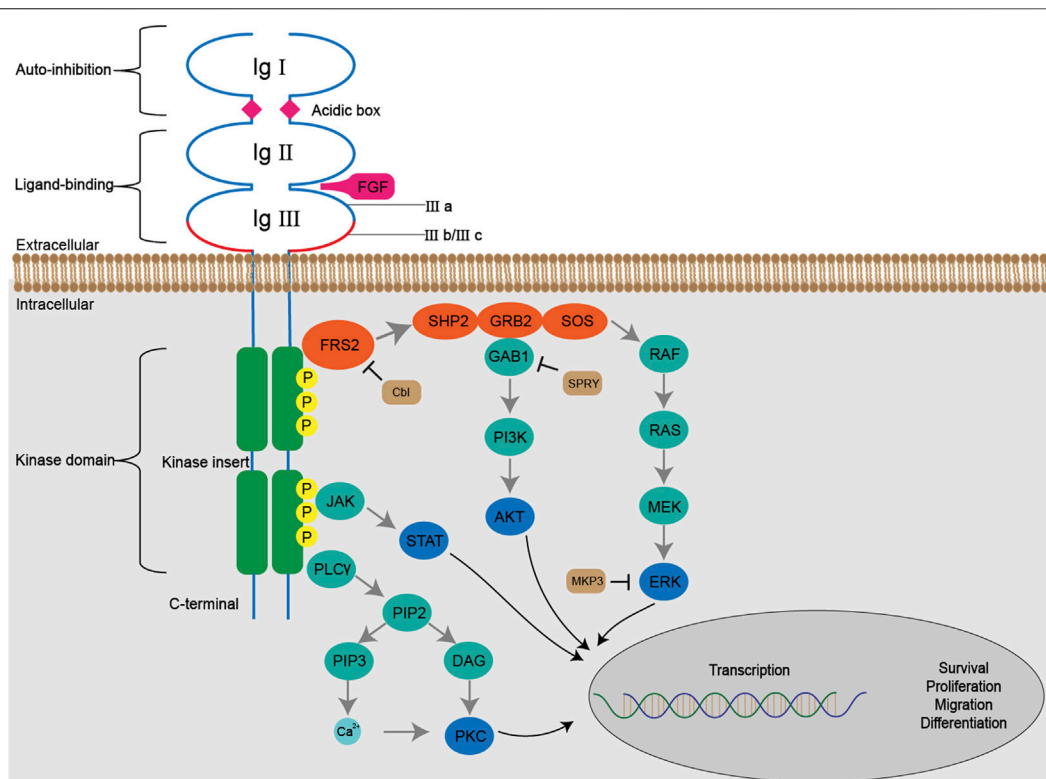


FIGURE 3 | The FGF/FGFR signaling pathways. The binding of FGFs with FGFRs initiates a series of conformational changes, which consequently result in phosphorylation of tyrosine residues in the kinase domain. The phosphorylated tyrosine triggers cascaded docking and phosphorylation of downstream molecules including SHP2, GRB2, GAB1 and SOS, forms a multi-complex, and subsequently activates RAS-MAPK-ERK and PI3K-AKT pathways. Activated FGFRs are also involved in JAK-STAT and PLC γ -PKC pathways. The Cbl, SPRY, MKP3 negatively regulate FGF/FGFR signaling by ubiquitination, docking prevention and dephosphorylation, respectively.

The activation of kinase domain is a finely-tuned process (Furdui et al., 2006). Several critical tyrosine residues including Y463, Y583, Y585, Y653, Y654, Y730, and Y766 are autophosphorylated by precisely ordered reactions while ATP binds to the highly conserved pocket located in the hinge region during the activation of FGFR1 (Mohammadi, Dikic, et al., 1996). The autophosphorylations of Y653 and Y654 in the A-loop, which appear to induce the binding of substrate but not ATP, have increased by 50–100 fold and 500–1,000 fold in the rate of substrate phosphorylation, respectively. This suggested that these autophosphorylations have an indispensable role in kinase activation. The function of other tyrosine autophosphorylation sites contributes to the activation of FGFRs and downstream signal transduction through diverse biochemical reactions yet to be discovered.

In addition to the phosphorylation of critical tyrosine residues, the DFG motif of kinase domain toggles between two different conformations in line with the state of FGFR (active or inactive). When the motif adopts a DFG-in conformation, its Asp coordinates with phosphate groups of ATP and/or magnesium ion and causes the A-loop to display an open conformation, rendering the kinase an active state. Conversely, a DFG-out conformation, where the Asp and Phe

point away from and toward the ATP binding pocket, respectively, is an indicator of inactive state of kinase. Noticeably, the flipped conformation of the DFG motif results in the formation of a large adjacent hydrophobic pocket (Hu et al., 2015; Vijayan et al., 2015). A valine in the ATP binding pocket (V561/564/555/550 in FGFR1/2/3/4), which is highly conserved in a variety of kinases and known as a “gatekeeper” residue, is the switch of the large hydrophobic pocket. The gatekeeper mutations give rise to many drug resistances due to hampered drug binding (Azam et al., 2008; Roskoski, 2010; Vijayan et al., 2015).

3.2.2 FGFR Signaling Pathways

The autophosphorylated kinase domain can recruit and phosphorylate multiple downstream effector molecules to initiate several signaling pathways (Figure 3).

The Fibroblast Growth Factor Receptor Substrate 2 (FRS2), a major FGFR substrate, binds to the juxtamembrane region of FGFR *via* its phospho-tyrosine binding domain (PTB) in a constitutive manner, regardless of the activation and phosphorylation state of the kinase domain. Following the activation of FGFR, multiple tyrosine residues of FRS2 are subject to phosphorylation and serve as docking sites for subsequent molecules.

The RAS-MAPK-ERK signaling pathway is activated by a serial docking of FRS2 with multiple proteins, including SH2-containing protein tyrosine phosphatase (SHP2), growth factor receptor-bound protein 2 (GRB2), Son of Sevenless (SOS) and noted RAS. Both SHP2 and GRB2 contain a Src homology domain (SH2 domain), which can recognize and bind the phosphorylated tyrosine residues of FRS2 and GRB2. Therefore, the GRB2-SOS complex is recruited to FRS2 directly or through the formation of the SHP2-GRB2-SOS complex (Hadari et al., 1998; Ong et al., 2000). The complex, in turn, initiates a phosphorylation cascade in the RAS-MAPK-ERK signaling pathway. Upon activation, ERK1/2 is translocated from cytoplasm into nucleus and regulates the activity of diverse transcription factors to influence cell proliferation, differentiation and signal transduction, which makes it the most persuasive signaling molecules in this pathway for the evaluation of FGFR inhibitors (Guo et al., 2020).

The docking protein GRB2 associated binding protein 1 (GAB1) is recruited to the complex *via* binding to the SH3 domain of GRB2, which enables tyrosine phosphorylation on itself. Similarly, the phosphorylated tyrosine residues of GRB2 are captured by the phosphoinositide 3 kinase (PI3K) containing a SH2 domain, thus initiating the activation of PI3K-AKT signaling pathway. The downstream effector molecules of AKT vary, including the well-known mTOR, which is closely related to cell metabolism, transcription and so forth (Quan et al., 2020).

Besides FRS2, the phospholipase C γ (PLC γ) binds to a phosphorylated tyrosine in the C-terminal of phosphorylated kinase domain, and hydrolyzes phosphatidylinositol 4,5-bisphosphate (PIP2) into two secondary messengers, inositol triphosphate (IP3) and diacyl glycerol (DAG). The binding between IP3 and its receptor on the endoplasmic reticulum leads to the release of Ca²⁺ from intracellular stores and thus increases Ca²⁺ concentration (Mikoshiba, 2007). When coordinated with Ca²⁺, DAG activates PKC signaling pathway, which causes crosstalk with RAS-MAPK pathway due to the competition between GRB2 and PLC γ to bind with FGFR (Fearon et al., 2014).

In addition, FGFR can activate the signal transducer and activator of transcription (STAT) proteins to partially mediate cell transformation (Hart et al., 2000).

The negative regulation of FGF/FGFR signaling includes dephosphorylation, ubiquitination and obstruction in a serial of docking. In response to FGF stimulation, an ubiquitin ligase called Casitas B-lineage lymphoma (Cbl) is recruited to the FRS2 (-SHP2)-GRB2-SOS complex and induces ubiquitination and subsequent degradation of FGFR and FRS2 α (Wong et al., 2002). In addition, the binding of Sprouty to GRB2 can block the interaction between GRB2 and FRS2 or SHP2 so as to exert an inhibitory effect on downstream RAS-MAPK signaling (Hanafusa et al., 2002). The dual-specificity MAPK phosphatases 3 (MKP3) also inhibits RAS-MAPK signaling by dephosphorylating activated MAPK (Farooq et al., 2004).

The activations of these FGFR-dependent or related signaling pathways converge into the regulation of diverse cellular events and physical functions.

3.3 FGF/FGFR Signaling in Cancer

FGFR genetic alterations have been involved in the development and progression of a variety of diseases, particularly cancers (Figure 4). The majority of FGFR aberrations are gene amplifications (66%), followed by gene mutations (26%) and, less frequently, rearrangements (8%), according to a recent sequencing study involving 4,853 patients with various types of cancers (Helsten et al., 2016). *FGFR* amplification leads to enhanced level of FGF binding. Generally, extracellular mutations increase binding affinity and disturb specificity between FGFs and FGFRs (Ibrahimi et al., 2001; Ibrahimi et al., 2004), or increase receptor dimerization by forming unexpected disulfide bridge (Plotnikov et al., 2000); while kinase domain mutations directly induce a higher level of intracellular phosphorylation. Despite the low incidence, chromosome rearrangements usually cause ligand-independent dimerization. However, most FGFR aberrations are oncogenic drivers, whereas prognostic indicators or “passenger co-aberrations” in different cancers remain ambiguous.

3.3.1 FGFR1

As the most commonly altered FGFR subtype, FGFR1 aberrations account for 49% of all cases with FGFR aberrations according to the sequencing analysis (Helsten et al., 2016). The most frequent type of FGFR1 aberrations is gene amplification, which is reported in 8.7–20.0% of non-small cell lung carcinoma (NSCLC) cases (Miao et al., 2016; Miao et al., 2020) and involved in several acquired resistances against NSCLC therapeutics (Gammelgaard et al., 2019; Zhang et al., 2019). *FGFR1* amplification is common in breast cancer (10%), predominantly in estrogen receptor-positive breast cancer, and harmful to the survival of patients (Gelsi-Boyer et al., 2005; Wang et al., 2017). *FGFR1* amplification is also seen in prostate cancer (15%) (Edwards et al., 2003), bladder cancer (9%) (Ross et al., 2014), and other cancers (ovarian cancer, colorectal carcinoma, and squamous non-lung tumors). *FGFR* amplification (mainly in *FGFR1* and 2) causes overexpression of proteins and increases the FGFR-dependency of cancer cells. Therefore, it is regarded as a biomarker for the efficacy of some FGFR inhibitors (Weiss et al., 2010). *FGFR1* mutation has been detected in several types of cancers, including midline gliomas (18%), glioblastoma and melanoma, whereas *FGFR1* fusion is rare.

3.3.2 FGFR2

Amplification (predominantly observed in triple-negative breast cancer, 4%) and mutation (e.g., K660N) of FGFR2 occur frequently in breast cancer. Besides, *FGFR2* also amplifies in gastric cancer (4.5–9%) and is associated with its venous and lymphatic invasion (Jung et al., 2012; Cancer Genome Atlas Research Network, 2014). Apart from breast cancer, 10–12% of endometrial carcinoma and 4–5% of NSCLCs bear *FGFR2* mutations (Mohammadi et al., 1998; Dutt et al., 2008; Kandath et al., 2013). *FGFR2* mutants are infrequently reported in urothelial cancers (1.2%). Several *FGFR2* fusions have been reported including *FGFR2-AFF3*, *FGFR2-CASP7* and *FGFR2-CCDC6* (Turner et al., 2010; Reintjes et al., 2013; Wu et al., 2013). In addition, *FGFR2* fusions occur in cholangiocarcinoma,

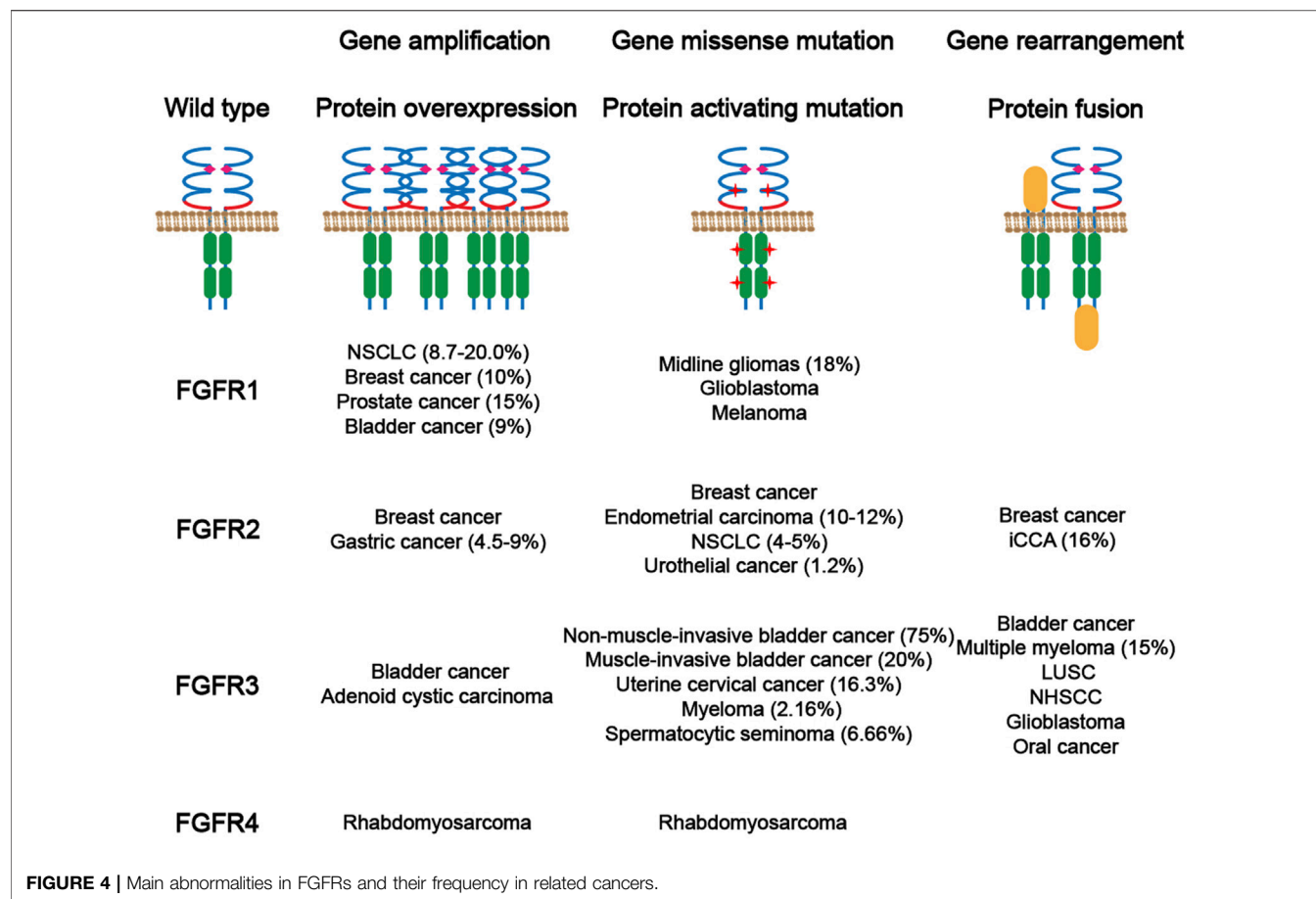


FIGURE 4 | Main abnormalities in FGFRs and their frequency in related cancers.

lung squamous cell carcinoma (LSCC), thyroid cancer, prostate cancer, according to a study of FGFR targetable gene fusions (Wu et al., 2013). Notably, a *FGFR2-PPH1N1* fusion generated by the chromosomal translocation t (10; 12) (q26; q12) is identified to possess oncogenic and transforming activity in 16% of intrahepatic cholangiocarcinoma (iCCA).

3.3.3 FGFR3

FGFR3 aberrations are predominantly implicated in bladder cancer (Baldia et al., 2016; Helsten et al., 2016). The incidence of *FGFR3* mutations in non-muscle-invasive bladder cancer is as high as 75%, as determined by the presence of mutations in the p53 suppressor gene (Zhang et al., 2015), whereas it is relatively low (20%) in muscle-invasive bladder cancer (Couffignal et al., 2015; Solomon et al., 2016; Siracusano et al., 2020). Suppression of FGFR3 activation is sufficient to reduce the survival and proliferation of carcinoma cells harboring *FGFR3* mutations (Markham, 2019; Montazeri et al., 2020). Furthermore, *FGFR3* mutations are found in uterine cervical cancer (16.3%) (Yoshimoto et al., 2020), including invasive cervical cancer (5%) (Rosty et al., 2005), myeloma (2.16%) (Walker et al., 2015), and spermatocytic seminoma (6.66%) (Goriely et al., 2009). *FGFR3* amplification is not frequent in cancers, but is sporadically reported in bladder cancer and adenoid cystic carcinomas (Vékony et al., 2007). Translocations at the t (4;

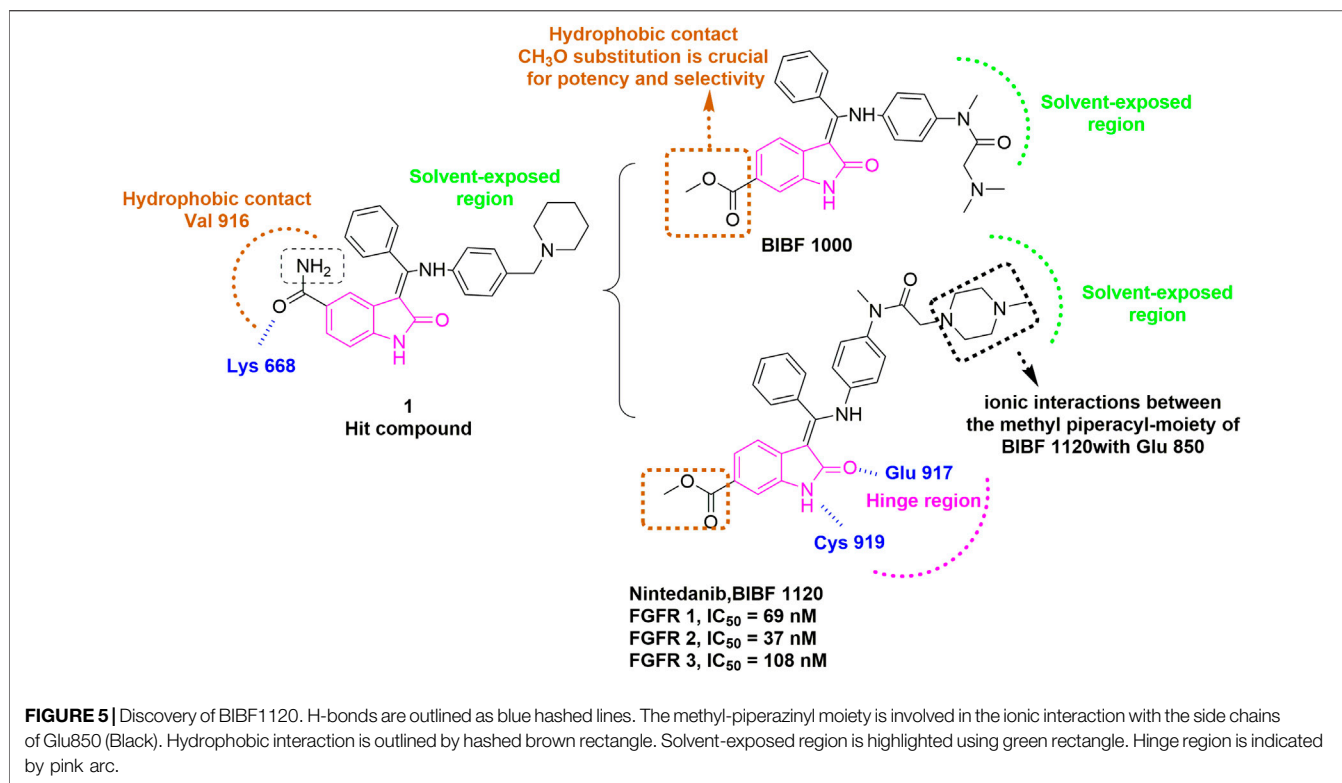
14), in which *FGFR3* is significantly mutated, occurs in multiple myeloma (15%) frequently (Walker et al., 2018). Fusions of *BAIAP2L1* or *TACC3* to 5' terminal of *FGFR3* can also cause aberrant activation of FGFR3 by inducing oligomerization of fusion proteins even in the absence of FGFs. These fusions are reported in a variety of cancers including bladder cancer, LSCC, NLSCC, glioblastoma and oral cancer.

3.3.4 FGFR4

Amplification or mutation of *FGFR4* is rarely perceived as an oncogene except in rhabdomyosarcoma (7.5%). It is confirmed that kinase inhibitor treatment increased cell apoptosis in *FGFR4*-mutant rhabdomyosarcoma (RMS) cell lines, which is consistent with increased SubG1 fraction and high level of activated caspase-3, suggesting the strong dependency of RMS on FGFR4 (Taylor et al., 2009).

4 SMALL-MOLECULE FGFR INHIBITORS

To fight against FGFR-driven abnormalities in various cancers, continuous efforts are devoted to various types of therapeutics, including monoclonal antibodies interacting with extracellular domain of FGFR, ligand traps restricting FGF, and small-molecule inhibitors targeting the kinase domain. During the



past decade, we have witnessed multiple preclinical and clinical breakthroughs of FGFR inhibitors. To help developing novel therapeutics, we reviewed the current status of discovery of small-molecule FGFR inhibitors as well as other small molecule-based modalities from the standing point of medicinal chemists.

Although the development of tyrosine kinase inhibitors started in the 20th century (Porta et al., 2017), targeting FGFR was validated as a therapeutic strategy for cancer treatment only recently, when FDA approved the use of erdafitinib (JNJ-42756493) in 2019 (Markham, 2019), pemigatinib (INCB054828) in 2020 (Qu et al., 2022) and infigratinib (BGJ-398) in 2021 (Yu et al., 2021) for the treatment of FGFR-altered cancers. In addition, a larger number of inhibitors are in clinical trial or preclinical investigation, such as LY2874455, ARQ-087, AZD4547, FGF401, BLU9931, and H3B6527s (**Supplementary Table S1**). The following part will elaborate the discovery of small-molecule FGFR inhibitors in structure-based fashion.

4.1 The First-Generation: Non-Selective FGFR Kinase Inhibitors

The FGFR kinase domain share high homology with other receptor tyrosine kinases. The first-generation FGFR inhibitors are non-selective tyrosine kinase inhibitors (TKIs) that compete with ATP for ATP-binding site. As a result, these inhibitors inhibit not only FGFR but also a variety of other tyrosine kinases, such as vascular endothelial growth factor receptor (VEGFR), platelet-derived growth factor receptor (PDGFR), fms-like tyrosine kinase 3 (FLT-3), c-Kit and BCR-ABL (Huang et al., 2020).

Many approved TKIs show mild to strong activity for FGFR, and some of them are being (or have been) assessed in clinical trials for diseases where FGFR alterations are implicated, including nintedanib, dovitinib, ponatinib, lucitanib, derazantinib, anlotinib, and so on. Nintedanib (BIBF1120), first discovered in 2009 by Roth et al. (2009), is an inhibitor targeting VEGFR, FGFR and PDGFR (Capdevila et al., 2014). Nintedanib was approved for the treatment of idiopathic pulmonary fibrosis and interstitial lung diseases (ILD) by FDA in 2014 and 2020, respectively. It is currently under active clinical trials, including the treatment of FGFR3 mutated urothelial carcinoma (Phase 2, NCT02278978), and the treatment of SARS-CoV-2 induced pulmonary fibrosis (Phase 3, NCT04541680). This inhibitor resulted from the optimization of a hit compound **1** bearing a 5-substituted indolinone core that was initially identified as a VEGFR-2 inhibitor (**Figure 5**). The computational modeling of hit compound **1** with VEGFR-2 suggested that the carbonyl oxygen of the amide group can form a hydrogen bond with Lys868. The hydrophobic region flanked by Val916 indicated that replacing the amide moiety with a more lipophilic substituent (e.g., methoxycarbonyl) could improve potency and maintain selectivity. Meanwhile, the basic side chain pointing toward the solvent was further modified with additional polar fragments, resulting in two compounds BIBF1000 and BIBF1120. The latter compound exhibited a favorable IC₅₀ values for VEGFR, FGFR, and PDGFR within nanomolar range and showed selectivity over other homologous kinases. The indolinone scaffold formed two hydrogen bonds with Cys919 and Glu917 in the hinge region. The methyl piperazinyl group directed into the solvent region, and its

4-nitrogen atom formed a bidentate ionic interaction with the carboxylate oxygens of Glu850 based on a published X-ray crystal structure in complex with VEGFR-2 (PDB: 3C7Q) (Hilberg et al., 2008).

Dovitinib (TKI258) inhibits VEGFR-2, FGFR-1, and PDGFR with IC₅₀ values below 0.1 μ M, and several clinical trials for advanced solid tumors have been conducted (Angevin et al., 2013; Taeger et al., 2011). Dovitinib contains a benzimidazole core, which makes critical contacts with the hinge region and also binds to FGFR1 and FGFR4 in a DFG-in mode as usually observed for this type of inhibitors (Bunney et al., 2015; Lesca et al., 2014). Ponatinib, which targets PDGFR, VEGFR and FGFR, was initially approved for the treatment of refractory chronic myeloid leukemia (CML) or Philadelphia chromosome-positive acute lymphoblastic leukemia (Ph + ALL) in 2012 (Pao et al., 2004; Cortes et al., 2018), then it entered two clinical trials in 2014 for the treatment of malignant neoplasm with *FGFR* fusions or activating mutations (NCT02265341, NCT02272998). Structural study revealed that ponatinib bound to either FGFR1 or FGFR4 in a unique DFG-out mode, which is distinct from most of reported FGFR inhibitors (Lesca et al., 2014). Liu et al. (2017) conducted extensive SAR study of ponatinib and obtained optimized analogs with improved activity and selectivity. Anlotinib, a quinoline-based inhibitor of VEGFR, FGFR, PDGFR and c-kit (Shen et al., 2018), is being investigated for treatment of advanced solid tumors with FGFR alterations (NCT03929965). Lucitanib (E3810) is also a TKI that targets VEGFR1/2/3, FGFR1/2 and PDGFR (Babina et al., 2017), and a phase 2 trial (NCT02053636) for testing Lucitanib in patients with *FGFR1*-amplified or non-amplified ER + metastatic breast cancer was completed. Derazantinib (ARQ087) inhibits multiple kinases including RET, DDR2, PDGFR, VEGFR, KIT and FGFR, and its phase 1/2 study in FGFR-altered patients was recently completed as well. Representative kinase small-molecule inhibitors in this category are shown in **Supplementary Figure S1**.

Although moderate suppression on tumors harboring FGFR aberrations was observed, these non-selective inhibitors still brought some issues of therapeutic regimen. The human kinome comprises ~535 protein kinases (Zhong et al., 2021). A wide range of off-target effects attributed to their poor selectivity leads to blockage of multiple signaling pathways and causes a multiplicity of related side effects such as diarrhea, vomiting and nausea (Konecny et al., 2015). Albeit these factors have restricted the broad application of multi-target TKIs, they are widely recognized as a decent treatment for tumors in absence or unawareness of the “oncogenic driver,” and have provided the impetus to the development of on target FGFR inhibitors.

4.2 The Second-Generation: Selective FGFR Kinase Inhibitors

Thanks to the rapidly evolving high throughput screening methods and structure-based strategies, a number of second-generation FGFR inhibitors have been discovered with higher potency, selectivity, safety as well as novel modality. Three inhibitors in this category, namely erdafitinib, pemigatinib,

and infigratinib, have been approved by FDA, and a lot more compounds are being evaluated in preclinical and clinical investigations. These second-generation inhibitors were tentatively divided into several subclasses on the basis of different modes of action. Chemical structures of these reported selective FGFR small molecule inhibitors are shown in **Supplementary Figure S2**.

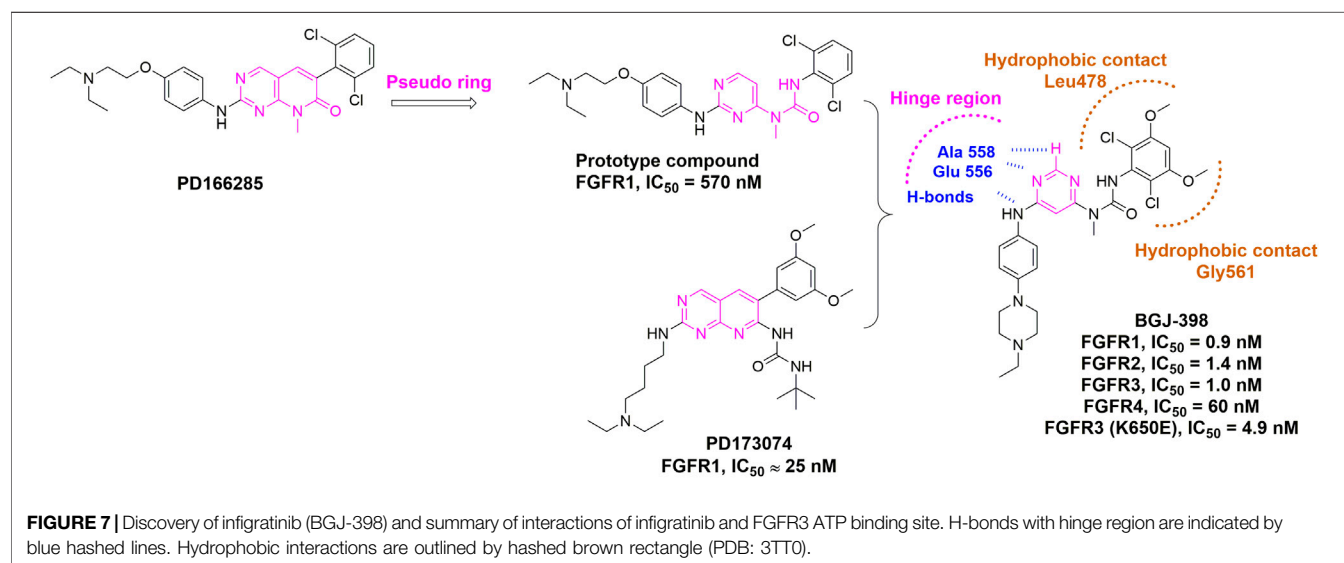
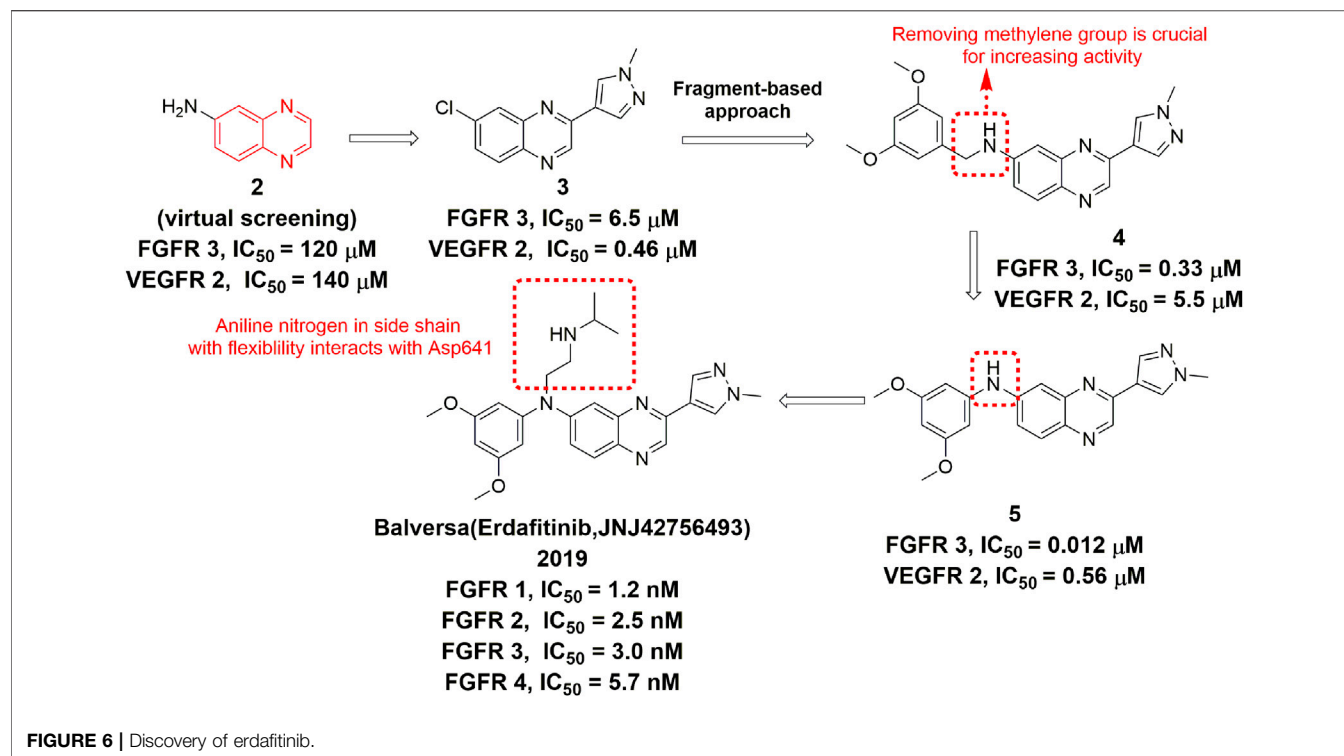
4.2.1 Non-Covalent Pan-FGFR Inhibitors

The three approved FGFR inhibitors and quite a few candidates are all non-covalent inhibitors with pan-FGFR inhibitory activity, although some of them showed reduced, yet still considerable, potency for FGFR4 because of its relatively notable difference from FGFR1-3.

Erdafitinib (JNJ-42756493) is the first approved FGFR inhibitor for treatment of adult patients with locally advanced or metastatic urothelial carcinoma. It is an orally active and selective pan-FGFR inhibitor (Perera et al., 2017) that inhibits the kinase activity of FGFR1-4 with similar potency (Markham, 2019). Erdafitinib features quinoxaline element, which was first identified through virtual screening based on the crystal structure with FGFR1. The compound **2** was next generated through fragment growing approach. Removal of the methylene group in compound **2** produced compound **3**, which has shown much improvement in activity due to better shape complementarity with the hydrophobic pocket. An additional substitution on the secondary nitrogen occupied the ribose-binding region, leading to the discovery of erdafitinib with increased affinity, better physicochemical and pharmacokinetic properties (**Figure 6**) (Murray et al., 2019).

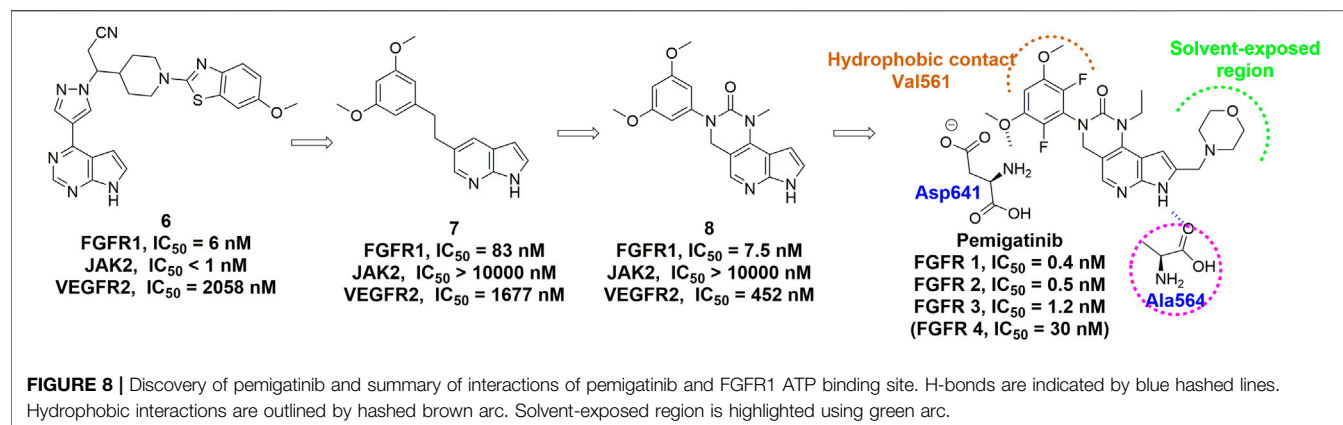
In order to replace the pyrido [2,3-*d*]pyrimidin-7-one core, which was a common feature in a well-established class of protein kinase inhibitors (e.g., PD166285), Guagnano et al. (2011) developed a pseudo six-membered ring structure stabilized by an intramolecular hydrogen bond (e.g., prototype compound) (**Figure 7**) (Furet et al., 2008). Using the same strategy, infigratinib was eventually discovered through a lead optimization of a known FGFR inhibitor PD173074. Structural studies confirmed that hydrogen bonds with hinge region were retained and both chlorines and methoxy groups would form favorable hydrophobic contacts with the deep pocket inside ATP binding site. It was also observed that the phenyl ring at the entrance of the pocket was hydrophobically sandwiched between Leu478 and Gly561. These hydrophobic effects contributed to the selectivity of infigratinib for FGFR, especially FGFR1-3, over other tyrosine kinases. Infigratinib was approved by FDA for the treatment of cholangiocarcinoma patients with FGFR2 fusion in 2021 (Botrus et al., 2021; Javle et al., 2021).

Pemigatinib is another FGFR inhibitor featuring a tricyclic urea scaffold for the treatment of adults with previously treated, unresectable locally advanced or metastatic cholangiocarcinoma with a FGFR2 fusion or other rearrangement. Like infigratinib, pemigatinib contains a 3,5-dimethoxyphenyl for the high affinity and selectivity by filling the hydrophobic pocket, and two fluorine atoms, which led to further improvements in potency (**Figure 8**) (Wu et al., 2021). Many rounds of optimization also demonstrated that the ethyl group on the N-1 position of the cyclic urea and the pyrrole ring were of great importance to the potency and PK profile.



Starting from erdafitinib and its quinazolinone analogue, a series of pyrido [1,2-*a*] pyrimidinone derivatives were designed as novel selective FGFR inhibitors through scaffold hopping (**Figure 9A**) (Ran et al., 2021). Molecular docking suggested an overall similar binding mode with erdafitinib, while the rotatable pyrazole ring could lead to increased potency. The rotation also disrupted the planarity, which might enhance the aqueous solubility owing to reduced crystal-stacking.

AZD4547 is another pan-FGFR inhibitor bearing the pyrazole scaffold and just completed phase 2 clinical trial (NCT04439240) in multiple cancers with FGFR alterations. Based on the structure of AZD4547, Zhao *et al.* developed 1H-Pyrazolo [3,4-*b*]pyridine derivatives using scaffold hopping strategy, and incorporated two chlorines at the dimethoxyphenyl ring (**Figure 9B**) (Zhao et al., 2016). Notably, AZD4547 maintains efficacy to FGFR1 harboring gatekeeper mutation V561M as the flexible linker between dimethoxyphenyl and pyrazole allows conformational adaption



within the hydrophobic region (Sohl et al., 2015). However, it remains unknown whether 1H-Pyrazolo [3,4-*b*]pyridine derivative (a) has compromised its activity for mutated FGFRs.

CH5183284 (Debio1374) is a potent pan-inhibitor of FGFR1-3 with IC_{50} values of 9.3, 7.6 and 22 nM, respectively. It was discovered through a conventional high throughput screening and its interactions with the hinge region, hydrogen bonding pattern and an additional π - π interaction were also identified (Ebiike et al., 2016). CH5183284 is under clinical investigation for the treatment of cancer patients with FGFR genetic alterations (Nakanishi et al., 2014). Turner et al. (2017) described the application of SPROUT, a *de novo* computation program, to develop the active indazole-based pharmacophore for the inhibition of FGFR kinases (Figure 9C). Beginning with the co-crystal structure of CH5183284-FGFR1, they modified the indole moiety and obtained a small library of 23 indazole derivatives. Subsequent biological evaluation indicated that these indazole-containing fragments inhibited FGFR1-3 with IC_{50} values of 0.8–90 μ M, suggesting that structure-based drug discovery (SBDD) is becoming an essential tool for identifying potent and selective FGFR inhibitors.

There are numerous other non-covalent pan-FGFR inhibitors in clinical trial or development. For example, ASP5878 inhibited cell proliferation of urothelial cancer cell lines harboring FGFR3 point mutation or fusion and has completed phase 1 clinical trial in 2017 (NCT02038673) (Kikuchi et al., 2017). LY2874455 is a phase 1 orally available inhibitor with IC_{50} values of 2.8, 2.6, 6.4, and 6.0 nM against FGFR1-4, respectively (Michael et al., 2017). Rogaratinib (BAY 1163877) is another potent and selective FGFR1-4 inhibitor (Collin et al., 2018). Rogaratinib alone or in combination with other agents have been in a few clinical trials. 3D185, a highly selective FGFR1-3 inhibitor, was approved for investigational new drug by the NMPA in 2018 and followed by a phase 1 study in patients with the advanced solid tumors (NCT04221204). ICP-192 is a pan-inhibitor against FGFR1-4 and entered the phase 1/2 clinical trial for the treatment of advanced solid tumors, urothelial carcinoma, and cholangiocarcinoma (NCT04565275). E7090 has favorable pharmacokinetic profiles and sub-nanomolar inhibitory activity against FGFR1-3 with IC_{50} values of 0.71, 0.50, and 1.2 nM, respectively (Watanabe Miyano et al., 2016). The phase 2 study of E7090 in participants with unresectable advanced or metastatic

cholangiocarcinoma with *FGFR2* fusion is recruiting (NCT04238715).

4.2.2 Covalent Pan-FGFR Inhibitors

Covalent inhibition is a re-emerging strategy especially in the development of kinase inhibitors, which can make a big difference in binding affinity and selectivity. A covalent inhibitor typically consists of a drug-like scaffold offering noncovalent interactions and an appropriate electrophilic warhead to react with nucleophilic residues of target proteins. Cysteine represents the most targeted amino acid in kinases, due to its non-catalytic roles, low abundance, high reactivity and chemical plasticity of the anionic thiolate (Abdeldayem et al., 2020; Galbiati et al., 2020). For FGFRs, the conserved cysteine in the P-loop (C488 in FGFR1, C491 in FGFR2, C482 in FGFR3 and C477 in FGFR4) and the unique C552 in FGFR4 in the hinge region are sites for covalent attachment (Dai et al., 2019). This section focuses on recent publications with regard to the discovery of covalent pan-FGFR covalent inhibitors.

Zhou et al. (2010) discovered FIIN-1 as the first irreversible inhibitor of FGFR1–4 in 2010. The acrylamide of FIIN-1 formed covalent bond with a conserved cysteine (Cys488 of FGFR1) located at the rim of the P-loop. Replacing the acrylamide with a propylamide led to the failure of covalent bond formation. In addition, its selectivity over some other kinases (e.g., c-Src, TNK1, and YES) bearing the P-loop cysteine at the same position as FGFRs was also confirmed. Tan et al. (2014) developed FIIN-2 and FIIN-3 as irreversible inhibitors with potent *in vitro* inhibitory activity against FGFR1 and FGFR2 gatekeeper mutants, which conferred resistance to first-generation FGFR inhibitors. The acrylamide moiety in both molecules was installed on the 4-position of their phenyl rings in contrast to 3-acrylamide as found in FIIN-1, which still maintained the bond formation with P-loop cysteine while changed the selectivity over other kinases (PDB 4QQC, 4R5S, 4R6V).

Brameld et al. (2017) developed another irreversible inhibitor, PRN-1371, which shared a common core with FIIN-1. PRN-1371 was proven to be highly selective for FGFR1–4 over other kinases, including KDR, FLT-4, etc., and showed high FGFR1 occupancy and ideal PK profile. Ding et al. focused on the modification of the

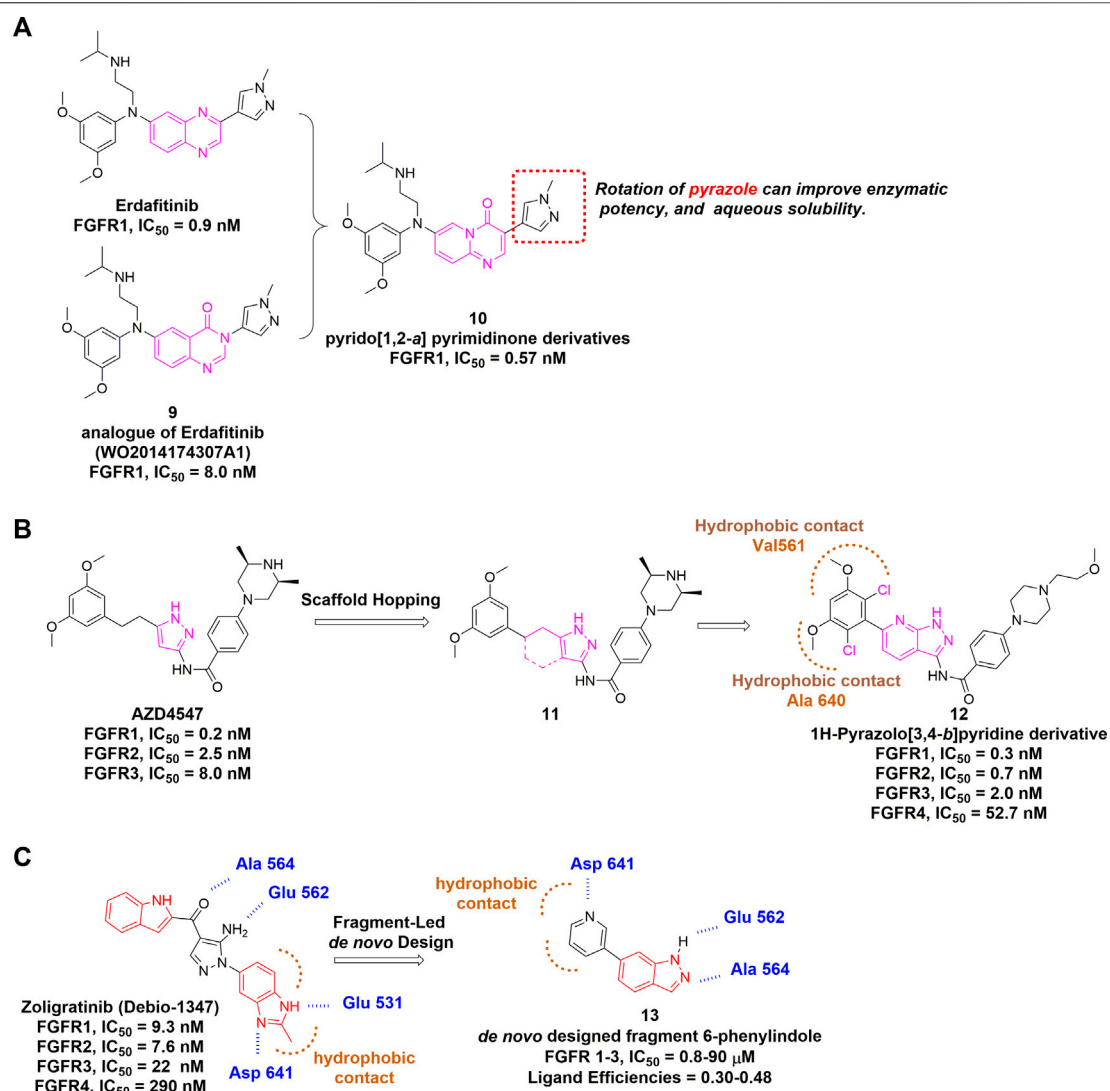


FIGURE 9 | (A) Discovery of pyrido [1,2-a] pyrimidinone derivatives as non-covalent pan-FGFR inhibitor. **(B)** Discovery of 1H-Pyrazolo [3,4-b]pyridine derivatives from AZD4547 and summary of its interactions with FGFR1 ATP binding site. Hydrophobic interactions are outlined by hashed brown arc (PDB: 4V05). **(C)** Summary of CH5183284 and designed fragment.

acrylamide-containing side chain of FIIN-1 and obtained the promising lead compound showing inhibitory effect in FGFR-amplified cancer cell lines (**Figure 10A**) (Li et al., 2017). The crystal structure of FGFR1 C488A in complex with lead compound revealed that the acrylamide side chain was located in the solvent accessible space and easily performed nucleophilic attack by the target cysteine.

Goyal et al. (2019) demonstrated that Futibatinib (TAS-120), a highly selective and irreversible pan-FGFR inhibitor, exhibited *in vitro* potency against wild-type FGFR1-4, as well as some FGFR2 kinase domain mutants. Hiroshi Sootome et al. (2020) reported the preclinical profile of futibatinib and suggested that it is an orally available, potent pan-FGFR inhibitor. Futibatinib is the most advanced candidate in the category of covalent pan-FGFR inhibitors because it is in phase 3 clinical trial to evaluate

the treatment of metastatic and recurrent unresectable cholangiocarcinoma harboring FGFR2 gene rearrangements.

Wang et al. (2018) designed and discovered a set of irreversible inhibitors bearing novel pyrrolopyrimidine scaffold. By analyzing the ATP binding pocket, they introduced a substituted phenyl moiety at the C-3 position of pyrrolopyrimidine to interact with hydrophobic region I (**Figure 10B**). Then the electrophilic warhead attached to N-1 via a pyrrolidine linker led to the identification of lead compound that showed excellent potencies against FGFR1-4 and acceptable selectivity over VEGFR2.

Wei et al. (2021) recently reported a class of 2H-pyrazolo [3,4-d]pyrimidine derivatives as a potent irreversible pan-FGFR inhibitor (**Figure 10C**). The lead compound was derived from BTK inhibitor ibrutinib and also shares a similar core with the

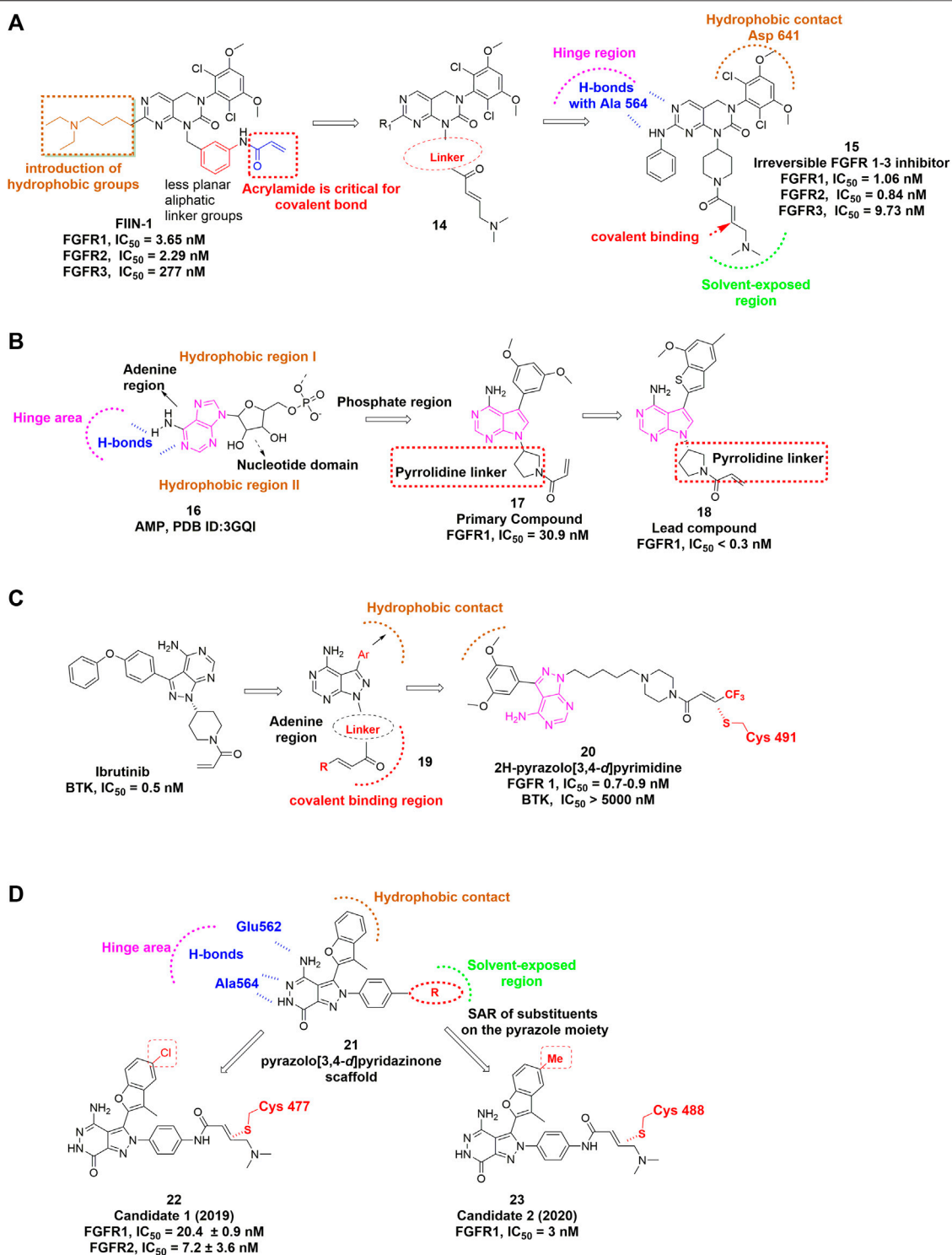


FIGURE 10 | (A) Structure optimization of FIIN-1. H-bonds are indicated by blue hashed lines. Hydrophobic interactions are outlined by hashed brown arc (PDB: 5B7V). The covalent bond-forming Michael acceptor carbon of the acrylamide is indicated by red arrow. **(B)** Discovery of irreversible inhibitors bearing novel pyrrolopyrimidine scaffold. **(C)** Discovery of 2H-pyrazolo [3,4-d]pyrimidine derivatives. Hydrophobic interaction region is outlined by hashed brown arc. Covalent binding region is highlighted by dashed red arc. **(D)** Covalent FGFR inhibitors bearing pyrazolo [3,4-d]pyridazinone.

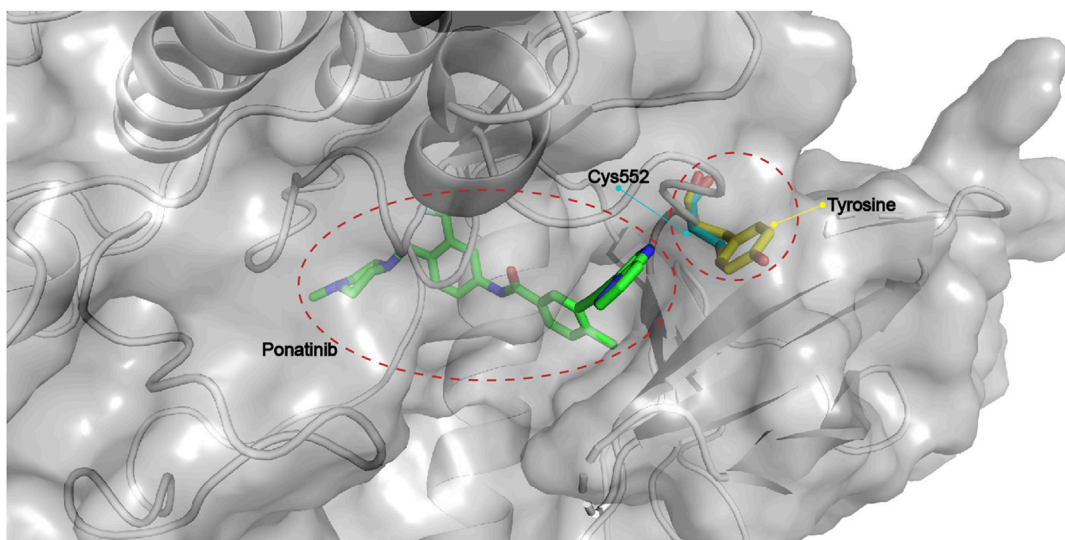


FIGURE 11 | Critical Cys552 in FGFR4 and replacement by tyrosine in FGFR1-3 (PDB: 4QRC, the crystal structure of FGFR4 in complex with Ponatinib).

above-mentioned lead compound. Interestingly, an electron-withdrawing terminal- CF_3 substituted acrylamide group provided the most potent inhibition against FGFRs.

There are several other covalent pan-FGFR inhibitors in development. For example, Yamani et al. (2021) discovered a pyrazole-benzimidazole CPL304110 as a pan-FGFR inhibitor for the treatment of bladder, gastric and squamous cell lung cancer, which also showed favorable pharmacokinetic properties after oral administration. Dai et al. (2020) reported that DW14383 simultaneously inhibited tumor proliferation and angiogenesis *via* inhibition of FGFR1–4 with similar potency. In addition, they claimed that its pan-tumor spectrum potential might overcome compensatory activation among FGFR1–4. Wang et al. (2019) developed a series of compounds featuring pyrazolo [3,4-*d*] pyridazinone as covalent FGFR inhibitors. Their structural optimization resulted in more analogues that could remarkably inhibit proliferation of various FGFR-dysregulated cancer cells and display potent antitumor efficacy in xenograft model as well (Figure 10D) (Xie et al., 2020).

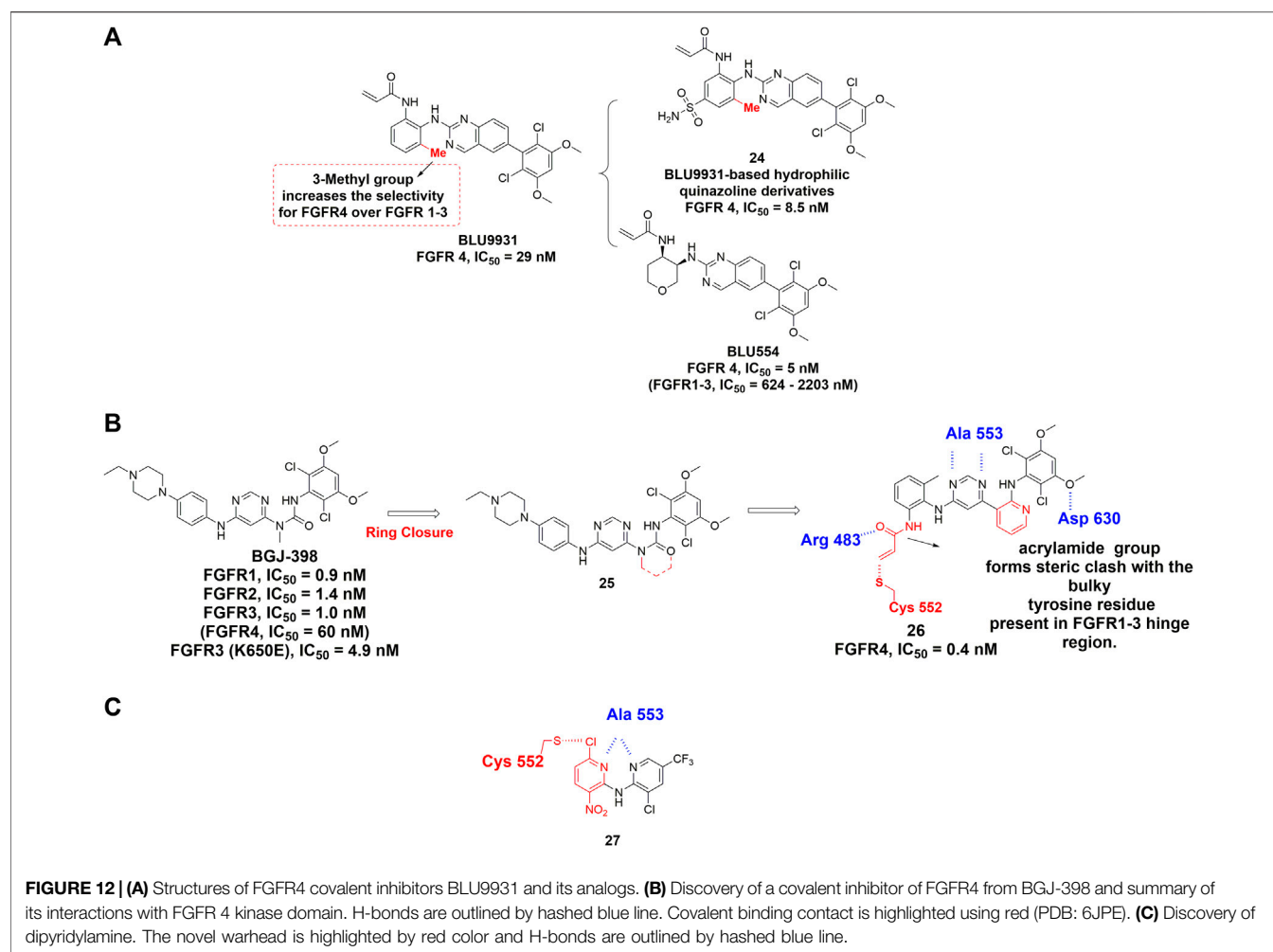
4.2.3 FGFR4-Specific Covalent Inhibitors

The kinase domains of FGFR1–3 share high structural similarity, whereas FGFR4 is relatively distinct from FGFR1–3 (Babina et al., 2017), which is consistent with the fact that many foregoing pan-FGFR inhibitors show strong inhibition of FGFR1–3 but reduced potency for FGFR4. Detailed comparison of the active sites of FGFR1–3 and FGFR4 revealed a key difference in the hinge region: Tyr563 in FGFR1–3 versus the Cys552 in FGFR4 (Figure 11) (Tucker et al., 2014). This unique Cys552 provides great opportunity for the design of highly selective, covalent inhibitors of FGFR4. Although there is no approved FGFR4-specific drug, the past years have witnessed growing numbers of promising compounds as discussed below.

Hagel et al. (2015) discovered BLU9931 as the first selective FGFR4 inhibitor for the treatment of hepatocellular carcinomas (HCC) with aberrant FGFR4 signaling. The dimethoxyphenyl group of BLU9931 occupied the hydrophobic pocket located near the gatekeeper valine of all FGFRs. In addition, an acrylamide at the ortho-position of the aniline can form the covalent bond with Cys552 in the hinge region of FGFR4. To achieve a better selectivity, the rotation of the phenyl ring was also taken into consideration because it could cause steric clash with the corresponding tyrosine in FGFR1–3 hinge region. Moreover, the addition of 3-methyl group on the aniline ring rendered BLU9931 with high selectivity for FGFR4 over FGFR1–3 (Figure 12A). Unfortunately, BLU9931 failed to enter clinical stage, presumably due to its rapid metabolism in liver microsomes. BLU554 (fisogatinib), an orally available analog of BLU9931, is now in phase 1 clinical trial to treat patients with HCC (NCT02508467) and in phase 1b/2 clinical trial in combination with CS1001.

H3B-6527 (Joshi et al., 2017) is another highly selective covalent FGFR4 inhibitor and is currently undergoing phase 1 study for the treatment of advanced HCC, liver neoplasms, hepatic carcinoma and so on. Co-crystal structure of FGFR4 in complex with H3B-6527 illustrated the covalent bond formation between Cys552 and the acrylamide at the ortho-position of the N-aryl substituent.

Fairhurst et al. (2020) reported the discovery of FGF401 (roblitinib) as a potent, selective FGFR4 inhibitor. Through high throughput screening, 2-formylquinoline amide (2-FQA) derivatives were identified as the starting hits. After optimization of the 2-FQA and the substituent groups on the hinge-binding pyridyl ring, roblitinib was eventually obtained with outstanding selectivity for FGFR4. Being assessed in phase 2 clinical trial, roblitinib is the most advanced covalent FGFR4-specific inhibitor. This inhibitor features a covalent yet rapidly



reversible mode of action that may reduce off-target related toxicity. Therefore, roblitinib is regarded as a promising next-generation drug to offer a new approach to target FGFR covalently.

Starting from BGJ-398 (infigratinib), Miranda et al. developed a novel covalent inhibitor of FGFR4 for the treatment of HCC (Rezende Miranda et al., 2020). According to the crystal structure of FGFR1-BGJ-398, the urea group and aminopyridine group should exhibit similar geometrical and electronic properties (Figure 12B). An acrylamide group was also attached to the ortho position of a 2-methylaniline ring for targeting Cys552 of FGFR4. Interestingly, crystallographic study revealed that the introduction of the methyl group into aniline phenyl rings facilitates the covalent reaction from a conformational perspective (PDB: 6JPE). As expected, its exceptional selectivity among the FGFR family is due to the fact that the acrylamide group formed steric clash with the bulky tyrosine residue present in FGFR1-3 hinge region.

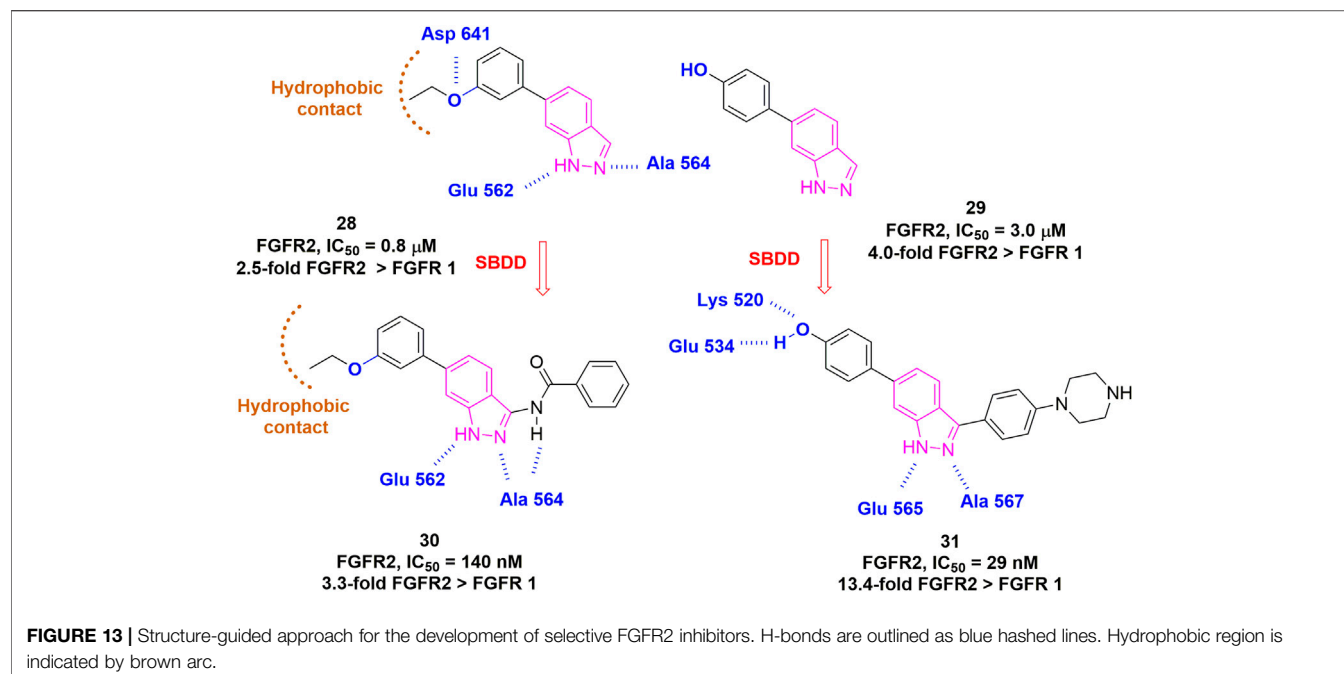
Fairhurst et al. (2017) reported the discovery of dipyrindylamine through high throughput screening (HTS). Dipyrindylamine contains a novel warhead 3-nitro-6-chloropyridyl, which was designed to achieve covalent binding

with Cys552 of FGFR4 (Figure 12C). The 6-chloro substituent in this warhead is positioned for attack by the Cys552 thiomethyl group through a nucleophilic aromatic substitution (S_NAr). Dipyrindylamine demonstrated high potency against FGFR4 with IC_{50} value of 53 nM while sparing the FGFR1-3 with IC_{50} values higher than 10 μ M. Besides, each nitrogen atom in pyridyl ring formed a hydrogen bond with hinge residue Ala553 (Lu et al., 2019). Dipyrindylamine features a relatively low molecular weight and novel mechanism of covalent binding that may serve as a promising lead compound for future discovery of FGFR4-specific covalent inhibitors.

Several candidates have entered clinical stages without full disclosure of chemical structures. For example, INCB-62079 entered phase 1 trial in 2017 but was terminated for business strategic consideration. ICP-105, a selective FGFR4 inhibitor, is now in phase 1 clinical trial for the treatment of solid tumor (NCT03642834). Other clinical trials involving inhibitors including ZSP-1241 and ABSK-011 are actively recruiting patients.

4.2.4 Selective FGFR2 Inhibitors

Unlike FGFR4, few FGFR1-3 subtype-specific kinase inhibitors have been reported to date, mainly aiming at FGFR2. Casaletto



et al. (2021) recently reported RLY-4008 as a highly selective inhibitor of FGFR2 WT/mutant, which exhibited >200-fold higher potency than FGFR1. Although the structure has not been disclosed, RLY-4008 showed no difference in binding modes with FGFR1 or FGFR2. Instead, a flexible loop in FGFR1/2 validated from MD simulation might be the cause of the selectivity. It is encouraging that a recent *de novo* design by Turner et al. (2021) has provided a paradigm for perhaps the next-generation member of FGFR-specific inhibitors. They started from a fragment with moderate potency and carried out iterative rounds of *de novo* design as well as a classical SAR study to generate compound **31**. Interestingly, compound **31** specifically inhibited FGFR2 with an IC_{50} of 29 nM, whereas 389 nM for FGFR1 and 758 nM for FGFR3, suggesting at least 10-fold selectivity for FGFR2 over FGFR1 (Figure 13).

4.3 Miscellaneous Types

4.3.1 Extracellular Allosteric Inhibitors

An extracellular allosteric inhibitor of FGFR can bind to its extracellular domain and modulate the receptor conformation, thus blocking the signaling pathway. The extracellular domains of FGFR1-4 exhibit discernible structural differences compared to their kinase domains, therefore it is possible to achieve selective inhibition within FGFR members. Alofanib (RPT835) belongs to this type of inhibitors and has entered a phase 1 clinical trial in Russia. By specifically binding to IgIII of FGFR2, alofanib is able to inhibit the FGF2-induced phosphorylation of FRS2 α with nanomolar activity in cancer cells expressing different FGFR2 isoforms (Tyulyandina et al., 2017). In addition, Tsimafeyeu et al. (2016) performed *in vivo* experiments to demonstrate that alofanib could ablate FGF-induced angiogenesis. Another example is SSR128129E, an orally-active, allosteric inhibitor of

FGFR1 (Herbert et al., 2013). It interacts with extracellular part of FGFR without interfering with FGF binding or receptor dimerization. Critical conformational changes were observed in IgIII subdomain when treated with SSR128129E, resulting in defective internalization of FGFRs.

4.3.2 Natural Products

Efforts have been made to identify natural products that act on FGFRs. These include a few phenolic compounds (resveratrol, caffeic acid phenethyl ester, kaempferol, etc.), stilbene glycosides, and sesterterpenes compounds (leucosesterterpenone, leucosterlactone, etc.), and a detailed review has been completed by Yin et al. (2019). Recently, Pagano et al. (2021) reported rosmarinic acid (RA), a natural phenolic compound, could induce FGF2/FGFR complex dissociation as verified by experimental mechanistic study. In addition, gambogic acid and ferulic acid, originated from natural plants, exhibited inhibitory effect of FGFR autophosphorylation. Taken together, natural products stand for a prime source of FGFR inhibitors, while more studies are needed to improve their activities and elucidate the molecular mechanisms. Chemical structures of these represent natural products are shown in Supplementary Figure S3.

5 OTHER SMALL MOLECULE-BASED THERAPEUTIC MODALITIES

5.1 Combination Therapy

Due to the extensive crosstalk between FGF/FGFR and other signaling pathways, the inhibition of FGF/FGFR signaling can be rescued by activation or upregulation of multiple signaling pathways. The most involved proteins are among the receptor tyrosine kinase

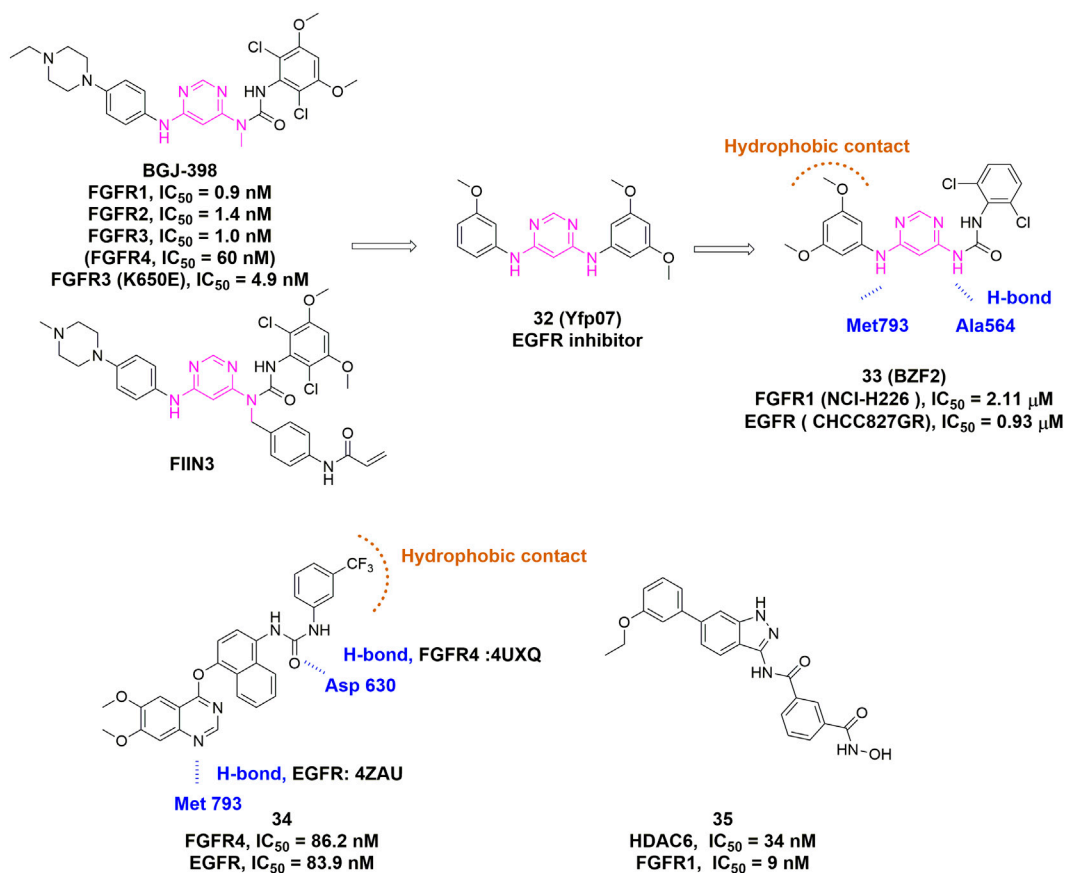


FIGURE 14 | Discovery of representative dual/multi-target inhibitors. H-bonds are outlined as blue hashed lines. Hydrophobic region is indicated by brown arc.

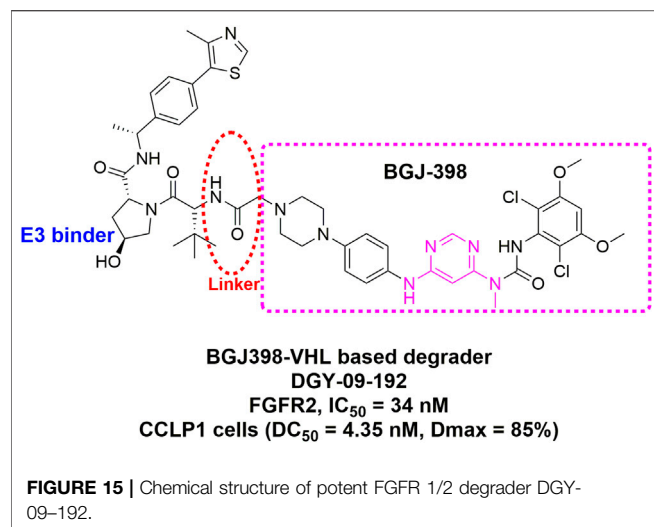
family, such as c-Met, EGFR, ErbB2/3 or even among four members of FGFR. The compensatory activation of alternative receptors or/and signaling pathways occurs frequently while a receptor function is suppressed specifically, and consequently the resistance to FGFR inhibitor is developed. Therefore, a combination of FGFR inhibitor with other types of drugs is a promising avenue to improve clinical efficacy of available therapeutics and overcome drug resistance.

Fischer et al. (2008) reported that cotreatment with FGFR inhibitors (SU5404/PD166866) and EGFR-targeting drugs (erlotinib/lapatinib) improved *in vivo* antiproliferative effects, indicating its potential as combination therapy in NSCLC. In addition to EGFR, other RTKs were also involved in the combination therapy with FGFR. The combined treatment of RET inhibitor (ST1571) and FGFR inhibitor (PD173074) significantly suppressed tumor growth of medullary thyroid cancer, which is intractable by surgery and has no widely accepted treatment (Ezzat et al., 2005). The addition of VEGFR1 inhibitors solved the limited practical effects of FGFR inhibitors in FGFR1-amplified breast cancers through blocking the contribution of FGFR1 to VEGF secretion (Golfmann et al., 2018).

Besides RTKs, many kinases are attractive targets in the combination therapy with FGFR inhibitors. The phosphoinositide 3-kinase (PI3K) inhibitor is used to achieve

superior antitumor effect in FGFR2 mutant endometrial cancer cell lines (Packer et al., 2017). PI3K also mediates resistance to FGFR inhibitors in urothelial cell carcinomas harboring alterations of FGFR3 gene, which both highlight the prospect of combination of their inhibitors (Wang et al., 2017). FGFR was also identified as a promoter to induce resistance to CDK4/6 inhibitors, which was diminished by complementary inhibition of FGFR in ER+/FGFR1-amplified breast cancers (Formisano et al., 2019). Similar antitumor effects were observed in synergism of mTOR and FGFR inhibitors, which resulted in significantly arrested cell cycle in G1 phase in AN3CA-derived endometrial tumor models (Gozgit et al., 2013). Krook et al. (2020) further implemented a combination therapy using an mTOR inhibitor (INK258) and demonstrated that this strategy may overcome the resistance to FGFR inhibitor like infigratinib. Moreover, through a kinome-wide CRISPR-based screening, Yang et al. identified PLK1 and FGFR as promising synthetic lethal targets for treating FGFR1-amplified lung cancer (Yang et al., 2021).

Overexpression of FGFs may also cause hyperactivated FGF/FGFR signaling, which is present in some tumors and can be co-targeted accordingly. The frequent presence of both BRAF mutations and FGF2 overexpression in melanomas, which lack a recognized systematic therapy so far, leads to the combination



of FGFR inhibitor PD166866 and BRAF V600E inhibitor, consequently increased cell apoptosis and restricted tumor growth (Metzner et al., 2011). Wang et al. (2019) further revealed that upregulated secretion of FGF1 gave rise to resistance to the combined therapy of RAF inhibitor vemurafenib and MEK inhibitor cobimetinib in BRAF V600E-driven tumors, which was abrogated by addition of FGFR inhibitors to achieve a triple BRAF/MEK/FGFR inhibition.

Tremendous potential also lies in cooperation of FGFR inhibitors with immune checkpoint inhibitors (Qin et al., 2020). For instance, Palakurthi *et al.* demonstrated the combination of erdafitinib and PD-1 blockade RMP1-14 could achieve remarkable tumor regression and significantly improve survival in mice with a FGFR2-driven lung tumor harboring dual mutations on FGFR2 and P53 genes (Palakurthi et al., 2019).

Despite a number of successful attempts of combination therapy, the drug-drug interactions may cause unpredictable toxicity and should be assessed with meticulousness. For example, the combination of infigratinib with imatinib encountered higher toxicity and frequent adverse effects, including CPK elevation, lipase elevation, hyperphosphatemia, anemia, and peripheral edema (NCT02257541).

5.2 Dual/Multi-Target Inhibitors

Dual/multi-target inhibitors have several potential advantages over combination therapy, such as more predictable pharmacokinetics, better patient compliance, reduced administration dosage and toxicities (Duan et al., 2021). Previous advances in the field of TKIs validated a diversity of promising and well-tolerated targets, including EGFR, ALK, ROS1, HER2, NTRK, VEGFR, RET, MET, MEK, FGFR, PDGFR, PI3K and KIT, which have inspired the discovery and rational design of dual/multi-target inhibitors.

From the perspective of medicinal chemistry, most of the present dual/multi-target inhibitors can be assigned to the first- or second-generation FGFR TKIs. In some cases, their low selectivity over aforementioned targets has in turn created a synergistic inhibitory effect in diseases involving abnormal

FGFR and the other target(s). MPT0L145, an alleged dual-target inhibitor of PIK3C3 and FGFR, not only increased autophagosome formation due to FGFR inhibition but also interfered with autophagic flux via PIK3C3 inhibition. It synergistically sensitized anticancer effects of targeted- or chemo-therapy in different cancer cell lines (Chen et al., 2018). Besides, FGFR/EGFR and FGFR/VEGFR dual inhibition strategies are also frequently reported. FGFR/EGFR dual inhibitors can be exemplified by FIIN3, while FGFR/VEGFR dual inhibitors include PD173074, AZD2171 (cediranib), BMS-540215 (brivanib), ODM-203, and so on (Chen et al., 2019).

Recently, several publications have paved the way for the rational design of dual/multi-target FGFR inhibitors. Chen *et al.* applied SVM machine learning algorithm to establish QSAR models for FGFR4 and EGFR, which led to the identification of **Cpd 34** as a potent inhibitor of FGFR and EGFR with similar IC₅₀ values but distinct binding modes (Figure 14) (Chen et al., 2020). Xie et al. developed a series of 4,6-pyrimidinediamine derivatives through incorporation of key scaffolds from FGFR inhibitors (FIIN3 and infigratinib) and EGFR inhibitors (Figure 14, **Cpd 32**) (Sacks et al., 2018). The most promising compound, **BZF2** (Figure 14, **Cpd 33**), potently inhibited cell proliferation and cell migration, and induced apoptosis in NSCLC cell lines with FGF2-FGFR1 autocrine loop. Moreover, it exhibited outstanding *in vivo* anti-tumor activity. Apart from FGFR/EGFR dual inhibitors, the FGFR/HDAC dual inhibitors were also reported by Liu et al. (2018). The 1-H-indazol-3-amine-derived FGFR/HDAC dual inhibitor (Figure 14, **Cpd 35**) exhibited HDAC6 and FGFR1 dual inhibitions with IC₅₀ values of 34 and 9 nM, respectively.

5.3 FGFR Degraders

Proteolysis targeting chimera (PROTAC) was first reported by the Crews and Deshaies laboratories in 2001 (Hu et al., 2020; Pettersson et al., 2019). Rather than acting as conventional inhibitors, PROTACs induce selective intracellular proteolysis of target proteins. This novel strategy is likely to circumvent the common disadvantages of traditional occupancy-driven inhibitors such as the toxicity due to off-target and drug resistance caused by compensatory feedback activation of alternative kinases (Paiva et al., 2019). Several kinase targets employing the PROTAC strategy have been explored, including EGFR, HER2, c-Met, ALK, Akt, CK2, ERK1/2, FLT3, PI3K, BTK, RIPK2, and BCR-ABL, most of which are cytosol- or nuclei-located proteins. As for membrane-associated tyrosine kinase receptors like EGFR, Burslem et al. (2018) conjugated a kinase inhibitor Lapatinib to a VHL ligand for degradation of EGFR, HER2, and c-Met. Interestingly, the PROTAC mediated the internalization of EGFR and sorted to lysosomal degradation, although the RTKs usually prefer to be internalized into a recycling endosome (Zou et al., 2019). Du et al. (2021) recently reported a bivalent degrader DGY-09-192, which coupled pan-FGFR inhibitor BGJ-398 to a CRL2^{VHL} E3 ligase (Figure 15). Surprisingly, DGY-09-192 preferentially induced FGFR1 and FGFR2 degradation while largely sparing FGFR3 and FGFR4. Despite multiple concerns regarding cellular permeability, the feasibility of scalable synthesis, and so on (Goracci et al., 2020; Liu et al., 2020), these pioneering studies have demonstrated that the

PROTAC approach has a great potential to expand the arsenal against a variety of FGFRs-altered cancers.

6 CONCLUDING REMARKS

As a type of membrane receptor, FGFR plays a critical role in cell signal transduction and mediates diverse cellular events and processes through a ligand-dependent characteristic. Genetic amplification, mutation, and/or fusion of *FGFR* occurring frequently in various kinds of cancers, can over-activate downstream signaling pathways and cause excessive common oncogenic inducements, such as cell proliferation, inadequate cell apoptosis and cell transformation.

Due to the increasing incidence of abnormal FGF/FGFR signaling axis in various malignancy, such as breast cancers, lung cancers and bladder cancers, FGFRs have been recognized as attractive therapeutic targets. A great number of FGFR inhibitors have been developed in the past decades. Erdafitinib, Pemigatinib and Infigratinib were approved by FDA in 2019, 2020 and 2021, respectively, to treat limited subsets of bladder cancer and cholangiocarcinoma patients with corresponding FGFR alterations, while dozens of other inhibitors are racing in preclinical and clinical development.

TKIs make up a major portion of FGFR-targeting small molecules. The first-generation FGFR inhibitors are general TKIs with a wide spectrum of inhibitory effects for multiple kinases. In contrast, second-generation FGFR inhibitors have improved selectivity, potency and lowered drug resistance, as a result of delicate structure-based design focusing on either optimizing non-covalent interactions with ATP-binding site or the use of covalent warheads to modify critical Cys residues.

The FGFR2 selective inhibitors generated by *de novo* design hold great promise for targeting specific members of FGFR1-3. These inhibitors may possess higher safety, as pan-FGFR inhibitors often display “FGFR1-specific” toxicity that leads to adverse side effects which are presumably originated from abnormal signaling of FGF23 (Chae et al., 2017).

Macrocyclization may serve as another potential strategy for novel FGFR inhibitors. Generally, macrocyclic molecules offer superior binding affinity with targets bearing large and featureless pockets. As seen in other kinase inhibitors, macrocyclic inhibitors also exhibit improved cell permeability, plasma stability and oral absorption when compared to traditional small molecules (Engelhardt et al., 2019; Begnini et al., 2021).

Although there is no allosteric TKI reported for FGFR, this strategy was applied to overcome the drug-resistant EGFR T790M mutant. Jia et al. (2016) described the rational discovery of EAI045, a fourth-generation EGFR inhibitor that targeted an allosteric pocket of the EGFR mutant but not the wild-type kinase. Given the structural similarity between EGFR and FGFR, this finding could give a hint about the design of allosteric TKIs for the latter.

Compared with conventional CADD, it is believed that artificial intelligence (AI) can expand chemical space in a more comprehensive way. Zhavoronkov et al. (2019) established the first deep-learning-based *de novo* design method (GENTRL) to discover inhibitors for a receptor tyrosine kinase called DDR1. In addition, the

forementioned work regarding FGFR4/EGFR dual inhibitor by Chen et al. (2020) also demonstrated the great potential of AI for the discovery of novel FGFR inhibitors with different modes of action.

Small molecules other than TKIs, such as extracellular domain binders or natural products, is another potential source of novel modalities. Many of these molecules show selectivity towards certain subtype of FGFR, probably because the extracellular domains of FGFR1-4 are structurally more distinct than kinase domains. The rapidly emerging resistance to current TKIs may also be overcome by these novel types of molecules. Additionally, it seems unnecessary to impose harsh criteria for cell permeability of these molecules as they typically function outside cells.

Combination therapy and dual/multi-target inhibitor are conceptually similar, while the latter apparently has more advantages since it circumvents any drug-drug interactions. While the rational design of dual inhibitors of FGFR/EGFR, FGFR/VEGFR, and FGFR/HDAC may inspire rapid discovery of more inhibitors simultaneously acting on FGFR and another target, identification of more genes that can robustly cause synthetic lethality with *FGFR* is the central problem and requires extensive in-depth research.

The thriving techniques of targeted protein degradation including PROTAC, molecular glue, as well as other TACs (AUTAC, LYTAC, ATTEC, etc.), have demonstrated broad applicability. PROTACs for RTKs including EGFR and FGFR, have been recently reported, all of which utilized current kinase inhibitors as the RTK binders. It can be envisaged that small molecules occupying a pocket of the kinase beyond ATP-binding site are especially suitable for designing new PROTACs. Such PROTACs are supposed to improve the selectivity and offer solutions to combat drug resistance.

This review encompassed most of the existing FGFR inhibitors and elaborated important structures from a medicinal chemistry perspective. We anticipate that more and more tailor-made novel small molecules of different types and modalities will be developed to improve future targeted therapy with higher efficacy and lower toxicity.

AUTHOR CONTRIBUTIONS

JZ and WZ conducted the literature review and wrote the draft. LL, SN and ZG edited the draft and made significant revisions. All authors read and approved the final.

FUNDING

This work was supported by the research foundation of talented scholars from Chongqing Medical University, the National Natural Science Foundation of China (22177017) and Innovative Group of Natural Science Foundation of Chongqing (CXQT21016).

SUPPLEMENTARY MATERIAL

The Supplementary Material for this article can be found online at: <https://www.frontiersin.org/articles/10.3389/fchem.2022.860985/full#supplementary-material>

REFERENCES

- Abdeldayem, A., Raouf, Y. S., Constantinescu, S. N., Moriggl, R., and Gunning, P. T. (2020). Advances in Covalent Kinase Inhibitors. *Chem. Soc. Rev.*, 49, 2617–2687. doi:10.1039/c9cs00720b
- Akbulut, O., Lengerli, D., Saatci, O., Duman, E., Seker, U. O. S., Isik, A., et al. (2020). A Highly Potent TACC3 Inhibitor as a Novel Anticancer Drug Candidate. *Mol. Cancer Ther.* 19, 1243–1254. doi:10.1158/1535-7163.MCT-19-0957
- Angelin, B., Larsson, T. E., and Rudling, M. (2012). Circulating Fibroblast Growth Factors as Metabolic Regulators-A Critical Appraisal. *Cel Metab.*, 16, 693–705. doi:10.1016/j.cmet.2012.11.001
- Angevin, E., Lopez-Martin, J. A., Lin, C.-C., Gschwend, J. E., Harzstark, A., Castellano, D., et al. (2013). Phase I Study of Dovitinib (TKI258), an Oral FGFR, VEGFR, and PDGFR Inhibitor, in Advanced or Metastatic Renal Cell Carcinoma. *Clin. Cancer Res.* 19, 1257–1268. doi:10.1158/1078-0432.CCR-12-2885
- Ayala-Aguilera, C. C., Valero, T., Lorente-Macias, A., Baillache, D. J., Croke, S., and Unciti-Broceta, A. (2022). Small Molecule Kinase Inhibitor Drugs (1995–2021): Medical Indication, Pharmacology, and Synthesis. *J. Med. Chem.*, 65, 1047–1131. doi:10.1021/acs.jmedchem.1c00963
- Azam, M., Seeliger, M. A., Gray, N. S., Kuriyan, J., and Daley, G. Q. (2008). Activation of Tyrosine Kinases by Mutation of the Gatekeeper Threonine. *Nat. Struct. Mol. Biol.*, 15, 1109–1118. doi:10.1038/nsmb.1486
- Babina, I. S., and Turner, N. C. (2017). Advances and Challenges in Targeting FGFR Signalling in Cancer. *Nat. Rev. Cancer*, 17, 318–332. doi:10.1038/nrc.2017.8
- Baldia, P. H., Maurer, A., Heide, T., Rose, M., Stoeck, R., Hartmann, A., et al. (2016). Fibroblast Growth Factor Receptor (FGFR) Alterations in Squamous Differentiated Bladder Cancer: a Putative Therapeutic Target for a Small Subgroup. *Oncotarget* 7, 71429–71439. doi:10.18632/oncotarget.12198
- Begnini, F., Poongavanam, V., Over, B., Castaldo, M., Geschwindner, S., Johansson, P., et al. (2021). Mining Natural Products for Macrocycles to Drug Difficult Targets. *J. Med. Chem.* 64, 1054–1072. doi:10.1021/acs.jmedchem.0c01569
- Bello, E., Colella, G., Scarlato, V., Oliva, P., Berndt, A., Valbusa, G., et al. (2011). E-3810 Is a Potent Dual Inhibitor of VEGFR and FGFR that Exerts Antitumor Activity in Multiple Preclinical Models. *Cancer Res.* 71, 1396–1405. doi:10.1158/0008-5472.CAN-10-2700
- Belov, A. A., and Mohammadi, M. (2013). Molecular Mechanisms of Fibroblast Growth Factor Signaling in Physiology and Pathology. *Cold Spring Harbor Perspect. Biol.*, 5, a015958. doi:10.1101/cshperspect.a015958
- Bhide, R. S., Cai, Z.-W., Zhang, Y.-Z., Qian, L., Wei, D., Barbosa, S., et al. (2006). Discovery and Preclinical Studies of (R)-1-(4-(4-fluoro-2-methyl-1H-indol-5-yloxy)-5-Methylpyrrolo[2,1-F][1,2,4]triazin-6-Yloxy)propan-2-ol (BMS-540215), an *In Vivo* Active Potent VEGFR-2 Inhibitor. *J. Med. Chem.* 49, 2143–2146. doi:10.1021/jm051106d
- Bono, F., De Smet, F., Herbert, C., De Bock, K., Georgiadou, M., Fons, P., et al. (2013). Inhibition of Tumor Angiogenesis and Growth by a Small-Molecule Multi-FGF Receptor Blocker with Allosteric Properties. *Cancer Cell* 23, 477–488. doi:10.1016/j.ccr.2013.02.019
- Botrus, G., Raman, P., Oliver, T., and Bekaii-Saab, T. (2021). Infigratinib (BGJ398): an Investigational Agent for the Treatment of FGFR-Altered Intrahepatic Cholangiocarcinoma. *Expert Opin. Investig. Drugs*, 30, 309–316. doi:10.1080/13543784.2021.1864320
- Brameld, K. A., Owens, T. D., Verner, E., Venetsanakos, E., Bradshaw, J. M., Phan, V. T., et al. (2017). Discovery of the Irreversible Covalent FGFR Inhibitor 8-(3-(4-Acryloylpiperazin-1-Yl)propyl)-6-(2,6-Dichloro-3,5-Dimethoxyphenyl)-2-(methylamino)pyrido[2,3-D]pyrimidin-7(8h)-One (PRN1371) for the Treatment of Solid Tumors. *J. Med. Chem.* 60, 6516–6527. doi:10.1021/acs.jmedchem.7b00360
- Brooks, A. N., Kilgour, E., and Smith, P. D. (2012). Molecular Pathways: Fibroblast Growth Factor Signaling: a New Therapeutic Opportunity in Cancer. *Clin. Cancer Res.* 18, 1855–1862. doi:10.1158/1078-0432.Ccr-11-0699
- Bunney, T. D., Wan, S., Thiagarajan, N., Sutto, L., Williams, S. V., Ashford, P., et al. (2015). The Effect of Mutations on Drug Sensitivity and Kinase Activity of Fibroblast Growth Factor Receptors: A Combined Experimental and Theoretical Study. *EBioMedicine* 2, 194–204. doi:10.1016/j.ebiom.2015.02.009
- Burbridge, M. F., Bossard, C. J., Saunier, C., Fejes, I., Bruno, A., Léonce, S., et al. (2013). S49076 Is a Novel Kinase Inhibitor of MET, AXL, and FGFR with strong Preclinical Activity Alone and in Association with Bevacizumab. *Mol. Cancer Ther.* 12, 1749–1762. doi:10.1158/1535-7163.MCT-13-0075
- Burslem, G. M., Smith, B. E., Lai, A. C., Jaime-Figueroa, S., McQuaid, D. C., Bondeson, D. P., et al. (2018). The Advantages of Targeted Protein Degradation over Inhibition: An RTK Case Study. *Cel Chem. Biol.* 25, 67–77. doi:10.1016/j.chembiol.2017.09.009
- Cancer Genome Atlas Research Network (2014). Comprehensive Molecular Characterization of Gastric Adenocarcinoma. *Nature* 513, 202–209. doi:10.1038/nature13480
- Cao, Z.-X., Zheng, R.-L., Lin, H.-J., Luo, S.-D., Zhou, Y., Xu, Y.-Z., et al. (2011). SKLB610: a Novel Potential Inhibitor of Vascular Endothelial Growth Factor Receptor Tyrosine Kinases Inhibits Angiogenesis and Tumor Growth *In Vivo*. *Cell Physiol Biochem* 27, 565–574. doi:10.1159/000329978
- Capdevila, J., Carrato, A., Tabernero, J., and Grande, E. (2014). What Could Nintedanib (BIBF 1120), a Triple Inhibitor of VEGFR, PDGFR, and FGFR, Add to the Current Treatment Options for Patients with Metastatic Colorectal Cancer? *Crit. Rev. Oncology/Hematology*, 92, 83–106. doi:10.1016/j.critrevonc.2014.05.004
- Carpinelli, P., Ceruti, R., Giorgini, M. L., Cappella, P., Gianellini, L., Croci, V., et al. (2007). PHA-739358, a Potent Inhibitor of Aurora Kinases with a Selective Target Inhibition Profile Relevant to Cancer. *Mol. Cancer Ther.* 6, 3158–3168. doi:10.1158/1535-7163.MCT-07-0444
- Casaleto, J., Maglic, D., Toure, B. B., Taylor, A., Schoenherr, H., Hudson, B., et al. (2021). Abstract 1455: RLY-4008, a Novel Precision Therapy for FGFR2-Driven Cancers Designed to Potently and Selectively Inhibit FGFR2 and FGFR2 Resistance Mutations. *Cancer Res.* 81, 1455. doi:10.1158/1538-7445.AM2021-1455
- Chae, Y. K., Ranganath, K., Hammerman, P. S., Vaklavas, C., Mohindra, N., Kalyan, A., et al. (2017). Inhibition of the Fibroblast Growth Factor Receptor (FGFR) Pathway: the Current Landscape and Barriers to Clinical Application. *Oncotarget* 8, 16052–16074. doi:10.18632/oncotarget.14109
- Chen, C.-H., Changou, C. A., Hsieh, T.-H., Lee, Y.-C., Chu, C.-Y., Hsu, K.-C., et al. (2018). Dual Inhibition of PIK3C3 and FGFR as a New Therapeutic Approach to Treat Bladder Cancer. *Clin. Cancer Res.* 24, 1176–1189. doi:10.1158/1078-0432.CCR-17-2066
- Chen, C.-H., Liu, Y.-M., Pan, S.-L., Liu, Y.-R., Liou, J.-P., and Yen, Y. (2016). Trichlorobenzene-substituted Azaaryl Compounds as Novel FGFR Inhibitors Exhibiting Potent Antitumor Activity in Bladder Cancer Cells *In Vitro* and *In Vivo*. *Oncotarget*, 7, 26374–26387. doi:10.18632/oncotarget.8380
- Chen, G., Bao, Y., Weng, Q., Zhao, Y., Lu, X., Fu, L., et al. (2019). Compound 15c, a Novel Dual Inhibitor of EGFR/858R/T790M and FGFR1, Efficiently Overcomes Epidermal Growth Factor Receptor-Tyrosine Kinase Inhibitor Resistance of Non-small-cell Lung Cancers. *Front. Pharmacol.* 10, 1533. doi:10.3389/fphar.2019.01533
- Chen, H., Ma, J., Li, W., Eliseenkova, A. V., Xu, C., Neubert, T. A., et al. (2007). A Molecular Brake in the Kinase Hinge Region Regulates the Activity of Receptor Tyrosine Kinases. *Mol. Cel* 27, 717–730. doi:10.1016/j.molcel.2007.06.028
- Chen, X., Xie, W., Yang, Y., Hua, Y., Xing, G., Liang, L., et al. (2020). Discovery of Dual FGFR4 and EGFR Inhibitors by Machine Learning and Biological Evaluation. *J. Chem. Inf. Model.* 60, 4640–4652. doi:10.1021/acs.jcim.0c00652
- Collin, M.-P., Lobell, M., Hübsch, W., Brohm, D., Schirok, H., Jautelat, R., et al. (2018). Discovery of Rogaratinib (BAY 1163877): a Pan-FGFR Inhibitor. *ChemMedChem* 13, 437–445. doi:10.1002/cmdc.201700718
- Cortes, J. E., Kim, D.-W., Pinilla-Ibarz, J., le Coutre, P. D., Paquette, R., Chuah, C., et al. (2018). Ponatinib Efficacy and Safety in Philadelphia Chromosome-Positive Leukemia: Final 5-year Results of the Phase 2 PACE Trial. *Blood* 132, 393–404. doi:10.1182/blood-2016-09-739086
- Couffignal, C., Desgrandchamps, F., Mongiat-Artus, P., Ravery, V., Ouzaid, I., Roupert, M., et al. (2015). The Diagnostic and Prognostic Performance of Urinary FGFR3 Mutation Analysis in Bladder Cancer Surveillance: A Prospective Multicenter Study. *Urology* 86, 1185–1191. doi:10.1016/j.urology.2015.07.036
- Dai, M.-d., Wang, Y.-L., Fan, J., Dai, Y., Ji, Y.-c., Sun, Y.-m., et al. (2020). DW14383 Is an Irreversible Pan-FGFR Inhibitor that Suppresses FGFR-dependent Tumor

- Growth *In Vitro* and *In Vivo*. *Acta Pharmacol. Sin* 42, 1498–1506. doi:10.1038/s41401-020-00567-3
- Dai, S., Zhou, Z., Chen, Z., Xu, G., and Chen, Y. (2019). Fibroblast Growth Factor Receptors (FGFRs): Structures and Small Molecule Inhibitors. *Cells*, 8, 614. doi:10.3390/cells8060614
- Ding, X., Boney-Montoya, J., Owen, B. M., Bookout, A. L., Coate, K. C., Mangelsdorf, D. J., et al. (2012). β Klotho Is Required for Fibroblast Growth Factor 21 Effects on Growth and Metabolism. *Cel Metab.* 16, 387–393. doi:10.1016/j.cmet.2012.08.002
- Dorey, K., and Amaya, E. (2010). FGF Signalling: Diverse Roles during Early Vertebrate Embryogenesis. *Development*, 137, 3731–3742. doi:10.1242/dev.037689
- Du, G., Jiang, J., Wu, Q., Henning, N. J., Donovan, K. A., Yue, H., et al. (2021). Discovery of a Potent Degradable for Fibroblast Growth Factor Receptor 1/2. *Angew. Chem. Int. Ed.* 60, 15905–15911. doi:10.1002/anie.202101328
- Duan, Y.-C., Zhang, S.-J., Shi, X.-J., Jin, L.-F., Yu, T., Song, Y., et al. (2021). Research Progress of Dual Inhibitors Targeting Crosstalk between Histone Epigenetic Modulators for Cancer Therapy. *Eur. J. Med. Chem.* 222, 113588. doi:10.1016/j.ejmech.2021.113588
- Dubreuil, P., Letard, S., Ciufolini, M., Gros, L., Humbert, M., Castéran, N., et al. (2009). Masitinib (AB1010), a Potent and Selective Tyrosine Kinase Inhibitor Targeting KIT. *PLoS One* 4, e2758. doi:10.1371/journal.pone.0007258
- Dutt, A., Salvesen, H. B., Chen, T.-H., Ramos, A. H., Onofrio, R. C., Hattton, C., et al. (2008). Drug-sensitive FGFR2 Mutations in Endometrial Carcinoma. *Proc. Natl. Acad. Sci. U.S.A.* 105, 8713–8717. doi:10.1073/pnas.080379105
- Ebiike, H., Taka, N., Matsushita, M., Ohmori, M., Takami, K., Hyohdoh, I., et al. (2016). Discovery of [5-Amino-1-(2-Methyl-3h-Benzimidazol-5-Yl)pyrazol-4-Yl]-(1h-Indol-2-Yl)methanone (CH5183284/Debio 1347), an Orally Available and Selective Fibroblast Growth Factor Receptor (FGFR) Inhibitor. *J. Med. Chem.* 59, 10586–10600. doi:10.1021/acs.jmedchem.6b01156
- Edwards, J., Krishna, N. S., Witton, C. J., and Bartlett, J. M. (2003). Gene Amplifications Associated with the Development of Hormone-Resistant Prostate Cancer. *Clin. Cancer Res.*, 9, 5271–5281.
- Engelhardt, H., Böse, D., Petronczki, M., Scharn, D., Bader, G., Baum, A., et al. (2019). Start Selective and Rigidify: The Discovery Path toward a Next Generation of EGFR Tyrosine Kinase Inhibitors. *J. Med. Chem.* 62, 10272–10293. doi:10.1021/acs.jmedchem.9b01169
- Ezzat, S., Huang, P., Dackiw, A., and Asa, S. L. (2005). Dual Inhibition of RET and FGFR4 Restrains Medullary Thyroid Cancer Cell Growth. *Clin. Cancer Res.*, 11, 1336–1341.
- Fairhurst, R. A., Knoepfel, T., Buschmann, N., Leblanc, C., Mah, R., Todorov, M., et al. (2020). Discovery of Roblitiinib (FGF401) as a Reversible-Covalent Inhibitor of the Kinase Activity of Fibroblast Growth Factor Receptor 4. *J. Med. Chem.* 63, 12542–12573. doi:10.1021/acs.jmedchem.0c01019
- Fairhurst, R. A., Knoepfel, T., Leblanc, C., Buschmann, N., Gaul, C., Blank, J., et al. (2017). Approaches to Selective Fibroblast Growth Factor Receptor 4 Inhibition through Targeting the ATP-Pocket Middle-Hinge Region. *Med. Chem. Commun.* 8, 1604–1613. doi:10.1039/c7md00213k
- Farooq, A., and Zhou, M.-M. (2004). Structure and Regulation of MAPK Phosphatases. *Cell Signal.* 16, 769–779. doi:10.1016/j.cellsig.2003.12.008
- Fearon, A. E., and Grose, R. P. (2014). Grb-ing Receptor Activation by the Tail. *Nat. Struct. Mol. Biol.* 21, 113–114. doi:10.1038/nsmb.2767
- Fernandes-Freitas, I., and Owen, B. M. (2015). Metabolic Roles of Endocrine Fibroblast Growth Factors. *Curr. Opin. Pharmacol.* 25, 30–35. doi:10.1016/j.coph.2015.09.014
- Fischer, H., Taylor, N., Allerstorfer, S., Grusch, M., Sonvilla, G., Holzmann, K., et al. (2008). Fibroblast Growth Factor Receptor-Mediated Signals Contribute to the Malignant Phenotype of Non-small Cell Lung Cancer Cells: Therapeutic Implications and Synergism with Epidermal Growth Factor Receptor Inhibition. *Mol. Cancer Ther.* 7, 3408–3419. doi:10.1158/1535-7163.Mct-08-0444
- Fletcher, G. C., Brox, R. D., Denny, T. A., Hembrough, T. A., Plum, S. M., Fogler, W. E., et al. (2011). ENMD-2076 Is an Orally Active Kinase Inhibitor with Antiangiogenic and Antiproliferative Mechanisms of Action. *Mol. Cancer Ther.* 10, 126–137. doi:10.1158/1535-7163.MCT-10-0574
- Formisano, L., Lu, Y., Servetto, A., Hanker, A. B., Jansen, V. M., Bauer, J. A., et al. (2019). Aberrant FGFR Signaling Mediates Resistance to CDK4/6 Inhibitors in ER+ Breast Cancer. *Nat. Commun.* 10, 1373. doi:10.1038/s41467-019-09068-2
- Furdui, C. M., Lew, E. D., Schlessinger, J., and Anderson, K. S. (2006). Autophosphorylation of FGFR1 Kinase Is Mediated by a Sequential and Precisely Ordered Reaction. *Mol. Cell*, 21, 711–717. doi:10.1016/j.molcel.2006.01.022
- Furet, P., Caravatti, G., Guagnano, V., Lang, M., Meyer, T., and Schoepfer, J. (2008). Entry into a New Class of Protein Kinase Inhibitors by Pseudo Ring Design. *Bioorg. Med. Chem. Lett.*, 18, 897–900. doi:10.1016/j.bmcl.2007.12.041
- Futami, T., Okada, H., Kihara, R., Kawase, T., Nakayama, A., Suzuki, T., et al. (2017). ASP5878, a Novel Inhibitor of FGFR1, 2, 3, and 4, Inhibits the Growth of FGF19-Expressing Hepatocellular Carcinoma. *Mol. Cancer Ther.* 16, 68–75. doi:10.1158/1535-7163.MCT-16-0188
- Galbiati, A., Zana, A., and Conti, P. (2020). Covalent Inhibitors of GAPDH: From Unspecific Warheads to Selective Compounds. *Eur. J. Med. Chem.*, 207, 112740. doi:10.1016/j.ejmech.2020.112740
- Gammelgaard, K. R., Vad-Nielsen, J., Clement, M. S., Weiss, S., Dagaard, T. F., Dagnæs-Hansen, F., et al. (2019). Up-Regulated FGFR1 Expression as a Mediator of Intrinsic TKI Resistance in EGFR-Mutated NSCLC. *Translational Oncol.* 12, 432–440. doi:10.1016/j.tranon.2018.11.017
- Gavine, P. R., Mooney, L., Kilgour, E., Thomas, A. P., Al-Kadhimi, K., Beck, S., et al. (2012). AZD4547: an Orally Bioavailable, Potent, and Selective Inhibitor of the Fibroblast Growth Factor Receptor Tyrosine Kinase Family. *Cancer Res.* 72, 2045–2056. doi:10.1158/0008-5472.CAN-11-3034
- Gelsi-Boyer, V., Orsetti, B., Cervera, N., Finetti, P., Sircoulomb, F., Rougé, C., et al. (2005). Comprehensive Profiling of 8p11-12 Amplification in Breast Cancer. *Mol. Cancer Res.* 3, 655–667. doi:10.1158/1541-7786.Mcr-05-0128
- Goldfarb, M., Schoorlemmer, J., Williams, A., Diwakar, S., Wang, Q., Huang, X., et al. (2007). Fibroblast Growth Factor Homologous Factors Control Neuronal Excitability through Modulation of Voltage-Gated Sodium Channels. *Neuron* 55, 449–463. doi:10.1016/j.neuron.2007.07.006
- Golfmann, K., Meder, L., Koker, M., Volz, C., Borchmann, S., Tharun, L., et al. (2018). Synergistic Anti-angiogenic Treatment Effects by Dual FGFR1 and VEGFR1 Inhibition in FGFR1-Amplified Breast Cancer. *Oncogene* 37, 5682–5693. doi:10.1038/s41388-018-0380-3
- Goracci, L., Desantis, J., Valeri, A., Castellani, B., Eleuteri, M., and Cruciani, G. (2020). Understanding the Metabolism of Proteolysis Targeting Chimeras (PROTACs): The Next Step toward Pharmaceutical Applications. *J. Med. Chem.* 63, 11615–11638. doi:10.1021/acs.jmedchem.0c00793
- Goriely, A., Hansen, R. M. S., Taylor, I. B., Olesen, I. A., Jacobsen, G. K., McGowan, S. J., et al. (2009). Activating Mutations in FGFR3 and HRAS Reveal a Shared Genetic Origin for Congenital Disorders and Testicular Tumors. *Nat. Genet.* 41, 1247–1252. doi:10.1038/ng.470
- Goyal, L., Shi, L., Liu, L. Y., Fece de la Cruz, F., Lennerz, J. K., Raghavan, S., et al. (2019). TAS-120 Overcomes Resistance to ATP-Competitive FGFR Inhibitors in Patients with FGFR2 Fusion-Positive Intrahepatic Cholangiocarcinoma. *Cancer Discov.* 9, 1064–1079. doi:10.1158/2159-8290.CD-19-0182
- Gozgit, J. M., Squillace, R. M., Wongchenko, M. J., Miller, D., Wardwell, S., Mohammad, Q., et al. (2013). Combined Targeting of FGFR2 and mTOR by Ponatinib and Ridaforolimus Results in Synergistic Antitumor Activity in FGFR2 Mutant Endometrial Cancer Models. *Cancer Chemother. Pharmacol.* 71, 1315–1323. doi:10.1007/s00280-013-2131-z
- Grünwald, S., Polit, O., Bender, S., Héroult, M., Lustig, K., Thuss, U., et al. (2019). Rogaratinib: A Potent and Selective pan-FGFR Inhibitor with Broad Antitumor Activity in FGFR-overexpressing Preclinical Cancer Models. *Int. J. Cancer* 145, 1346–1357. doi:10.1002/ijc.32224
- Guagnano, V., Furet, P., Spanka, C., Bordas, V., Le Douget, M., Stamm, C., et al. (2011). Discovery of 3-(2,6-Dichloro-3,5-Dimethoxy-Phenyl)-1-[6-[4-(4-Ethyl-Piperazin-1-Yl)-Phenylamino]-Pyrimidin-4-Yl]-1-Methyl-Urea (NVP-Bg398), A Potent and Selective Inhibitor of the Fibroblast Growth Factor Receptor Family of Receptor Tyrosine Kinase. *J. Med. Chem.* 54, 7066–7083. doi:10.1021/jm2006222
- Guimarães, C. R. W., Rai, B. K., Munchhof, M. J., Liu, S., Wang, J., Bhattacharya, S. K., et al. (2011). Understanding the Impact of the P-Loop Conformation on Kinase Selectivity. *J. Chem. Inf. Model.* 51, 1199–1204. doi:10.1021/ci200153c
- Guo, Y. J., Pan, W. W., Liu, S. B., Shen, Z. F., Xu, Y., and Hu, L. L. (2020). ERK/ MAPK Signalling Pathway and Tumorigenesis (Review). *Exp. Ther. Med.*, 19, 1997–2007. doi:10.3892/etm.2020.8454
- Hadari, Y. R., Kouhara, H., Lax, I., and Schlessinger, J. (1998). Binding of Shp2 Tyrosine Phosphatase to FRS2 Is Essential for Fibroblast Growth Factor-

- Induced PC12 Cell Differentiation. *Mol. Cell Biol.* 18, 3966–3973. doi:10.1128/mcb.18.7.3966
- Hagel, M., Miduturu, C., Sheets, M., Rubin, N., Weng, W., Stransky, N., et al. (2015). First Selective Small Molecule Inhibitor of FGFR4 for the Treatment of Hepatocellular Carcinomas with an Activated FGFR4 Signaling Pathway. *Cancer Discov.* 5, 424–437. doi:10.1158/2159-8290.CD-14-1029
- Hall, T. G., Yu, Y., Eathiraj, S., Wang, Y., Savage, R. E., Lapierre, J.-M., et al. (2016). Preclinical Activity of ARQ 087, a Novel Inhibitor Targeting FGFR Dysregulation. *PLoS One* 11, e0162594. doi:10.1371/journal.pone.0162594
- Hanafusa, H., Torii, S., Yasunaga, T., and Nishida, E. (2002). Sprouty1 and Sprouty2 Provide a Control Mechanism for the Ras/MAPK Signaling Pathway. *Nat. Cell Biol.* 4, 850–858. doi:10.1038/ncb867
- Harris, P. A., Boloor, A., Cheung, M., Kumar, R., Crosby, R. M., Davis-Ward, R. G., et al. (2008). Discovery of 5-[[4-[(2,3-Dimethyl-2H-Indazol-6-Yl)methylamino]-2-Pyrimidinyl]amino]-2-Methyl-Benzenesulfonamide (Pazopanib), a Novel and Potent Vascular Endothelial Growth Factor Receptor Inhibitor. *J. Med. Chem.* 51, 4632–4640. doi:10.1021/jm800566m
- Hart, K. C., Robertson, S. C., Kanemitsu, M. Y., Meyer, A. N., Tynan, J. A., and Donoghue, D. J. (2000). Transformation and Stat Activation by Derivatives of FGFR1, FGFR3, and FGFR4. *Oncogene*, 19, 3309–3320. doi:10.1038/sj.onc.1203650
- Helsten, T., Elkin, S., Arthur, E., Tomson, B. N., Carter, J., and Kurzrock, R. (2016). The FGFR Landscape in Cancer: Analysis of 4,853 Tumors by Next-Generation Sequencing. *Clin. Cancer Res.* 22, 259–267. doi:10.1158/1078-0432.Ccr-14-3212
- Herbert, C., Schieborr, U., Saxena, K., Juraszek, J., De Smet, F., Alcouffe, C., et al. (2013). Molecular Mechanism of SSR128129E, an Extracellularly Acting, Small-Molecule, Allosteric Inhibitor of FGF Receptor Signaling. *Cancer Cell* 23, 489–501. doi:10.1016/j.ccr.2013.02.018
- Hilberg, F., Roth, G. J., Krssak, M., Kautschitsch, S., Sommergruber, W., Tontschgrunt, U., et al. (2008). BIBF 1120: Triple Angiokinase Inhibitor with Sustained Receptor Blockade and Good Antitumor Efficacy. *Cancer Res.* 68, 4774–4782. doi:10.1158/0008-5472.CAN-07-6307
- Holmström, T. H., Moilanen, A.-M., Ikonen, T., Björkman, M. L., Linnanen, T., Wohlfahrt, G., et al. (2019). ODM-203, a Selective Inhibitor of FGFR and VEGFR, Shows Strong Antitumor Activity, and Induces Antitumor Immunity. *Mol. Cancer Ther.* 18, 28–38. doi:10.1158/1535-7163.Mct-18-0204
- Howard, S., Berdini, V., Boulstridge, J. A., Carr, M. G., Cross, D. M., Curry, J., et al. (2009). Fragment-based Discovery of the Pyrazol-4-Yl Urea (AT9283), a Multitargeted Kinase Inhibitor with Potent aurora Kinase Activity. *J. Med. Chem.* 52, 379–388. doi:10.1021/jm800984v
- Hu, B., Zhou, Y., Sun, D., Yang, Y., Liu, Y., Li, X., et al. (2020). PROTACs: New Method to Degrade Transcription Regulating Proteins. *Eur. J. Med. Chem.* 207, 112698. doi:10.1016/j.ejmech.2020.112698
- Hu, J., Ahuja, L. G., Meharena, H. S., Kannan, N., Kornev, A. P., Taylor, S. S., et al. (2015). Kinase Regulation by Hydrophobic Spine Assembly in Cancer. *Mol. Cell Biol.* 35, 264–276. doi:10.1128/mcb.00943-14
- Huang, L., Jiang, S., and Shi, Y. (2020). Tyrosine Kinase Inhibitors for Solid Tumors in the Past 20 Years (2001–2020). *J. Hematol. Oncol.* 13, 143. doi:10.1186/s13045-020-00977-0
- Ibrahimi, O. A., Eliseenkova, A. V., Plotnikov, A. N., Yu, K., Ornitz, D. M., and Mohammadi, M. (2001). Structural Basis for Fibroblast Growth Factor Receptor 2 Activation in Apert Syndrome. *Proc. Natl. Acad. Sci. U.S.A.*, 98, 7182–7187. doi:10.1073/pnas.121183798
- Ibrahimi, O. A., Zhang, F., Eliseenkova, A. V., Itoh, N., Linhardt, R. J., and Mohammadi, M. (2004). Biochemical Analysis of Pathogenic Ligand-dependent FGFR2 Mutations Suggests Distinct Pathophysiological Mechanisms for Craniofacial and Limb Abnormalities. *Hum. Mol. Genet.* 13, 2313–2324. doi:10.1093/hmg/ddh235
- Itoh, N., and Ornitz, D. M. (2004). Evolution of the Fgf and Fgfr Gene Families. *Trends Genet.* 20, 563–569. doi:10.1016/j.tig.2004.08.007
- Javle, M., Roychowdhury, S., Kelley, R. K., Sadeghi, S., Macarulla, T., Weiss, K. H., et al. (2021). Infigratinib (BGJ398) in Previously Treated Patients with Advanced or Metastatic Cholangiocarcinoma with FGFR2 Fusions or Rearrangements: Mature Results from a Multicentre, Open-Label, Single-Arm, Phase 2 Study. *Lancet Gastroenterol. Hepatol.* 6, 803–815. doi:10.1016/s2468-1253(21)00196-5
- Jia, Y., Yun, C.-H., Park, E., Ercan, D., Manuia, M., Juarez, J., et al. (2016). Overcoming EGFR(T790M) and EGFR(C797S) Resistance with Mutant-Selective Allosteric Inhibitors. *Nature* 534, 129–132. doi:10.1038/nature17960
- Jiang, X.-f., Dai, Y., Peng, X., Shen, Y.-y., Su, Y., Wei, M.-m., et al. (2018). SOMCL-085, a Novel Multi-Targeted FGFR Inhibitor, Displays Potent Anticancer Activity in FGFR-Addicted Human Cancer Models. *Acta Pharmacol. Sin.* 39, 243–250. doi:10.1038/aps.2017.96
- Joshi, J. J., Coffey, H., Corcoran, E., Tsai, J., Huang, C.-L., Ichikawa, K., et al. (2017). H3B-6527 Is a Potent and Selective Inhibitor of FGFR4 in FGF19-Driven Hepatocellular Carcinoma. *Cancer Res.* 77, 6999–7013. doi:10.1158/0008-5472.CAN-17-1865
- Jung, E.-J., Jung, E.-J., Min, S. Y., Kim, M. A., and Kim, W. H. (2012). Fibroblast Growth Factor Receptor 2 Gene Amplification Status and its Clinicopathologic Significance in Gastric Carcinoma. *Hum. Pathol.* 43, 1559–1566. doi:10.1016/j.humpath.2011.12.002
- Kikuchi, A., Suzuki, T., Nakazawa, T., Iizuka, M., Nakayama, A., Ozawa, T., et al. (2017). ASP5878, a Selective FGFR Inhibitor, to Treat FGFR3-dependent Urothelial Cancer with or without Chemoresistance. *Cancer Sci.* 108, 236–242. doi:10.1111/cas.13124
- Konecny, G. E., Finkler, N., Garcia, A. A., Lorusso, D., Lee, P. S., Rocconi, R. P., et al. (2015). Second-line Dovitinib (TKI258) in Patients with FGFR2-Mutated or FGFR2-Non-Mutated Advanced or Metastatic Endometrial Cancer: a Non-randomised, Open-Label, Two-Group, Two-Stage, Phase 2 Study. *Lancet Oncol.* 16, 686–694. doi:10.1016/s1470-2045(15)70159-2
- Kovalenko, M., Gazit, A., Böhmer, A., Rorsman, C., Rönnstrand, L., Heldin, C. H., et al. (1994). Selective Platelet-Derived Growth Factor Receptor Kinase Blockers Reverse SIs-Transformation. *Cancer Res.* 54, 6106–6114.
- Krook, M. A., Lenyo, A., Wilberding, M., Barker, H., Dantuono, M., Bailey, K. M., et al. (2020). Efficacy of FGFR Inhibitors and Combination Therapies for Acquired Resistance in FGFR2-Fusion Cholangiocarcinoma. *Mol. Cancer Ther.* 19, 847–857. doi:10.1158/1535-7163.MCT-19-0631
- Laird, A. D., Vajkoczy, P., Shawver, L. K., Thurnher, A., Liang, C., Mohammadi, M., et al. (2000). SU6668 Is a Potent Antiangiogenic and Antitumor Agent that Induces Regression of Established Tumors. *Cancer Res.* 60, 4152–4160.
- Lesca, E., Lammens, A., Huber, R., and Augustin, M. (2014). Structural Analysis of the Human Fibroblast Growth Factor Receptor 4 Kinase. *J. Mol. Biol.* 426, 3744–3756. doi:10.1016/j.jmb.2014.09.004
- Levine, D. A., Schultz, N., Cherniack, A. D., Akbani, R., Liu, Y., Shen, H., et al. (2013). Integrated Genomic Characterization of Endometrial Carcinoma. *Nature* 497, 67–73. doi:10.1038/nature12113
- Li, X., Guise, C. P., Taghipouran, R., Yosaatmadja, Y., Ashoorzadeh, A., Paik, W.-K., et al. (2017). 2-Oxo-3, 4-dihydropyrimido[4, 5- D]pyrimidinyl Derivatives as New Irreversible pan Fibroblast Growth Factor Receptor (FGFR) Inhibitors. *Eur. J. Med. Chem.* 135, 531–543. doi:10.1016/j.ejmech.2017.04.049
- Liu, J., Ma, J., Liu, Y., Xia, J., Li, Y., Wang, Z. P., et al. (2020). PROTACs: A Novel Strategy for Cancer Therapy. *Semin. Cancer Biol.* 67, 171–179. doi:10.1016/j.semcancer.2020.02.006
- Liu, J., Qian, C., Zhu, Y., Cai, J., He, Y., Li, J., et al. (2018). Design, Synthesis and Evaluate of Novel Dual FGFR1 and HDAC Inhibitors Bearing an Indazole Scaffold. *Bioorg. Med. Chem.* 26, 747–757. doi:10.1016/j.bmc.2017.12.041
- Liu, Y., Peng, X., Guan, X., Lu, D., Xi, Y., Jin, S., et al. (2017). Discovery of Novel Ponatinib Analogues for Reducing KDR Activity as Potent FGFRs Inhibitors. *Eur. J. Med. Chem.* 126, 122–132. doi:10.1016/j.ejmech.2016.10.003
- Lu, X., Chen, H., Patterson, A. V., Smail, J. B., and Ding, K. (2019). Fibroblast Growth Factor Receptor 4 (FGFR4) Selective Inhibitors as Hepatocellular Carcinoma Therapy: Advances and Prospects. *J. Med. Chem.* 62, 2905–2915. doi:10.1021/acs.jmedchem.8b01531
- Müller, A.-K., Meyer, M., and Werner, S. (2012). The Roles of Receptor Tyrosine Kinases and Their Ligands in the Wound Repair Process. *Semin. Cell Develop. Biol.* 23, 963–970. doi:10.1016/j.semcdb.2012.09.015
- Markham, A. (2019). Erdafitinib: First Global Approval. *Drugs* 79, 1017–1021. doi:10.1007/s40265-019-01142-9
- Matsui, J., Yamamoto, Y., Funahashi, Y., Tsuruoka, A., Watanabe, T., Wakabayashi, T., et al. (2008). E7080, a Novel Inhibitor that Targets Multiple Kinases, Has Potent Antitumor Activities against Stem Cell Factor Producing Human Small Cell Lung Cancer H146, Based on Angiogenesis Inhibition. *Int. J. Cancer* 122, 664–671. doi:10.1002/ijc.23131

- Matsuo, I., and Kimura-Yoshida, C. (2013). Extracellular Modulation of Fibroblast Growth Factor Signaling through Heparan Sulfate Proteoglycans in Mammalian Development. *Curr. Opin. Genet. Develop.*, 23, 399–407. doi:10.1016/j.gde.2013.02.004
- Metzner, T., Bedeir, A., Held, G., Peter-Vörösmarty, B., Ghassemi, S., Heinzel, C., et al. (2011). Fibroblast Growth Factor Receptors as Therapeutic Targets in Human Melanoma: Synergism with BRAF Inhibition. *J. Invest. Dermatol.* 131, 2087–2095. doi:10.1038/jid.2011.177
- Miao, J.-L., Liu, R.-J., Zhou, J.-H., and Meng, S.-H. (2016). Fibroblast Growth Factor Receptor 1 Gene Amplification in Non-small Cell Lung Cancer. *Chin. Med. J. (Engl.)*, 129, 2868–2872. doi:10.4103/0366-6999.194649
- Miao, J.-L., Zhou, J.-H., Cai, J.-J., and Liu, R.-J. (2020). The Association between Fibroblast Growth Factor Receptor 1 Gene Amplification and Lung Cancer: a Meta-Analysis. *Arch. Med. Sci.*, 16, 16–26. doi:10.5114/aoms.2020.91284
- Michael, M., Bang, Y.-J., Park, Y. S., Kang, Y.-K., Kim, T. M., Hamid, O., et al. (2017). A Phase 1 Study of LY2874455, an Oral Selective Pan-FGFR Inhibitor, in Patients with Advanced Cancer. *Targ. Oncol.* 12, 463–474. doi:10.1007/s11523-017-0502-9
- Mikoshiba, K. (2007). The IP3 receptor/Ca2+ Channel and its Cellular Function. *Biochem. Soc. Symp.* 74, 9–22. doi:10.1042/bss0740009
- Mohammadi, M., Dikic, I., Sorokin, A., Burgess, W. H., Jaye, M., and Schlessinger, J. (1996). Identification of Six Novel Autophosphorylation Sites on Fibroblast Growth Factor Receptor 1 and Elucidation of Their Importance in Receptor Activation and Signal Transduction. *Mol. Cell Biol.* 16, 977–989. doi:10.1128/mcb.16.3.977
- Mohammadi, M., Froum, S., Hamby, J. M., Schroeder, M. C., Panek, R. L., Lu, G. H., et al. (1998). Crystal Structure of an Angiogenesis Inhibitor Bound to the FGF Receptor Tyrosine Kinase Domain. *Embo j* 17, 5896–5904. doi:10.1093/emboj/17.20.5896
- Mohammadi, M., McMahon, G., Sun, L., Tang, C., Hirth, P., Yeh, B. K., et al. (1997). Structures of the Tyrosine Kinase Domain of Fibroblast Growth Factor Receptor in Complex with Inhibitors. *Science* 276, 955–960. doi:10.1126/science.276.5314.955
- Mohammadi, M., Schlessinger, J., and Hubbard, S. R. (1996). Structure of the FGF Receptor Tyrosine Kinase Domain Reveals a Novel Autoinhibitory Mechanism. *Cell*, 86, 577–587. doi:10.1016/s0092-8674(00)80131-2
- Montazeri, K., and Bellmunt, J. (2020). Erdafitinib for the Treatment of Metastatic Bladder Cancer. *Expert Rev. Clin. Pharmacol.*, 13, 1–6. doi:10.1080/17512433.2020.1702025
- Murray, C. W., Newell, D. R., and Angibaud, P. (2019). A Successful Collaboration between Academia, Biotech and Pharma Led to Discovery of Erdafitinib, a Selective FGFR Inhibitor Recently Approved by the FDA. *Med. Chem. Commun.*, 10, 1509–1511. doi:10.1039/c9md90044f
- Nakanishi, Y., Akiyama, N., Tsukaguchi, T., Fujii, T., Sakata, K., Sase, H., et al. (2014). The Fibroblast Growth Factor Receptor Genetic Status as a Potential Predictor of the Sensitivity to CH5183284/Debio 1347, a Novel Selective FGFR Inhibitor. *Mol. Cancer Ther.* 13, 2547–2558. doi:10.1158/1535-7163.MCT-14-0248
- O'Hare, T., Shakespeare, W. C., Zhu, X., Eide, C. A., Rivera, V. M., Wang, F., et al. (2009). AP24534, a Pan-BCR-ABL Inhibitor for Chronic Myeloid Leukemia, Potently Inhibits the T315I Mutant and Overcomes Mutation-Based Resistance. *Cancer Cell* 16, 401–412. doi:10.1016/j.ccr.2009.09.028
- Ong, S. H., Guy, G. R., Hadari, Y. R., Laks, S., Gotoh, N., Schlessinger, J., et al. (2000). FRS2 Proteins Recruit Intracellular Signaling Pathways by Binding to Diverse Targets on Fibroblast Growth Factor and Nerve Growth Factor Receptors. *Mol. Cell Biol.* 20, 979–989. doi:10.1128/mcb.20.3.979-989.2000
- Ornitz, D. M. (2000). FGFs, Heparan Sulfate and FGFRs: Complex Interactions Essential for Development. *Bioessays* 22, 108–112. doi:10.1002/(sici)1521-1878(200002)22:2<108::aid-bies2>3.0.co;2-m
- Packer, L. M., Geng, X., Bonazzi, V. F., Ju, R. J., Mahon, C. E., Cummings, M. C., et al. (2017). PI3K Inhibitors Synergize with FGFR Inhibitors to Enhance Antitumor Responses in FGFR2-mutant Endometrial Cancers. *Mol. Cancer Ther.* 16, 637–648. doi:10.1158/1535-7163.MCT-16-0415
- Pagano, K., Carminati, L., Tomaselli, S., Molinari, H., Tarabozetti, G., and Ragona, L. (2021). Molecular Basis of the Antiangiogenic Action of Rosmarinic Acid, a Natural Compound Targeting Fibroblast Growth Factor-2/FGFR Interactions. *Chembiochem*, 22, 160–169. doi:10.1002/cbic.202000610
- Paiva, S.-L., and Crews, C. M. (2019). Targeted Protein Degradation: Elements of PROTAC Design. *Curr. Opin. Chem. Biol.*, 50, 111–119. doi:10.1016/j.cbpa.2019.02.022
- Palakurthi, S., Kuraguchi, M., Zacharek, S. J., Zudaire, E., Huang, W., Bonal, D. M., et al. (2019). The Combined Effect of FGFR Inhibition and PD-1 Blockade Promotes Tumor-Intrinsic Induction of Antitumor Immunity. *Cancer Immunol. Res.* 7, 1457–1471. doi:10.1158/2326-6066.Cir-18-0595
- Pan, B.-S., Chan, G. K. Y., Chenard, M., Chi, A., Davis, L. J., Deshmukh, S. V., et al. (2010). MK-2461, a Novel Multitargeted Kinase Inhibitor, Preferentially Inhibits the Activated C-Met Receptor. *Cancer Res.* 70, 1524–1533. doi:10.1158/0008-5472.CAN-09-2541
- Pao, W., Miller, V. A., and Kris, M. G. (2004). 'Targeting' the Epidermal Growth Factor Receptor Tyrosine Kinase with Gefitinib (Iressa) in Non-small Cell Lung Cancer (NSCLC). *Semin. Cancer Biol.*, 14, 33–40. doi:10.1016/j.semcancer.2003.11.005
- Peng, X., Hou, P., Chen, Y., Dai, Y., Ji, Y., Shen, Y., et al. (2019). Preclinical Evaluation of 3D185, a Novel Potent Inhibitor of FGFR1/2/3 and CSF-1R, in FGFR-dependent and Macrophage-Dominant Cancer Models. *J. Exp. Clin. Cancer Res.* 38, 372. doi:10.1186/s13046-019-1357-y
- Perera, T. P. S., Jovcheva, E., Mevellec, L., Vialard, J., De Lange, D., Verhulst, T., et al. (2017). Discovery and Pharmacological Characterization of JNJ-42756493 (Erdafitinib), a Functionally Selective Small-Molecule FGFR Family Inhibitor. *Mol. Cancer Ther.* 16, 1010–1020. doi:10.1158/1535-7163.MCT-16-0589
- Pettersson, M., and Crews, C. M. (2019). PROTeolysis TARgeting Chimeras (PROTACs) - Past, Present and Future. *Drug Discov. Today Tech.*, 31, 15–27. doi:10.1016/j.ddtec.2019.01.002
- Plotnikov, A. N., Hubbard, S. R., Schlessinger, J., and Mohammadi, M. (2000). Crystal Structures of Two FGF-FGFR Complexes Reveal the Determinants of Ligand-Receptor Specificity. *Cell*, 101, 413–424. doi:10.1016/s0092-8674(00)80851-x
- Porta, R., Borea, R., Coelho, A., Khan, S., Araújo, A., Reclusa, P., et al. (2017). FGFR a Promising Druggable Target in Cancer: Molecular Biology and New Drugs. *Crit. Rev. Oncology/Hematology* 113, 256–267. doi:10.1016/j.critrevonc.2017.02.018
- Powers, C. J., McLeskey, S. W., and Wellstein, A. (2000). Fibroblast Growth Factors, Their Receptors and Signaling. *Endocr. Relat. Cancer*, 7, 165–197. doi:10.1677/erc.0.0070165
- Qin, Q., Patel, V., and Galsky, M. D. (2020). Urothelial Carcinoma: the Development of FGFR Inhibitors in Combination with Immune Checkpoint Inhibitors. *Expert Rev. Anticancer Ther.*, 20, 503–512. doi:10.1080/14737140.2020.1770600
- Qiu, H., Yashiro, M., Zhang, X., Miwa, A., and Hirakawa, K. (2011). A FGFR2 Inhibitor, Ki23057, Enhances the Chemosensitivity of Drug-Resistant Gastric Cancer Cells. *Cancer Lett.*, 307, 47–52. doi:10.1016/j.canlet.2011.03.015
- Qu, L., Chen, X., Wei, H., Guo, M., Dai, S., Jiang, L., et al. (2022). Structural Insights into the Potency and Selectivity of Covalent Pan-FGFR Inhibitors. *Commun. Chem.* 5. doi:10.1038/s42004-021-00623-x
- Quan, M.-Y., Guo, Q., Liu, J., Yang, R., Bai, J., Wang, W., et al. (2020). Corrigendum: An FGFR/AKT/SOX2 Signaling Axis Controls Pancreatic Cancer Stemness. *Front. Cell Dev. Biol.* 8, 594589. doi:10.3389/fcell.2020.594589
- Ran, K., Zeng, J., Wan, G., He, X., Feng, Z., Xiang, W., et al. (2021). Design, Synthesis and Biological Evaluations of a Series of Pyrido[1,2-A]pyrimidinone Derivatives as Novel Selective FGFR Inhibitors. *Eur. J. Med. Chem.* 220, 113499. doi:10.1016/j.ejmech.2021.113499
- Reintjes, N., Li, Y., Becker, A., Rohmann, E., Schmutzler, R., and Wollnik, B. (2013). Activating Somatic FGFR2 Mutations in Breast Cancer. *PLoS One*, 8, e60264. doi:10.1371/journal.pone.0060264
- Rezende Miranda, R., Fu, Y., Chen, X., Perino, J., Cao, P., Carpten, J., et al. (2020). Development of a Potent and Specific FGFR4 Inhibitor for the Treatment of Hepatocellular Carcinoma. *J. Med. Chem.* 63, 11484–11497. doi:10.1021/acs.jmedchem.0c00044
- Risuleo, G., Ciacciarelli, M., Castelli, M., and Galati, G. (2009). The Synthetic Inhibitor of Fibroblast Growth Factor Receptor PD166866 Controls Negatively the Growth of Tumor Cells in Culture. *J. Exp. Clin. Cancer Res.*, 28, 151. doi:10.1186/1756-9966-28-151
- Ronca, R., Giacomini, A., Di Salle, E., Coltrini, D., Pagano, K., Ragona, L., et al. (2015). Long-Pentraxin 3 Derivative as a Small-Molecule FGF Trap for Cancer Therapy. *Cancer Cell* 28, 225–239. doi:10.1016/j.ccell.2015.07.002

- Roskoski, R., Jr. (2010). RAF Protein-Serine/threonine Kinases: Structure and Regulation. *Biochem. Biophysical Res. Commun.* 399, 313–317. doi:10.1016/j.bbrc.2010.07.092
- Roskoski, R., Jr. (2020). The Role of Fibroblast Growth Factor Receptor (FGFR) Protein-Tyrosine Kinase Inhibitors in the Treatment of Cancers Including Those of the Urinary Bladder. *Pharmacol. Res.* 151, 104567. doi:10.1016/j.phrs.2019.104567
- Ross, J. S., Wang, K., Al-Rohil, R. N., Nazeer, T., Sheehan, C. E., Otto, G. A., et al. (2014). Advanced Urothelial Carcinoma: Next-Generation Sequencing Reveals Diverse Genomic Alterations and Targets of Therapy. *Mod. Pathol.* 27, 271–280. doi:10.1038/modpathol.2013.135
- Rosty, C., Aubriot, M.-H., Cappellen, D., Bourdin, J., Cartier, I., Thiery, J., et al. (2005). Clinical and Biological Characteristics of Cervical Neoplasias with FGFR3 Mutation. *Mol. Cancer* 4, 15. doi:10.1186/1476-4598-4-15
- Roth, G. J., Heckel, A., Colbatzky, F., Handschuh, S., Kley, J., Lehmann-Lintz, T., et al. (2009). Design, Synthesis, and Evaluation of Indolinones as Triple Angiokinase Inhibitors and the Discovery of a Highly Specific 6-Methoxycarbonyl-Substituted Indolinone (BIBF 1120). *J. Med. Chem.* 52, 4466–4480. doi:10.1021/jm900431g
- Sacks, D., Sacks, D., Baxter, B., Campbell, B. C. V., Carpenter, J. S., Cognard, C., et al. (2018). Multisociety Consensus Quality Improvement Revised Consensus Statement for Endovascular Therapy of Acute Ischemic Stroke. *AJNR Am. J. Neuroradiol* 39, E61–E632. doi:10.3174/ajnr.A5638
- Sanchez-Heras, E., Howell, F. V., Williams, G., and Doherty, P. (2006). The Fibroblast Growth Factor Receptor Acid Box Is Essential for Interactions with N-Cadherin and All of the Major Isoforms of Neural Cell Adhesion Molecule. *J. Biol. Chem.* 281, 35208–35216. doi:10.1074/jbc.M608655200
- Shen, G., Zheng, F., Ren, D., Du, F., Dong, Q., Wang, Z., et al. (2018). Anlotinib: a Novel Multi-Targeting Tyrosine Kinase Inhibitor in Clinical Development. *J. Hematol. Oncol.* 11, 120. doi:10.1186/s13045-018-0664-7
- Siracusano, S., Rizzetto, R., and Porcaro, A. B. (2020). Bladder Cancer Genomics. *Urologia*, 87, 49–56. doi:10.1177/0391560319899011
- Sohl, C. D., Ryan, M. R., Luo, B., Frey, K. M., and Anderson, K. S. (2015). Illuminating the Molecular Mechanisms of Tyrosine Kinase Inhibitor Resistance for the FGFR1 Gatekeeper Mutation: the Achilles' Heel of Targeted Therapy. *ACS Chem. Biol.* 10, 1319–1329. doi:10.1021/acscchembio.5b00014
- Solomon, J. P., and Hansel, D. E. (2016). The Emerging Molecular Landscape of Urothelial Carcinoma. *Surg. Pathol. Clin.*, 9, 391–404. doi:10.1016/j.path.2016.04.004
- Sootome, H., Fujita, H., Ito, K., Ochiwa, H., Fujioka, Y., Ito, K., et al. (2020). Futibatinib Is a Novel Irreversible FGFR 1-4 Inhibitor that Shows Selective Antitumor Activity against FGFR-Deregulated Tumors. *Cancer Res.* 80, 4986–4997. doi:10.1158/0008-5472.CAN-19-2568
- Sun, L., Tran, N., Liang, C., Tang, F., Rice, A., Schreck, R., et al. (1999). Design, Synthesis, and Evaluations of Substituted 3-[(3- or 4-Carboxyethylpyrrol-2-Yl)methylidene]indolin-2-Ones as Inhibitors of VEGF, FGF, and PDGF Receptor Tyrosine Kinases. *J. Med. Chem.* 42, 5120–5130. doi:10.1021/jm9904295
- Taeger, J., Moser, C., Hellerbrand, C., Mycielska, M. E., Glockzin, G., Schlitt, H. J., et al. (2011). Targeting FGFR/PDGR/VEGFR Impairs Tumor Growth, Angiogenesis, and Metastasis by Effects on Tumor Cells, Endothelial Cells, and Pericytes in Pancreatic Cancer. *Mol. Cancer Ther.* 10, 2157–2167. doi:10.1158/1535-7163.MCT-11-0312
- Tan, L., Wang, J., Tanizaki, J., Huang, Z., Aref, A. R., Rusan, M., et al. (2014). Development of Covalent Inhibitors that Can Overcome Resistance to First-Generation FGFR Kinase Inhibitors. *Proc. Natl. Acad. Sci. U.S.A.* 111, E4869–E4877. doi:10.1073/pnas.1403438111
- Trudel, S., Li, Z. H., Wei, E., Wiesmann, M., Chang, H., Chen, C., et al. (2005). CHIR-258, a Novel, Multitargeted Tyrosine Kinase Inhibitor for the Potential Treatment of T(4;14) Multiple Myeloma. *Blood* 105, 2941–2948. doi:10.1182/blood-2004-10-3913
- Tsimafeyeu, I., Ludes-Meyers, J., Stepanova, E., Daeyaert, F., Khochenkov, D., Joosse, J.-B., et al. (2016). Targeting FGFR2 with Alofanib (RPT835) Shows Potent Activity in Tumour Models. *Eur. J. Cancer* 61, 20–28. doi:10.1016/j.ejca.2016.03.068
- Tucker, J. A., Klein, T., Breed, J., Breeze, A. L., Overman, R., Phillips, C., et al. (2014). Structural Insights into FGFR Kinase Isoform Selectivity: Diverse Binding Modes of AZD4547 and Ponatinib in Complex with FGFR1 and FGFR4. *Structure* 22, 1764–1774. doi:10.1016/j.str.2014.09.019
- Turner, L. D., Summers, A. J., Johnson, L. O., Knowles, M. A., and Fishwick, C. W. G. (2017). Identification of an Indazole-Based Pharmacophore for the Inhibition of FGFR Kinases Using Fragment-Led De Novo Design. *ACS Med. Chem. Lett.*, 8, 1264–1268. doi:10.1021/acsmchemlett.7b00349
- Turner, L. D., Trinh, C. H., Hubball, R. A., Orritt, K. M., Lin, C.-C., Burns, J. E., et al. (2021). From Fragment to Lead: De Novo Design and Development toward a Selective FGFR2 Inhibitor. *J. Med. Chem.* 65, 1481–1504. doi:10.1021/acs.jmedchem.1c01163
- Turner, N., Lambros, M. B., Horlings, H. M., Pearson, A., Sharpe, R., Natrajan, R., et al. (2010). Integrative Molecular Profiling of Triple Negative Breast Cancers Identifies Amplicon Drivers and Potential Therapeutic Targets. *Oncogene* 29, 2013–2023. doi:10.1038/onc.2009.489
- Tyulyandina, A., Harrison, D., Yin, W., Stepanova, E., Kochenkov, D., Solomko, E., et al. (2017). Alofanib, an Allosteric FGFR2 Inhibitor, Has Potent Effects on Ovarian Cancer Growth in Preclinical Studies. *Invest. New Drugs* 35, 127–133. doi:10.1007/s10637-016-0404-1
- Vékony, H., Ylstra, B., Wilting, S. M., Meijer, G. A., van de Wiel, M. A., Leemans, C. R., et al. (2007). DNA Copy Number Gains at Loci of Growth Factors and Their Receptors in Salivary Gland Adenoid Cystic Carcinoma. *Clin. Cancer Res.* 13, 3133–3139. doi:10.1158/1078-0432.Ccr-06-2555
- Vi, J. G. t., Cheuk, A. T., Tsang, P. S., Chung, J.-Y., Song, Y. K., Desai, K., et al. (2009). Identification of FGFR4-Activating Mutations in Human Rhabdomyosarcomas that Promote Metastasis in Xenotransplanted Models. *J. Clin. Invest.* 119, 3395–3407. doi:10.1172/jci39703
- Vijayan, R. S. K., He, P., Modi, V., Duong-Ly, K. C., Ma, H., Peterson, J. R., et al. (2015). Conformational Analysis of the DFG-Out Kinase Motif and Biochemical Profiling of Structurally Validated Type II Inhibitors. *J. Med. Chem.* 58, 466–479. doi:10.1021/jm501603h
- Walker, B. A., Boyle, E. M., Wardell, C. P., Murison, A., Begum, D. B., Dahir, N. M., et al. (2015). Mutational Spectrum, Copy Number Changes, and Outcome: Results of a Sequencing Study of Patients with Newly Diagnosed Myeloma. *J. Clin. Oncol.* 33, 3911–3920. doi:10.1200/jco.2014.59.1503
- Walker, B. A., Mavrommatis, K., Wardell, C. P., Ashby, T. C., Bauer, M., Davies, F. E., et al. (2018). Identification of Novel Mutational Drivers Reveals Oncogene Dependencies in Multiple Myeloma. *Blood* 132, 587–597. doi:10.1182/blood-2018-03-840132
- Wang, L., Šuštić, T., Leite de Oliveira, R., Lieftink, C., Halonen, P., van de Ven, M., et al. (2017). A Functional Genetic Screen Identifies the Phosphoinositide 3-kinase Pathway as a Determinant of Resistance to Fibroblast Growth Factor Receptor Inhibitors in FGFR Mutant Urothelial Cell Carcinoma. *Eur. Urol.* 71, 858–862. doi:10.1016/j.eururo.2017.01.021
- Wang, N., Li, J.-y., Li, S., Guo, X.-c., Wu, T., Wang, W.-f., et al. (2018). Fibroblast Growth Factor 21 Regulates Foam Cells Formation and Inflammatory Response in Ox-LDL-Induced THP-1 Macrophages. *Biomed. Pharmacother.* 108, 1825–1834. doi:10.1016/j.biopha.2018.09.143
- Wang, S., and Ding, Z. (2017). Fibroblast Growth Factor Receptors in Breast Cancer. *Tumour Biol.*, 39, 101042831769837. doi:10.1177/1010428317698370
- Wang, V. E., Xue, J. Y., Frederick, D. T., Cao, Y., Lin, E., Wilson, C., et al. (2019). Adaptive Resistance to Dual BRAF/MEK Inhibition in BRAF-Driven Tumors through Autocrine FGFR Pathway Activation. *Clin. Cancer Res.* 25, 7202–7217. doi:10.1158/1078-0432.Ccr-18-2779
- Wang, Y., Dai, Y., Wu, X., Li, F., Liu, B., Li, C., et al. (2019). Discovery and Development of a Series of Pyrazolo[3,4-D]pyridazinone Compounds as the Novel Covalent Fibroblast Growth Factor Receptor Inhibitors by the Rational Drug Design. *J. Med. Chem.* 62, 7473–7488. doi:10.1021/acs.jmedchem.9b00510
- Wang, Y., Li, L., Fan, J., Dai, Y., Jiang, A., Geng, M., et al. (2018). Discovery of Potent Irreversible Pan-Fibroblast Growth Factor Receptor (FGFR) Inhibitors. *J. Med. Chem.* 61, 9085–9104. doi:10.1021/acs.jmedchem.7b01843
- Watanabe Miyano, S., Yamamoto, Y., Kodama, K., Miyajima, Y., Mikamoto, M., Nakagawa, T., et al. (2016). E7090, a Novel Selective Inhibitor of Fibroblast Growth Factor Receptors, Displays Potent Antitumor Activity and Prolongs

- Survival in Preclinical Models. *Mol. Cancer Ther.* 15, 2630–2639. doi:10.1158/1535-7163.MCT-16-0261
- Webster, M. K., D'Avis, P. Y., Robertson, S. C., and Donoghue, D. J. (1996). Profound Ligand-independent Kinase Activation of Fibroblast Growth Factor Receptor 3 by the Activation Loop Mutation Responsible for a Lethal Skeletal Dysplasia, Thanatophoric Dysplasia Type II. *Mol. Cell Biol.* 16, 4081–4087. doi:10.1128/mcb.16.8.4081
- Wedge, S. R., Kendrew, J., Hennequin, L. F., Valentine, P. J., Barry, S. T., Brave, S. R., et al. (2005). AZD2171: a Highly Potent, Orally Bioavailable, Vascular Endothelial Growth Factor Receptor-2 Tyrosine Kinase Inhibitor for the Treatment of Cancer. *Cancer Res.* 65, 4389–4400. doi:10.1158/0008-5472.Can-04-4409
- Wei, M., Peng, X., Xing, L., Dai, Y., Huang, R., Geng, M., et al. (2018). Design, Synthesis and Biological Evaluation of a Series of Novel 2-Benzamide-4-(6-Oxy-N-Methyl-1-Naphthamide)-Pyridine Derivatives as Potent Fibroblast Growth Factor Receptor (FGFR) Inhibitors. *Eur. J. Med. Chem.* 154, 9–28. doi:10.1016/j.ejmech.2018.05.005
- Wei, Y., Tang, Y., Zhou, Y., Yang, Y., Cui, Y., Wang, X., et al. (2021). Discovery and Optimization of a Novel 2H-Pyrazolo[3,4-D]pyrimidine Derivative as a Potent Irreversible Pan-Fibroblast Growth Factor Receptor Inhibitor. *J. Med. Chem.* 64, 9078–9099. doi:10.1021/acs.jmedchem.1c00174
- Weiss, J., Sos, M. L., Seidel, D., Peifer, M., Zander, T., Heuckmann, J. M., et al. (2010). Frequent and Focal FGFR1 Amplification Associates with Therapeutically Tractable FGFR1 Dependency in Squamous Cell Lung Cancer. *Sci. Transl. Med.* 2, 62ra93. doi:10.1126/scitranslmed.3001451
- Wiedemann, M., and Trueb, B. (2000). Characterization of a Novel Protein (FGFRL1) from Human Cartilage Related to FGF Receptors. *Genomics*, 69, 275–279. doi:10.1006/geno.2000.6332
- Wong, A., Lamothe, B., Lee, A., Schlessinger, J., and Lax, I. (2002). FRS2 α Attenuates FGF Receptor Signaling by Grb2-Mediated Recruitment of the Ubiquitin Ligase Cbl. *Proc. Natl. Acad. Sci. U.S.A.*, 99, 6684–6689. doi:10.1073/pnas.052138899
- Wu, L., Zhang, C., He, C., Qian, D., Lu, L., Sun, Y., et al. (2021). Discovery of Pemigatinib: A Potent and Selective Fibroblast Growth Factor Receptor (FGFR) Inhibitor. *J. Med. Chem.* 64, 10666–10679. doi:10.1021/acs.jmedchem.1c00713
- Wu, Y.-M., Su, F., Kalyana-Sundaram, S., Khazanov, N., Ateeq, B., Cao, X., et al. (2013). Identification of Targetable FGFR Gene Fusions in Diverse Cancers. *Cancer Discov.* 3, 636–647. doi:10.1158/2159-8290.Cd-13-0050
- Xie, Z., Wu, K., Wang, Y., Pan, Y., Chen, B., Cheng, D., et al. (2020). Discovery of 4,6-pyrimidinediamine Derivatives as Novel Dual EGFR/FGFR Inhibitors Aimed EGFR/FGFR1-positive NSCLC. *Eur. J. Med. Chem.* 187, 111943. doi:10.1016/j.ejmech.2019.111943
- Xu, J. M., Wang, Y., Chen, Y. L., Jia, R., Li, J., Gong, J. F., et al. (2017). Sulfatinib, a Novel Kinase Inhibitor, in Patients with Advanced Solid Tumors: Results from a Phase I Study. *Oncotarget* 8, 42076–42086. doi:10.18632/oncotarget.14942
- Xu, L., Meng, X., Xu, N., Fu, W., Tan, H., Zhang, L., et al. (2018). Gambogic Acid Inhibits Fibroblast Growth Factor Receptor Signaling Pathway in Erlotinib-Resistant Non-small-cell Lung Cancer and Suppresses Patient-Derived Xenograft Growth. *Cell Death Dis* 9, 262. doi:10.1038/s41419-018-0314-6
- Yamani, A., Zdzalik-Bielecka, D., Lipner, J., Stańczak, A., Piórkowska, N., Stańczak, P. S., et al. (2021). Discovery and Optimization of Novel Pyrazole-Benzimidazole CPL304110, as a Potent and Selective Inhibitor of Fibroblast Growth Factor Receptors FGFR (1-3). *Eur. J. Med. Chem.* 210, 112990. doi:10.1016/j.ejmech.2020.112990
- Yang, G.-W., Jiang, J.-S., and Lu, W.-Q. (2015). Ferulic Acid Exerts Anti-angiogenic and Anti-tumor Activity by Targeting Fibroblast Growth Factor Receptor 1-Mediated Angiogenesis. *Int. J. Mol. Sci.* 16, 24011–24031. doi:10.3390/ijms161024011
- Yang, Z., Liang, S.-Q., Yang, H., Xu, D., Bruggmann, R., Gao, Y., et al. (2021). CRISPR-mediated Kinome Editing Prioritizes a Synergistic Combination Therapy for FGFR1-Amplified Lung Cancer. *Cancer Res.* 81, 3121–3133. doi:10.1158/0008-5472.Can-20-2276
- Yin, B., Fang, D.-M., Zhou, X.-L., and Gao, F. (2019). Natural Products as Important Tyrosine Kinase Inhibitors. *Eur. J. Med. Chem.* 182, 111664. doi:10.1016/j.ejmech.2019.111664
- Yoshimoto, Y., Sasaki, Y., Murata, K., Noda, S.-e., Miyasaka, Y., Hamamoto, J., et al. (2020). Mutation Profiling of Uterine Cervical Cancer Patients Treated with Definitive Radiotherapy. *Gynecol. Oncol.* 159, 546–553. doi:10.1016/j.ygyno.2020.08.020
- Yu, J., Mahipal, A., and Kim, R. (2021). Targeted Therapy for Advanced or Metastatic Cholangiocarcinoma: Focus on the Clinical Potential of Infigratinib. *Onco Targets Ther.* 14, 5145–5160. doi:10.2147/OTT.S272208
- Yu, P., Wilhelm, K., Dubrac, A., Tung, J. K., Alves, T. C., Fang, J. S., et al. (2017). FGF-dependent Metabolic Control of Vascular Development. *Nature* 545, 224–228. doi:10.1038/nature22322
- Zhang, D., Han, L.-L., Du, F., Liu, X.-m., Li, J., Wang, H.-h., et al. (2019). FGFR1 Induces Acquired Resistance against Gefitinib by Activating AKT/mTOR Pathway in NSCLC. *Onco Targets Ther.* 12, 9809–9816. doi:10.2147/ott.S220462
- Zhang, X., Lv, H., Zhou, Q., Elkholi, R., Chipuk, J. E., Reddy, M. V. R., et al. (2014). Preclinical Pharmacological Evaluation of a Novel Multiple Kinase Inhibitor, ON123300, in Brain Tumor Models. *Mol. Cancer Ther.* 13, 1105–1116. doi:10.1158/1535-7163.MCT-13-0847
- Zhang, X., and Zhang, Y. (2015). Bladder Cancer and Genetic Mutations. *Cell Biochem Biophys*, 73, 65–69. doi:10.1007/s12013-015-0574-z
- Zhao, B., Li, Y., Xu, P., Dai, Y., Luo, C., Sun, Y., et al. (2016). Discovery of Substituted 1H-Pyrazolo[3,4-B]pyridine Derivatives as Potent and Selective FGFR Kinase Inhibitors. *ACS Med. Chem. Lett.* 7, 629–634. doi:10.1021/acsmchemlett.6b00066
- Zhao, G., Li, W.-Y., Chen, D., Henry, J. R., Li, H.-Y., Chen, Z., et al. (2011). A Novel, Selective Inhibitor of Fibroblast Growth Factor Receptors that Shows a Potent Broad Spectrum of Antitumor Activity in Several Tumor Xenograft Models. *Mol. Cancer Ther.* 10, 2200–2210. doi:10.1158/1535-7163.MCT-11-0306
- Zhavoronkov, A., Ivanenkov, Y. A., Aliper, A., Veselov, M. S., Aladinskiy, V. A., Aladinskaya, A. V., et al. (2019). Deep Learning Enables Rapid Identification of Potent DDR1 Kinase Inhibitors. *Nat. Biotechnol.* 37, 1038–1040. doi:10.1038/s41587-019-0224-x
- Zhong, L., Li, Y., Xiong, L., Wang, W., Wu, M., Yuan, T., et al. (2021). Small Molecules in Targeted Cancer Therapy: Advances, Challenges, and Future Perspectives. *Sig Transduct Target. Ther.* 6, 201. doi:10.1038/s41392-021-00572-w
- Zhou, W., Hur, W., McDermott, U., Dutt, A., Xian, W., Ficarro, S. B., et al. (2010). A Structure-Guided Approach to Creating Covalent FGFR Inhibitors. *Chem. Biol.* 17, 285–295. doi:10.1016/j.chembiol.2010.02.007
- Zou, Y., Ma, D., and Wang, Y. (2019). The PROTAC Technology in Drug Development. *Cell Biochem Funct.* 37, 21–30. doi:10.1002/cbf.3369

Conflict of Interest: The authors declare that the research was conducted in the absence of any commercial or financial relationships that could be construed as a potential conflict of interest.

Publisher's Note: All claims expressed in this article are solely those of the authors and do not necessarily represent those of their affiliated organizations or those of the publisher, the editors, and the reviewers. Any product that may be evaluated in this article, or claim that may be made by its manufacturer, is not guaranteed or endorsed by the publisher.

Copyright © 2022 Zheng, Zhang, Li, He, Wei, Dang, Nie and Guo. This is an open-access article distributed under the terms of the Creative Commons Attribution License (CC BY). The use, distribution or reproduction in other forums is permitted, provided the original author(s) and the copyright owner(s) are credited and that the original publication in this journal is cited, in accordance with accepted academic practice. No use, distribution or reproduction is permitted which does not comply with these terms.



3D Single Molecule Super-Resolution Microscopy of Whole Nuclear Lamina

Ashley M. Rozario^{1,2}, Alison Morey², Cade Elliott¹, Brendan Russ², Donna R. Whelan³, Stephen J. Turner^{2*} and Toby D. M. Bell^{1*}

¹School of Chemistry, Monash University, Clayton, VIC, Australia, ²Department of Microbiology, Monash Biomedicine Discovery Institute, Clayton, VIC, Australia, ³La Trobe Institute for Molecular Science, Bendigo, VIC, Australia

OPEN ACCESS

Edited by:

John D. Wade,
University of Melbourne, Australia

Reviewed by:

Shenfei Zong,
Southeast University, China
Leonel Malacrida,
Universidad de la República, Uruguay

*Correspondence:

Stephen J. Turner
stephen.j.turner@monash.edu
Toby D. M. Bell
toby.bell@monash.edu

Specialty section:

This article was submitted to
Chemical Biology,
a section of the journal
Frontiers in Chemistry

Received: 27 January 2022

Accepted: 28 March 2022

Published: 28 April 2022

Citation:

Rozario AM, Morey A, Elliott C, Russ B, Whelan DR, Turner SJ and Bell TDM (2022) 3D Single Molecule Super-Resolution Microscopy of Whole Nuclear Lamina.
Front. Chem. 10:863610.
doi: 10.3389/fchem.2022.863610

Single molecule (SM) super-resolution microscopies bypass the diffraction limit of conventional optical techniques and provide excellent spatial resolutions in the tens of nanometers without overly complex microscope hardware. SM imaging using optical astigmatism is an efficient strategy for visualizing subcellular features in 3D with a z-range of up to ~1 μm per acquisition. This approach however, places high demands on fluorophore brightness and photoswitching resilience meaning that imaging entire cell volumes in 3D using SM super-resolution remains challenging. Here we employ SM astigmatism together with multiplane acquisition to visualize the whole nuclear lamina of COS-7 and T cells in 3D. Nuclear lamina provides structural support to the nuclear envelope and participates in vital nuclear functions including internuclear transport, chromatin organization and gene regulation. Its position at the periphery of the nucleus provides a visible reference of the nuclear boundary and can be used to quantify the spatial distribution of intranuclear components such as histone modifications and transcription factors. We found Alexa Fluor 647, a popular photoswitchable fluorophore, remained viable for over an hour of continuous high laser power exposure, and provided sufficient brightness detectable up to 8 μm deep into a cell, allowing us to capture the entire nuclear lamina in 3D. Our approach provides sufficient super-resolution detail of nuclear lamina morphology to enable quantification of overall nuclear dimensions and local membrane features.

Keywords: astigmatism, multiplane imaging, T cell, nuclear envelope, convex hull

INTRODUCTION

Fluorescence microscopy techniques are routinely employed in biological research, making use of a variety of fluorophore labelling strategies to enable specific visualization of cellular structures and dynamics. The nuclear lamina is a continuous protein meshwork comprised of lamins, such as lamin A/C and B1, and is located within the inner membrane of the nuclear envelope. Lamins are key structural proteins that contribute to the structural integrity of the nucleus and provide a scaffold in which chromatin domains can be anchored. In addition, nuclear lamina has been shown to have roles in chromatin organization, gene regulation and transcription (Burke and Stewart 2013). Mutations in the genes encoding lamin proteins disrupt the integrity of the nuclear lamina resulting in structural aberrations, dysregulated gene expression and genomic instability, and have been associated with diseases collectively termed laminopathies (Rankin and Ellard 2006). Additionally, the nuclear lamina is a recognizable boundary of the nucleus that when imaged, can be used as a reference structure for describing the spatial arrangement of intranuclear components including histone modifications and transcription factors. Of particular interest, imaging the nuclear lamina could aid

in characterizing the nuclear interior of immune cells where the 3D spatial organization of the genome is associated with immune cell function i.e., activation, differentiation, and cell-type specific function (Pongubala and Murre 2021). Direct observation of specific nuclear features, however, can be challenging. This is partly due to the compactness of the nuclear space, but also because conventional optical methods are diffraction limited to ~200 nm imaging resolution at best, insufficient for resolving biomolecular and subcellular detail sized in the tens of nanometers.

Super-resolution fluorescence microscopies (SRFMs) are ideal for visualizing nuclear features (Miriklis et al., 2021), providing target specificity, subdiffraction resolution and capability for 3D imaging (Schermerle et al., 2019). SRFMs include the deterministic methods such as Stimulated Emission Depletion (STED) (Klar and Hell 1999; Klar et al., 2000) and Structured Illumination Microscopy (SIM) (Gustafsson 2000) that optically engineer the excitation source to yield subdiffraction output. SRFMs also include the stochastic methods that harness the photoswitching properties of fluorophores to achieve single molecule localization microscopies (SMLMs) (Betzig et al., 2006; Hess et al., 2006; Rust et al., 2006; Sharonov and Hochstrasser 2006) including direct stochastic optical reconstruction microscopy (*d*STORM) (Heilemann et al., 2008). SMLMs offer outstanding imaging gains—as good as 20 nm resolution—and make use of simple organic dye molecules as labels. SMLMs are performed by fitting diffraction-limited intensity profiles of individual SM emissions i.e., the point-spread function (PSFs) and deducing its spatial coordinates. Mapping several hundred thousand (up to a few million) SM coordinates yields the super-resolved image: a pointillistic reconstruction of the fluorophore-labelled structure.

2D-SMLMs can be upgraded for 3D imaging by optically engineering typically 2D symmetrical PSFs to be encoded with axial information. The astigmatism method (Huang et al., 2008a) uses a single cylindrical lens in the imaging path to laterally distort PSFs in *x* and *y* based on the *z* position of the emitter. Decoding these distorted PSFs during the localization procedure yields SM coordinates in all 3 spatial dimensions. Astigmatism provides ~1 μ m *z*-range, sufficient for capturing some cellular components such as individual cytoskeletal filaments (Xu et al., 2013) and subnucleolar bodies (Rawlinson et al., 2018) in 3D. Visualizing larger structures or across larger volumes, however, requires additional strategies to improve the imaging depth. One strategy is to stack multiple 1 μ m *z*-ranges by scanning the microscope objective through the whole cell, capturing SM emissions throughout. This was first demonstrated as a follow up of PSF astigmatism, employing a dual fluorophore system (activator and reporter dye for STORM) to capture multiple focal planes of mitochondria and microtubules up to a depth of 3 μ m (Huang et al., 2008b). A purpose-built multifocus microscope has also been reported to enable large depth 3D SMLM by introducing a focal-splitting prism to the imaging path for simultaneous acquisition of nine focal planes (Hajj et al., 2014). Alternatively, adaptive optics (Shechtman et al., 2014; Shechtman et al., 2015; Młodzianoski et al., 2018) or emission phase-modulating masks (for double-helix PSFs) (Pavani et al.,

2009; Carr et al., 2017) can engineer PSFs with more complex distortions for increased imaging depths up to 6 μ m without objective lens scanning. These latter strategies, however, utilize expensive optical hardware that require specialized expertise to install, align and calibrate. Furthermore, not all PSF engineering strategies are immediately compatible with the acquisition prerequisites for SMLM: bright emitting fluorophores and well resolved SM emission patterns. For this work, we demonstrate 3D *d*STORM of whole nuclei using hardware already available, a motorized objective turret on a home-built SM super-resolution microscope (Whelan and Bell 2015a) and a single cylindrical lens placed in the emission path.

Our method for whole nuclei 3D SMLM employs the stepwise acquisition of multiple imaging planes manipulated with astigmatism and the most popular fluorophore for *d*STORM, Alexa Fluor 647 (Alx647), an organic dye that exhibits ideal photoswitching properties for *d*STORM when subjected to a high laser flux and reducing thiol buffer [100 mM mercaptoethylamine (MEA)]. We harnessed the performance of Alx647 for whole nuclei 3D *d*STORM, maintaining bright photoswitching for over an hour that was detectable up to 8 μ m deep in a fixed cell. With such prolonged laser exposure throughout the entire labelled sample, a reasonable assumption is that some fluorophores would photobleach before being detected, resulting in lower fluorophore density and poorer image quality of the structure. A previous report to capture whole nuclear lamina in 3D employed a continuous re-labelling strategy of Alx647 throughout the SM acquisition to maintain sufficiently high fluorophore density (Venkataramani et al., 2018). We found conventional immunolabelling provided sufficient fluorophore density throughout the entire depth of the cell, even after an hour of continuous exposure to high laser power. With no signs of extensive photobleaching, whole nuclear lamina could be imaged comfortably, resulting in super-resolution detail throughout the structure.

Here we utilize the advantageous performance of Alx647 for whole nuclei 3D *d*STORM of lamin B1 in primary mouse T lymphocytes (T cells) and cultured COS-7 cells, as well as quantification of nuclear volume and surface areas using convex hull fitting. The fit also provides a 3D reference boundary of the nucleus, useful for mapping spatial distributions of intranuclear components. Interrogation of the 3D model also revealed sub-structures within the nuclear lamina membrane, including folds, blebs and cone-like invaginations potentially indicative of nuclear transport channels. Our assay for 3D whole nuclei super-resolution imaging reveals both the global microscopic perspective of the nuclear membrane as well as local nanoscopic features found therein.

MATERIALS AND METHODS

COS-7 Cell Culture

COS-7 cells (African green monkey kidney fibroblast-like, ATCC CRL1651) were cultured in Dulbecco's Modified Eagles Medium (DMEM—high glucose) supplemented with 10% fetal bovine serum and 1% penicillin-streptomycin, and incubated at 37°C,

5% CO₂. For imaging, cells were seeded onto high precision coverglass slides (Marienfeld 18 mm diameter #1.5H) and allowed to reach ~70% confluency before fixation and immunolabelling.

Isolation of Naive CD8⁺ T Cells

Female C57BL/6 mice of 6–8 weeks of age were housed in specific-pathogen free conditions at the Monash Animal Research Platform. Experimental procedures were conducted in agreement with the guidelines specified by the Monash Animal Ethics Committee. Spleens were extracted from female C57BL/6 mice and prepared for single cell suspensions. For cell sorting, single cell suspensions were resuspended in PBS and stained with anti-CD8 α -fluorescein isothiocyanate (BD Pharmingen), anti-CD44^{lo} phycoerythrin cyanine 7 (TONBO biosciences), anti-CD62L-allophycocyanin (Biolegend) and LIVE/DEADTM Fixable Aqua Dead Cell Stain (Thermo Fisher Scientific). Naive CD8⁺ T cells (CD44^{lo}, CD62L^{hi}) were sorted using a BD InfluxTM Cell Sorter and adhered to NuncTM Lab-TekTM II Chambered Coverglass (Thermo Scientific) using Cell-TakTM Cell and Tissue Adhesive (Corning) before fixations and immunolabelling.

Fixation and Immunolabelling

COS-7 and naive CD8⁺ T cells were fixed with 3.7% formaldehyde in PBS for 10 min at 37°C in a humid incubator, then washed twice with PBS followed by permeabilization with 0.1% Triton X-100 in PBS for 10 min at R.T. Fixed cells were blocked in 5% bovine serum albumin in PBS for 30 min at R.T., and immunolabelled first with rabbit anti-lamin B1 primary antibodies (1:1,000 dilution, Abcam) then anti-rabbit secondary antibodies conjugated to Alexa Fluor 647 (1:200 dilution, Thermo). Labelled cells were post-fixed with 3.7% formaldehyde in PBS for 5 min at R.T. before storage in 0.05% sodium azide in PBS at 4°C. Cells were imaged within 1 week of labelling.

Microscope Setup

SM imaging was performed on a home-built super-resolution microscope, as previously described (Whelan et al., 2014; Whelan and Bell 2015b; Rozario et al., 2020), based around an Olympus IX81 inverted fluorescence microscope frame fitted with a TIRF $\times 100$ 1.49 NA oil objective, Oxixus 638-nm laser diode and Andor iXon EM-CCD detector. Micromanager (Edelstein et al., 2010) was used to set acquisition parameters. To induce SM astigmatism for 3D imaging, a cylindrical lens ($f = 1,000$ mm) was placed in the emission path just after the exit port of the microscope frame (Supplementary Figure S1).

Astigmatism Calibration

Calibration for astigmatism was based on the original report of 3D SM astigmatic imaging (Huang et al., 2008a). The calibration sample comprised 100-nm Tetraspeck fluorescent beads (Thermo T7279, 1:10,000 dilution) suspended in a glycerol-based water soluble jelly (refractive index, RI ~ 1.46) diluted into water to yield a final RI of ~ 1.35 – 1.40 . The suspension was added to a NuncTM Lab-TekTM II Chambered Coverglass chamber and allowed to air dry overnight at 45°C before imaging. With the cylindrical lens (f

$= 1,000$ mm) placed in the imaging path, a Tetraspeck was scanned through 4 μm in z with 10-nm intervals and acquired for 100 ms at each step. Frames were processed through rapidSTORM (Wolter et al., 2012) to determine the PSF width in x and y at each z -step, by selecting “Store PSF width.” Similar to 2D dSTORM, the 2D Gaussian fitted onto each PSF provided the sigma value (width) in x and y used for the calibration. The data was cropped to a 1 μm z range such that the mid-point was where PSF width in x was nearest to PSF width in y , i.e., the ideal z imaging plane of objective. The calibration was smoothed with a 10-point B-spline function and exported from the rapidSTORM output “3D PSF width calibration table.” This calibration file was modified by increasing the z -coordinate value by increments of 400 nm to match the movement of the objective for each z -plane imaged using astigmatic 3D dSTORM.

Whole Nuclei Imaging

Cells were imaged in a switching buffer of 100 mM mercaptoethylamine (MEA) at pH 8.5 (adjusted with 1 M potassium hydroxide) in PBS. The laser was used at full power (150 mW resulting in ~ 3 kW/cm²) to induce Alexa Fluor 647 SM photoswitching, observed as “blinking” during acquisition. Cells were imaged from the bottom up where, at each step, 5,000 frames of photoswitching SM emissions were acquired at 50 Hz (20 ms exposure), then the objective was shifted up z by 400 nm to the next step. Typically 15–20 steps were required to cover the entire height of the nuclear lamina signal. The raw data from each step was processed for 3D SM localization in rapidSTORM using the appropriate calibration file that matched the step’s relative position through the cell, e.g., 1st step z -range: 0–1,000 nm, 2nd step z -range: 400–1,400 nm, etc. The resulting SM coordinate list from each step was compiled into a single text file that was imported into ViSP (Beheiry and Dahan 2013) for visualizing nuclear lamina structure and enabling colour coding each SM coordinate for its position in z (Figure 1).

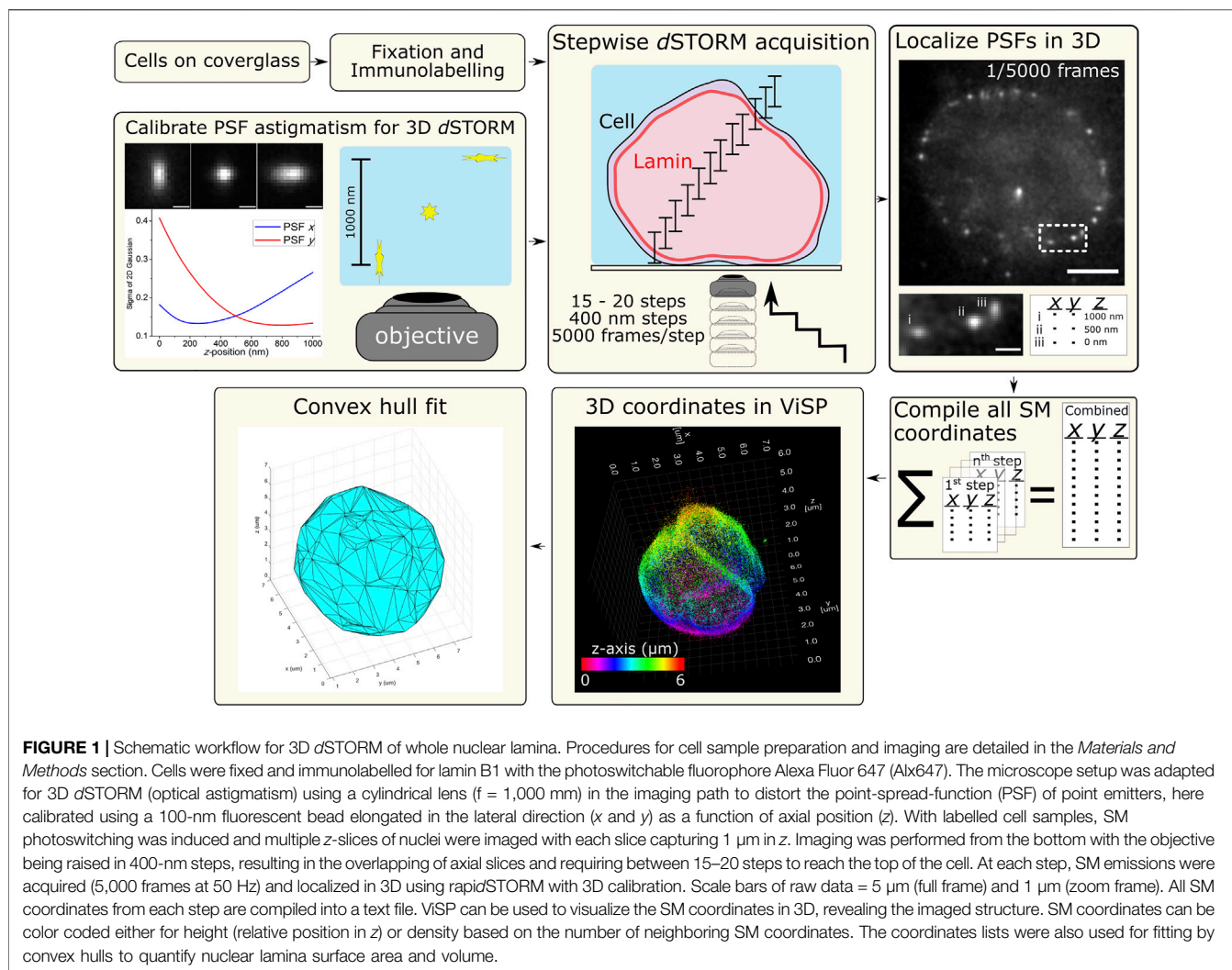
Convex Hull Fitting

SM coordinate lists from all z -slices were combined for each cell and imported into a custom written MATLAB 2020a script that processed the data through a DBSCAN (Ester et al., 1996)-based clustering function to identify individual nuclei based on coordinate density. Convex hull fitting was applied to determine the outer boundaries of each of these dense regions i.e., the nuclei boundaries as imaged with lamin B1. Hulls comprised the outermost coordinates of these dense regions and connected as triangular faces that wrapped around each nuclear boundary. For this work, the sum of these faces was used as the nuclear surface area, and the volume within the fitted hull was determined as nuclear volume.

RESULTS

Multiplane Astigmatic PSF Imaging for Whole Cell Super-Resolution

Conventional widefield imaging with z -scanning was capable of imaging whole cell nuclear lamina in 3D. As expected, the images



showed poor contrast of the nuclear boundary and lacked structural detail in the membrane. A side-on projection showed severely reduced fluorescence signal at the top of the cell compared to the bottom (**Supplementary Figure S2**), indicative of a reduced efficiency for imaging deeper into biological samples.

Application of dSTORM improved the resolution of the nuclear lamina (**Supplementary Figure S3**), revealing a more distinct boundary of the nucleus compared with diffraction-limited widefield imaging and enabled measurements of T cell nuclear lamina thickness within the subdiffraction range (96 nm, 81 and 160 nm); a ~3-fold improvement over diffraction-limited measurements of the same lamina sections (361 nm, 428 and 380 nm). Our dSTORM derived values for T cell nuclear lamina are comparable with those from previous SMLM measurements of nuclear lamina of U2OS cells: ~200 nm (Venkataramani et al., 2018) and MEF cells: ~100 nm (Nmezi et al., 2019).

For 3D dSTORM, astigmatism was induced using a cylindrical lens that distorted PSFs in x and y based on each emitting molecule's z position above or below the objective imaging plane, i.e., where the PSF is in focus. 100-nm fluorescent beads

(Tetraspecks) were used to calibrate PSF distortion as a function of z position by plotting the relative axial position from the focal plane of an emitting bead against the lateral elongation of its PSF (width in x and y). With this 3D calibration (as described in *Materials and Methods*), the 3D coordinates of SM emitters in labelled nuclei could be determined within a $1\ \mu\text{m}$ z range without the need for scanning in z (**Figure 1**).

The usable z range for this astigmatism approach is limited by the loss of integrity of distorted PSFs beyond approximately ± 500 nm in z from the focal plane. Beyond this $\sim 1\ \mu\text{m}$ z range, a defocused PSF from a single emitter becomes too challenging to distinguish from noise and may appear to have multiple lobes of maximum signal that, when rendered for dSTORM, would be imprecisely localized as multiple SM coordinates. Another issue with lateral distortions beyond ± 500 nm in z is that signal intensity from the emitter is spread across more pixels, reducing the likelihood of that PSF reaching the threshold for being selected for localization. While not affecting a calibration Tetraspeck bead that contains multiple fluorophores, a single fluorophore with a finite photon budget would become increasingly difficult to localize when its PSF is

excessively elongated. To increase the achievable z range for whole cell imaging, we captured multiple z planes affected by astigmatism, each providing 1 μm in z , stacked in a overlapping fashion accommodate the localization of less distinguished PSF elongations at either extreme of the range (+500 and -500 nm).

For d STORM acquisition, a switching buffer was added to the fixed and labelled cells, and the laser was turned to full power to induce Alx647 photoswitching. In order to penetrate the entire cell depth, the laser was aligned straight up (epifluorescence mode) and multiplane imaging was performed from the bottom up. This is different to inclined laser excitation modes [HILO (Tokunaga et al., 2008) or quasi-TIRF (Whelan et al., 2014)] typically used to improve SM photoswitching for 2D d STORM. We found Alx647 exhibited sufficient photoswitching properties up to 8 μm in z when induced with epifluorescence laser illumination (**Supplementary Figure S4**). The brightness and frequency of Alx647 photoswitching (blinking) observed during acquisition was a direct visual indication for the eventual quality of the rendered d STORM image. Individual frames of raw acquired data showed well resolved PSFs with a noticeable range of astigmatism lengths, enabling 3D localization using rapid d STORM with 3D calibration (**Supplementary Figure S4**). Remarkably, Alx647 maintained desirable brightness and photoswitching frequency throughout acquisition of the whole cell depth—a total duration of ~1 h with continuous high laser power exposure—to cover a total z range of up to 8 μm .

To capture the entire depth of nuclear lamina using 3D d STORM, we employed a stepwise acquisition strategy together with SM astigmatism (**Figure 1**). Each step of acquisition provided a 1 μm z range of 3D data—effectively a 1 μm z slice through the labelled nucleus. Following acquisition of each slice, the objective was raised by 400 nm so slices overlapped, allowing SM emitters to be localized more frequently throughout the sample. This is especially important for emitters at the extreme edges of the 1 μm z range that are not collected as efficiently as the in-plane emitters due to the spreading of photons across more elongated PSFs. The same 3D calibration file for 1 μm in z was applied for all z slices where only the final z coordinates were offset to match that slice's position in the sample, i.e., the z coordinates were offset incrementally by +400 nm to match the distance between each slice.

By inspecting rendered 3D segments from each imaged z slice, we can appreciate the spatial detail contained within a whole 3D nucleus model (**Supplementary Figure S4**). The bottom of the nucleus ($z = 1 \mu\text{m}$) shows a continuous layer of lamin B1, with some regions higher in z most notably at the edges where the nuclear lamina curves upward. At the middle of the nucleus ($z = 3 \mu\text{m}$) a distinct ring is observed with very few spurious localizations within the ring, indicative of the high labelling density and specificity of the lamin B1 antibodies. The ring, while revealing its axial position in z (by colour) also shows a steady lateral shift outward from its center highlighting curvature along the z plane. At the top of the nucleus ($z = 7 \mu\text{m}$), a much smaller area of lamin B1 is observed where the center portion is slightly higher than the edges, effectively the cap of the nuclear membrane. This also demonstrates that out-of-focus emission

between the objective and the desired focal plane 7 μm deep do not interfere with 3D SM imaging at these depths.

Applying multiplane 3D d STORM allowed visualization of whole nuclear lamina using the combined coordinate data. Upon inspection of the 3D image, ripples were observed when viewed from the side-on (**Supplementary Figure S5**). Scrutiny of the data from each slice revealed that the majority of localizations (59%) arose from emissions within the center third of the 1 μm z slice ($z \sim 330\text{--}660 \text{ nm}$). When combined with all other slices, each majority region formed an intensity peak that resulted in a rippling through the height of the nucleus. We found that rippling comes from the stacking of multiple astigmatic z slices and the spatial frequency of rippling could be modulated by varying the z increments during acquisition (100 nm, 400 and 1,000 nm). Smaller z increments increased the amount of overlap thereby reducing the space between the center regions of z slices and consequently the differences in intensity through z , resulting in a smoother 3D model (**Supplementary Figure S6**).

Lateral drift of the sample was minimal despite ~20 separate motions of the objective for z scanning during acquisition. Viewing all imaged z planes from the bottom up (xy view, **Supplementary Movie S1**), the zenith of nuclei were found to be positioned reasonably well in xy based on the middle and lower z planes. Allowing samples to settle on the oiled objective for at least 10 min prior to acquisition was crucial in minimizing drift.

Step size for multiplane 3D d STORM constitutes an important imaging parameter to consider alongside fluorophore choice, exposure time, frames acquired per slice and total duration of acquisition per cell. While using the smallest possible step size (100 nm) would be ideal for the smoothest possible 3D model, the increased objective movement and number of slices increases the chances for drift caused by hardware errors in z . Any error associated with the absolute z value of the motorized microscope objective turret (even if only a few tens of nanometers) together with the z localization precision of PSFs for 3D d STORM (~50 nm) would steadily worsen with each step through the height of the cell. This would lead to additional false SM coordinates occurring in z due to an apparent smearing of a single emitter as it is mis-localized across multiple z slices. For this work, we settled on using 400 nm steps to minimize the objective movement and total acquisition time required to capture whole nuclei, and despite incurring some rippling in the final model, we determined this would minimize overall localization artefacts.

Between 20–30 overlapping z slices (400 nm steps, 5,000 frames/step) were sufficient to capture the entire heights of COS-7 and T cell nuclei. Mouse T cells adhered onto microscope coverglass using Cell-Tak showed nuclei that were relatively spheroidal having similar width and heights of ~5–6 μm . COS-7 cells cultured directly onto the coverglass showed nuclei that were ~30 μm laterally but with heights only up to ~8 μm .

Measuring Area and Volume of Whole Nuclei

Whole nuclei were rendered in ViSP (Beheiry and Dahan 2013), a program built to visualize and process 3D SMLM output data. By

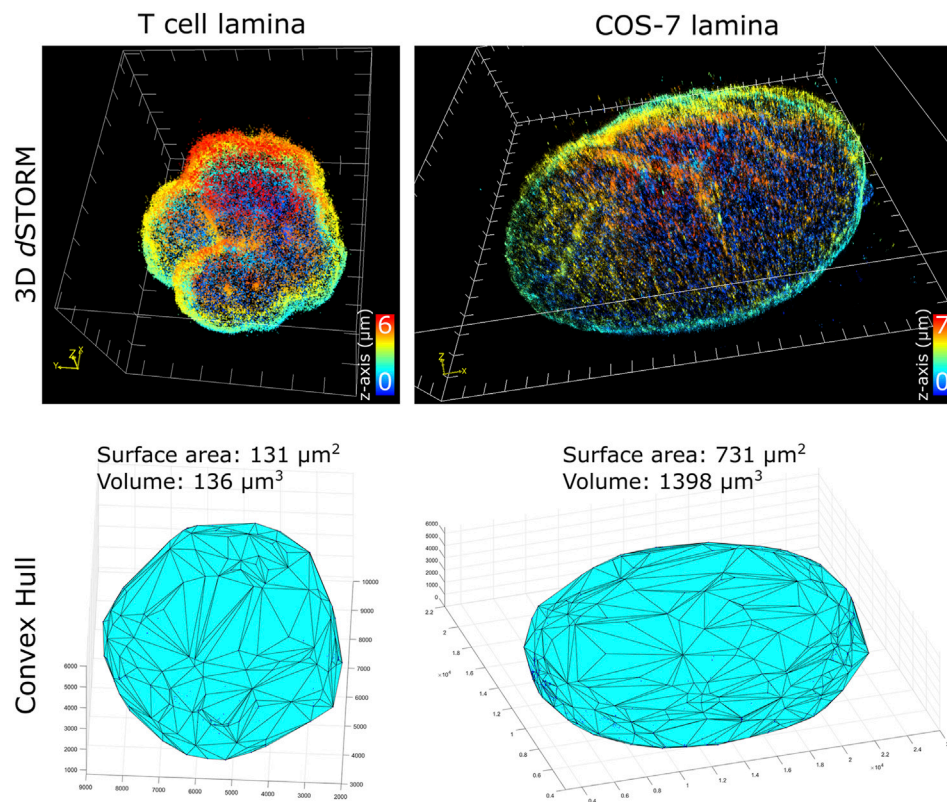


FIGURE 2 | Quantification of nuclei dimensions using 3D dSTORM of lamin B1 and convex hull fitting. (top row) Whole nucleus of T cell and COS-7 cell visualized in ViSP using SM coordinates acquired from 3D dSTORM up to 6 μm in z. (bottom row) 3D convex hull fitting using SM coordinates to determine approximate surface area and volume of whole nuclei.

assigning SM coordinates a colour based on z-position, for example, the entire volume and hollow nature of the nuclear lamina can be readily observed (**Figure 1**). Rendering a relatively continuous 3D structure with few spurious SM localizations highlights the efficiency of immunolabelling lamin B1 to reveal a complete nuclear boundary when imaged. As such, the nuclear lamina can serve as a distinct demarcation of the nuclear envelope and thereby nuclear space and volume when quantifying the spatial distributions of intranuclear components.

To characterize nuclei dimensions, we first used the DBSCAN algorithm (Ester et al., 1996) to identify individual nuclei based on overall SM density, then connected the outermost SM coordinates to form triangular faces that culminate into the 3D convex hull encapsulating the boundary of each nucleus. Transforming individual coordinates into a continuous structure allowed the surface area, as well as the volume within the enclosed hull, to be calculated. Comparing the cell types imaged (**Figure 2**), unsurprisingly, COS-7 nuclei were much larger with more nuclear surface area than T cell nuclei. In the same imaging field of view (25 μm by 25 μm), we could capture either a single COS-7 cell or multiple (up to 6) T cells within the same imaging period (~1 h), mitigating the time required to capture T cells compared to COS-7 cells. The convex hull fitting was useful to segregate individual nuclei and subsequently measure the dimensions of each T cell nucleus. The multi cell

imaging and analysis demonstrates a viable strategy to increase the throughput of quantitative super-resolution imaging of T cell nuclei.

Of the T cell nuclei imaged ($n = 8$ cells, avg. volume $\pm\text{SD} = 127 \pm 15 \mu\text{m}^3$, avg. surface area $\pm\text{SD} = 127 \pm 10 \mu\text{m}^2$), interestingly, the surface area to volume ratio (SA:V) of each nucleus was close to 1. Perfect spheres have a SA:V of 3/radius, and since the approximate radius of each T cell nuclei was ~3 μm , this shows empirically that our sample preparation and imaging assay results in nuclei being closely spherical. This indicates that our protocol for adhering T cells to the coverglass substrate using Cell-Tak and centrifugal force induced little to no compression of the cells. Determining the sphericity of nuclear lamina could be a useful parameter for characterizing lamin-related diseases where nuclear envelope structure or nuclear shape is affected. Additionally, since SA:V is used as a metric for bacterial growth (Ojkic et al., 2019; Shi et al., 2021), there may be potential application for using whole cell 3D dSTORM to study T cell metabolism based on measured SA:V.

Nuclei membrane substructures such as membrane folds and blebs being more concave were excluded from the convex hull fit and thus require more sophisticated fitting procedures to be mapped autonomously. In this work, we measured these membrane features individually based on the 3D nuclei models rendered in ViSP.

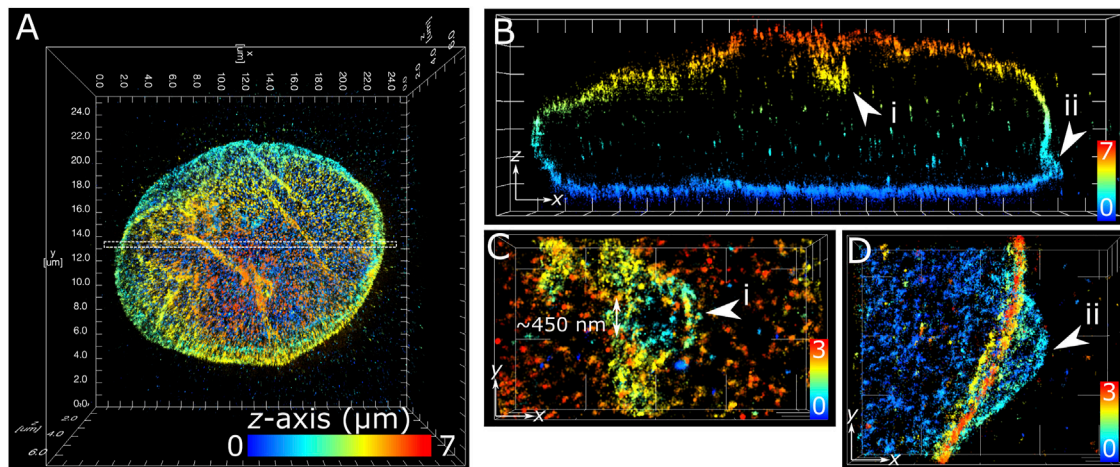


FIGURE 3 | Subdiffraction resolution of membrane features in COS-7 nuclear lamina. Fixed COS-7 cell labelled for lamin B1 with Alexa Fluor 647 and imaged using multiplane astigmatic 3D *d*STORM, 24 μm by 24 μm in *xy* and up to 7 μm in *z*. SM coordinates were rendered in ViSP and color-coded for height. Color scale in each panel indicates *z*-axis range. **(A)** Whole nuclei visualized from the top down *xy* 2D projection. **(B)** A 300 nm section in *xy* from the dotted region in **(A)** visualized from the side reveals sub-lamina features including (i) indentation at the top of nucleus and (ii) outward protrusion at the bottom of nucleus. **(C)** Magnified feature from (i) viewed from the top down reveals a circular indent of outer width $\sim 1 \mu\text{m}$ and inner width $\sim 450 \text{ nm}$. **(D)** Magnified feature from (ii) viewed from the top down reveals an outward swell $\sim 2 \mu\text{m}$ wide at the base of the nuclear lamina. Grid ticks in all images = 1 μm .

Membrane Features of Nuclear Lamina in COS-7 Cells and T Cells

The application of multiplane 3D *d*STORM provided excellent subdiffraction resolution along with the whole-cell spatial context of the target protein, demonstrated here with lamin B1 revealing membrane-like features in cultured COS-7 cells and surgically extracted mouse T cells. Some common features include shallow inward folding of the lamina ($<1 \mu\text{m}$), deep folds into the nucleus reaching up to several μm , and outward blebbing at local regions along the lamina (**Figures 3, 4**). Also observed along folds were ring-like features that extended into the nucleus of COS-7 cells (**Figure 3C**) and T cells (**Figure 4E**). While these features were sized just at or above the diffraction limit ($\sim 200 \text{ nm}$), performing *d*STORM improved their clarity in the rendered 3D SM model to enable more accurate measurement of their dimensions.

The structural complexity of the nuclear envelope (Agrawal and Lele 2019) was reflected in the features we observed when imaging lamin B1. The folds and tunnels observed along the lamina surface could be related to the nucleoplasmic reticulum (NR) (Malhas et al., 2011), a feature observed to reach deep into the nucleoplasm through accumulation with lamin proteins (Drozdz et al., 2017). While its cellular function is not fully understood, aberrations to NR morphology are associated with diseased states (Shoeman et al., 2001; Bussolati et al., 2008; Cornelison et al., 2019). Nuclear blebs observed protruding from the main nuclear lamina (**Figure 3D**) could be a consequence of altered chromatin compaction (Stephens et al., 2018), or early signs of apoptosis (Lindenboim et al., 2020). Cone-like structures protruding inward of the lamina with openings measured in the range of several hundred nanometers (**Figure 4F**) have been identified previously as nuclear invaginations with SMLM (Schoen et al., 2017) and may have

roles with lamin associated chromatin domains or intranuclear transport (Legartová et al., 2014).

DISCUSSION

Here we demonstrate that the photophysical properties of the organic fluorophore Alx647 are sufficient to provide an hour of continuous high laser power imaging up to 8 μm deep into fixed cell samples, enabling multiplane astigmatic 3D *d*STORM of whole nuclear lamina. Fluorophore performance did not deteriorate appreciably indicating potential for even longer imaging time, thereby allowing for greater *z* ranges than the $\sim 8 \mu\text{m}$ achieved here. This raises the possibility that multiplane 3D *d*STORM using Alx647 can also be useful not only for structures with greater *z* dimensions but also for imaging cells expanded with expansion microscopy (ExM) protocols. The emerging combination of ExM with SMLM (Zwettler et al., 2020) to yield cumulative resolution gain for so called ultra-resolution ($\sim 2\text{--}5 \text{ nm}$) has revealed unprecedented structural detail of biological samples previously only achievable with electron microscopies. Since ExM typically incurs a ~ 4 -fold lateral expansion (Chen et al., 2015; Tillberg et al., 2016), with some protocols and iterative strategies achieving 10-fold expansion (Chang et al., 2017; Truckenbrodt et al., 2019), sample volume in 3D is equivalently increased.

Implementing adaptive optics (AO) onto microscope setups have shown to increase the viable imaging depth in a sample and has enabled astigmatic SM imaging up to 90 μm in *z* into the sample (Młodzianowski et al., 2018). AO is also capable of engineering more complex PSF shapes that distort over larger *z* ranges of up to 6 μm (Shechtman et al., 2015), enabling a much

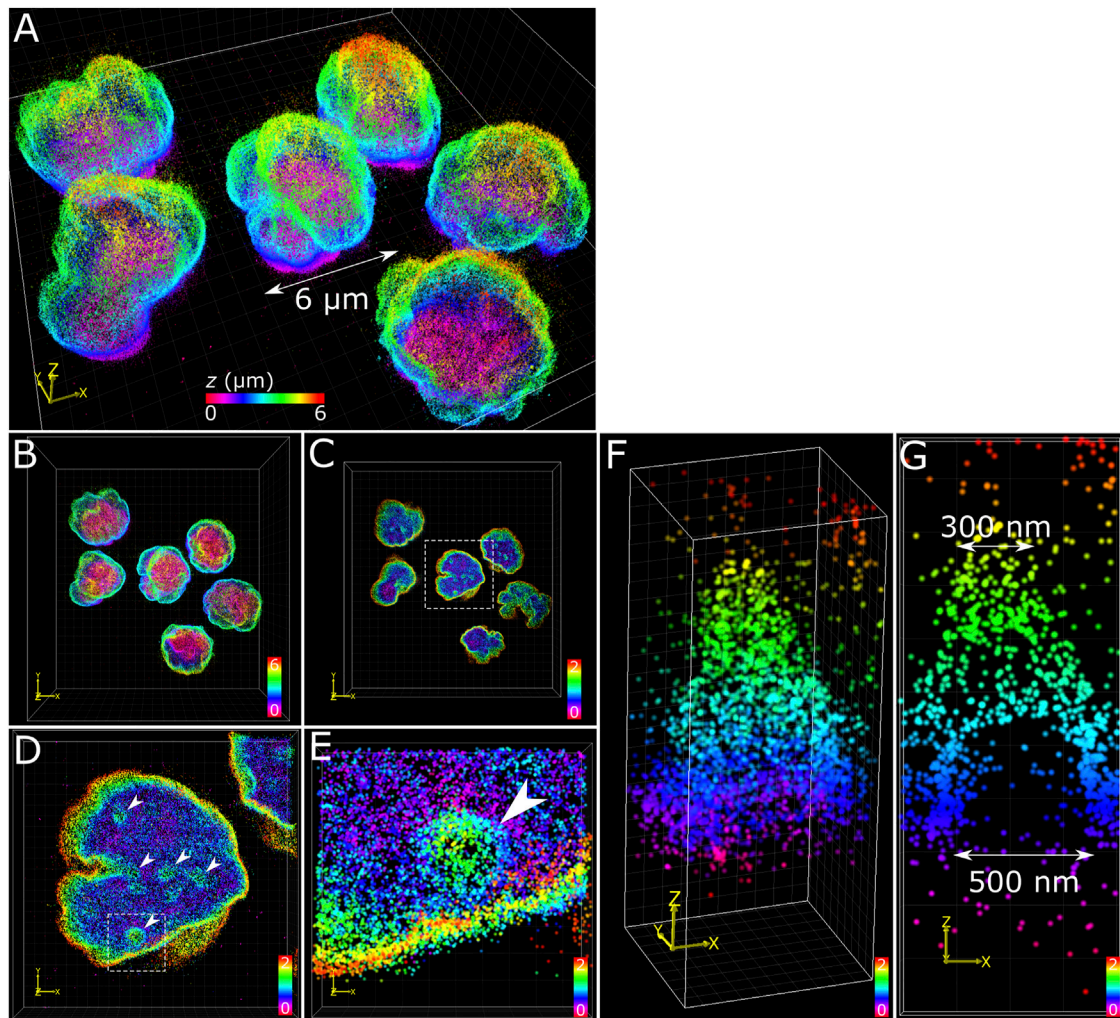


FIGURE 4 | T cell nuclear invaginations visualized with 3D *d*STORM. **(A)** Fixed mouse T cells labelled for lamin B1 with Alexa Fluor 647 and imaged using 3D *d*STORM. **(B)** Top-down projection of the entire height (6 μ m) of T cells from a. **(C)** The bottom 2 μ m of T cells with the same color gradient used. **(D)** Zoom in on a single nucleus (from white dotted box in c) showing distinct height protrusions, indicated by white arrows. **(E)** A single protrusion (from white dotted box in d). **(F)** 3D visualization of the feature isolated from e reveals a cone-like structure. **(G)** Cross-section through the feature in y shows the bottom portion to be relatively void of lamin B1 signal, suggesting a hollow structure. The feature measured 500 nm at the base and 300 nm at the top (toward the nuclear interior). Color bars in each panel indicate z-positions of SM coordinates in μ m.

greater z range in a single slice for 3D SMLM, which, when applied to multiplane *d*STORM of whole cells, would substantially reduce the number of z slices required and thereby the total imaging time and the occurrence of localization errors and artefacts. Ultimately, total imaging time is dependent on the resilience of fluorophores during extended *d*STORM acquisitions, which may be extended with more robust organic dyes and more accommodating switching buffer compositions (Nahidiazar et al., 2016), or by utilizing sophisticated experimental set-ups such as flow-through labelling systems that continuously replenish the fluorophore population (Venkataramani et al., 2018). Given the efficiency of Alx647 demonstrated in this work, and the fact that we did not detect an upper limit for SM imaging performance after 1 h, there is good reason to expect that Alx647 could be used for 3D

*d*STORM or ultra-resolution over longer acquisition periods (2–3 h) to capture larger expanded samples potentially up to ~ 20 μ m in z , or more with the addition of adaptive optics.

Aberrant nuclear membrane phenotypes have been associated with disease pathologies (Muchir and Worman 2004; Fichtman et al., 2019). Examination of whole nuclei morphology with the detail from super-resolution imaging could enhanced visualization of previously uncharacterized structural changes brought about by virally-induced differentiation (Li et al., 2021), genetic anomalies, or drug treatments (Rozario et al., 2021). The nuclear lamina, as imaged in this work via lamin B1, also provides a distinct outline of the nucleus. Fitting with the convex hull provides a quantifiable reference boundary, useful for characterizing intranuclear distributions of chromatin regions along with chromatin features such as histone modifications, as

well as other nuclear components including transcription factors and replication and repair proteins (Whelan and Rothenberg 2021), for example, and sub-nuclear structures such as nucleoli (Rawlinson et al., 2018). This would provide information about the nuclear interior at the single-cell level and would establish a standardized distribution parameter when interrogating multiple cells. Achieving this would require two imaging channels, one for lamin and one for the target of interest, and as such would require another suitable fluorophore, that is spectrally distinct from Alx647 and has desirable photophysical performance for whole cell 3D *d*STORM matching Alx647. Intranuclear features can then be spatially defined as a function of the nuclear lamina. For example, in the case of T cell nuclei that were observed to be closely spherical, radial plot analysis (Crosetto and Bienko 2020; Girelli et al., 2020) is a viable quantification method for the distribution of T cell intranuclear components. Because *d*STORM affords a highly precise SM coordinate list, more sophisticated analysis methods can be employed to map individual coordinates or coordinate clusters of the intranuclear components (Xu et al., 2018; Su et al., 2020) with respect the nuclear lamina.

Characterization of nuclear architecture, both in the interior and membrane-bound, remains challenging. The application of 3D super-resolution techniques, as well as next-generation ultra-resolution and AO imaging methods provide excellent visualization of specifically labelled proteins and structures. The structural detail provided with *d*STORM images and the accompanying SM coordinate dataset can be analyzed with various levels depending on the features of interest. We have shown that the convex hull analysis can extract useful parameters such as surface area and volume of the whole nucleus. Besides the convex hull fit, *d*STORM data may be processed using other methods that quantify volume such as the Voronoi tessellation-based 3DClusterViSu (Andronov et al., 2018). Another approach is to fit the 3D coordinates with an alpha shape (Gardiner et al., 2018), similar to the convex hull that wraps around the outermost datapoints, the alpha shape method additionally retains concave features, such as nuclear membrane folds observed from 3D ViSP models. Furthermore, the alpha shape method can be used for fitting internal surfaces of the nuclear membrane. Efforts to adapt the alpha shape method to quantify 3D SM data of the nuclear lamina are ongoing. The use of super-resolution microscopy to directly visualize and precisely quantify specific nuclear features is emerging as a powerful tool for investigations of genetic disease (Xu et al., 2020), immune cell functionality (Carr et al., 2017; Ponjavic et al., 2018), and understanding how chromatin is organized *in situ* (Otterstrom et al., 2019; Xu and Liu 2021). Achieving a complete nuclear atlas warrants further development in both the imaging technologies and analytical capabilities.

CONCLUSION

Our assay extending SM PSF astigmatism for multiplane 3D *d*STORM of whole nuclear lamina demonstrates the capability of modern modular microscope setups and harnesses the superior performance of the Alx647 organic fluorophore for over 1 h in a simple photoswitching buffer. The rendered 3D images encompassed the entire nuclear dimensions while retaining the excellent

subdiffraction resolution (~ 20 nm in x and y and ~ 50 nm in z) achieved with *d*STORM. Convex hull analysis allowed quantification of nuclear surface area and volume that revealed the sphericity of T cells by their SA:V values of ~ 1 . Observed 3D structures included membrane folds, blebs and invaginations that each may contribute or be consequence of specific nuclear phenotypes. We expect that imaging the nuclear lamina to determine the inner nuclear envelope boundary is ideal for quantifying spatial distributions of nuclear contents such as histone modifications which can readily be labelled and mapped using super-resolution methods.

DATA AVAILABILITY STATEMENT

The datasets presented in this study can be found in online repositories. The names of the repository/repositories and accession number(s) can be found below: doi: 10.26180/19358699.

ETHICS STATEMENT

The animal study was reviewed and approved by the Monash Animal Ethics Committee.

AUTHOR CONTRIBUTIONS

AR and AM: Prepared samples and imaged whole nuclei using 3D multiplane *d*STORM. AR, AM and CE: Analyzed data and performed fitting. TB, DW, BR and ST: Supervised the project. AR and AM: Wrote the manuscript with all authors editing and reviewing the manuscript. All authors read and approved the final manuscript.

FUNDING

Support from the National Health and Medical Research Council through the Ideas program (GA65914) is gratefully acknowledged. DW is the recipient of an Australian Research Council Australian Discovery Early Career Research Award (DE200100584) funded by the Australian Government.

ACKNOWLEDGMENTS

AR, TB and ST acknowledge support from the National Health and Medical Research Council. DW acknowledges the Bendigo Tertiary Education Anniversary Foundation for auspicing the Holsworth Biomedical Research Initiative.

SUPPLEMENTARY MATERIAL

The Supplementary Material for this article can be found online at: <https://www.frontiersin.org/articles/10.3389/fchem.2022.863610/full#supplementary-material>

REFERENCES

- Agrawal, A., and Lele, T. P. (2019). Mechanics of Nuclear Membranes. *J. Cel Sci* 132 (14), jcs229245. doi:10.1242/jcs.229245
- Andronov, L., Michalon, J., Ouarrarhni, K., Orlov, I., Hamiche, A., Vonesch, J.-L., et al. (2018). 3DClusterViSu: 3D Clustering Analysis of Super-resolution Microscopy Data by 3D Voronoi Tessellations. *Bioinformatics* 34 (17), 3004–3012. doi:10.1093/bioinformatics/bty200
- Betzig, E., Patterson, G. H., Sougrat, R., Lindwasser, O. W., Olenych, S., Bonifacio, J. S., et al. (2006). Imaging Intracellular Fluorescent Proteins at Nanometer Resolution. *Science* 313, 1642–1645. doi:10.1126/science.1127344
- Burke, B., and Stewart, C. L. (2013). The Nuclear Lamins: Flexibility in Function. *Nat. Rev. Mol. Cel Biol* 14 (1), 13–24. doi:10.1038/nrm3488
- Bussolati, G., Marchiò, C., Gaetano, L., Lupo, R., and Sapino, A. (2008). Pleomorphism of the Nuclear Envelope in Breast Cancer: a New Approach to an Old Problem. *J. Cel Mol Med* 12 (1), 209–218. doi:10.1111/j.1582-4934.2007.00176.x
- Carr, A. R., Ponjavic, A., Basu, S., McColl, J., Santos, A. M., Davis, S., et al. (2017). Three-Dimensional Super-resolution in Eukaryotic Cells Using the Double-Helix Point Spread Function. *Biophysical J.* 112 (7), 1444–1454. doi:10.1016/j.bpj.2017.02.023
- Chang, J.-B., Chen, F., Yoon, Y.-G., Jung, E. E., Babcock, H., Kang, J. S., et al. (2017). Iterative Expansion Microscopy. *Nat. Methods* 14 (6), 593–599. doi:10.1038/nmeth.4261
- Chen, F., Tillberg, P. W., and Boyden, E. S. (2015). Expansion Microscopy. *Science* 347 (6221), 543–548. doi:10.1126/science.1260088
- Cornelison, G. L., Levy, S. A., Jensen, T., and Frost, B. (2019). Tau-induced Nuclear Envelope Invagination Causes a Toxic Accumulation of mRNA in Drosophila. *Aging Cell* 18 (1), e12847. doi:10.1111/ace1.12847
- Crosetto, N., and Bienko, M. (2020). Radial Organization in the Mammalian Nucleus. *Front. Genet.* 11, 33. doi:10.3389/fgene.2020.00033
- Drozd, M. M., Jiang, H., Pytowski, L., Grovenor, C., and Vaux, D. J. (2017). Formation of a Nucleoplasmic Reticulum Requires De Novo Assembly of Nascent Phospholipids and Shows Preferential Incorporation of Nascent Lamins. *Sci. Rep.* 7 (1), 7454. doi:10.1038/s41598-017-07614-w
- Edelstein, A., Amodaj, N., Hoover, K., Vale, R., and Stuurman, N. (2010). Computer Control of Microscopes Using µManager. *Curr. Protoc. Mol. Biol.* 14 (1), 14–20. doi:10.1002/0471142727.mbl1420s92
- El Beheiry, M., and Dahan, M. (2013). ViSP: Representing Single-Particle Localizations in Three Dimensions. *Nat. Methods* 10, 689–690. doi:10.1038/nmeth.2566
- Ester, M., Kriegl, H.-P., Sander, J., and Xu, X. (1996). “A Density-Based Algorithm for Discovering Clusters in Large Spatial Databases with Noise,” in Proceedings of the Second International Conference on Knowledge Discovery and Data Mining, Portland, Oregon, August 2–4, 1996. (Portland, Oregon: AAAI Press), 226–231. doi:10.5555/3001460.3001507
- Fichtman, B., Zagair, F., Biran, N., Barsheshet, Y., Chervinsky, E., Ben Neria, Z., et al. (2019). Combined Loss of LAP1B and LAP1C Results in an Early Onset Multisystemic Nuclear Envelopathy. *Nat. Commun.* 10 (1), 605. doi:10.1038/s41467-019-08493-7
- Gardiner, J. D., Behnsen, J., and Brassey, C. A. (2018). Alpha Shapes: Determining 3D Shape Complexity across Morphologically Diverse Structures. *BMC Evol. Biol.* 18 (1), 184. doi:10.1186/s12862-018-1305-z
- Girelli, G., Custodio, J., Kallas, T., Agostini, F., Wernersson, E., Spanjaard, B., et al. (2020). GPSeq Reveals the Radial Organization of Chromatin in the Cell Nucleus. *Nat. Biotechnol.* 38 (10), 1184–1193. doi:10.1038/s41587-020-0519-y
- Gustafsson, M. G. (2000). Surpassing the Lateral Resolution Limit by a Factor of Two Using Structured Illumination Microscopy. *J. Microsc.* 198, 82–87. doi:10.1046/j.1365-2818.2000.00710.x
- Haji, B., Wisniewski, J., El Beheiry, M., Chen, J., Revyakin, A., Wu, C., et al. (2014). Whole-cell, Multicolor Superresolution Imaging Using Volumetric Multifocus Microscopy. *Proc. Natl. Acad. Sci. U.S.A.* 111 (49), 17480–17485. doi:10.1073/pnas.1412396111
- Heilemann, M., van de Linde, S., Schüttelpelz, M., Kasper, R., Seefeldt, B., Mukherjee, A., et al. (2008). Subdiffraction-Resolution Fluorescence Imaging with Conventional Fluorescent Probes. *Angew. Chem. Int. Ed.* 47 (33), 6172–6176. doi:10.1002/anie.200802376
- Hess, S. T., Girirajan, T. P., and Mason, M. D. (2006). Ultra-High Resolution Imaging by Fluorescence Photoactivation Localization Microscopy. *Biophys. J.* 91, 4258–4272. doi:10.1529/biophysj.106.091116
- Huang, B., Jones, S. A., Brandenburg, B., and Zhuang, X. (2008a). Whole-cell 3D STORM Reveals Interactions between Cellular Structures with Nanometer-Scale Resolution. *Nat. Methods* 5, 1047–1052. doi:10.1038/nmeth.1274
- Huang, B., Wang, W., Bates, M., and Zhuang, X. (2008b). Three-Dimensional Super-resolution Imaging by Stochastic Optical Reconstruction Microscopy. *Science* 319, 810–813. doi:10.1126/science.1153529
- Klar, T. A., and Hell, S. W. (1999). Subdiffraction Resolution in Far-Field Fluorescence Microscopy. *Opt. Lett.* 24 (14), 954–956. doi:10.1364/ol.24.000954
- Klar, T. A., Jakobs, S., Dyba, M., Egner, A., and Hell, S. W. (2000). Fluorescence Microscopy with Diffraction Resolution Barrier Broken by Stimulated Emission. *Proc. Natl. Acad. Sci. U.S.A.* 97 (15), 8206–8210. doi:10.1073/pnas.97.15.8206
- Legartová, S., Stixová, L., Laur, O., Kozubek, S., Sehnalová, P., and Bártová, E. (2014). Nuclear Structures Surrounding Internal Lamin Invaginations. *J. Cell Biochem.* 115 (3), 476–487. doi:10.1002/jcb.24681
- Li, J., Hardy, K., Olshansky, M., Barugahare, A., Gearing, L. J., Prier, J. E., et al. (2021). KDM6B-dependent Chromatin Remodeling Underpins Effective Virus-specific CD8+ T Cell Differentiation. *Cel Rep.* 34 (11), 108839. doi:10.1016/j.celrep.2021.108839
- Lindenboim, L., Zohar, H., Worman, H. J., and Stein, R. (2020). The Nuclear Envelope: Target and Mediator of the Apoptotic Process. *Cell Death Discov.* 6 (1), 29. doi:10.1038/s41420-020-0256-5
- Malhas, A., Goulbourne, C., and Vaux, D. J. (2011). The Nucleoplasmic Reticulum: Form and Function. *Trends Cel Biol.* 21 (6), 362–373. doi:10.1016/j.tcb.2011.03.008
- Miriklis, E. L., Rozario, A. M., Rothenberg, E., Bell, T. D. M., and Whelan, D. R. (2021). Understanding DNA Organization, Damage, and Repair with Super-resolution Fluorescence Microscopy. *Methods Appl. Fluoresc.* 9 (3), 032002 1–21. doi:10.1088/2050-6120/abf239
- Mlodzianowski, M. J., Cheng-Hathaway, P. J., Bemiller, S. M., McCray, T. J., Liu, S., Miller, D. A., et al. (2018). Active PSF Shaping and Adaptive Optics Enable Volumetric Localization Microscopy through Brain Sections. *Nat. Methods* 15 (8), 583–586. doi:10.1038/s41592-018-0053-8
- Muchir, A., and Worman, H. J. (2004). The Nuclear Envelope and Human Disease. *Physiology* 19 (5), 309–314. doi:10.1152/physiol.00022.2004
- Nahidiazar, L., Agronskaia, A. V., Broertjes, J., van den Broek, B., and Jalink, K. (2016). Optimizing Imaging Conditions for Demanding Multi-Color Super Resolution Localization Microscopy. *PLOS ONE* 11 (7), e0158884. doi:10.1371/journal.pone.0158884
- Nmezi, B., Xu, J., Fu, R., Armiger, T. J., Rodriguez-Bey, G., Powell, J. S., et al. (2019). Concentric Organization of A- and B-type Lamins Predicts Their Distinct Roles in the Spatial Organization and Stability of the Nuclear Lamina. *Proc. Natl. Acad. Sci. U.S.A.* 116 (10), 4307–4315. doi:10.1073/pnas.1810070116
- Ojic, N., Serbanescu, D., and Banerjee, S. (2019). Surface-to-volume Scaling and Aspect Ratio Preservation in Rod-Shaped Bacteria. *eLife* 8, e47033. doi:10.7554/eLife.47033
- Otterstrom, J., Castells-Garcia, A., Vicario, C., Gomez-Garcia, P. A., Cosma, M. P., and Lakadamyali, M. (2019). Super-resolution Microscopy Reveals How Histone Tail Acetylation Affects DNA Compaction within Nucleosomes In Vivo. *Nucleic Acids Res.* 47 (16), 8470–8484. doi:10.1093/nar/gkz593
- Pavani, S. R. P., Thompson, M. A., Biteen, J. S., Lord, S. J., Liu, N., Twieg, R. J., et al. (2009). Three-dimensional, Single-Molecule Fluorescence Imaging beyond the Diffraction Limit by Using a Double-helix point Spread Function. *Proc. Natl. Acad. Sci. U.S.A.* 106 (9), 2995–2999. doi:10.1073/pnas.0900245106
- Pongubala, J. M. R., and Murre, C. (2021). Spatial Organization of Chromatin: Transcriptional Control of Adaptive Immune Cell Development. *Front. Immunol.* 12, 633825. doi:10.3389/fimmu.2021.633825
- Ponjavic, A., McColl, J., Carr, A. R., Santos, A. M., Kulenkampff, K., Lippert, A., et al. (2018). Single-Molecule Light-Sheet Imaging of Suspended T Cells. *Biophysical J.* 114 (9), 2200–2211. doi:10.1016/j.bpj.2018.02.044
- Rankin, J., and Ellard, S. (2006). The Laminopathies: a Clinical Review. *Clin. Genet.* 70 (4), 261–274. doi:10.1111/j.1399-0004.2006.00677.x
- Rawlinson, S. M., Zhao, T., Rozario, A. M., Rootes, C. L., McMillan, P. J., Purcell, A. W., et al. (2018). Viral Regulation of Host Cell Biology by Hijacking of the

- Nucleolar DNA-Damage Response. *Nat. Commun.* 9 (1), 3057. doi:10.1038/s41467-018-05354-7
- Rozario, A. M., Duwé, S., Elliott, C., Hargreaves, R. B., Moseley, G. W., Dedecker, P., et al. (2021). Nanoscale Characterization of Drug-Induced Microtubule Filament Dysfunction Using Super-resolution Microscopy. *BMC Biol.* 19 (1), 260. doi:10.1186/s12915-021-01164-4
- Rozario, A. M., Zwettler, F., Duwé, S., Hargreaves, R. B., Brice, A., Dedecker, P., et al. (2020). 'Live and Large': Super-resolution Optical Fluctuation Imaging (SOFI) and Expansion Microscopy (ExM) of Microtubule Remodelling by Rabies Virus P Protein. *Aust. J. Chem.* 73 (8), 686–692. doi:10.1071/ch19571
- Rust, M. J., Bates, M., and Zhuang, X. (2006). Sub-diffraction-limit Imaging by Stochastic Optical Reconstruction Microscopy (STORM). *Nat. Methods* 3 (10), 793–796. doi:10.1038/nmeth929
- Schermelleh, L., Ferrand, A., Huser, T., Eggeling, C., Sauer, M., Biehlmair, O., et al. (2019). Super-resolution Microscopy Demystified. *Nat. Cell Biol.* 21 (1), 72–84. doi:10.1038/s41556-018-0251-8
- Schoen, I., Aires, L., Ries, J., and Vogel, V. (2017). Nanoscale Invaginations of the Nuclear Envelope: Shedding New Light on Wormholes with Elusive Function. *Nucleus* 8 (5), 506–514. doi:10.1080/19491034.2017.1337621
- Sharonov, A., and Hochstrasser, R. M. (2006). Wide-field Subdiffraction Imaging by Accumulated Binding of Diffusing Probes. *Proc. Natl. Acad. Sci. U.S.A.* 103 (50), 18911–18916. doi:10.1073/pnas.0609643104
- Shechtman, Y., Sahl, S. J., Backer, A. S., and Moerner, W. E. (2014). Optimal Point Spread Function Design for 3D Imaging. *Phys. Rev. Lett.* 113 (13), 133902. doi:10.1103/physrevlett.113.133902
- Shechtman, Y., Weiss, L. E., Backer, A. S., Sahl, S. J., and Moerner, W. E. (2015). Precise Three-Dimensional Scan-free Multiple-Particle Tracking over Large Axial Ranges with Tetrapod Point Spread Functions. *Nano Lett.* 15 (6), 4194–4199. doi:10.1021/acs.nanolett.5b01396
- Shi, H., Hu, Y., Odermatt, P. D., Gonzalez, C. G., Zhang, L., Elias, J. E., et al. (2021). Precise Regulation of the Relative Rates of Surface Area and Volume Synthesis in Bacterial Cells Growing in Dynamic Environments. *Nat. Commun.* 12 (1), 1975. doi:10.1038/s41467-021-22092-5
- Shoeman, R. L., Hüttermann, C., Hartig, R., and Traub, P. (2001). Amino-terminal Polypeptides of Vimentin Are Responsible for the Changes in Nuclear Architecture Associated with Human Immunodeficiency Virus Type 1 Protease Activity in Tissue Culture Cells. *MBoC* 12 (1), 143–154. doi:10.1091/mbc.12.1.143
- Stephens, A. D., Liu, P. Z., Banigan, E. J., Almassalha, L. M., Backman, V., Adam, S. A., et al. (2018). Chromatin Histone Modifications and Rigidity Affect Nuclear Morphology Independent of Lamins. *MBoC* 29 (2), 220–233. doi:10.1091/mbc.e17-06-0410
- Su, Q. P., Zhao, Z. W., Meng, L., Ding, M., Zhang, W., Li, Y., et al. (2020). Superresolution Imaging Reveals Spatiotemporal Propagation of Human Replication Foci Mediated by CTCF-Organized Chromatin Structures. *Proc. Natl. Acad. Sci. U.S.A.* 117 (26), 15036–15046. doi:10.1073/pnas.2001521117
- Tillberg, P. W., Chen, F., Piatkevich, K. D., Zhao, Y., Yu, C.-C., English, B. P., et al. (2016). Protein-retention Expansion Microscopy of Cells and Tissues Labeled Using Standard Fluorescent Proteins and Antibodies. *Nat. Biotechnol.* 34 (9), 987–992. doi:10.1038/nbt.3625
- Tokunaga, M., Imamoto, N., and Sakata-Sogawa, K. (2008). Highly Inclined Thin Illumination Enables clear Single-Molecule Imaging in Cells. *Nat. Methods* 5 (2), 159–161. doi:10.1038/nmeth1171
- Truckenbrodt, S., Sommer, C., Rizzoli, S. O., and Danzl, J. G. (2019). A Practical Guide to Optimization in X10 Expansion Microscopy. *Nat. Protoc.* 14 (3), 832–863. doi:10.1038/s41596-018-0117-3
- Venkataramani, V., Kardorff, M., Herrmannsdörfer, F., Wieneke, R., Klein, A., Tampé, R., et al. (2018). Enhanced Labeling Density and Whole-Cell 3D dSTORM Imaging by Repetitive Labeling of Target Proteins. *Sci. Rep.* 8 (1), 5507. doi:10.1038/s41598-018-23818-0
- Whelan, D. R., and Bell, T. D. M. (2015a). Image Artifacts in Single Molecule Localization Microscopy: Why Optimization of Sample Preparation Protocols Matters. *Sci. Rep.* 5, 7924. doi:10.1038/srep07924
- Whelan, D. R., and Bell, T. D. M. (2015b). Super-Resolution Single-Molecule Localization Microscopy: Tricks of the Trade. *J. Phys. Chem. Lett.* 6 (3), 374–382. doi:10.1021/jz5019702
- Whelan, D. R., Holm, T., Sauer, M., and Bell, T. D. M. (2014). Focus on Super-resolution Imaging with Direct Stochastic Optical Reconstruction Microscopy (dSTORM). *Aust. J. Chem.* 67 (2), 179–183. doi:10.1071/ch13499
- Whelan, D. R., and Rothenberg, E. (2021). Super-resolution Mapping of Cellular Double-Strand Break Resection Complexes during Homologous Recombination. *Proc. Natl. Acad. Sci.* 118 (11), e2021963118. doi:10.1073/pnas.2021963118
- Wolter, S., Löschberger, A., Holm, T., Aufmkolk, S., Dabauvalle, M. C., van de Linde, S., et al. (2012). RapidSTORM: Accurate, Fast Open-Source Software for Localization Microscopy. *Nat. Methods* 9, 1040–1041. doi:10.1038/nmeth.2224
- Xu, J., and Liu, Y. (2021). Probing Chromatin Compaction and its Epigenetic States *In Situ* with Single-Molecule Localization-Based Super-resolution Microscopy. *Front. Cell Dev. Biol.* 9, 653077. doi:10.3389/fcell.2021.653077
- Xu, J., Ma, H., Jin, J., Uttam, S., Fu, R., Huang, Y., et al. (2018). Super-Resolution Imaging of Higher-Order Chromatin Structures at Different Epigenomic States in Single Mammalian Cells. *Cel Rep.* 24 (4), 873–882. doi:10.1016/j.celrep.2018.06.085
- Xu, J., Ma, H., Ma, H., Jiang, W., Mela, C. A., Duan, M., et al. (2020). Super-resolution Imaging Reveals the Evolution of Higher-Order Chromatin Folding in Early Carcinogenesis. *Nat. Commun.* 11 (1), 1899. doi:10.1038/s41467-020-15718-7
- Xu, K., Zhong, G., and Zhuang, X. (2013). Actin, Spectrin, and Associated Proteins Form a Periodic Cytoskeletal Structure in Axons. *Science* 339 (6118), 452–456. doi:10.1126/science.1232251
- Zwettler, F. U., Reinhard, S., Gambarotto, D., Bell, T. D. M., Hamel, V., Guichard, P., et al. (2020). Molecular Resolution Imaging by post-labeling Expansion Single-Molecule Localization Microscopy (Ex-SMLM). *Nat. Commun.* 11 (1), 3388. doi:10.1038/s41467-020-17086-8

Conflict of Interest: The authors declare that the research was conducted in the absence of any commercial or financial relationships that could be construed as a potential conflict of interest.

Publisher's Note: All claims expressed in this article are solely those of the authors and do not necessarily represent those of their affiliated organizations, or those of the publisher, the editors and the reviewers. Any product that may be evaluated in this article, or claim that may be made by its manufacturer, is not guaranteed or endorsed by the publisher.

Copyright © 2022 Rozario, Morey, Elliott, Russ, Whelan, Turner and Bell. This is an open-access article distributed under the terms of the Creative Commons Attribution License (CC BY). The use, distribution or reproduction in other forums is permitted, provided the original author(s) and the copyright owner(s) are credited and that the original publication in this journal is cited, in accordance with accepted academic practice. No use, distribution or reproduction is permitted which does not comply with these terms.



Approaches to Improve the Quantitation of Oxytocin in Human Serum by Mass Spectrometry

Anke Hering^{1†}, Beverly Jieu^{1†}, Alun Jones¹ and Markus Muttenthaler^{1,2*}

¹Institute for Molecular Bioscience, The University of Queensland, Brisbane, QLD, Australia, ²Institute of Biological Chemistry, Faculty of Chemistry, University of Vienna, Vienna, Austria

OPEN ACCESS

Edited by:

John D. Wade,
University of Melbourne, Australia

Reviewed by:

Edouard Nice,
Monash University, Australia
Marcin Poreba,
Wrocław University of Science and
Technology, Poland

*Correspondence:

Markus Muttenthaler
m.muttenthaler@uq.edu.au

[†]These authors have contributed
equally to this work

Specialty section:

This article was submitted to
Chemical Biology,
a section of the journal
Frontiers in Chemistry

Received: 03 March 2022

Accepted: 03 May 2022

Published: 09 June 2022

Citation:

Hering A, Jieu B, Jones A and
Muttenthaler M (2022) Approaches to
Improve the Quantitation of Oxytocin in
Human Serum by Mass Spectrometry.
Front. Chem. 10:889154.
doi: 10.3389/fchem.2022.889154

The neuropeptide oxytocin (OT) regulates several peripheral and central functions and is a molecule of interest in psychiatric diseases such as autism spectrum disorder, schizophrenia, anxiety and depression. The study of OT in human serum samples is however hampered by inconsistent sample preparation and analysis as well as low endogenous blood concentration (1–10 pM). This results in varying reports on OT's blood levels and interpretation of OT's role in different (patho)physiological states. Quantitative mass spectrometry (MS) is a highly promising technology to address this problem but still requires large sample volumes to achieve adequate sensitivity and reliability for the quantitation of compounds at low concentrations. We therefore systematically evaluated sample preparation methods for MS to achieve a reliable sample preparation protocol with good peptide recovery, minimal matrix effects and good overall method efficiency in line with FDA guidelines for bioanalytic method development and validation. Additionally, we investigated a strategy to improve the ionization efficiency of OT by adding charged and/or hydrophobic moieties to OT to improve the lower limit of quantitation. Optimized sample preparation in combination with OT modification with a quaternary pyridinium ion improved the sensitivity of OT by ~40-fold on a tandem triple quadrupole mass spectrometer (API4000 QTRAP), resulting in a lower limit of quantitation of 5 pM in water (linear range 5 pM – 1 mM) and 2 nM in human serum (linear range 2 nM – 1 mM) compared to 200 pM in water and 86 nM in serum with unmodified OT. This approach and protocol provide a solid foundation towards method development for OT quantitation using MS, which should be of high value for fundamental research as well as clinical monitoring of OT upon drug treatments.

Keywords: oxytocin, LC-MS, neuropeptide, analytical method development, sample preparation

Abbreviations: ACN, Acetonitrile; HLB, Hydrophobic-lipophilic-balanced; HPLC, High-performance liquid chromatography; LCMS, Liquid chromatography-mass spectrometry; LC-MS/MS, Liquid chromatography-tandem mass spectrometry; LLOQ, Lower limit of quantitation; ME, Method efficiency; MX, Matrix effects; OT, Oxytocin; RE, Recovery.

INTRODUCTION

Oxytocin (OT) is an important neuropeptide and peptide hormone mediating several physiological functions. These range from peripheral functions like muscle contractions in the uterus during birth (Gimpl and Fahrenholz, 2001; Leng et al., 2008; Jurek and Neumann, 2018), ejaculation (Hib, 1974a; Hib, 1974b; Hib, 1977) and milk-ejection (McNeilly et al., 1983; Nishimori et al., 1996; Erickson et al., 2020), as well as anti-inflammatory effects in the cardiovascular (Jovanovic et al., 2019; Meusel et al., 2021) and gastrointestinal systems (Pfister et al., 2005; Welch et al., 2009; Welch et al., 2014; Tang et al., 2019), to central nervous system functions such as maternal care, pair-bonding, empathy, memory and learning (Heinrichs et al., 2009; Rasie Abdullahi et al., 2018; Salighedar et al., 2019). OT holds therapeutic potential for a wide variety of diseases including breast cancer (Ariana et al., 2018; Khorrami et al., 2018; Liu et al., 2020), cardiovascular disease (Merz et al., 2020), diabetes (Garrido-Urbani et al., 2018; Szeto et al., 2020; Yuan et al., 2020) and neurological disorders such as autism and schizophrenia (Green et al., 2001; Cyranowski et al., 2008; Goldman et al., 2008; Kéri et al., 2009; Feifel et al., 2010; Guastella et al., 2010; Bartholomeusz et al., 2015; Feifel et al., 2016; Alvares et al., 2017; Bradley and Woolley, 2017; Ooi et al., 2017). OT has also been studied for its potential as a biomarker, but progress has been hampered by inconsistent analysis methods and difficulties with reliably measuring the low levels of endogenous OT in the blood (1–10 pM) (Kagerbauer et al., 2013; Leng and Sabatier, 2016), resulting in contradicting measurements and rendering data interpretation difficult (Glovinsky et al., 1994; Bell et al., 2006; Jansen et al., 2006; Ozsoy et al., 2009; Miller et al., 2013; Strauss et al., 2015; Saxbe et al., 2019).

Radio- and enzyme-linked immunoassays are the most commonly used methods for OT analysis in biological samples, but they have been questioned for their lack of sensitivity and specificity as well as for their inconsistent sample preparation protocols (Szeto et al., 2011; McCullough et al., 2013; Robinson et al., 2014; Leng and Sabatier, 2016). Mass spectrometry (MS) is a promising alternative since it is a sensitive and mass-specific analytical method that can quantify a target analyte by its defined mass and fragmentation pattern, thereby excluding any metabolites that might still give a signal using immunoassays (McCullough et al., 2013). MS methods have been developed for OT quantitation using triple quadrupole (Zhang et al., 2011; Brandtzaeg et al., 2016) or orbitrap (Franke et al., 2019) mass spectrometers. However, achieving the required lower limit of quantitation (LLOQ) to reliably measure OT in the range of 1–10 pM remains challenging. We therefore set out to develop improved MS-based strategies and protocols towards the detection and quantitation of OT in biological samples.

The first challenge, one often overlooked, is that MS is susceptible to sample matrix interferences that cause ion suppression or enhancement, known as matrix effects (Mei et al., 2003; Panuwet et al., 2016). Matrix effects and their impact on analyte ionization depend on ionization type, biological matrix, chromatographic conditions, and sample preparation (Dams et al., 2003; Panuwet et al., 2016).

Appropriate sample preparation is particularly important in reducing matrix effects as it removes impurities and matrix interferences (Szeto et al., 2011; Christensen et al., 2014; Robinson et al., 2014; Lefevre et al., 2017). Most sample preparation protocols developed for OT analysis unfortunately do not evaluate such matrix effects and lack adequate characterization according to the US Food and Drug Administration (FDA) guidelines for bioanalytical method development (Kramer et al., 2004; Brandtzaeg et al., 2016; Franke et al., 2019). The second challenge is that MS sensitivity is still not good enough to reliably quantify OT's low endogenous levels, requiring large sample volumes to achieve adequate sensitivity or specialized equipment not available in most laboratories (e.g., 2D LC-MS/MS) (Dams et al., 2003; Zhang et al., 2011; Liu et al., 2019). When using electrospray ionization MS (ESI-MS), the sensitivity relies heavily on the analyte's ionization efficiency and ion transmission (Kearle and Tang, 1993; Page et al., 2007). These factors can be improved by introducing derivatizations to the peptide such as hydrophobic and charged amino acids, as well as quaternary ammonium, phosphonium, imidazolium and pyridinium salts (Bachor et al., 2014; Qiao et al., 2014; Qiao et al., 2015; Waliczek et al., 2016).

Here, we describe the development of a robust sample preparation protocol following FDA guidelines in terms of LLOQ (Administration, U.F.A.D., 2018) and an OT derivatization method to improve OT's ionization efficiency with the aim to improve the overall sensitivity of detecting and quantifying OT in biological samples.

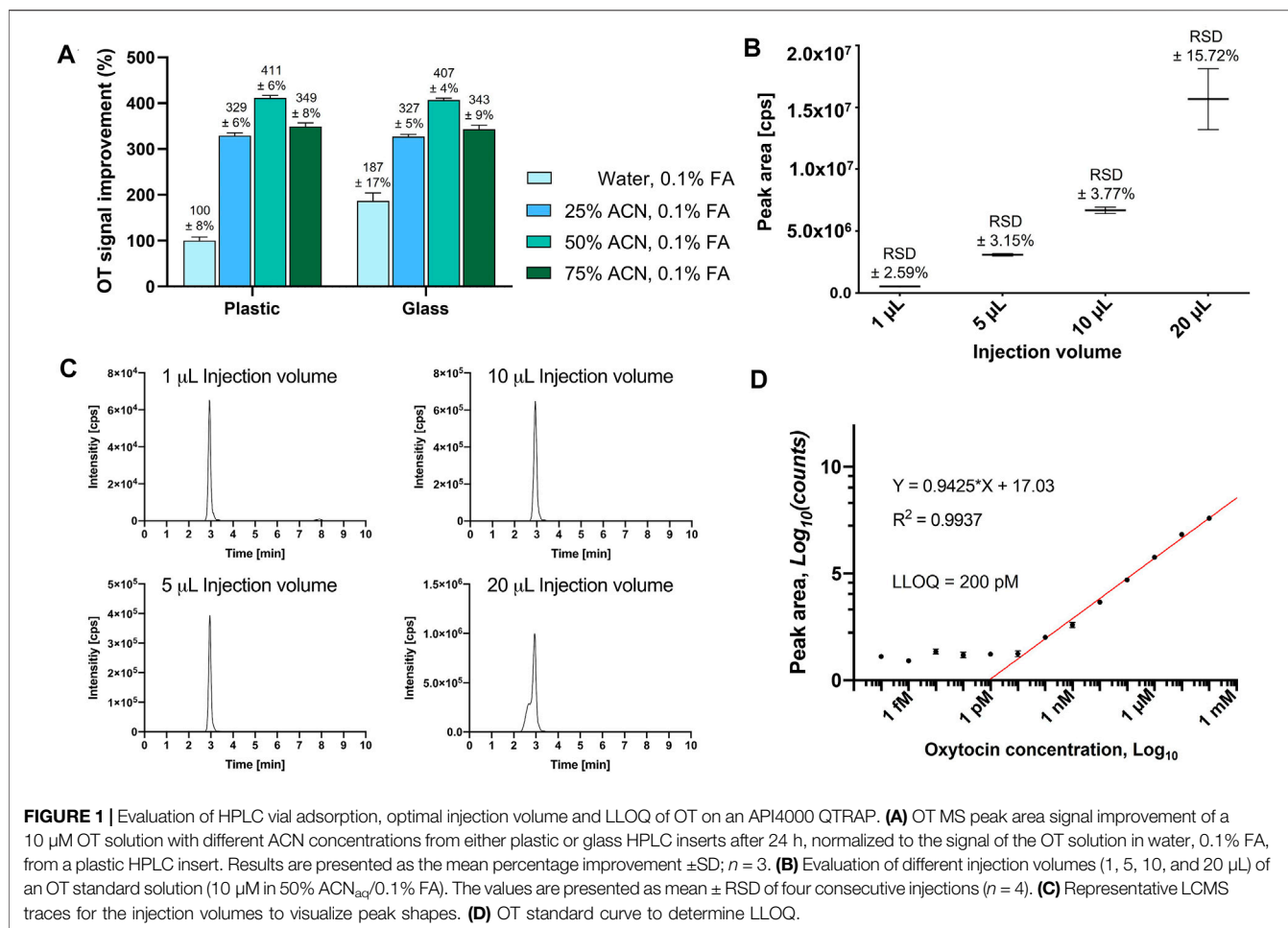
RESULTS

Method Development

OT was synthesized by manual Fmoc solid phase peptide synthesis (Kremsmayr and Muttenthaler, 2022). The exact concentration and purity of the peptide was determined *via* RP-HPLC (**Supplementary Table S1**) and compared against two peptide standards of known concentration.

Analyte Adsorption to HPLC Inserts

Adsorption of the analyte to sample preparation materials (e.g., HPLC inserts) can result in inconsistent and inaccurate measurements (Goebel-Stengel et al., 2011). Addition of organic solvent (e.g., ACN) can prevent this adsorption and improve ionization during MS analysis (Sterner et al., 2000; Gosetti et al., 2010). We therefore prepared OT standards (10 μ M) with different ACN concentrations (H₂O, 25, 50, 75% ACN) and analyzed them in plastic polypropylene or silanized glass HPLC inserts in three independent experiments every hour for 24 h. An API4000 QTRAP MS instrument tuned to OT and equipped with an Agilent C₁₈ column was used for this study (**Supplementary Table S2**). The OT MS signal (peak area) was twice as large in glass inserts than in plastic inserts (10 μ M OT in H₂O/0.1% formic acid, FA) (**Figure 1A**). The use of ACN as the organic co-solvent enhanced the MS signal for OT 3–4-fold in both plastic and glass inserts, with no significant differences



between plastic and glass inserts. The best signal was obtained in 50% ACN_{aq}/0.1% FA, which was selected for the rest of the study.

Injection Volume

We evaluated 1, 5, 10, and 20 μL injection volumes of a standard OT solution (10 μM , 50% ACN_{aq}/0.1% FA) by LC-MS/MS (Figure 1B). Injection volumes of 1–10 μL had sharp peaks, high signal-to-noise ratio, and low variability (relative standard deviation (RSD) \pm 2.59–3.77%), while injection volumes of 20 μL displayed broader peaks with a shoulder and higher variability (RSD \pm 15.72%) (Figure 1C). A 10 μL injection volume was therefore used for the rest of this study.

Standard Curve and Lower Limit of Quantitation

The linear range was determined by the maximum number of points that could be included for the R^2 coefficient to remain ≥ 0.9 . LLOQ was determined by visual evaluation of the calibration curve (smallest value on the linear range, before the plateau) and should be at least ≥ 5 of the blank signal (Supplementary Figure S2) (Shrivastava and Gupta, 2011). A dilution series of OT ranging from 0.1 mM to 0.1 fM in 50% ACN_{aq}/0.1% FA was prepared and analyzed on an API4000 QTRAP (Figure 1D). The calibration curve displayed a plateau

from 0.1 fM to 100 pM OT and formed a linear range from 1 nM to 0.1 mM ($R^2 = 0.9971$). 200 pM was the lowest value lying on the linear range before the plateau and thus determined as the LLOQ of OT.

Sample Preparation Methods and Parameters

Sample preparation is a critical step to reduce sample matrix interferences that affect the accuracy, precision and robustness of MS analysis (Panuwet et al., 2016). Six different sample preparation protocols (Table 1) were designed and evaluated regarding the matrix effect (MX), peptide recovery (RE), and overall method efficiency (ME) *via* the pre- and post-spike method (Matuszewski et al., 2003) by spiking serum at three OT concentrations (0.1, 10, and 50 μM) to give a final OT concentration of 4.5 μM , 0.91 μM and 9.09 nM. Briefly, the pre- and post-spike method involves (A) spiking a blank solution (50% ACN_{aq}/0.1% FA) with an OT standard, (B) spiking a serum sample with OT before sample preparation, and (C) spiking a serum sample with OT after sample preparation. Samples were injected (10 μL) into the API4000 QTRAP and peak areas were analyzed. The calculation of the RE, MX, and ME values and the overview of the sample preparation are described in Figure 2.

TABLE 1 | Overview of tested sample preparation protocols for OT analysis in human serum. Modified protocol parameters are bolded. RE values >115% were set to 0 for ME calculations. Results for protocols are presented qualitatively as a heat map with green, yellow and red representing good, average and poor values respectively. Exact values with errors and cut-off ranges can be found in **Supplementary Table S3**.

Protocol 1		Protocol 2	Protocol 3
Cartridge activation 3 mL MeOH for Sep-Pak (50 mg) or Oasis HLB (60 mg)			
Cartridge equilibration 3 mL 0.1% TFA		10 mL 1% TFA	10 mL 4% H ₃ PO ₄
Cartridge sample loading 200 µL 0.1% TFA		200 µL 0.1% TFA	400 µL 4% H ₃ PO ₄
Washes 1x 3 mL 0.1% TFA 1x 3 mL 5% MeOH		1x 3 mL 1% TFA 1x 3 mL 5% MeOH	1x 3 mL 4% H ₃ PO ₄ 1x 3 mL 5% MeOH
Elution and sample concentration 1x 2 mL 50% ACN, 0.1% FA; Speed-Vacuum			
Reconstitution 200 µL 50% ACN, 0.1% FA			
Spiked OT concentration range 10 nM – 50 µM			
Results (Sep-Pak)	RE [%]:	248 – 520	188 – 223
	MX [%]:	-94 – -85	-85 – -41
	ME [%]:	0	0
Results (Oasis HLB)	RE [%]:	94 – 138	120 – 884
	MX [%]:	-94 – -8	-91 – -17
	ME [%]:	0	0
Protocol 4		Protocol 5	Protocol 6
Protein precipitation 400 µL sat. NH ₄ SO ₄		200 µL ice-cold ACN	200 µL ice-cold ACN
Centrifugation 30 min, 17,000 g, 4°C			
Impurity extraction –		–	1 mL Et ₂ O
Cartridge activation 3 mL MeOH, Oasis HLB (60 mg)			
Cartridge equilibration		10 mL 4% H ₃ PO ₄	
Cartridge sample loading		2 mL 4% H ₃ PO ₄	
Washes		1x 3 mL 4% H ₃ PO ₄ 1x 3 mL 5% MeOH	
Elution and sample concentration 1x 2 mL 50% ACN, 0.1% FA; Speed-Vacuum			
Reconstitution 200 µL 50% ACN, 0.1% FA			
Spiked OT concentration range 10 nM – 50 µM			
Results (Oasis HLB)	RE [%]:	39 – 110	87 – 102
	MX [%]:	-29 – +1	+6 – +10
	ME [%]:	39 – 94	80 – 95

With Protocols 1, 2, and 3, we evaluated two acids commonly used for solid phase extraction, namely TFA (trifluoroacetic acid, 0.1 and 1%) and H₃PO₄ (phosphoric acid, 4%). We evaluated these protocols on two solid phase extraction cartridges, the Sep-Pak (50 mg) and Oasis Hydrophilic-Lipophilic-Balanced (HLB, 60 mg) cartridges (Table 1). A continuous pressure increase on the LC-MS/MS (API4000 QTRAP) was observed during analysis of samples prepared with Sep-Pak cartridges, indicating incomplete sample clean-up and a consequent accumulation of impurities on the HPLC column. Oasis HLB cartridges were therefore selected for the sample preparation step. Of the three protocols tested on Oasis HLB cartridges, Protocol 3 was selected for further method development since the MX values were the most consistent across the measured OT concentrations (Supplementary Table S3).

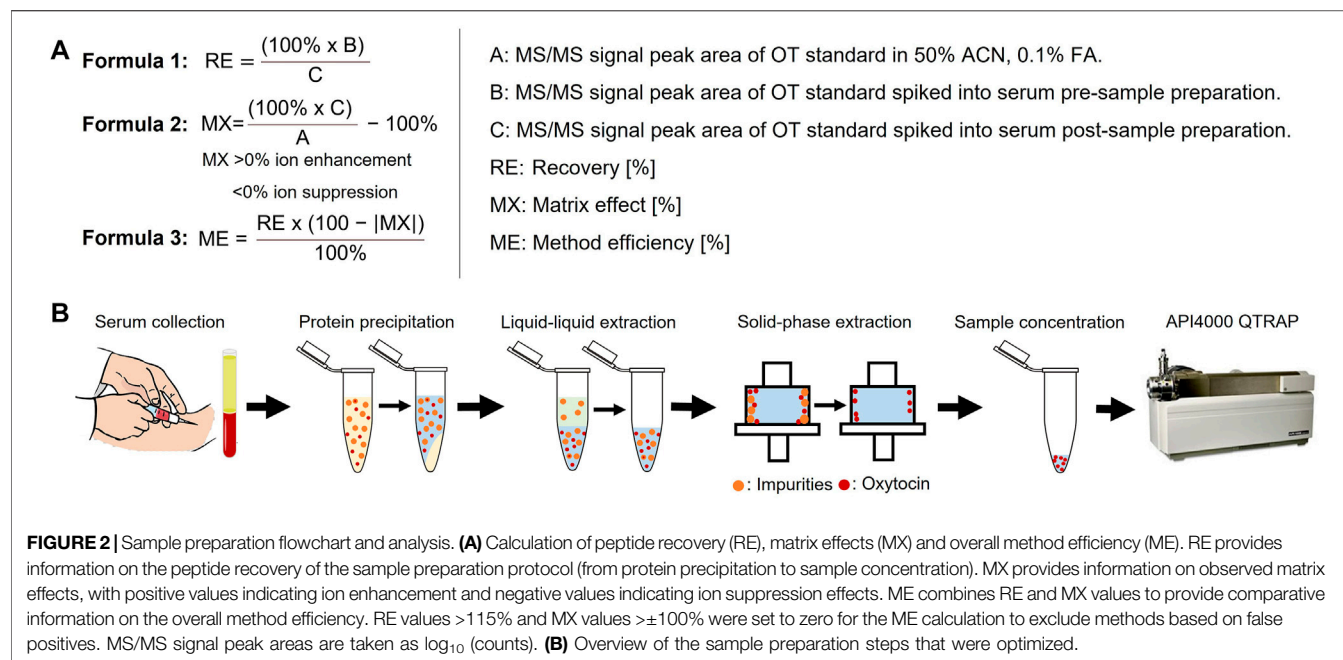
To improve sample clean-up and reduce matrix effects, an additional sample clean-up step prior to solid phase extraction was introduced. A saturated NH₄SO₄ solution (Protocol 4) or ice-cold ACN (Protocol 5 and 6) were used to precipitate larger serum proteins, leaving OT in the supernatant (Protocol 4: 1.25 μ M–2.5 nM OT in 400 μ L NH₄SO₄ solution; Protocol 5 & 6: 2.5 μ M–5 nM OT in 200 μ L ACN). The precipitated impurities were centrifuged into a pellet and removed. An additional liquid-liquid extraction step was introduced in Protocol 6 to further

remove hydrophobic compounds. In this step, ice-cold diethyl ether (Et₂O) was mixed with the supernatant after centrifugation, extracting hydrophobic molecules into the ether phase, leaving OT in the aqueous phase.

Protein precipitation with saturated NH₄SO₄ (Protocol 4) resulted in low OT recovery (3–47%), possibly due to co-precipitation of OT and serum proteins. Precipitation with cold ACN (Protocol 5) or cold ACN combined with Et₂O liquid-liquid extraction (Protocol 6) worked well with OT recoveries in the 39–110% and 87–102% range, respectively. Particularly the ACN precipitation with Et₂O liquid-liquid extraction resulted in substantial reduction of matrix effects across all concentration tested (MX <±12%). The resulting ME for Protocols 4, 5 and 6 were 3–31%, 39–94%, and 82–95% across the tested concentrations, and Protocol 6 was therefore selected for further characterization.

Evaluation of Reconstitution Volume of Sample Preparation Protocol

Decreasing the reconstitution volume increases the analyte's concentration and thereby its detection limits, but this can also lead to more pronounced matrix effects. To determine the RE, MX, and ME of different reconstitution volumes, serum samples were spiked with 50 μ M OT *via* the pre- and post-spike method and



prepared using Protocol 6. Samples were reconstituted in four different volumes (40, 60, 80, and 100 µL; 50% ACN_{aq}/0.1% FA) and evaluated compared to the initial reconstitution volume of 200 µL. Changing the reconstitution volume also affects the analyte's concentration, thus altering the LLOQ of the method. Hence, human serum samples were spiked with OT standards (0.1 pM–1 mM), prepared using Protocol 6, and reconstituted in 40, 60, 80 or 100 µL; 50% ACN_{aq}/0.1% FA). Samples were analyzed in the API4000 QTRAP and a standard curve was determined for each reconstitution volume. While reconstitution volumes of both 60 and 200 µL had good RE, MX, and ME results, a 60 µL reconstitution volume yielded a ~2-fold improvement in LLOQ as compared to the initially used 200 µL (**Supplementary Table S4**). 60 µL reconstitution volume was thus chosen for the final protocol (Protocol 6'). RE, MX, and ME of the final Protocol 6' was determined *via* the pre- and post-spike method with three OT concentrations (50, 10 and 0.1 µM). This gave a MX of -16--10%, 81–87% RE, 71–77% ME and a LLOQ of 86 ± 17 nM in human serum (**Supplementary Figure S3**, **Supplementary Table S5**). Protocol 6' was used for further method validation.

Method Validation: Precision and Accuracy

To determine precision and accuracy of the method, human serum was spiked with OT standard to give final serum OT concentrations of 1.5, 10 and 40 µM. The spiked human serum samples were purified with Protocol 6' and analyzed. The LCMS peak areas of these samples were compared against the OT standard curve to calculate the expected concentration present in serum ($n = 5$). Precision is expressed as a percentage of standard deviation from the mean value and accuracy as percentage error from the theoretical concentration. The intraday precision for the quantitation of OT in human serum was 6.4–7.6% and the intraday accuracy was -7.0–15.7% (**Supplementary Table S6**). The method therefore fulfills largely the FDA acceptance criteria for precision (±15%)

and accuracy (±15%) for bioanalytical method validation (except for one intraday accuracy measurement of 15.7%) (Administration, U.F.A.D., 2018).

Improving Sensitivity

To increase the sensitivity of our analytical method, we investigated different MS instruments and strategies to improve OT's ionization efficiency.

Protocol Evaluation Across Other Mass Spectrometry Instruments

A dilution series of OT (1 fM to 0.1 mM in 50% ACN_{aq}/0.1% FA) was analyzed across four quadrupole time-of-flight (QTOF) mass spectrometers (TripleTOF 6600, TripleTOF 5600, ×500R, QstarElite) and two triple quadrupole instruments (API4000 QTRAP, QTRAP6500) (**Supplementary Figure S4**). The sensitivity of each instrument was determined using the LLOQ of OT (50% ACN_{aq}/0.1% FA). The triple quadrupole mass spectrometers, API4000 QTRAP (LLOQ: 100 ± 12 pM) and QTRAP6500 (LLOQ: 40 ± 3 pM) had greater sensitivity for OT compared to the TOF instruments. The superior sensitivity of triple quadrupoles over QTOF instruments was expected due to their additional quadrupole, allowing them to be tuned to a specific potential for detection of one specific ion. However, it also highlighted that further improvement is necessary before being able to quantitatively measure OT out of complex biological samples. We continued with the method development on the API4000 QTRAP due to limited access to the QTRAP6500.

Improving the Analyte's Ionization Efficiency Through Derivatization

MS analyte detection sensitivity in ESI-MS can also be enhanced by improving the ionization efficiency of the analyte through modifications of its hydrophobicity and/or charge state

TABLE 2 | LLOQ values of OT analogues in 50% ACN_{aq}/0.1% FA. A dilution series of each peptide ranging from 1 fM to 1 mM in 50% ACN_{aq}/0.1% FA was measured (*n* = 3) on the API4000 QTRAP. LLOQ was determined by visual examination of the calibration curve and ensuring the signal was $\geq 5\times$ the blank. LLOQ values < 20 pM (more sensitive than OT) are highlighted in green, >200 pM in red, values between 20 and 200 pM in grey and the four sequences with the lowest LLOQ values in a darker shade of green. **(i)** 4-bromo-N,N,N-triethylbutan-1-ammonium, **(ii)** 3-(4-bromobutyl)-1-butyl-1H-imidazol-3-ium, **(iii)** iodoacetamide, **(iv)** 1-(4-bromobutyl)-4-methylpyridin-1-ium, * indicates C-terminal amide.

ID	Sequence	Charge	Linear/Reduced	Folded/Oxidized
			LLOQ (pM)	LLOQ (pM)
1	CYIQNCPLG*	0	2100 \pm 120	200 \pm 3
2	WCYIQNCPLG*	0	209 \pm 90	11 \pm 3
3	RCYIQNCPLG*	+1	29 \pm 15	13 \pm 1
4	FCYIQNCPLG*	0	61 \pm 10	82 \pm 30
5	KCYIQNCPLG*	+1	325 \pm 110	66 \pm 20
6	RWCYIQNCPLG*	+1	33 \pm 12	11 \pm 2
7	RKCYIQNCPLG*	+2	1000 \pm 360	12 \pm 0.3
8	RFCYIQNCPLG*	+1	236 \pm 30	11 \pm 3
9	WFCYIQNCPLG*	0	156 \pm 20	9 \pm 2
10	KFCYIQNCPLG*	+1	89 \pm 30	12 \pm 1
11	RWKCYIQNCPLG*	+2	676 \pm 290	12 \pm 2
12	RWFCYIQNCPLG*	+1	60 \pm 20	5 \pm 1.6
13	WFKCYIQNCPLG*	+1	516 \pm 63	17 \pm 4
14	RWKFCYIQNCPLG*	+2	20974 \pm 4900	6 \pm 2
15	WKCYIQNCPLG*	+1	54 \pm 6.7	68 \pm 10
16	RFKCYIQNCPLG*	+2	118 \pm 10	6 \pm 4.3
17	C(i)YIQNC(i)PLG*	+2	583 \pm 230	
18	C(ii)YIQNC(ii)PLG*	+2	95 \pm 60	
19	C(iii)YIQNC(iii)PLG*	0	12 \pm 2	
20	C(iv)YIQNC(iv)PLG*	+2	5 \pm 0.8	

(Konermann et al., 2013). During ionization in ESI-MS, hydrophobic analytes tend to sit on the outside of the ionization droplet, resulting in easier and more efficient ionization. Analytes with high proton affinity (e.g., Arg-containing peptides) also increase signal intensity in ESI-MS due to formation of pre-charged species.

We investigated two strategies: 1) addition of either charged or hydrophobic amino acids, and 2) addition of positively charged small molecule moieties. The API4000 QTRAP was tuned for the detection of the new peptide analogues and a calibration curve in water was prepared for each (Table 2). Removing the stabilizing disulfide bond on OT might also improve ionization; we therefore assessed the oxidized and reduced form of the new analogues. The hydrophobicity and charge of each analogue, oxidized and reduced, was compared against that of native OT (Table 2).

In the first strategy, Arg, Lys, Trp, and Phe were added in different combinations to the N-terminus of reduced and folded/oxidized OT (Table 2, compounds 1–16). The addition of single amino acids Arg, Lys, Trp and Phe yielded improved sensitivity (LLOQ of 13, 66, 11, and 82 pM respectively) compared to unmodified OT (200 pM); oxidized analogues generally yielded better sensitivity (Figure 3C). In particular, the Arg analogue (R-OT 3, 13 pM) and Trp analogue (W-OT 2, 11 pM) improved LLOQ in ESI-MS by 13–15-fold.

Addition of two amino acids to OT allowed the study of combinations of charged (Arg and Lys) and hydrophobic (Trp and Phe) amino acids. The addition of two charged or two hydrophobic residues did however not necessarily result in lower LLOQs than OT derivatives with a single residue

addition. For example, WK-OT 15 (68 pM) had a relatively high LLOQ, and RK-OT 7 (12 pM) had a LLOQ similar to W-OT 2 (11 pM) and R-OT 3 (13 pM). In line with the results of the single residue derivatives, the combination of a charged amino acid (Arg/Lys) with a hydrophobic (Trp/Phe) improved the LLOQ in oxidized analogues but less so in reduced analogues. Overall, the addition of two amino acids improved the LLOQ by 13–16-fold for the oxidized analogues, with WF-OT 9 (9 pM) having the best sensitivity. These improvements were similar to the improvements of single amino acid derivatives, i.e., R-OT 3 (13 pM) and W-OT 2 (11 pM).

The addition of three amino acids allowed us to combine a charged residue with two hydrophobic residues and vice versa. The trend of the oxidized forms having better sensitivity than their reduced counterparts continued with these derivatives. Two of the best performing analogues, were RWF-OT 12 (5 pM) and RFK-OT 16 (6 pM). The addition of all four amino acids, RWKF-OT 14 (6 pM), resulted in a more hydrophobic peptide than native OT 1 (100 pM). From all analogues tested, the modifications RWF-OT 12 (5 pM), RFK-OT 16 (6 pM) and RWKF-OT 14 (6 pM) had the biggest impact on sensitivity, resulting in 20–25-fold improvement compared to the LLOQ of OT. Also, R-OT 3 (13 pM) and W-OT 2 (11 pM) should be mentioned since they are in a similar LLOQ range through the N-terminal addition of just a single amino acid.

For the second strategy, three small molecules, 2-bromo-N, N, N-triethylethan-1-ammonium (quaternary ammonium ion), 3-(4-bromobutyl)-1-butyl-1H-imidazol-3-ium (imidazolium ion) and 1-

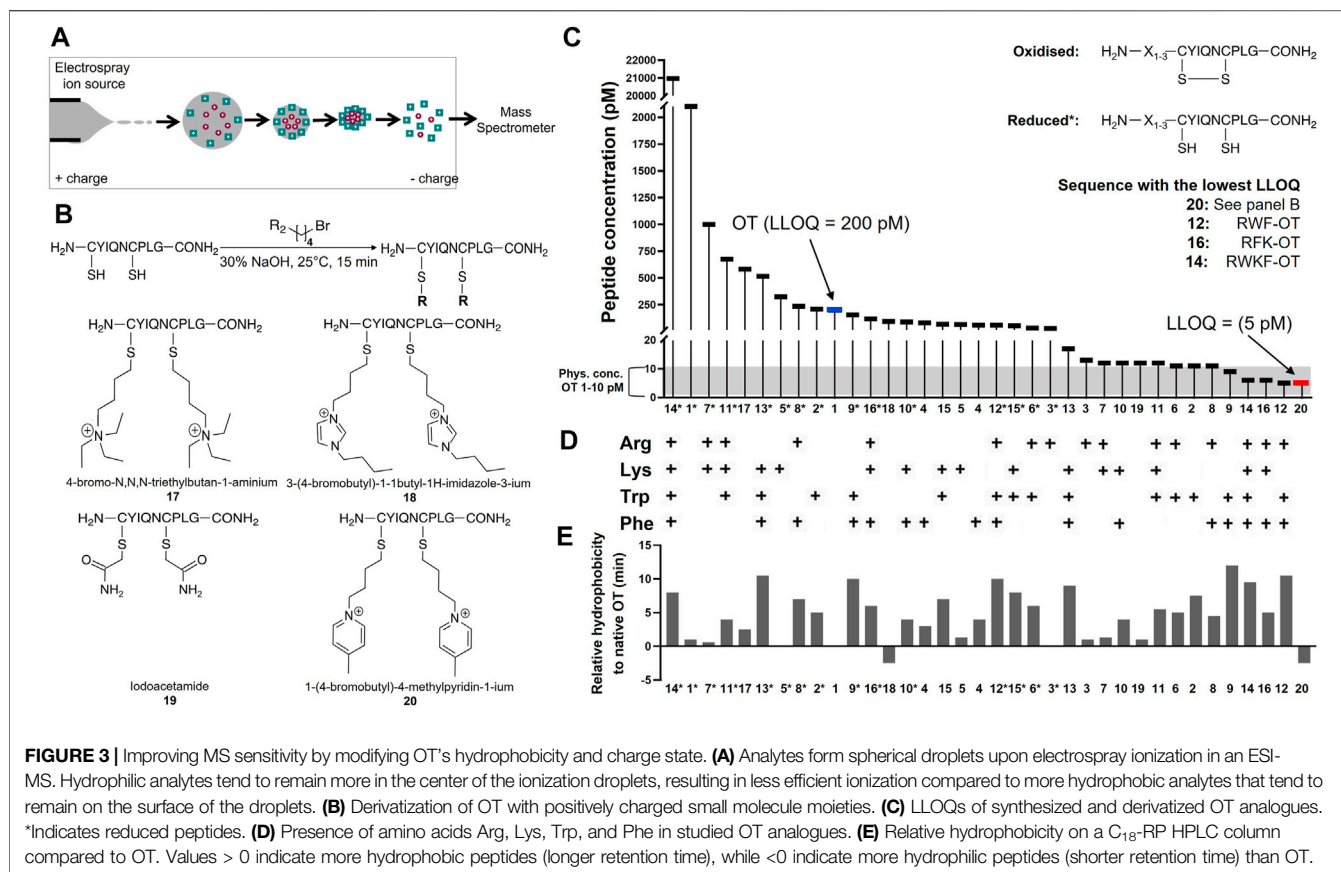


FIGURE 3 | Improving MS sensitivity by modifying OT's hydrophobicity and charge state. **(A)** Analytes form spherical droplets upon electrospray ionization in an ESI-MS. Hydrophilic analytes tend to remain more in the center of the ionization droplets, resulting in less efficient ionization compared to more hydrophobic analytes that tend to remain on the surface of the droplets. **(B)** Derivatization of OT with positively charged small molecule moieties. **(C)** LLOQs of synthesized and derivatized OT analogues. *Indicates reduced peptides. **(D)** Presence of amino acids Arg, Lys, Trp, and Phe in studied OT analogues. **(E)** Relative hydrophobicity on a C₁₈-RP HPLC column compared to OT. Values > 0 indicate more hydrophobic peptides (longer retention time), while < 0 indicate more hydrophilic peptides (shorter retention time) than OT.

(4-bromobutyl)-4-methylpyridin-1-ium (pyridinium ion) were synthesized (**Figure 3B**) and used to derivatize the free Cys thiol groups of reduced OT (**Figure 3B**; **ID 17–20**). Iodoacetamide was also added to the free Cys thiol of reduced OT as another analogue. The LLOQ for the resulting OT analogues alkylated by (i) 4-bromo-N, N, N-triethylbutan-1-aminium, (ii) 3-(4-bromobutyl)-1-butyl-1H-imidazol-3-ium, (iii) iodoacetamide and (iv) 1-(4-bromobutyl)-4-methylpyridin-1-ium were 583, 95, 12 and 5 pM respectively. The LLOQ of [1-(4-bromobutyl)-4-methylpyridin-1-ium]₂-OT (**20**) was 25-fold lower than the LLOQ of OT and was also the lowest LLOQ of all modified peptides. It was thus chosen for further evaluation in human serum.

To determine the LLOQ of [1-(4-bromobutyl)-4-methylpyridin-1-ium]₂-OT **20** in human serum, a dilution series of peptide **20** was prepared in 50% ACN_{aq}/0.1% FA ranging from 1 mM–1 fM. Sample preparation was performed according to Protocol 6' and samples were analyzed on the API4000 QTRAP. The LLOQ was determined by spiking 100 μL human serum samples with 10 μL peptide **20** standards (1 mM–1 fM). This yielded an LLOQ of 2 nM, representing a 43-fold improvement compared to human serum samples spiked with OT (LLOQ 86 nM).

DISCUSSION

A MS method that can reliably monitor endogenous peptide hormone levels in human blood would enable a wide range of

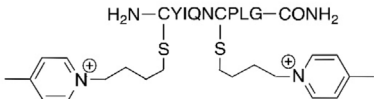
studies including fundamental (patho) physiological state studies as well as biomarker studies for clinical trials measuring treatment response or identifying patients with abnormal endogenous peptide levels. In the process of developing such a method, we focused on OT as it is one of the most studied neuropeptide/peptide hormone (including hundreds of clinical trials) due to its high relevance in social behavior and reproductive functions and its involvement in disorders such as autisms spectrum disorders, schizophrenia, anxiety and depression (Feifel et al., 2010; Alvares et al., 2017; Ooi et al., 2017). MS has the advantage that it identifies and quantifies analytes by their mass, therefore removing the possibility of detecting metabolites or similar recognition motifs, as it is often the case with immunoassays (McCullough et al., 2013). However, measuring low peptide concentrations in biological samples by MS remains challenging, with several contradicting results regarding the endogenous concentration of OT in blood (Zhang et al., 2011; Brandtzaeg et al., 2016), likely due to uncharacterized matrix effects.

In this work, we highlight the importance of sample preparation for OT analysis and investigated several strategies to improve the quantitation of OT in human serum by MS. This resulted in a robust sample preparation protocol and the introduction of novel derivatization strategies to improve the ionization efficiency of the analyte and thereby the LLOQ towards physiological levels of OT.

Our optimized sample preparation Protocol 6' (**Table 3**) displayed good peptide recovery (81–87%), low matrix effects (±16%) and

TABLE 3 | Optimized sample preparation Protocol 6'. RE, MX, and ME for optimized Protocol 6' were evaluated in human serum via the pre- and post-spike method (50 μ M, 10 μ M, 0.1 μ M). Precision and accuracy were determined by spiking samples with 40, 10 and 1.5 μ M OT. The OT analogue derivatized with 1-(4-bromobutyl)-4-methylpyridin-1-ium had the lowest LLOQ when evaluated in human serum.

	Protocol 6'
Protein precipitation	200 μ L ice-cold ACN
Centrifugation	30 min, 17,000 g, 4°C
Liquid-liquid extraction	1 mL Et ₂ O
Cartridge	Oasis HLB (60 mg)
Cartridge activation	3 mL MeOH
Cartridge equilibration	10 mL 4% H ₃ PO ₄
Cartridge sample loading	2 mL 4% H ₃ PO ₄
Washes	1x 3 mL 4% H ₃ PO ₄ 1x 3 mL 5% MeOH
Sample elution	1 x 2 mL 50% ACN _{aq} /0.1% FA
Sample concentration	Speed-Vacuum
Sample reconstitution	60 μ L 50% ACN _{aq} /0.1% FA
Recovery (RE)	81 – 87%
Matrix effects (MX)	-16 – -10%
Method efficiency (ME)	71 – 77%
Precision	6.4 – 7.6%
Accuracy	-7.0 – 15.7%

OT derivatization strategy	
LLOQ (OT, human serum)	86 nM
LLOQ (OT analogue, human serum)	2 nM

excellent overall method efficiency (71–77%) in human serum OT quantitation using the pre- and post-spike method (50, 10 and 0.1 μ M). Method precision (6.4–7.6%) and accuracy (–7.0–15.7%) were within or close to FDA guidelines ($\pm 15\%$). The optimized sample preparation includes an organic solvent (ice-cold ACN) protein precipitation step, followed by a liquid-liquid extraction with Et₂O step and solid-phase extraction on an Oasis HLB column (60 mg), before injection into an ESI-MS instrument. The advantage of this protocol lies in its simplicity and ability to provide consistent results over the observed OT concentration range (pM– μ M). The protocol was developed on a common MS instrument (API4000 QTRAP) available in many laboratories, and the LLOQ can be pushed further with more sensitive instruments (**Supplementary Figure S4**), indicating that it is just a matter of time until we will have reached the threshold of reliable quantifying endogenous OT and other peptide hormone levels in blood or other biological samples (e.g., urine, cerebrospinal fluid).

Since the optimized sample preparation method per se was not able to provide a low enough LLOQ for the quantitation of endogenous OT in human serum, we explored an OT derivatization strategy that resulted in another ~40-fold improvement of the LLOQ from 86 to 2 nM in human serum. The derivatization strategies are based on the hypothesis that sensitivity is affected by the analyte's ionization efficiency, which is directly linked to its physicochemical properties such as charge and hydrophobicity (Wahl et al., 1993; Page et al., 2007). However, no direct correlation between sensitivity and retention time nor overall charge was observed. However, there was a clear trend between oxidized vs. reduced OT analogues,

with oxidized analogues yielding better sensitivity. A likely explanation for this is that the thiol groups of the reduced peptide interact with water molecules through hydrogen bonding leading to the formation of a hydration shell around the peptide. Higher energy is then needed to evaporate the solvent and hydration shell, resulting in poorer ionization and sensitivity.

Given the trajectory of technological development in the MS space, we will continue to see substantial advances pushing the limits of sensitivity and quantitation, as already seen with the more sensitive QTRAP6500. The ability to detect specific masses by MS provides a clear advantage over the commonly used immunoassays that are often prone to specificity issues and false positives. Additionally, MS has a huge potential for further advancements, making it the technique of choice for future bioanalytical studies.

In conclusion, we have achieved the development of an optimized sample preparation protocol and introduced and evaluated new and promising derivatization strategies to improve the sensitivity of detecting OT in biological samples. This provides a solid foundation for a standardized and accessible MS method to quantitate OT levels in biological samples, valuable for OT biomarker studies supporting fundamental research, patient blood screens, treatment monitoring and clinical trials.

DATA AVAILABILITY STATEMENT

The original contributions presented in the study are included in the article/**Supplementary Material**, further inquiries can be directed to the corresponding author.

AUTHOR CONTRIBUTIONS

AH designed and synthesized OT and OT analogues. AH and BJ designed and performed the experiments. AJ advised on experiment design. MM conceived and supervised the project. The manuscript was drafted by BJ and AH. BJ, AJ, and MM reviewed and edited the manuscript. All authors have read and agreed to the published version of the manuscript.

FUNDING

This research was supported by the European Research Council under the European Union's Horizon 2020 research and innovation program (grant agreements no. 714366), by the Austrian Science Fund FWF (TAI 382-B), by Cancer Australia

and Cancer Council Queensland (1146504) and by the Australian Research Council (DP190101667, FT210100266).

ACKNOWLEDGMENTS

We thank Aaron Poth for his advice on the pre- and post-spike methods, instrument tuning and standard curve design.

SUPPLEMENTARY MATERIAL

The Supplementary Material for this article can be found online at: <https://www.frontiersin.org/articles/10.3389/fchem.2022.889154/full#supplementary-material>

REFERENCES

- Administration, U.F.A.D. (2018). *Bioanalytical Method Validation Guidance for Industry*. Rockville, MD: Food and Drug Administration.
- Alvares, G. A., Quintana, D. S., and Whitehouse, A. J. O. (2017). Beyond the Hype and Hope: Critical Considerations for Intranasal Oxytocin Research in Autism Spectrum Disorder. *Autism Res.* 10, 25–41. doi:10.1002/aur.1692
- Ariana, M., Pornour, M., Mehr, S. S., Vaseghi, H., Ganji, S. M., Alivand, M. R., et al. (2018). Preventive Effects of Oxytocin and Oxytocin Receptor in Breast Cancer Pathogenesis. *Per Med.* 16, 25–34. doi:10.2217/pme-2018-0009
- Bąchor, R., Mielczarek, P., Rudowska, M., Silberring, J., and Szewczuk, Z. (2014). Sensitive Detection of Charge Derivatized Peptides at the Attomole Level Using Nano-LC-ESI-MRM Analysis. *Int. J. Mass Spectrom.* 362, 32–38. doi:10.1016/j.ijms.2014.02.018
- Bartholomeusz, C. F., Ganella, E. P., Labuschagne, I., Bousman, C., and Pantelis, C. (2015). Effects of Oxytocin and Genetic Variants on Brain and Behaviour: Implications for Treatment in Schizophrenia. *Schizophrenia Res.* 168, 614–627. doi:10.1016/j.schres.2015.06.007
- Bell, C. J., Nicholson, H., Mulder, R. T., Luty, S. E., and Joyce, P. R. (2006). Plasma Oxytocin Levels in Depression and Their Correlation with the Temperament Dimension of Reward Dependence. *J. Psychopharmacol.* 20, 656–660. doi:10.1177/02698881106060512
- Bradley, E. R., and Woolley, J. D. (2017). Oxytocin Effects in Schizophrenia: Reconciling Mixed Findings and Moving Forward. *Neurosci. Biobehav. Rev.* 80, 36–56. doi:10.1016/j.neubiorev.2017.05.007
- Brandtzaeg, O. K., Johnsen, E., Roberg-Larsen, H., Seip, K. F., Maclean, E. L., Gesquiere, L. R., et al. (2016). Proteomics Tools Reveal Startlingly High Amounts of Oxytocin in Plasma and Serum. *Sci. Rep.* 6, 31693. doi:10.1038/srep31693
- Christensen, J. C., Shiyanov, P. A., Estep, J. R., and Schlager, J. J. (2014). Lack of Association between Human Plasma Oxytocin and Interpersonal Trust in a Prisoner's Dilemma Paradigm. *PLoS One* 9, e116172. doi:10.1371/journal.pone.0116172
- Cyranowski, J. M., Hofkens, T. L., Frank, E., Seltman, H., Cai, H.-M., and Amico, J. A. (2008). Evidence of Dysregulated Peripheral Oxytocin Release Among Depressed Women. *Psychosom. Med.* 70, 967–975. doi:10.1097/psy.0b013e318188ade4
- Dams, R., Huestis, M. A., Lambert, W. E., and Murphy, C. M. (2003). Matrix Effect in Bio-Analysis of Illicit Drugs with LC-MS/MS: Influence of Ionization Type, Sample Preparation, and Biofluid. *J. Am. Soc. Mass Spectrom.* 14, 1290–1294. doi:10.1016/s1044-0305(03)00574-9
- Erickson, E. N., Carter, C. S., and Emeis, C. L. (2020). Oxytocin, Vasopressin and Prolactin in New Breastfeeding Mothers: Relationship to Clinical Characteristics and Infant Weight Loss. *J. Hum. Lact.* 36, 136–145. doi:10.1177/0890334419838225
- Feifel, D., Macdonald, K., Nguyen, A., Cobb, P., Warlan, H., Galangue, B., et al. (2010). Adjunctive Intranasal Oxytocin Reduces Symptoms in Schizophrenia Patients. *Biol. Psychiatry* 68, 678–680. doi:10.1016/j.biopsych.2010.04.039
- Feifel, D., Shilling, P. D., and Macdonald, K. (2016). A Review of Oxytocin's Effects on the Positive, Negative, and Cognitive Domains of Schizophrenia. *Biol. Psychiatry* 79, 222–233. doi:10.1016/j.biopsych.2015.07.025
- Franke, A. A., Li, X., Menden, A., Lee, M. R., and Lai, J. F. (2019). Oxytocin Analysis from Human Serum, Urine, and Saliva by Orbitrap Liquid Chromatography-Mass Spectrometry. *Drug Test. Anal.* 11, 119–128. doi:10.1002/dta.2475
- Garrido-Urbani, S., Deblon, N., Poher, A. L., Caillon, A., Ropraz, P., Rohner-Jeanraud, F., et al. (2018). Inhibitory Role of Oxytocin on TNF α Expression Assessed *In Vitro* and *In Vivo*. *Diabetes & Metabolism* 44, 292–295. doi:10.1016/j.diabet.2017.10.004
- Gimpl, G., and Fahrenholz, F. (2001). The Oxytocin Receptor System: Structure, Function, and Regulation. *Physiol. Rev.* 81, 629–683. doi:10.1152/physrev.2001.81.2.629
- Glovinsky, D., Kalogeras, K., Kirch, D., Suddath, R., and Wyatt, R. (1994). Cerebrospinal Fluid Oxytocin Concentration in Schizophrenic Patients Does Not Differ from Control Subjects and Is Not Changed by Neuroleptic Medication. *Schizophrenia Res.* 11, 273–276. doi:10.1016/0920-9964(94)90021-3
- Goebel-Stengel, M., Stengel, A., Taché, Y., and Reeve, J. R., JR. (2011). The Importance of Using the Optimal Plasticware and Glassware in Studies Involving Peptides. *Anal. Biochem.* 414, 38–46. doi:10.1016/j.ab.2011.02.009
- Goldman, M., Marlow-O'Connor, M., Torres, I., and Carter, C. S. (2008). Diminished Plasma Oxytocin in Schizophrenic Patients with Neuroendocrine Dysfunction and Emotional Deficits. *Schizophrenia Res.* 98, 247–255. doi:10.1016/j.schres.2007.09.019
- Gosetti, F., Mazzucco, E., Zampieri, D., and Gennaro, M. C. (2010). Signal Suppression/enhancement in High-Performance Liquid Chromatography Tandem Mass Spectrometry. *J. Chromatogr. A* 1217, 3929–3937. doi:10.1016/j.chroma.2009.11.060
- Green, L., Fein, D., Modahl, C., Feinstein, C., Waterhouse, L., and Morris, M. (2001). Oxytocin and Autistic Disorder: Alterations in Peptide Forms. *Biol. Psychiatry* 50, 609–613. doi:10.1016/s0006-3223(01)01139-8
- Guastella, A. J., Einfeld, S. L., Gray, K. M., Rinehart, N. J., Tonge, B. J., Lambert, T. J., et al. (2010). Intranasal Oxytocin Improves Emotion Recognition for Youth with Autism Spectrum Disorders. *Biol. Psychiatry* 67, 692–694. doi:10.1016/j.biopsych.2009.09.020
- Heinrichs, M., Von Dawans, B., and Domes, G. (2009). Oxytocin, Vasopressin, and Human Social Behavior. *Front. Neuroendocrinol.* 30, 548–557. doi:10.1016/j.yfrne.2009.05.005
- Hib, J. (1977). The 'In Vivo' Effects of Oxytocin and Vasopressin on Spontaneous Contractility of the Rat Epididymis. *Int. J. Fertil.* 22, 63–64.
- Hib, J. (1974a). The Contractility of the Cauda Epididymidis of the Mouse, its Spontaneous Activity *In Vitro* and the Effects of Oxytocin. *Reproduction* 36, 191–193. doi:10.1530/jrf.0.0360191
- Hib, J. (1974b). The *In Vitro* Effects of Oxytocin and Vasopressin on Spontaneous Contractility of the Mouse Cauda Epididymidis. *Biol. Reprod.* 11, 436–439. doi:10.1095/biolreprod11.4.436
- Jansen, L. M. C., Gispén-De Wied, C. C., Wiegant, V. M., Westenberg, H. G. M., Lahuis, B. E., and Van Engeland, H. (2006). Autonomic and

- Neuroendocrine Responses to a Psychosocial Stressor in Adults with Autistic Spectrum Disorder. *J. Autism Dev. Disord.* 36, 891–899. doi:10.1007/s10803-006-0124-z
- Jovanovic, P., Spasojevic, N., Puskas, N., Stefanovic, B., and Dronjak, S. (2019). Oxytocin Modulates the Expression of Norepinephrine Transporter, β_3 -adrenoceptors and Muscarinic M2 Receptors in the Hearts of Socially Isolated Rats. *Peptides* 111, 132–141. doi:10.1016/j.peptides.2018.06.008
- Jurek, B., and Neumann, I. D. (2018). The Oxytocin Receptor: From Intracellular Signaling to Behavior. *Physiol. Rev.* 98, 1805–1908. doi:10.1152/physrev.00031.2017
- Kagerbauer, S. M., Martin, J., Schuster, T., Blobner, M., Kochs, E. F., and Landgraf, R. (2013). Plasma Oxytocin and Vasopressin Do Not Predict Neuropeptide Concentrations in Human Cerebrospinal Fluid. *J. Neuroendocrinol.* 25, 668–673. doi:10.1111/jne.12038
- Kebarle, P., and Tang, L. (1993). From Ions in Solution to Ions in the Gas Phase - the Mechanism of Electrospray Mass Spectrometry. *Anal. Chem.* 65, 972A–986A. doi:10.1021/ac00070a001
- Kéri, S., Kiss, I., and Kelemen, O. (2009). Sharing Secrets: Oxytocin and Trust in Schizophrenia. *Soc. Neurosci.* 4, 287–293. doi:10.1080/17470910802319710
- Khori, V., Alizadeh, A. M., Khalighfar, S., Heidarian, Y., and Khodayari, H. (2018). Oxytocin Effects on the Inhibition of the NF- κ B/miR195 Pathway in Mice Breast Cancer. *Peptides* 107, 54–60. doi:10.1016/j.peptides.2018.07.007
- Konermann, L., Ahadi, E., Rodriguez, A. D., and Vahidi, S. (2013). Unraveling the Mechanism of Electrospray Ionization. *Anal. Chem.* 85, 2–9. doi:10.1021/ac302789c
- Kramer, K. M., Cushing, B. S., Carter, C. S., Wu, J., and Ottinger, M. A. (2004). Sex and Species Differences in Plasma Oxytocin Using an Enzyme Immunoassay. *Can. J. Zool.* 82, 1194–1200. doi:10.1139/z04-098
- Kremsmayr, T., and Muttenthaler, M. (2022). Fmoc Solid Phase Peptide Synthesis of Oxytocin and Analogues. *Methods Mol. Biol.* 2384, 175–199. doi:10.1007/978-1-0716-1759-5_11
- Lefevre, A., Mottotese, R., Dirheimer, M., Mottotese, C., Duhamel, J.-R., and Sirigu, A. (2017). A Comparison of Methods to Measure Central and Peripheral Oxytocin Concentrations in Human and Non-human Primates. *Sci. Rep.* 7, 17222. doi:10.1038/s41598-017-17674-7
- Leng, G., and Sabatier, N. (2016). Measuring Oxytocin and Vasopressin: Bioassays, Immunoassays and Random Numbers. *J. Neuroendocrinol.* 28 (10). doi:10.1111/jne.12413
- Leng, G., Meddle, S., and Douglas, A. (2008). Oxytocin and the Maternal Brain. *Curr. Opin. Pharmacol.* 8, 731–734. doi:10.1016/j.coph.2008.07.001
- Liu, D., Han, X., Liu, X., Cheng, M., He, M., Rainer, G., et al. (2019). Measurement of Ultra-trace Level of Intact Oxytocin in Plasma Using SALLE Combined with Nano-LC-MS. *J. Pharm. Biomed. Analysis* 173, 62–67. doi:10.1016/j.jpba.2019.04.023
- Liu, H., Gruber, C. W., Alewood, P. F., Möller, A., and Muttenthaler, M. (2020). The Oxytocin Receptor Signalling System and Breast Cancer: a Critical Review. *Oncogene* 39, 5917–5932. doi:10.1038/s41388-020-01415-8
- Matuszewski, B. K., Constanzer, M. L., and Chavez-Eng, C. M. (2003). Strategies for the Assessment of Matrix Effect in Quantitative Bioanalytical Methods Based on HPLC–MS/MS. *Anal. Chem.* 75, 3019–3030. doi:10.1021/ac020361s
- McCullough, M. E., Churchland, P. S., and Mendez, A. J. (2013). Problems with Measuring Peripheral Oxytocin: Can the Data on Oxytocin and Human Behavior Be Trusted? *Neurosci. Biobehav. Rev.* 37, 1485–1492. doi:10.1016/j.neubiorev.2013.04.018
- Mcneilly, A. S., Robinson, I. C., Houston, M. J., and Howie, P. W. (1983). Release of Oxytocin and Prolactin in Response to Suckling. *BMJ* 286, 257–259. doi:10.1136/bmj.286.6361.257
- Mei, H., Hsieh, Y., Nardo, C., Xu, X., Wang, S., Ng, K., et al. (2003). Investigation of Matrix Effects in Bioanalytical High-Performance Liquid Chromatography/tandem Mass Spectrometric Assays: Application to Drug Discovery. *Rapid Commun. Mass Spectrom.* 17, 97–103. doi:10.1002/rcm.876
- Merz, T., Denoix, N., Wigger, D., Waller, C., Wepler, M., Vettorazzi, S., et al. (2020). The Role of Glucocorticoid Receptor and Oxytocin Receptor in the Septic Heart in a Clinically Relevant, Resuscitated Porcine Model with Underlying Atherosclerosis. *Front. Endocrinol.* 11, 299. doi:10.3389/fendo.2020.00299
- Meusel, M., Herrmann, M., Machleidt, F., Franzen, K., Vonthein, R., and Sayk, F. (2021). Intranasal Oxytocin Has Sympathoexcitatory Effects on Vascular Tone in Healthy Males. *Am. J. Physiology-Regulatory, Integr. Comp. Physiology* 320, R162–R172. doi:10.1152/ajpregu.00062.2020
- Miller, M., Bales, K. L., Taylor, S. L., Yoon, J., Hostetler, C. M., Carter, C. S., et al. (2013). Oxytocin and Vasopressin in Children and Adolescents with Autism Spectrum Disorders: Sex Differences and Associations with Symptoms. *Autism Res.* 6, 91–102. doi:10.1002/aur.1270
- Nishimori, K., Young, L. J., Guo, Q., Wang, Z., Insel, T. R., and Matzuk, M. M. (1996). Oxytocin Is Required for Nursing but Is Not Essential for Parturition or Reproductive Behavior. *Proc. Natl. Acad. Sci. U.S.A.* 93, 11699–11704. doi:10.1073/pnas.93.21.11699
- Ooi, Y. P., Weng, S. J., Kossowsky, J., Gerger, H., and Sung, M. (2017). Oxytocin and Autism Spectrum Disorders: A Systematic Review and Meta-Analysis of Randomized Controlled Trials. *Pharmacopsychiatry* 50, 5–13. doi:10.1055/s-0042-109400
- Ozsoy, S., Esel, E., and Kula, M. (2009). Serum Oxytocin Levels in Patients with Depression and the Effects of Gender and Antidepressant Treatment. *Psychiatry Res.* 169, 249–252. doi:10.1016/j.psychres.2008.06.034
- Page, J. S., Kelly, R. T., Tang, K., and Smith, R. D. (2007). Ionization and Transmission Efficiency in an Electrospray Ionization-Mass Spectrometry Interface. *J. Am. Soc. Mass Spectrom.* 18, 1582–1590. doi:10.1016/j.jasms.2007.05.018
- Panuwet, P., Hunter, R. E., JR., D'Souza, P. E., Chen, X., Radford, S. A., Cohen, J. R., et al. (2016). Biological Matrix Effects in Quantitative Tandem Mass Spectrometry-Based Analytical Methods: Advancing Biomonitoring. *Crit. Rev. Anal. Chem.* 46, 93–105. doi:10.1080/10408347.2014.980775
- Pfister, O., Mouquet, F., Jain, M., Summer, R., Helmes, M., Fine, A., et al. (2005). CD31 – but Not CD31 + Cardiac Side Population Cells Exhibit Functional Cardiomyogenic Differentiation. *Circulation Res.* 97, 52–61. doi:10.1161/01.res.0000173297.53793.f
- Qiao, X., Wang, R., Yan, H., Wang, T., Zhao, Q., Zhang, L., et al. (2014). Development of a Novel Imidazolium-Based Aromatic Quaternary Ammonium Tag: Synthesis and Application to the Efficient Analysis of Cysteiny-Peptides by Mass Spectrometry. *Rapid Commun. Mass Spectrom.* 28, 256–264. doi:10.1002/rcm.6785
- Qiao, X., Yang, Y., Liu, S., Chen, S., Wang, X., Li, G., et al. (2015). Novel Pyridinium-Based Tags: Synthesis and Characterization for Highly Efficient Analysis of Thiol-Containing Peptides by Mass Spectrometry. *Analyst* 140, 407–413. doi:10.1039/c4an01802h
- Rasie Abdullahi, P., Eskandarian, S., Ghanbari, A., and Rashidy-Pour, A. (2018). Oxytocin Receptor Antagonist Atosiban Impairs Consolidation, but Not Reconsolidation of Contextual Fear Memory in Rats. *Brain Res.* 1695, 31–36. doi:10.1016/j.brainres.2018.05.034
- Robinson, K. J., Hazon, N., Lonergan, M., and Pomeroy, P. P. (2014). Validation of an Enzyme-Linked Immunoassay (ELISA) for Plasma Oxytocin in a Novel Mammal Species Reveals Potential Errors Induced by Sampling Procedure. *J. Neurosci. Methods* 226, 73–79. doi:10.1016/j.jneumeth.2014.01.019
- Salighedar, R., Erfanparast, A., Tamaddonfar, E., and Soltanilinejad, F. (2019). Medial Prefrontal Cortex Oxytocin-Opioid Receptors Interaction in Spatial Memory Processing in Rats. *Physiology Behav.* 209, 112599. doi:10.1016/j.physbeh.2019.112599
- Saxbe, D., Khaled, M., Horton, K. T., and Mendez, A. J. (2019). Maternal Prenatal Plasma Oxytocin Is Positively Associated with Prenatal Psychological Symptoms, but Method of Immunoassay Extraction May Affect Results. *Biol. Psychol.* 147, 107718. doi:10.1016/j.biopsycho.2019.107718
- Shrivastava, A., and Gupta, V. (2011). Methods for the Determination of Limit of Detection and Limit of Quantitation of the Analytical Methods. *Chron. Young Sci.* 2, 21–25. doi:10.4103/2229-5186.79345
- Sterner, J. L., Johnston, M. V., Nicol, G. R., and Ridge, D. P. (2000). Signal Suppression in Electrospray Ionization Fourier Transform Mass Spectrometry of Multi-Component Samples. *J. Mass Spectrom.* 35, 385–391. doi:10.1002/(sici)1096-9888(200003)35:3<385:aid-jms947>3.0.co;2-o
- Strauss, G. P., Keller, W. R., Koenig, J. I., Gold, J. M., Ossenfort, K. L., and Buchanan, R. W. (2015). Plasma Oxytocin Levels Predict Olfactory Identification and Negative Symptoms in Individuals with Schizophrenia. *Schizophrenia Res.* 162, 57–61. doi:10.1016/j.schres.2014.12.023
- Szeto, A., Cecati, M., Ahmed, R., McCabe, P. M., and Mendez, A. J. (2020). Oxytocin Reduces Adipose Tissue Inflammation in Obese Mice. *Lipids Health Dis.* 19, 188–211. doi:10.1186/s12944-020-01364-x

- Szeto, A., McCabe, P. M., Nation, D. A., Tabak, B. A., Rossetti, M. A., McCullough, M. E., et al. (2011). Evaluation of Enzyme Immunoassay and Radioimmunoassay Methods for the Measurement of Plasma Oxytocin. *Psychosom. Med.* 73, 393–400. doi:10.1097/psy.0b013e31821df0c2
- Tang, Y., Shi, Y., Gao, Y., Xu, X., Han, T., Li, J., et al. (2019). Oxytocin System Alleviates Intestinal Inflammation by Regulating Macrophages Polarization in Experimental Colitis. *Clin. Sci.* 133, 1977–1992. doi:10.1042/cs20190756
- Wahl, J. H., Goodlett, D. R., Udseth, H. R., and Smith, R. D. (1993). Use of Small-Diameter Capillaries for Increasing Peptide and Protein Detection Sensitivity in Capillary Electrophoresis-Mass Spectrometry. *Electrophoresis* 14, 448–457. doi:10.1002/elps.1150140170
- Waliczek, M., Kijewska, M., Rudowska, M., Setner, B., Stefanowicz, P., and Szewczuk, Z. (2016). Peptides Labeled with Pyridinium Salts for Sensitive Detection and Sequencing by Electrospray Tandem Mass Spectrometry. *Sci. Rep.* 6, 37720. doi:10.1038/srep37720
- Welch, M. G., Margolis, K. G., Li, Z., and Gershon, M. D. (2014). Oxytocin Regulates Gastrointestinal Motility, Inflammation, Macromolecular Permeability, and Mucosal Maintenance in Mice. *Am. J. Physiology-Gastrointestinal Liver Physiology* 307, G848–G862. doi:10.1152/ajpgi.00176.2014
- Welch, M. G., Tamir, H., Gross, K. J., Chen, J., Anwar, M., and Gershon, M. D. (2009). Expression and Developmental Regulation of Oxytocin (OT) and Oxytocin Receptors (OTR) in the Enteric Nervous System (ENS) and Intestinal Epithelium. *J. Comp. Neurol.* 512, 256–270. doi:10.1002/cne.21872
- Yuan, J., Zhang, R., Wu, R., Gu, Y., and Lu, Y. (2020). The Effects of Oxytocin to Rectify Metabolic Dysfunction in Obese Mice Are Associated with Increased Thermogenesis. *Mol. Cell. Endocrinol.* 514, 110903. doi:10.1016/j.mce.2020.110903
- Zhang, G., Zhang, Y., Fast, D. M., Lin, Z., and Steenwyk, R. (2011). Ultra Sensitive Quantitation of Endogenous Oxytocin in Rat and Human Plasma Using a Two-Dimensional Liquid Chromatography-Tandem Mass Spectrometry Assay. *Anal. Biochem.* 416, 45–52. doi:10.1016/j.ab.2011.04.041

Conflict of Interest: The authors declare that the research was conducted in the absence of any commercial or financial relationships that could be construed as a potential conflict of interest.

Publisher's Note: All claims expressed in this article are solely those of the authors and do not necessarily represent those of their affiliated organizations, or those of the publisher, the editors and the reviewers. Any product that may be evaluated in this article, or claim that may be made by its manufacturer, is not guaranteed or endorsed by the publisher.

Copyright © 2022 Hering, Jieu, Jones and Muttenthaler. This is an open-access article distributed under the terms of the Creative Commons Attribution License (CC BY). The use, distribution or reproduction in other forums is permitted, provided the original author(s) and the copyright owner(s) are credited and that the original publication in this journal is cited, in accordance with accepted academic practice. No use, distribution or reproduction is permitted which does not comply with these terms.



Role of Helical Structure in MBP Immunodominant Peptides for Efficient IgM Antibody Recognition in Multiple Sclerosis

Agnieszka Staśkiewicz^{1,2}, Michael Quagliata¹, Felician Real-Fernandez¹, Francesca Nuti¹, Roberta Lanzillo³, Vincenzo Brescia-Morra³, Hendrik Rusche^{4,5}, Michal Jewginski², Alfonso Carotenuto⁶, Diego Brancaccio⁶, Rina Aharoni⁷, Ruth Arnon⁷, Paolo Rovero⁸, Rafal Latajka² and Anna Maria Papini^{1,5*}

¹Interdepartmental Research Unit of Peptide and Protein Chemistry and Biology, Department of Chemistry "Ugo Schiff", University of Florence, Sesto Fiorentino, Italy, ²Department of Bioorganic Chemistry, Faculty of Chemistry, Wrocław University of Science and Technology, Wrocław, Poland, ³Multiple Sclerosis Clinical Care and Research Centre, Department of Neurosciences, Reproductive Sciences and Odontostomatology, University of Naples "Federico II", Naples, Italy, ⁴Fischer Analytics GmbH, Weiler, Germany, ⁵CY PeptLab Platform of Peptide and Protein Chemistry and Biology and UMR 8076 CNRS-BioCIS, CNRS, CY Cergy Paris Université, Neuville sur Oise, France, ⁶Department of Pharmacy, University of Naples "Federico II", Naples, Italy, ⁷Department of Immunology, The Weizmann Institute of Science, Rehovot, Israel, ⁸Interdepartmental Research Unit of Peptide and Protein Chemistry and Biology, Department of NeuroFarBa, University of Florence, Sesto Fiorentino, Italy

OPEN ACCESS

Edited by:

John D. Wade,
University of Melbourne, Australia

Reviewed by:

Mark Del Borgo,
Monash University, Australia
Michele Saviano,
Institute of Crystallography, National
Research Council (IC-CNR), Italy

*Correspondence:

Anna Maria Papini
annamaria.papini@unifi.it

Specialty section:

This article was submitted to
Chemical Biology,
a section of the journal
Frontiers in Chemistry

Received: 27 February 2022

Accepted: 26 May 2022

Published: 20 June 2022

Citation:

Staśkiewicz A, Quagliata M, Real-Fernandez F, Nuti F, Lanzillo R, Brescia-Morra V, Rusche H, Jewginski M, Carotenuto A, Brancaccio D, Aharoni R, Arnon R, Rovero P, Latajka R and Papini AM (2022) Role of Helical Structure in MBP Immunodominant Peptides for Efficient IgM Antibody Recognition in Multiple Sclerosis. *Front. Chem.* 10:885180. doi: 10.3389/fchem.2022.885180

The involvement of Myelin Basic Protein (MBP) in Multiple Sclerosis (MS) has been widely discussed in the literature. This intrinsically disordered protein has an interesting α -helix motif, which can be considered as a conformational epitope. In this work we investigate the importance of the helical structure in antibody recognition by MBP peptides of different lengths. Firstly, we synthesized the peptide MBP (81–106) (1) and observed that its elongation at both N- and C-termini, to obtain the peptide MBP (76–116) (2) improves IgM antibody recognition in SP-ELISA, but destabilizes the helical structure. Conversely, in competitive ELISA, MBP (81–106) (1) is recognized more efficiently by IgM antibodies than MBP (76–116) (2), possibly thanks to its more stable helical structure observed in CD and NMR conformational experiments. These results are discussed in terms of different performances of peptide antigens in the two ELISA formats tested.

Keywords: multiple sclerosis, circular dichroism, immune response, synthetic helical peptides, myelin basic protein antigen, peptide-antigen based ELISA, NMR

1 INTRODUCTION

Multiple Sclerosis (MS) is a demyelinating disease of the central nervous system (CNS). Genetic and environmental factors, such as bacterial or viral infections, are involved in its multifactorial etiology. Among the viral agent putatively associated with the disease, Epstein-Barr virus (EBV) has been repeatedly reported (Meier et al., 2021; Robinson and Steinman, 2022), and the *Haemophilus influenzae* has been described as possible bacterial triggering agent in MS (Walvoort et al., 2016). Although MS etiology and pathogenesis are not fully clarified, it is widely accepted that a T-cell-mediated inflammatory process directed against myelin and other related proteins plays a crucial role, jointly with a possible role of B cells (Steinman, 1996; Rahmanzadeh et al., 2018; Díaz et al., 2019). Recent discoveries suggest that B lymphocytes substantially contribute to its initiation and chronic propagation. The fulminant clinical success of anti-CD20 antibodies in the treatment of MS,

raised awareness that besides T-cells, B cells play a decisive role in MS. Synergic interaction of B and T-cell mechanisms were recently implicated as possible causes of MS (van Langelaar et al., 2020).

Due to its heterogeneity, no fully specific MS biomarkers are available, thus hampering both diagnosis and patient stratification. Considering that recent studies on B cells demonstrated the critical role of antibodies in MS pathology, identification of the antigenic targets recognized by specific antibodies in MS patient sera may help in the patient stratification process.

One of the most deeply studied myelin antigens related to MS is the myelin basic protein (MBP), a 170 amino-acid protein, which is the second most abundant component of the myelin sheath and plays an essential role in the myelination process (Moscarello, 1997; Lolli et al., 2006). Moreover, MBP is involved in the adhesion of the cytosolic surfaces of multilayered compact myelin, interacting with several polyanionic proteins, including actin, tubulin, Ca^{2+} -calmodulin, and clathrin, and with negatively charged lipids, thus changing its structure upon binding to them (Boggs, 2006).

Although MBP has not been demonstrated to be the main autoantigen in MS, MBP-specific autoreactive T-cells have been found in blood of MS patients at a higher rate than in healthy individuals (Tejada-Simon et al., 2003). Moreover, immunization of susceptible mouse strains with MBP induces a T-cell response that causes experimental autoimmune encephalomyelitis (EAE), considered a valuable mouse model of human MS (Zamvil and Steinman, 1990). These evidences suggest that MBP may be a candidate autoantigen in MS. In fact, it has been reported that autoantibodies from MS patient sera recognize MBP and recruit inflammatory cells to focal areas, thereby targeting CNS myelin components and affecting their stability (Rozenblum et al., 2014). In this context, investigations of anti-MBP antibodies in MS have been largely described, reporting controversial results ranging from 0 to 100% of seropositivity (Cruz et al., 1987; Link, 1997). In particular, relapsing-remitting MS patients have been described to be seropositive to anti-MBP (84–100) antibodies (Lolli et al., 2005). Anti-MBP antibodies have been detected not only in sera, but also in the cerebrospinal fluid (CSF) (Warren et al., 1995; Sellebjerg et al., 2000) in 85% relapsing-remitting MS patients and 45% MS patients, respectively, compared to 2% in non-MS controls. In any case, anti-MBP antibodies and their pathogenic role have been a matter of debate for many years, while the role of myelin-reactive autoantibodies appears more defined (Martinsen and Kursula, 2021).

This discussion may be triggered by several factors, sometimes involving unclear changes at the molecular level in the composition and structure of MBP isoforms, as well as in compact myelin, during the pathogenesis of MS (Beniac et al., 1999; Boggs et al., 1999). The hypothesis of an abnormal isoform composition of MBP, leading to weakened membrane interactions and loosening the rigid myelin structure, could lead to the observed anti-MBP immune-

reactivity, as well as to the presence of MBP in the CSF. Then, structural changes in the MBP sequences used in immunosorbent assays could explain, at least in part, not only the controversial results reported about anti-MBP antibody recognition in sera samples, but also their described low affinity. In fact, cells secreting high-affinity anti-myelin antibodies have been described in CSF from MS patients, particularly when compared to circulating anti-MBP antibodies, which showed low affinity (Sellebjerg et al., 1995; O'Connor et al., 2003). In any case, the association of anti-MBP antibodies with earlier and more frequent disease relapses (Berger et al., 2003) highlights their interesting role in MS.

With all these considerations in mind, we focused our research on a further investigation of the factors involved in antibody recognition of MBP peptide antigens by MS patients. Herein, we present a study on the role of the sequence and structure of synthetic MBP peptides that have been used to identify specific antibodies in Multiple Sclerosis patient sera.

2 MATERIALS AND METHODS

2.1 Reagents

All Fmoc-protected amino acids, *N,N'*-diisopropylcarbodiimide (DIC), OxymaPure® (ethyl-2-cyano-2-(hydroxyimino)acetate), and Fmoc-Lys(Boc)-Wang Tentagel® resin were purchased from Iris Biotech GmbH (Marktredwitz, Germany). Tentagel® S RAM was purchased from Rapp Polymere (Tuebingen, Germany). Peptide-synthesis grade *N,N'*-dimethylformamide (DMF) and acetonitrile (ACN) were purchased from Carlo Erba (Milan, Italy). Dichloromethane (DCM), trifluoroacetic acid (TFA), triisopropylsilane (TIS), and piperidine were purchased from Sigma-Aldrich (Milan, Italy). 2,2,2-trifluoroethanol (TFE) was purchased from Alfa Aesar (Kandel, Germany). Myelin Basic Protein (MBP) was purchased from Merck (Milan, Italy).

2.2 Microwave-Assisted Solid Phase Peptide Synthesis

Peptides 1–6 were synthesized in solid-phase using a microwave-assisted protocol (MW-SPPS) on a Liberty Blue™ automated peptide synthesizer (CEM Corporation, Matthews, NC, United States), following the Fmoc/tBu strategy as previously described (Rizzolo et al., 2011; Pandey et al., 2013; Nuti et al., 2020). Tentagel® S RAM resin (loading 0.23 mmol/g) was used for the synthesis of peptides 1, 5, and 6. Fmoc-Lys(Boc)-Wang Tentagel® resin (loading 0.23 mmol/g) was used for the synthesis of peptides 2, 3, and 4. Fmoc-deprotections were performed with a solution of 20% (v/v) piperidine in DMF (2 M). Peptide assembly was performed by repeating the standard MW-SPPS coupling cycle for each amino acid, using Fmoc-protected amino acids (2.5 equiv, 0.4 M in DMF), OxymaPure® (2.5 equiv, 1 M in DMF), and DIC (2.5 equiv, 3 M in DMF). Uncertain peptide coupling steps were checked by the ninhydrin test described by

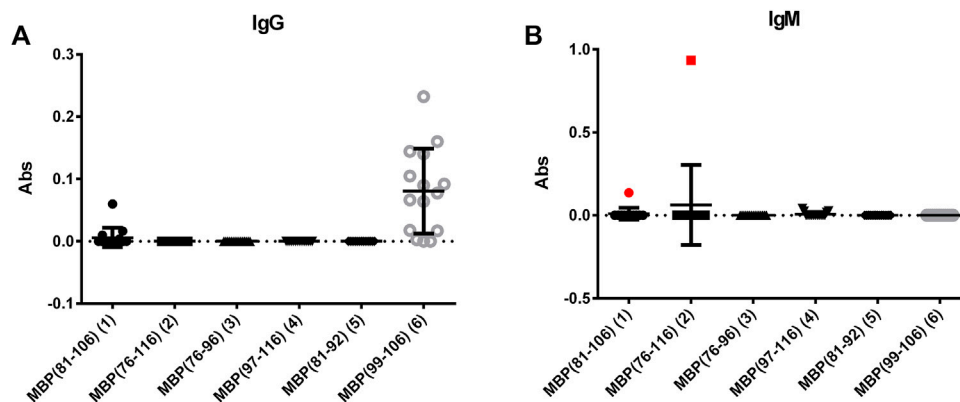


FIGURE 1 | Mean antibody titers to MBP peptide antigens for IgGs (A) and IgMs (B) of MS patient sera. IgM antibody responses of the MS serum to the coated peptides MBP (81–106) (1) and MBP (76–116) (2) are plotted in red.

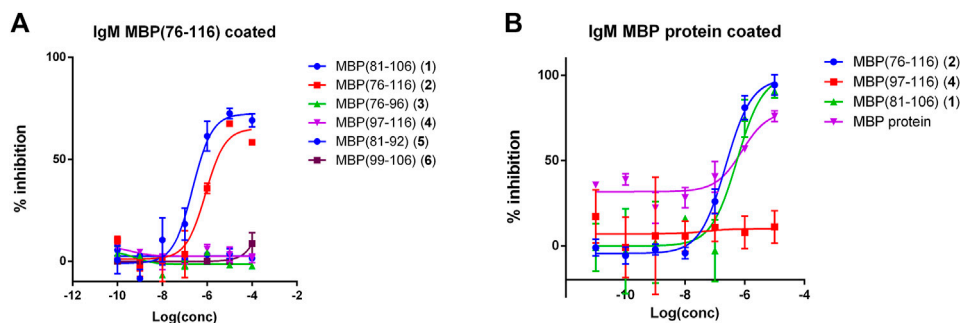


FIGURE 2 | Competitive ELISA obtained coating the peptide antigen MBP (76–116) (2) (A) or the MBP protein (B). Inhibition curve of IgMs using peptides and protein as inhibitors at different concentrations. Results show the inhibition activity % (ordinate axis) of the reference MS serum for IgMs vs. antigen concentrations on a logarithmic scale (abscissas axis). Antibody titer values were calculated as (mean Abs of serum triplicate) – (mean Abs of blank triplicate) representing graphically the calculated mean values \pm the standard deviation.

Kaiser (Kaiser et al., 1970), or micro-cleavages performed with a microwave apparatus CEM Discover™ single-mode MW reactor (CEM Corporation, Matthews, NC, United States). Resins with peptides 2–4 were N-terminal acetylated before cleavage, using twice Ac_2O in a DMF solution for 10 min at room temperature. Final cleavage and side-chain deprotections were performed using a mixture of TFA/TIS/ H_2O (95:2.5:2.5, v/v/v) at room temperature. After 2.5 h each resin was filtered off and the solution was concentrated flushing with N_2 . Each peptide was precipitated from cold Et_2O , centrifuged, and lyophilized.

The crude peptides were purified by Reverse-Phase Flash Liquid Chromatography (RP-HPLC) on an Isolera One Flash Chromatography (Biotage, Uppsala, Sweden) using a SNAP Ultra C18 column (25 g) at 20 ml/min. Eluent systems: 0.1% (v/v) TFA in H_2O (A), 0.1% (v/v) TFA in ACN (B) (elution gradient reported in **Supplementary Table S1**). The second step of purification of the peptides was performed by semipreparative RP-HPLC on a Waters instrument (Separation Module 2695, detector diode array 2996) using a Sepax Bio-C18 column (Sepax Technologies, Newark, United States) (5 μM , 250 mm \times 10 mm),

at 4 ml/min using the solvent systems A (0.1% TFA in H_2O) and B (0.1% TFA in ACN). Characterization of the peptides was performed by analytical HPLC using a Waters ACQUITY HPLC coupled to a single quadrupole ESI-MS (Waters® ZQ Detector, Waters Milford, MA, United States) supplied with a BEH C18 column (1.7 μm , 2.1 mm \times 50 mm) at 35°C, 0.6 ml/min with the solvent systems A (0.1% TFA in H_2O) and B (0.1% TFA in ACN). Gradient elution was performed with a flow of 0.6 ml/min and started at 10% B, with a linear increase to 90% B in 5 min. The analytical data are reported in the Supplementary Material (**Supplementary Table S1** and **Supplementary Figures S1–S6**).

2.3 Immunoassays

2.3.1 Sample Sera Collection

Fifteen Multiple Sclerosis (MS) patients were recruited in the Multiple Sclerosis Clinical Care and Research Centre, Department of Neurosciences, Reproductive Sciences and Odontostomatology, Federico II University (Naples, Italy). The relapsing-remitting MS (RR-MS) patients were previously diagnosed after a lumbar puncture, cerebrospinal fluid analysis, and MRI examination and fulfilled the

TABLE 1 | Synthesized MBP peptides.

Peptide	Fragment	Sequence
1	MBP (81–106)	-----TQDENPVWHFFKNIVTPRTPPPSQGK-----
2	MBP (76–116) ^a	SQHGRTQDENPVWHFFKNIVTPRTPPPSQGKGRGLSLSRFS
3	MBP (76–96) ^a	SQHGRTQDENPVWHFFKNIVT-----
4	MBP (97–116) ^a	-----PRTPPPSQGKGRGLSLSRFS
5	MBP (81–92)	-----TQDENPVWHFFK-----
6	MBP (99–106)	-----TPPPSQGK-----

^aN-terminal acetylated and C-terminal amide.

TABLE 2 | Calculated IC₅₀ values of anti-MBP (76–116) or anti-MBP protein IgM antibodies of MS serum to MBP (76–116) (2) and MBP (81–106) (1). Values are reported as 95% confidence interval for the calculated mean IC₅₀ ± the standard error (SEM).

Coated antigen	Inhibitor	IC ₅₀ (IgM)
MBP (76–116) (2)	MBP (81–106) (1)	(2.2 ± 0.18)·10 ⁻⁷
	MBP (76–116) (2)	(8.4 ± 0.24)·10 ⁻⁷
MBP protein	MBP (81–106) (1)	(5.5 ± 0.31)·10 ⁻⁷
	MBP (76–116) (2)	(2.3 ± 0.07)·10 ⁻⁷
	MBP protein	(7.9 ± 0.34)·10 ⁻⁷

established international diagnostic criteria (Polman et al., 2011; Thompson et al., 2018). The present study was conducted in accordance with the Declaration of Helsinki. The performed experimental protocols were approved by the Ethics Committee 2006 (protocol n. 120/06) and 2017 (protocol n. 160/17). Blood samplings were performed during the routine follow-up of patients, while the healthy control samplings were carried out during routine health checks or blood donations. Sera samples were obtained for diagnostic purposes from patients and healthy controls who had given their informed consent. Blood samples were centrifuged at 4,000 rpm for 10 min and sera supernatant was stored at -20°C until use.

2.3.2 Inhibition ELISA

Nunc-Immuno MicroWell 96 well polystyrene ELISA plates (NUNC Maxisorb, product code M9410, Merck, Milan, Italy) were coated with a solution 10 µg/ml of the peptide antigens in pure carbonate buffer 0.05 M (pH 9.6) adding 100 µL/well, and microplates were incubated at 4°C overnight. Wells were washed (5×) with washing buffer (0.9% NaCl, 0.05% Tween 20) using an automatic Hydroflex microplate washer (Tecan Italia, Milan, Italy). Nonspecific binding sites were blocked with 100 µL/well of fetal bovine serum (FBS) buffer solution (10% in washing buffer) at room temperature for 1 h. Antibody affinity was measured following the competitive ELISA previously reported (Real-Fernández et al., 2015). Semi-saturating sera dilution was previously calculated in preliminary titration curves (absorbance 0.7). Seven different concentrations of each synthetic antigenic peptide probe were used as inhibitors. Then, sera samples at the selected dilution were incubated in parallel with increasing

concentrations of antigens (range 1 × 10⁻¹⁰ to 1 × 10⁻⁴ M) for 1 h at room temperature. All competitive experiments were performed in triplicate. After washes (3×), uninhibited antibodies were identified by adding 100 µL/well of alkaline phosphatase-conjugated to anti-human immunoglobulin G or M (IgG and IgM, Merck, Milano, Italy) diluted 1:3,000 (IgG) and 1:200 (IgM) in FBS buffer. The microplates were then incubated 3 h at room temperature and, after washes (3×), 100 µL of substrate solution consisting of 1 mg/ml p-nitrophenyl phosphate pNPP (Merck, Milan, Italy) and MgCl₂ 0.01 M in carbonate buffer (pH 9.6) were added. After approximately 30 min, the reaction was stopped with 1 M NaOH solution (50 µL/well), and the absorbance was read in a multichannel ELISA reader (Tecan Sunrise, Männedorf, Switzerland) at 405 nm. Antibody titer values were calculated as (mean Abs of serum triplicate)—(mean Abs of blank triplicate) representing graphically the absorbance inhibition percentage. One positive and one negative serum, as references, were included in each plate for further normalization. Each experiment was performed at least twice in different days. Within-assays and between-assays coefficients of variations were below 10%. Calculated half maximal inhibitory concentrations (IC₅₀) are reported for each antigen.

2.3.3 Solid-Phase ELISA (SP-ELISA)

Immunoassays were performed to evaluate IgM or IgG antibodies in sera by SP-ELISA. At this purpose, the synthetic antigens were coated on 96-well plates (NUNC Maxisorb, product code M9410, Merck, Milan, Italy). Coating conditions were set-up independently for each peptide and results are reported in the **Supplementary Material**. Polystyrene 96-well ELISA plates were coated with 100 µL/well of a 10 µg/ml solution of synthetic peptide antigens 1-6 diluted in pure carbonate buffer 0.05 M (pH 9.6), independently. After overnight incubation at 4°C, plates were washed (3×) using washing buffer. Nonspecific binding sites were blocked with 100 µL/well of fetal bovine serum buffer (10% FBS in washing buffer) at room temperature for 1 h. FBS buffer was removed, and plates were incubated overnight at 4°C with sera (diluted 1:100 in FBS buffer, 100 µL/well). After three washes, plates were treated with 100 µL/well of anti-human IgG or IgM alkaline phosphatase-conjugated specific antibodies diluted in FBS buffer 1:3,000 (IgG) and 1:200 (IgM) for all tested

antigens. After 3 h of incubation at room temperature and washes (3×), 100 μ L of substrate buffer (1 mg/ml *p*NPP, MgCl_2 0.01 M in carbonate buffer, pH 9.6) was added to each well. Colorimetric reaction was carried out adding 100 μ L of substrate reaction solution (1 mg/ml *p*NPP, MgCl_2 0.01 M in carbonate buffer, pH 9.6) to each well and plates were read at 405 nm using a TECAN plate reader. After 30 min, the reaction was stopped with 1 M

NaOH solution (50 μ L/well) and the absorbance was read in a multichannel ELISA reader (Tecan Sunrise, Männedorf, Switzerland) at 405 nm. Antibody titer values were calculated as (mean Abs of serum triplicate) – (mean Abs of blank triplicate) representing graphically the calculated mean values. One positive and one negative serum, as references, were included in each plate for further normalization. Each experiment was performed at least twice in different days.

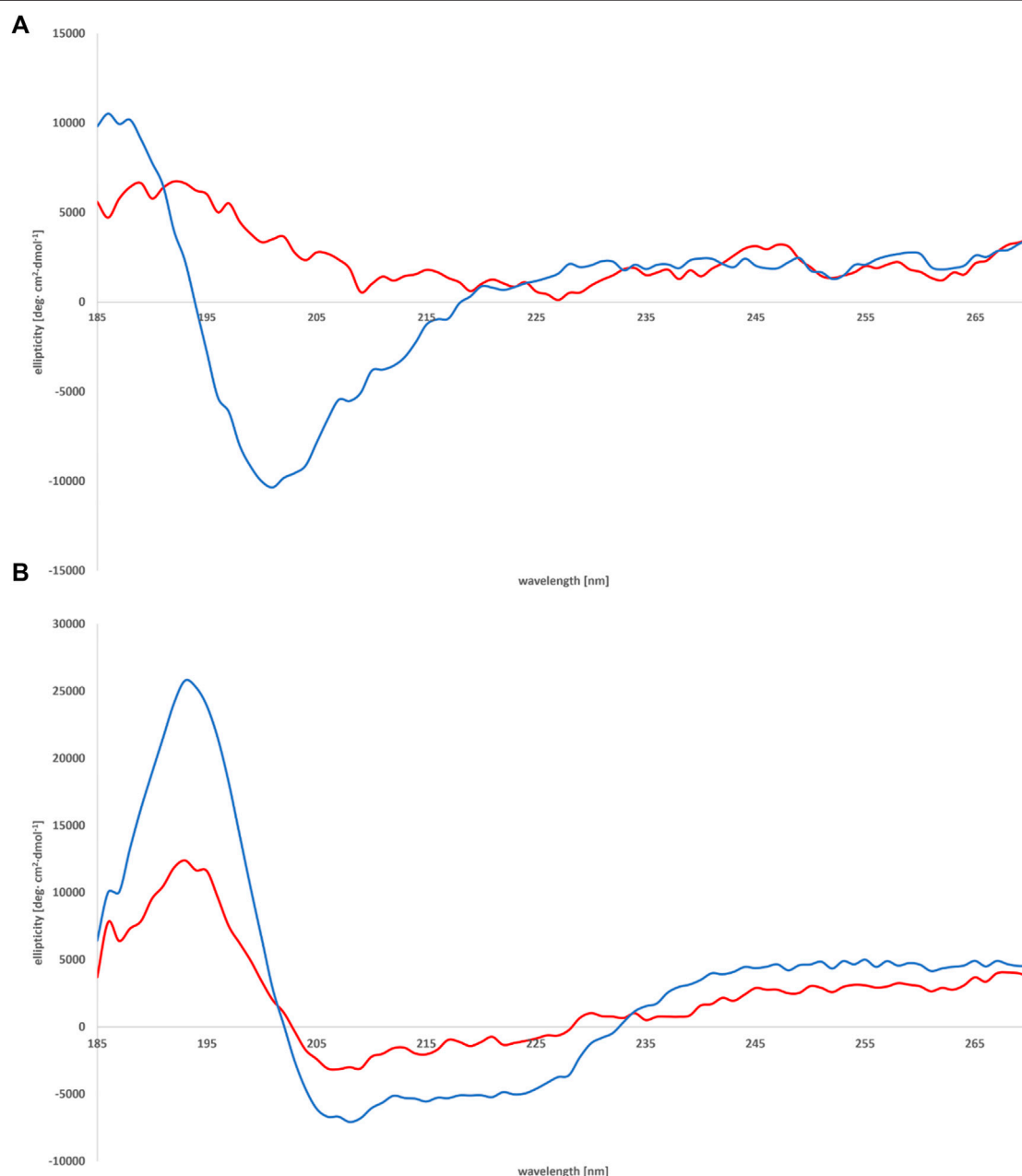
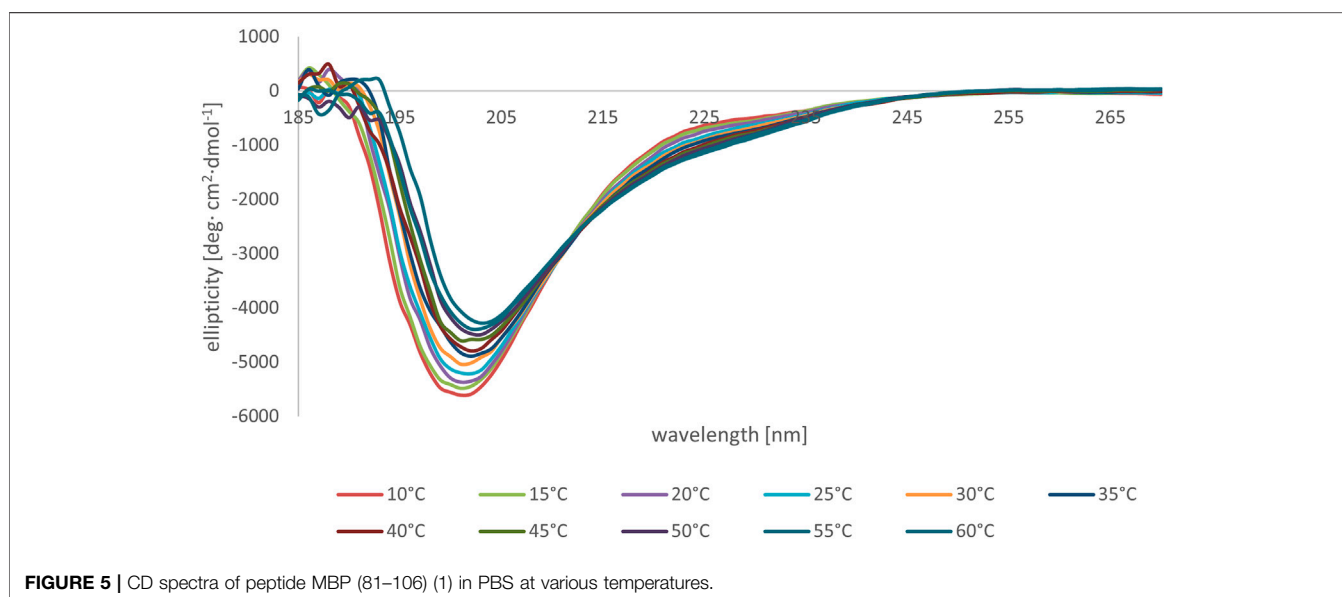
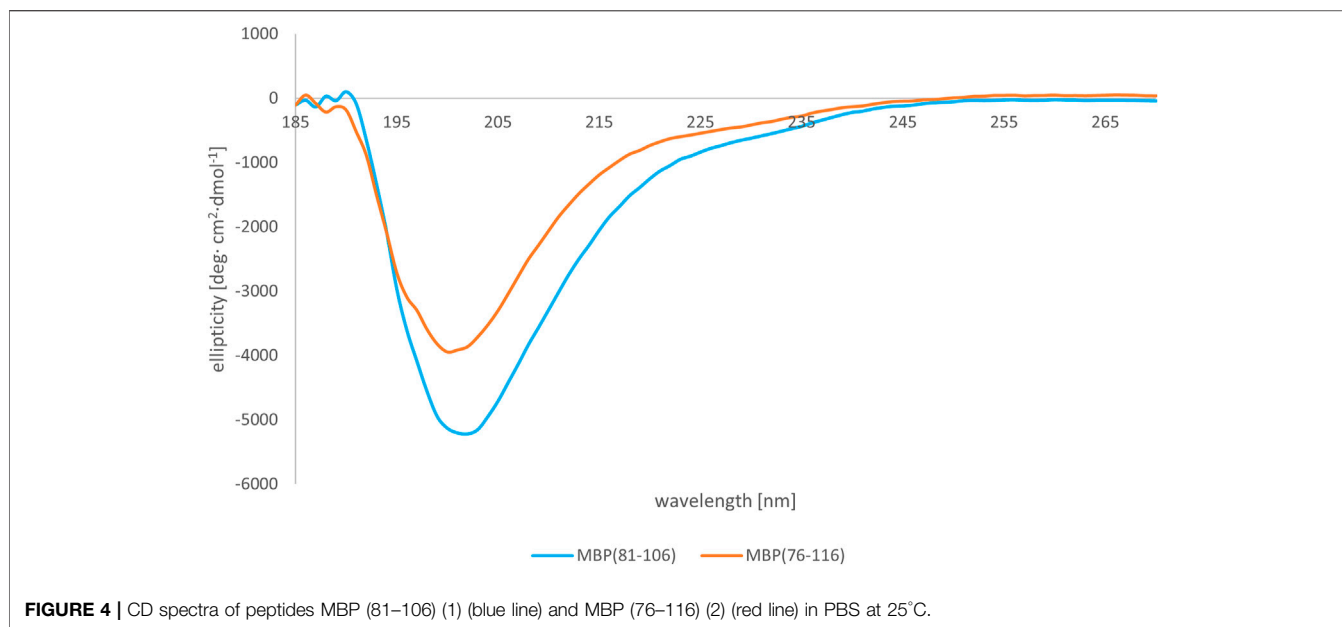


FIGURE 3 | CD spectra of peptides MBP (81–106) (1) (blue line) and MBP (76–116) (2) (red line) measured in water **(A)** and mixture of H_2O :TFE (50:50, v:v) **(B)** at 25°C.



Within-assays and between-assays coefficients of variations were below 10%.

2.4 Circular Dichroism

CD spectra were recorded on JASCO J-815 with increasing temperature from 10 to 60°C in increments of 5°C between $\lambda = 270$ and 185 nm. The CD measurements were carried out in H₂O, a mixture of H₂O:TFE (50:50, v:v) and PBS (phosphate buffered saline, pH 7.4, containing: sodium chloride, potassium chloride, sodium phosphate dibasic, potassium phosphate monobasic). The spectra were registered with the following parameters: 0.2 nm resolution, 1.0 nm bandwidth, 20 mdeg sensitivity, 0.25 s response, 100 nm min⁻¹ scanning speed, 5 scans, and 0.02 cm cuvette path

length. The CD spectra of solvents were recorded and subtracted from the raw data. The spectra were corrected by a baseline that was measured with the identical solvent in the same cell. The CD intensity is given as mean residue molar ellipticity (θ) [deg \times cm² \times dmol⁻¹].

2.5 NMR

The samples for NMR spectroscopy were prepared by dissolving the appropriate amount of peptide in 50 mM potassium phosphate buffer (pH 6.5), 10% D₂O, and 100 mM DPC-d₃₈. NMR spectra were recorded on a Varian INOVA 600 MHz spectrometer equipped with a z-gradient 5 mm triple-resonance probe head. Spectra were recorded at a temperature of 25°C. The spectra were calibrated relative

to TSP (0.00 ppm) as internal standard. One-dimensional (1D) NMR spectra were recorded in the Fourier mode with quadrature detection. The water signal was suppressed by gradient echo (Hwang and Shaka, 1995). 2D DQF-COSY (Piantini et al., 1982; Marion and Wüthrich, 1983), TOCSY (Braunschweiler and Ernst, 1983), and NOESY (Jenner et al., 1979) spectra were recorded in the phase-sensitive mode. Data block sizes were 2048 addresses in T2 and 512 equidistant T1 values. Before Fourier transformation, the time domain data matrices were multiplied by shifted sin2 functions in both dimensions. A mixing time of 70 ms was used for the TOCSY experiments. NOESY experiments were run with mixing time of 100 ms.

3 RESULTS AND DISCUSSION

3.1 Design of the Synthetic Myelin Basic Protein Peptides

Many publications indicate the presence of an immunodominant sequence in a specific region of MBP. One report described the sequence MBP (83–101) as a potential immunodominant T-cell epitope restricted to HLA-DR2b (DRB1*15:01) in MS (Ota et al., 1990), while others reported that MBP (89–101) peptide has two registers for binding to DR2a and DR2b (Kim et al., 2014). Other authors identified MBP (87–106) (Martin et al., 1990), MBP (83–101) (Hansen et al., 2007), and other overlapping sequences as T-cell epitopes inside the MBP protein. Importantly, these MBP regions match with B-cell epitopes previously described (Lolli et al., 2005; Warren et al., 2006; Mameli et al., 2014).

With the idea in mind to cover the whole immunodominant region of MBP, we synthesized and tested the peptide MBP (81–106) (1). Moreover, considering that the sensitivity of the peptide-based ELISA might be limited when short antigen sequences are used, we designed the elongated sequence MBP (76–116) (2), in order to achieve better antigen exposition in the solid-phase conditions of the ELISA (Nuti et al., 2020). With the aim of clarifying the amino-acid residues specifically involved in the B-cell epitope recognition, we divided the whole sequence of MBP (76–116) (2) into two fragments: MBP (76–96) (3) and MBP (97–116) (4). Amino- and carboxy-termini of peptides were acetylated and amidated, respectively, in order to remove free terminal charges, which are not present in the native protein sequence and may interfere with antibody recognition (Van Regenmortel, 2001). Finally, we also synthesized the shorter sequences MBP (81–92) (5) and MBP (99–106) (6), to be tested in competitive ELISA.

3.2 Biological Activity

3.2.1 Solid-phase ELISA

Fifteen sera from MS patients were screened using the synthetic peptides 1–6 as antigens in solid-phase ELISA. To this purpose, preliminary tests were performed to set-up the optimal conditions for the coating of the different peptide antigens onto the ELISA plates. Accordingly, we evaluated IgG and IgM antibody titres to each relevant peptide (Figure 1), observing a nonspecific IgG antibody reactivity against peptide MBP (99–106) (6). To a lesser extent, also against peptide MBP

(81–106) (1). A deeper analysis of these data indicated that peptide 6 is too short to be efficiently coated and/or exposed on the ELISA plate, favouring the nonspecific signals observed (Supplementary Figure S13). At variance, peptides 2–5 did not detect IgG-type antibodies. On the other hand, IgM antibodies were detected in one representative patient serum with peptide MBP (76–116) (2) and, to a lesser way, with peptide MBP (81–106) (1) [1 out of 15 patients (7%)] (Figure 1B). Interestingly, whereas the intensity of IgMs signal is clear for peptide MBP (76–116) (2), the peptide MBP (81–106) (1) slightly recognized IgGs and IgMs. This finding can be explained by the longer peptide MBP (76–116) (2), which may contain an extended epitope, or features an optimal exposition on the ELISA plate, not obtained by the shorter peptide MBP (81–106) (1), but important to capture pentameric IgM antibodies. This interesting result let us to hypothesize that the structures of peptide 1 may reproduce the correct antigen presentation, i.e., the one observed in the whole protein, thus enabling optimal antibody recognition of IgM antibodies. In fact, we already reported that, generally speaking, IgG antibodies can be more easily identified in ELISA using synthetic peptides as antigens, as compared to IgMs, possibly due to the pentameric spatial orientation of the latter. Previously, we overcome this problem using multivalent peptides to exploit IgMs higher avidity (Nuti et al., 2020; Mazzoleni et al., 2021). Interestingly, we herein observed that the monomeric, linear peptide MBP (76–116) (2) is able to detect a high, stable, and reproducible IgM antibody titer.

An additional explanation for the low reactivity generally observed for both IgGs and IgMs with most of the tested samples stems from the observation that a high percentage of patients are under immunosuppressive treatment, and they are not in the initial stage of the disease. In fact, it has been previously reported that anti-MBP IgM antibodies decrease in patients with a longer disease duration (Egg et al., 2001). Moreover, it should be noted that the recognized representative patient is not following any immunosuppressive treatment.

3.2.2 Inhibition ELISA

We focused our attention on the IgM antibody response to peptide MBP (76–116) (2), with the aim of verifying the specificity of the observed signals in a competitive solid-phase ELISA. To this purpose, MBP (76–116) (2) was coated on the plate and all the synthesized MBP sequences, including MBP (76–116) (2) itself, were individually tested at different concentrations as inhibitors of IgM antibody binding in the representative serum. The results showed in Figure 2A indicate that peptides MBP (81–106) (1) and MBP (76–116) (2) were able to inhibit IgM antibody binding to peptide 2 in the tested MS serum, showing an IC_{50} of $2.2 \cdot 10^{-7}$ and $8.4 \cdot 10^{-7}$, respectively (Table 2). These results confirm that IgM antibody response to peptide MBP (76–116) (2) is concentration-dependent and assess the specificity of the IgM recognition, previously observed in SP-ELISA. Moreover, we performed the inhibition experiments coating the MBP protein and using peptides MBP (81–106) (1), MBP (76–116) (2), MBP (97–116) (4), and the MBP protein as inhibitors (Figure 2B). Results showed the cross-reactivity between peptides MBP

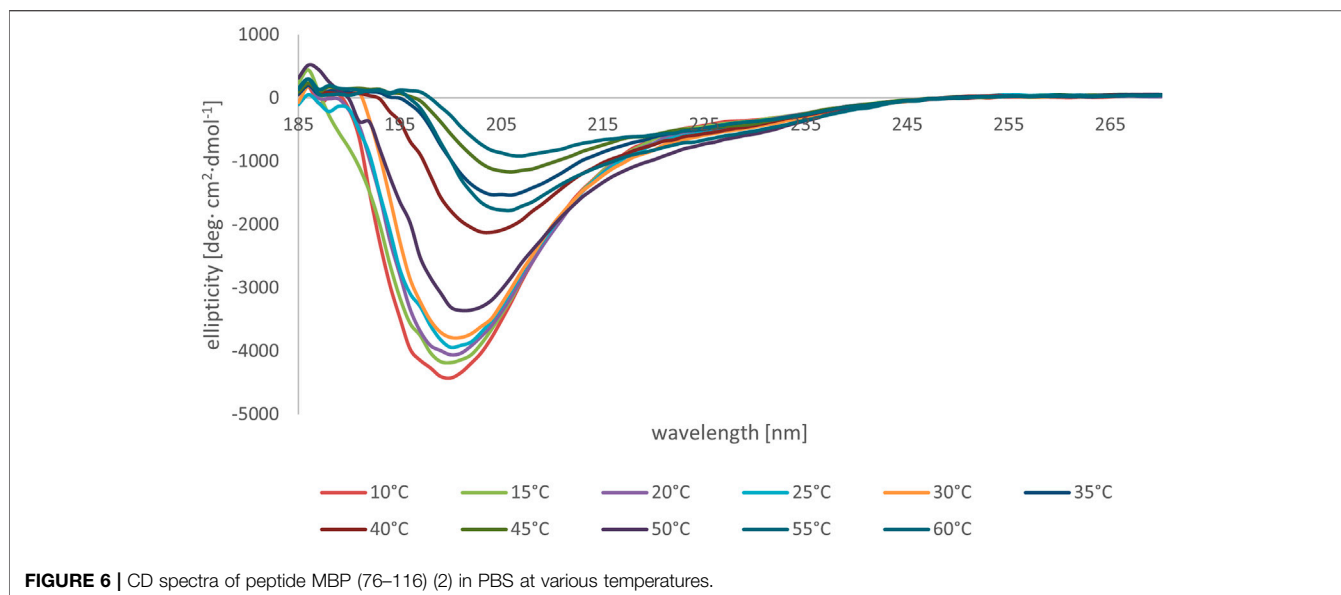


FIGURE 6 | CD spectra of peptide MBP (76–116) (2) in PBS at various temperatures.

(81–106) (1) and MBP (76–116) (2) and the whole MBP protein, and peptides were able to inhibit IgM antibody binding to MBP protein in the tested MS serum with comparable IC_{50} (Table 2). The greater affinity observed in the competitive experiment with peptide MBP (81–106) (1) indicates that, while the elongation of the sequence featured by peptide MBP (76–116) (2) is fundamental for antibody recognition in solid-phase ELISA, the shortened sequence MBP (81–106) (1) is recognized more efficiently by antibodies in the solution conditions of the competitive experiments. In light of these results, we decided to study the secondary structure of peptides MBP (81–106) (1) and MBP (76–116) (2) by circular dichroism.

3.3 Circular Dichroism

A preliminary screening of the conformational preferences of peptides MBP (81–106) (1) and MBP (76–116) (2) indicate that these peptides appear randomly structured in water solution (Figure 3A; Supplementary Figure S14). We subsequently studied the conformational behavior of these peptides in H₂O: TFE (50:50, v:v), a solvent mixture known to act as stabilizing agent (Campagna et al., 1998). Moreover, the use of fluoroalcohol provides additional stability by removing the water molecules from the surroundings of the peptides (Khandelwal et al., 1999). The spectra obtained in the solvent mixture displayed two negative bands at 222 and 208 nm ($n \rightarrow \pi^*$ and $\pi \rightarrow \pi^*$ transitions) and one positive band at 190 nm ($\pi \rightarrow \pi^*$ transition) (Figure 3B), characteristic for helical structures according to the literature (Bradley et al., 1990; Bates et al., 2004; Ahmed et al., 2012; Miles et al., 2022). Indeed, predictions based on amino acid composition of these peptides indicate that they show a tendency to form helical structures (Yang et al., 1997; Bates et al., 2004; Ahmed et al., 2012). Moreover, it may be assumed that there were no spectral differences of secondary peptide structure at various temperatures (Supplementary Figure S14, S15). Interestingly, the shorter peptide MBP (81–106) (1) displays higher tendency to

adopt an helical conformation, as compared to the longer analogue MBP (76–116) (2) (% helix 14 vs. 3) (Figure 3B) (Sommese et al., 2010). Apparently, the elongation at N- and C-termini of the peptide causes the disability in forming the helix. Furthermore, a different agent stabilizing the helix motif in the structure of MBP (81–106) (1) is the presence at the C- and N-termini of positively and negatively charged amino acids able to form salt bridges (Forood et al., 1993). At variance, the longer peptide MBP (76–116) (2) includes many positively charged residues, i.e., arginine residues that produce a destabilized effect on helix conformation by electrostatic repulsion (Sitkoff et al., 1994).

We subsequently studied the conformational preferences of peptides MBP(81–106) (1) and MBP (76–116) (2) in PBS, which is the most frequently used solvent to maintain physiological pH (White, 2002). These data indicate that the peptides present random coil structures (Figure 4). In fact, the obtained spectra displayed a single band with negative ellipticity at approximately 200 nm characteristic for unordered peptides. However, peptide MBP (81–106) (1) presents a more ordered structure, as can be inferred by the small but significant shift at higher wavelength of the minimum of MBP (81–106) (1) compared to MBP (76–116) (2) (Muruganandam et al., 2013; Lanthier et al., 2014). Moreover, we can assume there were no differences of secondary structure at various temperatures for MBP(81–106) (1) (Figure 5). In contrast, increasing the temperature of MBP (76–116) (2) led to a shift of the minimum to lower wavelength and a strong decrease of the signal intensity (Figure 6). This result can derive from a temperature-induced peptide self-aggregation, likely in beta structures (minimum at about 205 nm). The partial aggregation can account for the reduced ability of MBP (76–116) (2) to interact with the IgM antibody.

3.4 NMR

Conformational behavior of peptides MBP (81–106) (1) and MBP (76–116) (2) was studied in DPC micelle (100 mM) by solution

NMR spectroscopy. Almost complete ^1H NMR assignments were not obtained for peptide 1 while some residues of 2 could not be assigned due to strong signals overlapping (**Supplementary Tables S2, S3**). From chemical shift and NOE interaction patterns (**Supplementary Tables S2, S3; Supplementary Figure S16**), the two peptides have stable helical structure along residues 87–96, while the remaining regions did not show diagnostic parameters of any secondary structure. They are henceforth in random coil conformation. These results are in agreement with those reported in the literature (Ahmed et al., 2012) about a 36-residue peptide fragment of murine MBP corresponding to residues 76–111. Comparing the chemical shift values peptides MBP (81–106) (1) and MBP (76–116) (2), which are not significantly different, the helical structure turns out to have the same stability regardless of the sequence length. Superposition of chosen regions of the NOESY spectra of the two peptides (**Supplementary Figure S16**) gives a visual confirmation of this result.

4 CONCLUSION

In MS the myelin sheath is severely damaged by the autoimmune response, including autoreactive antibodies, therefore the characterization of antigens, particularly those expressed by proteins in the CNS, is highly relevant. In this study, we investigated the MBP protein, an important constituent of the myelin membrane. New insights in the anti-MBP antibodies and their pathogenicity can contribute to clarify their role, debated in the literature for many years. To this aim, we synthesized peptides covering the MBP (76–116) (2) fragment, including the immunodominant B-cell epitope MBP (84–104), and tested them both in solid-phase and competitive ELISA with MS patient sera. We focused our attention on IgM antibodies, observed in one representative serum using the peptides MBP (81–106) (1) and MBP (76–116) (2), while the other tested sequences showed in general low reactivity, for both IgGs and IgMs. The reactivity of peptides 1 and 2 is particularly relevant since frequency of serum anti-MBP IgMs is lower in patients with a long-term disease duration. Competitive ELISA experiments confirmed the specificity of the interaction and perhaps high antibody affinity to these peptide sequences.

NMR conformational analysis in DPC indicates that the two peptides MBP (81–106) (1) and MBP (76–116) (2) display a stable helical conformation along residues 87–96, while the remaining regions display unordered conformation. CD experiments in H_2O :TFE mixture showed that the shorter peptide MBP (81–106) (1) displays a slightly higher tendency to adopt an helical conformation, which may be considered the bioactive conformation of the epitope recognized by IgMs, since the competitive ELISA experiments show a 4-fold greater affinity of IgMs for this peptide, as compared to the longer analogue. However, the longer peptide MBP (76–116) (2) appears to be much more suitable to be efficiently coated on the plate, correctly exposing the helical epitope to capture IgMs in solid-phase. At variance, the correct epitope exposition is hampered by the flanking flexible N- and C-terminal regions, when the longer peptide is tested in solution.

In conclusion, the efficacy of the experimental approach based on the use of designed peptide sequences as synthetic antigenic probes

to characterize antibodies in patient sera is greatly enhanced by the optimization of the procedure to synthesize specifically modified and unique molecules (Nuti et al., 2010). Moreover, we demonstrated the possible positive role of chain elongation in solid-phase ELISA, enabling the detection of antibodies that cannot be identified by shorter sequences, even if they contain an epitope. These facts explain how minor changes in the MBP sequence and structure may contribute to the controversial results reported about its antibody reactivity. The selection of the methodology with the correct and well-exposed structures, is fundamental to improve antibody identification. Further studies based on a larger cohort of recently diagnosed and untreated MS patients could contribute to clarify the role of MBP in Multiple Sclerosis.

DATA AVAILABILITY STATEMENT

The raw data supporting the conclusions of this article will be made available by the authors, without undue reservation.

ETHICS STATEMENT

The studies involving human participants were reviewed and approved by the protocols n. 120/06 and n. 160/17. Comitato etico per le attività biomediche, Dipartimento di Medicina Pubblica e della Sicurezza Sociale, Facoltà di Medicina e Chirurgia, Università degli Studi di Napoli “Federico II,” Via S. Pansini 5, 80131 Napoli (Italy). The patients/participants provided their written informed consent to participate in this study.

AUTHOR CONTRIBUTIONS

AS, MQ, and FN synthesized the peptide antigens. AS, MJ, and RaL performed and interpreted the CD spectra. AC and DB performed and interpreted the NMR spectra. RuA and RiA participated to the conceptual discussions. MQ and FR-F performed the immunoassays and interpreted immunoassays data analyses. RL and VB-M recruited patients and analyzed the clinical data. AMP and PR developed the project, designed the experiments, interpreted the data. All authors contributed to write the manuscript.

FUNDING

This work was partly supported by the Rita Levi Montalcini Prize for scientific cooperation between Italy (University of Florence) and Israel (Weizmann Institute of Science, Hebrew University, and Bar Ilan University) to AMP (Israel Council for Higher Education grant 2018, attributed in 2019). Authors gratefully acknowledge the Italian Multiple Sclerosis Foundation (FISM) (grant n. 2017/R/5). AS is a participant of BioTechNan project—Interdisciplinary Environmental Doctoral Studies KNOW in the field of Biotechnology and Nanotechnology, co-financed by the European Union. The PhD of AS was performed in the context of a Cotutorate between the PhD Schools in

Chemical Sciences of the University of Florence (XXXV Ciclo) and of the Wrocław University of Science and Technology. The PhD scholarship of MQ is funded by the “Progetto Ministeriale Dipartimenti di Eccellenza 2018-2022” (58503_DIPECC-C.U.P. B96C17000200008).

REFERENCES

- Ahmed, M. A. M., De Avila, M., Polverini, E., Bessonov, K., Bamm, V. V., and Harauz, G. (2012). Solution Nuclear Magnetic Resonance Structure and Molecular Dynamics Simulations of a Murine 18.5 kDa Myelin Basic Protein Segment (S72-S107) in Association with Dodecylphosphocholine Micelles. *Biochemistry* 51, 7475–7487. doi:10.1021/bi300998x
- Bates, I. R., Feix, J. B., Boggs, J. M., and Harauz, G. (2004). An Immunodominant Epitope of Myelin Basic Protein Is an Amphipathic α -Helix. *J. Biol. Chem.* 279, 5757–5764. doi:10.1074/jbc.M311504200
- Beniac, D. R., Wood, D. D., Palaniyar, N., Ottensmeyer, F. P., Moscarello, M. A., and Harauz, G. (1999). Marburg's Variant of Multiple Sclerosis Correlates with a Less Compact Structure of Myelin Basic Protein. *Mol. Cell Biol. Res. Commun.* 1, 48–51. doi:10.1006/mcbr.1999.0111
- Berger, T., Rubner, P., Schautzer, F., Egg, R., Ulmer, H., Mayringer, I., et al. (2003). Antimyelin Antibodies as a Predictor of Clinically Definite Multiple Sclerosis after a First Demyelinating Event. *N. Engl. J. Med.* 349, 139–145. doi:10.1056/NEJMoa022328
- Boggs, J. M. (2006). Myelin Basic Protein: a Multifunctional Protein. *Cell. Mol. Life Sci.* 63, 1945–1961. doi:10.1007/s00018-006-6094-7
- Boggs, J. M., Rangaraj, G., Koshy, K. M., Ackerley, C., Wood, D. D., and Moscarello, M. A. (1999). Highly Deiminated Isoform of Myelin Basic Protein from Multiple Sclerosis Brain Causes Fragmentation of Lipid Vesicles. *J. Neurosci. Res.* 57, 529–535. doi:10.1002/(SICI)1097-4547(19990815)57:4<529::AID-JN12>3.0.CO;2-0
- Bradley, E. K., Thomason, J. F., Cohen, F. E., Kosen, P. A., and Kuntz, I. D. (1990). Studies of Synthetic Helical Peptides Using Circular Dichroism and Nuclear Magnetic Resonance. *J. Mol. Biol.* 215, 607–622. doi:10.1016/S0022-2836(05)80172-X
- Braunschweiler, L., and Ernst, R. R. (1983). Coherence Transfer by Isotropic Mixing: Application to Proton Correlation Spectroscopy. *J. Magnetic Reson.* (1969) 53, 521–528. doi:10.1016/0022-2364(83)90226-3
- Campagna, S., Vitoux, B., Humbert, G., Girardet, J. M., Linden, G., Haertle, T., et al. (1998). Conformational Studies of a Synthetic Peptide from the Putative Lipid-Binding Domain of Bovine Milk Component PP3. *J. Dairy Sci.* 81, 3139–3148. doi:10.3168/jds.S0022-0302(98)75879-5
- Cruz, M., Olsson, T., Ernerudh, J., Højeberg, B., and Link, H. (1987). Immunoblot Detection of Oligoclonal Anti-myelin Basic Protein IgG Antibodies in Cerebrospinal Fluid in Multiple Sclerosis. *Neurology* 37, 1515. doi:10.1212/wnl.37.9.1515
- Díaz, C., Zarco, L. A., and Rivera, D. M. (2019). Highly Active Multiple Sclerosis: An Update. *Multiple Scler. Relat. Disord.* 30, 215–224. doi:10.1016/j.msard.2019.01.039
- Egg, R., Reindl, M., Deisenhammer, F., Linington, C., and Berger, T. (2001). Anti-MOG and Anti-MBP Antibody Subclasses in Multiple Sclerosis. *Mult. Scler.* 7, 285–289. doi:10.1177/135245850100700503
- Forood, B., Feliciano, E. J., and Nambiar, K. P. (1993). Stabilization of Alpha-Helical Structures in Short Peptides by End Capping. *Proc. Natl. Acad. Sci. U.S.A.* 90, 838–842. doi:10.1073/pnas.90.3.838
- Hansen, B. E., Rasmussen, A. H., Jakobsen, B. K., Ryder, L. P., and Svejgaard, A. (2007). Extraordinary Cross-Reactivity of an Autoimmune T-Cell Receptor Recognizing Specific Peptides Both on Autologous and on Allogeneic HLA Class II Molecules. *Tissue Antigens* 70, 42–52. doi:10.1111/j.1399-0039.2007.00849.x
- Hwang, T. L., and Shaka, A. J. (1995). Water Suppression that Works. Excitation Sculpting Using Arbitrary Wave-Forms and Pulsed-Field Gradients. *J. Magnetic Reson. Ser. A* 112, 275–279. doi:10.1006/jmra.1995.1047
- Jeener, J., Meier, B. H., Bachmann, P., and Ernst, R. R. (1979). Investigation of Exchange Processes by Two-dimensional NMR Spectroscopy. *J. Chem. Phys.* 71, 4546–4553. doi:10.1063/1.438208

SUPPLEMENTARY MATERIAL

The Supplementary Material for this article can be found online at: <https://www.frontiersin.org/articles/10.3389/fchem.2022.885180/full#supplementary-material>

- Kaiser, E., Colescott, R. L., Bossinger, C. D., and Cook, P. I. (1970). Color Test for Detection of Free Terminal Amino Groups in the Solid-Phase Synthesis of Peptides. *Anal. Biochem.* 34 (2), 595–598. doi:10.1016/0003-2697(70)90146-6
- Khandelwal, P., Seth, S., and V. Hosur, R. (1999). CD and NMR Investigations on Trifluoroethanol-Induced Step-wise Folding of Helical Segment from Scorpion Neurotoxin. *Eur. J. Biochem.* 264, 468–478. doi:10.1046/j.1432-1327.1999.00641.x
- Kim, A., Hartman, I. Z., Poore, B., Boronina, T., Cole, R. N., Song, N., et al. (2014). Divergent Paths for the Selection of Immunodominant Epitopes from Distinct Antigenic Sources. *Nat. Commun.* 5, 5369. doi:10.1038/ncomms6369
- Lanthier, D. K., Vassall, K. A., and Harauz, G. (2014). Biophysical Characterization of 21.5-kDa Myelin Basic Protein (MBP) and the Effects of Zinc on its Structure. *Surgery* 7, 30–41. doi:10.21083/surg.v7i3.2958
- Link, H. (1997). “B Cells and Autoimmunity,” in *Molecular Biology of Multiple Sclerosis*. Editor WC. Russell (Chichester, UK: John Wiley & Sons), 161–191.
- Lolli, F., Mulinacci, B., Carotenuto, A., Bonetti, B., Sabatino, G., Mazzanti, B., et al. (2005). An N-Glucosylated Peptide Detecting Disease-specific Autoantibodies, Biomarkers of Multiple Sclerosis. *Proc. Natl. Acad. Sci. U.S.A.* 102, 10273–10278. doi:10.1073/pnas.0503178102
- Lolli, F., Rovero, P., Chelli, M., and Papini, A. M. (2006). Toward Biomarkers in Multiple Sclerosis: New Advances. *Expert Rev. Neurother.* 6, 781–794. doi:10.1586/14737175.6.5.781
- Mameli, G., Cossu, D., Cocco, E., Masala, S., Frau, J., Marrosu, M. G., et al. (2014). Epstein-Barr Virus and *Mycobacterium avium* Subsp. Paratuberculosis Peptides Are Cross Recognized by Anti-myelin Basic Protein Antibodies in Multiple Sclerosis Patients. *J. Neuroimmunol.* 270, 51–55. doi:10.1016/j.jneuroim.2014.02.013
- Marion, D., and Wüthrich, K. (1983). Application of Phase Sensitive Two-Dimensional Correlated Spectroscopy (COSY) for Measurements of ^1H - ^1H Spin-Spin Coupling Constants in Proteins. *Biochem. Biophysical Res. Commun.* 113, 967–974. doi:10.1016/0006-291X(83)91093-8
- Martin, R., Jaraquemada, D., Flerlage, M., Richert, J., Whitaker, J., Long, E. O., et al. (1990). Fine Specificity and HLA Restriction of Myelin Basic Protein-specific Cytotoxic T Cell Lines from Multiple Sclerosis Patients and Healthy Individuals. *J. Immunol.* 145, 540–548.
- Martinsen, V., and Kursula, P. (2021). Multiple Sclerosis and Myelin Basic Protein: Insights into Protein Disorder and Disease. *Amino Acids* 54, 99–109. doi:10.1007/s00726-021-03111-7
- Mazzoleni, A., Real-Fernandez, F., Nuti, F., Lanzillo, R., Brescia Morra, V., Dambruoso, P., et al. (2021). Selective Capture of Anti-N -glucosylated NTHi Adhesin Peptide Antibodies by a Multivalent Dextran Conjugate. *Chembiochem* 23. doi:10.1002/cbic.202100515
- Meier, U.-C., Cipian, R. C., Karimi, A., Ramasamy, R., and Middeldorp, J. M. (2021). Cumulative Roles for Epstein-Barr Virus, Human Endogenous Retroviruses, and Human Herpes Virus-6 in Driving an Inflammatory Cascade Underlying MS Pathogenesis. *Front. Immunol.* 12, 757302. doi:10.3389/fimmu.2021.757302
- Miles, A. J., Ramalli, S. G., and Wallace, B. A. (2022). DichroWeb, a Website for Calculating Protein Secondary Structure from Circular Dichroism Spectroscopic Data. *Protein Sci.* 31, 37–46. doi:10.1002/pro.4153
- Moscarello, M. A. (1997). “Myelin Basic Protein, the “Executive” Molecule of the Myelin Membrane,” in *Cell Biology and Pathology of Myelin: Evolving Biological Concepts and Therapeutic Approaches* (Juurlink B.H.J. Editors R.M. Devon, J.R. Doucette, A.J. Nazarali, D.J. Schreyer, and V.M.K. Verge (New York: Plenum), 13–25. doi:10.1007/978-1-4615-5949-8_2
- Muruganandam, G., Bürck, J., Ulrich, A. S., Kursula, I., and Kursula, P. (2013). Lipid Membrane Association of Myelin Proteins and Peptide Segments Studied

- by Oriented and Synchrotron Radiation Circular Dichroism Spectroscopy. *J. Phys. Chem. B* 117, 14983–14993. doi:10.1021/jp4098588
- Nuti, F., Fernandez, F. R., Sabatino, G., Peroni, E., Mulinacci, B., Paolini, I., et al. (2020). A Multiple N-Glucosylated Peptide Epitope Efficiently Detecting Antibodies in Multiple Sclerosis. *Brain Sci.* 10, 453. doi:10.3390/brainsci10070453
- Nuti, F., Peroni, E., Real-Fernández, F., Bonache, M. A., Le Chevalier-Isaad, A., Chelli, M., et al. (2010). Posttranslationally Modified Peptides Efficiently Mimicking Neoantigens: A Challenge for Theragnostics of Autoimmune Diseases. *Biopolymers* 94, 791–799. doi:10.1002/bip.21456
- O'Connor, K. C., Chitnis, T., Griffin, D. E., Piyasirisilp, S., Bar-Or, A., Khoury, S., et al. (2003). Myelin Basic Protein-Reactive Autoantibodies in the Serum and Cerebrospinal Fluid of Multiple Sclerosis Patients Are Characterized by Low-Affinity Interactions. *J. Neuroimmunol.* 136, 140–148. doi:10.1016/s0165-5728(03)00002-x
- Ota, K., Matsui, M., Milford, E. L., Mackin, G. A., Weiner, H. L., and Hafler, D. A. (1990). T-cell Recognition of an Immuno-Dominant Myelin Basic Protein Epitope in Multiple Sclerosis. *Nature* 346, 183–187. doi:10.1038/346183a0
- Pandey, S., Alcaro, M. C., Scrima, M., Peroni, E., Paolini, I., Di Marino, S., et al. (2012). Designed Glucopeptides Mimetics of Myelin Protein Epitopes as Synthetic Probes for the Detection of Autoantibodies, Biomarkers of Multiple Sclerosis. *J. Med. Chem.* 55 (23), 10437–10447. doi:10.1021/jm301031r
- Piantini, U., Sorensen, O. W., and Ernst, R. R. (1982). Multiple Quantum Filters for Elucidating NMR Coupling Networks. *J. Am. Chem. Soc.* 104, 6800–6801. doi:10.1021/ja00388a062
- Polman, C. H., Reingold, S. C., Banwell, B., Clanet, M., Cohen, J. A., Filippi, M., et al. (2011). Diagnostic Criteria for Multiple Sclerosis: 2010 Revisions to the McDonald Criteria. *Ann. Neurol.* 69, 292–302. doi:10.1002/ana.22366
- Rahmanzadeh, R., Brück, W., Minagar, A., and Sahraian, M. A. (2018). Multiple Sclerosis Pathogenesis: Missing Pieces of an Old Puzzle. *Rev. Neurosci.* 30, 67–83. doi:10.1515/revneuro-2018-0002
- Real Fernández, F., Di Pisa, M., Rossi, G., Auberger, N., Lequin, O., Larregola, M., et al. (2015). Antibody Recognition in Multiple Sclerosis and Rett Syndrome Using a Collection of Linear and cyclicN-Glucosylated Antigenic Probes. *Biopolymers* 104, 560–576. doi:10.1002/bip.22677
- Rizzolo, F., Testa, C., Lambardi, D., Chorev, M., Chelli, M., Rovero, P., et al. (2011). Conventional and Microwave-Assisted SPPS Approach: a Comparative Synthesis of PTHrP(1-34)NH₂. *J. Pept. Sci.* 17, 708–714. doi:10.1002/psc.1395
- Robinson, W. H., and Steinman, L. (2022). Epstein-Barr Virus and Multiple Sclerosis. *Science* 375, 264–265. doi:10.1126/science.abm7930
- Rozenblum, G. T., Kaufman, T., and Vitullo, A. D. (2014). Myelin Basic Protein and a Multiple Sclerosis-Related MBP-Peptide Bind to Oligonucleotides. *Mol. Ther. - Nucleic Acids* 3, e192. doi:10.1038/mtna.2014.43
- Sellebjerg, F., Jensen, C. V., and Christiansen, M. (2000). Intrathecal IgG Synthesis and Autoantibody-Secreting Cells in Multiple Sclerosis. *J. Neuroimmunol.* 108, 207–215. doi:10.1016/s0165-5728(00)00292-7
- Sellebjerg, F., Madsen, H. O., Frederiksen, J. L., Ryder, L. P., and Svejgaard, A. (1995). Acute Optic Neuritis: Myelin Basic Protein and Proteolipid Protein Antibodies, Affinity, and the HLA System. *Ann. Neurol.* 38, 943–950. doi:10.1002/ana.410380616
- Sitkoff, D., Lockhart, D. J., Sharp, K. A., and Honig, B. (1994). Calculation of Electrostatic Effects at the Amino Terminus of an Alpha Helix. *Biophysical J.* 67, 2251–2260. doi:10.1016/S0006-3495(94)80709-X
- Sommese, R. F., Sivaramakrishnan, S., Baldwin, R. L., and Spudich, J. A. (2010). Helicity of Short E-R/K Peptides. *Protein Sci.* 19, 2001–2005. doi:10.1002/pro.469
- Steinman, M. D., L. (1996). Multiple Sclerosis: a Coordinated Immunological Attack against Myelin in the Central Nervous System. *Cell* 85, 299–302. doi:10.1016/s0092-8674(00)81107-1
- Tejada-Simon, M. V., Zang, Y. C. Q., Hong, J., Rivera, V. M., and Zhang, J. Z. (2003). Cross-reactivity with Myelin Basic Protein and Human Herpesvirus-6 in Multiple Sclerosis. *Ann. Neurol.* 53, 189–197. doi:10.1002/ana.10425
- Thompson, A. J., Banwell, B. L., Barkhof, F., Carroll, W. M., Coetzee, T., Comi, G., et al. (2018). Diagnosis of Multiple Sclerosis: 2017 Revisions of the McDonald Criteria. *Lancet Neurology* 17, 162–173. doi:10.1016/S1474-4422(17)30470-2
- van Langelaar, J., Rijvers, L., Smolders, J., and van Luijn, M. M. (2020). B and T Cells Driving Multiple Sclerosis: Identity, Mechanisms and Potential Triggers. *Front. Immunol.* 11, 760. doi:10.3389/fimmu.2020.00760
- Van Regenmortel, M. H. V. (2001). Antigenicity and Immunogenicity of Synthetic Peptides. *Biologicals* 29 (3–4), 209–213. doi:10.1006/biol.2001.0308
- Walvoort, M. T. C., Testa, C., Eilam, R., Aharoni, R., Nuti, F., Rossi, G., et al. (2016). Antibodies from Multiple Sclerosis Patients Preferentially Recognize Hyperglucosylated Adhesin of Non-typeable Haemophilus Influenzae. *Sci. Rep.* 6, 39430. doi:10.1038/srep39430
- Warren, K. G., Catz, I., Ferenczi, L. Z., and Krantz, M. J. (2006). Intravenous Synthetic Peptide MBP8298 Delayed Disease Progression in an HLA Class II-Defined Cohort of Patients with Progressive Multiple Sclerosis: Results of a 24-month Double-Blind Placebo-Controlled Clinical Trial and 5 Years of Follow-Up Treatment. *Eur. J. Neurol.* 13, 887–895. doi:10.1111/j.1468-1331.2006.01533.x
- Warren, K. G., Catz, I., and Steinman, L. (1995). Fine Specificity of the Antibody Response to Myelin Basic Protein in the Central Nervous System in Multiple Sclerosis: the Minimal B-Cell Epitope and a Model of its Features. *Proc. Natl. Acad. Sci. U.S.A.* 92, 11061–11065. doi:10.1073/pnas.92.24.11061
- White, D. C. (2002). *Proteins, Peptides, and Amino Acids SourceBook*. New York, NY: Springer.
- Yang, J., Spek, E. J., Gong, Y., Zhou, H., and Kallenbach, N. R. (1997). The Role of Context on α -helix Stabilization: Host-Guest Analysis in a Mixed Background Peptide Model. *Protein Sci.* 6, 1264–1272. doi:10.1002/pro.5560060614
- Zamvil, S. S., and Steinman, L. (1990). The T Lymphocyte in Experimental Allergic Encephalomyelitis. *Annu. Rev. Immunol.* 8, 579–621. doi:10.1146/annurev.iy.08.040190.003051

Conflict of Interest: Author HR is employed by Fischer Analytics GmbH.

The remaining authors declare that the research was conducted in the absence of any commercial or financial relationships that could be construed as a potential conflict of interest.

Publisher's Note: All claims expressed in this article are solely those of the authors and do not necessarily represent those of their affiliated organizations, or those of the publisher, the editors and the reviewers. Any product that may be evaluated in this article, or claim that may be made by its manufacturer, is not guaranteed or endorsed by the publisher.

Copyright © 2022 Staškiewicz, Quagliata, Real-Fernandez, Nuti, Lanzillo, Brescia-Morra, Rusche, Jewginski, Carotenuto, Brancaccio, Aharoni, Arnon, Rovero, Latajka and Papini. This is an open-access article distributed under the terms of the Creative Commons Attribution License (CC BY). The use, distribution or reproduction in other forums is permitted, provided the original author(s) and the copyright owner(s) are credited and that the original publication in this journal is cited, in accordance with accepted academic practice. No use, distribution or reproduction is permitted which does not comply with these terms.

Advantages of publishing in Frontiers



OPEN ACCESS

Articles are free to read
for greatest visibility
and readership



FAST PUBLICATION

Around 90 days
from submission
to decision



HIGH QUALITY PEER-REVIEW

Rigorous, collaborative,
and constructive
peer-review



TRANSPARENT PEER-REVIEW

Editors and reviewers
acknowledged by name
on published articles

Frontiers

Avenue du Tribunal-Fédéral 34
1005 Lausanne | Switzerland

Visit us: www.frontiersin.org

Contact us: frontiersin.org/about/contact



REPRODUCIBILITY OF RESEARCH

Support open data
and methods to enhance
research reproducibility



DIGITAL PUBLISHING

Articles designed
for optimal readership
across devices



FOLLOW US

@frontiersin



IMPACT METRICS

Advanced article metrics
track visibility across
digital media



EXTENSIVE PROMOTION

Marketing
and promotion
of impactful research



LOOP RESEARCH NETWORK

Our network
increases your
article's readership